frontiers | Research Topics

Macroecology of coastal zone under global changes

Edited by
Meilin Wu, Hui Zhao, Luzhen Chen, Vetrimurugan Elumalai, Qiuying Han and Lin Hui

Published in
Frontiers in Marine Science

ISSN 1664-8714
ISBN 978-2-8325-2849-5
DOI 10.3389/978-2-8325-2849-5

About Frontiers

Frontiers is more than just an open access publisher of scholarly articles: it is a pioneering approach to the world of academia, radically improving the way scholarly research is managed. The grand vision of Frontiers is a world where all people have an equal opportunity to seek, share and generate knowledge. Frontiers provides immediate and permanent online open access to all its publications, but this alone is not enough to realize our grand goals.

Frontiers journal series

The Frontiers journal series is a multi-tier and interdisciplinary set of open-access, online journals, promising a paradigm shift from the current review, selection and dissemination processes in academic publishing. All Frontiers journals are driven by researchers for researchers; therefore, they constitute a service to the scholarly community. At the same time, the *Frontiers journal series* operates on a revolutionary invention, the tiered publishing system, initially addressing specific communities of scholars, and gradually climbing up to broader public understanding, thus serving the interests of the lay society, too.

Dedication to quality

Each Frontiers article is a landmark of the highest quality, thanks to genuinely collaborative interactions between authors and review editors, who include some of the world's best academicians. Research must be certified by peers before entering a stream of knowledge that may eventually reach the public - and shape society; therefore, Frontiers only applies the most rigorous and unbiased reviews. Frontiers revolutionizes research publishing by freely delivering the most outstanding research, evaluated with no bias from both the academic and social point of view. By applying the most advanced information technologies, Frontiers is catapulting scholarly publishing into a new generation.

What are Frontiers Research Topics?

Frontiers Research Topics are very popular trademarks of the *Frontiers journals series*: they are collections of at least ten articles, all centered on a particular subject. With their unique mix of varied contributions from Original Research to Review Articles, Frontiers Research Topics unify the most influential researchers, the latest key findings and historical advances in a hot research area.

Find out more on how to host your own Frontiers Research Topic or contribute to one as an author by contacting the Frontiers editorial office: frontiersin.org/about/contact

Macroecology of coastal zone under global changes

Topic editors

Meilin Wu — South China Sea Institute of Oceanology, Chinese Academy of Sciences (CAS), China

Hui Zhao — Guangdong Ocean University, China

Luzhen Chen — Xiamen University, China

Vetrimurugan Elumalai — University of Zululand, South Africa

Qiuying Han — Hainan Tropical Ocean University, China

Lin Hui — Third institute of Oceanography, Ministry of Natural Resources, China

Topic Coordinator

Keerthi Sri Senarathna Atapaththu — University of Ruhuna, Sri Lanka

Citation

Wu, M., Zhao, H., Chen, L., Elumalai, V., Han, Q., Hui, L., eds. (2023). *Macroecology of coastal zone under global changes*. Lausanne: Frontiers Media SA.

doi: 10.3389/978-2-8325-2849-5

Table of contents

frontiers | Frontiers in Marine Science

TYPE Editorial
PUBLISHED 14 June 2023
DOI 10.3389/fmars.2023.1208448

OPEN ACCESS

EDITED AND REVIEWED BY
Charitha Bandula Pattiaratchi,
University of Western Australia, Australia

*CORRESPONDENCE
Meilin Wu
mlwu@scsio.ac.cn
Hui Zhao
zhaohui@gdou.edu.cn

RECEIVED 19 April 2023
ACCEPTED 19 May 2023
PUBLISHED 14 June 2023

CITATION
Wu M, Zhao H, Han Q, Hui L, Elumalai V, Chen L and Atapaththu KSS (2023) Editorial: Macroecology of coastal zones under global changes.
Front. Mar. Sci. 10:1208448.
doi: 10.3389/fmars.2023.1208448

Editorial: Macroecology of coastal zones under global changes

Meilin Wu[1,2,3,4]*, Hui Zhao[1]*, Qiuying Han[5], Lin Hui[6], Vetrimurugan Elumalai[7], Luzhen Chen[8] and Keerthi Sri Senarathna Atapaththu[9]

[1]College of Chemistry and Environmental Science, Guangdong Ocean University, Zhanjiang, China, [2]State Key Laboratory of Tropical Oceanography, South China Sea Institute of Oceanology, Chinese Academy of Sciences (CAS), Guangzhou, China, [3]Southern Marine Science and Engineering Guangdong Laboratory (Guangzhou), Guangzhou, China, [4]Innovation Academy of South China Sea Ecology and Environmental Engineering, Chinese Academy of Sciences, Guangzhou, China, [5]Yazhou Bay Innovation Institute, Hainan Tropical Ocean University, Sanya, China, [6]Laboratory of Marine Ecological Environment Early Warning and Monitoring, Third institute of Oceanography, Ministry of Natural Resources, Xiamen, China, [7]Department of Hydrology, University of Zululand, KwaDlangezwa, South Africa, [8]College of the Environment and Ecology, Xiamen University, Xiamen, China, [9]Department of Limnology and Water Technology, Faculty of Fisheries and Marine Sciences & Technology, University of Ruhuna, Matara, Sri Lanka

KEYWORDS

human activity, natural change, mangrove, seagrass, nutrient biogeochemistry

Editorial on the Research Topic
Macroecology of coastal zone under global changes

Introduction

Coastal areas are important for maintaining the ecological integrity of both marine and terrestrial ecosystems but they are sensitive to both human activities and nature changes (Dong et al., 2010; Wu et al., 2010; Wu et al., 2015; Wu et al., 2017). These areas are subject to dramatic stress due to rapid population growth, as well as intensive industrial aggregation and expansion. Environmental problems have arisen in coastal environments from degraded water quality, resulting in highly undesirable conditions that affect coastal ecosystem structures and functions. In this context, it is important to develop sustainable socio-economics for coastal environmental issues and draft relevant management policies (Ling et al., 2014; Wu et al., 2015; Wu et al., 2020). Therefore, short-term and/or long-term environmental and ecological monitoring networks have been established in some coastal areas to evaluate environmental problems such as eutrophication, heavy metal pollution, harmful algal blooms (HABs), microplastic, and organic pollutants along with their biomagnifications. The measurement and analysis of hydro-biogeochemical variables in the marine environment are helpful for a better understanding of aquatic status (Wang et al., 2011; Wu et al., 2023). Coastal ecosystems can also be affected by natural changes, including hurricanes, droughts, and floods. Therefore, a better understanding of both natural and anthropogenic influences on coastal ecosystems has paramount validity in coastal ecosystem management and conservation.

Aiming to address the issues caused by anthropogenic activities and the natural occurrences that can influence coastal environments and ecosystems, this Research Topic concentrates on global patterns of change in the macroecology of coastal zones by identifying these research interests, as follows:

Dataset monitoring

The huge datasets on hydro-biogeochemical parameters created by the growing number of coastal environment and ecological monitoring projects need to be collected and the datasets of all parameters examined to provide a better understanding of anthropogenic activities and natural changes in coastal environments and ecologies.

Coastal responses

The responses of coastal environments and their ecologies such as coral reefs, seagrass, and mangrove resistance against biotic and abiotic parameters.

Ocean-land orientation

The dynamics of coastal ecosystems as a function of ocean-land orientation have also been explored in recent years. In addition, phytoplankton such as the harmful algal bloom have experienced in coastal water.

This Research Topic aims to identify sharp changes in coastal ecosystems, paying special attention to the macroecology of coastal zones with respect to land-ocean interactions.

Hydro-ecosystem identified by remote sensing

Remote sensing is a field that extends from sensor design, validation, and calibration to the application of sensors in environmental sciences, geosciences, and ecology. It is widely used in coastal zones and the open ocean. This Research Topic includes a simple method for estimating macroalgae area under clouds (Area_cloud_GT) on MODIS imagery, which used the principle behind the lowpass filter processes (An et al.). The mean relative difference between the estimation results and the 'real' value was 30.09%. In all, the results supply a reference for quantitating the green tide abundance and its areas. Both satellite observation and numerical simulation were used to study the mechanism of the abrupt decay.

Another contribution to the Research Topic explores the spatiotemporal variation of the Zhejiang-Fujian coastal current, which was assessed by examining the riverine discharge and tidal forcing (Li et al.). Secchi disk depth in the spatial distribution were assessed by multi-source remote sensing data and other fused data from 2011 to 2020 along southeastern Vietnam (Sun et al.). This study includes four sea surface models examining the maximum monthly number of the cyclonic cold-core eddy anticyclonic warm-core eddy, cyclonic warm-core eddy, and anticyclonic cold-core eddy from the monthly distribution over multiple years (2008 ~ 2017), in the months of December (765.70 ± 52.05), January (688.20 ± 82.53), April (373.40 ± 43.09), and August (533.00 ± 56.92), respectively (Sun et al.).

Coastal ecosystem

Coastal ecosystems are located at the interface between land and sea, meaning they are subject to the processes of both of their interactions. For instance, coastal ecosystems often have large volumes of freshwater inputs from terrestrial environments while simultaneously being subject to a massive load of marine inputs via waves and ocean currents. Both of these inputs may consist of an array of toxic or non-toxic constituents. However, coastal zones are rich in biodiversity and highly sensitive to changes in their environment (Balasuriya, 2018) with biological communities that include almost all biological components, ranging from microscopic to macroscopic in size. For example, coastal coral reefs are a diverse habitat that support a large number of invertebrates, vertebrates, algae, and seaweeds. Furthermore, mangroves, sea grass meadows, marshes, and coastal wetlands have been recognized as the most productive ecosystems in the world. However, the integrity of these ecosystems is highly interconnected and largely depends upon inputs from both marine and terrestrial ecosystems. For example, floods caused by river runoff stimulate the spawning of certain fish and other aquatic species. Furthermore, changes in salinity in coastal lagoons and estuaries are important for migratory species (Ishitobi et al., 2000). However, extreme events and manmade influences often disturb the ecological integrity of these ecosystems (Aguilera et al., 2020). In this context, cultural eutrophication, ocean acidification, hypoxia, HABs, heavy metal pollution, and biomagnifications of these issues are highlighted in literature on this subject. Therefore, a proper understanding of the interactions between biotic components and their interactions with their environment is particularly important. In this context, advanced analytical tools such as HPLC-based pigment analysis are superior to conventional microscopic analysis, enabling better understanding of this subject.

Dissolved inorganic nitrogen (DIN) (ammonium and nitrate) and dissolved organic nitrogen (DON) (urea and glycine) were used to quantify the absorption ability of the seagrass *Zostera japonica* and the macroalgae *Ulva pertusa*. The results showed that *Ulva pertusa* had higher absorption rates for ammonium and nitrate after being exposed to higher light (14.67 ± 2.50 and 1.29 ± 0.16 mg^{-1} dry weight (DW) h^{-1}) compared with lower light (4.52 ± 0.95 and 0.18 ± 0.12 mg^{-1} DW h^{-1}) treatments. While *Zostera japonica* adsorbed rates of the belowground seagrass, parts for glycine were 14.71 ± 1.85 and 6.38 ± 0.52 mg^{-1} DW h^{-1} after the high- and low-light treatments. This indicates that eutrophication plays an important role in macroalgae and seagrasses, providing insights into protecting seagrass meadows

(Han et al.). Both optical microscopy and HPLC-pigment analysis were used to analyze the feeding selectivity of blue mussel Mytilus coruscus on natural phytoplankton assemblages. The results showed that cryptophytes dominated the phytoplankton community and concentrated 66.1% of the total phytoplankton abundance (Jiang et al.). Image analysis combined with biological measures established the seagrass-epiphyte dynamic relationship and how it changes with environmental conditions (Huang et al.).

Phytoplankton play an important role in the cooling water systems of nuclear power plants, with the risk of phytoplankton blockage being highest between April to July. Wang et al.'s examination of the available control measures for high-risk phytoplankton species provides new ideas for nuclear power plants. In this study, the relationships between inorganic nutrients and the diversity of dinoflagellate cysts were studied in relation to the range of nutrient concentrations. The relationship between all diversity metrics and nutrients was negative, further proving that eutrophication may result from a low diversity of cysts (Gao and Su).

Modeling ecosystem

Real-time environmental forecasting systems based on modeling approaches in terms of three-dimensional, coupled hydrodynamic-biogeochemistry models are important for providing information on spatio-temporal variations in environmental conditions (Wang, 2001). The Coupled Great Bay Ecological Environmental Prediction System is a real-time marine biogeochemical and ecosystem forecast tool and module, providing daily real-time nowcasts and 2-day forecasts of temperature, salinity, NO2 + NO3, chlorophyll, and pH. It also predicts the spatio-temporal variability of the ecological environmental changes associated with extreme weather events (Luo et al.). The medium and high-risk composition and its distribution characteristics are used in an ecosystem service value model. The results show that the optimized coastal zone landscape pattern and the total ecological value are 462.02 km2 and 105,01.71 million yuan, providing new ideas that could help in implementing ecological development and protection strategies in coastal cities (Yi et al.). Another study in the Research Topic examined the red tide that took place in the central sea area of Lingdingyang Bay using the Delft3D model. Tide and wind, with minimal influence from runoff, were shown to mainly influence the red tide drift-diffusion process (Xu et al.). A coupled dynamical diagnostic framework assessed four factors, including phase speed, the damping rate, and the strength of the annual and semi-annual harmonic forcing of SSTAC. Most coupled models were shown to have a relatively weaker (an average of 18%) propagation speed and stronger annual (18%) and semi-annual (39%) external forcing. Half of the models show a relatively stronger (about one time) damping rate, while the rest show a weaker (30%) damping rate (Chen and Yu).

Contribution and perspectives

This Research Topic, introduces the Research Topic *Macroecology of Coastal Zones under Global Changes*, analyzing different diverse coastal ecosystems around the globe and addressing topics related to hydro-ecosystem identified by remote sensing, coastal ecosystem and modeling ecosystem. It includes 14 articles that provide insights for understanding the macroecology of coastal zones under global changes. The knowledge and insights brought together in this Research Topic are by no means closed, and we believe this Research Topic provides a valid scientific platform for exploring new insights into coastal ecology that are beneficial for the management of coastal ecosystems by integrating scientific, administrative, and financial constituents from coastal environmental and ecological sciences.

Author contributions

All the listed authors made a substantial contribution to the work and approved it for publication.

Acknowledgments

We would like to thank the reviewers and scientists who contributed to this Research Topic.

Conflict of interest

The authors declare that the research was conducted in the absence of any commercial or financial relationships that could be construed as a potential conflict of interest.

Publisher's note

References

Aguilera, M. A., Tapia, J., Gallardo, C., Núñez, P., and Varas-Belemmi, K. (2020). Loss of coastal ecosystem spatial connectivity and services by urbanization: natural-to-urban integration for bay management. *J. Environ. Manag.* 276, 111297. doi: 10.1016/j.jenvman.2020.111297

Balasuriya, A. (2018). "Chapter 25 - coastal area management: biodiversity and ecological sustainability in Sri Lankan perspective," in *Biodiversity and climate change adaptation in tropical islands*. Eds. C. Sivaperuman, A. Velmurugan, A. K. Singh and I. Jaisankar (USA:Academic Press), 701–724.

Dong, J. D., Zhang, Y. Y., Wang, Y. S., Wu, M. L., Zhang, S., and Cai, C. H. (2010). Chemometry use in the evaluation of the sanya bay water quality. *Braz. J. Oceanogr.* 58, 339–352. doi: 10.1590/S1679-87592010000400008

Ishitobi, Y., Hiratsuka, J.-i., Kuwabara, H., and Yamamuro, M. (2000). Comparison of fish fauna in three areas of adjacent eutrophic estuarine lagoons with different salinities. *J. Mar. Syst.* 26, 171–181. doi: 10.1016/S0924-7963(00)00052-X

Ling, J., Wu, M. L., Chen, Y. F., Zhang, Y. Y., and Dong, J. D. (2014). Identification of spatial and temporal patterns of coastal waters in sanya bay, south China Sea by chemometrics. *J. Environ. Inf.* 23, 37–43. doi: 10.3808/jei.201400255

Wang, J. (2001). A Nowcast/Forecast system for coastal ocean circulation using simple nudging data assimilation. *J. Atmos. Ocean. Technol.* 18, 1037–1047. doi: 10.1175/1520-0426(2001)018<1037:anfsfc>2.0.co;2

Wang, Y. S., Sun, C. C., Lou, Z. P., Wang, H. L., Mitchell, B. G., Wu, M. L., et al. (2011). Identification of water quality and benthos characteristics in daya bay, China, from 2001 to 2004. *Oceanological Hydrobiological Stud.* 40, 82–95. doi: 10.2478/s13545-011-0009-4

Wu, M. L., Lin, Y. P., Ruiz-Fernaandez, A. C., and Sahu, B. K. (2023). Coastal environmental and ecological data analysis. *Front. Mar. Sci.* 9. doi: 10.3389/fmars.2022.1126086

Wu, M. L., Wang, Y. T., Cheng, H., Sun, F. L., Fei, J., Sun, C. C., et al. (2020). Phytoplankton community, structure and succession delineated by partial least square regression in daya bay, south China Sea. *Ecotoxicology* 29, 751–761. doi: 10.1007/s10646-020-02188-2

Wu, M. L., Wang, Y. S., and Gu, J. D. (2015). Assessment for water quality by artificial neural network in daya bay, south China Sea. *Ecotoxicology* 24, 1632–1642. doi: 10.1007/s10646-015-1453-5

Wu, M. L., Wang, Y. S., Sun, C. C., Wang, H. L., Dong, J. D., Yin, J. P., et al. (2010). Identification of coastal water quality by statistical analysis methods in daya bay, south China Sea. *Mar. Pollut. Bull.* 60, 852–860. doi: 10.1016/j.marpolbul.2010.01.007

Wu, M. L., Wang, Y. S., Wang, Y. T., Yin, J. P., Dong, J. D., Jiang, Z. Y., et al. (2017). Scenarios of nutrient alterations and responses of phytoplankton in a changing daya bay, south China Sea. *J. Mar. Syst.* 165, 1–12. doi: 10.1016/j.jmarsys.2016.09.004

frontiers | Frontiers in Marine Science

TYPE Original Research
PUBLISHED 18 August 2022
DOI 10.3389/fmars.2022.995731

OPEN ACCESS

EDITED BY
Qiuying Han,
Hainan Tropical Ocean University, China

REVIEWED BY
Deyong Sun,
Nanjing University of Information Science and Technology, China
Mengquqn Wu,
Ludong University, China

*CORRESPONDENCE
Dingfeng Yu
dfyu@qlu.edu.cn

SPECIALTY SECTION
This article was submitted to Coastal Ocean Processes, a section of the journal Frontiers in Marine Science

RECEIVED 16 July 2022
ACCEPTED 01 August 2022
PUBLISHED 18 August 2022

CITATION
An D, Xing Q, Yu D and Pan S (2022) A simple method for estimating macroalgae area under clouds on MODIS imagery.
Front. Mar. Sci. 9:995731.
doi: 10.3389/fmars.2022.995731

A simple method for estimating macroalgae area under clouds on MODIS imagery

Deyu An[1,2,3], Qianguo Xing[2,3,4], Dingfeng Yu[1]* and Shunqi Pan[5]

[1]Institute of Oceanographic Instrumentation, Qilu University of Techonology (Shandong Academy of Sciences), Qingdao, China, [2]Chinese Academy of Sciences (CAS) Key Laboratory of Coastal Environmental Processes and Ecological Remediation, Yantai Institute of Coastal Zone Research, Chinese Academy of Sciences, Yantai, China, [3]University of Chinese Academy of Sciences, Beijing, China, [4]Center for Ocean Mega-Science, Chinese Academy of Sciences, Qingdao, China, [5]Hydro-Environmental Research Centre, School of Engineering, Cardiff University, Cardiff, United Kingdom

The presence of clouds interferes with optical remote sensing monitoring of macroalgae blooms. To solve this problem, we propose a simple method for estimating macroalgae area under clouds ($Area_{\_cloud\_GT}$) on MODIS imagery using the principle behind the lowpass filter. The method is based on a rectangle with clouds and eight identical adjacent rectangles surrounding it that contain macroalgae. The cloud rectangle is a central 'pixel' (Cloud) and the eight adjacent rectangles are 'pixels' GT1–GT8. The core operation is to calculate the central 'pixel' value, i.e., the macroalgae coverage rate in the Cloud rectangle. The macroalgae area detected by semi-simultaneous fine resolution images in the same region was taken as the 'real' value. A comparison of the estimation results and the 'real' value shown that the mean relative difference between them (MRD) was 30.09% when the time interval of the images within 10 minutes. When the time interval was over 3 hours, the MRD was more than 60%. The MRD increased significantly with increasing time interval because of the constant movement of the macroalgae and the limitations of the remote sensing image. The results indicate that this simple method is effective to a certain extent. These results can provide a reference for the quantitative analysis of green tide.

KEYWORDS

macroalgae blooms, MODIS imagery, clouds, method of estimating macroalgae area, multi-sensor images

1 Introduction

Macroalgae blooms (MABs), caused by outbreaks of macroalgae, have increased remarkably in the global oceans in recent years, becoming a worldwide marine ecological problem (Morand and Merceron, 2005; Ye et al., 2011; Smetacek and Zingone, 2013; Wang et al., 2019). The world's largest transregional MABs of *Ulva prolifera* ("green

tide") have occurred every summer in the Yellow Sea since 2007, causing serious ecological, environmental, and socioeconomic problems (Song et al., 2015; Zhou et al., 2015). Both the scientific communities and the public have shown a strong interest in identifying the causes of MABs and addressing the environmental impacts and implications (Hu and He, 2008; Sun et al., 2008; Ye et al., 2008; Liu et al., 2009). In much of the research, satellite data have played a vital role because of the advantages of having a synoptic view and repeated observations. The patterns associated with MABs, especially their origin and development, have become fairly well understood with the help of remote sensing data (Hu, 2009; Son et al., 2012; Xu et al., 2014; Zhou et al., 2014; Qi et al., 2016; Min et al., 2017; Qiu et al., 2018; Cao et al., 2019; Chen et al., 2020).

Optical images, such as GOCI (Geostationary Ocean Color Imager), MODIS (Moderate Resolution Imaging Spectroradiometer), HJ-1A/1B (HuanJing-1A/1B), and GF-1 (GaoFen-1) are the primarily remote sensing images for monitoring MABs (Hu et al., 2010; Xing et al., 2011; Qiu and Lu, 2015; Xing et al., 2015; Xing and Hu, 2016; Zhang et al., 2016; Xing et al., 2019; An et al., 2021; Cui et al., 2022). However, during the MAB outbreaks, which occur in early June to early August, it is the rainy season in the Yellow Sea because of the influence of the East Asian summer monsoon (Feng et al., 1998). When clouds contaminate optical images, macroalgae patches under clouds are missed. Figure 1A shows macroalgae patches south and north of an area obscured by clouds. It is reasonable to assume that there are also macroalgae patches under the clouds. Figures 1B, C confirms this assumption. After local linear enhancement, Sentinel-2 can observe macroalgae patches in images with a small amount of cloud coverage because of its fine spatial resolution (10 m). MODIS cannot observe macroalgae patches in the same images due to its coarse resolution (250 m). This demonstrates that clouds can affect the estimated area of MAB in MODIS images with a small amount of cloud coverage, thereby affect quantitative analysis results. However, in most current research using remote sensing to estimate macroalgae area and biomass, the presence of clouds would be masked by preprocessing (Hu et al., 2017; Cui et al., 2018; Hu et al., 2019; Xiao et al., 2019), regardless of whether macroalgae are present underneath the clouds. This would increase the difference between the estimated and actual area or biomass.

To reduce the quantitative analysis error, we must obtain information about the macroalgae obscured by the cloud mask. How to do this is an interesting problem. Microwave remote sensing seems like an effective method because microwaves can penetrate clouds and fog due to their greater wavelength compared to visible and infrared radiation. As a result, the atmosphere has little effect on microwave remote sensing images. Nevertheless, the monitoring of MABs used by microwave remote sensing is still in its initial stage. The noise signal in microwave remote sensing data has an obvious impact on the interpretation of small macroalgae

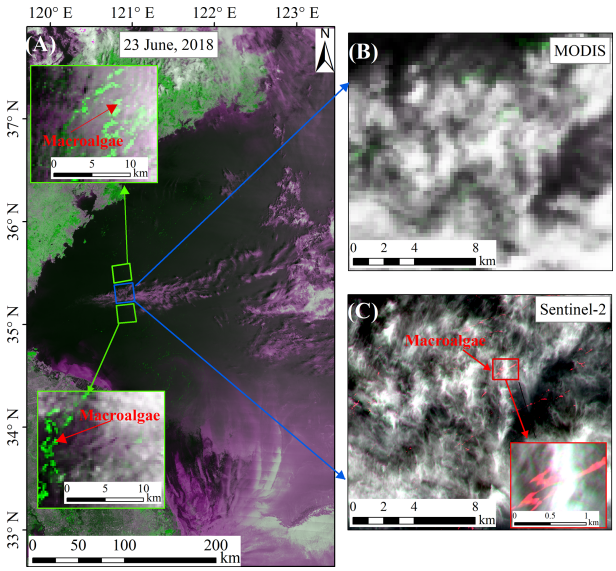

FIGURE 1
(A) Macroalgae shown in a false color composite by MODIS bands 1, 2, 1 acquired over the Yellow Sea on 23 June 2018. The green patches indicated by red arrows in green frame are floating green macroalgae, and the white patches in blue frame are clouds. **(B)** Details of blue frame shown in MODIS false color image. **(C)** Details of blue frame shown in Sentinel-2 false color image composite by bands 8, 4, 3 acquired on the same day as MODIS. In the false color images, the floating macroalgae patches are in red color.

patches (Qiu and Lu, 2015), so currently it is mostly used as auxiliary monitoring data.

Another possible method is to reconstruct missing information obscured by clouds in remote sensing images and then detect macroalgae using the reconstructed image. Many methods for reconstructing missing information in remote sensing images have been previously proposed, including spatial-based methods (Ballester et al., 2001; Chan and Shen, 2001; Zhang et al., 2007; Shen et al., 2010; Yu et al., 2011), spectral-based methods (Rakwatin et al., 2008; Shen et al., 2010; Gladkova et al., 2012; Li et al., 2014a), and temporal-based methods (Julien and Sobrino, 2010; Zhu et al., 2011; Lorenzi et al., 2013; Li et al., 2014b; Zeng et al., 2014; Zhang et al., 2014b; Shen et al., 2015). Shen et al. (2015) summarized that the spatial-based methods are susceptible to blurring and usually fail to reconstruct large area of missing information, whereas the spectral-based methods usually target missing information problems caused by the sensor, such as black strip. Therefore, these two categories of methods are not suitable for the detection of macroalgae under cloud. The temporal-based methods are also not suitable obviously for the detection of macroalgae because macroalgae are constantly drifting (Cui et al., 2012; Harun-Al-Rashid and Yang, 2018).

For accurate MAB analysis and effective prevention and control, it is extremely important to reduce the impact of clouds on macroalgae estimates based on optical images. In this study, we propose a simple method to solve the impact of clouds on estimates of macroalgae area under clouds on MODIS imagery. It is based on the principle of the lowpass filter. Results detected by semi-simultaneous fine resolution images (GF-1, Sentienl-2 and Sentinel-1) in the same region are used for comparisons to determine the feasibility of the method.

2 Data and methods

2.1 Satellite data and processing

Fourteen satellite images (listed in Table 1) were used including eight Terra and Aqua MODIS images (250 m resolution), two GF-1 WFV images (16 m resolution), two Sentinel-2 MSI images (10 m resolution) and two Sentienl-1 SAR images. In this study, we used the Sentinel-1 Level-1 Interferometric Wide Swath (IW) Ground Range Detected (GRD) High Resolution product. The spatial resolution was 20 m × 22 m and the pixel spacing was 10 m × 10 m.

TABLE 1 Acquisition time of the satellite images.

Sensor	Acquisition time (hh:mm dd/mm/yyyy)
MODIS	11:45 21/06/2015; 10:45 01/07/2015; 11:20 04/07/2015; 13:10 28/06/2017; 11:00 21/06/2018; 10:45 23/06/2018; 10:30 20/07/2018; 11:50 23/06/2019
GF-1	11:20 21/06/2018; 11:26 20/07/2018
Sentinel-2	10:35 23/06/2018; 10:35 28/06/2017
Sentinel-1	17:55 23/06/2019

Optical image preprocessing included georeferencing and atmospheric correction. The FLAASH (Fast Line of Sight Atmospheric Analysis of Spectral Hypercubes) atmospheric correction module *via* ENVI 5.3 software (Exelis Visual Information Solutions, Inc., Boulder, CO, USA) was applied to MODIS and GF-1 images to derive the reflectance (R, unitless), while the Sen2Cor atmospheric correction module from European Space Agency (ESA) was used on the Sentinel-2 images. For microwave images, the radiometric calibration module *via* SNAP (Sentinel Application Platform, ESA) was applied to Sentinel-1 images to derive the radar backscattering coefficient (NRCS, not converted to decibel value). The speckle filtering module and the range-doppler terrain correction *via* SNAP were also applied to Sentinel-1 images to reduce speckle impact and correct geometric distortion. All of the images were transformed into WGS_1984_UTM_Zone_51N coordinate system after preprocessing.

2.2 Macroalgae and cloud detection methods

2.2.1 Optical image macroalgae detection method

Many macroalgae information detection algorithms have been proposed by scholars based on the distinct spectral difference between natural seawater and macroalgae-covered seawater in the red light (Red) and near infrared (NIR) bands. The difference index algorithm, such as Difference Vegetation Index (DVI), Floating Algae Index (FAI), Virtual-Baseline Floating macroalgae Height (VB-FAH), is little affect by sunlight and aerosol changes and is not particularly sensitive to the accuracy of the atmospheric correction (Hu, 2009; Xing and Hu, 2016; Xing et al., 2018). In this work, the DVI index (Eq. (1)) is selected for detecting pixels containing macroalgae since MODIS 250m images only have two bands of Red and NIR.

$$DVI = R_{\mathrm{NIR}} - R_{\mathrm{Red}} \tag{1}$$

where R_{NIR} is the reflectance at the near-infrared (NIR) band and R_{Red} is the red light band reflectance.

Given the significant variability in atmospheric turbidity, ocean background, and sun glint (Xing and Hu, 2016; Cui et al., 2018), a dynamic threshold of DVI was used to extract the macroalgae. The DVI images were segmented into small windows, and a set of thresholds was used to classify the macroalgae pixels window by window. For further details, please refer to Xing and Hu, 2016 and Xing et al., 2018.

Next, the macroalgae area (Area, km^2) was derived by multiplying the pixel size of the satellite image (PS, km^2) by

the total number of pixels (N) that were identified as macroalgae (Cui et al., 2018), as shown in Eq. (2).

$$\mathbf{Area = N \times PS} \quad (2)$$

2.2.2 Microwave image macroalgae detection method

The Sentinel-1 IW-GRD image used in this study contained two polarization modes, VV and VH. From a qualitative perspective, the macroalgae pixels are shown more clearly with VV- (VV image) than VH-polarization (VH image) (Figure 2).

From a quantitative perspective, the statistical analysis of NRCS including high NRCS pixels (i.e., pixels contained ships or islands), pixels containing macroalgae and pure seawater pixels showed that the mean value of high NRCS pixels is much larger than NRCS mean value of pixels containing macroalgae and pure seawater pixels (Figures 3A, B). Therefore, a high threshold was used to mask high NRCS pixels. The mean NRCS value of pixels containing macroalgae was larger than pure seawater pixels in both VV and VH images. The reason for this is that sea surface covered by macroalgae is rougher than a sea surface without macroalgae and the radar echo signal increases with increasing roughness. The difference between pixels containing macroalgae and pure seawater pixels was greater in the VV image than in the VH images (Figures 3A, B). The NRCS histogram analysis showed the same results (Figures 3C, D). Since it was easier to classify the floating macroalgae and other objects in the VV image than in the VH image. The VV image was used to detect the macroalgae. Given the variability in ocean background, a dynamic threshold of DVI was also used to extract the macroalgae. The detection details and the calculation method for macroalgae were same as for the optical image.

2.2.3 Consistency of macroalgae area detected from multi-sensor images

Macroalgae patches vary in size from centimetres to kilometres, which means that pixel-mixing is common for most remote sensing images (Xiao et al., 2017; Li et al., 2018). This situation can lead to biased results derived from images with different resolutions (Kim et al., 2018). Image pairs over the same macroalgae region with the same acquisition dates were selected to investigate the consistency in the retrieved macroalgae coverage area (Xing et al., 2019; An et al., 2021). The areas derived from different image pairs were then compared. Three linear regression functions ($R^2 \geq 0.9$, MRD $\leq$ 25.71%) were performed on the areas derived from GF-1, Sentinel-2 and Sentinel-1 images and the areas from MODIS image (Figure 4). R^2 is the linear regression coefficient and MRD is the mean relative difference. MRD could be expressed by formulas as shown in Eq. (3).

$$MRD = \frac{1}{N}\sum_{i=1}^{N}\frac{|(y_i - x_i)|}{x_i} \times 100\,\% \quad (3)$$

where N is the number of image pairs. y is $FArea_{\_Fine}$, i.e., the macroalgae fitted area converted by the macroalgae area detected by MODIS images based on the linear regression functions. x is the 'real' value, i.e., the macroalgae area detected by fine resolution images (GF-1, Sentinel-2 and Sentinel-1).

2.2.4 Cloud detection method

Clouds have significantly higher reflectance than underlying surfaces in the visible spectrum (Tan et al., 2000). Macroalgae has low reflectance in the red band because of the strong

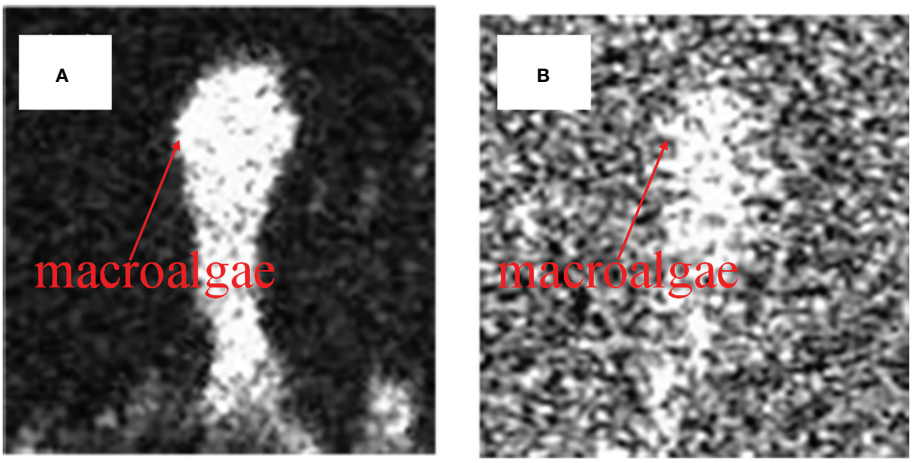

FIGURE 2
Comparison of visual interpretation quality of the floating macroalgae in two polarization modes of Sentinel-1: **(A)** VV; **(B)** VH.

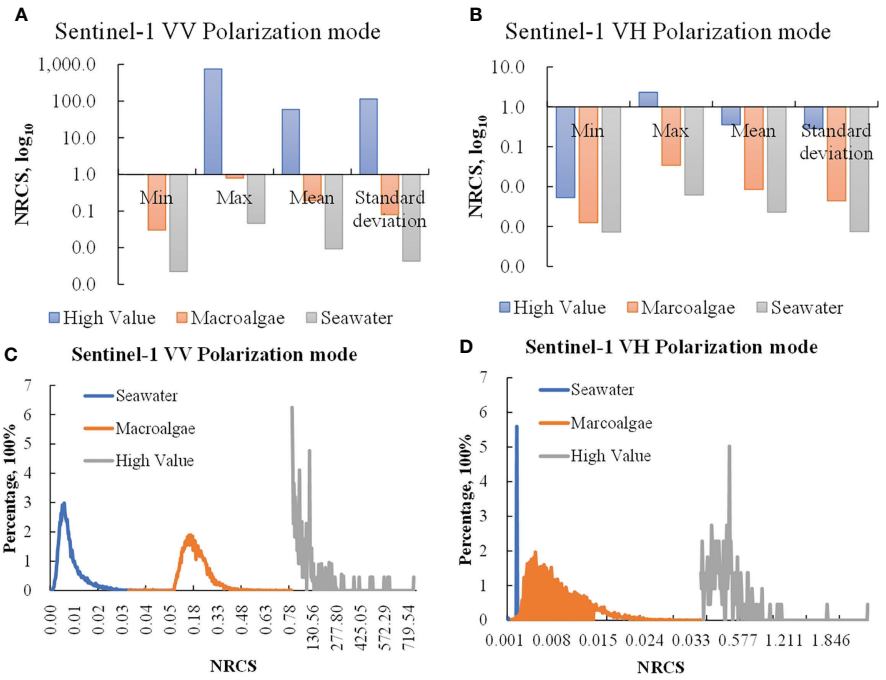

FIGURE 3
The radar backscattering coefficient (NRCS) comparison of pure seawater pixels (Seawater), pixels containing macroalgae (Macroalgae) and high NRCS pixels (High Value) in VV and VH polarization mode. **(A, B)** are the comparison of maximum value (Max), minimum value (Min), mean value (Mean) and standard deviation. **(C, D)** are the histogram comparison of Seawater, Macroalgae and High Value.

absorption caused by photosynthetic pigments (Dierssen et al., 2015). Thus, we also used a dynamic threshold method of the red band reflectance was used to detect clouds in MODIS images. The specific detection process was the same as for macroalgae. And the calculation method for clouds area ($Area_{\_cloud}$) was also the same as for Area.

2.3 Simple method for estimating macroalgae area under clouds

We proposed a simple method for estimating macroalgae area under clouds ($Area_{\_cloud\_GT}$) based on the principle behind the lowpass filter. The lowpass filter is a filter commonly used for

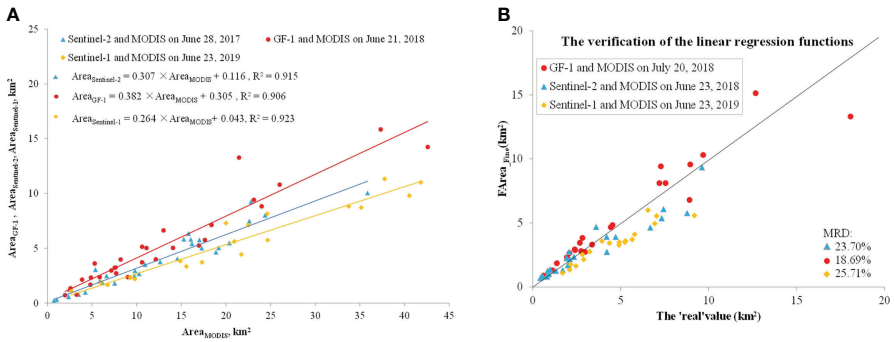

FIGURE 4
(A) Comparison in the macroalgae coverage areas derived from optical images of MODIS, GF-1, Sentinel-2 and Sentinel-1, i.e., $Area_{MODIS}$, $Area_{GF-1}$, $Area_{Sentinel-2}$, $Area_{Sentinel-1}$, respectively. **(B)** The verification of the linear regression functions in Figure **(A)**. The 'real' values are the macroalgae area detected by fine resolution images (GF-1, Sentinel-2 and Sentinel-1), and $FArea_{\_Fine}$ is the macroalgae fitted area converted by the macroalgae area detected by MODIS images based on the linear regression functions. MRD is the mean relative difference between $FArea_{\_Fine}$ values and the 'real' values. The black line in figure is the 1:1 line.

smoothing images in ENVI software. ENVI's default low pass filter contains the same weights in each kernel element, replacing the center pixel value with an average of the surrounding values. The default kernel size was 3×3 (Deng, 2010). Figure 5 shows a simple estimation method of $Area_{\_cloud\_GT}$ in the case of clouds surrounded by macroalgae. The process was as follows.

First, we used a rectangle to determine the distribution range of the clouds. We designated this rectangle and eight identical rectangles containing macroalgae around the clouds as a central 'pixel' (Cloud) and eight adjacent 'pixels' (GT1~GT8).

Next, we calculated the macroalgae coverage rate of GT as the ratio of the macroalgae area to the corresponding rectangle area. We took this ratio as the 'pixel' value of GT. The average of the eight GT 'pixels' values from GT1 to GT8 was calculated and taken as the central 'pixel' value.

Finally, we derive the $Area_{\_cloud\_GT}$ of this cloud by multiplying the cloud area ($Area_{\_cloud}$) in the central 'pixel' region with the central 'pixel' value.

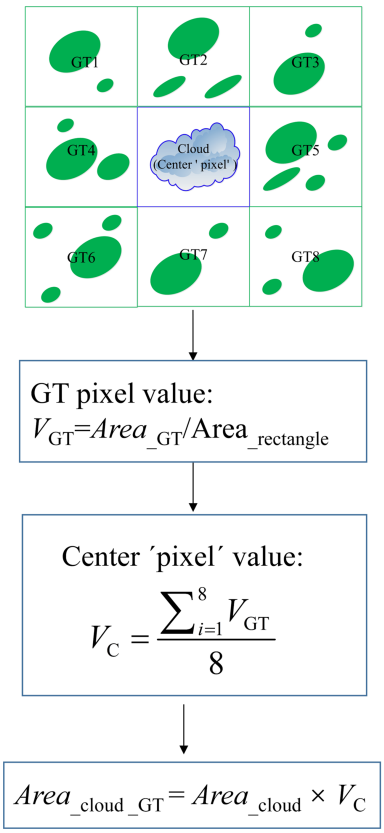

FIGURE 5
Methods for estimating macroalgae area under clouds ($Area_{\_cloud\_GT}$) in the case of clouds surrounded by macroalgae. These rectangles are the same size. In the surrounding rectangles (GT1-GT8), green ellipses represent different macroalgae patches. In the center rectangle (Cloud), the blue shape represents cloud patches.

This method was used to calculate $Area_{\_cloud\_GT}$ of eight MODIS images. The $Area_{\_cloud\_GT}$ was converted into the macroalgae fitted area ($FArea_{\_cloud\_GT}$) of the corresponding fine resolution image. Next, $FArea_{\_cloud\_GT}$ was compared with the macroalgae area estimated ($Area_{GF}$, $Area_{Sentinel\text{-}2}$, or $Area_{Sentinel\text{-}1}$) using semi-simultaneous fine resolution images in the same region. $Area_{GF}$ ($Area_{Sentinel\text{-}2}$ or $Area_{Sentinel\text{-}1}$) was considered to be the 'real' value. The feasibility of the method was verified through the mean relative difference (MRD) between $FArea_{\_cloud\_GT}$ and the 'real' value.

3 Results and discussion

3.1 Application of the simple method for estimating macroalgae area under clouds

In practice, it is not common for images to contain clouds surrounded by macroalgae. As a result, using the proposed method to estimate the $Area_{\_cloud\_GT}$ will result in an underestimate. To avoid underestimating $Area_{\_cloud\_GT}$, we divided the distribution patterns of macroalgae and clouds into five cases. These five cases are as follows:

Case 1: If clouds are surrounded by macroalgae, the central 'pixel' value is the average of the eight GT 'pixels' values from GT1 to GT8, as shown in Figure 6B.

Case 2: If the rectangles in a south-north direction (or east-west or northeast-southwest, or northwest-southeast) of the clouds have macroalgae, the central 'pixel' value is the average of GT4 and GT5 (or GT2 and GT7, or GT3 and GT6, or GT1 and GT8), as shown in Figure 6A.

Case 3: If only one side of the cloud rectangle has macroalgae, the central 'pixel' value is the 'pixel value' of GT2 (north) [or GT7 (south) or GT4 (east) or GT5 (west)], as shown in Figure 6C.

Case 4: If the distribution of macroalgae around the clouds is scattered, the number of GT rectangles involved in the calculation can be judged on a case-by-case basis, as shown in Figure 6B. In this example, there are macroalgae in GT4, GT5, GT6, and GT7, so the average of these four 'pixels' is taken as the central 'pixel' value.

Case 5: If there is no macroalgae on one side of the clouds, while there is macroalgae on the other side of the clouds, there may be macroalgae under the clouds. As shown in Figure 6C, there is no macroalgae on the right side of cloud rectangle D, while there are macroalgae around adjacent cloud rectangles A, B, and C. The central 'pixel' value of cloud rectangles A, B, and C are first calculated according to the above four cases. The average of these three values is taken as the central 'pixel' value of cloud rectangle D.

Owing to the random distribution of clouds and macroalgae, there may be one of the above cases in a remote sensing image, such as June 23, 2018 (Figure 6A). There may also be two or

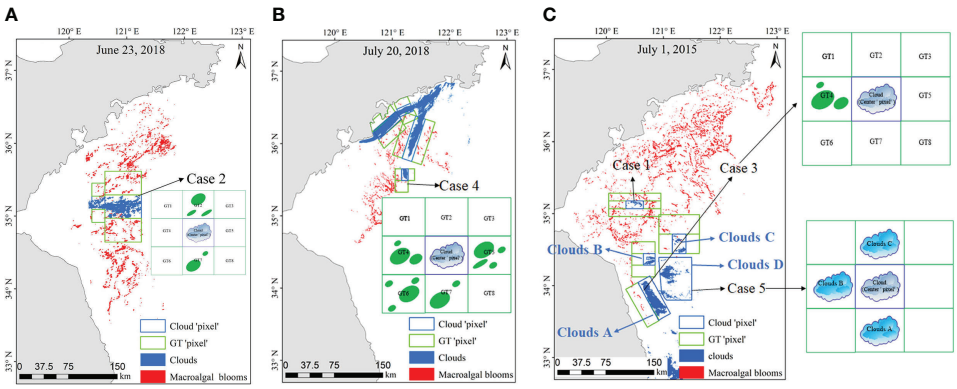

FIGURE 6
Application of the simple method for estimating macroalgae area under clouds under various scenarios. **(A)** The scenario of Case 2. **(B)** The scenario of Case 4. **(C)** The scenarios of Case 1, Case 3 and Case 5.

three of the above cases, such as July 1, 2015 and July 20, 2018 (Figures 6B, C). There may also be four or all of the above cases, such as June 21, 2015 and July 4, 2015 (Figure 7).

3.2 Verification of the simple method for estimating $Area_{\_cloud\_GT}$

The equations should be inserted in editable format from the equation editor. The $Area_{\_cloud\_GT}$ derived from this simple method must be validated with field measurements to verify its accuracy. However, field verification is difficult because we cannot guarantee consistency between the region covered by aerial survey (or ship survey) and the area of clouds on an image. Instead, we selected fifteen pairs of cloud sub-regions on MODIS images and fine spatial images acquired on the same day to verify the feasibility of the simple method of estimating $Area_{\_cloud\_GT}$, as shown in Figure 8A.

The $FArea_{\_cloud\_GT}$ on MODIS images was obtained according to section 2.3 and 3.1, and compared with the 'real' value, i.e., $Area_{GF}$ ($Area_{Sentinel\text{-}2}$ or $Area_{Sentinel\text{-}1}$). As shown in Figure 8A, when the time interval was within 10 minutes,

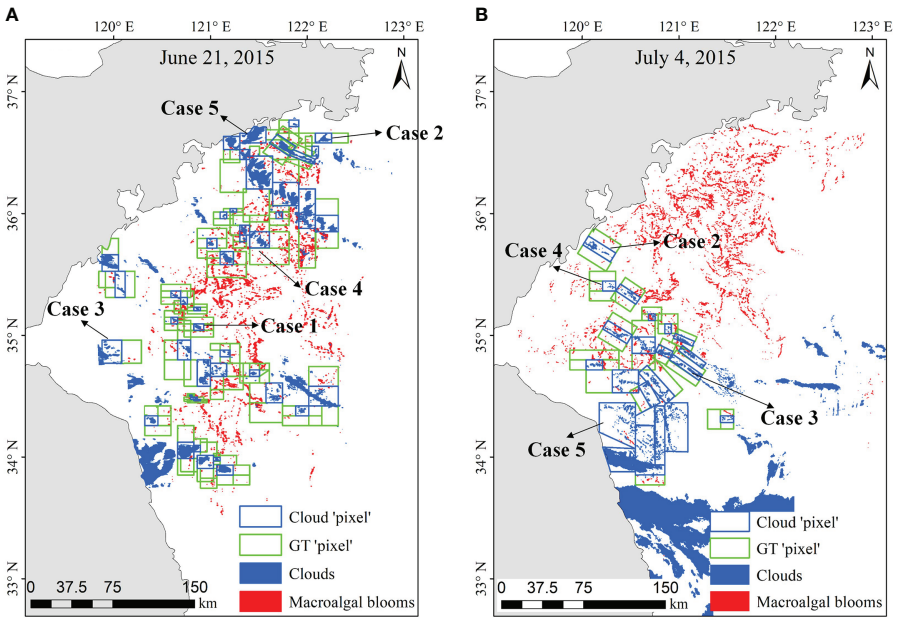

FIGURE 7
Application of the simple method for estimating macroalgae area under clouds under complex scenarios. **(A)** The scenario including four above cases; **(B)** The scenario including all above cases.

FArea$_{cloud_GT}$ converted from MODIS images was relatively close to the 'real' value except for the individual regions in red circle. The MRD between FArea$_{cloud_GT}$ and the 'real' value was 30.09%. When the time interval was within about one hour, the MRD increased significantly to 57.18%. When the time interval was over three hours, the MRD was more than 60%. The increase in MRD with time is easily understood. The macroalgae is constantly moving (Cui et al., 2012; Harun-Al-Rashid and Yang, 2018) and macroalgal aggregation morphology is changing at any time. In addition, we used here only extract the surface floating macroalgae, and less considering of the distribution of macroalgae in the upper water column because of the limitations of the remote sensing image, so the longer the time interval, the larger the MRD. From this study, we can conclude that the simple method has a relatively good accuracy.

For individual regions in red circle, the difference between FArea$_{cloud_GT}$ and the 'real' value is extremely obvious. We speculate that there are two possible reasons besides time interval. One reason is the difference in macroalgal aggregation morphology caused by sea surface wind and sea surface current (Xu et al., 2016; Cao et al., 2019). This difference can affect the calculation result of the macroalgae coverage rate, causing the larger MRD between FArea$_{cloud_GT}$ and the 'real' value. The other reason is the impact of cloud top height, cloud optical thickness, cloud effective particle radius, and other factors. These factors can affect the reflectance of underlying surfaces (Tan et al., 2000), and thus affect macroalgae detection, leading to uncertainty in FArea$_{cloud_GT}$.

The range of MRD was 10.89% to 87.26% after applying the simple method for estimating macroalgae area under clouds on MODIS imagery, while the range of MRD was 74.83% to 100% before applying the method. The estimation accuracy of semi-simultaneous cloud sub-regions was improved by 11.75% to 69.91% on average (Figure 8B). These results indicate the method can significantly improve the estimation accuracy of macroalgae area under cloudy conditions and has an evident effect in reducing the impact of clouds on the macroalgae area estimated on MODIS imagery.

4 Conclusions and prospective

Optical remote sensing images are seriously affected by clouds. Most current research about macroalgae area and biomass does not consider whether the sea surface under clouds is covered by macroalgae. This omission causes an increase in the difference between the estimated and actual biomass. The novelty of this study is that a simple method for estimating macroalgae area under clouds on MODIS imagery is proposed to address this challenge. The accuracy of the method is verified by a comparison of the estimation results and results detected by semi-simultaneous fine resolution images in the same region. The verification results show that the simple method has a relatively good accuracy, and can provide a technological reference for MAB quantitative analysis.

This method can be extended to other remote sensing images with coarse spatial resolution, such as GOCI. In practical application, the MRD between the 'real' results and the estimation results using this method may be larger in individual regions because of the impacts from macroalgal aggregation morphology, cloud optical thickness, cloud effective particle radius, and other factors. Further study is needed to reduce the impact of these factors to improve the method.

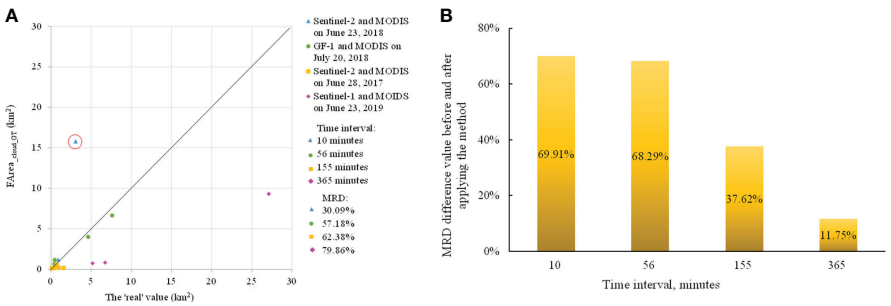

FIGURE 8
(A) The verification results of the simple method for estimating macroalgae area under clouds on MODIS imagery. The 'real' values are the macroalgae area detected by fine resolution images. FArea$_{cloud_GT}$ is the macroalgae fitted area converted by Area_cloud_GT, and Area$_{cloud_GT}$ is the macroalgae area under clouds estimated by the method. The black line in figure is the 1:1 line. **(B)** The MRD difference value before and after applying the method.

Data availability statement

The original contributions presented in the study are included in the article/supplementary material. Further inquiries can be directed to the corresponding author.

Author contributions

Conceptualization, DA and QX; methodology, DA; formal analysis, QX, DA, and DY; writing—original draft preparation, DA and QX; writing—review and editing, DY, QX, and SP. All authors have read and agreed to the published version of the manuscript.

Funding

This research was funded by, the Chinese Academy of Science Strategic Priority Research Program—the Big Earth Data Science Engineering Project (No. XDA19060203 and XDA19060501), the National Natural Science Foundation of China (No.42076188, 41676171, 42106172 and 41911530), the National Key Research and Development Program of China (No. 2017YFC1404802), Natural Science Foundation of Shandong Province (No. ZR2021QD135, ZR2019PD021), the Key Research and Development Program of Shandong (No. 2019GHY112017), State Key Laboratory of Tropical Oceanography, South China Institute of Oceanology, Chinese Academy of Sciences (No. LTO2017), the Project plan of pilot project of integration of science, education and Industry (No.2022GH004, 2022PY041), the Foundation of Institute of Oceanographic Instrumentation, Shandong Academy of Sciences (No. HYPY202107), and the University-Industry Collaborative Education Program (No. 202102245036 and 202101044002).

Acknowledgments

Thanks to China Center for Resources Satellite Data and Application and NASA's Goddard Space Flight Center for providing GF-1 and MODIS data, and to European Space Agency for Sentinel-2 and Sentinel-1 data. The authors are grateful for the encouragement and suggestions from reviewers.

Conflict of interest

The authors declare that the research was conducted in the absence of any commercial or financial relationships that could be construed as a potential conflict of interest.

Publisher's note

All claims expressed in this article are solely those of the authors and do not necessarily represent those of their affiliated organizations, or those of the publisher, the editors and the reviewers. Any product that may be evaluated in this article, or claim that may be made by its manufacturer, is not guaranteed or endorsed by the publisher.

References

An, D., Yu, D., Zheng, X., Zhou, Y., Meng, L., and Xing, Q. (2021). Monitoring the dissipation of the floating green macroalgae blooms in the yellow Sea, (2007–2020) on the basis of satellite remote sensing. *Remote Sensing.* 13 (19), 3811. doi: 10.3390/rs1319381

Ballester, C., Bertalmio, M., Caselles, V., Sapiro, G., and Verdera, J. (2001). Filling-in by joint interpolation of vector fields and gray levels. *IEEE Trans. Image. Processing.* 10 (8), 1200–1211. doi: 10.1109/83.935036

Cao, Y., Wu, Y., Fang, Z., Cui, X., Liang, J., and Song, X. (2019). Spatiotemporal patterns and morphological characteristics of *Ulva prolifera* distribution in the yellow Sea, China in 2016–2018. *Remote Sensing.* 11 (4), 445. doi: 10.3390/rs11040445

Chan, T., and Shen, J. (2001). Nontexture inpainting by curvature-driven diffusions. *J. Visual Commun. Image. Representation.* 12 (4), 436–449. doi: 10.1006/jvci.2001.0487

Chen, Y., Sun, D., Zhang, H., Wang, S., Qiu, Z., and He, Y. (2020). Remote-sensing monitoring of green tide and its drifting trajectories in yellow Sea based on observation data of geostationary ocean color imager. *Acta Optica. Sin.* 40 (03), 7–19. doi: 10.3788/AOS202040.0301001

Cui, T., Liang, X., Gong, J., Tong, C., Xiao, Y., Liu, R., et al. (2018). Assessing and refining the satellite-derived massive green macro-algal coverage in the yellow Sea with high resolution images. *ISPRS. J. Photogramm. Remote Sensing.* 144, 315–324. doi: 10.1016/j.isprsjprs.2018.08.001

Cui, B., Zhang, H., Jing, W., Liu, H., and Cui, J. (2022). SRSe-net: Super-resolution-based semantic segmentation network for green tide extraction. *Remote Sensing.* 14 (3), 710. doi: 10.3390/rs14030710

Cui, T., Zhang, J., Sun, L., Jia, Y., Zhao, W., Wang, Z., et al. (2012). Satellite monitoring of massive green macroalgae bloom (GMB): Imaging ability comparison of multi-source data and drifting velocity estimation. *Int. J. Remote Sensing.* 33 (17), 5513–5527. doi: 10.1080/01431161.2012.663112

Deng, S. (2010). ""Image enhancement"," in *ENVI remote sensing image processing methods* (Beijing: Science Press), 103.

Dierssen, H., Chlus, A., and Russell, B. (2015). Hyperspectral discrimination of floating mats of seagrass wrack and the macroalgae sargassum in coastal waters of greater Florida bay using airborne remote sensing. *Remote Sens. Environment.* 167, 247–258. doi: 10.1016/j.rse.2015.01.027

Feng, S., Li, F., and Li, S. (1998). "Regional oceanography of china's coastal waters"," in *Introduction to marine science* (Beijing: Higher Education Press), 329.

Gladkova, I., Grossberg, M., Shahriar, F., Bonev, G., and Romanov, P. (2012). Quantitative restoration for MODIS band 6 on aqua. *IEEE Trans. Geosci. Remote Sensing.* 50 (6), 2409–2416. doi: 10.1109/TGRS.2011.2173499

Harun-Al-Rashid, A., and Yang, C. (2018). Hourly variation of green tide in the yellow Sea during summer 2015 and 2016 using geostationary ocean color imager data. *Int. J. Remote Sensing.* 39 (13), 4402–4415. doi: 10.1080/01431161.2018.1457228

Hu, C. (2009). A novel ocean color index to detect floating algae in the global oceans. *Remote Sens. Environment.* 113 (10), 2118–2129. doi: 10.1016/j.rse.2009.05.012

Hu, C., and He, M. (2008). Origin and offshore extent of floating algae in Olympic sailing area. *Eos. Trans. Am. Geophys. Union.* 89 (33), 302–303. doi: 10.1029/2008EO330002

Hu, L., Hu, C., and He, M. (2017). Remote estimation of biomass of *Ulva prolifera* macroalgae in the yellow Sea. *Remote Sens. Environment.* 192, 217–227. doi: 10.1016/j.rse.2017.01.037

Hu, C., Li, D., Chen, C., Ge, J., Muller-Karger, F., Liu, J., et al. (2010). On the recurrent *Ulva prolifera* blooms in the yellow Sea and East China Sea. *J. Geophys. Res.: Oceans.* 115, C05017. doi: 10.1029/2009JC005561

Hu, L., Zeng, K., Hu, C., and He, M. (2019). On the remote estimation of *Ulva prolifera* areal coverage and biomass. *Remote Sens. Environment.* 223, 194–207. doi: 10.1016/j.rse.2019.01.014

Julien, Y., and Sobrino, J. (2010). Comparison of cloud-reconstruction methods for time series of composite NDVI data. *Remote Sens. Environment.* 114 (3), 618–625. doi: 10.1016/j.rse.2009.11.001

Kim, K., Shin, J., and Ryu, J. (2018). Application of multi-satellite sensors to estimate the green-tide area. *Korean. J. Remote Sens.* 34 (2_2), 339–349. doi: 10.7780/kjrs.2018.34.2.2.4

Li, X., Shen, H., Zhang, L., Zhang, H., and Yuan, Q. (2014a). Dead pixel completion of aqua MODIS band 6 using a robust m-estimator multiregression. *IEEE Geosci. Remote Sens. Lett.* 11 (4), 768–772. doi: 10.1109/LGRS.2013.2278626

Li, X., Shen, H., Zhang, L., Zhang, H., Yuan, Q., and Yang, G. (2014b). Recovering quantitative remote sensing products contaminated by thick clouds and shadows using multitemporal dictionary learning. *IEEE Trans. Geosci. Remote Sensing.* 52 (11), 7086–7098. doi: 10.1109/TGRS.2014.2307354

Liu, D., Keesing, J. K., Xing, Q., and Shi, P. (2009). World's largest macroalgal bloom caused by expansion of seaweed aquaculture in China. *Mar. pollut. Bull.* 58 (6), 888–895. doi: 10.1016/j.marpolbul.2009.01.013

Li, L., Zheng, X., Wei, Z., Zou, J., and Xing, Q. (2018). A spectral-mixing model for estimating sub-pixel coverage of sea-surface floating macroalgae. *Atmosphere-Ocean* 56 (4), 296–302. doi: 10.1080/07055900.2018.1509834

Lorenzi, L., Melgani, F., and Mercier, G. (2013). Missing-area reconstruction in multispectral images under a compressive sensing perspective. *IEEE Trans. Geosci. Remote Sensing.* 51 (7), 3998–4008. doi: 10.1109/TGRS.2012.2227329

Min, S., Oh, H., Hwang, J., Suh, Y., Park, M., Shin, J., et al. (2017). Tracking the movement and distribution of green tides on the yellow Sea in 2015 based on GOCI and landsat images. *Korean. J. Remote Sensing.* 33 (1), 97–109. doi: 10.1109/TGRS.2012.2227329

Morand, P., and Merceron, M. (2005). Macroalgal population and sustainability. *J. Coast. Res.* 21 (5), 1009–1020. doi: 10.2112/04-700A.1

Qi, L., Hu, C., Xing, Q., and Shang, S. (2016). Long-term trend of *Ulva prolifera* blooms in the western yellow Sea. *Harmful. Algae.* 58, 35–44. doi: 10.1016/j.hal.2016.07.004

Qiu, Z., Li, Z., Bilal, M., Wang, S., Sun, D., and Chen, Y. (2018). Automatic method to monitor floating macroalgae blooms based on multilayer perceptron: Case study of yellow Sea using GOCI images. *Optics. Express.* 26 (21), 26810–26829. doi: 10.1364/OE.26.026810

Qiu, Y., and Lu, J. (2015). Advances in the monitoring of *Enteromorpha prolifera* using remote sensing. *Acta Ecol. Sin.* 35 (15), 4977–4985. doi: 10.5846/stxb201309232339

Rakwatin, P., Takeuchi, W., and Yasuoka, Y. (2008). Restoration of aqua MODIS band 6 using histogram matching and local least squares fitting. *IEEE Trans. Geosci. Remote Sensing.* 47 (2), 613–627. doi: 10.1109/TGRS.2008.2003436

Shen, H., Liu, Y., Ai, T., Wang, Y., and Wu, B. (2010). Universal reconstruction method for radiometric quality improvement of remote sensing images. *International Journal of Applied Earth Observation and Geoinformation* 12 (4), 278–286. doi: 10.1016/j.jag.2010.04.002

Shen, H., Zeng, C., and Zhang, L. (2010). Recovering reflectance of aqua MODIS band 6 based on within-class local fitting. *IEEE J. Selected. Topics. Appl. Earth Observ. Remote Sensing.* 4 (1), 185–192. doi: 10.1109/JSTARS.2010.2077620

Shen, H., Li, X., Cheng, Q., Zeng, C., Yang, G., Li, H., et al (2015). Missing information reconstruction of remote sensing data: A technical review. *IEEE Geoscience and Remote Sensing Magazine* 3 (3), 61–85. doi: 10.1109/MGRS.2015.2441912

Smetacek, V., and Zingone, A. (2013). Green and golden seaweed tides on the rise. *Nature* 504 (7478), 84–88. doi: 10.1038/nature12860

Song, X., Huang, R., Yuan, K., Zhao, Y., Wen, R., and Zhang, H. (2015). Characteristics of the green tide disaster of east Shandong peninsula. *Mar. Environ. Sci.* 34 (3), 391–395. doi: 10.13634/j.cnki.mes.2015.03.012

Son, Y., Min, J., and Ryu, J. (2012). Detecting massive green algae (*Ulva prolifera*) blooms in the yellow Sea and East China Sea using geostationary ocean color imager (GOCI) data. *Ocean. Sci. J.* 47 (3), 359–375. doi: 10.1007/s12601-012-0034-2

Sun, S., Wang, F., Li, C., Qin, S., Zhou, M., Ding, L., et al. (2008). Emerging challenges: Massive green algae blooms in the yellow Sea. *Nat. Precedings.* 3, 1–13. doi: 10.1038/npre.2008.2266.1

Tan, J., Zhou, H., and Yang, C. (2000). Research and establishment in operation system of cloud detection and rehabilitation applied to NOAA satellite. *Remote Sens. Technol. Application.* 15 (4), 228–231. doi: 10.11873/j.issn.1004-0323.2000.4.228

Wang, M., Hu, C., Barnes, B., Mitchum, G., Lapointe, B., and Montoya, J. (2019). The great Atlantic sargassum belt. *Science* 365 (6448), 83–87. doi: 10.1126/science.aaw7912

Xiao, Y., Zhang, J., and Cui, T. (2017). High-precision extraction of nearshore green tides using satellite remote sensing data of the yellow Sea, China. *Int. J. Remote Sensing.* 38 (6), 1626–1641. doi: 10.1080/01431161.2017.1286056

Xiao, Y., Zhang, J., Cui, T., Gong, J., Liu, R., Chen, X., et al. (2019). Remote sensing estimation of the biomass of floating *Ulva prolifera* and analysis of the main factors driving the interannual variability of the biomass in the yellow Sea. *Mar. pollut. Bull.* 140, 330–340. doi: 10.1016/j.marpolbul.2019.01.037

Xing, Q., An, D., Zheng, X., Wei, Z., Wang, X., Li, L., et al. (2019). Monitoring seaweed aquaculture in the yellow Sea with multiple sensors for managing the disaster of macroalgal blooms. *Remote Sens. Environment.* 231, 111279. doi: 10.1016/j.rse.2019.111279

Xing, Q., and Hu, C. (2016). Mapping macroalgal blooms in the yellow Sea and East China Sea using HJ-1 and landsat data: Application of a virtual baseline reflectance height technique. *Remote Sens. Environment.* 178, 113–126. doi: 10.1016/j.rse.2016.02.065

Xing, Q., Hu, C., Tang, D., Tian, L., Tang, S., Wang, X., et al. (2015). World's largest macroalgal blooms altered phytoplankton biomass in summer in the yellow Sea: Satellite observations. *Remote Sensing.* 7 (9), 12297–12313. doi: 10.3390/rs70912297

Xing, Q., Wu, L., Tian, L., Cui, T., Li, L., Kong, F., et al. (2018). Remote sensing of early-stage green tide in the yellow Sea for floating-macroalgae collecting campaign. *Mar. pollut. Bull.* 133, 150–156. doi: 10.1016/j.marpolbul.2018.05.035

Xing, Q., Zheng, X., Shi, P., Hao, J., Yu, D., Liang, S., et al. (2011). Monitoring "Green tide"in the yellow Sea and the East China Sea using multi-temporal and multi-source remote sensing images. *Spectrosc. Spectral. Analysis.* 31 (6), 1644–1647. doi: 10.3964/j.issn.1000-0593(2011)06-1644-04

Xu, Q., Zhang, H., Cheng, Y., Zhang, S., and Zhang, W. (2016). Monitoring and tracking the green tide in the yellow Sea with satellite imagery and trajectory model. *IEEE J. Selected. Topics. Appl. Earth Observ. Remote Sensing.* 9 (11), 5172–5181. doi: 10.1109/JSTARS.2016.2580000

Xu, Q., Zhang, H., Ju, L., and Chen, M. (2014). Interannual variability of *Ulva prolifera* blooms in the yellow Sea. *Int. J. Remote Sensing.* 35 (11-12), 4099–4113. doi: 10.1080/01431161.2014.916052

Ye, N., Zhang, X., Mao, Y., Liang, C., Xu, D., Zou, J., et al. (2011). 'Green tides' are overwhelming the coastline of our blue planet: taking the world's largest example. *Ecol. Res.* 26 (3), 477–485. doi: 10.1007/s11284-011-0821-8

Ye, N., Zhuang, Z., Jin, X., Wang, Q., Zhang, X., Li, D., et al. (2008). China Is on the tracking enteromorpha spp. forming green tide. *Nat. Precedings* 3, 1–10. doi: 10.1038/npre.2008.2352.1

Yu, C., Chen, L., Su, L., Fan, M., and Li, S. (2011). "Kriging interpolation method and its application in retrieval of MODIS aerosol optical depth," in *2011 19th International Conference on Geoinformatics*. (IEEE) 1–6. doi: 10.1109/GeoInformatics.2011.5981052

Zeng, C., Shen, H., Zhong, M., Zhang, L., and Wu, P. (2014). Reconstructing MODIS LST based on multitemporal classification and robust regression. *IEEE Geosci. Remote Sens. Lett.* 12 (3), 512–516. doi: 10.1109/LGRS.2014.2348651

Zhang, J., Clayton, M., and Townsend, P. (2014). Missing data and regression models for spatial images. *IEEE Trans. Ggeosci. Remote Sensing.* 53 (3), 1574–1582. doi: 10.1109/TGRS.2014.2345513

Zhang, C., Li, W., and Travis, D. (2007). Gaps-fill of SLC-off landsat ETM+ satellite image using a geostatistical approach. *Int. J. Remote Sensing.* 28 (22), 5103–5122. doi: 10.1080/01431160701250416

Zhang, H., Sun, D., Li, J., Qiu, Z., Wang, S., and He, Y. (2016). Remote sensing algorithm for detecting green tide in China coastal waters based on GF1-WFV and HJ-CCD data. *Acta Optica. Sin.* 36 (6), 601004. doi: 10.3788/AOS201636.0601004

Zhou, M., Liu, D., Anderson, D., and Valiela, I. (2015). Introduction to the special issue on green tides in the yellow Sea. *Estuarine. Coast. Shelf. Sci.* 163, 3–8. doi: 10.1016/j.ecss.2015.06.023

Zhou, Y., Zhou, B., and Gai, Y. (2014). *Ulva prolifera* monitoring study in the yellow Sea from multi-temporal remote sensing images. *Appl. Mechanics. Materials.* 675–677, 1201–1206. doi: 10.4028/www.scientific.net/AMM.675-677.1201

Zhu, W., Pan, Y., He, H., Wang, L., Mou, M., and Liu, J. (2011). A changing-weight filter method for reconstructing a high-quality NDVI time series to preserve the integrity of vegetation phenology. *IEEE Trans. Geosci. Remote Sensing.* 50 (4), 1085–1094. doi: 10.1109/TGRS.2011.2166965

frontiers | Frontiers in Marine Science

TYPE Original Research
PUBLISHED 18 October 2022
DOI 10.3389/fmars.2022.1003313

OPEN ACCESS

EDITED BY
Hui Zhao,
Guangdong Ocean University, China

REVIEWED BY
Yangfan Li,
Xiamen University, China
Changchun Huang,
Nanjing Normal University, China
Zhifeng Jin,
Jiangsu Land and Resources Research Center, China

*CORRESPONDENCE
Jiujuan Wang
jjuanwang@gmail.com

SPECIALTY SECTION
This article was submitted to Coastal Ocean Processes, a section of the journal Frontiers in Marine Science

RECEIVED 26 July 2022
ACCEPTED 28 September 2022
PUBLISHED 18 October 2022

CITATION
Yi L, Ma S, Tao S, Zhang J and Wang J (2022) Coastal landscape pattern optimization based on the spatial distribution heterogeneity of ecological risk.
Front. Mar. Sci. 9:1003313.
doi: 10.3389/fmars.2022.1003313

Coastal landscape pattern optimization based on the spatial distribution heterogeneity of ecological risk

Lin Yi[1], Sunjie Ma[1], Shiwei Tao[1], Jiyi Zhang[2] and Jiujuan Wang[3,4]*

[1]College of Earth Science, Chengdu University of Technology, Chengdu, China, [2]College of Geographic Science, Nantong University, Nantong, China, [3]Southern Marine Science and Engineering Guangdong Laboratory (Guangzhou), Guangzhou, China, [4]Shenzhen Institute of Advanced Technology, Chinese Academy of Sciences, Shenzhen, China

The increasingly intensified development of coastal cities causes excessive consumption of natural resources, leading to environmental damage and increasing conflict between development and ecological protection. In addition to emphasizing ecological development, planners should pay more attention to the practical optimization and regulation of the developed landscape pattern. Taking Dafeng as an example, this study constructs a landscape-pattern optimization method suitable for the spatial distribution heterogeneity of ecological risk-level units in the coastal zone. The study is based on (a) an analysis of the composition and evolution characteristics of Dafeng's coastal landscape elements, (b) the landscape pattern index of the ecosystem's overall risk assessment, and (c) the minimal cumulative resistance (MCR) model. The study uses an ecosystem service value to build a resistance model by analyzing the medium and high-risk composition and distribution characteristics of space unit elements. Finally, 23 ecological sources, 14 ecological nodes, and 17 ecological corridors (total length 169.63 km) were built. The optimized coastal zone landscape pattern jointly protects the landscape area of high ecological value by 462.02 km^2. The total ecological value is 105,01.71 million yuan. Landscape connectivity has been optimized, as well as the ecosystem's stability and total service value. The optimization method proposed in this paper can reduce the protection area and cost. The spatial optimization unit is highly targeted, providing new ideas for the coastal cities to implement their ecological development and protection strategies.

KEYWORDS

Coastal zone, ecological risk heterogeneity, landscape pattern optimization, MCR model, ecosystem service value (ESV)

1 Introduction

As a transitional zone connecting the sea and the land, the coastal zone is of great significance to the expansion of human living space due to its abundant natural resources and dynamic expandable land space (Knecht, 1975). However, the coastal zone is simultaneously affected by natural and human-made external disturbances from the sea and land (Hepcan et al., 2013; Rodrigues et al., 2021; Hoel et al., 2022), and its ecosystem is sensitive and fragile (Doney, 2010), especially in recent decades, due to increasing development. Its ecological problems have become prominent and have a significant impact on the global ecological environment (He and Silliman, 2019). Eco-environmental problems in coastal zones have received extensive attention (Kantamaneni et al., 2018; Rangel-Buitrago et al., 2020). The United Nations has proposed the decade of 2021–2030 as the Decade of Ocean Science for Sustainable Development (UNESCO, 2019; Dai, 2021), while the international scientific community has launched projects such as Future Earth Coasts (FEC, https://www.futureearthcoasts.org/). More and more attention is being paid to research on measures to ensure the sustainable development of coastal zones (Liu et al., 2020).

The research on sustainable development measures is gradually changing from monitoring and evaluating ecological problems in the early stages to optimizing and regulating research for different ecological problems (Li et al., 2019; Zhang et al., 2020; Anfuso et al., 2021; Yan et al., 2021). Some scholars have carried out landscape pattern optimization research on rural settlements (Qu et al., 2021), agricultural land, and wetlands (He and Chen, 2021) in the coastal zone, but less consideration is given to the spatial heterogeneity of human interference. The degree of human interference in the coastal zone shows spatial heterogeneous, so the landscape ecological optimization measures taken should follow this spatial heterogeneity, and focus on the spatial units that have a large degree of disturbance. Therefore, coastal landscape optimization should focus more on those spatial units that are more disturbed. It is also an inevitable trend in current regional sustainable development measures.

The landscape space is adjusted and combined to achieve maximum ecological benefits and regional sustainable development (Chen et al., 2014). In recent years, the minimum cumulative resistance model (MCR) (Li et al., 2015; Xu et al., 2021) has become more and more mature in landscape optimization. It analyzes the relationship between the internal units of the landscape through distance and resistance factors and comprehensively understands the relationship between landscape pattern, ecological process, and function (Dai et al., 2021; Wei et al., 2022). Although the construction of this model in some studies (Cui et al., 2022) considers the impact of human activities, less consideration has been given to the impact of on regional ecological risks and sustainable development (Chen et al., 2017a; Han et al., 2022). For this, based on the spatial heterogeneity of the coastal landscape ecological pattern, targeted optimization of the landscape pattern is more practical and less costly for improving the coastal ecological pattern and achieving regional sustainable development.

The study built a landscape-pattern optimization method considering the spatial distribution characteristics of human activity disturbance in the coastal zone based on an analysis of the spatial distribution characteristics of the structure, function and risk of coastal ecosystem. The study selected China's Dafeng District as an example for analysis. This paper aims to: (1) construct a low-cost ecological pattern optimization method based on an analysis of the current characteristics of the coastal zone's ecology; and (2) provide theoretical guidance for landscape ecological risk prevention and control and landscape-pattern optimization in the Dafeng coastal zone to afford new thoughts for implementing sustainable development strategies in coastal zones.

2 Materials and methods

2.1 Study area

Dafeng is located at 32°56'~33°36' N, 120°13'~120°56' E in the east of Jiangsu Province and borders the Yellow Sea to the east (Figure 1). It is a coastal plain formed by long-term siltation from the eastern inflow of the Yangtze and Yellow rivers to the sea. It has a total area of about 3008 km² and a coastline of 112 km. As a node for China's "coastal development" strategy and the integration of the Yangtze River Delta, it has seen increasingly intensified development and construction (Zhao et al., 2020). However, Dafeng also has rich mudflat wetland resources and contains the world's largest Milu deer nature reserve. The outlook for coordinating Dafeng's economic development and construction with wetland protection and construction is grim. Therefore, taking Dafeng as the study area is of great significance for studying the optimization method of ecological patterns in a coastal zone.

Six types of data were selected from 2000 to 2018: land cover; administrative division, GDEM; vegetation type; national average profit of agricultural products; grain crop cultivation area; and yield (Table 1). In view of the comparability of the research results to others, this study reclassified the land-cover types (Table 2, Figure 2) into paddy field, dry land, woodland, grassland, water, wetland, urban land, and bare land. The wetland type is composed of tidal flats, shoals, and swamps.

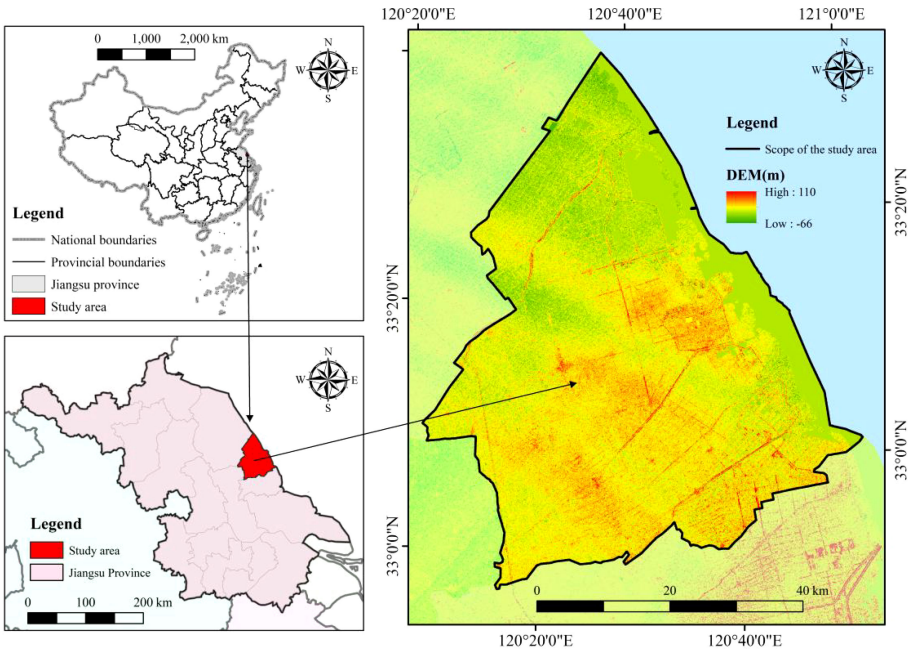

FIGURE 1
Study area.

2.2 Methodology

This study combined global and local perspectives and used a mixed-methods design to build a more refined optimization scheme for a coastal city (Figure 3). The whole landscape pattern optimization scheme is based on the ecological risk evaluation results, considering the spatial and temporal evolution characteristics of the landscape pattern in the coastal zone. The distribution area of various landscape types at different levels is analyzed according to the spatial distribution range of ecological risk assessment results at different levels. Then, the results of the spatial distribution characteristics of ecological service value estimations are combined. Finally, the landscape resistance value and ecological source value area threshold are calculated to optimize global and local patterns, respectively. An ecological corridor, landscape-type adjustment, ecological source identification, and ecological node construction form the coastal zone's final ecological landscape configuration scheme.

2.2.1 Estimation of ecological service value of coastal zone system based on modified equivalent factor

This study refers to the ecosystem service function value evaluation model (Robert et al., 1998) by the ecological service value equivalent factor method (Xie et al., 2015; Sun et al., 2019).

As the basis, modify the service value equivalent of woodland and grassland ecosystem services (as woodland is the only broad-leaved forest, take the basic broad-leaved forest equivalent; as grassland is the only meadow, take the basic meadow equivalent). The ecosystem service value of the

TABLE 1 Data sources.

Data type	Resolution (m)	Time	Source
Land cover	30	2000–2018	http://geodata.nnu.edu.cn/index.html
Administrative division	–	2015	https://www.resdc.cn/
ASTER GDEM V3	30	2019	http://nnu.geodata.cn:8008
1:1 000 000 China vegetation atlas	1000	2001	https://www.resdc.cn/
Official statistical yearbook (grain crop cultivation area, yield, etc.)	–	2000–2019	http://tjj.yancheng.gov.cn/
National average profit of agricultural products	–	2000–2019	Compilation of national agricultural product cost benefit data

TABLE 2 Land cover classification system.

Land cover type	Definition
Paddy field	Arable land with guaranteed water sources and irrigation facilities, which can be irrigated normally in normal years and used to grow aquatic crops such as rice and lotus roots, including arable land where rice and dryland crops are rotated.
Dry land	The cultivated land without irrigation water sources and facilities, and relying on natural precipitation to grow crops; and irrigation facilities, dry farmland that can be irrigated normally in normal years; to grow vegetables mainly cultivated land; leisure and resting land in normal rotation.
Woodland	Forestry land for growing trees, shrubs, bamboos, and coastal mangroves.
Grassland	All kinds of grasslands are dominated by growing herbs and cover more than 5%.
Water	Natural land waters and land for water conservancy facilities, except tidal flats, flats and marshes.
Wetland	Tidal flats, shoals, and swamps.
Urban land	Urban and rural residential areas and other land for industrial, mining, transportation, etc.
Bare land	Unused land, including difficult-to-use land.

standard unit area value equivalent factor, equal to 1/7 of the economic value of food production per unit area of farmland, is used to characterize and quantify the potential contribution capacity of different types of ecosystems to the ecological service function (Grimm et al., 2008; Xu et al., 2018; Guo et al., 2022). The corrected equivalent factor defines 1 km^2. The national average yield of farmland, the annual economic value of natural grain production, is 0.01. The ecological service value estimation method of a coastal zone system, based on a modified equivalent factor, is constructed as follows (Costanza et al., 1998; Xie et al., 2015; Xu et al., 2018):

$$ESV_j = \sum_k^n A_j \times VC_{jk} \quad (1)$$

In the formula, ESV_j is the total service value of the ecosystem j (yuan); and A_j is the area of the ecosystem (km^2); VC_{jk} is the economic value per unit area of the k-th species of ecological function of the ecosystem (yuan/km^2); n is the number of ecological service functions. The calculation method of VC_{jk} is as follows:

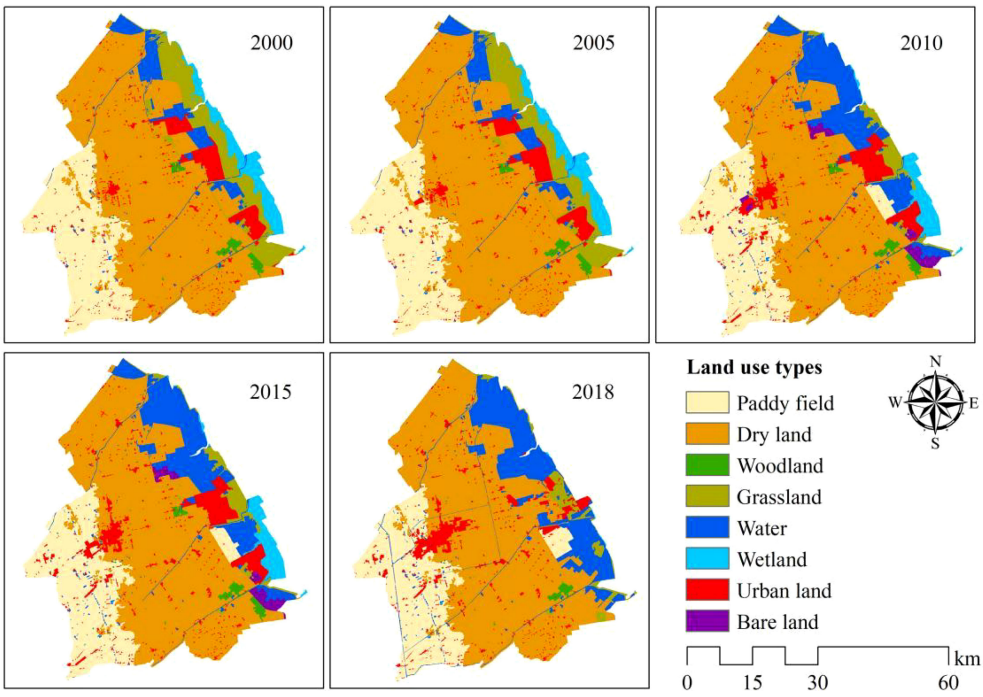

FIGURE 2
Landscape classification of Dafeng (2000–2018).

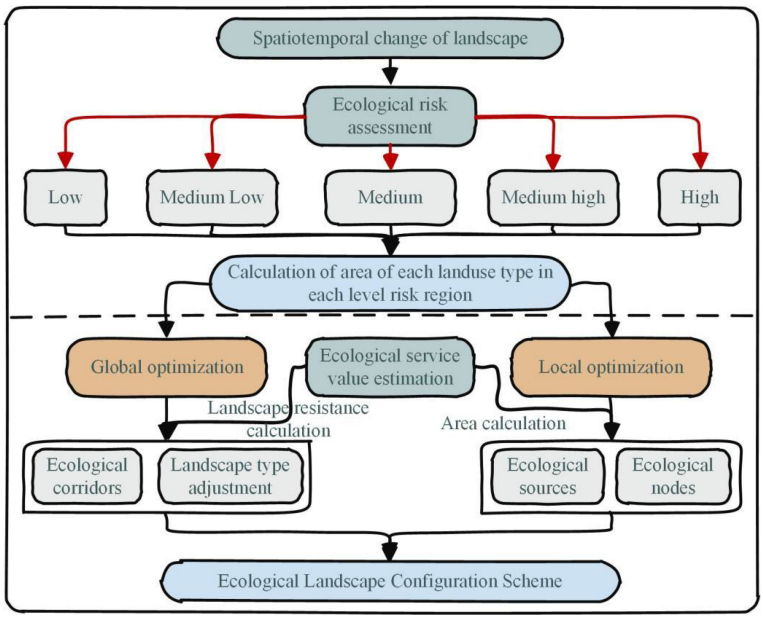

FIGURE 3
Method of landscape pattern optimization of the coastal city of this study.

$$VC_{jk} = Ef_k \frac{1}{7} \Sigma_{i=1}^{n} \frac{m_i p_i q_i}{M} \quad (2)$$

Ef_k is the modified equivalent factor of the ecosystem k (Table A2). The i is the crop type; $p_i$is the national average price of the i-th crop in a certain year (yuan/kg); q_i is the yield per unit area of the i-th crop (1000kg/km^2); m_i is the planting area of the i-th crop (km^2); M is the planting area (km^2) of the three main crops.

2.2.2 Landscape ecological risk assessment

The analysis of landscape pattern indexes can reflect the degree of human intervention on the natural landscape of the coastal zone (Chen et al., 2022) and is widely used in regional ecological risk assessment (Li et al., 2021; Pomara and Lee, 2021). This paper constructs an ecological risk-evaluation method based on the landscape fragmentation index, landscape separation index, landscape dominance index, and landscape vulnerability index to characterize the degree of the ecological service value loss of the coastal zone ecosystem when subjected to both natural and human-made interference (Zhang et al., 2020). The paper will divide the study into 3 km × km evaluation units, calculate the ecological risk index (ERI) of grid center elements, through the ordinary Kerry gold interpolation method of ecological risk index, and adopt the natural break-point grading method. ERI is divided into five levels (low, medium-low, medium, medium-high, and high); the higher the ERI value, the higher the ecological risk. The specific calculation formula (Zhang et al., 2020) is as follows:

$$ERI_k = \sum_{i=1}^{m} \frac{A_{ki}}{A_k} \times aC_i \times bN_i \times cD_i \times F_i \quad (3)$$

In the formula, k is the grid unit; i is the landscape type; m is the total number of landscape types. A_{ki} stands for the area of landscape i in the grid unit; A_k for the total area of the grid k; a, b, and c are the weights. According to the existing research experience combined with expert opinions (Zhang et al., 2014; Zhang et al., 2020), the weights are assigned 0.5, 0.3, and 0.2, respectively (where bare land is assigned 0.2, 0.3, and 0.5); $C_i$as the landscape fragmentation degree index, can reflect the process of landscape-type transition from continuous whole patches to complex discontinuous patches under natural or human interference. The larger the value, the lower the stability of the corresponding landscape ecosystem. N_i,as the landscape separation degree index, can reveal the complexity and integrity degree of the spatial distribution of a certain landscape type. The larger the values, the higher the separation degree. D_i, which is the landscape dominance index, refers to the importance of a certain type of landscape in the study area and its role in forming landscape patterns and maintaining pattern stability. The smaller the value, the greater the landscape diversity. F_i, as the landscape vulnerability index, can reflect the resistance ability of different landscape types to external interference. The greater the value, the smaller the ability to resist external interference. For F_i, the value is as follows. Landscape-type vulnerability was classified into six levels by the expert scoring method and normalized (Zhang et al., 2020). (That is, from high to low: bare land-6, water area and wetland-

5, cultivated land-4, grassland-3, woodland-2, urban land-1). Other landscape indexes are calculated as follows:

$$C_i = \frac{n_i}{A_i}, N_i = \frac{A}{2A_i}\sqrt{\frac{n_i}{A}}, D_i = u\frac{n_i}{N} + V\frac{A_i}{A} \quad (4)$$

Among them, A_i is the total area of the i-th landscape type; n_i is the total number of patches in the i-th-type landscape; A is the total landscape area. Based on the research experience of others and the actual research area, weights u and v are set at 0.6 and 0.4, respectively (Zhang et al., 2014).

2.2.3 Optimization of the urban ecosystem landscape pattern in the coastal zone

Promoting the sustainable development of the coastal zone requires its ecological processes to be healthy, stable, and safe. Different landscape types can be classified into "source" and "sink" based on the role of species, material, and energy flows in coastal zone ecosystems. Large woodland, grassland, wetland, and water areas can promote the development of landscape processes, namely "source"; others, such as biological production land and urban land, can "sink"; and various rivers and green corridors can transmit matter and energy. The source extraction requires integrating the landscape pattern continuity and service value per unit area, referring to the current ecological source extraction standard (Chen et al., 2017b).

The cumulative cost distance model can reflect the spatial trend of the source image element motion and can analyze the spatial operation of the landscape flow to explore ways and methods conducive to the regulation of the ecological process (Han et al., 2021). Based on Arc Map Desktop 10.1, Cost Distance and Cost Path modules, and fully considering factors such as landscape source, distance, and surface friction resistance, it is possible to construct a cumulative cost resistance model to express the spatial span characteristics of landscape type:

$$MCR = f_{min}\sum_{j=n}^{i=m}(D_{ij} \times R_i) \quad (5)$$

In the formula, *MCR* is the minimum cumulative resistance value; f is the positive function between *MCR*, and the variable ($D_{ij} \times R_i$); $D_{ij}$is the spatial distance that spreads from the source j to a point in space across the ecological surface i; $R_i$is the resistance to the direction of the source dispersal by the ecological surface i.

The medium-high-risk and high-risk area source constitute the "target"; the low-risk, medium-low-risk and medium-risk area source constitute the "ecological source." The landscape resistance depends on the landscape ecological service value — the higher the service value, the easier the landscape grid unit between material and energy transmission. The smoother the ecological flow, the smaller the landscape resistance, and vice versa. Therefore, in this study, the reciprocal of the unit ecological service value was taken as the resistance value cost to obtain the cumulative cost distance surface (Figure 9) of the landscape ecological function.

3 Results

3.1 Changes in the structure and function of a coastal ecosystem (2000–2018)

The overall structure of coastal ecosystem in Dafeng is composed of dry land, paddy field, water, urban land, grassland, wetland, woodland and bare land. In recent years (2000–2018), cultivated land (containing dry land and paddy field) has always been the dominant land type in Dafeng District, accounting for about 70% of the total area. Dry land is the largest component, accounting for about 50% of the total area, while paddy fields only account for about 20%. Landscape elements with high ecological service value have always accounted for a very small proportion (Figure 4). Overall, urban land and water have increased year by year. The water area increased from 145.49 km^2 to 402.84 km^2 and the area proportion increased by 9.63%. The area of urban land increased from 155.46 km^2 to 19265.39 km^2 from 2000 to 2015, and the proportion rose from 5.82% to 7.21%. The decrease in urban land from 2015 to 2018 is due to implementing the ecological red line protection plan and the promotion of the wetland restoration project in the ecological function area (Zhang et al., 2021a). The increases in these two landscape elements have been at the expense of decrease in wetland, grassland and woodland. They continued to decrease from 2000 to 2018, reducing 106.56 km^2, 179.57 km^2, and 13.62 km^2 The area proportion decreased by 3.99%, 6.72%, and 0.51%.

Spatial distribution from 2000 to 2018, including the factor transfer characteristics of different periods in space, shows typical sea-gradient characteristics (Figure 5) — namely, the conversion of frequent elements is mainly concentrated in the coastline strip space; which is close to the coastline internal space. This means that human activities here disturb the ecological environment more intensely. In the internal space, year by year, other characteristics of cultivated land transfer into urban land have been given priority with paddy field and dry land distribution. However, the spatial characteristics of element transfer in the strip space near the coastline were mainly concentrated in the southern region, and the transfer makes the spatial distribution of landscape elements become more broken. The main types of transfer were: ① woodland into water from 2000 to 2005, ②grassland into water, wetland into grassland, and bare land into paddy fields between 2005 and 2010, ③ bare land into woodland, and wetland into grassland from 2010 to 2015, ④dry land into woodland, bare land into water area, bare land into grassland, and grassland into urban

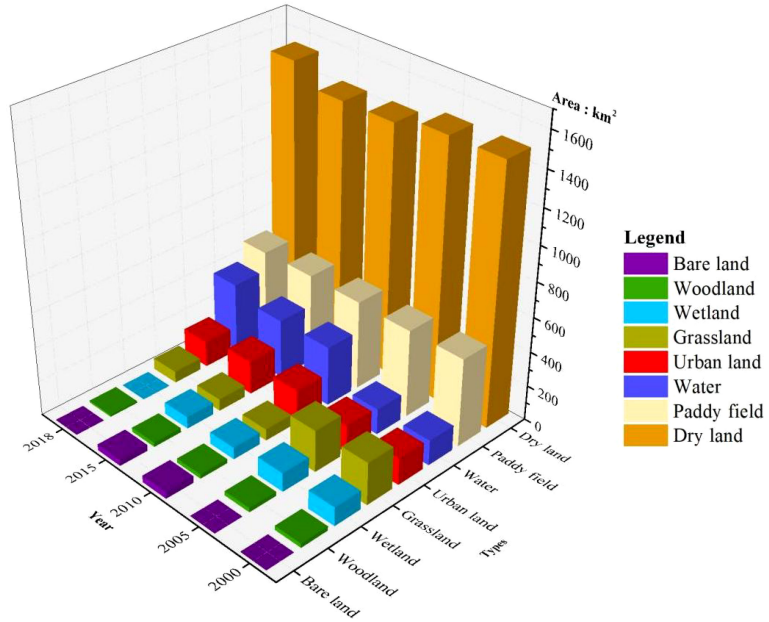

FIGURE 4
Changes in the proportion of land use types.

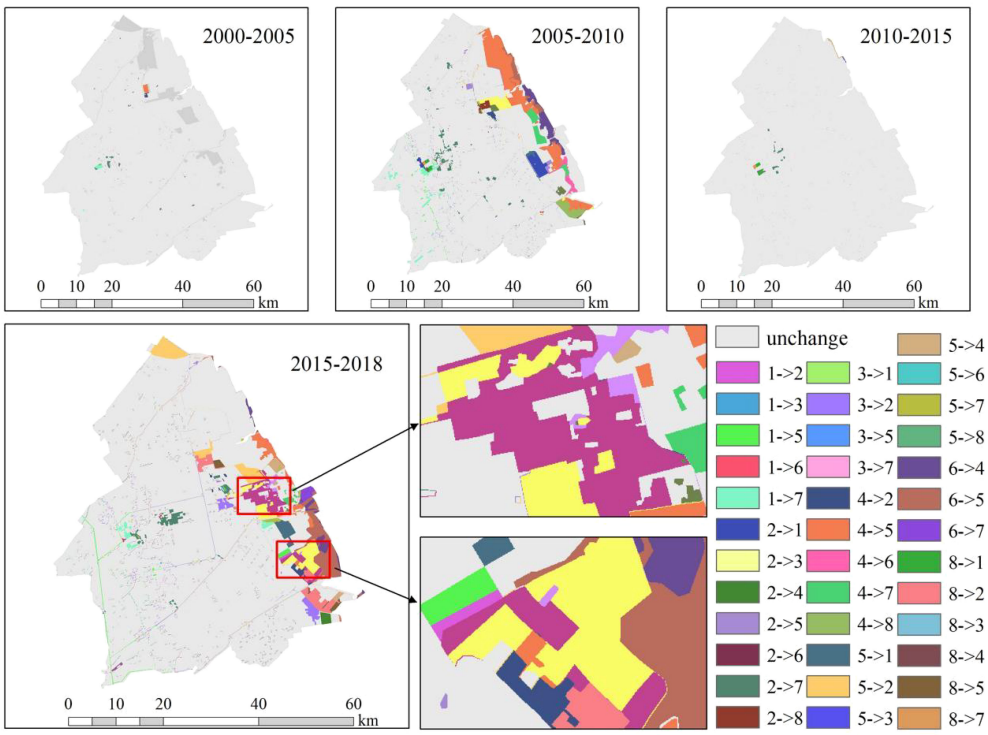

FIGURE 5
Land use types transfer from 2000 to 2018, Sankey diagram.

land from 2015 to 2018. Conversely, the transfer of features makes the spatial distribution of features in the northern area more continuous. The main types of transfer were grassland to water (2005-2010).

In summary, in addition to finding that sea reclamation is increasing, we find the embodiment of wetland ecological restoration in development.

3.2 Functional characteristics of coastal ecosystem services

The function of the coastal zone ecosystem (Figure 6) is seen from the analysis of the Dafeng ecological service value. In this study, wheat, rice, and corn from the largest sown area in Dafeng District were taken as the three main crops. The average data (Table A1) of price, yield per unit area, and sown area from 2000 to 2018 were counted. The unit price (Table A2) of the food production service function of each ecosystem was calculated according to formula 2. The ecological service value equivalent factor of urban land was 0, so the value of each ecological function service was 0 (Figure 6). In 2018, the value of ecological service per unit area in Dafeng District was in space. The landscape elements with high value were mainly concentrated in the offshore area but with discontinuous distribution, especially in the south, which was relatively broken, and there were elements with low ecological service value per unit area. The value was distributed away from the coastline to the inland area. The distribution of the total value of the ecosystem service functions of different land use types, and the overall value, ranked from large to small, was successively: water area> dry land> paddy field> wetland> grassland> woodland> bare land> urban land. From 2000 to 2018, the service value of the overall ecosystem in Dafeng showed a decreasing trend year by year, indicating that the ecosystem function was declining year by year.

3.3 Ecological risk assessment of Dafeng

Through the ecological risk assessment of Dafeng, the spatial units that should be optimized and adjusted are further defined. In the ecological risk assessment of Dafeng in 2018, the results (Figures 7, 8) show that the areas with risk levels of medium, medium-high, and high were concentrated in the eastern coastal strip areas; the intensive cultivated land and building areas in the central and western regions basically showed low risk or low-risk areas. The ecological risk presents a transition distribution from the west (low risk) to the east (high risk), which reflects the characteristics of strong aggregation and strong sea-gradient distribution of human activities in the coastal zone cities. The north and south of the coastal strip area are adjacent to Yancheng Red-crowned Crane Nature Reserve (①), Dafeng Milu National Nature Reserve (②), and Dongtai Huanghai Seaside National Forest Park (③) in Figure 8. To a certain extent, they will be affected by the higher-risk ecology in the east of Dafeng, so the group is potentially dangerously escalated. Therefore, the eastern medium-risk, medium-high, and high-risk areas are the key optimization areas.

From the different risk levels of landscape type area analysis (Figure 7), the high-risk unit spatial distribution water area accounts for 58.80%, urban land only 14.39%, and grassland 15.51%. The rest of the area accounts for less than 10%, hence the need to optimize the high-risk distribution area of water, urban land, and grassland-type landscape configuration and

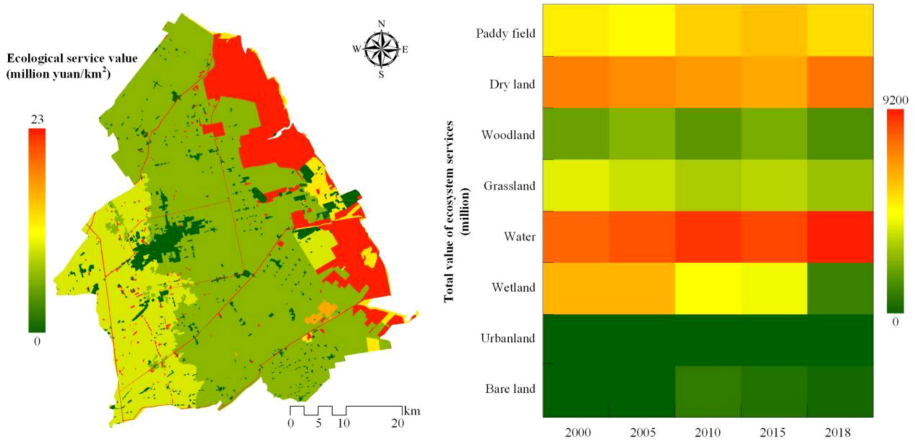

FIGURE 6
Spatiotemporal distribution of the total value of ecosystem services of each landscape type.

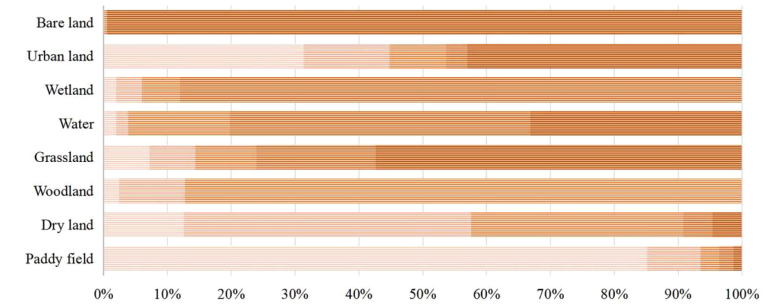

	Paddy field	Dry land	Woodland	Grassland	Water	Wetland	Urban land	Bare land
Low	60.56%	23.44%	0.06%	1.95%	3.50%	0.01%	10.48%	0.00%
Medium low	5.91%	83.96%	0.25%	1.95%	3.40%	0.02%	4.51%	0.00%
Medium	2.12%	61.97%	2.12%	2.58%	28.21%	0.03%	2.97%	0.01%
Medium high	1.59%	8.46%	0.00%	5.05%	83.36%	0.44%	1.10%	0.00%
High	0.92%	8.66%	0.00%	15.51%	58.80%	0.00%	14.39%	1.74%

FIGURE 7
The proportion of each type of landscape at various risk levels.

improve regional overall ecological function. The spatial distribution of medium-high risk units and the water area accounts for 83.36%. These are the main types of units that need to be optimized. In the medium-risk unit, dry land and water area account for relatively large areas, 61.97% and 28.21%, respectively — hence, the need to focus on optimizing the spatial pattern of these two landscape types.

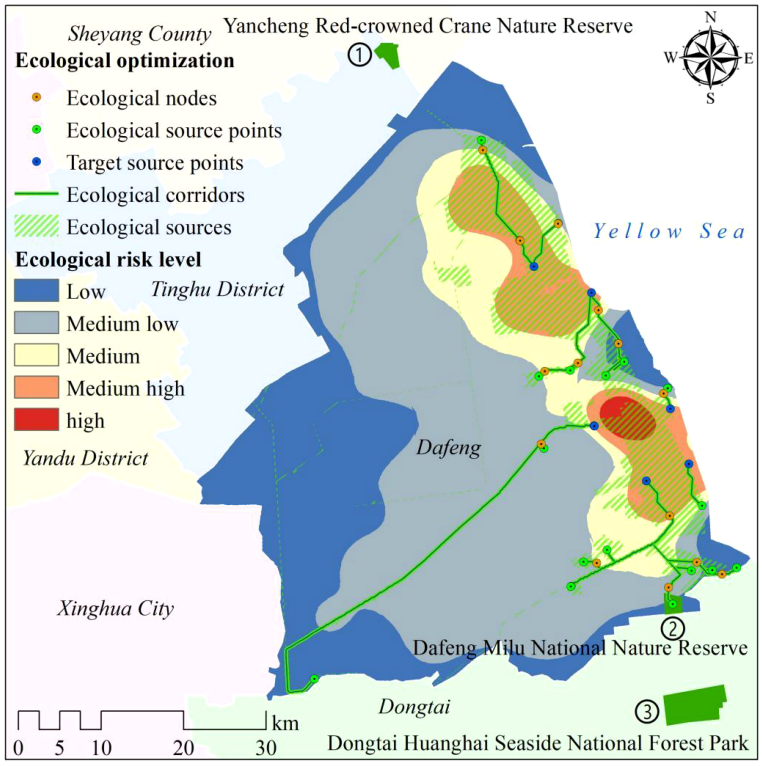

FIGURE 8
Ecological risk assessment and landscape pattern optimization (2018).

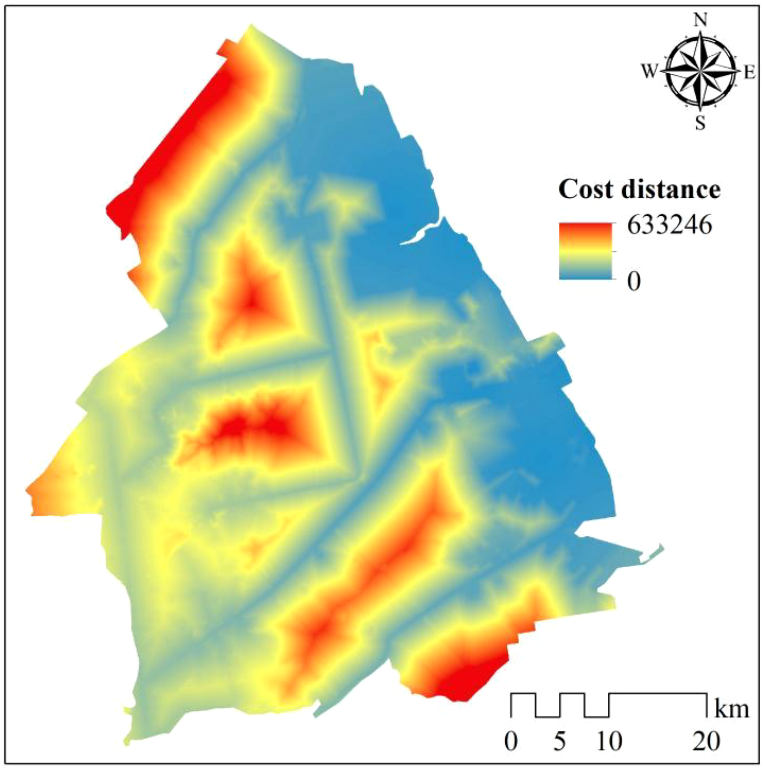

FIGURE 9
Landscape cumulative cost distance surface.

4 Coastal ecological optimization

The above analysis of the Dafeng District is a comprehensive example of coastal zone ecological pattern optimization. The final coastal urban ecological landscape configuration scheme is formed by:

- building the ecological source;
- building an ecological node in medium-risk, medium-high-risk, and high-risk area internal local optimization; and
- establishing an ecological corridor, adjusting the landscape-type configuration of the medium, medium-high, and high-risk areas across regional global optimization.

4.1 Creating ecological sources

Ecological sources have a certain spatial expansion and continuity, which is an important landscape component to promote the development of the landscape process (Chen et al., 2008). After merging the relatively aggregated small spots, 23 sources (Table 3, Figure 8) were built:

- the area of each source was more than 0.4 km^2, considering the study scale and the continuity of the landscape pattern, and based on multiple trials;
- the service value per unit area of each source was high;
- landscape type had priority with grassland and water system, which all cover the low, medium-low, medium and medium-high level ecological risk area;
- the spatial distribution was concentrated in the east and southeast;
- a small part of the source was distributed in the central and west, mainly for long and narrow river system sources, but overall distribution was uneven and connectivity poor;
- water source was the largest area, followed by wetland source — 326.20 km^2 and 125.99 km^2, respectively; they accounts for 57% and 22% of the total ecological source area, respectively.
- the eastern and western sources mainly relied on rivers, ditches, and corridors for material and energy exchange, and the interaction capacity between sources and places was not strong.

From the perspective of the source area, the share of woodland, grassland, and other landscape types should be increased. The spatial neighborhood of a certain scale of ecological source should be maintained to ensure the input and connectivity of the "source" in the process of "source-sink" ecological flow.

4.2 Building ecological corridors

Ecological corridors refer to the linear and banded landscape elements that act as channels or barriers. They are a vital bridge between the "sources" for the diffusion of species and material and energy flow (Zhang et al., 2020).

The landscape pattern of the eastern coastal area of Dafeng is broken, the landscape type of the central and western regions is relatively unbroken, and the connectivity between the eastern landscape unit and the western cultivated land and aquaculture ponds is not strong. The ecological corridor should be strengthened, and the connectivity of landscape elements, especially between sources, should be enhanced (Table 4). The low value cumulative consumption distance is mainly distributed in the east strip areas near the coastline. The overall high-resistance values are in the central and western regions, while the few low-resistance values are mainly distributed along the water system (Figure 9). A stronger ecological corridor is required between cultivated land, grassland, and coastal areas in the central and western regions.

Therefore, based on the combination of the landscape characteristics, determine the minimum cost path of the landscape functional flow operation, and build 17 ecological corridors, four of which are already existing ones that need to be transformed and repaired (Figure 8).

4.3 Building ecological nodes

Identifying and constructing ecological nodes can help increase the connectivity of a landscape ecological network, which will maintain the performance of the landscape ecological function and regional sustainable development (Zhang et al., 2020). Therefore, any weak ecological function points in the ecological corridor (i.e., those that have a large spatial distance span, making it difficult for species to spread their energy and where there is no material circulation) should be extracted. Fourteen ecological nodes were created in these areas (Table 3), including 2 low-risk areas, 5 medium-low-risk areas, 5 medium-risk areas, and 2 medium- high-risk areas.

To increase the connectivity of the landscape ecological network, resist external interference and impact, and improve the stability of landscape function:

- reference hydrological analysis tools, based on the cumulative cost distance surface, through multiple experiments to determine the optimal threshold extraction landscape pattern resistance surface "ridge line" and its intersection with the ecological corridor;
- extract the ecological flow running minimum cost path and maximum cost path intersection;
- refer to the previous landscape pattern characteristic analysis results to determine the spatial distribution of the ecological node (Figure 8).

4.4 Configuration scheme for landscape types

The essence of the landscape function is to maintain the spatial effects between adjacent landscape elements and the respective edge effects through landscape flow (Zhang et al., 2020). From the distribution of ecological resistance (Table 3), the resistance value of urban land and bare land is highest, followed by woodland. To avoid direct conflict with the spatial pattern of the landscape function, grassland, water and other landscape types can be configured in the vicinity of urban lands. It can act as a buffer role for the high-resistance landscape, contributing to the maintenance and coordination of ecological functions. Considering that the aquaculture ponds are the second step in soil desalination, and are close to the coastline, the low-cost and high-effect salt-resistant plants and protective woodlands can be configured according to the surrounding soil

TABLE 3 Ecological source and risk level.

Ecological source type	Ecological risk level					Source area (km^2)/ratio
	Low	Medium-low	Medium	Medium-high	High	
Woodland source	–	1	1	–	–	24.11/4%
Grassland source	1	3	2	1	–	91.72/16%
Water source	4	4	1	2	–	326.20/57%
Wetland source	–	–	–	3	–	125.99/22%
Ecological node	**2**	**5**	**5**	**2**	–	–

TABLE 4 Landscape ecological resistance value.

Types	Landscape types								Total
	Paddy field	Dry land	Wood land	Grass land	Water	Wetland	Urban land	Bare land	
Percentage of unit ecosystem service value (%)	4.06	1.78	10.19	5.07	55.76	23.09	0.00	0.05	100
Resistance value	24.62	56.18	9.82	19.71	1.79	4.33	100.00*	100.00*	–

*The ecological resistance with zero proportion of ecosystem service function value is the largest, which is set to 100.

characteristics of the aquaculture ponds to prevent pollutants from being directly discharged into offshore areas.

Arrange woodland and grassland around agricultural land; select salt-tolerant cash crops such as sea buckthorn, wolfberry, and jujube for saline land for ecological desalination.

5 Discussion

Coastal zone resources and location advantages are prominent, and coastal zone development such as beach reclamation and port city construction play a significant role in the economic development of various countries (Chen et al., 2018). However, the sensitivity of the coastal zone makes its ecological environment vulnerable to human activities, excessive consumption of natural resources, and environmental damage, exacerbating the contradiction between development and sustainable development (Cui et al., 2021). In recent years, various countries and global international organizations have paid more attention to the ecologically sustainable development of coastal zones (Duxbury and Dickinson, 2007; Göran and Karl-Henrik, 2017; Pradhan et al., 2017), with more emphasis on ecological development in coastal-zone planning (Zhang et al., 2021b). The optimization of the landscape ecological pattern of the coastal-developed zone also deserves attention (Wang et al., 2021). In addition to the current macro-optimization strategy, more practical and feasible targeted optimization solutions are required.

This paper took Dafeng District as an example. Based on an understanding of the overall ecosystem structure and function evolution characteristics, it determined the spatial distribution and element composition of different levels of risk units to establish a global and local landscape ecological pattern optimization scheme for different spatial unit levels. According to the above analysis, Dafeng, as an important node in China's coastal zone development strategy, continued to strengthen development efforts from 2000 to 2018. The reclamation-based development efforts of the coastal zone also continued to strengthen. However, high ecological service value elements such as coastal wetlands and woodland were largely sacrificed (Zhao et al., 2020). The research results are consistent. The reclamation and development of tidal flat wetlands and urban economic construction have transformed coastal wetlands into cultivated land, aquaculture pools, and urban land, of which aquaculture pools account for the largest proportion. At the same time, the conversion of some bare land and grassland into woodland also reflects the Chinese government's ecological development strategy. However, the gradually increasing landscape fragmentation still makes the structure and function of the ecosystem in Dafeng, especially near the coastal area, decline year by year, which seriously damages the ecological service value of the strip in the area near the coastline, showing a dense situation of intermediate, middle, and high-level ecological risks.

This paper uses the MCR model to combine the ecosystem service value of this area and conducts local and global optimization by constructing ecological sources, ecological nodes, ecological corridors, and landscape-type configuration. Compared with the unoptimized ecological layout, the optimized landscape elements' connectivity and ecological stability are stronger, with a total value of ecological protection of 105,01.71 million yuan. Thus, this paper's method can improve the connectivity and stability of landscape elements in the medium-risk, medium-high-risk and high-risk areas in a targeted manner, reducing the protection area and cost. It can also balance protection and development and provide new ideas for implementing ecological development and protection strategies for coastal urbanization.

The coastal area of Dafeng is muddy due to the rich wetland resources and is greatly disturbed by human activities. As a result, it is undergoing complex and dynamic changes. Only the value and area were considered in determining the importance of the plaque, and factors such as the morphology and geographical location of the origin were under-considered. In future research, the value of ecological service and the evolution form of the coastal wetland landscape should be considered together when constructing the resistance surface model. At the same time, the actual process of optimizing the landscape pattern also involves the roads and the habitat of the key protected species, so the optimization scheme needs to be further refined and adjusted according to the specific regional situation.

6 Conclusion

This study constructed a coastal zone landscape ecological pattern optimization method by:

- taking Dafeng District as an example to analyze the coastal zone ecosystem structure, functional evolution characteristics, and the spatial distribution characteristics of ecological risk, and
- combined the MCR model and the spatial distribution of ecosystem service values.

The results show that the landscape ecological risk in the Dafeng District is distributed in a sea-step gradient in space. The medium, medium-high, and high-risk areas are mainly concentrated in the strip area near the coastline, where human interference is intense. In this paper, through global and local optimization of risk-intensive distribution areas, 26 ecological sources, 14 ecological nodes, and 17 ecological corridors were constructed with a total area of 462.02km^2. After optimization, the total ecological value of the coastal ecosystem protection is 10,5,01.71 million yuan, and the landscape connectivity has also been greatly improved. The optimization method proposed in this paper is more targeted toward the coastal zone ecological landscape pattern, and it is more beneficial to improving regional landscape pattern connectivity and the overall value of the ecosystem service.

Data availability statement

The original contributions presented in the study are included in the article/supplementary material. Further inquiries can be directed to the corresponding author.

Author contributions

Conceptualization, LY, JW, and JZ. Methodology, LY and SM. Writing—original draft preparation, SM, ST, and LY. Writing—review and editing, LY, SM, ST, JZ, and JW. Visualization, JW, SM, and ST. All authors have read and agreed to the published version of the manuscript.

Funding

This study was financially supported by the National Natural Science Foundation of China (42230406), the National Natural Science Foundation of China (41801223) and the Fundamental Research Foundation of Shenzhen Technology and Innovation Council (Project No: JCYJ20190806170814498).

Acknowledgments

We acknowledge the data support from Yangtze River Delta Science Data Center, National Earth System Science Data Center, National Science & Technology Infrastructure of China (http://nnu.geodata.cn:8008).

Conflict of interest

The authors declare that the research was conducted in the absence of any commercial or financial relationships that could be construed as a potential conflict of interest.

Publisher's note

References

Anfuso, G., Postacchini, M., Di, L. D., and Benassai, G. (2021). Coastal Sensitivity/Vulnerability characterization and adaptation strategies: A review. *J. Mar. Sci. Eng.* 9 (1), 72. doi: 10.3390/jmse9010072

Chen, L. D., Fu, B. J., and Zhao, W. W. (2008). Source-sink landscape theory and its ecological significance. *Front. Biol. China* 3 (2), 131–136. doi: 10.1007/s11515-008-0026-x

Chen, Y. H., Li, G. S., Cui, L. L., Li, L. J., He, L., and Ma, P. P. (2022). The effects of tidal flat reclamation on the stability of the coastal area in the jiangsu province, China, from the perspective of landscape structure. *Land* 11, 421. doi: 10.3390/land11030421

Chen, L. D., Li, X. Z., Fu, B. J., Xiao, D. N., and Zhao, W. W. (2014). Development history and future research priorities of landscape ecology in China. *Acta Ecologica Sin.* 34 (12), 3129–3141. doi: 10.5846/stxb201405040878

Chen, X., Peng, J., Liu, Y. X., Yang, Y., and Li, G. C. (2017b). Constructing ecological security patterns in yunfu city based on the framework of importance-Sensitivity-Connectivity. *Geographical Res.* 3, 471–484. doi: 10.11821/dlyj201703006

Chen, L., Ren, C. Y., Zhang, B., Li, L., Wang, Z. M., and Song, K. S. (2018). Spatiotemporal dynamics of coastal wetlands and reclamation in the Yangtze

estuary during past 50 years, (1960s–2015). *Chin. Geographical Sci.* 28 (03), 386–399. doi: 10.1007/s11769-017-0925-3

Chen, L. L., Thapa, B., Kim, J., and Yi, L. (2017a). Landscape optimization in a highly urbanized tourism destination: An integrated approach in nanjing, China. *Sustainability* 9 (12), 2364. doi: 10.3390/su9122364

Costanza, R., d'Arge, R., de Groot, R., Farber, S., Grasso, M., Hannon, B., et al. (1998). The value of the world's ecosystem services and natural capital. *Ecol. Economics* 25 (1), 3–15. doi: 10.1016/S0921-8009(98)00020-2

Cui, X., Deng, W., Yang, J., Huang, W., and de Vries, W. T. (2022). Construction and optimization of ecological security patterns based on social equity perspective: A case study in wuhan, China. *Ecol. Indic.* 136, 108714. doi: 10.1016/j.ecolind.2022.108714

Cui, L. L., Li, G. S., Chen, Y. H., and Li, L. J. (2021). Response of landscape evolution to human disturbances in the coastal wetlands in northern jiangsu province, China. *Remote Sens.* 13 (11), 2030. doi: 10.3390/rs13112030

Dai, M. H. (2021). "Boundary regions: Land-ocean continuum and air-Sea interface," in *Integrated ocean carbon research: a summary of ocean carbon research, and vision of coordinated ocean carbon research and observations for the next decade* (Paris: The Intergovernmental Oceanographic Commission of UNESCO (UNESCO-IOC), 14–15.

Dai, L., Liu, Y. B., and Luo, X. L. (2021). Integrating the MCR and DOI models to construct an ecological security network for the urban agglomeration around poyang lake, China. *Sci. Total Environ.* 754, 141868. doi: 10.1016/j.scitotenv.2020.141868

Doney, S. C. (2010). The growing human footprint on coastal and open-ocean biogeochemistry. *Science* 328, 985, 1512–1516. doi: 10.1126/science.1185198

Duxbury, J., and Dickinson, S. (2007). Principles for sustainable governance of the coastal zone: In the context of coastal disasters. *Ecol. Economics* 63 (2–3), 319–330. doi: 10.1016/j.ecolecon.2007.01.016

Göran, I. B., and Karl-Henrik, R. (2017). A framework for strategic sustainable development. *J. Cleaner Production* 140, 17–31. doi: 10.1016/j.jclepro.2015.10.121

Grimm, N. B., Faeth, S. H., Golubiewski, N. E., Redman, C. L., Wu, J., Bai, X., et al. (2008). Global change and the ecology of cities. *Science* 319. doi: 10.1126/science.1150195

Guo, X. M., Fang, C. L., Mu, X. F., and Chen, D. (2022). Coupling and coordination analysis of urbanization and ecosystem service value in Beijing-Tianjin-Hebei urban agglomeration. *Ecol. Indic.* 137, 108782. doi: 10.1016/j.ecolind.2022.108782

Han, Y., Yu, C. Y., Feng, Z., Du, H. C., Huang, C. S., and Wu, K. N. (2021). Construction and optimization of ecological security pattern based on spatial syntax classification–taking ningbo, China, as an example. *Land* 10, 380. doi: 10.3390/land10040380

Han, R. Y., Zhao, Z. P., Xiao, N. W., Shi, N. N., Sun, G., and Gao, X. Q. (2022). Construction of ecological security pattern in Beijing city based on minimum resistance model. *Bull. Soil Water Conserv.* 42 (3), 95–102. doi: 10.13961/j.cnki.stbctb.20220518.001

Hu, Q. Y., and Chen, S. L. (2021). Optimizing the ecological networks based on the supply and demand of ecosystem services in xiamen-Zhangzhou-Quanzhou region. *J. Natural Resour.* 36 (2), 342–355. doi: 10.31497/zrzyxb.20210206

Hepcan, S., Hepcan, C. C., Ozkan, K., and Kocan, B. M. (2013). Analyzing landscape change and urban sprawl in a Mediterranean coastal landscape: A case study from izmi, Turkey. *J. Coast. Res.* 29, 301–310. doi: 10.2112/JCOASTRES-D-11-00064.1

He, Q., and Silliman, B. R. (2019). Climate change, human impacts, and coastal ecosystems in the anthropocene. *Curr. Biol.* 29 (19), R1021–R1035. doi: 10.1016/j.cub.2019.08.042

Hoel, P., Fredston, A., and Halpern, B. S. (2022). An evaluation framework for risk of coastal marine ecological diversity loss from land-based impacts. *Front. Mar. Sci.* 9, 796050. doi: 10.3389/fmars.2022.796050

Kantamaneni, K., Phillips, M., Thomas, T., and Jenkins, R. (2018). Assessing coastal vulnerability: Development of a combined physical and economic index. *Ocean Coast. Manage.* 158, 164–175. doi: 10.1016/j.ocecoaman.2018.03.039

Knecht, R. W. (1975). Coastal zone management. *Science* 187 (4179), 789–790. doi: 10.1126/science.187.4179.789-a

Li, X., Li, S., Zhang, Y., O'Connor, P. J., Zhang, L., and Yan, J. (2021). Landscape ecological risk assessment under multiple indicators. *Land* 10, 739. doi: 10.3390/land10070739

Li, F., Ye, Y. P., Song, B. W., and Wang, R. S. (2015). Evaluation of urban suitable ecological land based on the minimum cumulative resistance model: A case study from Changzhou, China. *AEcological Modelling* 318, 194–203. doi: 10.1016/j.ecolmodel.2014.09.002

Li, Q. P., Zhang, Z. D., Wan, L. W., Yang, C. X., Zhang, J., Ye, C., et al. (2019). Landscape pattern optimization in ningjiang river basin based on landscape ecological risk assessment. *Acta Geographica Sin.* 74 (7), 1420–1437. doi: 10.11821/dlxb201907011

Liu, R. J., Pu, L. J., Zhu, M., Huang, S. H., and Jiang, Y. (2020). Coastal resource-environmental carrying capacity assessment: A comprehensive and trade-off analysis of the case study in jiangsu coastal zone, Eastern China. *Ocean Coast. Manage.* 186, 105092. doi: 10.1016/j.ocecoaman.2020.105092

Pomara, L. Y., and Lee, D. C. (2021). The role of regional ecological assessment in quantifying ecosystem services for forest management. *Land* 10, 725. doi: 10.3390/land10070725

Pradhan, P., Costa, L., Rybski, D., Lucht, W., and Kropp, J. P. (2017). A systematic study of sustainable development goal (SDG) interactions. *Earth's Future* 5, 1169–1179. doi: 10.1002/2017EF000632

Qu, M., Zhou, Y. W., Cao, F. C., and Li, X. J. (2021). Layout optimization of rural residential land in the yellow Sea based on theory of landscape security pattern–a case study on pulandian district in dalian city of liaoning province. *Res. Soil Water Conserv.* 28 (1), 228–233, 241. doi: 10.13869/j.cnki.rswc.2021.01.029

Rangel-Buitrago, N., Neal, W. J., and de Jonge, V. N. (2020). Risk assessment as tool for coastal erosion management. *Ocean Coast. Manage.* 186, 105099. doi: 10.1016/j.ocecoaman.2020.105099

Rodrigues, E., Cohen, M. C. L., Liu, K. B., Pessenda, L. C. R., Yao, Q., Ryu, J. H., et al. (2021). The effect of global warming on the establishment of mangroves in coastal Louisiana during the Holocene. *Geomorphology* 381, 107648. doi: 10.1016/j.geomorph.2021.107648

Sun, Y. X., Liu, S. L., Dong, Y. H., An, Y., Shi, F. N., Dong, S. K., et al. (2019). Spatio-temporal evolution scenarios and the coupling analysis of ecosystem services with land use change in China. *Sci. Total Environ.* 681 (1), 211–225. doi: 10.1016/j.scitotenv.2019.05.136

UNESCO (2019) *United nations decade of ocean science for sustainable development, (2021–2030)*. Available at: https://www.oceandecade.org/.

Wang, X. X., Xiao, X. M., Xu, X., Zou, Z. H., Chen, B. Q., Qin, Y. W., et al. (2021). Rebound in china's coastal wetlands following conservation and restoration. *Nat. Sustainability* 4, 1076–1083. doi: 10.1038/s41893-021-00793-5

Wei, Q. Q., Halike, A., Yao, K. X., Chen, L. M., and Balati, M. (2022). Construction and optimization of ecological security pattern in ebinur lake basin based on MSPA-MCR models. *Ecol. Indic.* 138, 108857. doi: 10.1016/j.ecolind.2022.108857

Xie, G. D., Zhang, C. X., Zhang, L. M., Chen, W. H., and Li, S. M. (2015). Improvement of the evaluation method for ecosystem service value based on per unit area. *J. Natural Resour.* 30 (8), 1243–1254. doi: 10.11849/zrzyxb.2015.08.001

Xu, W. X., Wang, J. M., Zhang, M., and Li, S. J. (2021). Construction of landscape ecological network based on landscape ecological risk assessment in a Large-scale opencast coal mine area. *J. Cleaner Production* 286, 125523. doi: 10.1016/j.jclepro.2020.125523

Xu, Z. H., Wei, H. J., Fan, W. G., Wang, X. C., Huang, B. L., Lu, N. C., et al. (2018). Energy modeling simulation of changes in ecosystem services before and after the implementation of a grain-for-Green program on the loess plateau–a case study of the zhifanggou valley in ansai county, shaanxi province, China. *Ecosystem Serv.* 31, 32–43. doi: 10.1016/j.ecoser.2018.03.013

Yan, Y. C., Ju, H. R., Zhang, S. R., and Chen, G. K. (2021). The construction of ecological security patterns in coastal areas based on landscape ecological risk assessment–a case study of jiaodong peninsula, China. *Int. J. Environ. Res. Public Health* 18, 12249. doi: 10.3390/ijerph182212249

Zhang, W., Chang, W. J., Zhu, Z. C., and Hui, Z. (2020). Landscape ecological risk assessment of Chinese coastal cities based on land use change. *Appl. Geogr.* 117, 102174. doi: 10.1016/j.apgeog.2020.102174

Zhang, Z., Hu, B. Q., and Qiu, H. H. (2021a). Comprehensive assessment of ecological risk in southwest guangxi-beibu bay based onDPSIR Model and OWA-GIS. *Ecol. Indic.* 132, 108334. doi: 10.1016/j.ecolind.2021.108334

Zhang, X. B., Shi, P. J., Luo, J., Liu, H. L., and Wei, W. (2014). The ecological risk assessment of arid inland river basin at the landscape scale: A case study on shiyang river basin. *J. Natural Resour.* 29 (03), 410–419. doi: 10.11849/zrzyxb.2014.03.005

Zhang, S. S., Zhang, L., Chen, T., Dong, Y. W., Zhu, X. D., and Qi, L. Y. (2021b). Spatial variation and optimization of ecological carrying capacity in jiangsu coastal area, China. *Chin. J. Appl. Ecol.* 32 (6), 2158–2168. doi: 10.13287/j.1001-9332.202106.015

Zhao, X. D., Wang, J., Guo, B. S., Zhai, T. L., and Liu, J. J. (2020). Construction land expansion, utilization efficiency and decoupling relationship in coastal area–a case study of dafeng district of jiangsu province. *Res. Soil Water Conserv.* 27 (05), 340–348. doi: 10.13869/j.cnki.rswc.2020.05.043

10.3389/fmars.2022.1003313

Appendix

TABLE A1 Crop yield, area and national average selling price.

Crop information	Crop type	Year				
		2000	2005	2010	2015	2018
Production (1000kg/km)	Wheat	510.50	546.20	603.10	595.30	564.30
	Rice	829.70	828.70	903.50	921.80	921.60
	Corn	683.00	564.10	690.10	667.60	654.00
Planting area (km^2)	Wheat	368.30	252.20	419.70	489.70	524.00
	Rice	193.60	247.60	288.00	305.30	396.20
	Corn	152.00	111.10	201.60	203.30	231.60
Sales price (yuan/kg)	Wheat	1.06	1.38	1.98	2.33	2.24
	Rice	1.03	1.55	2.36	2.76	2.59
	Corn	0.86	1.11	1.86	1.88	1.76

TABLE A2 Ecosystem service value per unit area.

Ecosystem services		Ecosystem classification						
		I	II	III	IV	V	VI	VII
Provisioning services	A	2461.26	1538.28	524.83	398.14	1447.80	922.97	0.00
	B	162.88	723.90	1194.43	597.22	416.24	904.87	0.00
	C	4759.63	36.19	615.31	325.75	15002.80	4687.24	0.00
Regulating Services	D	2008.82	1212.53	3927.15	2063.11	1393.51	3438.52	36.19
	E	1031.56	651.51	11763.36	5465.44	4144.32	6515.09	0.00
	F	307.66	180.97	3492.81	1809.75	10044.10	6515.09	18.10
	G	4922.51	488.63	8578.20	3999.54	185028.53	43850.17	54.29
Supporting Services	H	18.10	1864.04	4795.83	2515.55	1683.06	4180.52	36.19
	I	343.85	217.17	361.95	199.07	126.68	325.75	0.00
	J	380.05	235.27	4361.49	2298.38	4614.85	14242.71	36.19
Cultural Services	K	162.88	108.58	1918.33	1013.46	3420.42	8560.10	18.10
Total		16559.19	7257.09	41533.69	20685.41	227322.32	94143.04	199.06

A: Food production, B: Material production, C: Water supply, D: Gas regulation, E: Climate control, F: Purify environment, G: Hydrological regulation, H: Soil conservation, I: Nutrients cycle maintenance, J: Biodiversity, K: Aesthetic Landscape, I: Paddy field, II: Dry land, III: Woodland, IV: Grass land, V: Water system, VI: Wetland, VII: Barren land.

frontiers | Frontiers in Marine Science

TYPE Original Research
PUBLISHED 17 November 2022
DOI 10.3389/fmars.2022.1034876

OPEN ACCESS

EDITED BY
Meilin Wu,
South China Sea Institute of Oceanology (CAS), China

REVIEWED BY
Kaizhi Li,
South China Sea Institute of Oceanology (CAS), China
Changling Ding,
Tianjin university of Science &Technology, China

*CORRESPONDENCE
Peng Xiang
xiangpeng@tio.org.cn
Heshan Lin
linheshan@tio.org.cn

†These authors share first authorship

SPECIALTY SECTION
This article was submitted to Coastal Ocean Processes, a section of the journal Frontiers in Marine Science

RECEIVED 02 September 2022
ACCEPTED 25 October 2022
PUBLISHED 17 November 2022

CITATION
Wang Y, Chen X, Lin Y, Zhang S, Chang L, Tang X, Xiang P and Lin H (2022) Potential risk from and prevention of phytoplankton outbreaks in blocking the cooling water system in a nuclear power plant on the Southeast China coast. *Front. Mar. Sci.* 9:1034876. doi: 10.3389/fmars.2022.1034876

Potential risk from and prevention of phytoplankton outbreaks in blocking the cooling water system in a nuclear power plant on the Southeast China coast

Yu Wang[1†], Xiaoyin Chen[1†], Yingyue Lin[2], Shuyi Zhang[1], Lin Chang[1], Xiaoming Tang[1], Peng Xiang[1*] and Heshan Lin[1*]

[1]Third Institute of Oceanography, Ministry of Natural Resources, Xiamen, China, [2]Fujian Fuqing Nuclear Power Company Limited, Fuqing, China

The invasion or aggregation of marine biota in coastal waters has become a common problem, threatening the safety of cooling water systems in the context of environmental and climate changes. However, studies on issues of coastal nuclear power plants from the view of marine ecology have mostly focused on the thermal effluent, entrainment effect on organisms, residual chlorine, radioactivity, etc. There is a lack of information on the safety of cooling water systems in nuclear power plants blocked by marine biota. Based on field and historical datasets, this study screened phytoplankton species that may potentially block the cooling water system of the Fuqing nuclear power plant on the Southeast China coast, identified the phytoplankton risk and a risk calendar, and established a catalog of risk phytoplankton species for the cooling water system. The screening criteria were simultaneously required as follows: (1) particle size of cells or group >2000 μm; (2) phytoplankton bloom or aggregation events occurred in surrounding areas; (3) and species abundance maintained at >0.5×10^5 cells/L in the surrounding area. Nine high-risk species were screened out that can easily form colonies, clusters, and groups, including *Thalassiosira diporocyclus*, *Thalassiosira subtilis*, *Noctiluca scintillans*, *Phaeocystis globosa*, *Pseudo-nitzschia pungens*, *Pseudo-nitzschia delicatissima*, *Skeletonema costatum*, *Skeletonema dohrnii*, *Paralia sulcata*. Due to small cells or the formation of short chains, some dominant phytoplankton species, even those with advantages in abundance and occurrence, had difficulty threatening the reliability of cooling water systems in nuclear power plants. The outbreak of different phytoplankton species varied daily, and the risk of blockage was highest from April to July. The biological characteristics, ecological mechanisms underlying outbreaks of high-risk phytoplankton species are reviewed and discussed, suggesting a high degree of temporal and spatial variability of blockage risk. Finally, main prevention and control measures used

against high-risk phytoplankton species are provided to imply new ideas and methods for nuclear power plants. These strategies have very important practical and scientific significance.

KEYWORDS

phytoplankton outbreak, cooling water system, blockage risk, nuclear power plants, ecological mechanism, preventive measures

Highlights

1. Nuclear power plants face a high risk of blockage by marine biota outbreaks in cooling water systems.
2. Blockages risk from phytoplankton was concentrated from April to July.
3. Nine high-risk species of phytoplankton that can easily form colonies, clusters, and groups were screened out.
4. The biological characteristics, ecological mechanisms underlying outbreaks of high-risk phytoplankton species suggested a huge temporal and spatial variability of blockage.
5. Main prevention and control measures used against high-risk phytoplankton species are provided.

1 Introduction

With the depletion of traditional power sources, such as coal and oil, nuclear energy has been developed and utilized by more countries as a clean and efficient alternative (Dagnall, 2005; Yang et al., 2020). Nuclear power plants are mainly located on the coast, and water supply systems using seawater as the final cooling water source are widely used. The main cooling water system, also known as the circulating water system, is the cold end system for operating the power plant (Dagnall, 2005; Liu, 2019). The operational state of the cooling water system directly affects the safety of the power plant (Alsaffar and Zheng, 1999; Ruan, 2015).

The reliability of the cooling water system in nuclear power plants is crucial for their safe operation. The intrusion or aggregation of marine biota into cooling water systems seriously threatens nuclear safety in the context of environmental and climate changes (Alsaffar and Zheng, 1999; ERPI, 2015; Fu et al., 2020). The increasing amount of waste, marine biota, sediment, sea ice, etc. can block cooling water systems (Chen, 2009; Ruan, 2015; Arefiev et al., 2015; Yan and Lu, 2016). If a large number of blockages are pumped into the system, clogging the water intake components, it will seriously threaten the normal operation and cause huge hidden dangers to the safe operation of nuclear power plants (Mark, 2012; Kumar et al., 2017; Fu et al., 2020). The World Association of Nuclear Operators (WANO) announced that 38% of the 60 blocking events from 2008 to 2015 were caused by marine biota; 38% were sand, silt, and debris; and 24% were other sources (sediment, plastic). Among the blockage events caused by marine biota since 1980, jellyfish account for 59%, phytoplankton for 11%, fish and shrimp for 10%, and microalgae and aquatic plants for 7% (ERPI, 2015; Han et al., 2018). Therefore, the aggregation and outbreak of marine biota is an important threat to cooling water systems of coastal nuclear power plants (Table 1). Table 1 indicates the most common issue occurs when jellyfish block the water intake filter screen and even cause the reactor to shut down (Matsumura et al., 2005; Mark, 2012; Florin et al., 2013). In addition to jellyfish, other marine biota have caused blockages, such as that caused by an outbreak of pelagic tunicates (*Salpa fusiformis*) and Euphausiids (Chae et al., 2008). In recent years, coastal nuclear power plants in China have also experienced incidents that threaten their cooling water systems, due to outbreaks of marine biota (Table 1). In July 2014, the water intake of the Hongyanhe nuclear power plant in northern China was blocked by *A. aurita*, resulting in a 10 day shutdown (Zhang et al., 2019). From December 2014 to February 2015, a bloom of *Phaeocystis globosa* erupted in the area of the Fangchenggang nuclear power plant, blocking some filtration equipment to varying degrees (He et al., 2019b; Kang et al., 2020). In January 2015, *Acetes chinensis*, *Acetes erythraeus*, and *Acetes japonicus* tripped the single circulating pump in Daya Bay nuclear power plant (Meng et al., 2018). In August 2015, the blocking of the Ningde nuclear power plant in Fujian by benthos, sea cucumbers *Acaudina molpadioidea*, was related to typhoons (Chen, 2018; Tang, 2018). Therefore, it can be seen that for phytoplankton or algae species, the blockage risk is relatively low, with relatively short time during blockage.

The monitoring and prevention of organisms that typically block coastal nuclear power plants aims to provide an analysis of contributing factors and prevention methods for outbreaks or aggregations (Chae et al., 2008; Moreau et al., 2013; Florin et al., 2013; Arefiev et al., 2015; Fu et al., 2020). The ecological mechanisms of outbreaks of some marine biota in areas near nuclear power plants have been preliminarily analyzed. Chae et al. (2008) found

TABLE 1 List of shutdown cases or threats to nuclear power plants caused by substances and invasion or aggregation of marine biota.

Year	Nuclear power plant	Country	Caused blockage	Operations
Jan. 1997	FitzPatrick	USA	Sticklebacks	reactor emergency shutdown
Jun. 2003	Uljin	Korea	*Euphausia pacifica* and *Salpa fusiformis*	reactor emergency shutdown
Aug. 2005	Stockholm's Oskarshamn	Sweden	*Aurelia aurita*	reactor emergency shutdown
Aug. 2005	Oyster Creek	USA	Sea weeds	reactor emergency shutdown
Sep. 2007	FitzPatrick	USA	Cladophora	multiple shutdown
Oct. 2008	Diablo in California	USA	Jellyfish	canyon 2 reactor shutdown
Dec. 2009	Cruas	France	Sea weeds	power reduction of 20%
2011	Shimane prefecture	Japan	Jellyfish	outlet generation reduced by 6%
Jun. 2011	Torness nuclear power station	UK	Jellyfish	reactor emergency shutdown
Jul. 2011	Hadera	Israel	Jellyfish	facing the risk of shutdown
Aug. 2011	St. Lucie Nuclear Plant in Florida	USA	*Aurelia aurita*	reactor emergency shutdown
Jul. 2012	San Luis Obispo in California	USA	*Salpa fusiformis*	reactor emergency shutdown
Sep. 2013	Stockholm's Oskarshamn	Sweden	*Aurelia aurita*	reactor emergency shutdown
Jul. 2007	Tianwan in Guangdong	China	Wheat straw	power reduction
2009	Dayawan in Guangdong	China	Mussels	power reduction
Jun. 2011	Qinshan in Zhejiang	China	Flotsam and jetsam	power reduction
Jul. 2014	Honhyanhe in Niaoning	China	Jellyfish	reactor automatic shutdown
Dec. 2014	Fangchenggang in Guangxi	China	*Phaeocystis globosa*	power reduction
Jan. 2015	Linao in Guangodng	China	*Acetes* spp.	power reduction
Jul. 2015	Honhyanhe in Niaoning	China	*Aurelia aurita*	power reduction
Aug. 2015	Ningde in Fujian	China	*Acaudina molpadioidea*	reactor emergency shutdown
Jan. 2016	Linao in Guangodng	China	*Acetes* spp.	reactor emergency shutdown

that the warm surface current that occasionally extends to the nearshore area, makes *Salpa fusiformis* enter the cooling waters of Uljin nuclear power plant in South Korea. Prakash et al. (2012) used hydrological and seaweed migration models and found that the Salem power plant was invaded by seaweed from the intertidal swamp 3 miles away. Florin et al. (2013) traced the mussels, *Mytilus edulis*, that first appeared around the Bothnian Sea nuclear power plant in Sweden. Chen (2018) speculated that the block of the Ningde nuclear power plant may have been caused by the combinded effect of ocean currents caused by typhoons, the disturbance of the bottom habitat, and the self reproduction and growth of *A. molpadioidea*. Consequently, the biggest threat to the cooling water system of nuclear power plants is the uncertainty of outbreaks of marine biota in the context of environmental and climate changes (Deretz, 2007; King et al., 2010; Prakash et al., 2012; Kumar et al., 2017; Fu et al., 2020). In general, these outbreaks have no obvious signs or specific times, which causes problems for studying bio-blocking in cooling water systems. Changes in the marine environment and climate, the impact of thermal effluent, and species distribution are all potential factors for the aggregation or outbreak of marine biota (Kumar et al., 2017; Wu et al., 2017; Chen, 2018; Tang, 2018; Fu et al., 2020; Yu et al., 2021).

Harmful algae blooms (HABs), mainly composed of phytoplankton, are an ecological anomaly caused by the proliferation of tiny unicellular organisms under specific environmental conditions (Berdalet et al., 2017). Fujian in Southeast China has a long coastline with numerous bays. As a result of global change and human activities, marine environment pollution is increasing in this area, making Fujian prone to HABs, with the occurrence of toxic HABs increasing rapidly (Li, 2012). Specifically, in 2012, a toxic *Karenia mikimotoi* bloom in Fujian resulted in the death of numerous more than 70% of cultured abalones and a direct economic loss of 2.1 billion yuan, which had a serious impact on fishery production, coastal tourism, and human health. This was the most serious economic loss caused by HABs reported in China (Lin et al., 2016). Once a large number of HABs organisms gather, the rotating filter screen (usually 3 or 5 mm) of the circulating water filtration system can be blocked, tripping the seawater circulating pump of nuclear power plants (Deretz, 2007; Mark, 2012; Fu et al., 2019; He et al., 2019b; Zhang et al., 2019; Kang et al., 2020). Therefore, as a potential risk organism, phytoplankton may accumulate, with a high number of cells that then deposit on the filter screen surface. Based on field monitoring data of phytoplankton in the 15 km around Fuqing nuclear power plant, combined with historical HABs datasets from the Marine Environmental Quality Bulletin in Fujian that covered 16 years from 2006 to 2021, phytoplankton species were screened and evaluated that may potentially block the cooling water system, a three principle of screening risk phytoplankton specie was established, a catalog of risk phytoplankton species and monthly risk calendar were determined. Finally, the ecological mechanisms of high-risk phytoplankton outbreak were reviewed and discussed, and an

effective solution for prevention was provided. These strategies have very important practical and scientific significance.

2 Material and methods

2.1 Data recourse

Field monitoring data of phytoplankton species were obtained by water sampling quantitative method that followed the UNESCO Manuals and Guides (Karlson et al., 2010). Twelve stations (Figure 1) were set within 15 km around Fuqing nuclear power plant area according to technical guidelines for sea area utilization demonstration in China (General Administration of Quality Supervision, Inspection and Quarantine of the People's Republic of China 2010). Water samples (500 mL) from the surface (0.5 m) and bottom (0.5 m above the seabed) were taken in December 2020, February 2021, April 2021, May 2021, June 2021, August 2021, and November 2021. The samples were fixed with 1% neutral formalin and brought back to the laboratory for analysis. Data on phytoplankton species included species composition, abundance, and dominant species. Dominant species were defined as the dominance ≥0.02 (Xu, 2006). HABs organisms and outbreak events were screened out from historical datasets of the Marine Environmental Quality Bulletin in Fujian on Southeast China coast between 2006 and 2021. Based on the field monitoring and historical datasets, the potential phytoplankton species of risk in the target area were screened, and the risk of blockage was assessed.

2.2 Analytical method

The treatment and analysis of phytoplankton species of risk were carried out in accordance with the relevant provisions of the Survey of Marine Biology (General Administration of Quality Supervision, Inspection and Quarantine of the People's Republic of China, 2008), Technical Guidelines for Treatment with Red Tide Disaster (General Administration of Quality Supervision, Inspection and Quarantine of the People's Republic of China, 2014). Phytoplankton species were identified and counted at 200× to 400× magnification under an inverted optical microscope (Zeiss Z1, Germany). Phytoplankton cell or group or chain length was measured using AxioVision Rel. 4.8 lnk software connected with microscopy. Phytoplankton abundance was calculated as cells/L. HABs events in Fujian coastal waters over 16 years, including phytoplankton causing species, occurrence, and duration days, were classified. According to the ecological status of phytoplankton around Fuqing nuclear power plant and the HABs events previously recorded, combined with the quantitative assignment risk level assessment method suggested by Tang (2018); Zhang et al. (2019) and Yu et al. (2021), the screening criteria for blockage organisms, catalog of potential phytoplankton species of risk, and the monthly risk calendar were obtained. Furthermore, ecological mechanisms of high-risk species outbreaks and preventive measures are discussed in the context of a comprehensive literature review. This study provides a scientific basis to carry out purposeful monitoring to control marine biota of risk for cooling water system, and also provides a reference for further research.

3 Results

3.1 Ecological status of phytoplankton based on field monitoring around Fuqing nuclear power plant in Southeast China

A total of 147 phytoplankton species were recorded in the waters 15 km around Fuqing nuclear power plant, including 117 species of diatoms that dominated the community, 25 species of dinoflagellates, two species of Cyanobacteria, and two species of Chrysophyta (Figure 2A). In terms of monthly variation, the maximum species richness was 74 in June 2021, which was the

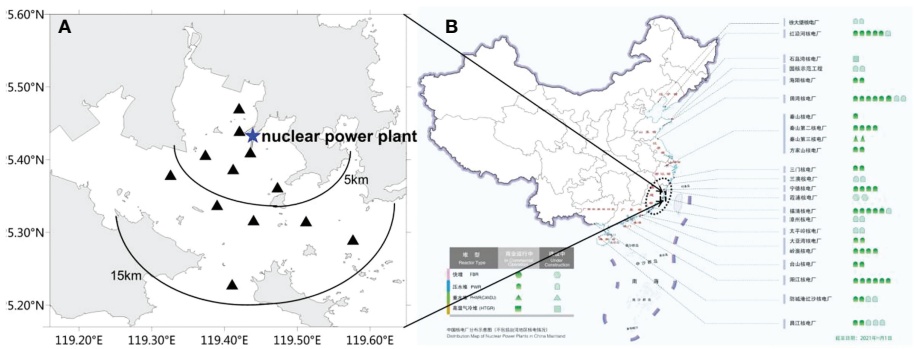

FIGURE 1
(A) Field monitoring stations within 15 km around Fuqing nuclear power plant area on southesast China coast. **(B)** Distribution map of nuclear power plants in China mainland cited from China Nuclear Energy Association (http://www.china-nea.cn/).

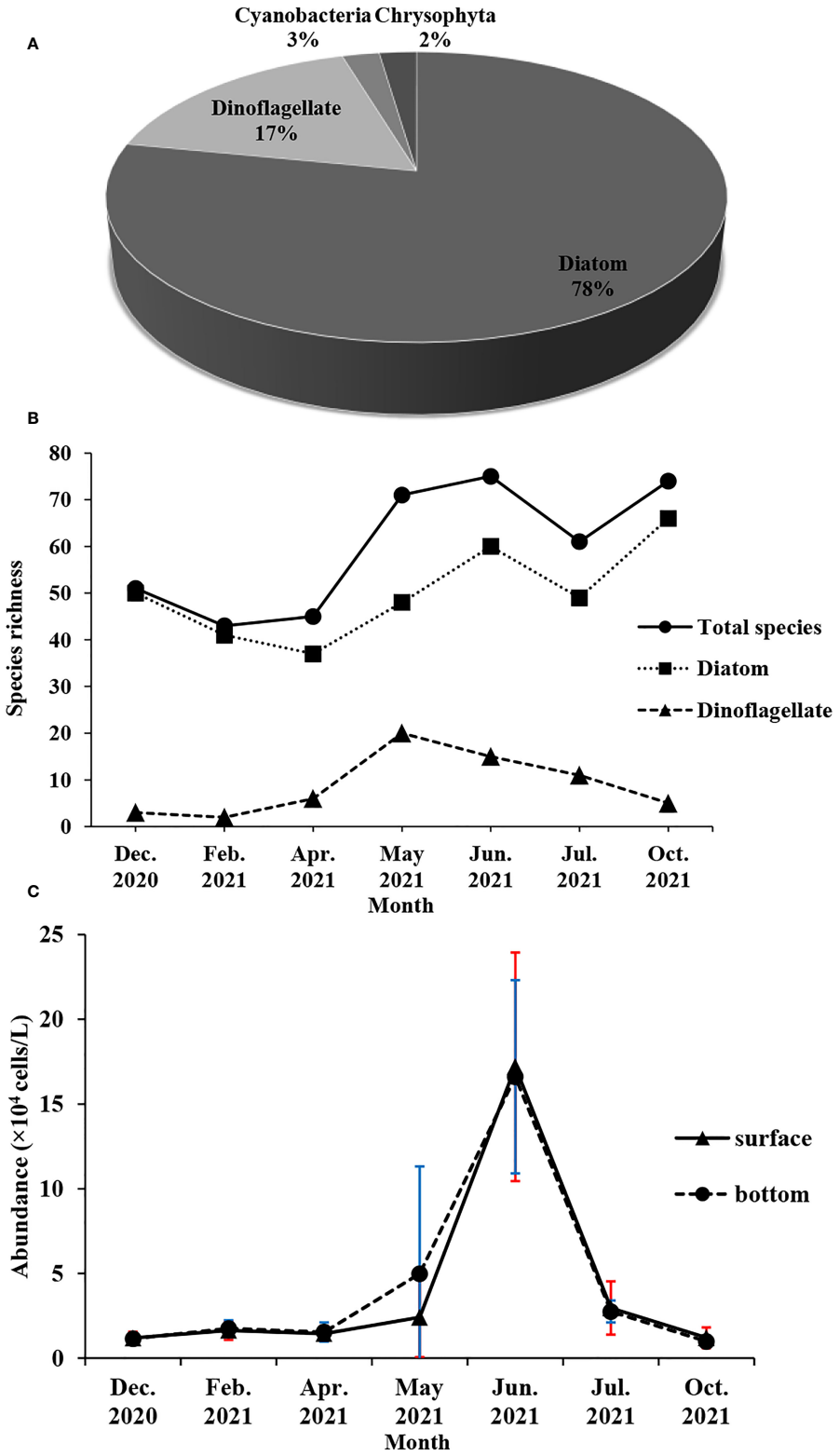

FIGURE 2
Monthly variation of phytoplankton composition **(A)**, species richness **(B)** and abundance **(C)** around Fuqing nuclear power plant on southeast China coast.

same as in October 2021. The minimum species richness was 43 in February 2021. The monthly variation of diatom species richness was basically the same as that of the total phytoplankton. However, dinoflagellates had the maximum species richness in May 2021 (Figure 2B). The abundance of phytoplankton was the highest in June 2021, followed by May 2021, and the lowest in October 2021 (Figure 2C).

The monthly variation of dominant species was evident (Table 2). The dominant species taking a greater advantage in months were chain-forming, mainly including *Paralia sulcata*, *Skeletonema costatum*, *Skeletonema dohrnii*, *Pseudo-nitzschia pungens*, *Pseudo-nitzschia delicatissima*, *Eucampia zodiacus*, *Chaetoceros curvisetus*, *Leptocylindrus danicus*, and *Lauderia annulata*. The major dominant species were diatoms. From December 2020 to April 2021, the major dominant species remained as chain-forming *P. sulcata* and *S. costatum*. From May 2021 to July 2021, chain-forming diatoms maintained high abundance and occurrence in the surrounding waters. These species are an important component of potential blocking organisms.

The spatial distribution of major dominant species varied significantly (Figure 3). The most highly abundant species found in waters close to the nuclear power plant were *S. dohrnii* in December, *L. annulata*, *E. zodiacus*, *C. curvisetus* in June, and *P. delicatissima* and *Bacillaria paradoxa* in July. While the most highly abundant species found offshore from the nuclear power plant was *Thalassiosira diporocyclus* in May, *P. pungens* in June, *P. sulcata*, and *S. costatum* in February (Figure 3). Specifically, the maximum abundance of *S. dohrnii* in December was 1.10×10^5 cells/L with an average of 0.57×10^4 cells/L; the maximum abundance of *L. annulata*, *E. zodiacus*, *C. curvisetus* in June were 0.54×10^5 cells/L, 0.90×10^5 cells/L, 1.10×10^5 cells/L, respectively; and *P. delicatissima* and *B. paradoxa* in July had the maximum abundance of 1.07×10^5 cells/L and 0.97×10^5 cells/L, respectively. Subsequently, *T. diporocyclus* in May had the maximum abundance of 1.13×10^5 cells/L with an average of 3.01×10^4 cells/L, while *P. pungens* in June had 1.11×10^5 cells/L in maximum. The maximum abundance of *P. sulcata*, and *S. costatum* in February were 1.03×10^5 cells/L and 1.11×10^5 cells/L, respectively.

TABLE 2 Monthly variation of phytoplankton dominant species and its dominance around Fuqing nuclear power plant on southesast China coast.

Dominant speciesand dominance	Time						
	Dec. 2020	Feb.2021	Apr. 2021	May 2021	Jun. 2021	Jul. 2021	Oct. 2021
Paralia sulcata	0.21	0.39	0.20	ND	< 0.02	0.13	0.25
Skeletonema costatum	< 0.01	0.37	0.17	ND	< 0.02	< 0.01	0.20
Skeletonema dohrnii	0.31	< 0.01	ND	ND	ND	ND	ND
Coscinodiscus bipartitus	0.06	0.04	0.05	ND	< 0.01	< 0.01	< 0.01
Coscinodiscus jonesianus	ND	ND	0.02	ND	< 0.01	< 0.01	ND
Nitzschia longissima v. *reversa*	< 0.01	< 0.01	< 0.01	< 0.01	< 0.01	< 0.02	0.04
Nitzschia closterium	< 0.01	0.04	0.07	< 0.01	< 0.01	< 0.01	0.02
Nitzschia sigma	0.04	< 0.01	< 0.01	0.04	< 0.01	0.03	< 0.01
Pleurosigma affine	0.02	0.02	< 0.01	ND	< 0.01	< 0.01	< 0.01
Pleurosigma elongatum	0.04	< 0.01	< 0.01	ND	< 0.01	< 0.01	< 0.01
Ditylum brightwellii	0.02	ND	ND	ND	ND	0.06	< 0.01
Cyclotella caspia	< 0.01	0.02	ND	ND	< 0.01	ND	ND
Leptocylindrus danicus	ND	< 0.01	0.13	ND	0.11	< 0.01	< 0.01
Leptocylindrus minus	ND	ND	ND	ND	< 0.02	0.13	< 0.01
Pseudo-nitzschia delicatissima	< 0.01	< 0.01	0.02	< 0.01	0.02	0.06	< 0.02
Pseudo-nitzschia pungens	< 0.01	< 0.01	0.02	0.02	0.07	0.02	< 0.02
Chaetoceros curvisetus	ND	< 0.01	< 0.01	ND	0.14	< 0.01	< 0.01
Eucampia zodiacus	ND	< 0.01	< 0.01	ND	0.18	< 0.01	< 0.01
Eucampia cornuta	ND	ND	ND	ND	0.05	< 0.01	ND
Guinardia striata	ND	ND	ND	ND	0.02	< 0.01	< 0.01
Lauderia annulata	ND	ND	ND	ND	0.21	< 0.01	< 0.01
Bacillaria paradoxa	ND	ND	ND	ND	ND	0.13	< 0.01
Asterionella japonica	ND	ND	ND	ND	ND	0.06	< 0.01
Thalassionema nitzschioides	< 0.01	< 0.01	< 0.01	ND	< 0.01	< 0.01	0.02
Thalassionema nitzschioides v. *parva*	ND	< 0.01	< 0.01	ND	< 0.01	< 0.01	0.02
Thalassiosira diporocyclus	ND	ND	ND	0.68	ND	ND	ND

ND indicates non-detected.

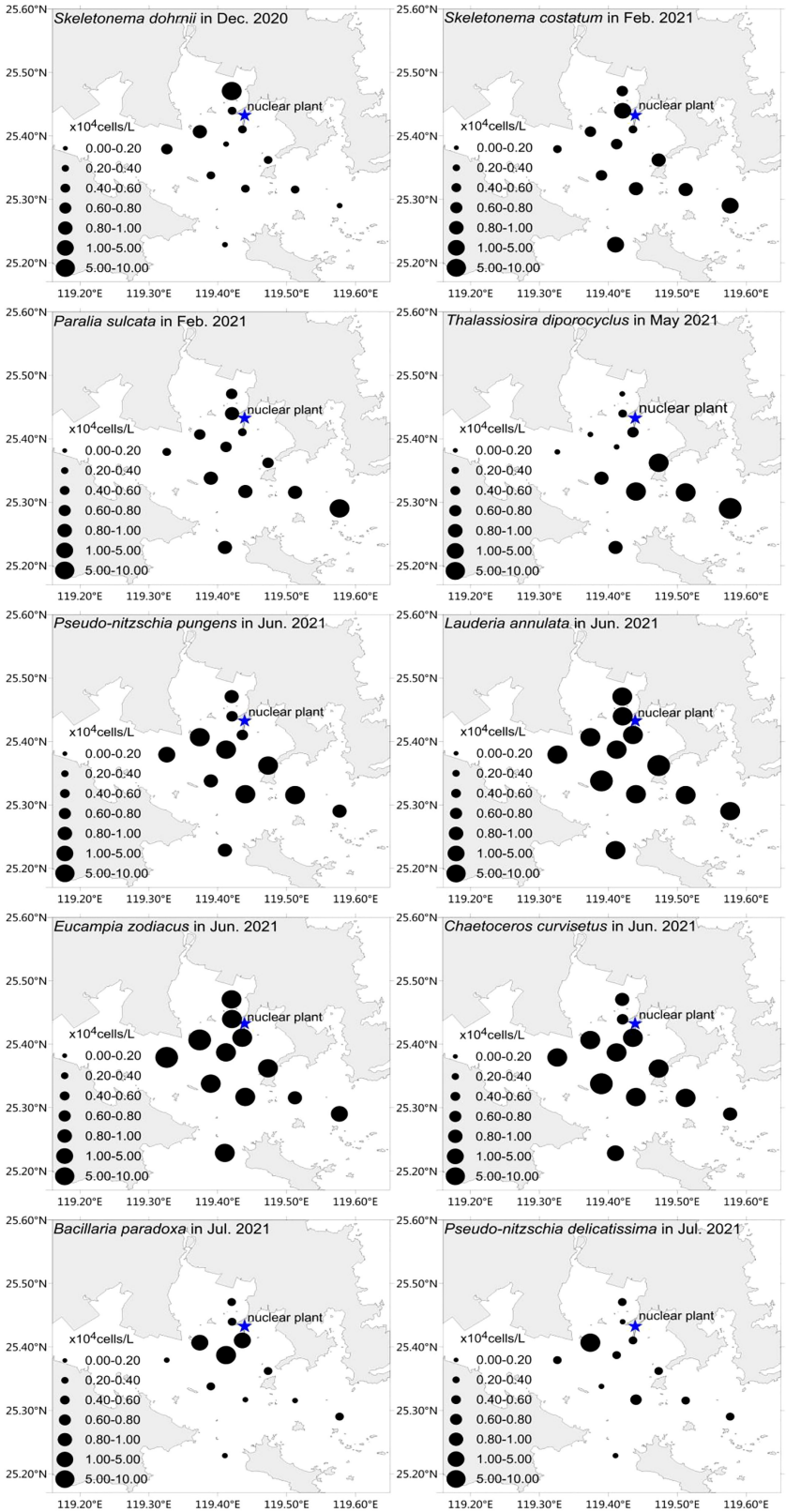

FIGURE 3
Horizontal distribution of 10 major phytoplankton dominant species around Fuqing nuclear power plant on southeast China coast.

3.2 Phytoplankton bloom events and annual changes based on historical datasets in the Fujian coast, Southeast China

Over 16 years, HABs outbreaks along the coast of Fujian in Southeast China were seasonal (Figure 4B), with 90.5% occurring from April to July. The highest incidence period of HABs was in May and June, with dinoflagellates as the majority of HABs causing species. The occurrence of HABs in May and June accounted for 60.0% of the total number, while the duration days accounted for 46.4% during the whole year. HABs showed a downward trend from 2014 to 2021, and there was a small increase by 2021 (Figure 4A). There were 13 HABs causing species from 2006 to 2021 in common, including *S. costatum*, *Chaetoceros* sp., *Thalassiosira* sp., *E. zodiacus*, *P. pungens*, *Prorocentrum micans*, *Karenia mikimotoi*, *Scrippsiella trochoidea*, *Noctiluca scintillans*, *Gymnodinium catenatum*, *Chattonella marina*, *Akashiwo sanguine*, and *Phaeocystis globosa*. The phytoplankton species that repeatedly cause HABs were *P. micans*, *S. costatum*, *Thalassiosira* sp., *N. scintillans*, and *A. sanguine*. Specifically, *P. micans* caused outbreaks from April to July each year along the coast of Fujian in Southeast China (Figure 4B).

3.3 Blockages caused by phytoplankton species: Screening criteria, catalog, and monthly calendar of potential risk species

According to the HABs events previously recorded within 16 years along the coast of Fujian, 87 phytoplankton species belonging to 39 genera of four phyla were selected as HABs organisms around Fuqing nuclear power plant (Figure 5A). Of these, 68 species of 27 genera belonging to diatoms accounted for 78% of the total species; 15 species of 10 genera from dinoflagellate accounted for 17%; two species of two genera from Chrysophyta accounted for 2%; and two species of one genus from cyanobacteria accounted for 3% (Figure 5A).

Based on the diameter of the drum net of the circulating water system (usually 3 or 5 mm) in nuclear power plants,

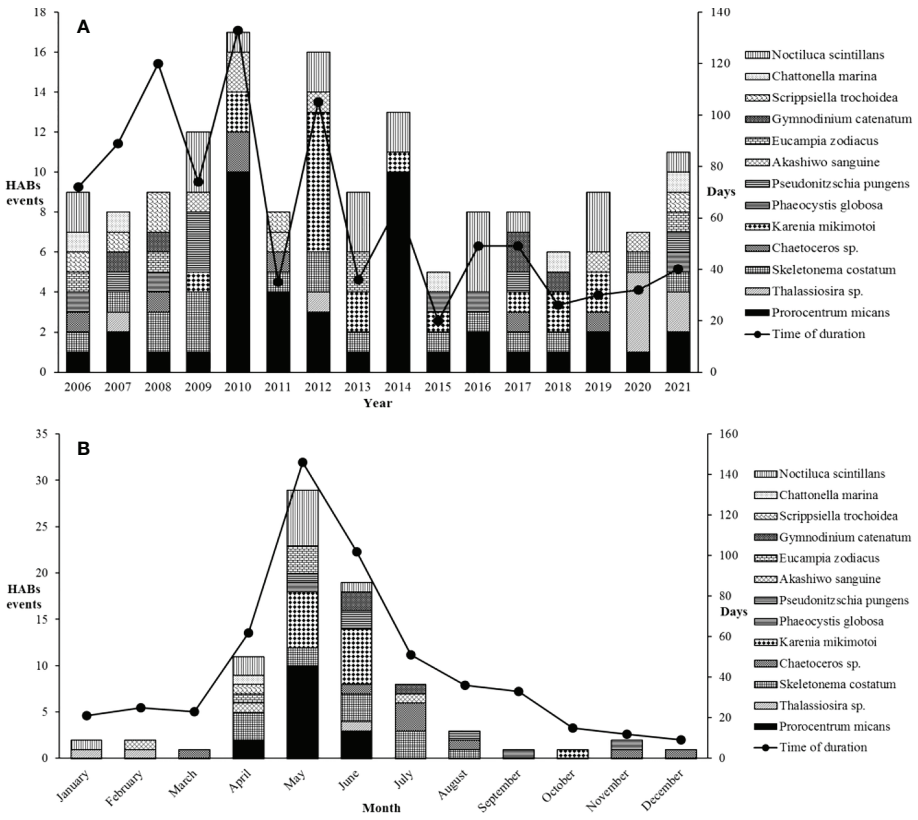

FIGURE 4
(A) Yearly variation and **(B)** monthly variation of HABs numbers and the duration days causing by major phytoplankton species in Fujian coastal waters during the last 16 years.

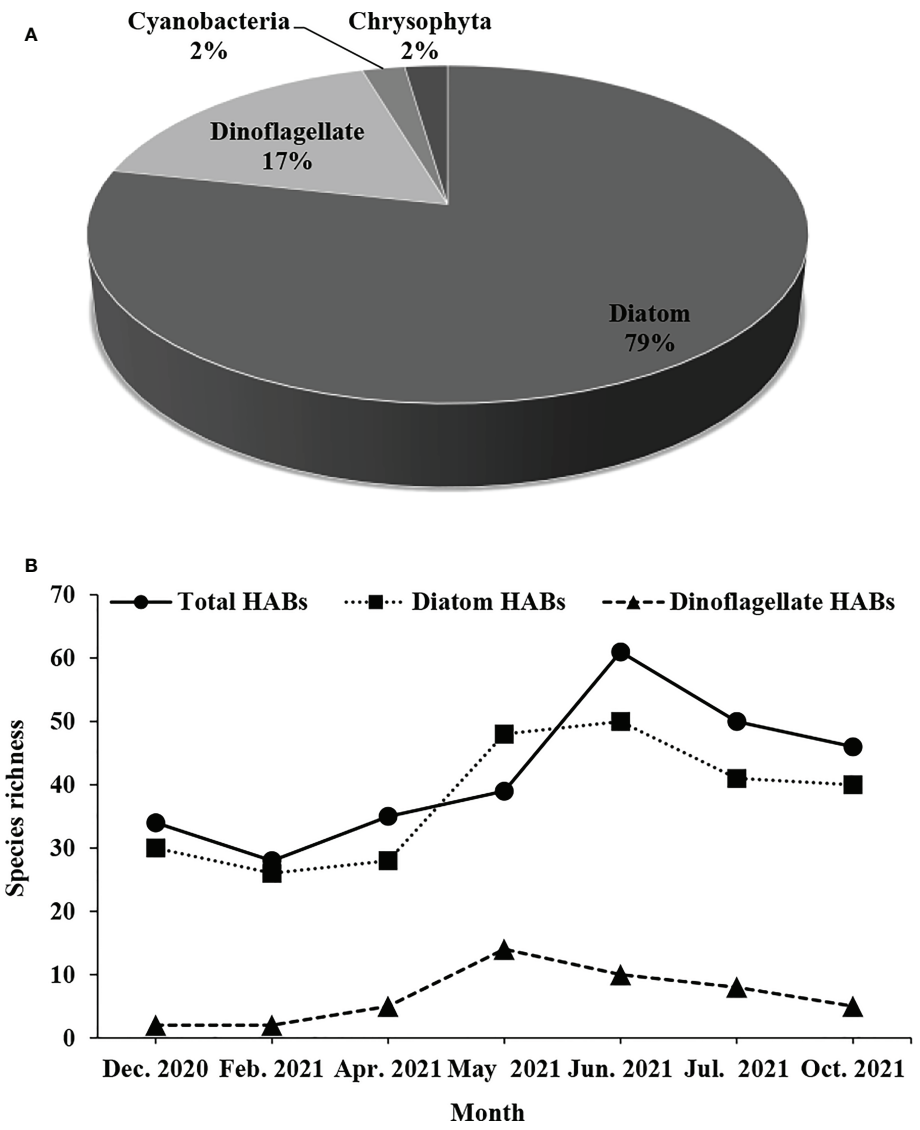

FIGURE 5
Monthly variation of HABs composition **(A)** and causing species richness **(B)** around Fuqing nuclear power plant on southeast China coast.

combined with blockage events in cooling water system documented by marine biota, the screening criteria for potential risk phytoplankton species were as follows: (1) particle size of cells or groups >2000 μm; (2) phytoplankton bloom or aggregation events recorded in surrounding areas; and (3) high species abundance of $>0.5\times10^5$ cells/L in the surrounding sea area. Notably, the entire three principles should be simultaneously required instead of optional selection. Consequently, 38 potential risk species among the above 87 HABs organisms and a monthly risk calendar were established for Fuqing nuclear power plant (Table 3). This includes species with high dominance over multiple months, such as *S. costaum*, S. *dohrnii*, *P. sulcata*, *P. pungens*, and *L. danicus*, as well as other non-dominant species with high abundance in the adjacent waters close to the nuclear power plant. Based on field monitoring and historical datasets, the phytoplankton of risk in the sea area around Fuqing nuclear power plant could be roughly determined (Table 3). Furthermore, the HABs events recorded in the adjacent waters or offshore from the nuclear power plant were referred to (Figure 5B). The potential risk from phytoplankton species may exist in a certain area in real time. Blockages in cooling water systems may occur when phytoplankton species abundance reaches a high level. Phytoplankton species that can easily form colonies, clusters, filaments, and groups were selected as high-risk organisms (Table 3).

TABLE 3 Totally 38 phytoplankton species as potential risk species and a monthly risk calendar for Fuqing nuclear power plant based on screening criteria.

Species	Dec. 2020	Feb. 2021	Apr. 2021	May 2021	Jun. 2021	Jul. 2021	Oct. 2021	Morphology	Particle size (cm)	Abundance (10^5 cells/L)	Comprehensive risk level
Asterionella japonica								catenoid colony	< 0.03	0.03–0.77	★
Bacillaria paradoxa								catenoid colony	0.01–0.03	0.03–0.97	★
Chaetoceros affinis								long chains	0.01–0.03	0.01–1.10	★
Chaetoceros curvisetus								long chains	> 0.1	0.03–1.10	★★
Chaetoceros tortissimus								long chains	0.01–0.03	0.01–1.00	★
Chaetoceros densus								long chains	> 0.1	0.01–1.00	★★
Eucampia zodiacus								catenoid colony	0.01–0.03	0.07–0.90	★
Guinardia striata								catenoid colony	> 0.5	0.02–0.90	★★
Guinardia delicatula								catenoid colony	0.01–0.03	0.02–0.91	★
Lauderia annulata								long chains	0.01–0.03	0.02–0.66	★
Leptocylindrus danicus								long chains	> 0.1	0.02–0.93	★★
Leptocylindrus minus								long chains	> 0.1	0.02–0.55	★★
Odontella mobiliensis								large cell	0.0–0.03	0.01–0.65	★
Odontella regia								large cell	> 0.1	0.02–0.55	★
Odontella sinensis								large cell	> 0.1	0.2–0.75	★
Paralia sulcata								long chains	> 0.1	0.7–1.03	★★★
Pseudo-nitzschia pungens								long chains	> 0.1	0.04–1.11	★★★
Pseudo-nitzschia delicatissima								long chains	> 0.1	0.04–1.07	★★★
Rhizosolenia setigera								long cell	> 0.5	0.02–0.61	★
Rhizosolenia alata								long cell	> 0.5	0.02–0.61	★
Skeletonema costatum								long chains	> 0.1	0.7–1.11	★★★
Skeletonema dohrnii								long chains	> 0.1	0.2–1.10	★★★
Stephanopyxis palmeriana								long chains	0.01-0.03	0.02–1.03	★
Thalassiosira diporocyclus								colony	1–2	0.01–1.13	★★★
Thalassiosira rotula								long chains	> 0.1	0.02–0.83	★★
Thalassiosira subtilis								colony	1–2	0.02–0.71	★★★
Thalassiothrix frauenfeldii								catenoid colony	0.01–0.03	0.02–0.72	★
Thalassionema nitzschioides								catenoid colony	0.01–0.03	0.07–0.62	★★
Akashiwo sanguinea								large cell	< 0.003	0.03–0.62	★
Ceratium furca								large cell	0.01–0.03	0.03–0.62	★

(Continued)

TABLE 3 Continued

Species	Dec. 2020	Feb. 2021	Apr. 2021	May 2021	Jun. 2021	Jul. 2021	Oct. 2021	Morphology	Particle size (cm)	Abundance (10^5 cells/L)	Comprehensive risk level
Ceratium fusus								large cell	0.01–0.03	0.03–0.61	★
Noctiluca scintillans								large cell	1–2	0.02–0.68	★★★
Gymnodinium catenatum								long chains	< 0.4	0.03–0.66	★
Karenia mikimotoi								large cell	< 0.003	0.03–0.66	★
Prorocentrum donghaiense								large cell	< 0.03	0.03–0.63	★
Scrippsiella trochoidea								large cell	< 0.003	0.03–0.62	★
Trichodesmium erythaeum								long cell	< 0.4	0.03–0.63	★
Phaeocystis globosa								granular colony	< 3	0.01–0.38	★★★

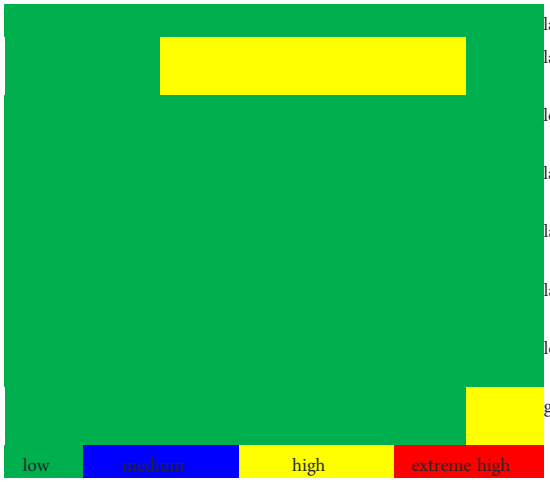

The symbol ★ suggests the risk level of blockage from marine phytoplankton species, the more number of ★ showing, the high the blockage risk being.

4 Discussion

4.1 Assessment on potential blocking risk from phytoplankton species for a nuclear power plant on the Southeast China coast

In terms of the relationship between nuclear power plants and the marine environment, the impact of thermal effluent on marine biology is the most well studied (Kaplan et al., 2016; Dvorniko et al., 2017; Wei et al., 2018). However, with changes in the marine environment and climate, the safety of cooling water systems has become a new research area. The safe operation of cooling water systems requires establishing a catalog of risk organisms in the surrounding area, and developing monitoring systems, early warning technologies, and preventive countermeasures (Moreau et al., 2013; Tang et al., 2017; Zhang et al., 2018; Kirsti et al., 2018; Lu et al., 2018; Yu et al., 2021). It is a complex problem, and factors such as population composition, distribution, abundance of marine biota, trends and intensity into water intake components are important issues for evaluating the threat or risk. Tang (2018) used the Analytic Hierarchy Process, which initially proposed the principle of Ningde nuclear blockage causing organisms screening and determined the possibility blockage in accordance with the criteria: 0.000 to 0.249 for low risk, 0.250 to 0.499 for medium risk, 0.500 to 0.749 for high risk, 0.750 to 1.000 for very high risk. Some studies have established a catalog of risk organisms and a biological screening index system for jellyfish. For example, Zhang et al. (2019) according to relative biomass, i.e. the number of jellyfish caught per net per hour, suggested the risk level was "High" when relative density of jellyfish was ≥ 500 ind./(net.h), called the red level; level "Medium" was when the relative density was > 300 but < 500 ind./(net.h), called the yellow level; level "Low" was > 100 and < 300 ind./(net.h), called the blue level. Subsenquently, over the past 5 years, several monitoring plans, early warning technologies, and decision support systems have been developed for marine biota that block cooling water systems (Tang et al., 2017; Zhang et al., 2018; Kirsti et al., 2018; Lu et al., 2018; Meng et al., 2018).

In present study, utilizing the quantitative risk level evaluation method suggested by Tang (2018); Zhang et al. (2019) and Yu et al. (2021), the risk level of 38 potential risk phytoplankton species preliminarily screened were assigned to quantitative values of 1, 2, 3, and 4, with corresponding levels of low, medium, high, and extremely high. Consequently, a comprehensive quantitative analysis showed that the organisms of potential risk to Fuqing nuclear power plant mainly appeared between April and July, with occasional high abundance aggregation events occurring in May (Figure 6). At the species level, there were nine major high-risk species, including *T. diporocyclus*, *T. subtilis*, *N. scintillans*, *Phaeocystis globosa*, *P. pungens*, *P. delicatissima*, *S. costatum*, *S. dohrnii*, and *P. sulcata* (Figure 6A). There were seven species of medium risk, 22 species of low risk, and no species of extremely high risk. Temporally, the high-risk species were most abundant in June and July, and the risk of blockage was highest. In the other months, there was a low to medium risk of blockage (Figure 6B).

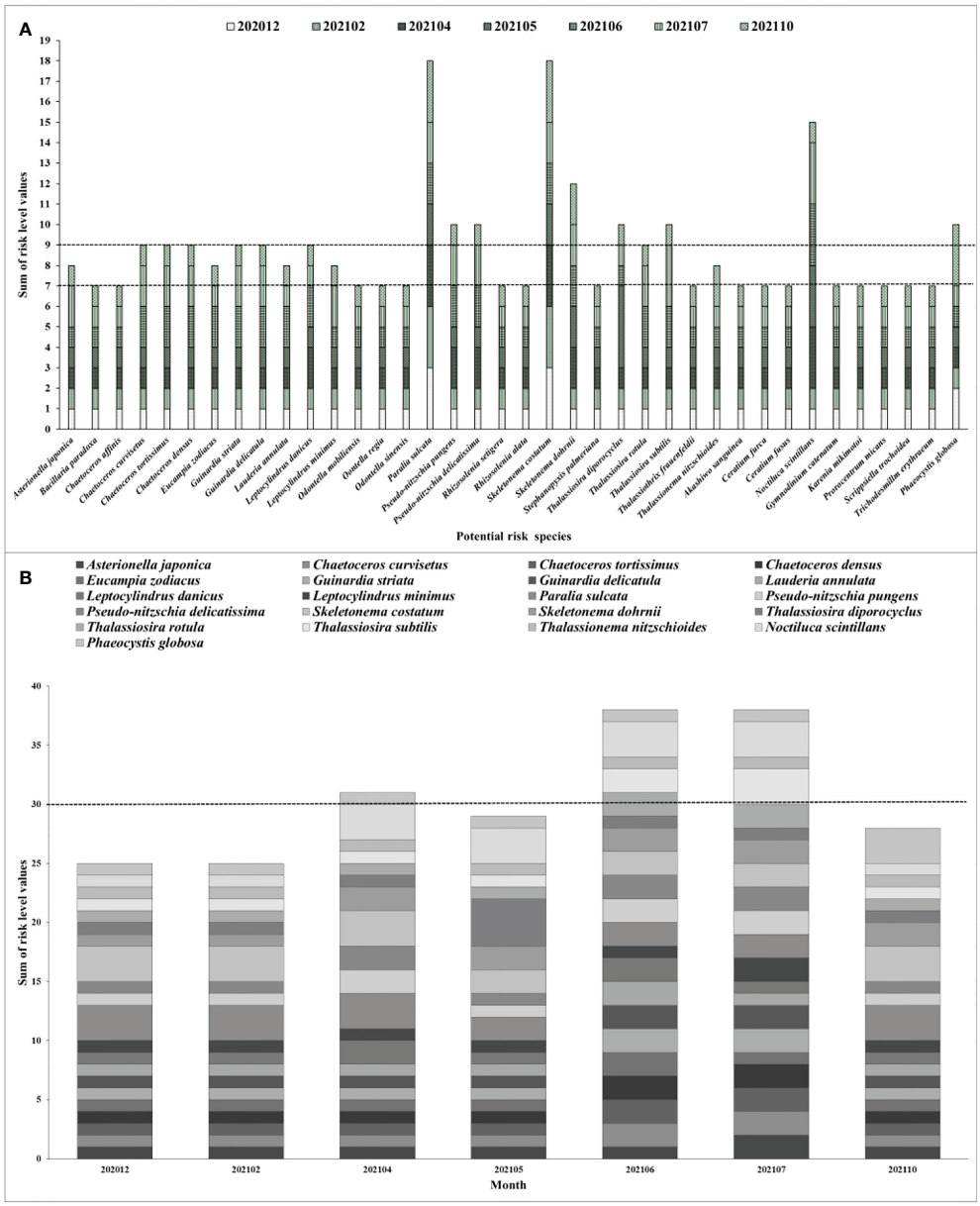

FIGURE 6
(A) The quantitative risk evaluation of 38 potential risk phytoplankton species and **(B)** monthly quantitative risk variation of 21 top potential risk phytoplankton species for Fuqing nuclear power plant.

Notably, the nine high-risk species in this study were only treated as a risk for the cooling water systems in nuclear power plants. For the entire ecosystem, these species had corresponding niches, and there was no distinction between mentions of high, medium, and low risk. The investigation and evaluation of marine biota should be guided by the data requirements of the calendar of marine organism outbreak risk (Mark, 2012; Florin et al., 2013; Tang, 2018; Zhang et al., 2019; He et al., 2019b; Yu et al., 2021).

4.2 Characteristics and ecological mechanism of outbreaks or aggregations of potential risk phytoplankton species for a nuclear power plant on the Southeast China coast

The increasing severity of HABs in the coastal waters of China has a close relationship with the intensified eutrophication, especially in the estuaries and bays (GEOHAB, 2010; Yu and

Chen, 2019). Besides, the alteration of natural habitat by mariculture industry and other anthropogenic activities also contributes to the occurrence of HABs events (Figure 7), such as the green tides in the southern Yellow Sea. Other factors like climate change also influence the distribution, dynamics, and impacts of HABs in the coastal waters of China directly or indirectly, through the effects on water temperature, stratification, and currents (Figure 7) (Anderson et al., 2012; Glibert et al., 2018; Yu and Chen, 2019).

The presence of phytoplankton species was the main cause of HABs. Appropriate external conditions, including physical, chemical, biological, hydrological, meteorological, and other factors were the environmental cause of HABs. The formation of HABs requires certain species and specific environmental factors (Figure 7). However, predicting and understanding the ecological mechanism of HABs formations remains difficult because it has a high degree of temporal and spatial variability (GEOHAB, 2010; Anderson et al., 2012; Glibert et al., 2018; Yu and Chen, 2019). In this study, the biological characteristics and ecological mechanism of outbreaks for major high-risk phytoplankton species are discussed below.

4.2.1 Biological properties and mechanisms underlying outbreak of *Phaeocystis globosa*

Phaeocystis globosa belongs to the genus *Phaeocystis* of Haptophyta. It is a major causative agent of HABs in oceans globally, featuring a complex polymorphic life cycle, alternating between free-living solitary cells (3–8 μm) and colonial cells (maximum 3 cm) (Shen and Qi, 2021). A colony is the dominant morphotype during *P. globosa* blooms (Figures 8A-C). The sticky and elastic carbohydrate skins of colonies can block the cooling water system of nuclear power plants (He et al., 2019b; Wang et al., 2021). Colony skin reportedly blocked the entrance of the cooling water filtration system of the Fangchenggang Nuclear Power Plant in China (Kang et al., 2020). According to the historical datasets and field investigation of this study, *Phaeocystis* blooms were not found in Fuqing nuclear power plant but were detected in July and October in lower abundance (0.07×10^5 cells/L, 0.11×10^5 cells/L), so may become a germplasm source of *Phaeocystis* blooms (Table 3, Figure 6). In general, *P. globosa* is prone to bloom in coastal waters with abundant or eutrophic nutrients. The restriction of nitrogen and phosphate will inhibit the growth and life cycle transformation of *P. globosa*. *P. globosa* colonies are more susceptible to phosphate restriction than free single cells, so colonies cannot form at low phosphate concentrations (Wang, 2006). When nitrate is the nitrogen source, colonies can easily develop, while other forms of nitrogen lead to the dissipation of colonies (Tungaraza et al., 2003). The colonies can be formed in a wide range of salinities, but temperature plays a key role in the colony size (He et al., 2019a). Higher external temperatures will accelerate colony

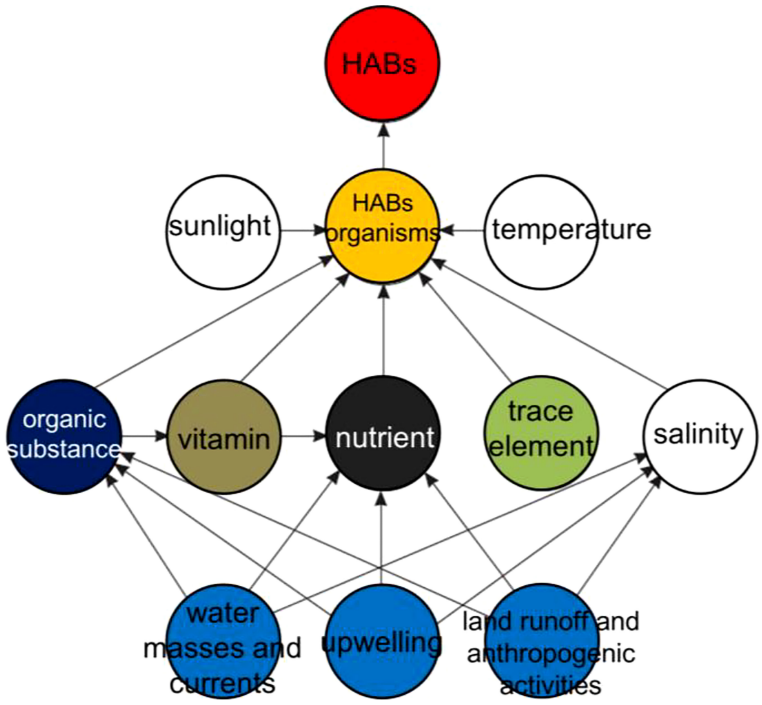

FIGURE 7
Ecological mechanism for HABs formation modified from GEOHAB (2010) suggests main environmental conditions and anthropogenic activities in coastal areas.

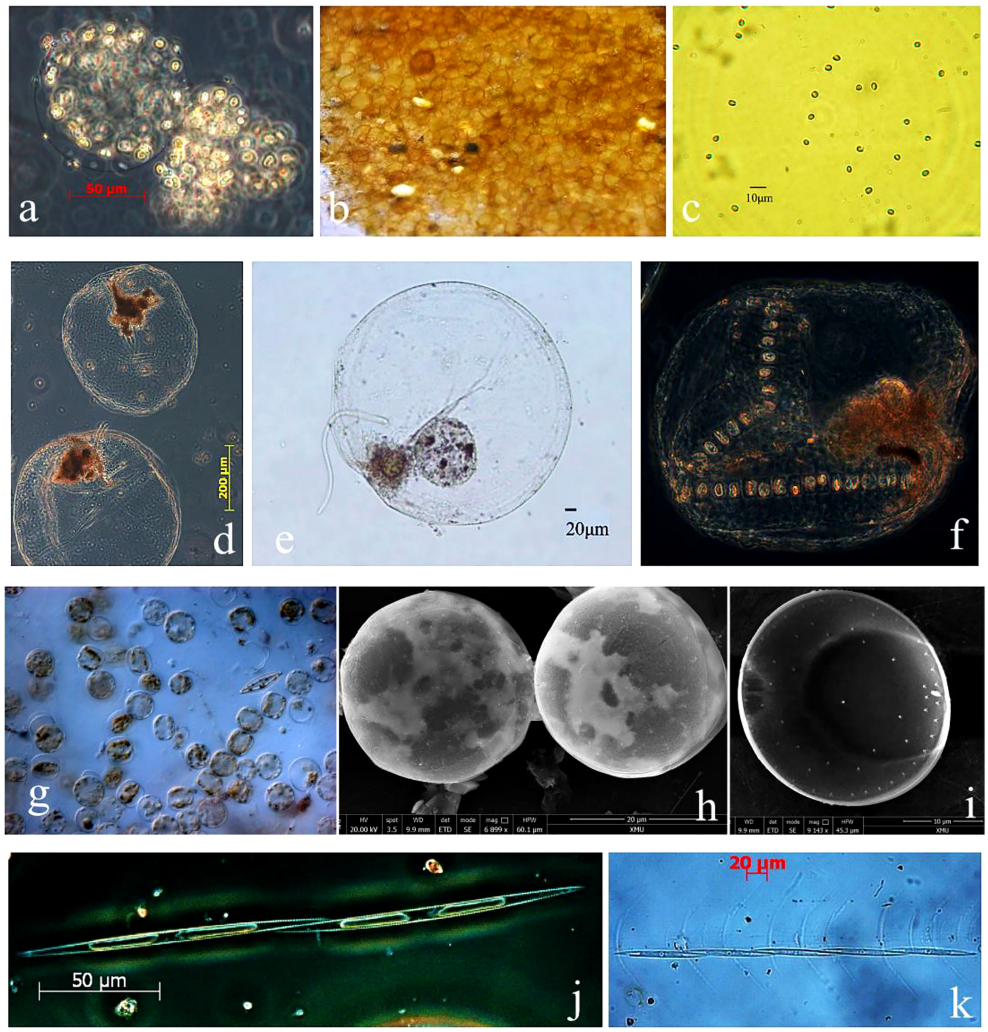

FIGURE 8
Morphological observation and mensuration of four high-risk phytoplankton species for Fuqing nuclear power plant. *P. globosa*: **(A–C)**, *N. scintillans*: **(D–F)**, *T. diporocyclus*: **(G–I)**, *P. pungens*: **(J, K)**.

rupture, and make single cells rapidly form large colonies. Specifically, Wang and Tang (2010) found that the maximum size of the colonies can be obtained at a salinity of 28 and a temperature of 25°C or at a salinity of 25 and temperature of 20° C. In addition, the formation of *P. globosa* colonies also requires light intensity of more than 40 μmol/(m^2s) (Deng, 2013). Water disturbance can promote the proliferation of *P. globosa* cells and prolong the growth time (Li et al., 2010; Cai et al., 2011). Therefore, water disturbance caused by monsoons may be one of the main factors of *P. globosa* blooms (Hai et al., 2010). Diatoms are often associated with the occurrence and dissipation of *P. globosa* blooms, especially chain diatoms, including *Chaetoceros* sp., *Skeletonema costatum*, and *Pseudo-nitzschia* sp. (Peperzak et al., 1998; Hamm and Rousseau, 2003). The formation and increase of *P. globosa* colonies causes a discrepancy in particle size between the food and the feeders, inhibits the feeding efficiency, and protects the colonies (Nejstgaard et al., 2007; Wang et al., 2011). Moreover, *P. globosa* can improve the inner space of colony formation when facing the feeding of mesozooplankton. In summary, the frequent occurrence of *P. globosa* blooms may be attributed to the competitive advantage of its life cycle transformation and colony formation.

4.2.2 Biological properties and mechanisms underlying outbreak of *Noctiluca scintillans*

N. scintillans, belonging to the genus *Noctiluca* of Pyrrophyta, is a unicellular species with a nearly spherical body and a cell diameter of 150–2000 μm, visible to the naked eye, especially giving off blue light at night (Figures 8D-F). It has both plant

attributes and some animal functions; therefore, its floristic classification includes red heterotrophic species and green amphotropic species (Mikaelyan et al., 2014; Song et al., 2016). *N. scintillans* blooms frequently occur on the China coast, and its occurrence can reach about 50% of the total HABs (Tang et al., 2006). During the blooms, *N. scintillans* are concentrated on the surface or near the surface (Turkoglu, 2013), distributed in strips or blocks of dark pink and orange, with bloom abundance of $>10^4$ cells/L (Qian et al., 1994). The *N. scintillans* cell is large and has colloidal substances on its surface and so it may block the cooling water system and cause potential safety hazards during outbreaks. This species has frequently caused HABs in Fujian since 2007, and near the Yangtze River Estuary in 2021, which can easily block Fuqing nuclear power plant on Southeast China coast (Table 3, Figure 6).

The population dynamics of *N. scintillans* are affected by many factors, such as the environment, biological characteristics, and population structure. Water temperature is the main factor affecting the seasonal variation of *N. scintillans* (Harrison et al., 2011). A study in Jangmok Bay, South Korea, showed that *N. scintillans* abundance decreased sharply when the water temperature was >28°C (Jang et al., 2010). Le Fèvre and Grall (1970) reported that, as *N. scintillans* is a cold-water species, high temperatures would inhibit population growth (e.g. Huang et al., 1997; Tada et al., 2004). *N. scintillans* is a heterotrophic dinoflagellate, and its population dynamics will also be affected by food availability. Harrison et al. (2011) reported that the abundance of zooplankton also controlled *N. scintillans* abundance due to competition. Miyaguchi et al. (2006) found that the large number of sexual-multiplication cells is one of the necessary conditions for *N. scintillans* blooms. Excessive nutrients or eutrophication are important prerequisites and foundations for *N. scintillans* outbreaks (Turkoglu, 2013; Baliarsingh et al., 2016). Eutrophication provides a rich nutritional basis for the phytoplankton, which is beneficial for the proliferation of *N. scintillans* (Xu, 2009). Furthermore, Miyaguchi et al. (2006) documented that wind speed and precipitation can significantly affect the abundance of *N. scintillans*. Several recent studies have demonstrated the potential of satellite remote sensing in assessing *N. scintillans* blooms (Van Mol et al., 2007; Qi et al., 2019). *N. scintillans* cells have strong absorption in the blue–green wavelengths and strong scattering in all wavelengths (Astoreca et al., 2005), leading to distinguishable spectral reflectance shapes, for example, a sharp reflectance increases from 520 to 600 nm (Van Mol et al., 2007), where the enhanced reflectance continues to near-infrared wavelengths.

4.2.3 Biological properties and mechanisms underlying outbreak of *Thalassiosira diporocyclus*

Thalassiosira diporocyclus is a diatom with a rounding, convex, or flat, rarely concave, cell shell, and a circle of small or long thorns arranged radially around the shell surface (Hasle and Vertsen, 1997). In the center of the shell surface, there is a hole for secreting colloid, from which thick or thin colloidal filaments are generated, connecting the cells into a straight or slightly curved chain group (Figures 8G-I). Many *T. diporocyclus* cells live together in a colloidal colony (1–2 cm), while few single cells live. The colloidal colony of *T. diporocyclus* is solid spherical or ellipsoidal in shape and tawny or milky white. The tawny group is a normal healthy colony, while the milky white group is a colony in decline. Each colloidal colony is generally composed of *T. diporocyclus* cells distributed in the outer layer and pennatae diatoms embedded in the colloid (Figure 8G). This species must be identified by electron microscope, so previous historical datasets are often missed or misjudged. In this study, *T. diporocyclus* was listed as a high-risk species for blockages (Table 3, Figure 6). *T. diporocyclus* often developed into HABs along the coast of Fujian in recent years (Figure 3). Therefore, it was classified as a high-risk organism for Fuqing nuclear power plant on Southeast China coast.

In January 2002, a *T. diporocyclus* bloom occurred in the waters around Nanao Island on the southeast coast of China, which was the first record in China of an outbreak of *T. diporocyclus* (Chen et al., 2004). *T. diporocyclus* has a low bloom occurrence, originating from the open sea. The ecological mechanism of *T. diporocyclus* outbreaks may be related to the abnormal increase of water temperature caused by El Niño (Nagai et al., 1995; Miyahara et al., 1996; Chen et al., 2004). In normal years, the wind in autumn and winter seasons along the coast of China is generally northwesterly, forcing strong coastal currents from north to south. If the weather is abnormal and the northwest wind weakens while the southeast wind prevails, the southward coastal current may lessen accordingly, providing an opportunity for *T. diporocyclus* from the open sea to invade the coast of China (Yin et al., 1999). The occurrence of *T. diporocyclus* blooms is closely related to low salinity (23–28). Consequently, the sudden decrease in salinity during El Niño may also be one of the factors in the *T. diporocyclus* outbreak (Nagai et al., 1995; Miyahara et al., 1996; Chen et al., 2004).

4.2.4 Biological properties and mechanisms underlying outbreak of *Pseudo-nitzschia pungens*

Pseudo-nitzschia pungens is a typical species of the genus *Pseudonitzschia*, a chain-forming cosmopolitan marine pennate diatom (Casteleyn et al., 2008; Kimon et al., 2012). Cells of *P. pungens* are 74–142 µm long and 2.9–4.5 µm wide, with 9–15 striae in 10 µm and 9–15 fibulae in 10 µm, mainly lanceolate in both valve and girdle views, forming a long stepped colony (Hasle and Vertsen, 1997; Li, 2005) (Figures 8J, K). Blooms have been reported in Dalian, Qingdao, the Yangtze River estuary, Xiamen Port, and many harbors in the northern South China Sea (Lu and Qi, 1992; Zou et al., 1993; Qi et al., 1994; Yang and Hodgkiss, 2002). In addition, *P. pungens* is also one of the important toxigenic species, and reports from New Zealand (Rhodes et al., 1996), Washington (Trainer et al., 1998), Montreal Bay, and

California (Bates et al., 1998) found that it produces toxicants and is poisonous to aquatic organisms and humans. Chinese scholars have also tested the toxins of *P. pungens* in the East China Sea, but no domoic acid has been detected (Li, 2005).

Bates et al. (1998) identified that *P. pungens* blooms usually occur in summer, in the form of a chain-like multicellular population, while Dortch et al. (1997) reported that *P. pungens* is euryhaline, with a tolerance range of 0–36, which confers an advantage in salinities of 15–20. *P. pungens* has a strong ability to absorb inorganic nitrogen, which may make it competitive over other species for nitrogen to form blooms. However, its ability to absorb phosphate was weak, which may be a factor limiting its proliferation in the natural environment (Zhang and Zou, 1997). Experiments suggested that the nitrogen and phosphate demand for *P. pungens* growth did not show a proportional increase, but a certain range was required, with a relatively rapid growth in the range of 10–32 for c(N)/c(P). When c(N)/c(P) =5 or c(N)/c(P) =100, *P. pungens* growth was significantly inhibited (Lu et al., 2006). A long-term field observation on the south China coast showed that *P. pungens* blooms were positively correlated with nitrite and total nitrogen (Chen et al., 2002). Overall in this study, *P. pungens* was a high-risk, potential blocking organism in the sea area around the Fuqing nuclear power plant on Southeast China coast (Table 3, Figure 6).

4.3 Preventive measures against high-risk phytoplankton species for a nuclear power plant on the Southeast China coast

According to the Important Operation Event Report of WANO and relevant datasets, nuclear power plants usually adopt the "prevention first and control combined" method for blockages of marine biota in the cooling water system (Zhan and Zhao, 2005; ERPI, 2015; Tang et al., 2017; He et al., 2019b). The specific methods are mainly divided into physical, biological, and chemical prevention, according to the relevant mechanism (Mark, 2012; Wu et al., 2017; Tang, 2018; Fu et al., 2020; Yu et al., 2021). In view of the characteristics of phytoplankton outbreaks, in terms of early warning technology, focus should be on investigating phytoplankton distribution and dynamic monitoring, long-term water temperature monitoring in the thermal effluent mixed area, and satellite remote sensing monitoring (Kaplan et al., 2016; Dvorniko et al., 2017; Tang et al., 2017; Wei et al., 2018; Lu et al., 2018; Yu et al., 2021).

In terms of algae disinfection and sterilization, measures and methods with mature technology application, reasonable economic cost control, and low damage to biological resources and the marine environment are preferred (Cao et al., 2017; Yu et al., 2017; He et al., 2019b; Kang et al., 2020). Specifically, the modified clay method is a HABs emergency treatment technology that can be applied on a large scale in the field (GEOHAB, 2010; Yu et al., 2017; Getchis and Shumway, 2017). There have been many successful applications of modified clay, such as for the treatment of *P. globosa* in Fangchenggang nuclear power plant, in which it has been very effective in removing microalgae cells, with a removal rate of >90%. *P. globosa* sank into the seabed with the modified clay, where it decomposed and was inactivated (Yu et al., 2017; Cao et al., 2017). Based on the results of long-term dynamic monitoring and analyses of historical datasets, modified clay removal research should be carried out in the laboratory for potential phytoplankton outbreaks, and the modified clay formula and sterilization strategy should be optimized to provide technical support for the safety of cooling water systems in nuclear power plants (He et al., 2019b; Kang et al., 2020).

Chemical reagents are also a common method for algae bloom sterilization. These reagents include thiazolidinedione derivative TD49, suitable for semi enclosed bays, which has the highest inhibition rate of HABs at 2.0 μM (Baek et al., 2014); Sophorolipid, which significantly inhibits the activity and growth of algal cells between 20 and 5 mg/L, with no recurrence at higher concentrations (Lee et al., 2008); Hydrogen peroxide (Burson et al., 2014); Chitosan (Divakaran and Pillai, 2002), and NaOCl (Jeong et al., 2008). However, attention should be paid to the toxic effects of these chemical reagents on another marine biota (Cao et al., 2017; Yu et al., 2017).

5 Conclusions

A number of marine biota cause outbreaks, blocking cooling water systems, leading to the shutdown of nuclear power plants, while the invasion of marine biota seriously affects their safe operation. Based on the field monitoring data of phytoplankton in the sea area within 15 km of the Fuqing nuclear power plant, in combination with HABs datasets in Fujian on Southeast China coast from 2006 to 2021, this study determined the risk from phytoplankton species that may potentially block the cooling water system. Three principles of screening blocking organisms were determined, and a catalog of risk organisms and a monthly risk calendar were established. Nine high-risk species of phytoplankton that can easily form colonies, clusters, and groups in case of outbreaks were screened out in this study. The outbreak of various phytoplankton species varied between days, and the risk of blockages from phytoplankton was concentrated from April to July. In addition, a preliminary discussion on the biological characteristics and ecological mechanism of four high-risk species is given, including *Phaeocystis globosa*, *Noctiluca scintillans*, *Thalassiosira diporocyclus*, and *Pseudo-nitzschia pungens*, suggesting that the ecological mechanism of HABs had a high degree of temporal and spatial variability. As for preventive measures against high-risk phytoplankton species, the modified clay method was an effective technology, while use of chemical reagents should be aware of their toxic effects on marine biota. The results of this study show that nuclear power

plants face a high risk of blockage by marine biota in cooling water systems. It is recommended that the administration of nuclear power plants establish a regular monitoring mechanism for cooling water intake safety.

Data availability statement

The data that support the findings of this study are available from the corresponding author or the first author upon reasonable request.

Author contributions

YW: conceptualization, data curation, investigation, methodology, writing–original draft, and funding acquisition. XC and YL: conceptualization, funding acquisition, and validation. SZ, LC, and XT: investigation, formal analysis, and data analysis. PX and HL: project administration and supervision. All authors contributed to the article and approved the submitted version.

Funding

This study was supported by the National Natural Science Foundation of China (Nos. 41506136 and 41306115) and the Project of Ministry of Science and Technology (No. GASI-01-02-04).

Acknowledgments

The authors acknowledge Dr. Senming Tang from Hongkong University for fruitful discussion and for helping to revise the manuscript. Thanks to the team workers from Third Institute of Oceanography for HABs analysis. We would like to thank MogoEdit (https://www.mogoedit.com) for its English editing during the preparation of this manuscript. We sincerely appreciate the constructive comments and suggestions of the reviewers.

Conflict of interest

YL was employed by Fujian Fuqing Nuclear Power Company Limited.

The remaining authors declare that the research was conducted in the absence of any commercial or financial relationships that could be construed as a potential conflict of interest.

Publisher's note

References

Alsaffar, A. M., and Zheng, Y. F. (1999). Water intakes - Siting and design approaches. *Congress of the International Association for Hydraulics Research* (Maryland, USA: Biennial congress of the International Association for Hydraulics Research), 1–7.

Anderson, D. M., Cembella, A. D., and Hallegraeff, G. M. (2012). Progress in understanding harmful algal blooms: paradigm shifts and new technologies for research, monitoring, and management. *Annu. Rev. Mar. Sci.* 4, 143–176. doi: 10.1146/annurev-marine-120308-081121

Arefiev, N., Mikhalev, M., Zotov, D., Zotov, K., Vatin, N., Nikonova, O., et al. (2015). Physical modeling of suspended sediment deposition in marine intakes of nuclear power plants. *Proc. Eng.* 117, 32–38. doi: 10.1016/j.proeng.2015.08.120

Astoreca, R., Rousseau, V., Ruddick, K., Van Mol, B., Parent, J. Y., and Lancelot, C. (2005). "Optical properties of algal blooms in an eutrophicated coastal area and its relevance to remote sensing," in *Remote sensing of the coastal oceanic environment*. Eds. R. J. Frouin, M. Babin and S. Sathyendranath (San Diego, California, USA: Proc. SPIE), 245–255.

Baek, S. H., Son, M., Jung, S. W., Na, D. H., Cho, H., Yamaguchi, M., et al. (2014). Enhanced species-specific chemical control of harmful and non-harmful algal bloom species by the thiazolidinedione derivative TD49. *J. Appl. Phycol* 26, 311–321. doi: 10.1007/s10811-013-0046-z

Baliarsingh, S. K., Lotliker, A. A., Trainer, V. L., Wells, M. L., Parida, C., Sahu, B. K., et al. (2016). Environmental dynamics of red *Noctiluca scintillans* bloom in tropical coastal waters. *Mar. pollut. Bull.* 111, 277–286. doi: 10.1016/j.marpolbul.2016.06.103

Bates, S. S., Garrison, D. L., and Horner, R. A. (1998). "Bloom dynamics and physiology of domoic-acid- producing pseudo-nitzschia species," in *Physiological ecology of harmful algal blooms*. Eds. D. M. Anderson, A. D. Cembella and G. M. Hallegraeff (Heidelberg: Springer-Verlag), 267–292.

Berdalet, E., Kudela, R., Urban, E., Enevoldsen, H., Banas, N. S., Bresnan, E., et al. (2017). Global HAB: A new program to promote international research, observations, and modeling of harmful algal blooms in aquatic systems. *Oceanography* 30, 70–81. doi: 10.5670/oceanog.2017.111

Burson, A., Matthijs, H. C., de Bruijne, W., Talens, R., Hoogenboom, R., Gerssen, A., et al. (2014). Termination of a toxic alexandrium bloom with hydrogen peroxide. *Harmful Algae* 31, 125–135. doi: 10.1016/j.hal.2013.10.017

Cai, Z. P., Duan, L. Y., Xiao, Q., and Duan, S. S. (2011). Simulation study on promoted proliferation of *Skeletonema costatum* and *Phaeocystis globosa* disturbed by wave. *Mar. Environ. Sci.* 50, 630–643. doi: 10.1631/jzus.B1000171

Cao, X. H., Yu, Z. M., and Qiu, L. X. (2017). Field experiment and emergent application of modified clays for *Phaeocystis globosa* blooms mitigation. *Oceanologia Limnologia Sin.* 48, 753–759. doi: 10.11693/hyhz20170200026

Casteleyn, G., Chepurnov, V. A., Leliaert, F., Mann, D. G., Bates, S. S., Lundholm, N., et al. (2008). *Pseudo-nitzschia pungens* (Bacillariophyceae): a cosmopolitan diatom species? *Harmful Algae* 7, 241–257. doi: 10.1016/j.hal.2007.08.004

Chae, J., Choi, H. W., Lee, W. J., Kim, D., and Lee, J. H. (2008). Distribution of a pelagic tunicate, salpa fusiformis in warm surface current of the eastern Korean waters and its impingement on cooling water intakes of uljin nuclear power plant. *J. Environ. Biol.* 29, 585–590.

Chen, F. (2009). The principle of choosing tunnel gate location for nuclear power plants in the coastal sites in China. *Nucl. Saf.* 2, 25–29. doi: 10.3969/j.issn.1672-5360.2009.02.005

Chen, H. (2018). *Research on the causes, prevention and control measures of bio-blogging on nuclear power cold source by acaudina molpadioidea. master thesis* (Shanghai: Shanghai Ocean University).

Chen, S. W., Gao, Y. H., Du, H., Dong, Q. X., and Huang, C. J. (2004). First recording of *Thalassiosira diporocyclus* bloom in the southeast China Sea. *Oceanologia Limnologia Sin.* 35, 130–137. CNKI:SUN:HYFZ.0.2004-02-003

Chen, J. F., Xu, N., Wang, Z. H., Huang, W. J., and Qi, Y. Z. (2002). Dynamics of *Pseudo-nitzschia* spp. and environmental factors in daya bay, the south china sea. *Acta Scientiae Circumstantiae* 22, 743–748. CNKI:SUN:HJXX.0.2002-06-010

Dagnall, S. (2005). Nuclear fission: continuing evolution of a future generation. *Proc. Institution Civil Engineers-Civil Eng.* 158, 12–19. doi: 10.1680/cien.2005.158.6.12

Deng, K. (2013). *The life cycle of phaeocystis globosa and the effects of light, nutrient and co-existing diatom, dinoflagellates* (Guangzhou: Jinan University).

Deretz, D. (2007). *Manual reactor scram due to blocked circulating water intake screens* (Washington D.C, USA: United States Nuclear Regulatory Commission).

Divakaran, R., and Pillai, V. N. S. (2002). Flocculation of algae using chitosan. *J. Appl. Phycology* 14, 419–422. doi: 10.1023/A:1022137023257

Dortch, Q., Robichaux, R., Pool, S., Milsted, D., and Parsons, M. L. (1997). Abundance and vertical flux of *Pseudo-nitzschia* in the northern gulf of mexico. *Mar. Ecol. Prog.* 146, 249–264. doi: 10.3354/meps146249

Dvorniko, A. Y., Martyanov, S. D., Ryabchenko, V. A., Eremina, T. R., Isaev, A. V., and Sein, D. V. (2017). Assessment of extreme hydrological conditions in the bothnian bay, Baltic Sea, and the impact of the nuclear power plant "Hanhikivi-1" on the local thermal regime. *Earth System Dynamics* 8, 265–282. doi: 10.5194/esd-8-265-2017

ERPI (2015). *Service water intake blockages event forecasting for minimizing impacts* (Palo Alto: EPRI).

Florin, A. B., Mo, K., Svensson, F., Schagerström, E., Kautsky, L., and Bergström, L. (2013). First records of conrad's false mussel, mytilopsis leucophaeata (Conrad 1831) in the southern bothnian Sea, Sweden, near a nuclear power plant. *Ann-Britt Florin Kerstin Mo Filip Svensson BioInvasions Records* 4, 1–7. doi: 10.3391/bir.2013.2.4.07

Fu, X. C., Du, F. L., Pu, X., Wang, X., and Han, F. Z. (2020). Analysis on critical factors of marine organism impacts on water intake safety at nuclear power plants. *J. Nucl. Eng. Radiat. Sci.* 6, 1–6. doi: 10.1115/1.4048112

Fu, Y. Z., Han, C. W., and Xu, S. G. (2019). Review on mechanisms and mitigation measures of harmful algal blooms in coastal regions. *Mar. Environ. Sci.* 7, 146–152. doi: 10.13634/j.cnki.mes.2019.01.045

General Administration of Quality Supervision, Inspection and Quarantine of the People's Republic of China (2008). *Specifications for oceanographic survey-part 5: Survey of marine biology* (Beijing, China: China Standard Press), 1–40.

General Administration of Quality Supervision, Inspection and Quarantine of the People's Republic of China (2010). *Technical guidelines for sea area utilization demonstration in China* (Beijing, China: China Standard Press), 1–23.

General Administration of Quality Supervision, Inspection and Quarantine of the People's Republic of China (2014). *Technical guidelines for treatment with red tide disaster* (Beijing, China: China Standard Press), 1–70.

GEOHAB (2010). *Global ecology and oceanography of harmful algal blooms: Harmful algal blooms in Asia* (Paris and Newark, Delaware: IOC and SCOR), 68.

Getchis, T. L., and Shumway, S. E. (2017). *Harmful algae: An executive summary*. Connecticut Sea grant college program. CTSG-17-08, 1–16.

Glibert, P. M., Al-Azri, A., Allen, J. I., Bouwman, A. F., Beusen, A. H. W., Burford, M. A., et al. (2018). "Key questions and recent research advances on harmful algal blooms in relation to nutrients and eutrophication," in *Global ecology and oceanography of harmful algal blooms*. Eds. P. M. Glibert, E. Berdalet, M. A. Burford, G. Pitcher and M. J. Zhou (Cham: Springer), 229–259.

Hai, D. N., Lam, N. N., and Dippner, J. W. (2010). Development of *Phaeocystis globosa* blooms in the upwelling waters of the south central coast of Viet nam. *J. Mar. Syst.* 83, 253–261. doi: 10.1016/j.jmarsys.2010.04.015

Hamm, C. E., and Rousseau, V. (2003). Composition, assimilation and degradation of *Phaeocystis globosa*-derived fatty acids in the north Sea. *J. Sea Res.* 50, 271–283. doi: 10.1016/S1385-1101(03)00044-3

Han, D., Ji, P., Zhao, Y. J., Liu, Y., and Kang, Z. S. (2018). Investigation and analysis of water intake blockage in binhai nuclear power plant. *Water Wastewater Eng.* 44, 75–79. doi: 10.13789/j.cnki.wwe1964.2018.0265

Harrison, P. J., Furuya, K., Glibert, P. M., Xu, J., Liu, H. B., Yin, K., et al. (2011). Geographical distribution of red and green noctiluca scintillans. *J. Oceanology Limnology* 29, 807–831. doi: 10.1007/s00343-011-0510-z

Hasle, G. R., and Vertsen, E. E. (1997). "Marine diatoms," in *Identifying marine phytoplankton*. Ed. C. R. Tomas (San Diego: Academic Press), 5–385.

He, C., Song, S. Q., and Li, C. W. (2019a). The spatial-temperal distribution of phaeocystis globosa colonies and related affecting factors in guangxi beibu gulf. *Oceanologia Limnologia Sin.* 50, 630–643. doi: 10.11693/hyhz20180800192

He, L. Y., Song, X. X., Yu, F., Wang, K., Song, S. Q., and Yu, Z. M. (2019b). Potential risk and prevention of phytoplankton outbreak to water-cooling system in nuclear power plant in fangchenggang, guangxi. *Oceanologia Limnologia Sin.* 50, 700–706. doi: 10.11693/hyhz20190100004

Huang, C. J., Qi, S., Qi, Y. Z., and Lin, X. (1997). The position and function of *Noctiluca scintillans* in its ecological community in dapeng bay, the south China Sea. *Oceanologia Limnologia Sin.* 28, 348–355. doi: 10.1007/BF02951625

Jang, M. C., Shin, K. S., Jang, P. G., and Lee, W. J. (2010). Relationship between environmental factors and short-term variations of mesozooplankton during summer in jangmok bay, south coast of Korea. *Ocean Polar Res.* 32, 41–52. doi: 10.4217/OPR.2010.32.1.041

Jeong, H. J., Kim, J. S., Yoo, Y. D., Kim, S. T., Song, J. Y., Kim, T. H., et al. (2008). Control of the harmful alga *Cochlodinium polykrikoides* by the naked ciliate strombidinopsis jeokjo in mesocosm enclosures. *Harmful Algae* 7, 368–377. doi: 10.1016/j.hal.2007.12.004

Kang, Z., Yang, B., Lai, J., Ning, Y., Zhong, Q., Lu, D. L., et al. (2020). *Phaeocystis globosa* bloom monitoring: Based on *P. globosa* induced seawater viscosity modification adjacent to a nuclear power plant in qinzhou bay, china. J. *Ocean Uni. China* 19, 1207–1220. doi: 10.1007/s11802-020-4481-6

Kaplan, E. M., Shvarts, A. A., Luneva, E. V., Makushenko, M. E., and Rumynin, V. G. (2016). Transboundary aspect of assessing the impact of NPPs under construction on aquatic ecosystems: Case study of the baltiiskaya NPP. *Water Resour* 43, 911–922. doi: 10.1134/S0097807816070046

Karlson, B., Cusack, C., and Bresnan, E. (2010). *Microscopic and molecular methods for quantitative phytoplankton analysis. IOC manuals and guides, 55* (Paris: UNESCO), 114.

Kimon, K. M., Athanasios, D. B., Panagiota, K., Dimitra, P., Georgios, N., and Theodore, J. A. (2012). Inter- and intra-specific diversity of *Pseudo-nitzschia* (Bacillariophyceae) in the northeastern mediterranean. *Eur. J. Phycology* 47, 321–339. doi: 10.1080/09670262.2012.713998

King, R. G., Seegert, G., Vondruska, J., Perry, E. S., and Dixon, D. A. (2010). Factors influencing impingement at 15 Ohio river power plants. *N. Am. J. Fish Manage* 30, 1149–1175. doi: 10.1577/M09-121.1

Kirsti, J., Matti, K., Carl, F., Hilppa, G., Juho, H., Otto, H., et al. (2018). Recent meteorological and marine studies to support nuclear power plant safety in finland. *Energy* 165, 1102–1118. doi: 10.1016/j.energy.2018.09.033

Kumar, S. B., Mohanty, A. K., Das, N. P. I., Satpathy, K. K., and Sarkar, S. K. (2017). Impingement of marine organisms in a tropical atomic power plant cooling water system. *Mar. pollut. Bull.* 124, 555–562. doi: 10.1016/j.marpolbul.2017.07.067

Lee, Y. J., Choi, J. K., Kim, E. K., Youn, S. H., and Yang, E. J. (2008). Field experiments on mitigation of harmful algal blooms using a sophorolipid–yellow clay mixture and effects on marine plankton. *Harmful Algae* 7, 154–162. doi: 10.1016/j.hal.2007.06.004

Le Fèvre, J., and Grall, J. R. (1970). On the relationships of noctiluca swarming off the western coast of Brittany with hydrological features and plankton characteristics of the environment. *J. Exp. Mar. Biol. Ecol.* 4, 287–306. doi: 10.1016/0022-0981(70)90040-7

Li, A. F. (2005). *Studies on the analytical methods of marine biotoxins with liquid chromatography mass spectrometry (LC-MS)* (Qingdao: Institute of Oceanology, Chinese Academy of Sciences).

Li, X. D. (2012). Analysis on characteristics of red tide in fujian coastal waters during the last 10 years. *Environ. Sci.* 33, 2210–2216. CNKI:SUN:HJKZ.0.2012-07-011

Li, D. M., Gao, Y. L., Tian, T., Cyrus, L., and Yin, K. D. (2010). Effects of turbulence on phytoplankton: species differences. *J. Trop. Oceanography* 29, 65–70. doi: 10.3969/j.issn.1009-5470.2010.06.010

Lin, J. N., Tian, Y., Zhang, Q. C., Wang, Y. F., Liu, Q., and Zhou, M. J. (2016). The detrimental impacts of *Karenia mikimotoi* blooms on the abalone *Haliotis discus hannai* in fujian province. *Mar. Environ. Sci.* 35, 27–34. doi: 10.13634/j.cnki.mes.2016.01.005

Liu, H. Y. (2019). The importance of cold source in nuclear power plant. *Ind. Sci. Tribune* 18, 69–70. CNKI:SUN:CYYT.0.2019-09-036

Lu, S. H., Chen, H. L., and He, Z. Q. (2006). The effects of different c(N)/c(P) ratios on the growth of *Pseudo-nitzschia pungens*. *Ecol. Environ.* 15, 697–701. doi: 10.3969/j.issn.1674-5906.2006.04.008

Lu, H. R., Meng, Y. H., Zhang, X. C., and Duan, Y. B. (2018). Research on monitoring and early-warning system of marine organisms for the intake of nuclear power plants. *Anim. Husbandry Feed Sci.* 10, 236–240. CNKI:SUN:AHFS.0.2018-04-006

Lu, S. H., and Qi, Y. Z. (1992). Main red tide causative species of da peng bay, south China Sea. *J. Jinan Univ. (Natural Science)* 13, 130–133.

Mark, S. (2012). Marine ecology: Attack of the blobs. *Nature* 482, 20–21. doi: 10.1038/482020a

Matsumura, K., Kamiya, K., Yamashita, K., Hayashi, F., Watanabe, I., Murao, Y., et al. (2005). Genetic polymorphism of the adult medusae invading an electric

power station and wild polyps of aurelia aurita in wakasa bay, Japan. *J. Mar. Biol. Assoc. Uk* 85, 563–568. doi: 10.1017/S0025315405011483

Meng, Y. H., Liu, L., Guo, X. J., Liu, N., and Liu, Y. (2018). An early warning and decision support system of marine organisms in a water cooling system in a nuclear power plant. *J. Dalian Ocean Univ.* 33, 108–112. doi: 10.16535/j.cnki.dlhyxb.2018-020

Mikaelyan, A. S., Malej, A., Shiganova, T. A., Turk, V., Sivkovitch, A. E., Musaeva, E. I., et al. (2014). Populations of the red tide forming dinoflagellate *Noctiluca scintillans* (Macartney): A comparison between the black Sea and the northern Adriatic Sea. *Harmful Algae* 33, 29–40. doi: 10.1016/j.hal.2014.01.004

Miyaguchi, H., Fujiki, T., Kikuchi, T., Kuwahara, V. S., and Toda, A. T. (2006). Relationship between the bloom of *Noctiluca scintillans* and environmental factors in the coastal waters of sagami bay, Japan. *J. Plankton Res.* 28, 313–324. doi: 10.1093/plankt/fbi127

Miyahara, K., Nagai, S., Itakura, S., Yamamoto, K., Fujisawa, K., Iwamoto, T., et al. (1996). First record of a bloom of thalassiosira diporocyclus in the eastern seto inland Sea. *Fisheries Sci.* 62, 878–882. doi: 10.2331/fishsci.62.878

Moreau, O., Beddek, K., Clénet, S., and Le Menach, Y. (2013). Stochastic nondestructive testing simulation: sensitivity analysis applied to material properties in clogging of nuclear power plant steam generators. *IEEE Trans. Magnetics* 49, 1873–1876. doi: 10.1109/TMAG.2013.2243409

Nagai, S., Miyahara, K., and Hori, Y. (1995). Blooming of *Thalassiosira* sp. in harima-nada, the eastern seto inland Sea, in the winters of 1994 and 1995. *Bull. Hyogo Prefect* 32, 9–17.

Nejstgaard, J. C., Tang, K. W., Steinke, M., Dutz, J., Koski, M., and Long, A. (2007). Phaeocystis, major link in the biogeochemical cycling of climate-relevant elements || zooplankton grazing on phaeocystis: A quantitative review and future challenges. *Biogeochemistry* 83, 147–172. doi: 10.1007/s10533-007-9098-y

Peperzak, L., Colijn, F., Gieskes, W., and Peeters, J. (1998). Development of the diatom-phaeocystis spring bloom in the Dutch coastal zone of the north Sea: The silicon depletion versus the daily irradiance threshold hypothesis. *J. Plankton Res.* 20, 517–537. doi: 10.1093/plankt/20.3.517

Prakash, S., Kolluru, V. S., and Tutton, P. (2012). "Semi-Lagrangian approach to studying grassing issue on a nuclear power plant cooling water intake," in *Proceedings of 10th International Conference on Hydroscience and Engineering (ICHE 2012)*. (Orlando, Florida, USA)., 1–26.

Qian, H. L., Liang, S., Qi, Y. Z., Deng, A. Q., and Chen, J. H. (1994). Study on ecology model of *Noctiluca scintillans* red tide in north coastal waters of south China Sea. *Ecol. Sci.* 40, 39–46.

Qi, L., Tsai, S. F., Chen, Y., Le, C., and Hu, C. (2019). In search of red *Noctiluca scintillans* blooms in the East China Sea. *Geophys. Res. Lett.* 46, 5997–6004. doi: 10.1029/2019GL082667

Qi, Y. Z., Wang, J., and Zheng, L. (1994). "The taxonomy and bloom ecology of pseudo-nitzschia on the coasts of China," in *Proceedings IOC-WESTPAC third international scientific symposium* (Bali, Indonesia: Indonesia Institute of Sciences), 88–95.

Rhodes, L. L., White, D., Syhre, M., and Atkinson, M. (1996). "Pseudo-nitzschia species isolated from new Zealand coastal waters: Domoic acid production in vitro and links with shellfish toxicity,". Eds. T. Yasumoto, Y. Oshima and Y. Fukuyo. *Harmful and Toxic Algal Blooms* (Paris: IOC UNESCO), 155–158.

Ruan, G. P. (2015). Reason analysis and corresponding strategy for cooling water intake blockage at nuclear power plants. *Nucl. Power Eng.* 36, 151–154. doi: 10.13832/j.jnpe.2015.S1.0151

Shen, P. P., and Qi, Y. Z. (2021). Research progress on species diversity and distribution of the genus phaeocystis. *Oceanol Et Limnol Sin.* 52, 1–15. doi: 10.11693/hyhz20200300085

Song, S. Q., Li, C., and Sun, J. (2016). Progress on studies of sexual reproduction in *Noctiluca scintillans*. *Acta Ecologica Sin.* 36, 2451–2459. doi: 10.5846/stxb201312212994

Tada, K., Pithakpol, S., and Montani, S. (2004). Seasonal variation in the abundance of *Noctiluca scintillans* in the seto inland Sea, Japan. *Plankton Biol. Ecol.* 51, 7–14.

Tang, Y. F. (2018). *Study on typical disaster-causing organisms of coastal nuclear power operation safety:Taking ningde nuclear power as an example* (Shanghai: Shanghai Ocean University).

Tang, Z., Cheng, F., Jin, X., Sun, L., Bao, R. Y., and Liu, Y. (2017). An automatic marine-organism monitoring system for the intake water of the nuclear power plant. *Ann. Nucl. Energy* 109, 208–211. doi: 10.1016/j.anucene.2017.05.040

Tang, D. L., Di, B. P., Wei, G. F., Ni, I. H., Oh, I. S., and Wang, S. F. (2006). Spatial, seasonal and species variations of harmful algal blooms in the south yellow Sea and East China Sea. *Hydrobiologia* 568, 245–253. doi: 10.1007/s10750-006-0108-1

Trainer, V. L., Adams, N. G., Bill, B. D., Anulacion, B. F., and Wekell, J. C. (1998). Concentration and dispersal of a *Pseudo-nitzschia* bloom in Penn Cove, Washington, USA. *Nat. Toxins* 6, 1–13. doi: 10.1002/(SICI)1522-7189(199805/08)6:3/4<113::AID-NT14>3.0.CO;2-B

Tungaraza, C., Rousseau, V., Brion, N., Lancelot, C., Gichuki, J., Baeyens, W., et al. (2003). Contrasting nitrogen uptake by diatom and phaeocystis dominated phytoplankton assemblages in the north Sea. *J. Exp. Mar. Biol. Ecol.* 292, 19–41. doi: 10.1016/S0022-0981(03)00145-X

Turkoglu, M. (2013). Red tides of the dinoflagellate *Noctiluca scintillans* associated with eutrophication in the Sea of marmara (the dardanelles, Turkey). *Oceanologia* 55, 709–732. doi: 10.5697/oc.55-3.709

Van Mol, B., Ruddick, K., Astoreca, R., Park, Y. J., and Nechad, B. (2007). Optical detection of a *Noctiluca scintillans* bloom. *EARSeL eProceedings* 6, 130–137. doi: 10.3354/meps132299

Wang, M. (2006). *Study on determination of biomass and the effects of salinity, nitrogen, phosphorus, iron on the growth of phaeocystis globosa* (Guangzhou: Jinan University).

Wang, K., Chen, B. H., Gao, Y. H., and Lin, H. (2021). Harmful algal blooms caused by phaeocystis globosa from 1997 to 2018 in Chinese coastal waters. *Mar. pollut. Bull.* 173, 112949. doi: 10.1016/j.marpolbul.2021.112949

Wang, X. D., and Tang, K. W. (2010). Buoyancy regulation in *Phaeocystis globosa* scherffel colonies. *Open Mar. Biol. J.* 4, 115–121. doi: 10.2174/1874450801004010115

Wang, X. D., Wang, Y., and Smith, J. R. W. O. (2011). The role of nitrogen on the growth and colony development of *Phaeocystis globosa* (Prymnesiophyceae). *Eur. J. Phycology* 46, 305–314. doi: 10.1080/09670262.2011.602430

Wei, X. Y., Wang, Y. C., Zhang, K., Dang, Y. Q., Xiong, X. W., and Shang, Z. R. (2018). Review of impact assessments of thermal discharges from power plants on aquatic biota. *J. Hydroecology* 39, 1–10. doi^ 978-1-5386-1243-9/18/$31.00_c2018IEEE

Wu, Y. N., Wang, Y. Q., Hou, Q. M., Jiao, F., and Sun, G. C. (2017). Experience feedbacks on events of nuclear power plants cold source systems blocked by oceanic foreign matter. *Nucl. Saf.* 16, 26–32. doi: 10.16432/j.cnki.1672-5360.2017.01.006

Xu, Z. (2006). Ecological characters of the *Eucalanus subcrassus* population in the East China Sea. *Acta Ecologica Sin.* 26, 1151–1158. doi: 10.3321/j.issn:1000-0933.2006.04.024

Xu, Z. L. (2009). The inter annual variations in *Noctiluca scintillans* abundance and eutrophication in changjiang estuary. *Oceanologia Limnologia Sin.* 40, 743–748. doi: 10.11693/hyhz200906019019

Yang, Z. B., and Hodgkiss, I. J. (2002). "Potentially harmful pseudo-nitzschia species in Hong Kong coastal waters," in *Prevention and management of harmful algal blooms in the south China Sea*. Eds. K. C. Ho, H. Y. Lin and Z. X. Yu (Hong Kong: Environmental Publication House), 123–128.

Yang, J., Zhang, E. H., Guo, Z. H., Wu, A. G., Wang, B. Q., Shi, L. H., et al. (2020). Recent progress of frontier nuclear energy science and technology. *Sci. Technol. Rev.* 38, 35–49. doi: 10.3981/j.issn.1000-7857

Yan, G. C., and Lu, W. T. (2016). Prevention and management of invasions blockage in water intake of power plant. *Ind. Technol.* 14, 119–119. CNKI:SUN:CXYY.0.2016-14-091

Yin, K. D., Harrison, P. J., Chen, J., Huang, W., and Qian, P. Y. (1999). Red tides during spring 1998 in Hong Kong:Is El niño responsible? *Mar. Ecol. Prog. Ser.* 187, 289–294. doi: 10.3354/meps187289

Yu, Z. M., and Chen, N. S. (2019). Emerging trends in red tide and major research progresses. *Oceanologia Limnologia Sin.* 050, 474–486. CNKI:SUN:HYFZ.0.2019-03-003

Yu, Z. M., Kai, W., Cao, X. H., Wang, B. Z., and Xin, X. (2017). "Feasibility and implementation of the modified clay technique in control of *Phaeocytstis globosa* blooms in the water-intake area of the fangchenggang nuclear power plant," in *2017 25th International Conference on Nuclear Engineering, American Society of Mechanical Engineers Digital Collection*. (Shanghai, China) 1–7. doi: 10.13634/j.cnki.mes.2021.01.019

Yu, F., Xu, B. T., Wu, X., Bai, J., and Li, Y. (2021). Study on the method of marine organisms investigation, screening and evaluation based on nuclear power plant cold source safety. *Mar. Environ. Sci.* 40, 139–143.

Zhang, C. W., Guan, C. J., Peng, X. U., Liu, G. Z., Xu, Q. M., Ye, J., et al. (2019). Analysis on risk organisms for the cold source water of nuclear power plant in the eastern waters of liaodong bay. *Mar. Environ. Sci.* 38, 41–45. doi: 10.13634/j.cnki.mes.2019.01.030

Zhang, Q., Zhou, S., Wang, X. H., and Zhang, J. Q. (2018). Design and implementation of marine biological preparedness monitoring system of nuclear power plant. *DEStech Trans. Comput. Sci. Eng. (wcne)* 453–457. doi: 10.12783/dtcse/wcne2017/19897

Zhang, C., and Zou, J. Z. (1997). Nutrient uptake kinetics and growth under nutrient limitation of *Pseudo-nitzschia*. *Oceanologia Limnologia Sin.* 28, 599–603. doi: 10.1007/BF02951625

Zhan, L., and Zhao, M. (2005). Statistics and analysis of WANO human factor events. *Nucl. Power Eng.* 26, 291–296. doi: 10.3969/j.issn.0258-0926.2005.03.019

Zou, J. Z., Zhou, M. J., and Zhang, C. (1993). "Ecological features of toxic nitzschia pungens grunow in Chinese coastal waters," in *Toxic phytoplankton blooms in the Sea*. Eds. T. J. Smayda and Y. Shimizu (Amsterdam: Elsevier), 651–657.

frontiers | Frontiers in Marine Science

TYPE Original Research
PUBLISHED 22 November 2022
DOI 10.3389/fmars.2022.1070737

OPEN ACCESS

EDITED BY
Meilin Wu,
South China Sea Institute of Oceanology (CAS), China

REVIEWED BY
Zhanhui Qi,
Key Laboratory of South China Sea Fishery Resources Exploitation and Utilization, South China Sea Fisheries Research Institute (CAFS), China
Jeffrey Ren,
National Institute of Water and Atmospheric Research (NIWA), New Zealand

*CORRESPONDENCE
Tao Jiang
jiangtaophy@163.com
Zhengguo Cui
cuizg@ysfri.ac.cn

SPECIALTY SECTION
This article was submitted to Coastal Ocean Processes, a section of the journal Frontiers in Marine Science

RECEIVED 15 October 2022
ACCEPTED 31 October 2022
PUBLISHED 22 November 2022

CITATION
Jiang T, Pan H, Steeves L, Jiang Z, Filgueira R, Strand Ø, Strohmeier T, Cranford PJ and Cui Z (2022) Effect of *Mytilus coruscus* selective filtration on phytoplankton assemblages. *Front. Mar. Sci.* 9:1070737. doi: 10.3389/fmars.2022.1070737

Effect of *Mytilus coruscus* selective filtration on phytoplankton assemblages

Tao Jiang[1]*, Huizhu Pan[2,3], Laura Steeves[4], Zengjie Jiang[2], Ramón Filgueira[4,5], Øivind Strand[5], Tore Strohmeier[5], Peter J. Cranford[6] and Zhengguo Cui[2]*

[1]School of Ocean, Yantai University, Yantai, China, [2]Key Laboratory of Sustainable Development of Marine Fisheries, Ministry of Agriculture, Yellow Sea Fisheries Research Institute, Chinese Academy of Fishery Sciences, Qingdao, China, [3]Guangxi Key Laboratory of Marine Environmental Science, Guangxi Beibu Gulf Marine Research Center, Guangxi Academy of Sciences, Nanning, China, [4]Marine Affairs Program, Dalhousie University, Halifax, NS, Canada, [5]Institute of Marine Research, Bergen, Norway, [6]Department of Fisheries and Oceans, St. Andrews Biological Station, St. Andrews, NB, Canada

The feeding selectivity of bivalves can play an important role in shaping the structure of phytoplankton communities of natural waters. This could be particularly true in waters with intensive bivalves farming, like Sungo Bay, Northern China. Understanding the role of bivalve feeding behavior is important for assessing how the dense cultivation of bivalves may affect phytoplankton community composition and food web structure in farm areas. In this study, we investigated the feeding selectivity of blue mussel *Mytilus coruscus* on natural phytoplankton assemblages in Sungo Bay using both optical microscopy and HPLC-pigment analysis. Results showed that cryptophytes dominated the phytoplankton community and made up 66.1% of the total phytoplankton abundance. A comparison of phytoplankton composition between natural and filtered seawater showed that *M. coruscus* preferred cryptophytes and dinoflagellates than *Chaetoceros* spp. and *Skeletonema* spp. Cryptophytes were not detected in gut contents by microscopic observation, while their marker pigment alloxanthin was present, suggesting they were also consumed by *M. coruscus* and can be readily digested. This highlights the shortcomings of microscopic methods and the significance of HPLC-pigment analysis in obtaining a comprehensive understanding of feeding selectivity of bivalves. The proportions of *Chaetoceros* spp. and *Skeletonema* spp. in gut contents were significantly lower than their proportions in the seawater, and contrastingly, the proportions of *Cocconeis* spp. and *Pinnularia* spp. showed opposite patterns. The marker pigments prasinoxanthin and zeaxanthin were detected in the gut of *M. coruscus* indicating that picophytoplankton (e.g., prasinophytes and *Synechococcus*) are also food sources for this bivalve. This information furthers our understanding of bivalve aquaculture and environment interactions.

KEYWORDS

feeding selectivity, preferential feeding, phytoplankton, pigments, *Mytilus coruscus*, Sungo Bay

Introduction

Bivalves like mussels, oysters, and scallops are key species for mariculture in coastal waters worldwide (Ward and Shumway, 2004; Filgueira et al., 2016). It is well known that filter-feeding bivalves play an important role in shaping the structure of phytoplankton community (Dame and Prins, 1998; Nakamura and Kerciku, 2000; Filgueira et al., 2012). However, there remain unknowns about the relationship between bivalve filter-feeding and phytoplankton assemblages, particularly for dense populations of bivalves in farming areas (Cédric et al., 2003).

Bivalves are exposed to diverse particles (living and nonliving; large and small) in the marine environment. Generally, suspension-feeding bivalves capture particles of increasing size with increasing efficiency, until some size threshold is met, beyond which all particles cannot be effectively captured (reviewed by Rosa et al., 2018); for example, the threshold for *M. edulis* is ~4 μm (Riisgård, 1988; Riisgård & Larsen, 2010). It has been found that some particles are more likely to be captured by bivalves than others, despite being similar in size (Shumway et al., 1985; Naddafi et al., 2007). This suggests that qualitative aspects apart from size can influence selective feeding (Grizzle et al., 2001; Ward & Shumway, 2004; Rosa et al., 2021). Previous studies have found that some bivalves may have flexible feeding behaviors in response to changes in particle composition and concentrations (e.g. Bayne & Worrall, 1980; Hawkins et al., 1996; Beninger et al., 2008; Strohmeier et al., 2012).

In some previous studies, the issue of feeding selectivity in bivalves has been addressed using various combinations of laboratory cultured algae (Shumway et al., 1985; Bougrier et al., 1997; Pales Espinosa et al., 2016; Rosa et al., 2017). These studies have found that bivalves can preferentially select different algal species based on the size, morphology, particle shape, and motility (Ward & Shumway, 2004); toxicity, nutritional contents (Ren et al., 2006); and membrane composition of the prey (Rosa et al., 2018). Feeding experiments conducted in a laboratory with a cultured diet may not appropriately reflect *in situ* conditions. Short-term variations of phytoplankton biomass and species composition may continually occur in response to the changing marine environments (Filgueira et al., 2016). Previous studies have explored particle selection by suspension feeders using natural algal assemblages (Cognie et al., 2001; Yahel et al., 2006; Naddafi et al., 2007; Yahel et al., 2009; Safi and Hayden, 2010; Frau et al., 2016). In those studies, the microscopic method has generally been used to study the feeding of phytoplankton by bivalves. The comparison of phytoplankton assemblages between gut contents and the surrounding seawater has also been performed to deal with their differential utilization by bivalves (Kamermans, 1994; Rouillon et al., 2005). However, the microscopic method can easily omit fragile or small phytoplankton cells in seawater, especially in gut contents of bivalves (Trottet et al., 2008). This would introduce a bias into evaluating the effects of selective feeding of bivalves on phytoplankton biomass and community, as well as bivalve diet in the natural environment. In recent decades, high-performance liquid chromatography (HPLC) based pigments analysis has been developed, which provides a chemotaxonomic qualitative and quantitative analysis for phytoplankton as certain key pigments are sensitive indicator of different algal groups (Zapata et al., 2000). The HPLC-pigment method is appropriate for the identification of fragile cells and small cells, but it cannot provide accurate taxonomical information (to species or genus) of phytoplankton (Pan et al., 2020). Nevertheless, this method has provided much important information in the studies of both feeding and digestion of molluscs (Loret et al., 2000; Lavaud et al., 2018; Jiang et al., 2019). Consequently, a combination of these two methods might provide a further understanding of the effects of bivalve selective feeding on the profile of phytoplankton communities in aquaculture sites (Trottet et al., 2008).

In the present study, we investigated the selective feeding of phytoplankton assemblages by *M. coruscus* in farming waters of Sungo Bay. We focused on two aspects of feeding selectivity: clearance (also referred to as 'retention') efficiency in the seawater, and a comparison between seawater and gut contents. The species compositions of phytoplankton in seawater and mussel gut contents were identified using microscopic counting and HPLC-pigment analysis. This study furthers our understanding of feeding selectivity and diet composition of *M. coruscus*, and more broadly about the potential effects of bivalve aquaculture on phytoplankton communities.

Materials and methods

Experimental design

Sungo Bay is located in northern China and characterized by a temperate climate. It has been used for farming bivalves (e.g., oyster *Crassostrea gigas* and Chinese scallop *Chlamys farreri*) and seaweed (*Saccharina japonica*) for several decades. The feeding experiments were conducted on a floating platform in a semi-enclosed dock of Sungo Bay (37°02′07′′ N, 122°32′58′′ E), China. The seawater used for the experiments was pumped from 50 m off the shore at a depth of 3m (Fig 1), which is about 3 km away from an aquaculture area. The water temperature and salinity were around 24°C and 31, respectively. Previous study showed that the diatoms are the most common species and dominate the phytoplankton community in this area (Wang, 2017; Hou et al., 2021). During the past several decades, the species number and Shannon's diversity index of phytoplankton in Sungo Bay have declined, which has been ascribed to the high biomass of cultured shellfish (Hou et al., 2021).

Eight groups of feeding experiments with *M. coruscus* were performed. The experimental groups NO. 1-6 and NO. 7-8 were performed on Sept. 16 and 20, 2018, respectively (Table 1). Before the experiments, all mussels were placed in a large plastic chamber (20 l) over 24 h with continuous seawater influx from a branch pipe of the headwater, which was the same source as the feeding experiments (Figure 1). In each experimental group, three mussels were placed in independent 1.0 l PVC chambers (as described in Cranford et al., 2016) supplied with seawater. The chambers were mounted on magnetic stirrers to ensure that the water was well mixed. The chambers were maintained in flow-through until all mussels were observed to be open. At that point, the flow of water was interrupted, and the chambers became static. The size distribution of the particles in each chamber was monitored using a PAMAS S40 GO instrument (PAMAS, Rutesheim, Germany) (Figure 1). Particle counts were measured once every 30 seconds throughout the static incubations. Particles were both counted across different size bins. Static incubations were run either until ~50% of particles larger than 8.0 μm were depleted, or for a maximum of one hour, which resulted in different incubations times across experimental groups (Table 1). The length of *M. coruscus* ranged from 45 to 56 mm. The experimental groups NO. 1-5 and 7 were used for studying the clearance of phytoplankton cells by *M. coruscus* using the microscopic method and the experimental groups NO. 6 and 8 were for the clearance of phytopigments by the HPLC pigments determination.

Microscopic observations for phytoplankton

For the experimental groups NO. 1-5 and 7, triplicate aliquots of 1.0 L seawater from the headwater were collected for microscopic analyses. After completion of each experiment, the filtered seawater in the chamber was also collected, and its volume was measured. Seawater samples were fixed by Lugol's solution and concentrated to 5–15 mL overnight settling, with 0.1 mL placed in a counting chamber and counted under light microscopy (Olympus BH-2, Olympus, Tokyo, Japan). Each

TABLE 1 Experimental design and total phytoplankton biomass in each experimental group (n=3 mussels for each group).

Experimental groups	Phytoplankton biomass before feeding experiment	Phytoplankton biomass after feeding experiment	Clearance efficiency (%)	Experiment time (h)	Refiltration index (RI)
Microscopic method	Cell density (10^4 cell l^{-1})				
NO. 1	24.8 ± 5.3	3.3	86.8	1.00	0.82
		1.3	94.9	1.00	1.47
		3.0	87.8	1.00	1.56
NO. 2	24.7 ± 5.3	4.0	83.8	0.71	0.35
		5.0	79.6	0.72	0.93
		8.7	64.7	0.71	1.04
NO. 3	36.6 ± 1.8	22.6	38.2	0.29	0.04
		18.0	50.9	0.28	0.65
		7.3	80.0	0.29	0.57
NO. 4	36.7 ± 5.1	21.6	41.1	0.28	0.05
		25.0	32.0	0.27	0.24
		20.3	44.7	0.26	0.40
NO. 5	36.5 ± 3.2	14.9	59.2	0.33	0.60
		1.8	95.2	0.33	1.41
		17.0	53.3	0.33	0.11
NO. 7	14.3 ± 1.7	1.1	92.2	0.68	1.61
		2.2	84.7	0.68	1.38
		2.5	82.6	0.68	1.45
HPLC method	Chl *a* concentration (ng l^{-1})				
NO. 6	575.9 ± 267.9	137.8	76.1	0.31	0.34
		87.0	84.9	0.33	0.67
		391.6	32.1	0.32	0.07
NO. 8	122.1 ± 4.3	76.4	37.5	0.41	1.16
		55.1	54.9	0.41	0.13
		105.9	13.3	0.41	0.36

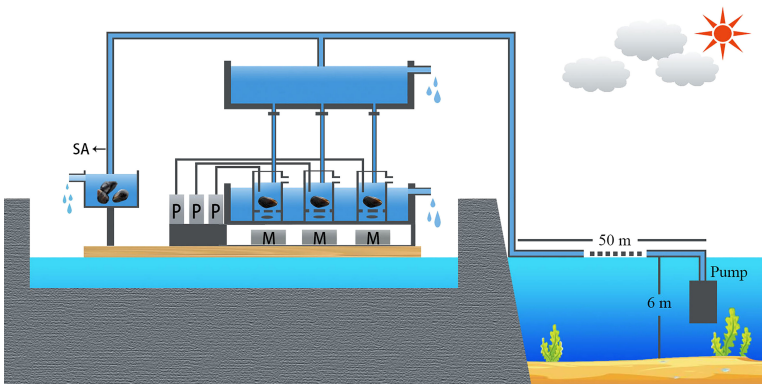

FIGURE 1
Feeding experiments in the Sungo Bay. (P, PAMAS; M, Magnetic stirrer; SA, Maintenance of *M. coruscus* samples).

sample was counted in triplicate and at least 350 cells were identified per counting.

HPLC-pigment analysis for sea water

For the experimental groups NO. 6 and 8, 1.0 L seawater (n=3) from the headwater was filtered through GF/F filters (0.7 μm pore size, 47 mm diameter, Whatman). After feeding experiments, the volume of remaining seawater in each chamber was measured, and then filtered as described above. The filters were immediately put into liquid nitrogen and stored until HPLC analysis. Pigment extraction and determination were performed according to Zapata et al. (2000). The 21 pigment standards were purchased from DHI (Denmark) (Table S1). All HPLC procedures were described by Pan et al. (2020).

Gut content analysis

After completion of the feeding experiments, mussel gut contents were immediately collected into a plastic tube by making an incision through to the gut cavity and rinsing of contents using filtered seawater (GF/F filter (< 0.7 μm)). Gut contents of the 15 individuals in experimental Groups NO. 1-5 were fixed in Lugol's solution for phytoplankton analysis by microscope described as in Section Microscopic observations for phytoplankton. Due to heavy disturbance by detritus, only 7 out of 15 mussel gut samples could achieve counts of > 200 algal cells (note that cryptophyte species were not observed due to digestion, see Section 3.4), which was the adopted threshold to guarantee the accuracy of the data (Venrick, 1978). Consequently, the other 8 samples were excluded in this study. The gut content of the 3 individuals of Group NO. 6 and 8 were filtered onto independent GF/F filters for pigments analysis described as in Section HPLC-pigment analysis for sea water.

Clearance and selectivity of phytoplankton

In each experimental group, clearance efficiency (CE) of phytoplankton for each *M. coruscus* was calculated as follows (Vahl, 1972):

$$CE\,\% = \left(1 - \frac{PB_{af}}{PB_{bf}}\right) \times 100 \quad (1)$$

where, PB_{bf} and PB_{af} are the phytoplankton biomass (cell density (cell l^{-1}) by microscopic counting and pigments concentration (ng l^{-1}) by HPLC analysis) in the natural seawater (headwater) and experimental water before and after the experiment, respectively.

For the whole experiment, the ratios of clearance efficiency (RCE) for certain phytoplankton genera or groups against total phytoplankton were calculated to describe the degree of selective clearance by *M. coruscus*, as shown in formula (2):

$$RCE = \frac{CE_{phyto}}{CE_{total}} \quad (2)$$

where CE_{phyto} is CE of certain phytoplankton genera or group; CE_{total} is CE of total phytoplankton. For certain phytoplankton genera or group, RCE > 1 means it is selectively filtered by *M. coruscus*, while RCE < 1 means it is selectively rejected.

Refiltration index

Given the different static incubation times and individual variability in terms of pumping activity, a refiltration index was calculated for comparative purposes across different mussels.

This index describes the total amount of water that was pumped by each mussel in the individual chamber during the measurements. This refiltration index was calculated as a ratio between the volume of water pumped by the mussel and the total volume of the chamber. To calculate the volume of water pumped by the mussel, pumping rate (PR) was calculated as:

$$PR = \lambda_{average} \times V \times 60 \quad (3)$$

Where $\lambda_{average}$ is the slope of ln (particle concentration) over time of particles which are captured with 100% efficiency by the mussel (see Cranford et al., 2016 for a detailed description of this equation). In this study, particles ranging between 8.25 and 10.75 µm were assumed to be 100% captured and used to calculate $\lambda_{average}$. To avoid error generated from non-constant pumping, or very low particle counts, only slopes with an associated $r^2 \geq 0.90$ were used (Cranford et al., 2016). V is the chamber volume, and PR is pumping rate in units of l h^{-1}. The refiltration index (RI) was calculated dividing the total volume pumped by the mussel by the volume of the chamber. A RI greater than 1 indicates that the mussel pumped more water than the volume of the chamber.

Statistical analysis

One-way ANOVA (Fisher LSD Test) was performed to evaluate the differences in the composition of phytoplankton assemblages in seawater and gut contents of *M. coruscus*, which was performed using SPSS 19.0. The agreement between RCE of phytoplankton assemblages and CE of total phytoplankton was evaluated using linear regression analysis. The relationships between CE of phytoplankton assemblages (and pigments) and RI were determined using logarithmic fit analysis. The above correlation analysis was performed by Origin 2017 software.

Results

Phytoplankton assemblage in the natural seawater

A total of 57 phytoplankton species were identified by microscope, including 48 diatoms, 6 dinoflagellates and 1 cryptophyte sp. (Figure 2). Cryptophytes, around 5-8 µm in diameter, were found as the dominant group, with average abundance of 19.69×10^4 cell l^{-1}, and it made up 66.1% of the total phytoplankton abundance. Diatoms *Chaetoceros* spp. (1.58×10^4 cell l^{-1}) and *Cocconeis scutellum* (1.08×10^4 cell l^{-1}) followed in abundance. Dinoflagellates (including *Gymnodinium* spp., *Gonyaulax spinifera*, *Gyrodinium* spp. and *Prorocentrum* spp.) only comprised 3.5% of total phytoplankton abundance.

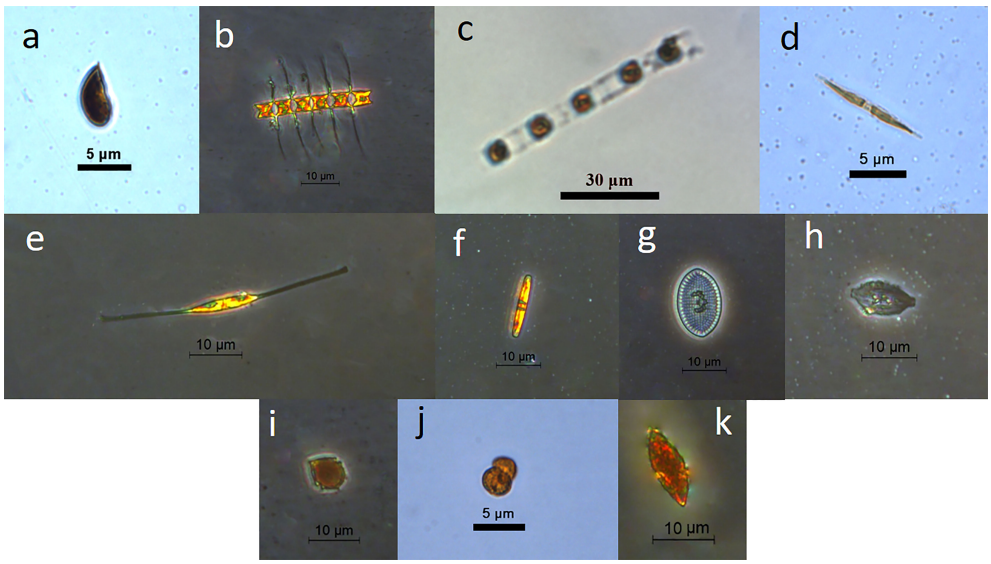

FIGURE 2
Some dominant phytoplankton species in this study. **(A)** Cryptophytes sp.; **(B)** *Chaetoceros* sp.; **(C)** *Skeletonema costatum*; **(D)** *Pseudo-nitzschia* sp.; **(E)** *Nitzschia* sp.; **(F)** *Pinnularia* sp.; **(G)** *Cocconeis scutellum*; **(H)** *Amphora* sp.; **(I)** *Gonyaulax spinifera*; **(J)** *Gymnodinium* sp.; **(K)** *Gyrodinium spirale* (**A** cryptophytes; **B, C**: centric diatoms; **D–H**: Pennatae diatoms; **I–K**: dinoflagellates).

Clearance efficiency of different phytoplankton genus/taxa by *Mytilus coruscus*

Phytoplankton biomass (cell abundance and Chl *a* concentration) before feeding experiments varied among different experimental groups due to the fluctuation of natural seawater (Table 1). Due to different incubation times and pumping rate across individuals, large differences of RI among the triplicate parallel experiments existed within each group (e.g., NO. 3, 5) (Table 1). Consequently, different experimental groups showed some variations of clearance efficiency of different phytoplankton genus/groups (Figure S1).

Given that the RI by *M. coruscus* varied between individual mussels in the experiments (Table 1), the clearance efficiency of phytoplankton cells was explored in relation to refiltration index (RI) (Figure 3) rather than comparing the proportions of phytoplankton before vs. after feeding experiments (Figure S1). Significant statistical relationships were found between RI and total phytoplankton cells (F=247; P< 0.01), as well as different groups (P< 0.01) (Figure 3). Moreover, these relationships revealed a differential clearance efficiency for the different algal groups. For a RI of 1.0, cryptophytes had the highest clearance efficiency (83%) while centric diatoms had the lowest (63%) (Figures 3B, F, respectively).

There was a large variation in the ratio of clearance efficiency (RCE) of different phytoplankton assemblages to total

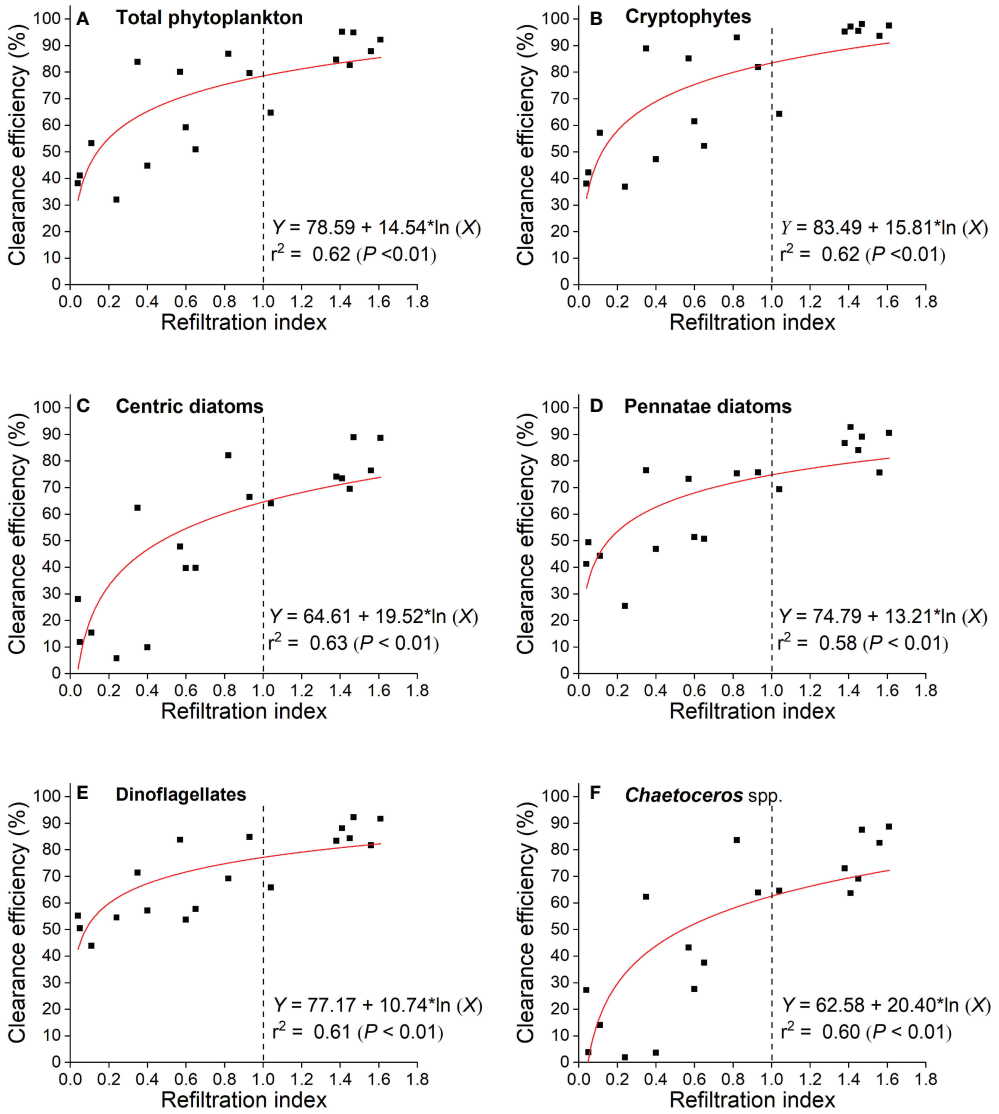

FIGURE 3
Logarithmic relationships between clearance efficiency of phytoplankton cells and refiltration index (RI) by *M. coruscus*.

phytoplankton at RI = 1 by *M. coruscus* (Figure 4). The RCE of cryptophytes against total phytoplankton was the highest (1.06) while *Chaetoceros* spp. Showed the lowest (0.80), representing preferential filtration and rejection, respectively. The other centric diatom *Skeletonema* spp. Also showed a relatively low RCE. By comparison, the pennate diatoms and dinoflagellates showed similar RCR within a range of 0.91-0.99.

The relationship between RCE and CE of total phytoplankton by *M. coruscus* differed across phytoplankton groups (Figure 5). With an increasing CE and decreasing total phytoplankton density in the remaining seawater after feeding experiments, the RCE of the dinoflagellates decreased ($P< 0.01$) while the centric diatoms showed an increasing trend ($P< 0.01$). It was noteworthy that the RCE of centric diatoms never exceeded 1.0. By comparison, the RCE of cryptophytes was relatively stable and always above 1.0. The average RCE of cryptophytes was significantly higher than centric diatoms ($P< 0.01$). No significant difference of RCE was observed among the other phytoplankton assemblages ($P > 0.05$) (Figure 5).

Clearance efficiency of different phytopigments by *Mytilus coruscus*

Significant relationships were found between the CE of different pigments and RI (F=8.98; $P< 0.05$) except for zeaxanthin (F=2.37; $P = 0.19$) (Figure 6). These relationships differed across pigments. When the RI was 1.0, alloxanthin and peridinin (marker pigment of cryptophytes and dinoflagellates, respectively) had the highest CE (77%-78%), and fucoxanthin (marker pigment of diatoms) ranked the third (Figures 6A–C). By comparison, prasinoxanthin and zeaxanthin (marker pigment of prasinophytes and *Synechococcus*, respectively) had the lowest clearance efficiency (27%-31% at RI = 1.0) (Figures 6D, E, respectively). Chl *a*, as an estimation of the total phytoplankton biomass, showed a moderate clearance efficiency (56% at RI = 1.0) (Figure 6G).

Comparison of phytoplankton composition in seawater and gut contents

The 7 samples having counts > 200 cells were distributed over five experimental groups, and the total amount of phytoplankton cells in gut contents ranged from 1.7×10^3 to 15.3×10^3 cells ind^{-1} (Table S2). Therefore, the pooled data of 15 water samples was compared to 7 mussels (Table 2 and Table S2) to explore differences in the composition of phytoplankton between them. A total of 31 phytoplankton species (or genera) were observed in the gut contents (Table S2). It is noteworthy that cryptophyte cells were not observed in the gut contents. The proportion of *Chaetoceros* spp. and *Skeletonema* spp. was significantly lower in the gut contents than in the seawater ($P< 0.05$). By contrast, *Cocconeis* spp. and *Pinnularia* spp. showed significantly higher proportion in the former than the latter ($P< 0.05$) (Table 2).

Similarly, a comparison of the seawater and gut contents showed different pigment structure (Table 3; Figure S2). In the natural seawater, fucoxanthin and prasinoxanthin contributed the highest proporation of total marker pigments (Table 3). By comparison, the proportion of prasinoxanthin significantly

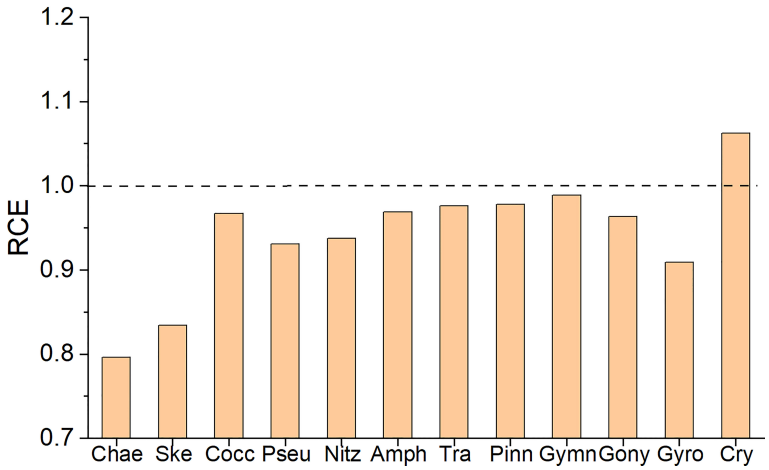

FIGURE 4
The ratio of clearance efficiency (RCE) of dominant phytoplankton assemblages against total phytoplankton at Refiltration Index = 1. The following abbreviations were used for the different communities: Chae, *Chaetoceros* spp.; Ske, *Skeletonema* spp.; Cocc, *Cocconeis* spp.; Pseu, *Pseudo-nitzschia* spp.; Nitz, *Nitzschia* spp.; Amph, *Amphora* spp.; Tra, *Trachyneis* spp.; Pinn, *Pinnularia* spp.; Gymn, *Gymnodinium* spp.; Gony, *Gonyaulax* spp.; Gyro, *Gyrodinium* spp.; Cry, cryptophytes

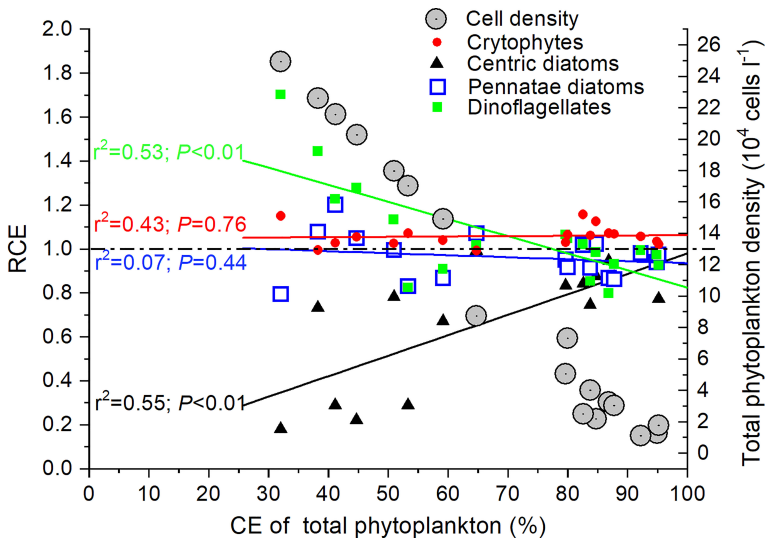

FIGURE 5
The relationship between the ratio of clearance efficiency of different phytoplankton groups against total phytoplankton (RCE) and CE of total phytoplankton by *M. coruscus*.

decreased in the gut contents of *M. coruscus* ($P< 0.01$). Zeaxanthin and lutein showed similar changes. Meanwhile, proportion of alloxanthin showed a significant increasing trend, from 6.65 ± 0.65% to 31.46 ± 4.41% ($P< 0.01$) (Table 3).

Discussion

Preferential feeding selection of *Mytilus coruscus*

The results indicated that cryptophytes dominated the phytoplankton community in Sungo Bay, which was not observed in previous studies (Wang, 2017; Hou et al., 2021). In natural seawater, cryptophytes were rarely reported to be a dominant phytoplankton group, largely due to the omission by microscopic methods (easily deformed or broken in fixed seawater samples) (Gieskes & Kraay, 1983).

HPLC-pigments analysis demonstrated that cryptophytes contribute a high proportion to algal biomass along the coastal areas of China (Wang et al., 2018; Pan et al., 2020). Our results showed that *M. coruscus* preferentially filtered the cryptophytes and dinoflagellates (Figures 3, 5). The preferential feeding on flagellates has been previously observed in bivalves (Dupuy et al., 2000b; Safi and Hayden, 2010). The mussel *Perna canaliculus* preferentially ingested flagellated cells, including dinoflagellates and other small flagellates, in the natural seawater from Pelorus Sound (New Zealand) (Safi and Hayden, 2010). Moreover, Naddafi et al. (2007) revealed that a freshwater bivalve species (*Dreissena polymorpha*) could selectively clear cryptophytes, chrysophyceaens and dinoflagellates. Ren et al. (2006) found the assimilation efficiency of flagellates by mussels was significantly higher than diatoms. Shellfish may have ability to select more nutritious dinoflagellates over diatoms (Menden-Deuer and Lessard, 2000).

Similarly, the laboratory study of Pales Espinosa et al. (2016) reported that cryptophyte *Rhodomonas lens* and *R. salina* tended to be more easily filtered by *Crassostrea virginica* and *M. edulis* and less rejected through pseudofeces than others.

Retention efficiency of bivalves in the natural seawater is generally dependent on the diameter of particles, which increases non-linearly with particle size (Strohmeier et al., 2012; Rosa et al., 2015). However, the retention efficiency of different particle sizes "varies spatially and seasonally and possibly in direct response to changes in the seston" (Strohmeier et al., 2012). Bivalves may capture smaller particles more efficiently than larger particles due to differences of cell shape, flexibility and swimming ability (Ward and Shumway, 2004). In this study, cryptophytes dominated the phytoplankton community with the size ranging 5-8 μm in diameter, which was much smaller than the other dominant chained diatom *Chaetoceros* spp. (composing 3-6 cells, 3-4 μm for width and 15-30 μm for length of chains), while the latter was poorly cleared during these experiments. Similar to *Chaetoceros* spp., also *Skeletonema* spp. had the chained shapes (composing 4-9 cells, 8-10 μm for width and 50-100 μm for length of chains) (Figure 2). It has previously been suggested bivalves would retain the phytoplankton with narrow widths (e.g.,<3 μm) and length to width ratio >3 at a low efficiency (Rosa et al., 2015), which may be one reason for low

10.3389/fmars.2022.1070737

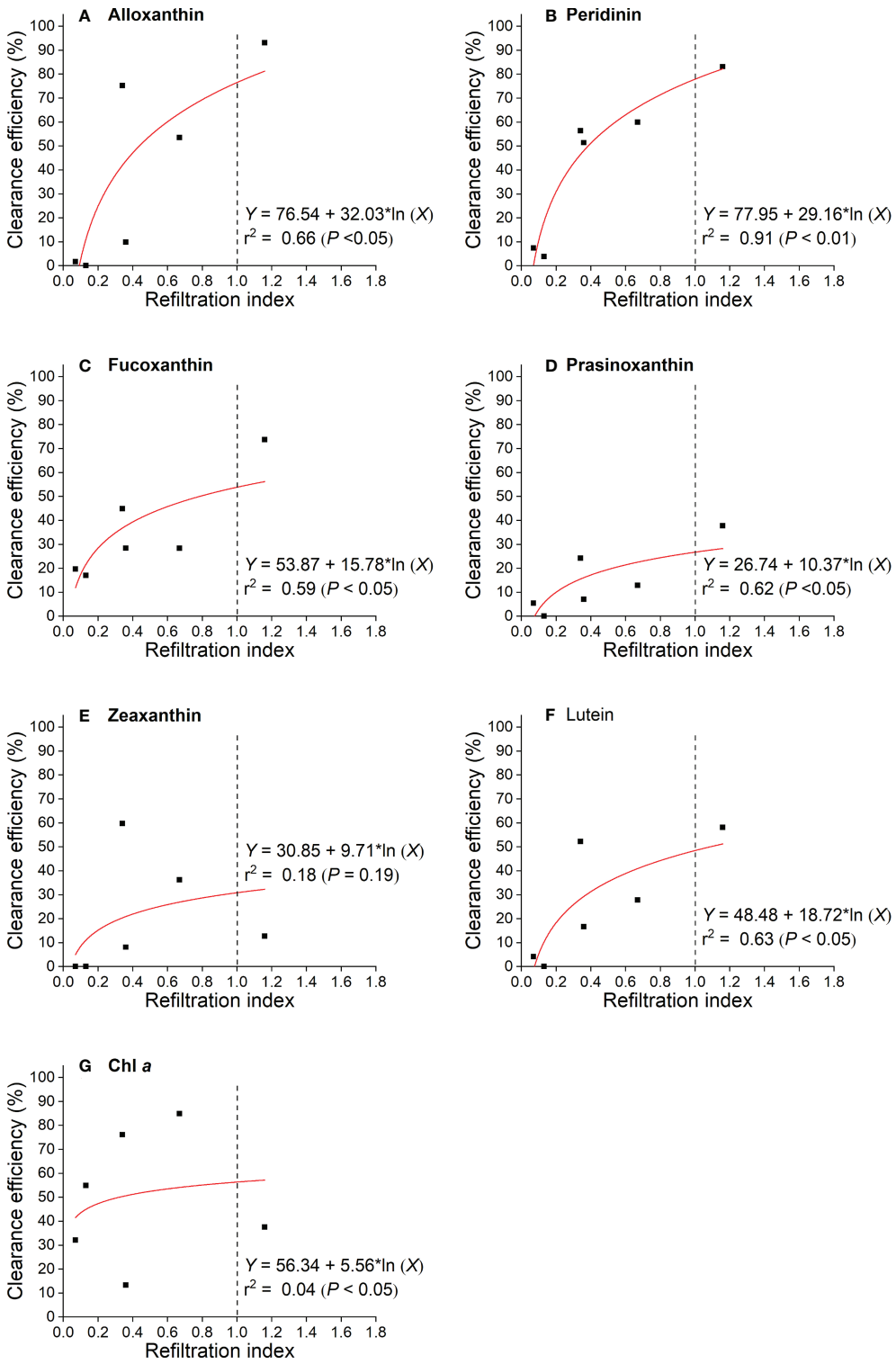

FIGURE 6
Logarithmic relationships between clearance efficiency of phytopigments and refiltration index by *M. coruscus*.

capture efficiency of both the large sized diatom species in this study. By comparison, most diatom species (i.e., Pennatae diatoms), which were unicellular and small, and some of which are elliptical (e.g., *Pinnularia* sp. and *Cocconeis scutellum*), showed relatively high clearance efficiency (Figures 2, 4). Diatoms may still be the most important food resources for mussels due to their high density and diversity along the Chinese coasts (Wang, 2017; Wang et al., 2018; Pan et al., 2020).

Preferential feeding selection in bivalves occurs in three stages: the first pre-ingestive processing (selective particle retention), the second pre-ingestive processing (particle transport) and post-ingestive processing (Cognie et al., 2001; Ward and Shumway, 2004; Frau et al., 2016). Particle retention is the first step in the feeding process during which captured particles are retained by the ctenidia of bivalves (Rosa et al., 2018). In this study, the preferential filtration of cryptophytes and several diatom genus did not indicate that those contributed significantly to the food source of bivalves because the second pre-ingestive selection (i.e., pseudofeces) was not investigated. A comparison of phytoplankton assemblages between seawater and gut contents could help understand preferential feeding selection (especially for cryptophytes) in bivalves as discussed in Section Comparison of phytoplankton assemblages between seawater and gut contents.

Our results suggested that CE of phytopigments was an effective proxy of evaluating the degree of selective clearance of different phytoplankton groups by *M. coruscus*. Size-fractionated pigment analysis showed that alloxanthin, peridinin and fucoxanthin distributed in micro- and nano-fractions while prasinoxanthin and zeaxanthin were mainly concentrated in pico-fraction (< 2.7 μm) in the seawater of Sungo Bay (Jiang, unpublished data). Like the results of the microscopic method (Figure 3), the HPLC-pigment analysis indicated that cryptophytes (i.e., alloxanthin) and dinoflagellates (i.e., peridinin) were preferentially cleared by *M. coruscus* (Figures 6A, B). In agreement with the previous studies (Dupuy et al., 2000b; Strohmeier et al., 2012), our results further demonstrated that *M. coruscus* filters pico-plankton prasinophytes and *Synechococcus* (i.e. prasinoxanthin and zeaxanthin, respectively) at lower efficiency than larger planktonic species (Figures 6D, E).

TABLE 3 Composition of the 7 detectable marker pigments in sea water and gut contents (n=3) in Experimental Group NO.6.

Dignostic pigments*	Sea water (%)	Gut contents (%)
Peridinin	2.37 ± 0.15	7.28 ± 2.67**↑
Fucoxanthin	40.15 ± 1.69	56.24 ± 1.43**↑
Prasinoxanthin	36.70 ± 0.85	0.83 ± 0.21**↓
Alloxanthin	6.65 ± 0.65	31.46 ± 4.41**↑
Zeaxanthin	9.27 ± 1.41	4.19 ± 2.34**↓
Lutein	4.86 ± 0.60	0 ± 0**↓

*Note that other pigments were not included and calculated.
**Values of pigment composition in the same row indicate significant difference (LSD Test, P< 0.01).
Comparison of phytoplankton assemblages between seawater and gut contents.
Arrows indicate the changing direction of the pigments from sea water to gut contents.

TABLE 2 Average density and composition of phytoplankton assemblages in sea water and gut contents (in accordance with gut contents, phytoplankton composition in seawater was only calculated for total diatoms and dinoflagellates but cryptophytes).

Phytoplankton taxa	Sea water (n=15)		Gut contents (n=7)	
	Density (10^3 cell l^{-1})	Composition (%)	Density (cells ind^{-1})	Composition (%)
Cryptophytes	235.5 ± 67.0	— (72.9 ± 7.4)[a]	0	0
Chaetoceros spp.	17.7 ± 5.4	22.6 ± 4.7*	39 2± 664	4.6 ± 5.3**↓
Skeletonema spp.	4.9 ± 1.2	6.6 ± 2.2*	0	0*
Other centric diatoms	1.5 ± 0.5	2.0 ± 0.7	52 ± 69	1.1 ± 1.2
Cocconeis spp.	16.9 ± 4.7	21.6 ± 3.7*	3511 ± 3797	50.6 ± 6.8**↑
Pseudo-nitzschia spp.	4.6 ± 2.5	5.6 ± 2.4	173 ± 174	3.4 ± 4.0
Nitzschia spp.	2.2 ± 0.5	2.9 ± 0.8	128 ± 132	1.8 ± 1.0
Amphora spp.	7.9 ± 2.4	10.2 ± 2.3*	295 ± 380	3.9 ± 2.9**↓
Trachyneis spp.	4.6 ± 2.0	6.0 ± 3.4	67 ± 91	1.8 ± 2.8
Pinnularia spp.	5.6 ± 2.1	7.0 ± 1.7*	634 ± 665	9.8 ± 2.0**↑
Synedra spp.	1.2 ± 0.7	1.5 ± 0.8	171 ± 247	2.0 ± 1.5
Other pennitae diatoms	2.4 ± 0.8	3.2 ± 1.1	425 ± 529	5.7 ± 3.2
Total dinoflagellates	8.4 ± 2.3	10.8 ± 2.2	519 ± 330	15.3 ± 11.7
Total phytoplankton	318.6 ± 70.4		6373 ± 6183	

[a]This value in brace is the ratio of cryptophytes to total phytoplankton abundance.
**Values of phytoplankton composition in the same row with different asterisks indicate significant difference (LSD Test, P< 0.05).
Arrows indicate the changing direction of the phytoplankton from sea water to gut contents.

Comparison of phytoplankton assemblages between seawater and gut contents

Comparisons of phytoplankton composition between natural seawater and gut contents of bivalves have been conducted with a single sampling, similarly to previous studies (Loret et al., 2000; Tan and Ransangan, 2017; Jiang et al., 2019). The comparisons revealed differences in phytoplankton composition between gut contents and surrounding seawater supporting previous findings (Loret et al., 2000; Tan and Ransangan, 2017; Jiang et al., 2019; Asaduzzaman et al., 2020). Our study has shown that cryptophyte cells dominated in seawater but were not observed in gut contents. By comparison, alloxanthin, the marker pigment of cryptophytes, was selectively cleared from seawater and showed a relatively high proportion in gut content compared to most of the other pigments (Figure 6; Table 3). This demonstrated fast digestion of cryptophytes by *M. coruscus*. Our results are similar to other studies in which alloxanthin is preferentially accumulated in the gut contents, suggesting the preferential feeding selectivity on cryptophytes by bivalves (Loret et al., 2000; Jiang et al., 2019). This contribution could also be affected by the presence of detrital matter (e.g., aggregates of dead cells) in the water column, which has not been assessed in this study. Similarly, Cucci et al. (1985) revealed that the cryptomonad *Chroomonas salina* was not found in the feces of *M. edulis* whereas diatom and dinoflagellate cells could be detected without significant digestion. Moreover, *C. salina* cells were completely digested and absorbed during passage through the gut by several other bivalve species (Shumway et al., 1985). The non-existence of cryptophyte cells in gut was presumably due to its fragile cell membrane which was broken during the digestion process. Results from this study highlight the importance of HPLC-pigment method in studying food composition in the gut contents of bivalves. Although some fragile flagellates such as cryptophytes may not be easily detected in gut contents by the microscopic method, they can be an important food supply for bivalves in the natural environment (Cucci et al., 1985; Shumway et al., 1985; Loret et al., 2000; Jiang et al., 2019).

Selective filtration of different diatom species by *M. coruscus* was also observed, with significantly lower proportions of *Chaetoceros* spp. and *Skeletonema* spp. in the gut contents than the seawater (Table 2). Rejection of diatoms by bivalves is understood to be species-dependent (also might be size-dependent) (Cucci et al., 1985; Defossez and Hawkins, 1997; Naddafi et al., 2007). Tan & Ransangan (2017) reported *P. viridis* showed a tendency to reject *Chaetoceros* spp. Similarly, Bougrier et al. (1997) observed that the ratio of rejection to filtration for some diatoms species (e.g., *Chaetoceros* and *Nitzschia*) was greater than that of the flagellates by the oyster *Crassostrea gigas*. The shape of diatom *Chaetoceros* spp. and *Skeletonema* spp. were characterized by spicules and long-chains in the natural seawater as described in Section Preferential feeding selection of Mytilus coruscus. Moreover, the intercalary and terminal setae along two sides of the *Chaetoceros* chain will greatly span to nearly 30 µm. Defossez and Hawkins (1997) suggested that particles larger than 22.5 µm were preferentially rejected as pseudofeces by *M. coruscus*. Although the size of single *Chaetoceros* and *Skeletonema* cells was around 5-12 µm (Figure 2), the chained cells greatly exceeded this threshold (22.5 µm). In comparison, a significant feeding selectivity of *Cocconeis* spp. and *Pinnularia* spp. by *M. coruscus* was observed. As shown in Figure 2, both diatom species are oval or with rounded ends, without spiny surface and sharp edges. Similarly, Asaduzzaman et al. (2020) showed that *P. viridis* preferentially ingested the Coscinodiscophyceae, Bacillariophyceae, Fragillariophyceae, as well as Dinophyceae, in the south-east coast of the Bay of Bengal. Therefore, we suggest that the size and shape of diatom species (even flagellates) might be an important factor influencing the feeding selectivity of *M. coruscus* in this study, which is in agreement with the results of Defossez and Hawkins (1997). Nevertheless, it should be acknowledged that feces and pseudofeces were not collected in this study, and hence the current data are not sufficient for estimating the assimilation efficiency of different diatom assemblages, as well other algal groups. Future efforts should quantitatively analyze the phytoplankton biomass in water, feces, pseudofeces and gut contents, which would further our understanding of filtration and egestion of shellfish on different algal assemblages in natural waters.

According to Sonier et al. (2016), picophytoplankton can contribute to mussel growth in intensive culture environments where picophytoplankton biomass is high. Retention efficiencies of picophytoplankton by *Mytilus edulis* was estimated 20 ± 2.0% in eastern Prince Edward Island (Sonier et al., 2016). In agreement with Sonier et al. (2016), our results suggested that picoplankton could be an important fraction of the diet. In this study, prasinoxanthin and zeaxanthin had the clearance efficiency of 27%-31% at RI = 1.0 (Figures 6D, E), and it was further evidenced by their presence in gut contents (Figure S2). Aggregation of picoplankton might be an important way for the filtration of these small particles by of bivalves (Ward and Shumway, 2004). Moreover, compared with other filter-feeding bivalves (e.g., oysters), mussels more efficiently filter and retain picophytoplankton (Richard et al., 2022).

Environmental implications of feeding selectivity by intensive bivalve aquaculture

Feeding experiments were carried out in short time (0.26-1 h) with high biomass of *M. coruscus* (1 mussel l^{-1}) in a static chamber. Under these conditions, our results suggested *M. coruscus* can change the composition of phytoplankton

community by selective clearance. Flagellated phytoplankton cells, especially cryptophytes, may be subject to greater filtration pressure than some diatom species under the feeding behavior of *M. coruscus*. Similarly, field investigation revealed that flagellates were selectively cleared by intensive oyster aquaculture (Jiang et al., 2016). This study also showed that mussels removed picoplankton at lower efficiency than the larger planktonic species (Figure 6), which was consistent with previous reports (Dupuy et al., 2000b; Strohmeier et al., 2012). This process may skew the phytoplankton community toward the relatively fast-growing pico-sized species. It was reported that picoplankton contributed a high proportion to total phytoplankton biomass in some shellfish aquaculture areas (Vaquer et al., 1996; Safi and Gibbs, 2003; Cranford et al., 2008; Jiang et al., 2016). Weissberger and Glibert (2021) reported that the oyster *Crassostrea virginica* preferentially filtered large phytoplankton cells (e.g., diatoms and flagellates) and rejected small cells (cyanobacteria), which would be another mechanism by which bivalve filter-feeding may impact phytoplankton communities. In addition to small cell size, low nutritional value may be a reason why filter-feeding bivalves do not feed extensively on picoplankton (Weissberger and Glibert, 2021). The selective feeding process of bivalves may be the dominant factor that determines the size distribution of the phytoplankton community in semi-enclosed areas with high cultured bivalve biomass (Vaquer et al., 1996; Jiang et al., 2016).

Several diatom species, such as *Chaetoceros* spp. and *Skeletonema* spp. showed lower clearance efficiency than other diatoms from seawater by *M. coruscus*, and also less aggregation in gut contents (Table 2). Other studies have found that *Chaetoceros* spp. and *Pseudo-nitzschia* spp. are easily rejected in pseudofeces in some bivalves (Mafra et al., 2009; Safi and Hayden, 2010; Tan & Ransangan, 2017). Furthermore, some algal species can survive in the pseudofeces and feces and return to the water column (Santelices and Correa, 1985; Barillé & Cognie, 2000). These diatoms are the most common species and frequently dominate the phytoplankton community in the near shore waters along the coasts of China, especially in aquaculture areas (Wang et al., 2006; Wang, 2017). Lower filtration and/or higher rejection for these species than other diatoms might increase the potential tendency toward their domination in seawater.

Intensive bivalve cultivation could cause a significant reduction of the micro and nano-sized diatoms and dominance of picophytoplankton in the farm area (Jiang et al., 2016). Apart from bivalve filtration activity, dynamics and size distribution of phytoplankton are influenced by combined environmental factors, such as water residence time, light intensity and nutrients regime (Naddafi et al., 2007; Filgueira et al., 2012; Filgueira et al., 2016). Consequently, the environmental impact of bivalve aquaculture is site-specific, which highlights the importance of site selection for shellfish aquaculture (Silva et al., 2011). Researchers rarely considered the size structure and taxa composition of phytoplankton when they investigated the environmental impact and carrying capacity of shellfish aquaculture by numerical models, such as FARM model (Ferreira et al., 2007; Silva et al., 2011). This study further suggests that species-dependent (also size-dependent) disturbance of phytoplankton community should be considered for evaluating the environmental impact of bivalve cultivation in future studies.

Conclusions

This study highlights the usefulness of combining HPLC-pigment analysis with microscopic methods in providing a better understanding of the effect of feeding behavior of bivalves on phytoplankton communities. Of the available phytoplankton diet, *M. coruscus* preferentially filtered larger sized flagellates e.g., cryptophytes, compared to smaller species. However, cryptophytes were not observed in gut contents by microscopy while the marker pigment (i.e., alloxanthin) showed a relatively high proportion by HPLC-pigment analysis. This result suggests fast digestion of cryptophytes by *M. coruscus* and implied that microscopic observation of gut contents could underestimate their contribution to the diet of mussels. Selective feeding of different diatom species by *M. coruscus* was also observed, with significantly lower proportions of *Chaetoceros* spp. and *Skeletonema* spp. in gut contents than the seawater. The size and shape of diatom species might be an important factor influencing the feeding selectivity of mussels. Picoplankton cannot be neglected as potential food in the natural environment, as evidenced by the presence of their characteristic pigments in the gut. This selective feeding suggests that intensive mariculture of *M. coruscus* may skew the phytoplankton community toward the relatively fast-growing pico-sized species.

Data availability statement

The raw data supporting the conclusions of this article will be made available by the authors, without undue reservation.

Ethics statement

Ethical review and approval was not required for the animal study because the bivalve *Mytilus coruscus* used in this experiment were provided by Rongcheng Chudao Aquatic Products Co. Ltd. Ethical approval was not required for this study because no endangered animals were involved. Specimen collection and maintenance were performed in strict accordance with the recommendations of Animal Care Quality Assurance in China.

Author contributions

TJ, HP and LS wrote the original manuscript. ZJ, RF, ØS, TS, PC, and ZC attended the experiments and took part in the data analysis. All authors contributed to the article and approved the submitted version.

Funding

This study was funded by the National Key Research and Development Program of China (2019YFD0901401), the National Natural Science Foundation of China (42176206), Natural Science Foundation of Shandong Province (ZR2021MD071), the project Environment and Aquaculture Governance (CHN17/0033, Ministry of Foreign Affairs, Norway), Major Scientific and Technological Innovation Project of Shandong Provincial Key Research and Development Program (2019JZZY020706).

Acknowledgments

We would like to thank Dr. X. Xing and Mr. J. Cen for their help in identifying the species of phytoplankton. We are also grateful to Miss M. Bai and Dr. W. Jiang who aided in field investigation and sample analysis.

Conflict of interest

The authors declare that the research was conducted in the absence of any commercial or financial relationships that could be construed as a potential conflict of interest.

Publisher's note

All claims expressed in this article are solely those of the authors and do not necessarily represent those of their affiliated organizations, or those of the publisher, the editors and the reviewers. Any product that may be evaluated in this article, or claim that may be made by its manufacturer, is not guaranteed or endorsed by the publisher.

Supplementary material

The Supplementary Material for this article can be found online at: https://www.frontiersin.org/articles/10.3389/fmars.2022.1070737/full#supplementary-material

References

Asaduzzaman, M., Akter, S., Hoque, N. F., Shakil, A., Noor, A. R., Akter, M. N., et al. (2020). Multifaceted linkages among eco-physiological factors, seasonal plankton dynamics and selective feeding behavior of the green mussel (*Perna viridis*) in the south-east coast of the bay of Bengal. *J. Sea Res.* 164, 101933. doi: 10.1016/j.seares.2020.101933

Barillé, L., and Cognie, B. (2000). Revival capacity of diatoms in bivalve pseudofaeces and faeces. *Diatom Res.* 15 (1), 11–17. doi: 10.1080/0269249x.2000.9705483

Bayne, B., and Worrall, C. (1980). Growth and production of mussels *Mytilus edulis* from two populations. *Mar. Ecol. Prog. Ser.* 3 (4), 317–328. doi: 10.3354/meps003317

Beninger, P. G., Valdizan, A., Decottignies, P., and Cognie, B. (2008). Impact of seston characteristics on qualitative particle selection sites and efficiencies in the pseudolamellibranch bivalve *Crassostrea gigas*. *J. Exp. Mar. Biol. Ecol.* 360, 9–14. doi: 10.1016/j.jembe.2008.03.003

Bougrier, S., Hawkins, A. J. S., and Héral, M. (1997). Preingestive selection of different microalgal mixtures in crassostrea gigas and mytilus edulis, analysed by flow cytometry. *Aquaculture* 150 (1-2), 123–134. doi: 10.1016/s0044-8486(96)01457-3

Cédric, B., Jon, G., Anthony, H., Fang, J., Zhu, M., and Mélanie, B. (2003). Modelling the effect of food depletion on scallop growth in sungo bay (China). *Aquat. Living Resour.* 16 (1), 10–24. doi: 10.1016/s0990-7440(03)00003-2

Cognie, B., Barillé, L., and Rincé, Y. (2001). Selective feeding of the *Oystercrassostrea gigas* fed on a natural microphytobenthos assemblage. *Estuaries* 24 (1), 126–134. doi: 10.2307/1352819

Cranford, P. J., Li, W., Strand, Ø., and Strohmeier, T. (2008). *Phytoplankton depletion by mussel aquaculture, high resolution mapping, ecosystem modeling, and potential indicators of ecological carrying capacity*. International Council for the Exploration of the Seas (ICES).

Cranford, P. J., Strohmeier, T., Filgueira, R., and Strand, Ø. (2016). Potential methodological influences on the determination of particle retention efficiency by suspension feeders: *Mytilus edulis* and *Ciona intestinalis*. *Aquat. Biol.* 25, 61–73. doi: 10.3354/ab00660

Cucci, T. L., Shumway, S. E., Newell, R. C., Selvin, R., Guillard, R. L., and Yentsch, ,. C. M. (1985). Flow cytometry: a new method for characterization of differential ingestion, digestion and egestion suspension feeders. *Mar. Ecol. Prog. Ser.* 24, 201–204. doi: 10.3354/meps024201

Dame, R. F., and Prins, ,. T. C. (1998). Bivalve carrying capacity in coastal ecosystems. *Aquat. Ecol.* 31, 409–421. doi: 10.1023/A:1009997011583

Defossez, J. M., and Hawkins, ,. A. J. S. (1997). Selective feeding in shellfish: size-dependent rejection of large particles within pseudofaeces from *Mytilus edulis*, *Ruditapes philippinarum* and *Tapes decussatus*. *Mar. Biol.* 129 (1), 139–147. doi: 10.1007/s002270050154

Dupuy, C., Vaquer, A., Lam-Hoai, T., Rougier, C., Mazouni, N., Lautier, J., et al. (2000b). Feeding rate of the oyster *crassostrea gigas* in a natural planktonic community of the Mediterranean thau lagoon. *Mar. Ecol. Prog. Ser.* 205 (1), 171–184. doi: 10.3354/meps205171

Ferreira, J. G., Hawkins, A. J. S., and Bricker, S. B. (2007). Management of productivity, environmental effects and profitability of shellfish aquaculture — the farm aquaculture resource management (FARM) model. *Aquaculture* 264, 160–174. doi: 10.1016/j.aquaculture.2006.12.017

Filgueira, R., Grant, J., Bacher, C., and Carreau, M. (2012). A physical-biogeochemical coupling scheme for modeling marine coastal ecosystems. *Ecol. Inform.* 7, 71–80. doi: 10.1016/j.ecoinf.2011.11.007

Filgueira, R., Guyondet, T., Comeau, L. A., and Tremblay, R. (2016). Bivalve aquaculture-environment interactions in the context of climate change. *Global Change Biol.* 22, 3901–3913. doi: 10.1111/gcb.13346

Frau, D., Molina, F. R., and Mayora, G. (2016). Feeding selectivity of the invasive mussel *Limnoperna fortune* (Dunker 1857) on a natural phytoplankton assemblage: what really matters? *Limnology* 17 (1), 47–57. doi: 10.1007/s10201-015-0459-2

Gieskes, W. W. C., and Kraay, G. W. (1983). Dominance of cryptophyceae during the phytoplankton spring bloom in the central north Sea detected by HPLC analysis of pigments. *Mar. Biol.* 75 (2-3), 179–185. doi: 10.1007/bf00406000

Grizzle, R. E., Bricelj, V. M., and Shumway, S. E. (2001). Chapter 8 physiological ecology of mercenaria mercenaria. *Dev. Aquacult. Fish. Sci.* 31 (1), 305–382. doi: 10.1016/s0167-9309(01)80036-3

Hawkins, A., Smith, R., Bayne, B. L., and Héral, M. (1996). Novel observations underlying the fast growth of suspension-feeding shellfish in turbid environments: *Mytilus edulis*. *Mar. Ecol. Prog. Ser.* 131 (1-3), 179–190. doi: 10.3354/meps131179

Hou, X., Gao, Y., Du, M., Jiang, W., Li, F., Dong, S., et al. (2021). Temporal and spatial variation in phytoplankton community structure and their relationship with environmental factors in sanggou bay. *Prog. Fish Sci.* 42 (2), 18–27. doi: 10.19663/j.issn2095-9869.20200130001

Jiang, T., Chen, F., Yu, Z., Lu, L., and Wang, Z. (2016). Size-dependent depletion and community disturbance of phytoplankton under intensive oyster mariculture based on HPLC pigment analysis in daya bay, south China Sea. *Environ. Pollut.* 219, 804–814. doi: 10.1016/j.envpol.2016.07.058

Jiang, T., Wang, L., Zhang, F., Fang, X., Lu, L., Zhang, J., et al. (2019). Selective feeding of bay scallop *Argopecten irradians* on phytoplankton community revealed by HPLC analysis of phytopigments in bohai Sea, China. *J. Oceanol. Limnol.* 37, 1746–1755. doi: 10.1007/s00343-019-8280-0

Kamermans, P. (1994). Similarity in food source and timing of feeding in deposit- and suspension-feeding bivalves. *Mar. Ecol. Prog. Ser.* 104 (1), 63–75. doi: 10.3354/meps104063

Lavaud, R., Artigaud, S., Le Grand, F., Donval, A., Soudant, P., Flye-Sainte-Marie, J. F., et al. (2018). New insights into the seasonal feeding ecology of *Pecten maximus* using pigments, fatty acids and sterols analyses. *Mar. Ecol. Prog. Ser.* 590, 109–129. doi: 10.3354/meps12476

Loret, P., Pastoreaud, A., Bacher, C., and Delesalle, B. (2000). Phytoplankton composition and selective feeding of the pearl oyster *Pinctada margaritifera* in the takapoto lagoon (Tuamotu archipelago, French polynesia): *in situ* study using optical microscopy and HPLC pigment analysis. *Mar. Ecol. Prog. Ser.* 199, 55–67. doi: 10.3354/meps199055

Mafra, L. L., Bricelj, V. M., and Ward, J. E. (2009). Mechanisms contributing to low domoic acid uptake by oysters feeding on *Pseudo-nitzschia* cells. II. selective rejection. *Aquat. Biol.* 6 (1-3), 213–226. doi: 10.3354/ab00122

Menden-Deuer, S., and Lessard, ,. E. J. (2000). Carbon to volume relationships for dinoflagellates, diatoms, and other protist plankton. *Limnol. Oceanogr.* 45, 569–579. doi: 10.4319/lo.2000.45.3.0569

Naddafi, R., Pettersson, K., and Eklöv, P. (2007). The effect of seasonal variation in selective feeding by zebra mussels (*Dreissena polymorpha*) on phytoplankton community composition. *Freshw. Biol.* 52, 823–842. doi: 10.1111/j.1365-2427.2007.01732.x

Nakamura, Y., and Kerciku, F. (2000). Effects of filter-feeding bivalves on the distribution of water quality and nutrient cycling in a eutrophic coastal lagoon. *J. Mar. Syst.* 26, 209–221. doi: 10.1016/s0924-7963(00)00055-5

Pales Espinosa, E. P., Cerrato, R. M., Wikfors, G. H., and Allam, B. (2016). Modeling food choice in the two suspension-feeding bivalves, *Crassostrea virginica* and *Mytilus edulis*. *Mar. Biol.* 163 (2), 40. doi: 10.1007/s00227-016-2815-0

Pan, H., Li, A., Cui, Z., Ding, D., Qu, K., Zheng, Y., et al. (2020). A comparative study of phytoplankton community structure and biomass determined by HPLC-CHEMTAX and microscopic methods during summer and autumn in the central bohai Sea, China. *Mar. pollut. Bull.* 155, 111172. doi: 10.1016/j.marpolbul.2020.111172

Ren, J. S., Ross, A. H., and Hayden, B. J. (2006). Comparison of assimilation efficiency on diets of nine phytoplankton species of the greenshell mussel *Perna canaliculus*. *J. Shellfish Res.* 25, 887–892. doi: 10.2983/0730-8000(2006)25[887:coaeod]2.0.co;2

Richard, M., Bec, B., Bergeon, L., Hébert, M., Mablouké, C., and Lagarde, F. (2022). Are mussels and oysters capable of reducing the abundances of picochlorum sp., responsible for a massive green algae bloom in thau lagoon, France? *J. Exp. Mar. Biol. Ecol.* 556, 151797. doi: 10.1016/j.jembe.2022.151797

Riisgård, H. (1988). Efficiency of particle retention and filtration rate in 6 species of northeast American bivalves. *Mar. Ecol. Prog. Ser.* 45, 217–223. doi: 10.3354/meps045217

Riisgård, H., and Larsen, P. (2010). Particle capture mechanisms in suspension-feeding invertebrates. *Mar. Ecol. Prog. Ser.* 418, 255–293. doi: 10.3354/meps08755

Rosa, M., Ward, J. E., Holohan, B. A., Shumway, S. E., and Wikfors, G. H. (2017). Physicochemical surface properties of microalgae and their combined effects on particle selection by suspension-feeding bivalve molluscs. *J. Exp. Mar. Biol. Ecol.* 486, 59–68. doi: 10.1016/j.jembe.2016.09.007

Rosa, M., Ward, J. E., Ouvrard, M., Holohan, B. A., Espinosa, E. P., Shumway, S. E., et al. (2015). Examining the physiological plasticity of particle capture by the blue mussel, *Mytilus edulis*, (L.): Confounding factors and potential artifacts with studies utilizing natural seston. *J. Exp. Mar. Biol. Ecol.* 473, 207–217. doi: 10.1016/j.jembe.2015.09.005

Rosa, M., Ward, J. E., and Shumway, S. E. (2018). Selective capture and ingestion of particles by suspension-feeding bivalve molluscs: A review. *J. Shellfish Res.* 37 (4), 727–746. doi: 10.2983/035.037.0405

Rosa, M., Ward, J. E., and Shumway, S. E. (2021). Examining the effects of microalgal metabolites on ciliary activity of the Eastern oyster crassostrea virginica. *J. Shellfish Res.* 40 (2), 231–237. doi: 10.2983/035.040.0204

Rouillon, G., Guerra Rivas, J., Ochoa, N., and Navarro, E. (2005). Phytoplankton composition of the stomach contents of the mussel *Mytilus edulis* l. from two populations: comparison with its food supply. *J. Shellfish Res.* 24 (1), 5–14. doi: 10.2983/0730-8000(2005)24[5:PCOTSC]2.0.CO;2

Safi, K. A., and Gibbs, M. M. (2003). Importance of different size classes of phytoplankton in beatrix bay, Marlborough sounds, new Zealand, and the potential implications for the aquaculture of the mussel, *Perna canaliculus*. *N. Z. J. Mar. Freshw. Res.* 37, 267–272. doi: 10.1080/00288330.2003.9517164

Safi, K. A., and Hayden, B. (2010). Differential grazing on natural planktonic populations by the mussel *Perna canaliculus*. *Aquat. Biol.* 11, 113–125. doi: 10.3354/ab00297

Santelices, B., and Correa, J. (1985). Differential survival of macroalgae to digestion by intertidal herbivore molluscs. *J. Exp. Mar. Biol. Ecol.* 88, 183–191. doi: 10.1016/0022-0981(85)90037-1

Shumway, S. E., Cucci, T. L., Newell, R. C., and Yentsch, C. M. (1985). Particle selection, ingestion, and absorption in filter-feeding bivalves. *J. Exp. Mar. Biol. Ecol.* 91 (1-2), 77–92. doi: 10.1016/0022-0981(85)90222-9

Silva, C., Ferreira, J. G., Bricker, S. B., DelValls, T. A., Martín-Díaz, M. L., and Yáñez, E. (2011) Site selection for shellfish aquaculture by means of GIS and farm-scale models, with an emphasis on data-poor environments. *Aquaculture* 318 (3–4), 444–457. doi: 10.1016/j.aquaculture.2011.05.033

Sonier, R., Filgueira, R., Guyondet, T., Tremblay, R., Olivier, F., Meziane, T., et al. (2016). Picophytoplankton contribution to *Mytilus edulis*, growth in an intensive culture environment. *Mar. Biol.* 163, 1–15. doi: 10.1007/s00227-016-2845-7

Strohmeier, T., Strand, Ø., Alunno-Bruscia, M., Duinker, A., and Cranford, ,. P. J. (2012). Variability in particle retention efficiency by the mussel *Mytilus edulis*. *J. Exp. Mar. Biol. Ecol.* 412 (3), 96–102. doi: 10.1016/j.jembe.2011.11.006

Tan, K. S., and Ransangan, J. (2017). Feeding behaviour of green mussels, *Perna viridis* farmed in marudu bay, Malaysia. *Aquacult. Res.* 48, 1216–1231. doi: 10.1111/are.12963

Trottet, A., Roy, S., Tamigneaux, E., Lovejoy, C., and Tremblay, R. (2008). Impact of suspended mussels (*Mytilus edulis* l.) on plankton communities in a magdalen islands lagoon (Québec, canada): A mesocosm approach. *J. Exp. Mar. Biol. Ecol.* 365 (2), 103–115. doi: 10.1016/j.jembe.2008.08.001

Vahl, O. (1972). Efficiency of particle retention in *Mytilus edulis* l. *Ophelia* 10, 17–25. doi: 10.1080/00785326.1972.10430098

Vaquer, A., Troussellier, M., Courties, C., and Bibent, B. (1996). Standing stock and dynamics of picoplankton in the thau lagoon (northwest Mediterranean coast). *Limnol. Oceanogr.* 41 (8), 1821–1828. doi: 10.4319/lo.1996.41.8.1821

Venrick, E. L. (1978). "How many cells to count?," in *Phytoplankton manual*. Ed. A. Sournia (UNESCO), 167–180.

Wang, X. (2017). *Studies on phytoplankton community under integrated multi-trophic aquaculture modes in sanggou bay* (Guangzhou: MSc dissertation, Jinan University).

Wang, L., Ou, L., Huang, K., Chai, C., Wang, Z., Wang, X., et al. (2018). Determination of the spatial and temporal variability of phytoplankton community structure in daya bay *via* HPLC-CHEMTAX pigment analysis. *J. Oceanol. Limnol.* 36 (3), 750–760. doi: 10.1007/s00343-018-7103-z

Wang, Z., Qi, Y., Chen, J., Ning, X., and Yang, Y. (2006). Phytoplankton abundance, community structure and nutrients in cultural areas of daya bay, south China Sea. *J. Mar. Syst.* 62 (1), 85–94. doi: 10.1016/j.jmarsys.2006.04.008

Ward, J. E., and Shumway, ,. S. E. (2004). Separating the grain from the chaff: particle selection in suspension- and deposit-feeding bivalves. *J. Exp. Mar. Biol. Ecol.* 300 (1-2), 83–130. doi: 10.1016/j.jembe.2004.03.002

Weissberger, E. J., and Glibert, P. M. (2021). Diet of the eastern oyster, crassostrea virginica, growing in a eutrophic tributary of Chesapeake bay, Maryland, USA. *Aquacult Rep.* 20, 100655. doi: 10.1016/j.aqrep.2021.100655

Yahel, G., Eerkes-Medrano, D. I., and Leys, S. P. (2006). Size dependent selective filtration of ultraplankton by hexactinellid glass sponges. *Aquat. Microb. Ecol.* 45 (2), 181–194. doi: 10.3354/ame045181

Yahel, G., Marie, D., Beninger, P. G., Eckstein, S., and Genin, A. (2009). *In situ* evidence for pre-capture qualitative selection in the tropical bivalve lithophaga simplex. *Aquat. Biol.* 6 (1-3), 235–246. doi: 10.3354/ab00131

Zapata, M., Rodriguez, F., and Garrido, J. L. (2000). Separation of chlorophylls and carotenoids from marine phytoplankton: a new HPLC method using reversed phase C8 column and pyridine-containing mobile phases. *Mar. Ecol. Prog. Ser.* 195, 29–45. doi: 10.3354/meps195029

frontiers | Frontiers in Marine Science

TYPE Original Research
PUBLISHED 15 December 2022
DOI 10.3389/fmars.2022.1092984

OPEN ACCESS

EDITED BY
Hui Zhao,
Guangdong Ocean University, China

REVIEWED BY
Wenjin Sun,
Nanjing University of Information Science and Technology, China
Kai Yu,
Hohai University, China
Dezhou Yang,
Institute of Oceanology (CAS), China

*CORRESPONDENCE
Peng Bai
pengbai@zjou.edu.cn
Yanzhen Gu
guyanzhen@zju.edu.cnn

SPECIALTY SECTION
This article was submitted to Coastal Ocean Processes, a section of the journal Frontiers in Marine Science

RECEIVED 08 November 2022
ACCEPTED 05 December 2022
PUBLISHED 15 December 2022

CITATION
Li J, Li P, Bai P, Zhai F, Gu Y, Liu C, Sun R and Wu W (2022) Abrupt change of a thermal front in a high-biomass coastal zone during early spring.
Front. Mar. Sci. 9:1092984.
doi: 10.3389/fmars.2022.1092984

Abrupt change of a thermal front in a high-biomass coastal zone during early spring

Jian Li[1,2], Peiliang Li[1,2], Peng Bai[3,4]*, Fangguo Zhai[5], Yanzhen Gu[1,2]*, Cong Liu[2], Ruili Sun[2] and Wenfan Wu[5]

[1]Institute of Physical Oceanography and Remote Sensing, Ocean College, Zhejiang University, Zhoushan, China, [2]Hainan Institute, Zhejiang University, Sanya, China, [3]Marine Science and Technology College, Zhejiang Ocean University, Zhoushan, China, [4]Donghai Laboratory, Zhoushan, China, [5]Donghai Laboratory, College of Oceanic and Atmospheric Sciences, Ocean University of China, Qingdao, China

Coastal fronts play vital roles in local biogeochemical environment. An abrupt change of Zhejiang-Fujian coastal front (ZFCF) during early spring was well captured by multi-source satellite-retrieved sea surface temperature images. Here in this study, we investigated the mechanism of the abrupt decay with a combination of satellite observation and numerical simulation. Correlation analysis of long-term reanalysis data indicates that the variability of wind, heat flux and the Zhejiang-Fujian coastal current (ZFCC) have significant relationships with the variation of ZFCF in winter. Following heat budget analysis points out that net heat flux and horizontal advection are important in determining the net temperature tendency difference between two water masses of ZFCF during this process. To further explore the intrinsic physical roles of different dynamic factors, a comprehensive numerical investigation was conducted. Compared with the observations, the model reproduced the abrupt change process of the ZFCF satisfyingly. Sensitive experiments reveal that the weakening of the ZFCC, caused by the relaxation of the monsoon, contributes to the abrupt decay of ZFCF in the first half period, and heating effect of the Kuroshio Intrusion (KI) water gives rise to the following half period of the decay under the recovered monsoon. Further, with the impact of the KI water after the change, the ZFCF can be maintained even if the ZFCC is weak, whereas in January, the contribution of the KI water to the formation of the ZFCF seems to be limited under the prevailing monsoon. Besides, the riverine discharge and the tidal forcing can also modulate the spatiotemporal variation of ZFCF, the decrease of the river input also intensifies that decay, while tides fix the front at a specific depth.

KEYWORDS

thermal front, schism, Kuroshio intrusion, East China Sea, net heat flux

1 Introduction

Coastal front is a significant hydrodynamic phenomenon located on the boundary between two distinct water masses with remarkably high gradients of temperature, salinity, density, nutrient, or other environmental variables (Cromwell and Reid, 1956; Belkin and O'Reilly, 2009). The frontal process is one of the most important physical processes in the coastal marine environment (McWilliams, 2021), playing a vital role in the regional ecosystem, fishery, and carbon cycling system (Alemany et al., 2014; Lohmann and Belkin, 2014; Androulidakis et al., 2018).

Occurring along the 50-m isobath off the Zhejiang-Fujian coast (Figure 1), the Zhejiang–Fujian coastal front (ZFCF) is known as a major part of the East China Sea (ECS) coastal front system (Hickox et al., 2000), and generally exists as a multi-type front (Chen, 2009; He et al., 2016; Cao et al., 2021). Thus, the ZFCF is closely associated with fish abundance (Huang et al., 2010). For instance, the famous Zhoushan fishing ground is right located around the ZFCF, of which the total fishery production is 1.8 million tons in 2021. Moreover, algal bloom (Zhang et al., 2018) and suspended sediments (Qiao et al., 2020) are also significantly modulated by ZFCF.

Former investigations date back to the 1980s have clarified the spatiotemporal variation of the ZFCF through *in-situ* observation, satellite remote sensing and numerical modeling. The ZFCF characterizes significant seasonal variability, it appears in autumn, strengthens in winter, and dissipates in summer (Hickox et al., 2000; Huang et al., 2010; He et al., 2016). Based on satellite retrieved sea surface temperature (SST), He et al. (2016) demonstrated that the ZFCF is a double coastal front system consisting of a Zhejiang-Fujian offshore thermal coastal front along the 50-m isobath and a near-shore coastal thermal front along the 20-m isobath, of which the width is about 73.5 km.

Most of previous studies share the same perspective that the Zhejiang-Fujian coastal current (ZFCC) and Taiwan Warm Current (TWC) are two essential factors in modulating the ZFCF (Tseng et al., 2000; Hsieh et al., 2004; Komatsu et al., 2007; Chen, 2009; Bian et al., 2013). Driven by the northeast monsoon, ZFCC usually forms in boreal autumn and winter, travelling southward with fresh, cold and eutrophic water sourced along the eastern Chinese coast. Zhang et al. (2005) pointed out that wind stress is a critical factor controlling the ZFCC's variation on the diurnal timescale. Through a de-tiding analysis on the ZFCC, Wu et al. (2013) summarized that buoyancy also makes vital contributions to the water transport along local coast. Recently, wind-induced sea level variation and buoyancy forcing from river discharge were reported to make quasi-equivalent contributions in driving ZFCC (Zhang et al., 2022).

The TWC is usually considered as the current originating from Taiwan Strait or Kuroshio Intrusion (KI), flowing toward north all year around within the 50-100m isobaths (Mao, 1964). The TWC significantly impacts the shelf environment and ecosystem of ECS, however, its origin and flow pathway are still controversial. To date, it is widely accepted that in summer, the TWC consists of both the northward flow through Taiwan

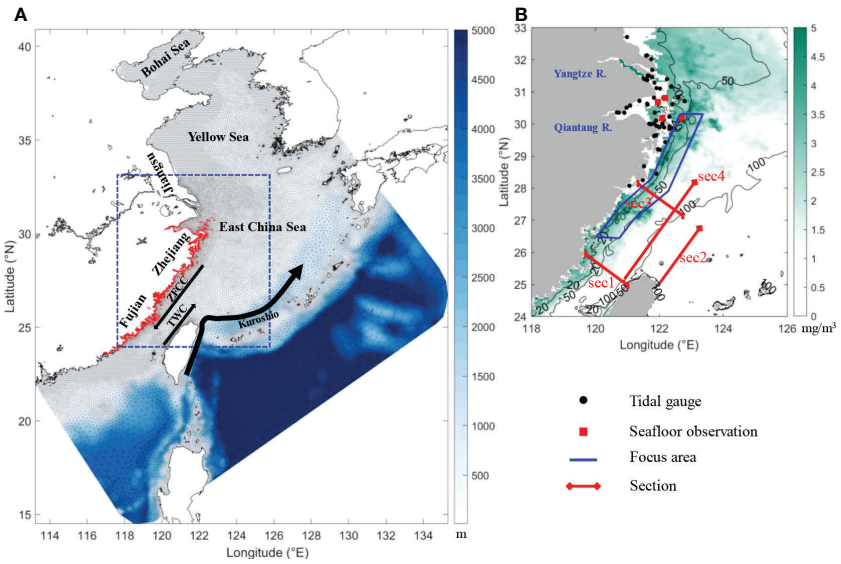

FIGURE 1
(A) Bathymetry and mesh grid of the studied region, the Zhejiang-Fujian coast is highlighted in the red line. **(B)** Monthly MODIS-Aqua chlorophyll-a concentration off the Zhejiang-Fujian coast in March, 2021.

Strait and the branch of Kuroshio intruding into the ECS. But in winter, no consensus has been reached so far (Isobe, 2008; Lian et al., 2016b). Therefore, impacts of TWC on the ZFCF exerted either by Taiwan Strait warm water or the Kuroshio Current (KC) remains to be elucidated.

Except for the large-scale background circulation, other factors also can modulate the ZFCF. He et al. (2016) indicated that the steep bottom bathymetry off the Zhejiang-Fujian coast and surface cooling jointly contribute to the formation of the ZFCF. Cao et al. (2021) analyzed the relationships between the potential driving forces (e.g., alongshore wind, river discharge and SST) and fronts probability using linear regression method, whose results highlighted the significant roles of alongshore wind and the river discharge in the frontogenesis of ZFCF.

Previous studies have achieved a comprehensive understanding of the ZFCF over a seasonal scale, however, the spatiotemporal variability and regulatory mechanisms of ZFCF over a shorter time scale remain unclear. Using multi-source remote-sensed SST data, a new phenomenon was captured: there is an abrupt change in the intensity of the ZFCF in early spring, 2021, which certainly will exert a significant impact on local coastal ecosystem. In order to explore the intrinsic mechanisms controlling the abrupt change of the ZFCF and achieve a better understanding of local marine environment, a series of numerical investigations together with remote sensing data analysis and heat budget analysis were conducted. Following this introduction, section 2 introduces the remote sensing data, numerical model configuration, and model validations; section 3 presents the three-dimensional structures of the ZFCF and its variability; section 4 documents a systematic discussion of factors controlling the abrupt change of ZFCF, and finally, section 5 summarizes the current study.

2 Data and methodology

2.1 Satellite-observed SST

Three sources of satellite data were employed in this study, including the Moderate Resolution Imaging Spectroradiometer (MODIS) -Aqua Daytime SST, Multiscale Ultrahigh Resolution (MUR) SST and Himawari-8 SST. The available periods of these data are 2002-07 to ongoing, 2002-06 to ongoing and 2015-06 to ongoing, respectively.

Monthly averaged MODIS -Aqua SST Level 3 Mapped data with a spatial resolution of 4 km × 4 km during 2003 to 2021 were obtained from the U.S. National Aeronautics and Space Administration (NASA) website[1]. Together with MODIS-Aqua SST, two more datasets were used for comparison and verification. The MURSST Level 4 SST, produced by NASA JPL Physical Oceanography DAAC[2] with a 0.01-degree resolution, is based upon nighttime GHRSST L2P skin and subskin SST observations from several instruments, including the AMSR-E, AMSR-2, MODIS, WINDSAT radiometer, AVHRR, and *in situ* SST observations from the NOAA iQuam project. In this study, daily MURSST data from October 2020 to June 2021 are used. The monthly Level 3 Himawari-8 SST data with a 2 km spatial resolution from October 2020 to June 2021 were provided by the Japan Meteorological Agency (JMA)[3], this product is mainly based on the observations by the new generation geostationary satellite Himawari-8. Notably, the Himawari-8 SST has been validated against the *in-situ* SST data (iQuam) and shows reliable quality.

2.2 Seafloor observations

The seafloor observations are achieved through the submarine cable observation systems (Zhai et al., 2020). These systems were applied to online monitor temporal variations in marine environment of the ecologically important regions. Four submarine cable observation systems are marked off with red squares around the Changjiang and Qiantangjiang estuaries in Figure 1B. The submarine cable online observation systems were placed at 20 cm above the sea floor and equipped with a HydroCAT conductivity-temperature-depth (CTD) recorder to continuously observe temperature, salinity, pressure and other variables in the bottom layer. In this study, hourly averaged temperature in bottom layer and the water elevation were used to examine the performance of the numerical model.

2.3 ERA5 product

ERA5[4] is the fifth generation ECMWF reanalysis of the global climate and weather, which provides hourly estimates for a large number of atmospheric, ocean-wave and land-surface quantities. In this study, 0.25-degree hourly wind vectors and surface radiation flux data, including Surface net solar radiation (SNSR), Surface net thermal radiation (SNTR), Surface sensible heat flux (SSHF), and Surface latent heat flux (SLHF), of 2020 to 2021 are used as the atmospheric forcing in our model. Meanwhile, ERA5 data from 2003 to 2021 were also utilized in the correlation analysis in section 4. The ECMWF convention for vertical fluxes is positive downwards, and net heat flux from ERA5 is calculated following:

1 http://oceancolor.gsfc.nasa.gov

2 https://podaac.jpl.nasa.gov

3 https://www.eorc.jaxa.jp/ptree/index.html

4 https://cds.climate.copernicus.eu/

$$Q_{net} = SNSR + SNTR + SSHF + SLHF \quad (1)$$

2.4 Algorithm for front intensity

SST gradient magnitude was calculated by the central difference method as:

$$\nabla_x SST(i,j) = \frac{(SST(i+1,j) - SST(i-1,j))}{2\Delta X} \quad (2)$$

$$\nabla_y SST(i,j) = \frac{(SST(i,j+1) - SST(i,j-1))}{2\Delta Y} \quad (3)$$

$$|\nabla SST|(i,j) = \left(\nabla_x SST(i,j)^2 + \nabla_y SST(i,j)^2\right)^{\frac{1}{2}} \quad (4)$$

Where $\nabla_x SST$ and $\nabla_y SST$ are the zonal and meridional components of the SST gradient, ΔX and ΔY are the distances in kilometers between the neighboring grid points in the longitudinal and latitudinal directions, respectively. $|\nabla SST|$ is the gradient magnitude. This algorithm has been widely used in the calculation of coast SST gradient (Vazquez-Cuervo et al., 2013; Saldias and Lara, 2020; Saldias et al., 2021).

2.5 Circulation model

The studied region characterizes irregular coastline and rugged topography, therefore the traditional circulation model working under structured grid is no longer capable. For this reason, the Semi-implicit Cross-scale Hydroscience Integrated System Model (SCHISM) was employed in this study (Zhang et al., 2016a; Zhang et al., 2016b). SCHISM is a 3D unstructured-grid model developed from the original Eulerian-Lagrangian Finite Element model, using the semi-implicit time stepping and hybrid finite-element/finite-volume method with the Eulerian-Lagrangian algorithm to solve the Navier-Stokes equations in hydrostatic form. In addition, it provided a new hybrid SZ coordinate called Localized Sigma Coordinates with Shaved Cells (LSC^2) in the vertical dimension, which makes no bathymetry smoothing possible. More details about the SCHISM model can be found on its official website[5].

The model region covers the whole Bohai sea, Yellow sea, and East China Sea with three open boundaries (Figure 1A). In order to better simulate the hydrodynamics in the nearshore areas and save computational resources, the locally-refined grid was designed. The horizontal resolution near the open boundaries is depth-dependent varying between 7 to 50 km, while for the refined regions (blue dotted box in Figure 1A), the horizontal resolution ranges from 2 km in the shallow coastal water to 8 km in the deeper area. The whole mesh grid contains 24742 nodes and 47319 triangle elements. In the vertical direction, 59 layers LSC^2 grid was applied and the bathymetry was interpolated from the Shuttle Radar Topography Mission (SRTM) 15Plus V2.1 (Tozer et al., 2019).

The 3-D water temperature, salinity, velocity, and sea surface height for initial and boundary conditions were interpolated from the 41-layer Hybrid Coordinate Ocean Model and Navy Coupled Ocean Data Assimilation (HYCOM + NCODA) Global 1/12° Analysis data. Additionally, we prescribed the tidal forcing of eight tidal components, including M_2, S_2, K_2, N_2, K_1, O_1, Q_1, and P_1 at the open boundaries. All the tidal information comes from the latest version of the Finite Element Solution (FES2014) tide model by AVISO+[6]. We considered two major river sources, the Yangtze River and the Qiantang River, the monthly averaged river discharge data is from the *River and Sediment Bulletin of China*[7], besides, the temperature of the rivers is based on MODIS-Aqua 4km daily SST product, and the salinity is set to 3 PSU uniformly. Hourly atmospheric forcing was generated using the ERA5 product originated from Climate Data Store[4]. The simulation period was initialized on October 1, 2020 and ended on December 31, 2021. During the integration, the time step was 120s and hourly outputs were saved.

3 Result

3.1 Abruptly-changed ZFCF

Figure 2 displays the monthly mean SST gradient magnitude and the 10m-high wind vectors from October, 2020 to March, 2021 within the study area. In November, the ZFCF started to form under the strong prevailing northeast monsoon, then its intensity kept strengthening along the 50-m isobath and peaked in January, with a maximum intensity of 0.2°C/km. In the following February and March, there was a significant decrease in both the intensity and spatial range of the ZFCF, especially in the area south of the 28°N, the SST gradient has dropped by more than 0.12°C/km and the front almost disappeared by March. However, compared with the evolution of winds in January, there is no significant change in the local wind both in speed and direction.

To show this phenomenon in more detail, we calculated the time series of spatially-averaged daily SST gradient as well as the local wind vectors of the focus region (blue dashed box in Figure 1A) and presented them in Figure 3. As revealed by Figure 3, when entering January, the SST gradient shows a high correlation with the southward meridional wind, e.g., it increases

5 http://ccrm.vims.edu/schismweb/

6 https://www.aviso.altimetry.fr

7 http://www.mwr.gov.cn/

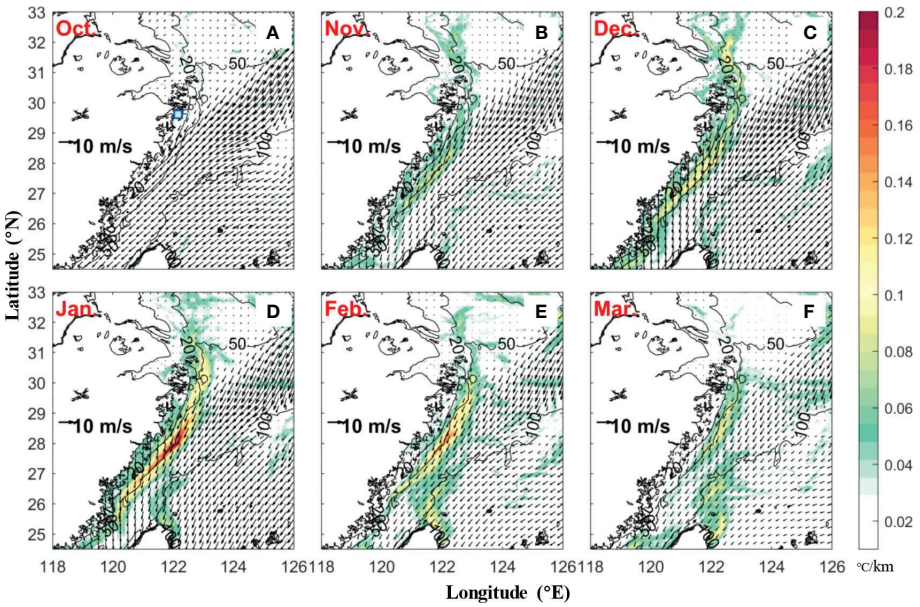

FIGURE 2
MURSST monthly mean SST gradient magnitude and ERA5 10m wind vectors in the Zhejiang-Fujian coastal sea from October **(A)** to March **(F)** of 2020-2021.

significantly during these two strong northerly wind processes around early January and mid-February, respectively, which agrees with the points of previous works (Cao et al., 2021). Then an abnormal abrupt decrease of the SST gradient occurred: the magnitude of SST gradient in the focus region quickly dropped by more than 0.05 °C/km during 15 days after late January, which is highlighted in red in Figure 3. This phenomenon can be divided into two periods: in the first period, the northerly wind significantly weakens and there is a synchronous dramatic decrease in SST gradient; in the second period, after the recovery of the northerly monsoon, the SST gradient does not recover as expected but oppositely a repaid decline process occurs. So, how does this phenomenon develop?

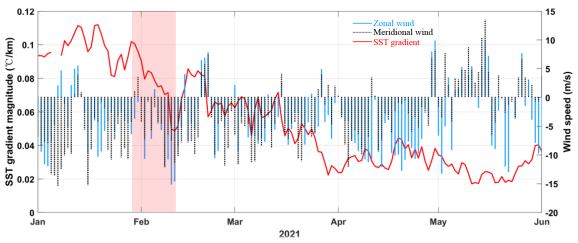

FIGURE 3
The spatially-averaged SST gradient magnitude of the focus region (Figure 1B) is shown in the red line, while the speed of zonal and meridional wind from ERA5 is in the blue line and black-dots-line (eastward and northward positive), respectively. The red shaded region marks off the sudden decrease of the SST gradient.

3.2 Model validation

The satellite observed SST has captured the rapid changes of the ZFCF successfully, however, it is hard to further investigate the regulatory mechanism of this phenomenon, thus the numerical model is employed to make further explorations. To ensure the reliability of the discussions, we first validated the model performance in describing local hydrodynamics.

3.2.1 Sea level height

Previous studies indicated that tides make significant contributions to the hydrodynamic field in ECS by generating internal solitary waves, tidal fronts and other processes (Hu et al., 2016; Teng et al., 2017; Liu et al., 2018; Wang et al., 2020). So, we first compared the simulated hourly sea elevation against the observations from the submarine cable observation system in January (Figure 4). As displayed, the model well reproduced the time series of elevation at stations Dajishan and Dongjidao 1 only with minor differences. To further evaluate the performance of the model, we calculate three statistical parameters, including Root Mean Square Error (RMSE), Correlation Coefficient (CC) and model Skill, and the model skill assessment parameter is defined as (Bai et al., 2016; Lai et al., 2018):

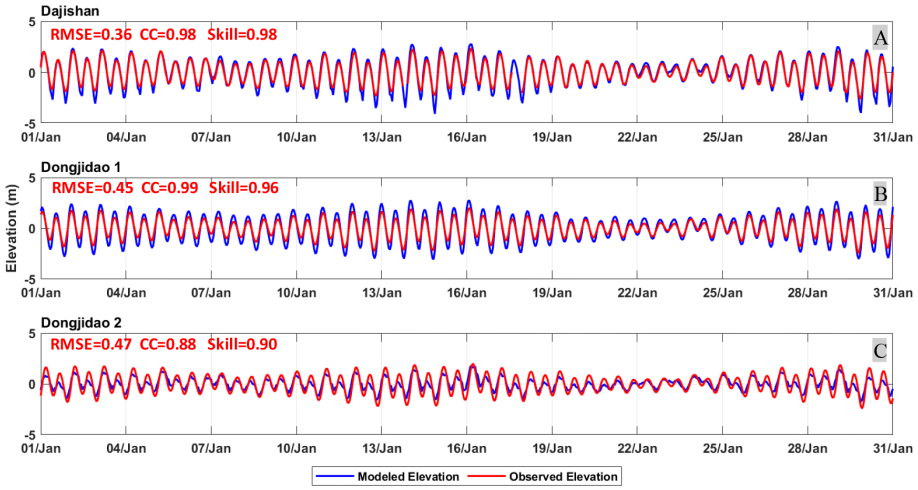

FIGURE 4
Comparison of modeled and observed elevations at three seafloor observation systems. Each station's statistical parameters (RMSE, CC and Skill).

$$\text{Skill} = -\frac{\sum_{i=1}^{N}(\eta-\zeta)^2}{\sum_{i=1}^{N}\left(|\eta-\bar{\zeta}|+|\eta-\bar{\eta}|\right)^2} \quad (5)$$

where η and ζ represent the modeled and the observed sea elevation, respectively, the overbar donates the temporal average. The RMSE of these stations are 0.36, 0.45, 0.47; CC are 0.98, 0.99, 0.88 and Skill are 0.98, 0.96, 0.90, respectively. The comparison indicates that the model has a good capability of simulating tidal motions in the study area.

Further, tidal harmonic analysis is applied using the T_TIDE MATLAB toolbox (Pawlowicz et al., 2002) to obtain the tidal harmonic constants of four major tidal components (M_2, S_2, K_1 and O_1) in those tide gauges around the Zhejiang-Fujian coast (black dots in Figure 1B). The comparisons of amplitude and phase of four major tidal constituents are shown in Tables 1 and 2. In general, model results have satisfying consistency with observations. The Mean Errors (ME) of the M_2, S_2, K_1 and O_1 tidal components are 0.30, 0.10, 0.04 and 0.03 m in amplitudes, 31.1°, 31.6°, 15.1° and 16.8° in phases, respectively. The simulation errors may come from the insufficient horizontal resolution near each tidal gauge. Nevertheless, such tidal performance of the coastal region model is acceptable in complicated coastline and bathymetry.

3.2.2 Water temperature

The model performance in temperature is crucial for studying temperature fronts, therefore, we evaluated the model output of sea temperature from bottom to surface based on the seafloor observations, MODIS-Aqua SST and MURSST products. The comparison between the modeled and observed bottom temperature is shown in Figure 5. Due to lack of measurement, only observations at stations Dajishan and Yujing 5 were used to validate the modeled bottom temperature. Figure 5 shows that the model satisfyingly simulates both the magnitude and the trend of temperature variation from winter to autumn, only minor overestimation in summer and underestimation in winter occurred. Three statistical parameters RMSE, CC, and Skill are applied in this part as well. The relatively small RMSE, high CC and Skill at two stations suggest that the model could reasonably simulate the bottom temperature in the study area.

The modeled SST is further validated by satellite SST products. Figure 6 compares the monthly-mean SST from October 2020 to March 2021, showing good consistency between the simulated and observed SST in spatial pattern (southward extension of the ZFCC and northwestward intrusion of KC) as well as in temperature values. Notably, the cold tongue which plays a significant role in the ZFCC off the Jiangsu coast is also well simulated.

In general, validations of simulated temperature at both surface and bottom layers indicate satisfactory model performance, which certainly ensures the reliability of following analyses.

3.2.3 Flow pattern

As the large-scale background circulation remarkably dominates variation of ZFCF (Hsu et al., 2021), the modeled flow pattern is further evaluated. Figure 7 shows the surface current field off the Zhejiang-Fujian coast from October 2020 to March 2021, two main currents, the ZFCC and KC, can be easily distinguished from Figure 7. The ZFCC has a relatively high intensity in October, December and January due to the powerful northeast monsoon, it gradually weakens in February and March following the decay of prevailing monsoon. There are three

TABLE 1 The comparison of amplitudes (m) between the observation and simulation of the major four tidal components.

Station	M2			S2			K1			O1		
	OBS	MOD	|DIF|	OBS	MOD	|DIF|	OBS	MOD	|DIF|	OBS	MOD	|DIF|
1	1.10	1.28	0.18	0.46	0.50	0.04	0.30	0.32	0.02	0.21	0.24	0.03
2	1.52	1.78	0.26	0.64	0.65	0.01	0.46	0.38	0.08	0.21	0.25	0.04
3	1.88	2.17	0.29	0.68	0.75	0.07	0.30	0.29	0.01	0.23	0.23	0.00
4	1.38	1.70	0.32	0.69	0.84	0.15	0.28	0.30	0.02	0.19	0.18	0.01
5	1.43	1.79	0.36	0.54	0.69	0.15	0.32	0.37	0.05	0.19	0.24	0.05
6	1.77	2.29	0.52	0.64	0.80	0.16	0.35	0.41	0.06	0.22	0.27	0.05
7	1.50	1.84	0.34	0.53	0.67	0.14	0.33	0.39	0.06	0.21	0.26	0.05
8	0.92	1.19	0.27	0.36	0.46	0.10	0.31	0.33	0.02	0.20	0.24	0.04
9	0.90	0.92	0.02	0.36	0.35	0.01	0.31	0.34	0.03	0.20	0.25	0.05
10	1.65	2.10	0.45	0.66	0.80	0.14	0.30	0.31	0.01	0.22	0.24	0.02

major branches of KI north to Taiwan Island, the first- and second-branch turn southwestward and northward, and then merge with the downstream and midstream of ZFCC, respectively. The third branch turns westward but finally merges into the KC mainstream again. Compared with former investigations, the flow pattern produced by our model is in good consistence with previous investigations (Liu et al., 2014; Yang et al., 2018; Cui et al., 2021), again suggesting reliable model performance.

3.3 Vertical structure of ZFCF

The vertical structure of temperature and current across the ZFCF in two representative sections (sec1 and sec3, Figure 1B.) from October 2020 to March 2021 are shown in Figures 8 and 9, respectively. As Figures 8A-F reveal, in October, despite the presence of strong ZFCC, no significant thermal fronts occurred because the water column is well stratified. As it comes to November, the whole water column is sufficiently mixed under the strong wind stress, meanwhile the cold ZFCC dominates the coastal area, therefore the horizontal temperature gradient begins to strengthen and an apparent thermal front (ZFCF) forms at regions 20~50 km off the coast. After reaching its peak in January, the vertical isotherm of the ZFCF gradually shifts direction and transforms into a horizontal distribution, suggesting the decay of ZFCF. From Figures 8G-L, the boundary of the northward and southward current can be clearly distinguished by the black dotted lines; interestingly, the boundary of two reversed current is located about 60 km off the coast, which is remarkably different with the location of ZFCF. This feature seems to be contradictory to the formation

TABLE 2 The comparison of phases (°) between the observation and simulation of the major four tidal components.

Station	M2			S2			K1			O1		
	OBS	MOD	|DIF|	OBS	MOD	|DIF|	OBS	MOD	|DIF|	OBS	MOD	|DIF|
1	261.00	236.32	24.68	305.00	282.22	22.78	220.00	200.03	19.97	175.00	156.84	18.16
2	334.00	327.06	6.94	18.00	11.84	6.16	210.00	212.66	2.66	165.00	158.60	6.40
3	341.00	317.27	23.73	23.00	2.36	20.64	213.00	208.15	4.85	171.00	154.51	16.49
4	344.00	325.45	18.55	30.00	13.60	16.40	213.00	204.23	8.77	170.00	150.18	19.82
5	286.00	268.69	17.31	331.00	315.97	15.03	193.00	182.36	10.64	151.00	132.83	18.17
6	334.00	327.06	6.94	18.00	11.84	6.16	210.00	212.66	2.66	165.00	158.60	6.40
7	292.00	277.32	14.68	335.00	321.16	13.84	216.00	209.31	6.69	169.00	157.85	11.15
8	348.00	333.15	14.85	41.00	21.32	19.68	196.00	188.26	7.74	144.00	128.68	15.32
9	297.00	282.70	14.30	334.00	327.02	6.98	209.00	207.48	1.52	166.00	154.84	11.16
10	32.00	20.15	11.85	89.00	79.32	9.68	221.00	218.73	2.27	168.00	155.48	12.52

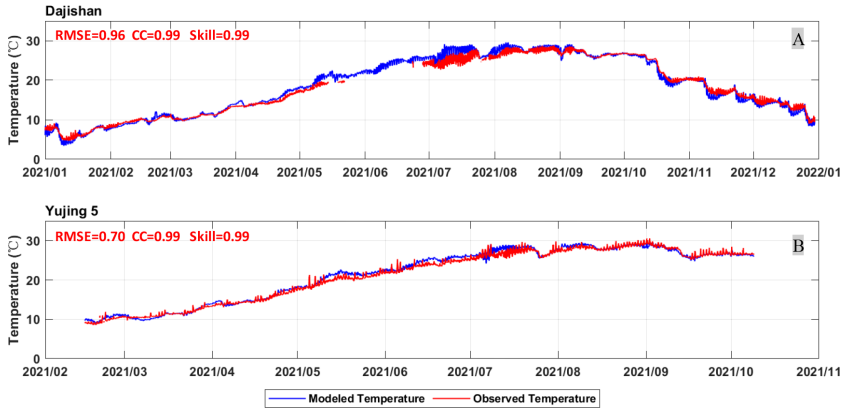

FIGURE 5
Comparison of modeled bottom temperature with the seafloor observation in Dajishan **(A)** and Yujing 5 **(B)**.

mechanism of the front raised by former studies, which will be explained in section 4. The first branch of KI carries relatively warm water and joins into the ZFCC near the coast. Thus, a front closer to the coast is formed. Meanwhile, the weakening of northward flow in January also suggests that the strong KI and northly monsoon could inhibit the southward flow within the Taiwan Strait. Obviously, Figure 8 provides a piece of clear evidence that the ZFCF is affected by the KI.

Sec 3 is located at the junction of the Zhejiang and Fujian coasts. Along sec 3 (Figures 9A-F), the temperature structure of the upper water has the same pattern as sec 1 in regions shallower than 50 m, while the deep water has strong stratification during October to December. The water column could be well mixed only in January, and then it stratifies again accompanied by the weakening of the front. The variation in the stratification of the water column is usually dominated by the heat fluxes, and thus exerts potential impact on the ZFCF, which will be discussed in the next section. In addition, the flow structure reveals that the southward (ZFCC) and northward (TWC) flows have a clear decreasing tendency through February and March, which is a strong indicator that the change of background flow may be the direct cause of the abrupt change of ZFCF.

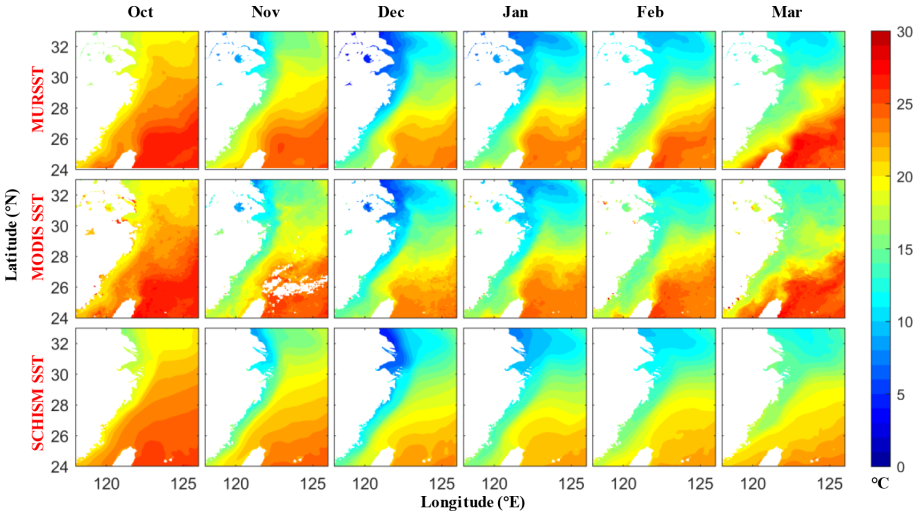

FIGURE 6
Comparison of monthly averaged SST between simulated and satellite-observed (MURSST and MODIS-Aqua) SST from October 2020 to March 2021.

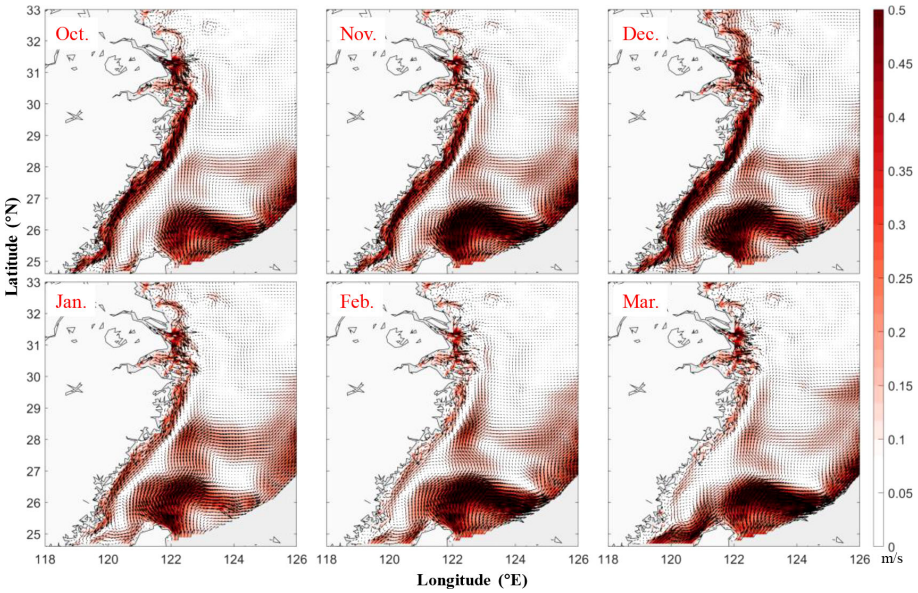

FIGURE 7
Monthly-average surface currents off the Zhejiang-Fujian coast from October 2020 to March 2021, the arrows represent the flow direction while color indicates current magnitude.

4 Discussion

We have analyzed the three-dimension structure and variation of the ZFCF based on satellite observations and numerical results. Above analyses suggest that the abrupt change of ZFCF is closely related with the variations in wind, background circulation, and also the stratification. Moreover, we noticed that the decay of ZFCF still persisted even after the

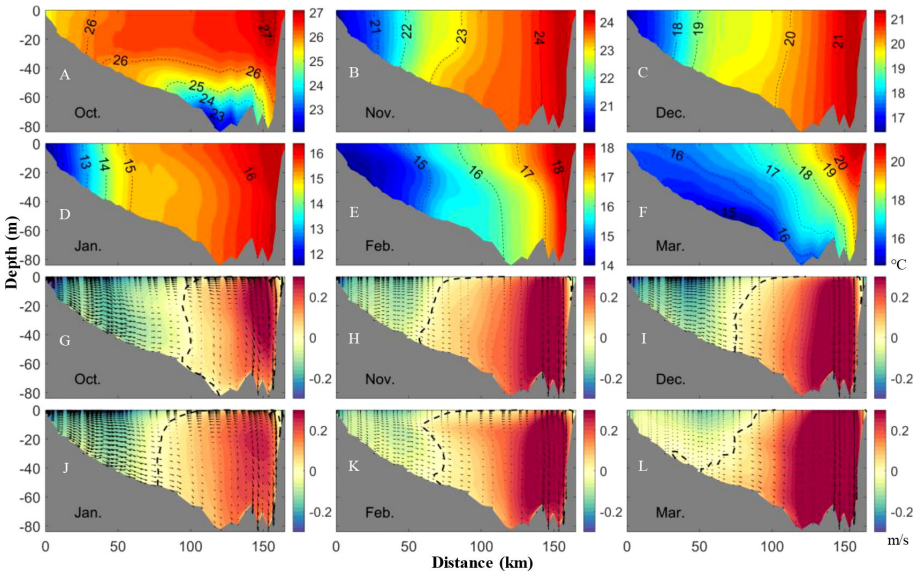

FIGURE 8
Vertical structure of temperature **(A-F)** and flow (**G-L**, along-isobath component in colors, northward positive; cross-isobath and vertical components in arrows, vertical velocity is multiplied by 1000) along sec1 from October 2020 to March 2021. The dotted lines in subgraphs **(G–L)** indicate the location of 0 m/s of along-isobath velocity.

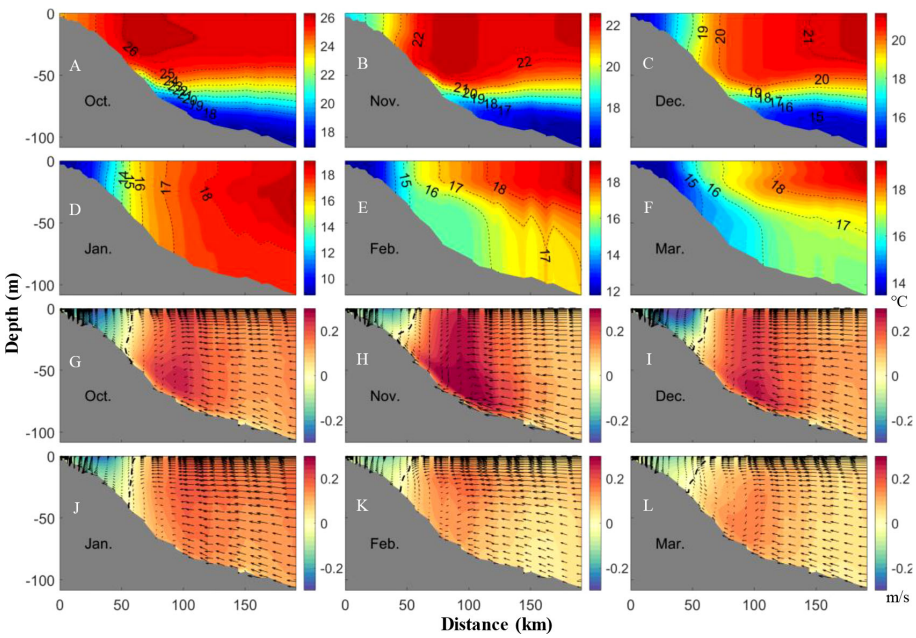

FIGURE 9
Same as Figure 8 but for sec 3.

recovery of northerly wind. In this section, the roles of different dynamic factors will be carefully discussed based on correlation analysis, heat budget and a series of numerically diagnostic experiments.

4.1 Role of heat flux and wind stress

The intensity of the ZFCF is closely related to the northeast monsoon (Figure 2): the monsoon weakened to some extent during the sudden drop of the ZFCF. Further, the stratification of the water column caused by variation of the net heat flux may also contribute to the sudden drop in thermal front (Figures 8 and 9). Therefore, based on correlation analysis, the relationships between the heat flux, wind stress, and the ZFCF were analyzed. We calculated the area-averaged local winds, net heat flux, and the SST gradient from January to March through 2003-2021 and the results are presented in Figure 10. As displayed, the intense heat loss (negative net heat flux) corresponds well with higher SST gradients, the regression analysis result (R=-0.72, P<0.001) also confirms their significant correlation. During a heat loss process, the shallow nearshore area tends to be cooled down more completely compared with the deep offshore region due to stronger vertical mixing and relatively lower heat content over the whole water column. Therefore, the temperature difference between nearshore and offshore waters gets further expanded, triggering a stronger ZFCF.

Winds can directly modulate the circulation, vertical mixing, and the air-sea heat exchange process (Qiao et al., 2006; Wang et al., 2015; Zhou et al., 2015; Park et al., 2020), further adjusting the ZFCF. Thus, as speculated, Figure 10 shows significant correlationship between SST gradient and wind stress (R=0.75, P<0.01). However, effect of winds on ZFCF is a comprehensive process and next we will explore the contribution of winds from different aspects.

4.2 Role of background currents

The encounter of two different water masses or currents is one of the major frontogenesis mechanisms, as section 3.3

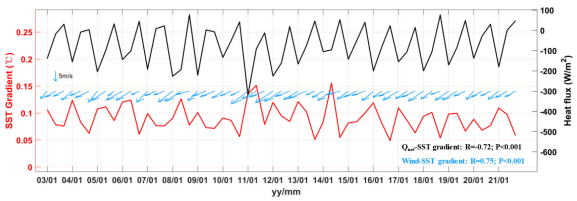

FIGURE 10
Comparison of the SST gradient magnitude (red line), surface net heat flux (black line, positive downwards) and wind stress vectors (blue arrows), all three are area-average results of the focus region. The correlation coefficients for the regression are labeled.

reveals, the weakening of ZFCC and TWC is highly correlated with the abrupt decay of ZFCF. We used the monthly-averaged HYCOM current product and MODIS-Aqua SST data to find out the relationship between the currents and ZFCF from January to March over an interannual scale. Expect for sec 1 and 3 presented above, two more sections (sec 2 and 4, Figure 1B) are selected to investigate the role of KI. The heat flux Q_T through four representative sections are calculated to diagnose the interactions between the background flow and ZFCF following:

$$Q_T = \int_0^l \delta_T dw,\ \delta_T = \int_{-h}^{\eta} TVdz \tag{6}$$

where T is the temperature of the water column, V is the cross-section velocity, η is sea water level, h is the water depth, and l is the width of the section. The southward current through sec 1 and 3 represent the ZFCC, while the northward current across sec 1 represents the flow through Taiwan Strait, and the westward currents crossing sec 2 and 4 represent the KI.

Figure 11 shows the time series of area-averaged SST gradient and Q_T through sec 1-4, meanwhile, results of linear regression analysis (at 95% confidence level) are shown in Table 3. For the ZFCC (southward current through sec 1 and 3), the variation of Q_T and SST gradient synchronize well with each other and significantly correlated (R=0.46 and 0.56, respectively). The ZFCC flows southward along the coast, bringing cold and fresh water to the focus area, and therefore directly maintains and regulates the ZFCF.

For the warm flow through Taiwan strait (northward current across sec 1), it leads to a significantly negative correlation between the Q_T and SST gradient (R=-0.66, P<0.001). This seems to be inconsistent with common sense, as the encounter of two different flows with larger temperature gradients tends to establish a strong thermal front. And here, the Taiwan Strait current and ZFCC have opposite directions, strong northerly winds will strengthen southward ZFCC and weaken northward Taiwan Strait current, thus the Q_T of Taiwan Strait current through sec 1 is reducing. The ZFCC and TWC could be regarded as the cool and warm water sources for forming ZFCF, when TWC weakens, extra warm water sources are needed to maintain the strength of ZFCF. For the ZFCF, KI is the possible one which might supply warm water except for the Taiwan Strait current.

Wang and Oey (2014) indicated that the strengthened northeast wind would significantly enhance the KI. Recently, Kang and Na (2022) further reported significant correlation relationships between KI and wind stress and wind stress curl. Does this mean stronger northeast winds will generate stronger KI, and thus leads to a stronger ZFCF? The answer is uncertain because stronger northeast winds enhance the KI but will inhibit the northward transport of warm KC water. This is why Figure 11 and Table 3 both suggest no significant relationship between the KI (westward current in sec 2 and 4) and the SST gradient.

4.3 Heat budget analysis

Discussions above point out that the ZFCF is closely modulated by the heat flux and background circulation in long term. To find out the key factors leading to this abrupt change of ZFCF in early spring, 2021, heat budget analysis was conducted based on numerical results. Since the onshore water column was well mixed during the abrupt change, we selected a series of representative points (blue and red dots in Figure 12E) located on either side of ZFCF, and the average heat budget through the whole water column at each point was calculated following Vijith et al. (2020) and the equation was written as:

$$\underbrace{\frac{\partial T_a}{\partial t}}_{Tendency} = \underbrace{-\left(u_a\frac{\partial T_a}{\partial x} + v_a\frac{\partial T_a}{\partial y}\right)}_{Horizontal\ advection} \underbrace{+\kappa_H\left(\frac{\partial^2 T_a}{\partial x^2} + \frac{\partial^2 T_a}{\partial y^2}\right)}_{Horizontal\ mixing} \underbrace{-\frac{1}{h}\left(\kappa_z\frac{\partial T}{\partial z}\right)_{-h}}_{Vertical\ mixing}$$
$$\underbrace{-\left(\frac{T_a - T_{-h}}{h}\right)\left(\underbrace{\frac{\partial h}{\partial t}}_{ML\ tendency} \underbrace{+u_{-h}\frac{\partial h}{\partial x} + v_{-h}\frac{\partial h}{\partial y}}_{Lateral\ induction} + \underbrace{w_{-h}}_{Vertical\ advection}\right)}_{Entrainment}$$
$$+\underbrace{\frac{q_0 - q_{pen}}{\rho_0 c_p h}}_{Net\ heat\ flux} \tag{7}$$

Where T, ρ_0, c_p and h represent the temperature, mean density, water column depth and specific heat capacity of

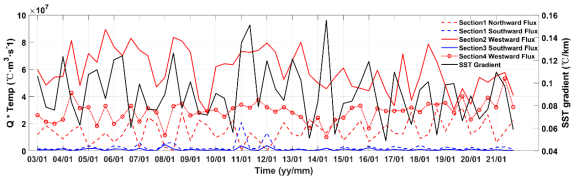

FIGURE 11
Time series of Q_T (heat flux) through four representative sections and the area-averaged SST gradient.

TABLE 3 Results of linear regression analysis between Q_T and SST gradient.

Section	Current	R	P
1	Northward	-0.66	0.0001
	Southward	0.46	0.0001
2	Westward	0.25	0.0624
3	Southward	0.56	0.0001
4	Westward	-0.21	0.1324

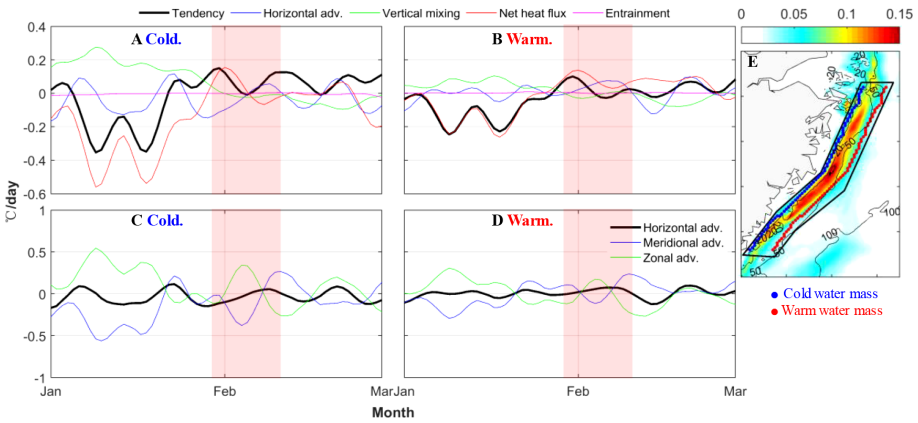

FIGURE 12
(A, B) Time series of the terms of the heat budget equation in cold water (blue dots in **E**) and warm water (red dots in **E**), the red shaded represents the same abrupt change period as Figure 3. **(C, D)** Zonal and meridional components of the horizontal advection in cold and warm water. **(E)** Average modeled SST gradient of January to March, 2021, and the points used for heat budget analysis.

seawater, respectively. *u,v* and *w* are the zonal, meridional and vertical velocity. The suffix *a* are the vertically-averaged quantity and the subscript *-h* denotes the quantity at the base of the water column. q_0 and q_{pen} are the surface net heat flux and penetrative loss of shortwave radiation, respectively. K_H and K_z represent the horizontal and vertical eddy diffusivities, respectively.

The sum of the horizontal advection, horizontal mixing, vertical mixing, entrainment and net heat flux well consist the overall pattern of the tendency term with a correlation of 0.87 and 0.83, RMSE of 0.13 and 0.09 °C/day (within 95% confidence interval) in cold water and warm water, respectively. The result is a satisfyingly good closure of the whole water column heat budget for such short time scales. Our analysis points out that net heat flux is important in determining the net tendency of the temperature on both sides of the front (Figures 12A and B), while in the cold water west to the front, vertical mixing and horizontal advection also greatly contribute to the tendency before February. For the abrupt change around later January, the temperature tendency in cold water has already been positive, while that in warm water east to the front was still negative. That indicates the temperature in cold water begins to warm up thus the temperature difference between two water masses is reduced. When the positive tendency reached its peak (~0.18°C/day) in cold water, the intensity of the ZFCF starts abruptly decreasing, and the net heat flux was the predominant contributor.

Interestingly, during the change period, the contributor of the positive tendency changed from net heat flux to horizontal advection in cold water, which provides a good answer to the question at the end of section 3.1. Although the recovery of the monsoon causes the net heat flux tends to cool the onshore water again, the heat carried by the horizontal advection compensated for the loss and kept the tendency positive, then resulting the decrease of ZFCF in the second period. Besides, the decomposition of the horizontal advection reveals that the flow pattern might change during the abrupt change of the ZFCF, because the zonal advection term changed from positive to negative and the meridional advection changed from negative to positive on both sides of the front. Combined with the analysis of the above sections, the variations of the horizontal advection of ZFCC and KI might induce the positive temperature tendency.

4.4 Numerical diagnosis

To further illustrate the contributions of different dynamic factors in triggering the abrupt decay of ZFCF in February, we conducted a series of sensitive numerical experiments based on above analyses. Each experiment runs for seven months from October 1, 2020, the control conditions of these sensitive experiments are listed in Table 4.

TABLE 4 Key configurations of sensitive experiments.

Numerical Experiments	Descriptions
No-wind	Zero Wind stress is used
No-river	No river inputs
No-tide	Tidal forcing is turned off
Rad-Jan	Longwave and shortwave radiations in Feb. and Mar. are replaced by that in Jan.
Wind-Jan	Wind stresses in Feb. and Mar. are replaced by that in Jan.
No-KI	The intrusion of Kuroshio is closed by adding a 'wall' on the northeastern Taiwan island

The differences in SST gradient between the sensitive experiments and control run are shown in Figure 13. When the wind stress forcing is closed (No-wind case), the SST gradient have changed dramatically in both distribution and intensity, the ZFCF almost disappears; in this case, thermal fronts mainly occurred around the Yangtze River estuary or regions with complicated bathymetry as a result of river discharge and modulation of current by topography. Moreover, the fronts triggered by the KI to the northeast of Taiwan Island are further away from the shelf, indicating a decreased KI under weak northerly monsoon, which agrees well with previous study (Wang and Oey, 2014). We found that the ZFCC almost disappeared with a small velocity lower than 0.1 m/s; thus, local wind stress is a key factor during the formation of ZFCF through modulating the intensity of ZFCC. When the wind stress in February and March were replaced by that in January (Exp. Wind-Jan, Figure 13E), the ZFCF was significantly enhanced, again proving that the weakening of the northeast wind stress plays a vital role during the abrupt decay process in February and March.

When no river discharge was considered (Exp. No-river, Figure 13B), the location of ZFCF is closer to the coastline in January compared with the control run, besides, the intensity of ZFCF decreases slightly in February and March. As an essential component of the ZFCC, the riverine flow merges with the ZFCC, increasing the flow flux and strengthening the zonal width of the ZFCC (Wu et al., 2021), which then leads to a farther ZFCF off the coast. Besides, buoyancy forcing produced by the Yangtze River discharge can strengthen the southward flow of the Zhejiang-Fujian coastal water (Wu et al., 2021; Zhang et al., 2022), so the ZFCF decreases in February and March under the condition of no river discharge. Further, runoff of the Yangtze River reduced from January (40.6×10^9 m^3) to February (33.53×10^9 m^3), which might also contribute to the decrease of the ZFCF in February.

From experiments No-tide and Rad-Jan (Figures 13C and D), limited effect of solar radiation and tidal forcing on the intensity of ZFCF could be speculated, and the front is fixed on the topographic slope under the tidal mixing (Cheng et al., 2017). When tidal forcing is neglected, the location of the front moves onshore. Moreover, the result also points out that the net heat flux, which is important in determining the net temperature tendency, is mainly modulated by latent and sensible heat flux controlled by winds.

To investigate the influence of the KI, Exp. No-KI was designed by blocking the western passage of the KI (Figure 13F) to simulate the situation of the weak KI. Notably, KI and the shelf circulation are vital components of the ECS, to balance the mass flux in and out of the continental shelf, when the KI was cut off, the currents through the Taiwan Strait will be influenced (Yang et al., 2020; Wu, 2021). In this case, the front formed by the KI in northern Taiwan Island has disappeared completely, meanwhile, the ZFCF has significantly changed. The reduction of frontal intensity in January is much weaker than that in February and March, this phenomenon indicates that the KI can hardly reach the focus region under the strong northeast

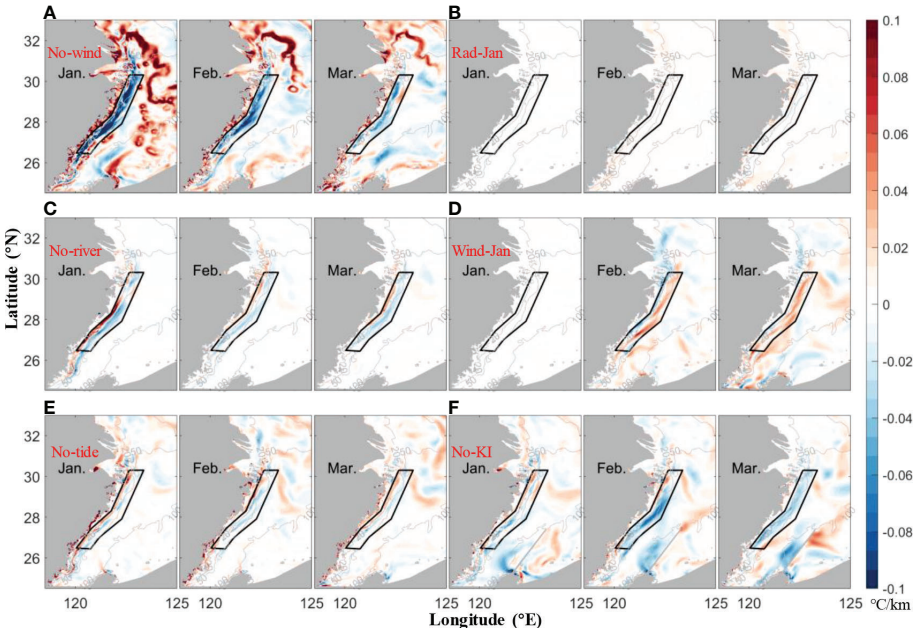

FIGURE 13
Differences in SST gradient between six sensitive experiments and the control run **(A–F)**. The focus region is marked off with a black polygon.

monsoon in January, so the reduction of ZFCF in the southern area is much remarkable than that in the northern area. Tracer experiments by Yang et al. (2018) suggested that the Kuroshio subsurface water cannot reach the algal bloom area along the Zhejiang coast in winter, when the prevailing monsoon relaxes, the onshore intrusion of the Kuroshio will be less prohibited by the barotropic pressure force created by the onshore Ekman transport (Yang et al., 2012; Xu et al., 2018). The intensity of ZFCF decreases distinctly in February under the absence of the KI, the maximum reduction reaches 0.08 °C/km inside the focus region, which is comparable with the change in the No-wind experiment, and even larger in March. Exp. No-KI indicates that the ZFCF is formed by the southward advection of the ZFCC, which was mainly forced by the northeast wind forcing, and the TWC water. As Figure 13F revealed, only a minor change of ZFCF occurred in January when the KI is cut off. However, this circumstance changed dramatically in Feb and Mar when the prevailing monsoon relaxed. This is attributed to the impact of KI, which can reach the focus region and then further affect the ZFCF more efficiently under the weak northeast monsoon. At this point, assisted by the heat budget analysis, the mechanism of the decrease in the second period can be revealed. During the weak of ZFCF in the first period which was caused by relaxation of the monsoon, the invaded water tended to transport to the focus region at the same time. And after this period of monsoon relaxation, the invaded water reached the focus area and heated the weak ZFCC water, so the component of horizontal advection term contributed positive temperature tendency changed from zonal shelf warm water advection to meridional KI advection (Figures 12C and D). Although, the monsoon recovered and tended to cool the onshore water again, the heating effect by KI was stronger than wind cooling effect, thus ZFCF was continually weakening in the second period until the winds forced the cool ZFCC southward and impeded the northward transport of the KI water again. However, Figure 3 shows that the intensity of ZFCF gets stronger after the abrupt decrease, which is caused by the interaction of cool water forced by recovered winds and the residual warm KI water left on the shelf. Also, in the following period with relatively weak northeast monsoon, the continuously invaded water maintained the less intense ZFCF until the onshore water was heating up in the middle March.

5 Conclusions

Former investigations have clarified the spatiotemporal variation of the ZFCF on seasonal scale as well as the basic mechanism of its variation, however, the abrupt change of the ZFCF on short-time scale requires to be further explored. Based on the multi-source satellite data, we found that the ZFCF has an abrupt change in early Spring, to improve understanding of the sudden variation and its internal mechanism of the ZFCF, we used a three-dimensional numerical model to simulate the variability of the coastal front along the ECS, investigated the key controlling factors of the variability of the ZFCF and revealed the main reason for its abrupt change in February.

Based on long-term regression analysis, heat budget analysis and sensitivity experiment, we found that the variation of wind stress is the main factor in the formation and disappearance of the ZFCF. The ZFCC and the KI, influenced by wind, heat flux and river discharge, are two key factors controlling the intensity and region of the ZFCF. For the abrupt change of the ZFCF in early spring, 2021, heat budget analysis indicated that net heat flux and horizontal advection were the most significant terms in determining the net temperature tendency difference between the two water masses of the ZFCF. Followed sensitivity experiment pointed out that the variation of the net heat flux is mainly modulated by the winds and the temperature tendency contributed by horizontal advection is affected by KI and ZFCC. In later January, under the relaxation of the northeast monsoon, the intensity of the ZFCC weakened subsequently, directly inducing the abruptly decreasing of the ZFCF in the first period. Then a second period decrease followed after the KI water transported to the focus region even if the northeast monsoon was recovered. The heating effect of the invaded water was stronger than the cooling effect of the wind, thus the intensity of the ZFCF kept decreasing until the monsoon forced the ZFCC southwardly and impeded the northward transport of the KI again.

The ZFCC and KI, closely associated with the abrupt change of the thermal front, delivered the eutrophication, phosphate and heat to the Zhejiang-Fujian coastal area, respectively, which will impact the algal bloom or other ecosystem influence (Lian et al., 2016; Zhang et al., 2018; Liu et al., 2021). However, the biogeochemical responses associated with the coastal front plunge remain to be investigated by the field or remote sensing observation to fully understand the regional dynamics in the future. In addition, this finding also provides a shred of specific evidence for the source of Taiwan Warm water in winter.

Data availability statement

The original contributions presented in the study are included in the article/supplementary material. Further inquiries can be directed to the corresponding authors.

Author contributions

JL and WW analyzed and visualized the data and wrote the manuscript. PL conceived the study and provided the methods and resources. FZ and YG reviewed and edited the manuscript.

PB assisted with the formal analysis, and reviewed and edited the manuscript. All authors contributed to the article and approved the submitted version.

Funding

This study was jointly financed by the National Natural Science Foundation of China (Grant Number 42106017), the Scientific and technological projects of Zhoushan (Grant Number 2022C81010), the Guangdong Basic and Applied Basic Research Foundation (Grant Number 2020A1515110516), the Special Fund for Technology Development of Zhanjiang City (Grant Number 2020A01008), and the Scientific Research Foundation for Advanced Talents of Zhejiang Ocean University (Grant Number 11105093522), the Key Research and Development Plan of Zhejiang Province Funding (Grant Number 2020C03012), the Major Science and Technology Project of Sanya (Grant Number SKJC-KJ-2019KY03), the High-level Personnel of Special Support Program of Zhejiang Province (Grant Number 2019R52045), the Science Foundation of Donghai Laboratory (Grant Number DH-2022KF0208) and the Hainan Provincial Joint Project of Sanya Yazhou Bay Science and Technology City (Grant Number 120LH001).

Conflict of interest

The authors declare that the research was conducted in the absence of any commercial or financial relationships that could be construed as a potential conflict of interest.

Publisher's note

References

Alemany, D., Acha, E. M., and Iribarne, O. O. (2014). Marine fronts are important fishing areas for demersal species at the Argentine Sea (Southwest Atlantic ocean). *J. Sea Res.* 87, 56–67. doi: 10.1016/j.seares.2013.12.006

Androulidakis, Y., Kourafalou, V., Ozgokmen, T., Garcia-Pineda, O., Lund, B., Le Henaff, M., et al. (2018). Influence of river-induced fronts on hydrocarbon transport: A multiplatform observational study. *J. Geophys. Res.-Oceans* 123 (5), 3259–3285. doi: 10.1029/2017JC013514

Bai, P., Gu, Y., Li, P., and Wu, K. (2016). Tidal energy budget in the zhujiang (Pearl river) estuary. *Acta Oceanol. Sin.* 35 (5), 54–65. doi: 10.1007/s13131-016-0850-9

Belkin, I. M., and O'Reilly, J. E. (2009). An algorithm for oceanic front detection in chlorophyll and SST satellite imagery. *J. Mar. Syst.* 78 (3), 319–326. doi: 10.1016/j.jmarsys.2008.11.018

Bian, C., Jiang, W., Quan, Q., Wang, T., Greatbatch, R. J., and Li, W. (2013). Distributions of suspended sediment concentration in the yellow Sea and the East China Sea based on field surveys during the four seasons of 2011. *J. Mar. Syst.* 121, 24–35. doi: 10.1016/j.jmarsys.2013.03.013

Cao, L., Tang, R., Huang, W., and Wang, Y. (2021). Seasonal variability and dynamics of coastal sea surface temperature fronts in the East China Sea. *Ocean Dyna.* 71 (2), 237–249. doi: 10.1007/s10236-020-01427-8

Chen, C.-T. A. (2009). Chemical and physical fronts in the bohai, yellow and East China seas. *J. Mar. Syst.* 78 (3), 394–410. doi: 10.1016/j.jmarsys.2008.11.016

Cheng, X., Sun, Q., Wang, Y., and Yang, Y. (2017). Analysis on seasonal variations and structures of the tidal front outside of the subei shoal. *Mar. Sci.* 41 (12), 1. doi: 10.11759/hykx20151108001

Cromwell, T., and Reid, J. L. (1956). A study of oceanic fronts. *Tellus* 8 (1), 94–101. doi: 10.3402/tellusa.v8i1.8947

Cui, X., Yang, D., Sun, C., Feng, X., Gao, G., Xu, L., et al. (2021). New insight into the onshore intrusion of the kuroshio into the East China Sea. *J. Geophys. Res.: Oceans* 126 (2), e2020JC016248. doi: 10.1029/2020JC016248

He, S., Huang, D., and Zeng, D. (2016). Double SST fronts observed from MODIS data in the East China Sea off the zhejiang–fujian coast, China. *J. Mar. Syst.* 154, 93–102. doi: 10.1016/j.jmarsys.2015.02.009

Hickox, R., Belkin, I., Cornillon, P., and Shan, Z. (2000). Climatology and seasonal variability of ocean fronts in the East China, yellow and bohai seas from satellite SST data. *Geophys. Res. Lett.* 27 (18), 2945–2948. doi: 10.1029/1999GL011223

Hsieh, C.-h., Chiu, T.-S., and Shih, C.-T. (2004). Copepod diversity and composition as indicators of intrusion of the kuroshio branch current into the northern Taiwan strait in spring 2000. *Zool. Stud.* 43 (2), 393–403. doi: 10.3390/biology11091357

Hsu, P.-C., Centurioni, L., Shao, H.-J., Zheng, Q., Lu, C.-Y., Hsu, T.-W., et al. (2021). Surface current variations and oceanic fronts in the southern East China Sea: Drifter experiments, coastal radar applications, and satellite observations. *J. Geophys. Res.: Oceans* 126 (10), e2021JC017373. doi: 10.1029/2021JC017373

Huang, D., Zhang, T., and Zhou, F. (2010). Sea-Surface temperature fronts in the yellow and East China seas from TRMM microwave imager data. *Deep Sea Res. Part II: Top. Stud. Oceanogr.* 57 (11-12), 1017–1024. doi: 10.1016/j.dsr2.2010.02.003

Hu, Z. F., Wang, D. P., Pan, D. L., He, X. Q., Miyazawa, Y., Bai, Y., et al. (2016). Mapping surface tidal currents and changjiang plume in the East China Sea from geostationary ocean color imager. *J. Geophys. Res.-Oceans* 121 (3), 1563–1572. doi: 10.1002/2015JC011469

Isobe, A. (2008). Recent advances in ocean-circulation research on the yellow Sea and East China Sea shelves. *J. oceanogr.* 64 (4), 569–584. doi: 10.1007/s10872-008-0048-7

Kang, J., and Na, H. (2022). Long-term variability of the kuroshio shelf intrusion and its relationship to upper-ocean current and temperature variability in the East China Sea. *Front. Mar. Sci.* 9. doi: 10.3389/fmars.2022.812911

Komatsu, T., Tatsukawa, K., Filippi, J. B., Sagawa, T., Matsunaga, D., Mikami, A., et al. (2007). Distribution of drifting seaweeds in eastern East China Sea. *J. Mar. Syst.* 67 (3-4), 245–252. doi: 10.1007/978-1-4020-9619-8_44

Lai, W., Pan, J., and Devlin, A. T. (2018). Impact of tides and winds on estuarine circulation in the pearl river estuary. *Continent. Shelf Res.* 168, 68–82. doi: 10.1016/j.csr.2018.09.004

Lian, E., Yang, S., Wu, H., Yang, C., Li, C., and Liu, J. T. (2016). Kuroshio subsurface water feeds the wintertime Taiwan warm current on the inner East China Sea shelf. *J. Geophys. Res.: Oceans* 121 (7), 4790–4803. doi: 10.1002/2016JC011869

Liu, X., Dong, C., Chen, D., and Su, J. (2014). The pattern and variability of winter kuroshio intrusion northeast of Taiwan. *J. Geophys. Res.: Oceans* 119 (8), 5380–5394. doi: 10.1002/2014JC009879

Liu, Z., Gan, J., Hu, J., Wu, H., Cai, Z., and Deng, Y. (2021). Progress of studies on circulation dynamics in the East China Sea: The kuroshio exchanges with the shelf currents. *Front. Mar. Sci.* 8. doi: 10.3389/fmars.2021.620910

Liu, S. D., Qiao, L. L., Li, G. X., Shi, J. H., Huang, L. L., Yao, Z. G., et al. (2018). Variation in the current shear front and its potential effect on sediment transport over the inner shelf of the East China Sea in winter. *J. Geophys. Res.-Oceans* 123 (11), 8264–8283. doi: 10.1029/2018JC014241

Lohmann, R., and Belkin, I. M. (2014). Organic pollutants and ocean fronts across the Atlantic ocean: A review. *Prog. Oceanogr.* 128, 172–184. doi: 10.1016/j.pocean.2014.08.013

Mao, H. (1964). A preliminary investigation on the application of using TS diagram for a quantitative analysis of the water masses in the shallow water area. *Oceanol. Limnol. Sin.* 6, 1–22.

McWilliams, J. C. (2021). Oceanic frontogenesis. *Annu. Rev. Mar. Sci.* 13, 227–253. doi: 10.1146/annurev-marine-032320-120725

Park, G. S., Lee, T., Min, S.-H., Jung, S.-K., and Son, Y. B. (2020). Abnormal Sea surface warming and cooling in the East China Sea during summer. *J. Coast. Res.* 95 (SI), 1505–1509. doi: 10.2112/SI95-290.1

Pawlowicz, R., Beardsley, B., and Lentz, S. (2002). Classical tidal harmonic analysis including error estimates in MATLAB using T_TIDE. *Comput. Geosci.* 28 (8), 929–937. doi: 10.1016/S0098-3004(02)00013-4

Qiao, L., Liu, S., Xue, W., Liu, P., Hu, R., Sun, H., et al. (2020). Spatiotemporal variations in suspended sediments over the inner shelf of the East China Sea with the effect of oceanic fronts. *Estuar. Coast. Shelf Sci.* 234, 106600. doi: 10.1016/j.ecss.2020.106600

Qiao, F., Yang, Y., Lü, X., Xia, C., Chen, X., Wang, B., et al. (2006). Coastal upwelling in the East China Sea in winter. *J. Geophys. Res.: Oceans* 111 (C11S06). doi: 10.1029/2005JC003264

Saldias, G. S., Hernandez, W., Lara, C., Munoz, R., Rojas, C., Vasquez, S., et al. (2021). Seasonal variability of SST fronts in the inner Sea of chiloe and its adjacent coastal ocean, northern Patagonia. *Remote Sens.* 13 (2), 181. doi: 10.3390/rs13020181

Saldias, G. S., and Lara, C. (2020). Satellite-derived sea surface temperature fronts in a river-influenced coastal upwelling area off central-southern Chile. *Reg. Stud. Mar. Sci.* 37, 101322. doi: 10.1016/j.rsma.2020.101322

Teng, F., Fang, G. H., and Xu, X. Q. (2017). Effects of internal tidal dissipation and self-attraction and loading on semidiurnal tides in the bohai Sea, yellow Sea and East China Sea: a numerical study. *Chin. J. Oceanol. Limnol.* 35 (5), 987–1001. doi: 10.1007/s00343-017-6087-4

Tozer, B., Sandwell, D. T., Smith, W. H. F., Olson, C., Beale, J. R., and Wessel, P. (2019). Global bathymetry and topography at 15 arc sec: SRTM15+. *Earth Space Sci.* 6 (10), 1847–1864. doi: 10.1029/2019EA000658

Tseng, C., Lin, C., Chen, S., and Shyu, C. (2000). Temporal and spatial variations of sea surface temperature in the East China Sea. *Continent. Shelf Res.* 20 (4-5), 373–387. doi: 10.1016/S0278-4343(99)00077-1

Vazquez-Cuervo, J., Dewitte, B., Chin, T. M., Armstrong, E. M., Purca, S., and Alburqueque, E. (2013). An analysis of SST gradients off the Peruvian coast: The impact of going to higher resolution. *Remote Sens. Environ.* 131, 76–84. doi: 10.1016/j.rse.2012.12.010

Vijith, V., Vinayachandran, P. N., Webber, B. G. M., Matthews, A. J., George, J. V., Kannaujia, V. K., et al. (2020). Closing the sea surface mixed layer temperature budget from *in situ* observations alone: Operation advection during BoBBLE. *Sci. Rep.* 10 (1), 7062. doi: 10.1038/s41598-020-63320-0

Wang, G., Kang, J., Yan, G., Han, G., and Han, Q. (2015). Spatio-temporal variability of sea level in the East China Sea. *J. Coast. Res.* 73 (10073), 40–47. doi: 10.2112/SI73-008.1

Wang, J., and Oey, L. Y. (2014). Inter-annual and decadal fluctuations of the kuroshio in East China Sea and connection with surface fluxes of momentum and heat. *Geophys. Res. Lett.* 41 (23), 8538–8546. doi: 10.1002/2014GL062118

Wang, Y., Sheng, J. Y., and Lu, Y. Y. (2020). Examining tidal impacts on seasonal circulation and hydrography variability over the eastern Canadian shelf using a coupled circulation-ice regional model. *Prog. Oceanogr.* 189. doi: 10.1016/j.pocean.2020.102448

Wu, H. (2021). Beta-plane arrested topographic wave as a linkage of open ocean forcing and mean shelf circulation. *J. Phys. Oceanogr.* 51 (3), 879–893. doi: 10.1175/jpo-d-20-0195.1

Wu, H., Deng, B., Yuan, R., Hu, J., Gu, J. H., Shen, F., et al. (2013). Detiding measurement on transport of the changjiang-derived buoyant coastal current. *J. Phys. Oceanogr.* 43 (11), 2388–2399. doi: 10.1175/JPO-D-12-0158.1

Wu, R., Wu, H., and Wang, Y. (2021). Modulation of shelf circulations under multiple river discharges in the East China Sea. *J. Geophys. Res.: Oceans* 126 (4), e2020JC016990. doi: 10.1029/2020JC016990

Xu, L., Yang, D., Benthuysen, J. A., and Yin, B. (2018). Key dynamical factors driving the kuroshio subsurface water to reach the zhejiang coastal area. *J. Geophys. Res.: Oceans* 123 (12), 9061–9081. doi: 10.1029/2018JC014219

Yang, D., Huang, R. X., Feng, X., Qi, J., Gao, G., and Yin, B. (2020). Wind stress over the pacific ocean east of Japan drives the shelf circulation east of China. Continent. *Shelf Res.* 201, 104122. doi: 10.1016/j.csr.2020.104122

Yang, D., Yin, B., Chai, F., Feng, X., Xue, H., Gao, G., et al. (2018). The onshore intrusion of kuroshio subsurface water from February to July and a mechanism for the intrusion variation. *Prog. Oceanogr.* 167, 97–115. doi: 10.1016/j.pocean.2018.08.004

Yang, D., Yin, B., Liu, Z., Bai, T., Qi, J., and Chen, H. (2012). Numerical study on the pattern and origins of kuroshio branches in the bottom water of southern East China Sea in summer. *J. Geophys. Res.: Oceans* 117, C02014. doi: 10.1029/2011JC007528

Zhai, F., Li, P., Gu, Y., Li, X., Chen, D., Li, L., et al. (2020). Review of the research and application of the submarine cable online observation system. *Mar. Sci.* 44 (8), 14–28. doi: 10.11759/hykx20200331003

Zhang, Y., Chai, F., Zhang, J., Ding, Y., Bao, M., Yan, Y. W., et al. (2022). Numerical investigation of the control factors driving zhe-Min coastal current. *Acta Oceanol. Sin.* 41 (2), 127–138. doi: 10.1007/s13131-021-1849-4

Zhang, C., Shang, S., Chen, D., and Shang, S. (2005). Short-term variability of the distribution of zhe-Min coastal water and wind forcing during winter monsoon in the Taiwan strait. *J. OF Remote SENSING-BEIJING-* 9 (4), 452. doi: 10.11849/zrzyxb.1991.01.010

Zhang, Y. L. J., Stanev, E. V., and Grashorn, S. (2016a). Unstructured-grid model for the north Sea and Baltic Sea: Validation against observations. *Ocean Model.* 97, 91–108. doi: 10.1016/j.ocemod.2015.11.009

Zhang, Z., Wu, H., Yin, X., and Qiao, F. (2018). Dynamical response of changjiang river plume to a severe typhoon with the surface wave-induced mixing. *J. Geophys. Res.: Oceans* 123 (12), 9369–9388. doi: 10.1029/2018JC014266

Zhang, Y. L. J., Ye, F., Stanev, E. V., and Grashorn, S. (2016b). Seamless cross-scale modeling with SCHISM. *Ocean Model.* 102, 64–81. doi: 10.1016/j.ocemod.2016.05.002

Zhou, F., Xue, H., Huang, D., Xuan, J., Ni, X., Xiu, P., et al. (2015). Cross-shelf exchange in the shelf of the e ast c hina s ea. *J. Geophys. Res.: Oceans* 120 (3), 1545–1572. doi: 10.1002/2014JC010567

frontiers | Frontiers in Marine Science

TYPE Original Research
PUBLISHED 22 December 2022
DOI 10.3389/fmars.2022.1100510

OPEN ACCESS

EDITED BY
Hui Zhao,
Guangdong Ocean University, China

REVIEWED BY
Yi Yu,
Ministry of Natural Resources, China
Peng Bai,
Zhejiang Ocean University, China
Kenny TC. Lim Kam Sian,
Wuxi University, China

*CORRESPONDENCE
Kai Yu
yukai041@hhu.edu.cn

SPECIALTY SECTION
This article was submitted to Coastal Ocean Processes, a section of the journal Frontiers in Marine Science

RECEIVED 16 November 2022
ACCEPTED 05 December 2022
PUBLISHED 22 December 2022

CITATION
Chen Y-Y and Yu K (2022) The responses of SST annual cycle in the eastern equatorial Pacific to global warming.
Front. Mar. Sci. 9:1100510.
doi: 10.3389/fmars.2022.1100510

The responses of SST annual cycle in the eastern equatorial Pacific to global warming

Ying-Ying Chen[1] and Kai Yu[2,3,4]*

[1]School of Marine Sciences, Nanjing University of Information Science and Technology, Nanjing, China, [2]Key Laboratory of Marine Hazards Forecasting, Ministry of Natural Resources, Hohai University, Nanjing, China, [3]State Key Laboratory of Satellite Ocean Environment Dynamics (SOED), Second Institute of Oceanography, Ministry of Natural Resources, Hangzhou, China, [4]College of Oceanography, Hohai University, Nanjing, China

The eastern equatorial Pacific exhibits a pronounced westward propagating sea surface temperature annual cycle (SSTAC). The responses of the equatorial Pacific SSTAC to CO2-induced global warming are examined using 15 Coupled Model Intercomparison Project Phase 5 (CMIP5) experiments. The annual cycle patterns of global-warming simulations over 2006-2100 are compared with that of present-day simulations over 1850-2005. We see no statistically significant changes in SSTAC amplitude in the future. A coupled dynamical diagnostic framework is adopted to assess four factors, including the damping rate, phase speed and strength of the annual and semi-annual harmonic forcing of SSTAC. Under global warming, changes relative to the present-day simulations in these four diagnostic factors have a clear multi-model trend. Most coupled models exhibit relatively weaker (an average of 18%) propagation speed, and stronger annual (18%) and semi-annual (39%) external forcing. Half of the models show a relatively stronger (about one time) damping rate, while the rest show a weaker (30%) damping rate. When these four diagnostic factors are further condensed into a dynamical response factor and a forcing factor, it is revealed that the same annual cycle amplitudes with respect to the present-day simulations may result from the compensations in terms of bias in the dynamical response factor and forcing factor under increased CO2-induced warm climate.

KEYWORDS

global warming, SST annual cycle, westward propagation, external forcing, CMIP

1 Introduction

Sea surface temperature (SST) in the eastern tropical Pacific cold tongue region exhibits a pronounced annual cycle, with a warm phase during boreal spring and a cold phase during fall, although the sun moves across the equator twice yearly (Wyrtki and Meyers, 1976; Horel, 1982; Mitchell and Wallace, 1992; Wang, 1994; Xie, 1994). The

main cause for the generation of this SST annual cycle (SSTAC) is the hemispheric asymmetries of the tropical Pacific climatological mean conditions (Mitchell and Wallace, 1992; Xie, 1994). These asymmetries are caused by the distribution of continents and maintained by coupled ocean-atmosphere interaction (Philander et al., 1996; Xie, 2004). In the eastern Pacific, the northern position of the intertropical convergence zone (ITCZ) (e.g., Hanson et al., 1967; Manabe et al., 1974; Philander and Seigel, 1985; Xie and Philander, 1994) maintains the southeast trade winds across the equator year-round with annually varying intensity. This annually-varying cross-equatorial wind brings the off-equatorial annual insolation onto the equator and remotely forces a westward propagating SSTAC at the equator by controlling the strength of cold-water upwelling, wind-driven evaporation and the amount of the stratus clouds *via* ocean-atmosphere interactions (Chen and Jin, 2018; Wengel et al., 2018). SSTAC in the eastern equatorial Pacific arises from the hemispheric asymmetries of the climate mean states and is amplified by coupled tropical ocean-atmosphere interactions. The tropical SSTAC interacts with ENSO (e.g., Tziperman et al., 1994; Jin et al., 1994; Chang and Philander, 1994; Jin, 1996; Stuecker et al., 2013; Stuecker et al., 2015), as well as with anthropogenic greenhouse warming. The increasing concentrations of the greenhouse gases, such as CO_2, are the main cause of the acceleration of global warming. The increasing ocean temperatures will have substantial effects on marine ecosystems (Doney et al., 2012; Hollowed et al., 2013; Brander, 2013). Ocean temperature modulates physiological processes in all marine organisms (Rivkin and Legendre, 2001; Drinkwater et al., 2010; Ottersen et al., 2010; Deutsch et al., 2015). SST, as an important driver of marine ecosystem, is dominated by the seasonal variability in the tropical coastal regions. The cross-equatorial wind forces coastal upwelling and brings subsurface cold water and nutrients to the surface, resulting in a high production in the eastern boundary of the Pacific Ocean.

Future climate projection is mostly based on climate model simulations. Under greenhouse warming, many climate models have projected a significant change in the SSTAC from low to high latitudes (Timmermann et al., 2004; Biasutti and Sobel, 2009; Xie et al., 2010; Sobel and Camargo, 2011; Stine and Huybers, 2012; Dwyer et al., 2012; Carton et al., 2015; Liu et al., 2017; Alexander et al., 2018; Liu et al., 2020). In particular, models display a great diversity of equatorial Pacific SST changes, including the east-west gradient of the annual mean SST (Liu et al., 2005; Collins and Modeling Groups, 2005; DiNezio et al., 2009) and SSTAC (Timmermann et al., 2004; Xie et al., 2010; Sobel and Camargo, 2011) in response to global warming. Timmermann et al. (2004) simulated a strong intensification of the SSTAC in the eastern equatorial Pacific in response to greenhouse warming in a coupled general circulation model. They illustrated that the tropical Pacific mean climate changes due to greenhouse warming provide seeding for the anomalous SSTAC and the tropical ocean-atmosphere interactions lead to amplification. Xie et al. (2010) showed a pronounced annual cycle in the equatorial Pacific under greenhouse warming in a climate model. They pointed out that the upwelling damping mechanism (Clement et al., 1996; Cane et al., 1997) dominates the equatorial Pacific annual cycle in SST warming. Sobel and Camargo (2011) studied 24 Coupled Model Intercomparison Project Phase 3 (CMIP3) models and analyzed changes in the tropical SST under greenhouse warming. They found that the SST annual mean warming, with a local maximum in the equatorial Pacific, is greater in the Northern Hemisphere than in the Southern Hemisphere and the SST seasonal change is a warming in the summer hemisphere and cooling in the winter hemisphere, inducing an enhanced seasonal cycle in the mid-latitudes. They attributed these SST change patterns to thermodynamic consequences of surface trade winds, which increase in the winter hemisphere and decrease in the summer hemisphere. However, they did not address the seasonal cycle on the equator in detail.

In summary, tropical patterns of SSTAC under global warming and relevant physical processes are still not systematically studied as has been the global annual mean warming. SSTAC can be caused by several factors, such as mean circulation advection, zonal advection, Ekman pumping feedback, thermocline feedback and thermodynamic feedback (Jin et al., 2006; Chen and Jin, 2018). The various relative importance of these feedbacks among models induces diverse properties of SSTAC and its uncertainties. To discern and separate the possible factors, Chen and Jin (2017; 2018) proposed a coupled dynamic diagnostics framework to analyze the equatorial Pacific SSTAC in terms of damping rate, propagation speed, external annual and semi-annual forcing and apply it to explore the diversities of the SSTACs in CMIP5 simulations. To illustrate the changes of the equatorial Pacific SSTAC in response to global warming, we describe its major patterns in global warming simulations of the CMIP5 models and use this framework to systematically analyze the dynamics and inter-model diversities of these SSTACs in this study.

The remainder of this paper is structured as follows. Section 2 describes the coupled models and observational datasets and introduces the coupled dynamic diagnostics framework of SSTAC. Section 3 presents the features of equatorial Pacific SSTAC change response to global warming based on CMIP5 simulations. Section 4 describes the dynamical diagnostic results of SSTAC change. In section 5, we examine the dynamic and forcing controls of SSTAC change and discuss the possible reasons for the diversities of SSTAC change. In section 6, we give a summary and discussion.

2 Data and method

2.1 Coupled models and observational datasets

In this study, we analyze 15 model simulations from the CMIP5 coupled general circulation models (CGCMs) (Table 1). Representative concentration pathway 4.5 (RCP4.5) is a high greenhouse gas emission scenario that reaches a radiative forcing level of 4.5 W/m^2 by the year 2100 (Taylor et al., 2011). RCP4.5 simulations over 2006-2100 represent the global-warming climate. Historical simulations, which cover the period 1850-2005, represent the present-day climate. We select these 15 models from which all variables required for dynamical diagnoses of the annual cycle of the surface layer (constant 25 m in this study), including monthly mean SST, ocean current, surface meridional wind, shortwave/longwave radiation, latent heat flux, and sensible heat flux, are available in the eastern equatorial Pacific. All model outputs are interpolated from the native model grid onto the same uniform 1°×1° horizontal grid prior to any diagnostic computation. The 'observed' SST, current velocity, surface wind and surface heat flux components are taken from the monthly ERA40 atmospheric reanalysis (Uppala et al., 2005) on a 2.5°×2.5° horizontal grid and the monthly ORA-S3 (Balmaseda et al., 2008) of ocean analysis system produced at ECMWF on a 1°×1° horizontal grid, from 1959 to 2001.

2.2 Dynamic diagnostics of SSTAC

Following Chen and Jin (2017; 2018), we establish an approximate coupled dynamic diagnostics framework for understanding the nature of the annual cycle in the equatorial Pacific cold tongue region. This framework utilizes a heat budget equation for SSTAC, which can be written as follows.

$$\begin{aligned}\frac{\partial T}{\partial t} &= -\left(\bar{u}\cdot\frac{\partial T}{\partial x}+u\cdot\frac{\partial \bar{T}}{\partial x}\right)-\left(\bar{v}\cdot\frac{\partial T}{\partial y}+v\cdot\frac{\partial \bar{T}}{\partial y}\right)\\ &\quad-\left(M(\bar{w}_e)\frac{\partial T}{\partial z}+\left[M(\bar{w}_e+w_e)-M(\bar{w}_e)\right]\frac{\partial \bar{T}}{\partial z}\right)\\ &\quad+\frac{Q}{\rho_0 C_p h}+\mathrm{NL}+res\\ &= \mathrm{MC}+\mathrm{ZA}+\mathrm{EK}+\mathrm{TH}+\mathrm{TD}+\mathrm{NL}+res,\end{aligned} \tag{1}$$

where

$$\mathrm{MC} = -\bar{u}\cdot\frac{\partial T}{\partial x}-\bar{v}\cdot\frac{\partial T}{\partial y}-M(\overline{w_e})\frac{T}{h}, \tag{2}$$

$$\mathrm{ZA} = -u\cdot\frac{\partial \bar{T}}{\partial x}, \tag{3}$$

TABLE 1 List of the CMIP5 models used in this study.

No.	Model	Modeling center
1	ACCESS1.0	The Centre for Australian Weather and Climate Research (Australia)
2	BCC-CSM1-1	Beijing Climate Center, China Meteorological Administration (China)
3	BCC-CSM1-1-m	
4	BNU-ESM	College of Global Change and Earth System Science, Beijing Normal University (China)
5	CMCC-CM	Centro Euro-Mediterraneo per I Cambiamenti Climatici (Canada)
6	CMCC-CMS	
7	CNRM-CM5	Centre National de Recherches Météorologiques (France)
8	CSIRO-Mk3-6-0	Commonwealth Scientific and Industrial Research Organization in collaboration with Queensland Climate Change Centre of Excellence (Australia)
9	GFDL-ESM2G	NOAA Geophysical Fluid Dynamics Laboratory (USA)
10	GISS-E2-R	NASA Goddard Institute for Space Studies (USA)
11	GISS-E2-R-CC	
12	MIROC-ESM	Japan Agency for Marine-Earth Science and Technology, Atmosphere and Ocean Research Institute (The University of Tokyo), and National Institute for Environmental Studies (Japan)
13	MIROC-ESM-CHEM	
14	MPI-ESM-MR	Max Planck Institute for Meteorology (Germany)
15	NorESM1-ME	Norwegian Climate Centre (Norway)

$$\mathrm{EK} = -v \cdot \frac{\partial \bar{T}}{\partial y} - [M(\bar{w}_e + w_e) - M(\bar{w}_e)] \frac{\partial \bar{T}}{\partial z}, \quad (4)$$

$$\mathrm{TH} = M(\overline{w_e}) \frac{T_{sub}}{h}, \quad (5)$$

$$\mathrm{TD} = \frac{Q}{\rho_0 C_p h}, \quad (6)$$

$$\mathrm{NL} = -u \cdot \frac{\partial T}{\partial x} - v \cdot \frac{\partial T}{\partial y} - [M(\bar{w}_e + w_e) - M(\bar{w}_e)] \frac{\partial T}{\partial z} \quad . \quad (7)$$

Here, all variables with an overbar denote the annual mean climate state. The variables T, u, v and Q denote the annual cycles of SST, horizontal surface currents and net surface heat flux, respectively. P_o is the density of seawater, C_p is the heat capacity, h is specified as the depth of the surface layer, NL is the nonlinear term, and *Res* is the residual. The vertical entrainment is defined as $w_e\partial T/\partial z = w_e(T - T_{sub})/h$, where T_{sub} and $w_e = h \cdot \Delta \boldsymbol{v}$ are the subsurface temperature and vertical entrainment velocity at the base of the mixed layer. $M(x)$ is a Heaviside function where $M(x)=0$, if $x<0$, and $M(x)=x$, otherwise. We regroup the SST heat budget into seven terms as in the ENSO heat budget analysis (An et al., 1999; Jin et al., 2006; Chen and Jin, 2018). The right hand of Eq. (1) represents, from left to right, the mean circulation term (MC), the zonal advection term (ZA), the Ekman pumping term (EK), the thermocline effect term (TH), the thermodynamic term (TD), the nonlinear term (NL), and the residual term (res), respectively.

We adopt four main assumptions to develop a simple coupled framework for the equatorial SSTAC as described in Chen and Jin (2017; 2018): (1) the decomposition of the equatorial annually varying wind into a coupled part as the direct response to the annual equatorial SST and an external part serving as external forcing; (2) the quasi-equilibrium approximation of oceanic dynamic response to the equatorial annual wind forcing or so-called fast-wave limit as termed in Jin and Neelin (1993); (3) the decomposition of the thermodynamic heating into a coupled part related directly to the equatorial annual SST and an external part serving as forcing; and (4) the assumption that the linear compounding coupled operator of the SST derived under assumptions (1-3) can be further approximated by a linear damping and a zonal propagation term. It should be noted that because we have adopted the fast-wave limit approximation to assume that annual variations in ocean current, upwelling and thermocline are in quasi-equilibrium with the annual wind stress, the coupled framework does not involve the ocean memory residing in adjustment through the ocean wave dynamics. Thus, the coupled framework could be considered equivalent to the SST-mode framework described in Neelin (1991) and Jin and Neelin (1993), except here, we also consider the external annual forcing.

With these assumptions, we may approximately define the equatorial SST in the following equation:

$$\frac{\partial T}{\partial t} = \lambda T + c \cdot \frac{\partial T}{\partial x} + f_1 \cos(\omega t - \varphi) - f_2 \cos(2\omega t) + R \, . \quad (8)$$

Here, $\omega = 2\pi/1yr$, φ is the relative phase of the annual forcing to the semi-annual forcing, R is the remainder. In this simple form, SSTAC is expressed by four factors (λ, c, f_1, f_2), which are the damping rate, westward phase speed, annual and semi-annual forcing amplitudes, respectively. More details can be found in Chen and Jin (2017; 2018). These four factors (λ, c, f_1, f_2) are estimated using least-squares regressions. By turning the heat budget equation (1) into an approximate coupled and forced linear model in the form of Eq. (8), we can describe SSTAC in terms of the four factors mentioned above. Sections 3-5 demonstrate how this simplification may offer insights into the response of the equatorial Pacific SSTAC to global warming in simulations.

3 Change of SST annual cycle

To illustrate the change in simulated SSTAC of the equatorial Pacific under global warming, we plot and contrast the equatorial (5°S-5°N) SST annual evolutions in the eastern Pacific (150-90°W). Figures 1A, B show the observation and the multi-model ensemble mean (MME) SSTAC of the present-day simulations. The observed equatorial SST in the cold tongue region shows a strong westward propagation. This annual cycle reaches its warm peak at 1.5°C during March and April, while cold peak at -1.0°C during August and October. Its amplitude, defined as half the peak-to-peak range, is largest at about 1.25°C and mainly confined to the cold tongue region between 110 and 80°W. Compared to the observation, the MME of the present-day simulated SSTAC shows a weaker amplitude of 1°C and is displaced westward. The warm phase arrives 1 month later than that in observation. Although the timing of the cold phase in August is represented successfully, it decays more rapidly.

In the present-day simulations, the models show a range of spatial and temporal patterns of the equatorial SSTAC, as shown in Figure 2. Most of the models roughly capture the major features of SSTAC, while a few of them (e.g., BCC-CSM1-1, BCC-CSM1-1-m) have their simulated annual cycle whose behavior to a large extent is dominated by the semi-annual component. Under enhanced CO2 conditions, The MME of the global-warming simulations is almost the same as that of the present-day simulations (Figures 1C, D).

Compared with the present-day simulations, most models show a slight change in the equatorial SSTAC patterns under global warming (Figure 3). The ACCESS1-0, CNRM-CM5 and NorESM1-ME models are exceptions, with a weakening of the annual cycle, which has colder SSTs during spring and warmer

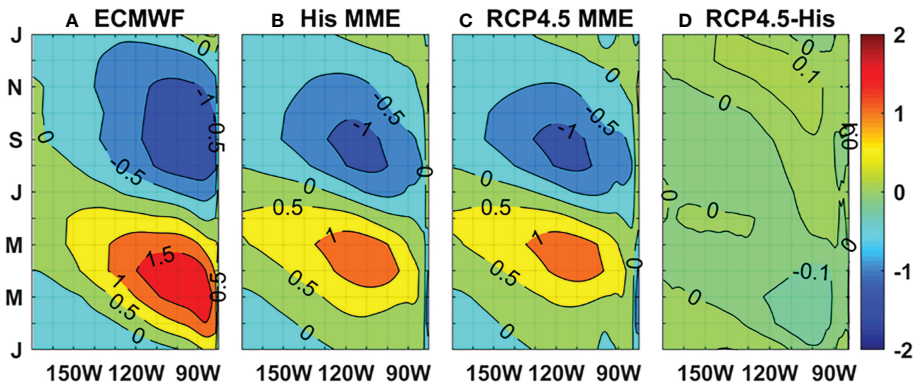

FIGURE 1
Time-longitude plots of SSTAC (°C) averaged between 5°S and 5°N in the eastern equatorial Pacific based on **(A)** ECMWF reanalysis dataset, and MME of **(B)** the historical and **(C)** RCP4.5 simulations, and **(D)** their difference (contour interval = 0.5°C).

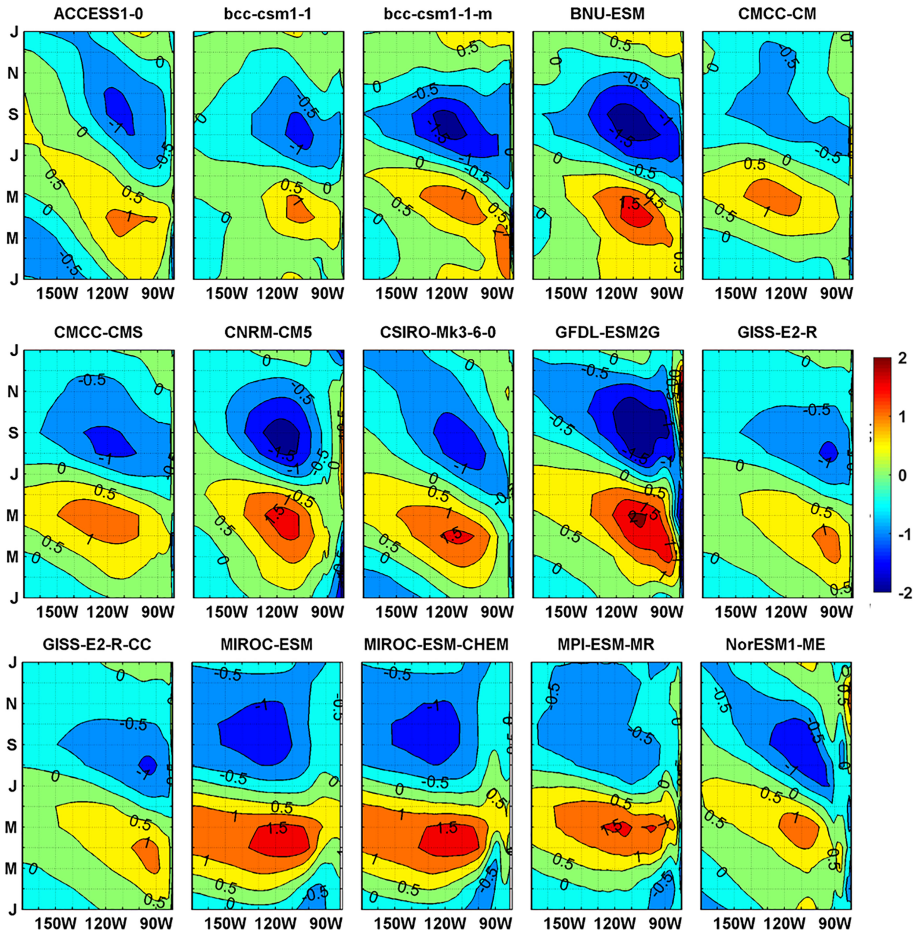

FIGURE 2
Same as Figure 1B, but for the individual 15 models in the historical period.

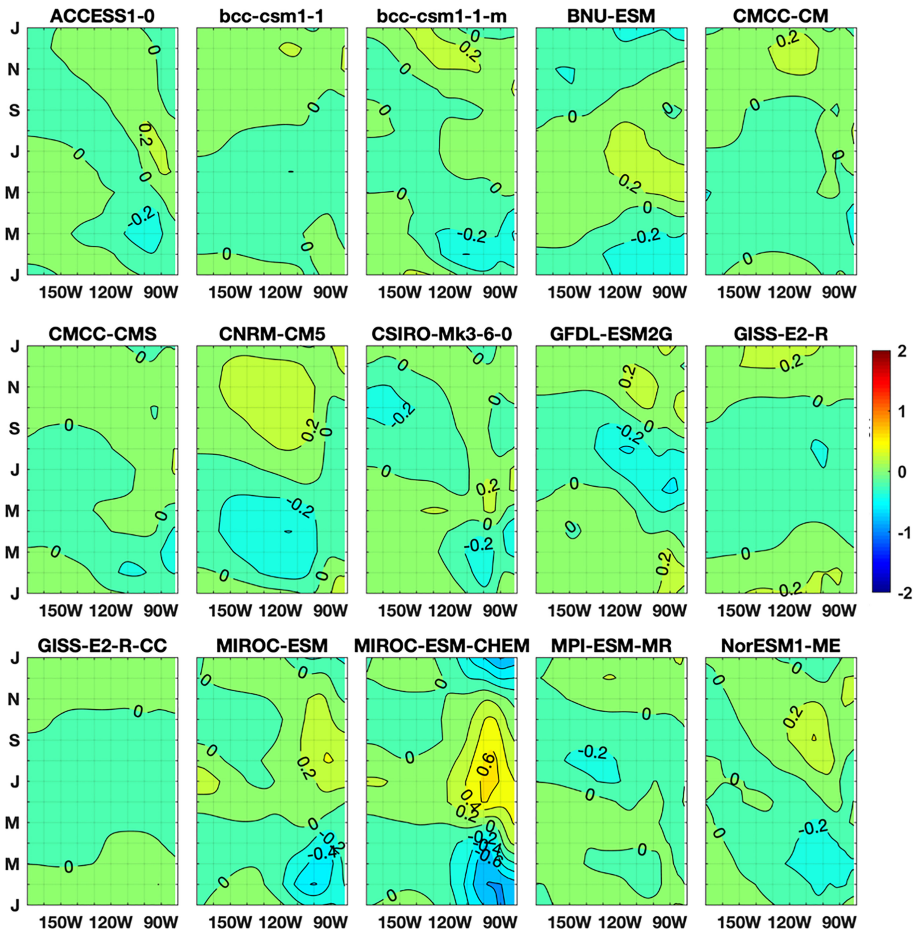

FIGURE 3
Same as Figure 1D, but for the difference between historical and RCP4.5 (where the difference is calculated as RCP4.5 minus historical).

SSTs during fall. It is worth noting that compared to the present-day scenario, although MIROC-ESM and MIROC-ESM-CHEM have enhanced amplitudes in the region between 110 and 90°W where it shows a semi-annual cycle, their amplitudes have no obvious change between 150 and 110°W where it shows a pronounced annual cycle under global warming. Both of their simulated equatorial SSTACs in the present-day and global warming climates are displaced more westward between 150 and 100°W compared with the observation.

We calculate the zonal averages of SSTAC amplitude over the main domain, which is defined by the amplitude being higher than the average of the entire domain (170-80°W). Figure 4A shows that under enhanced CO_2 conditions, the MME amplitude of SSTAC (A) in the eastern equatorial pacific region has almost the same magnitude as that in the present-day. However, nearly all (13 of 15) models underestimate the amplitudes of the annual cycle in these two climates compared to observations. In fact, it is not clear whether the SSTAC is stronger in the projections on a future climate change compared to the present-day simulations, as 4 of 15 models (ACCESS1-0, BNU-ESM, CNRM-CM5 and NorESM1-ME) show weakened SSTAC amplitudes, 4 of 15 models (GFDL-ESM2G, GISS-E2-R, GISS-E2-R-CC and MPI-ESM-MR) show increased SSTAC amplitudes and the remaining 7 of 15 models show no change. Figures 4B, C show the amplitudes of annual (A1) and semi-annual (A2) harmonic component of observed and simulated SSTAC, respectively. The annual harmonic component has a similar trend of total amplitude and is compensated by the semi-annual harmonic component (e.g., BCC-CSM1-1-m), which shows a systematic trend toward an increase under a warmer climate. Both the MME of total amplitude (A) of the present-day and global warming climates are about 15% lower than the observed, and their annual components (A1) are about 23% and 27% lower than the observed, respectively, whereas their semi-annual components (A2) are about 20% and 32% higher.

In summary, compared to the present-day scenario, most models have roughly equivalent SSTAC strengths in the eastern

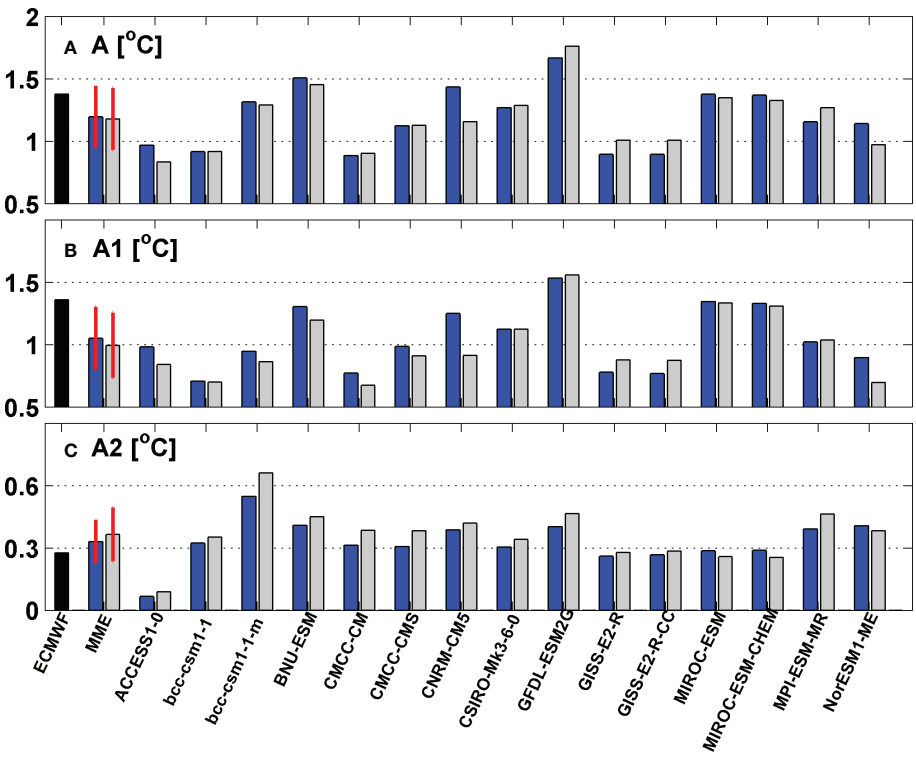

FIGURE 4
The amplitude (°C) of **(A)** SSTAC, and its **(B)** annual and **(C)** semi-annual components based on ECMWF reanalysis dataset (black bars), MME and each of 15 models in the historical period (blue bars) and RCP4.5 scenario (grey bars).Red lines represent the inter-model standard deviation.

equatorial Pacific, with a slightly reduced annual component and consistently increased semi-annual component under RCP4.5. In the next section, we further identify the contributions to the diverse magnitudes of change from model to model by employing the dynamical diagnostic framework (section 2).

4 Dynamic diagnostics of SSTAC change under a warmer climate

To investigate the causes of change in SSTAC in response to global warming, this section uses the dynamical diagnostic framework formulated in Section 2 to explore the physical mechanisms. This framework may approximately describe the equatorial annual cycle by four factors (λ, c, f_1, f_2), in terms of the damping rate, westward propagation speed, annual and semi-annual external forcing, respectively.

These four factors are estimated for the 15 couple models in the present-day and global warming climate, as shown in Figure 5. Here for the damping rate and westward propagation speed, we estimate the zonal averages over the main domain. For the annual and semi-annual external forcing, we calculate the averages over the eastmost 70% of the main domain., the zonal averages of (λ, c, f_1, f_2) of the observed SSTAC are (-0.4 month^{-1}, 0.58 m s^{-1}, 0.61°C month^{-1}, 0.13°C month^{-1}). There are wide ranges of these four factors among coupled models. The zonal average MMEs of (λ, c, f_1, f_2) are (-0.25 month^{-1}, 0.56 m s^{-1}, 0.42°C month^{-1}, 0.19°C month^{-1}) and (-0.26 month^{-1}, 0.46 m s^{-1}, 0.49°C month^{-1}, 0.26°C month^{-1}) for present-day and global-warming climate, respectively. The results indicate that compared with observations, most models of two climate periods produce lower annual external forcing and damping rate and higher semi-annual external forcing, but comparable propagation speed. The results also show that in a majority of models, the annual and semi-annual external forcing increase from the present-day to global warming simulations, while the propagation speed decrease. It should be noted that under warming climate, the increase of the semi-annual forcing, close to 39%, is larger than the annual forcing (18%). Although the MME of the damping rate does not change much, the inter-model differences in its change are substantial.

Moreover, further detailed analysis of changes of (λ, c, f_1, f_2) and the respective components of the different feedback terms in Eq. (1) in these four factors under enhanced CO_2 conditions is performed in Figure 6. The result shows how the MMEs of these four factors change under a warmer climate and their

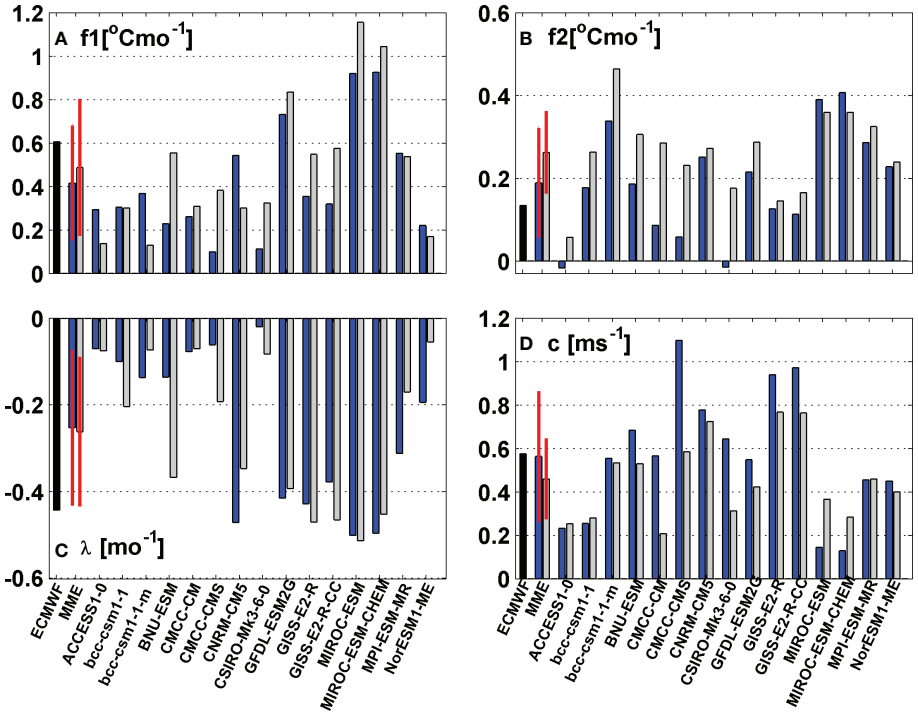

FIGURE 5
(A) Annual and **(B)** semi-annual external forcing (°C month^{-1}), **(C)** the damping rate (month^{-1}) and **(D)** the westward propagation speed (m/s) based on ECMWF reanalysis dataset (black bars), MME and each of 15 models in the historical period (blue bars) and RCP4.5 scenario (grey bars). Red lines represent the inter-model standard deviation.

contributions from the mean circulation, the zonal advection, the Ekman pumping feedback, the thermocline feedback, the thermodynamic feedback, the nonlinear effect and the residual.

Under a warmer climate, compared to the observation, the weak annual forcing is mainly due to the weakening of the contribution from the thermodynamic term, and there is some cancelation by the residual term, which might be the effect of sub-grid processes (Figure 6A). The increase of the semi-annual forcing derived from the Ekman pumping and thermodynamic terms are the two main positive contributors to the increase of the total semi-annual forcing. The decrease of the semi-annual forcing derived from the thermocline effect term is the main negative contributor, which tends to reduce the overall increase of the semi-annual forcing in response to global warming (Figure 6B). There is a stronger positive growth rate in the thermocline effect term and a weaker negative growth rate in the damping rate from the thermodynamic term. Both of them give rise to lower damping of the annual cycle. Although the damping rate derived from the mean circulation and residual terms are slightly stronger negative, they are still insufficient to encounter the two contributors above. As a result, the SSTAC has a lower damping rate than the observation in response to a warmer climate (Figure 6C). There is a notable weakening of propagation speed from the thermodynamic and Ekman pumping terms, which are partly canceled by the nonlinear and residual terms. This leads to a slightly weak westward propagation (Figure 6D). Figure 6 also clearly shows that the thermodynamic term is the key source of the increase of the annual and semi-annual external forcing and the decrease of the propagation speed from the present-day to global warming simulations.

Since the dominant contribution from the thermodynamic term (TD), we further decompose it into its four components of short-wave (SW), long-wave (LW), latent (LH) and sensible (SH) heat flux. As shown in Figure 7, TD, SW and LH all have substantial changes among different climates, suggesting that various behaviors of thermodynamics are attributable to the diversity of the response of the short wave radiation and latent heat flux to anomalous forcing (e.g., enhanced CO_2 conditions).

The main contributor to the differences between the two climate periods and between the observation and models is the short-wave radiation, as can be inferred from Figure 7. As an exception, the differences in the annual forcing may be primarily attributed to the latent heat flux. Under a warmer climate, compared to observation, the decreased annual forcing (increased semi-annual forcing) may be largely attributed to the weakened annual forcing (strengthened semi-annual forcing) from the LH as a result of decreased annual forcing (increased semi-annual forcing) from thermodynamics.

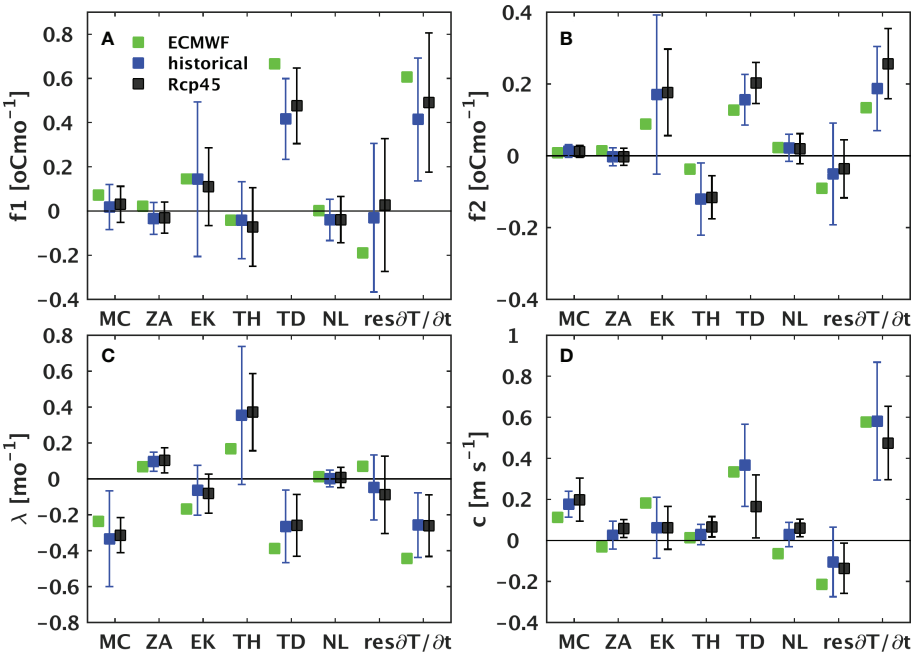

FIGURE 6
Diagrams for total and individual contribution from the different feedback terms (MC, ZA, EK, TH, TD, NL and Res) of the SST tendency (Tt) to **(A)** the annual and **(B)** semi-annual harmonic external forcing (ºC month^{-1}), **(C)** the damping rate (month^{-1}) and **(D)** the westward propagation speed (m s^{-1}) based on the ECMWF reanalysis dataset (green squares), MME in the historical period (blue squares) and RCP4.5 scenario (black squares). Whiskers represent the inter-model standard deviation.

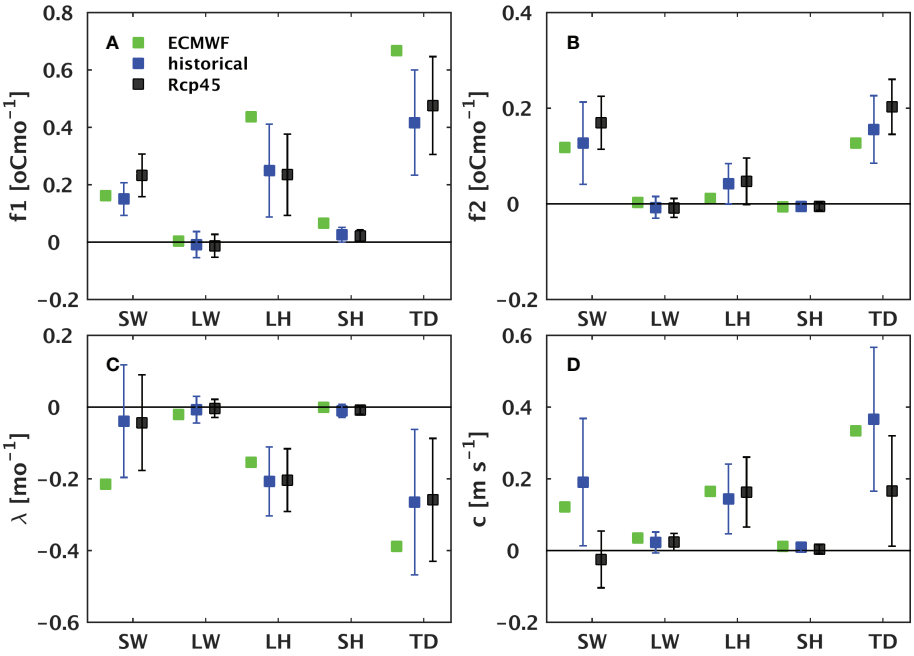

FIGURE 7
Same as Figure 6, but for contributions from the thermodynamic (TD) process and its components, the SW, LW, LH and SH. Whiskers represent the inter-model standard deviation.

5 The dynamic and forcing controls of SSTAC change

The above discussion shows that the SSTAC in the Pacific cold tongue region is mainly controlled by the internal dynamic factors, namely the damping rate λ and westward propagation speed c, and the external forcing factors that depend on the annual harmonic f_1 and semi-annual harmonic f_2 forcing. Under a warmer climate, despite the small change in the SSTAC amplitude (A), the changes in the internal dynamics and external forcing as measured by (λ, c, f_1, f_2) are remarkable and have great inter-model spreads. In this section, we propose a theory for better understanding the impact of climate change on the SSTAC. To further examine the effect of the internal dynamics and forcing on the SSTAC amplitude change under increased CO_2 conditions, we combine the two internal dynamical factors of the damping rate and propagation speed into a single dynamical response factor. Here we briefly define and describe the dynamical response factor (refer to Chen and Jin, 2017; Chen and Jin, 2018 for a detailed explanation). The dynamical response factor can be driven using the temporal and volume averaged form of the linearized SST perturbation equation (8) that is based on several approximations as follows:

$$D = \sqrt{\overline{\langle T^* \rangle^2}^t / \overline{\langle \left(\frac{\partial}{\partial t} - \lambda - c\frac{\partial}{\partial x}\right) T^* \rangle^2}^t} \quad . \qquad (9)$$

In the above, $\overline{B}^t$ denotes the temporal average quantities, $\langle B \rangle$ the volume average quantities over the zonal domain region. We solve the dynamical response factor D by using the individual longitudinally varying factors (λ, c, f_1, f_2) estimated from the CMIP5 models of two climate periods and observation shown in Figure 5. Figure 8 shows scatterplots of the SSTAC amplitudes A versus the total external forcing that includes the annual and semi-annual harmonic components multiplied by the dynamical response factor f·D. The SSTAC amplitude and the combination of the external forcing with the dynamical response factor are highly correlated at 0.81 and statistically significant at 99% confidence level. Due to this good correlation, f·D may be considered a simplified measurement of the SSTAC amplitude in the observation and coupled models. In other words, changes in SSTAC properties in coupled models under a warmer climate scenario can be attributed to the changes in the external forcing factor and dynamical response factor.

To contrast the dependence of A on f and D, the different SSTAC amplitudes that span a two-dimensional factors space are constructed to test the behaviors of A, under various f and D. For f continuously varying from 0 to 1.5°C month^{-1} and D from 0 to 8 months, we find that A vary greatly, from 0 to 10°C, as seen in Figure 9. The points in Figure 9 show a wide range of A that is mainly restricted in the range 0.5 to 2°C when f and D are taken as the domain averaged values identified in Figure 5. Our results clearly show that despite the MME of SSTAC amplitude in the future warming climate being close to that of the present-day climate, the former has higher external forcing and lower dynamical response factor in response to enhanced CO_2 conditions. Eight of the fifteen models (BCC-CSM1-1, BCC-CSM1-1-m, BNU-ESM, CMCC-CM, CMCC-CMS, CSIRO-Mk3-

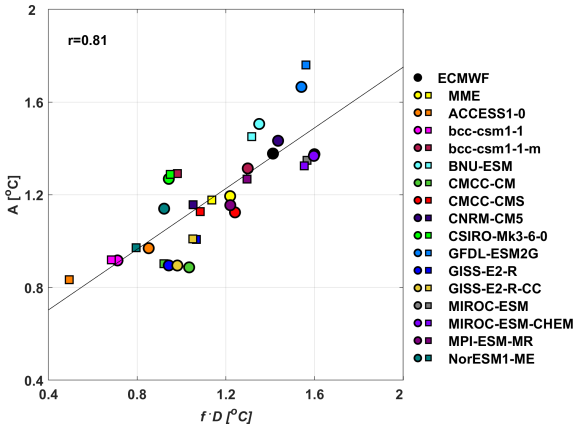

FIGURE 8
Amplitudes of SSTAC related to the total external forcing f, which includes the annual and semi-annual components, multiplied by the dynamical response factor D, based on ECMWF reanalysis dataset (black circle), MME and each of 15 models in the historical period (colored circles) and RCP4.5 scenario (colored squares).

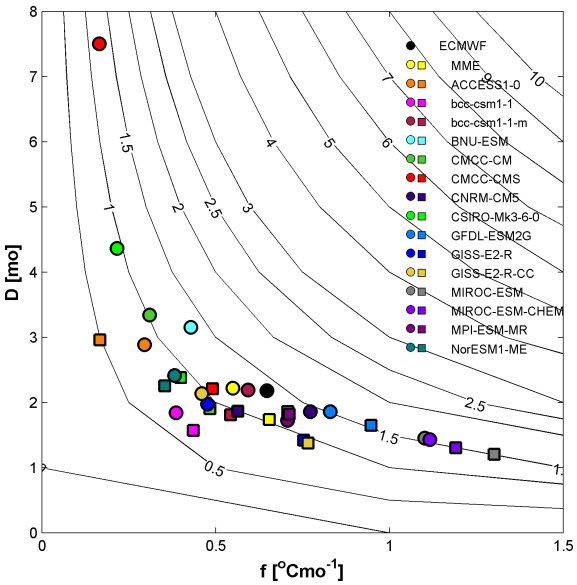

FIGURE 9
Scatterplots of SSTAC amplitudes (°C) as a function of the dynamical response factor D (month) and total external forcing f (°C month^{-1}) from ECMWF reanalysis dataset (black circle), MME and each of 15 models in the historical period (colored circles) and RCP4.5 scenario (colored squares).

6-0, MIROC-ESM and MIROC-ESM-CHEM) exhibit similar feature as the MME of SSTAC but with different relative strengths for the changes in f and D. Moreover, the relative contributions of the external forcing factor and dynamical response factor to the SSTAC amplitude change in response to global warming is different among the different models. For instance, ACCESS1-0 (CNRM-CM5) has a smaller SSTAC amplitude under RCP4.5 than that in the present-day scenario. To a large extent, it can be attributed to a much smaller external forcing with a value of 0.2°C month^{-1} (0.5°C month^{-1}) for the global warming scenario and 0.4°C month^{-1} (0.7°C month^{-1}) for the present-day scenario, since the dynamical response factor in two scenarios is almost equal. NorESM1-ME has a smaller amplitude in response to global warming. However, that is caused by the smaller dynamical response factor and the smaller external forcing.

6 Conclusions

The response of SSTAC in the eastern equatorial Pacific to global warming is investigated using 15 CMIP5 CGCMs under the historical and RCP4.5 scenarios. Historical and RCP4.5 simulations represent the present-day and global-warming climates, respectively. First, we examine pattern formations in SSTAC response to global warming. Compared with observations, the simulated SSTACs of two clime scenarios have weaker amplitudes and are displaced systematically westward. The warm phase occurs nearly one month later and the cold phase decays more rapidly. In future climate, 4 of 15 models simulate a weakening of the seasonal cycle, 4 of 15 models simulate a strengthening of the seasonal cycle and the remaining 7 of 15 models show no significantly changing compared to present-day climate. The annual harmonic component of the seasonal cycle weakens in nearly half of the models, and the semi-annual harmonic component commonly strengthens in most models.

To better evaluate the response of the SSTAC to enhanced CO_2 concentration in the future climate, we conduct a coupled dynamic diagnostics framework to diagnose its four main controlling factors, damping rate, propagation speed and external forcing factors. Compared with observations, most simulated SSTACs of two clime scenarios have lower damping rates, comparable propagation speeds, lower annual external forcing and higher semi-annual external forcing. Under global warming, most models exhibit relatively stronger annual and semi-annual external forcing and relatively weaker propagation speed compared to the present-day climate. The damping rate is relatively stronger in half of the models while weaker in the rest. These differences in four controlling factors between two climate periods and between the observation and models are largely attributed to the thermodynamic feedback, especially from the contribution of the short wave radiation.

By combining the damping rate and propagation speed into one dynamical response factor and the two forcings into one forcing factor, we demonstrate that the changes in the SSTAC amplitude under global warming can be simply measured by the forcing factor and the dynamical response factor multiplied together (f·D). Our analysis results show that under global warming, most models have SSTAC amplitudes close to that in the present-day climate, while their dynamical and external forcing factors have obvious changes. Some models' agreement in the annual cycle amplitudes between the two climate periods may stem from the adjustments and compensations of internal dynamics and external forcing from underlying processes.

Data availability statement

The datasets presented in this study can be found in online repositories. The names of the repository/repositories and accession number(s) can be found below: https://pcmdi.llnl.gov/ and http://apdrc.soest.hawaii.edu/.

Author contributions

YC conceived the study, developed the theoretical framework and wrote the manuscript. KY assisted with the analysis and reviewed the manuscript. All authors contributed to the article and approved the submitted version.

Funding

This research was supported by Fundamental Research Funds for the Central Universities (Grant B220201024), the Open Fund of State Key Laboratory of Satellite Ocean Environment Dynamics, Second Institute of Oceanography (Grant QNHX2120), the National Science Foundation of China (Grant 41806017), and the Natural Science Foundation of Jiangsu Province (Grant BK20180800).

Acknowledgments

The authors are grateful to the ESG-PCMDI for providing the CMIP5 historical and RCP4.5 simulations. The ECWMF ORA-S3 and ERA40 datasets were downloaded from Asia Pacific Data Research Center (APDRC) of International Pacific Research Center (IPRC).

Conflict of interest

The authors declare that the research was conducted in the absence of any commercial or financial relationships that could be construed as a potential conflict of interest.

Publisher's note

References

Alexander, M. A., Scott, J. D., Friedland, K. D., Mills, K. E., and Thomas, A. C. (2018). Projected sea surface temperatures over the 21st century: Changes in the mean, variability and extremes for large marine ecosystem regions of northern oceans. *Elementa Scie Anthropocene* 6 (1), 9. doi: 10.1525/elementa.191

An, S. I., Jin, F.-F., and Kang, I. S. (1999). The role of zonal advection feedback in phase transition and growth of ENSO on the cane-zebiak model. *J. Met Soc. Japan* 77, 1151–1160. doi: 10.2151/jmsj1965.77.6_1151

Balmaseda, M. A., Vidard, A., and Anderson, D. L. (2008). ECMWF ocean analysis system: ORA-S3. *Mon Wea Rev.* 136, 3018–3034. doi: 10.1175/2008MWR2433.1

Biasutti, M., and Sobel, A. H. (2009). Delayed sahel rainfall and global seasonal cycle in a warmer climate. *Geophys. Res. Lett.* 36, L23707. doi: 10.1029/2009GL041303

Brander, K. (2013). Climate and current anthropogenic impacts on fisheries. *Climatic Change* 119 (1), 9–21. doi: 10.1007/s10584-012-0541-2

Cane, M. A., Clement, A.C., Kaplan, A., Kushnir, Y., Pozdnyakov, D., Seager, R., et al (1997). Twentieth-century sea surface temperature trends. *Science* 275 (5302), 957–960. doi: 10.1126/science.275.5302.957

Carton, J. A., Ding, Y., and Arrigo, K. R. (2015). The seasonal cycle of the Arctic ocean under climate change. *Geophys. Res. Lett.* 42, 7681–7686. doi: 10.1002/2015GL064514

Chang, P., and Philander, S. G. H. (1994). A coupled ocean-atmosphere instability of relevance to the seasonal cycle. *J. Atmos. Sci.* 51, 3627–3648. doi: 10.1175/1520-0469(1994)051<3627:ACOIOR>2.0.CO;2

Chen, Y.-Y., and Jin, F.-F. (2017). Dynamical diagnostics of the SST annual cycle in the Eastern equatorial pacific: Part II analysis of CMIP5 simulations. *Clim. Dyn.* 49 (11-12), 3923–3936. doi: 10.1007/s00382-017-3550-z

Chen, Y.-Y., and Jin, F.-F. (2018). Dynamical diagnostics of the SST annual cycle in the eastern equatorial pacific: part I a linear coupled framework. *Clim. Dyn.* 50 (5-6), 1841–1862. doi: 10.1007/s00382-017-3725-7

Clement, A. C., Seager, R., Cane, M. A., and Zebiak, S. E. (1996). An ocean dynamic thermostat. *J. Clim.* 9, 2190–2196. doi: 10.1175/1520-0442(1996)009<2190:AODT>2.0.CO;2

Collins, M., and Modeling Groups, C. M. I. P. (2005). El Nino-or la Nina-like climate change? *Clim. Dyn.* 24, 89–104. doi: 10.1007/s00382-004-0478-x

Deutsch, C., Ferrel, A., Seibel, B., Pörtner, H. O., and Huey, R. B. (2015). Climate change tightens a metabolic constraint on marine habitats. *Science* 348, 1132–1135. doi: 10.1126/science.aaa1605

DiNezio, P. N., Clement, A. C., Vecchi, G. A., Soden, B. J., Kirtman, B. P., and Lee, S.-K. (2009). Climate response of the equatorial pacific to global warming. *J. Clim.* 22, 4873–4892. doi: 10.1175/2009JCLI2982.1

Doney, S. C., Ruckelshaus, M., Duffy, J. E., Barry, J. P., Chan, F., English, C., et al. (2012). Climate change impacts on marine ecosystems. *Ann. Rev. Mar. Sci.* 4, 11–37. doi: 10.1146/annurev-marine-041911-111611

Drinkwater, K. F., Beaugrand, G., Kaeriyama, M., Kim, S., Ottersen, G., Perry, R., et al. (2010). On the processes linking climate to ecosystem changes. *J. Mar. Sys* 79, 374–388. doi: 10.1016/j.jmarsys.2008.12.014

Dwyer, J. G., Biasutti, M., and Sobel, A. H. (2012). Projected changes in the seasonal cycle of surface temperature. *J. Clim* 25, 6359–6374. doi: 10.1175/JCLI-D-11-00741.1

Hanson, K. J., Hasler, A. F., Kornfield, J., and Suomi, V. E. (1967). Photographic cloud climatology from ESSA III and V computer produced mosaics. *Bull. Am. Meteorol. Soc.* 48, 878–883. doi: 10.1175/1520-0477-48.12.878

Hollowed, A. B., Barange, M., Beamish, R., Brander, K., Cochrane, K., Drinkwater, K., et al. (2013). Projected impacts of climate change on marine fish and fisheries. *ICES J. Mar. Sci.* 70 (5), 1023–1037. doi: 10.1093/icesjms/fst081

Horel, J. D. (1982). On the annual cycle of the tropical pacific atmosphere and ocean. *Mon Wea Rev.* 110, 1863–1878. doi: 10.1175/1520-0493(1982)110<1863:OTACOT>2.0.CO;2

Jin, F.-F. (1996). Tropical ocean-atmosphere interaction, the pacific cold tongue, and the El niño southern oscillation. *Science* 274, 76–78. doi: 10.1126/science.274.5284.76

Jin, F.-F., Kim, S. T., and Bejarano, L. (2006). A coupled-stability index for ENSO. *Geophys. Res. Lett.* 33, L23708. doi: 10.1029/2006GL027221

Jin, F.-F., and Neelin, J. D. (1993). Modes of interannual tropical ocean-atmosphere interaction-a unified view. part I: Numerical results. *J. Atmos Sci.* 50, 3477–3503. doi: 10.1175/1520-0469(1993)050<3477:MOITOI>2.0.CO;2

Jin, F.-F., Neelin, J. D., and Ghil, M. (1994). El Niño on the devil's staircase: annual and subharmonic steps to chaos. *Science* 264, 70–72. doi: 10.1126/science.264.5155.70

Liu, F., Lu, J., Luo, Y., Huang, Y., and Song, F. (2020). On the oceanic origin for the enhanced seasonal cycle of SST in the midlatitudes under global warming. *J. Clim.* 33 (19), 8401–8413. doi: 10.1175/JCLI-D-20-0114.1

Liu, F., Luo, Y., Lu, J., and Wan, X. (2017). Response of the tropical pacific ocean to El niño versus global warming. *Clim. Dyn.* 48, 935–956. doi: 10.1007/s00382-016-3119-2

Liu, Z., Vavrus, S., He, F., Wen, N., and Zhong, Y. (2005). Rethinking tropical ocean response to global warming: the enhanced equatorial warming. *J. Clim.* 18, 4684–4700. doi: 10.1175/JCLI3579.1

Manabe, S., Hahn, D. G., and Hollaway, J. (1974). The seasonal variation of tropical circulation as simulated by a global model of atmosphere. *J. Atmos. Sci.* 32, 43–83. doi: 10.1175/1520-0469(1974)031<0043:TSVOTT>2.0.CO;2

Mitchell, T. P., and Wallace, J. M. (1992). The annual cycle in equatorial convection and sea-surface temperature. *J. Clim.* 5, 1140–1156. doi: 10.1175/1520-0442(1992)005<1140:TACIEC>2.0.CO;2

Neelin, J. D. (1991). The slow sea surface temperature mode and the fast-wave limit: Analytic theory for tropical interannual oscillations and experiments in a hybrid coupled model. *J. Atmos. Sci.* 48, 584–606. doi: 10.1175/1520-0469(1991)048<0584:TSSSTM>2.0.CO;2

Ottersen, G., Kim, S., Huse, G., Polovina, J. J., and Stenseth, N. C. (2010). Major pathways by which climate may force marine fish populations. *J. Mar. Sys* 79, 343–360. doi: 10.1016/j.jmarsys.2008.12.013

Philander, S. G. H., Gu, D., Halpern, D., Lambert, G., Lau, N. C., Li, T., et al. (1996). Why the ITCZ is mostly north of the equator. *J. Clim.* 9, 2958–2972. doi: 10.1175/1520-0442(1996)009<2958:WTIIMN>2.0.CO;2

Philander, S. G. H., and Seigel, A. D. (1985). "Simulation of El niño of 1982-1983," in *Coupled ocean-atmosphere models*, vol. 40 . Ed. J. C. J. Nihoul (Elsevier Oceanogr Ser), 517–541.

Rivkin, R. B., and Legendre, L. (2001). Biogenic carbon cycling in the upper ocean: effects of microbial respiration. *Science* 291 (5512), 2398–2400. doi: 10.1126/science.291.5512.2398

Sobel, A. H., and Camargo, S. J. (2011). Projected future seasonal changes in tropical summer climate. *J. Clim.* 24 (2), 473–487. doi: 10.1175/2010JCLI3748.1

Stine, A. R., and Huybers, P. (2012). Changes in the seasonal cycle of temperature and atmospheric circulation. *J. Clim.* 25, 7362–7380. doi: 10.1175/JCLI-D-11-00470.1

Stuecker, M. F., Jin, F.-F., and Timmermann, A. (2015). El Niño-Southern oscillation frequency cascade. *Proc. Nat. Acad. Sci.* 112 (44), 13490–13495. doi: 10.1073/pnas.1508622112

Stuecker, M. F., Timmermann, A., Jin, F.-F., McGregor, S., and Ren, H.-L. (2013). A combination mode of the annual cycle and the El Niño/Southern oscillation. *Nat. Geosci.* 6, 540–544. doi: 10.1038/ngeo1826

Taylor, K. E., Stou_er, R. J., and Meehl, G. A. (2011). An overview of CMIP5 and the experiment design. *Bull. Am. Meteorol. Soc.* 93 (4), 485–498. doi: 10.1175/BAMS-D-11-00094.1

Timmermann, A., Jin, F.-F., and Collins, M. (2004). Intensification of the annual cycle in the tropical pacific due to greenhouse warming. *Geophys. Res. Lett.* 31, L12208. doi: 10.1029/2004GL019442

Tziperman, E., Stone, L., Cane, M. A., and Jarosh, H. (1994). El Niño chaos: Overlapping of resonances between the seasonal cycle and the pacific ocean-atmosphere oscillator. *Science* 263, 72–74. doi: 10.1126/science.264.5155.72

Uppala, S. M., Kållberg, P. W., Simmons, A. J., Andrae, U., Bechtold, V. D. C., Fiorino, M., et al. (2005). The ERA-40 re-analysis. *Quart J. Roy Meteor. Soc.* 131, 2961–3012. doi: 10.1256/qj.04.176

Wang, B. (1994). On the annual cycle in the tropical eastern central pacific. *J. Clim.* 7, 1926–1942. doi: 10.1175/1520-0442(1994)007<1926:OTACIT>2.0.CO;2

Wengel, C., Latif, M., Park, W., Harlass, J., and Bayr, T. (2018). Seasonal ENSO phase locking in the Kiel climate model: The importance of the equatorial cold sea surface temperature bias. *Clim. Dyn.* 50 (3-4), 901–919. doi: 10.1007/s00382-017-3648-3

Wyrtki, K., and Meyers, G. (1976). The trade wind field over the pacific ocean. *J. Appl. Meteor.* 15, 698–704. doi: 10.1175/1520-0450(1976)015<0698:TTWFOT>2.0.CO;2

Xie, S. P. (1994). On the genesis of the equatorial annual cycle. *J. Clim* 7, 2008–2013. doi: 10.1175/1520-0442(1994)007<2008:OTGOTE>2.0.CO;2

Xie, S. P. (2004). "The shape of continents, air-sea interaction, and the rising branch of the Hadley circulation," in *The Hadley circulation: present, past and future*. Eds. H. F. Diaz and R. S. Bradley (Kluwer Academic Publishers), 121–152.

Xie, S. P., Deser, C., Vecchi, G. A., Ma, J., Teng, H., and Wittenberg, A. T. (2010). Global warming pattern formation: sea surface temperature and rainfall. *J. Clim.* 23, 966–986. doi: 10.1175/2009JCLI3329.1

Xie, S. P., and Philander, S. G. H. (1994). A coupled ocean-atmosphere model of relevance to the ITCZ in the eastern pacific. *Tellus* 46A, 340–350. doi: 10.3402/tellusa.v46i4.15484

frontiers | Frontiers in Marine Science

TYPE Original Research
PUBLISHED 23 December 2022
DOI 10.3389/fmars.2022.1096497

OPEN ACCESS

EDITED BY
Meilin Wu,
South China Sea Institute of Oceanology (CAS), China

REVIEWED BY
Dake Chen,
Nanjing Hydraulic Research Institute, China
Yi Pan,
Hohai University, China
Zhenwei Zhang,
Xiamen University of Technology, China

*CORRESPONDENCE
Yuanmin Sun
sunyuanmin@tio.org.cn

SPECIALTY SECTION
This article was submitted to Coastal Ocean Processes, a section of the journal Frontiers in Marine Science

RECEIVED 12 November 2022
ACCEPTED 08 December 2022
PUBLISHED 23 December 2022

CITATION
Jiang B, Zhang H, You T, Sun Y, Fu C, Liao W and Cai F (2022) Experimental study on the effect of an oyster reef on the nonlinear characteristics of irregular waves.
Front. Mar. Sci. 9:1096497.
doi: 10.3389/fmars.2022.1096497

Experimental study on the effect of an oyster reef on the nonlinear characteristics of irregular waves

Beihan Jiang[1], Hui Zhang[1], Tuofu You[1,2,3], Yuanmin Sun[2]*, Chenming Fu[1], Weijie Liao[1] and Feng Cai[1]

[1]College of Civil Engineering, Fuzhou University, Fuzhou, China, [2]Third Institute of Oceanography, Ministry of Natural Resources, Xiamen, China, [3]Lianjiang Water Conservancy Bureau, Fuzhou, China

As a "marine ecological engineer", the oyster reefs not only perform important ecological functions, but also reduce the damage caused by waves to protective structures such as seawalls. However, oyster reefs in shallow water change the nonlinear characteristics of waves and affect sediment transport and coastal evolution. Based on Fourier spectrum and analysis of Wavelet Transform, the influence of artificial bag oyster reefs on the energy and nonlinear phase coupling of irregular waves are studied through physical experiment. The results show that oyster reefs have a substantial effect on the energy of primary harmonic, which transfer to higher harmonics through triad interactions, and a considerable reduction in primary harmonic energy and an increase in higher harmonics energy are reflected in the energy spectra. The transmission spectrum behind the oyster reefs shows three peaks at primary, secondary and third harmonics. The bicoherence spectrum indicates that the peaks at secondary and third harmonics mainly result from the self-coupling of the primary harmonics and phase coupling between the primary and secondary harmonics respectively. As the water depth increases, the degree of nonlinear coupling between wave components decreases, which leads to the energy of wave components at different frequencies increases. With increasing top width, the length of the shoaling region increases, and the growth of triad nonlinear interactions are observed in wavelet-based bicoherence spectra, resulting in the spectral peak energy decreasing while the secondary harmonics energy increasing in the spectrum. Finally, the potential application of an ecological system composed by "oyster reefs + mangroves" is discussed. As the effect of water depth on wave energy is much greater than that of top width, in artificial oyster reef construction, it is recommended that keep the oyster reefs non-submerged in terms of wave dissipation. Further studies should take the dynamic growth effect of oyster reefs into account.

KEYWORDS

oyster reef, nonlinear triad interaction, wavelet bicoherence, wave energy, spectrum analysis

1 Introduction

With the global warming and sea level rise, coastal areas, as high-risk and high-vulnerability areas of climate change, face many risks such as land inundation, strong storm surge, saltwater intrusion, coastal erosion and flood damage (Hoegh-IPCC et al., 2014). A comprehensive protection system combining engineering and ecology should be adopted to improve the resilience of coasts and minimize disaster losses.

At present, the "gray" rigid structures built with concrete, such as seawalls and submerged breakwaters, play a dominant role in coastal protection (Spalding et al., 2014). The submerged breakwaters mainly have significant impact on wave resistance, sand prevention and flow diversion. At the same time, when the wave propagates over the submerged breakwaters, the wave breaks with a large amount of energy dissipation, which will reduce the impact of the current against the shore. Many studies have pointed out that the main factors affecting the wave dissipation coefficient of the submerged breakwaters are the top water depth, incident wave elements, relative width, etc. The wave dissipation effect of submerged breakwaters is obvious at low water level, but is relatively poor on long period waves, and increases with the increase of the top width (Daemen, 1991; D'angermound et al., 1996; Bian et al., 2020). As for the changes of waves before and after passing through submerged breakwaters, most scholars focus on the study of external structures such as wave reflection coefficient, transmission coefficient, wave pattern and wave height (Beji and Battjes, 1993; Ohyama and Nadaoka, 1994; Rambabu and Mani, 2005), but few on the internal structure of waves.

Although the "gray" structures such as submerged breakwaters can sufficiently alleviate shoreline retreat, the ecological damage they cause can be enormous (Kennish, 2002; National Research Council, 2007). These "gray" structures destroy the natural landscape of the coast and negatively impacts the coastal ecosystem (Saleh and Weinstein, 2016). In recent years, continuous research has shown that "green" coastal ecological projects, such as mangrove restoration, coral reef and oyster reef restoration, can dissipate wave energy and mitigate coastal erosion. At the same time, "green" structures such as oyster reefs can quickly self-restore after being damaged by storms. Compared with rigid protective structures, "green" structures have the advantage of lower maintenance costs and can substantially improve coastal ecosystem services (Morris et al., 2019; Jiang et al., 2022; Lipcius et al., 2021; Wang et al., 2022). Therefore, the "green" coastal ecological protection project is gradually paid attention to and applied by governments all over the world.

In addition to the artificial oyster reefs made of concrete directly, part of the collected oysters will also be put into net bags to construct the reef (Morris et al., 2019). Compared with the submerged breakwaters, the profile of oyster reefs is irregular, with a relatively high porosity and roughness. In addition, with the growth of oysters, the volume of oyster reef increases, and may not be always submerged. The influence on the wave is different from that of the submerged breakwaters. Oyster reefs change the offshore hydrodynamic conditions by increasing bed friction (Whitman and Reidenbach, 2012; Styles, 2015; Kibler et al., 2019), promoting wave attenuation (Manis et al., 2015), and increasing deposition on the leeward of the reef (De Paiva et al., 2018; Chowdhury et al., 2019). However, few studies investigate the influence of "green" structures composed of organisms such as oyster reefs on waves. Only a few institutions have issued disaster prevention design guidelines related to oyster reefs. In recent years, Allen (2013) examined the wave dissipation effect of three artificial reefs, namely, bag oyster reefs, concrete prism and triangular steel frame oyster reefs, under different hydrodynamic conditions through the physical models. Spiering et al. (2018) measured the wave dissipation effect and hydrodynamic influence of oyster reefs by using ADV and wave altimeters on site. Chauvin (2018) used pressure gauge to measure the wave attenuation of oyster reef breakwater and studied the wave attenuation law of various oyster reefs. Wiberg et al. (2019) measured the intertidal oyster reefs in four oyster reef restoration areas and found that oyster reefs close to the average sea level can substantially reduce the wave energy. Carter et al. (2017) predicted the nonlinearity of wave attenuation effect of various oyster reefs by numerical simulation.

In nearshore shallow water where oyster reefs grow, waves show strong nonlinear characteristics through physical phenomena such as shallow water deformation, refraction, reflection, diffraction, energy dissipation and breaking, and the wave speed, length, height and waveform will be substantially changed (Yu, 2013). Many studies have shown that the nonlinear interaction is accompanied by the whole process of wave propagation and deformation, which is the key to understand the wave dynamics. This strong nonlinear characteristic is also closely related to the extreme wave, sediment transport and coastal deformation (Nielsen, 1992; Drake and Calantoni, 2001; Nielsen and Callaghan, 2003; Saprykina et al., 2013). The variation of energy spectrum in the process of wave deformation in shallow water shows different characteristics compared with that in deep water. The study on the variation of wave energy in this nonlinear process will help to understand the energy transfer phenomenon between different wave components (Zanuttigh and Martinelli, 2018). Elgar and Guza (1985) found that when the wave propagates to a nearshore shoal, the wave asymmetry gradually increases, with the wave skewness gradually reaching a maximum during the shoaling process and then decreasing to zero in shallower water. Peng et al. (2009) studied the asymmetry and skewness of wave propagation by measured wave data, analyzed the influence of the local Ursell number on the asymmetry and skewness of waves, and fitted the relationship between the Ursell number, asymmetry and skewness to obtain a series of empirical formulas.

However, there are limitations to predict the waveform by local wave parameters in shallow water. Even if the height,

period and water depth of the waves are completely the same, because of the difference in topographic conditions and the rapid change of hydrodynamic conditions, the incident wave and the conversion to locked wave may be different, resulting in different nonlinear parameters (Ma et al., 2015). Since the locked wave and the free wave follow different dispersion relationship, triad interaction analysis is a relatively simple method for distinguishing the locked wave and the free wave energy (De Wit et al., 2020). Analyzing the complete three-dimensional spectrum requires high-resolution spatial information, which is difficult to obtain. Therefore, Fourier bispectrum analysis, as an alternative to three-dimensional spectrum analysis, can be used to characterize the binding energy in a given frequency range. On the basis of the bispectrum, Doering and Bowen (1995) analyzed the data measured at a natural beach and derived several empirical relationships between the nonlinear parameters and the local Ursell number describing the variation of phase coupling between the primary harmonics. Young and Eldeberky (1998) investigated the nonlinear process of wave growth in deeper water and reported that the triad interactions play an important role in the evolution of wind waves. Additionally, Eldeberky and Battje (1996); Beji and Nadaoka (1999), and Dong et al. (2008) gave a proper description of the nonlinear evolution mechanism in shallow water through the theory of triad interactions.

Compared with the Fourier transform, the wavelet transform is a localized analysis of signal time and frequency (Ma, 2010). It performs step-by-step multiscale refinement of the signal through scaling and translation operations, and finally realizes time subdivision at high frequencies and frequency subdivision at low frequencies. It can also automatically adapt to the requirements of time-frequency signal analysis, thereby focusing on any details of the signal (Newman et al., 2021). In recent years, wavelet transform theory has been gradually applied to wave analysis. Wavelet-based bispectrum theory was first proposed by Van Milligen et al. (1995) and applied to the phase coupling of plasma turbulent. Chung and Powers (1998); Larsen and Hanssen (2000) proved that wavelet-based bispectrum had more degrees of freedom than Fourier-based bispectrum. Dong et al. (2009) successfully applied this method to the interaction of irregular waves on curved shoals. Ma et al. (2010) studied the nonlinear deformation of focused waves in medium water depth conditions by this method. The wavelet transform theory is also applied to analyze wave data collected in the nearshore area of lakes (Muchebve et al., 2016). Elsayed (2006) successfully applied the wavelet-based bispectrum to analyze the frequency coupling phenomenon in the process of wind wave growth. On the basis of wavelet-based bispectrum theory, Chen et al. (2018) studied the nonlinear characteristics of wave propagation on three bottom slopes and investigated the change in wave energy caused by nonlinear interactions. All these studies have confirmed the reliability of wavelet-based bispectrum on nonlinear feature analysis.

Investigating the wave evolution and energy transfer process around the oyster reefs is the basis for analyzing the wave dissipation mechanism of oyster reefs. Currently, only a few experimental studies have considered triad interactions under the impact of the oyster reefs. Therefore, through physical model experiment, Fourier analysis and wavelet-based bispectrum are adopted to study the evolution process of the wave energy spectrum and the nonlinear interactions among wave components during the irregular waves propagating through artificial bag oyster reefs, with a view to providing references for research and engineering in coastal ecological restoration and near-shore sediment transport.

2 Materials and methods

2.1 Wave flume

The physical experiment is conducted in the wave flume at the Fujian Key Laboratory of Hydrodynamics and Hydraulic Engineering, China. The wavemaker is installed at one end of the wave flume, with a length of 60 m, a width of 1.0 m, and a depth of 1.5 m deep. The minimum and maximum water depths are 0.2 m and 1.0 m, respectively. An energy dissipation network is equipped behind the wave maker, and wave absorbers are installed to help mitigate wave reflection at the other end of the flume, with an energy dissipation more than 95%. The description about this experiment set-up is shown in Figure 1.

The distance from the model to the wavemaker and to the wave elimination device should be 6 times and 2 times longer than the effective wavelength, respectively. All the conditions in this experiment meet the requirements. The No.0 wave gauge is arranged 14 m away from the wavemaker to measure the incident wave. Five wave gauge measuring points are arranged every 0.5 m from the center of the model, to measure the wave parameters after the oyster reefs, as shown in Figure 1. At the beginning of the experiment, the first four to five waves generated by the wave maker are generally unstable, which are ignored before data collection. Each record is 163.84 s in length with a sample interval of 0.02 s. For obtaining sufficient and accurate data of waves for statistical analysis, each record is repeatedly collected three times.

2.2 Oyster reef type

The bag type oyster reef, which has been widely used in the past years, is selected in the experiment. The material of oyster reef is composed of 4-6 cm long natural shells, with a length scale

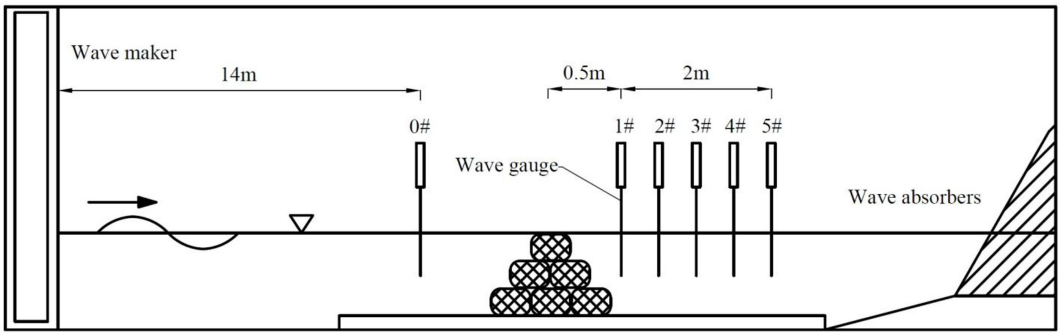

FIGURE 1
Experimental set-up.

of 4 and a porosity of 0.7 approximately, which is consistent with the practical situation. Four types of oyster reefs are designed in this experiment, as shown in Figure 2. The green part indicates that the oyster reefs are covered by biodegradable materials with better water resistance, while the grid part is covered by net bags. M1 are three-layer oyster reefs to study the influence of different hydrodynamic conditions on the nonlinear characteristics of waves. M2-M4 are double-layer oyster reefs to study the influence of the top width of the oyster reefs on the nonlinear characteristics of waves. Each layer of the oyster reef is composed of two connected parts of the same reef. The width of each part is 0.47 m, and the top center height d of the reefs is 0.272 m (three layers), or 0.18 m (double layers). Due to the flexibility of the oyster reefs, the reef in the center top is higher, while in the junction and the sidewall are lower, as shown in Figure 3.

2.3 Hydrodynamic conditions

In the experiment of three-layer oyster reef, five water depths D of 0.26 m, 0.27 m, 0.28 m, 0.3 m and 0.32 m were considered respectively. Among them, D = 0.26 m and 0.27 m are the emerged conditions, and the rest water depths are submerged conditions. The range of incident wave height H_i (significant wave height) is 0.023 m - 0.043 m, corresponding to the actual wave height of 0.13 m - 0.17 m, which is suitable for the conservation and growth of oyster reefs. In the double-layer oyster reef experiment, two water depths of 0.27 m and 0.3 m were considered, both of which were submerged conditions, and the incident wave height is H_i = 0.043 m. The peak period of spectra is set as T = 1 s, and 1.5 s, as a comparison between short and long periods. The experimental parameters are shown in Table 1.

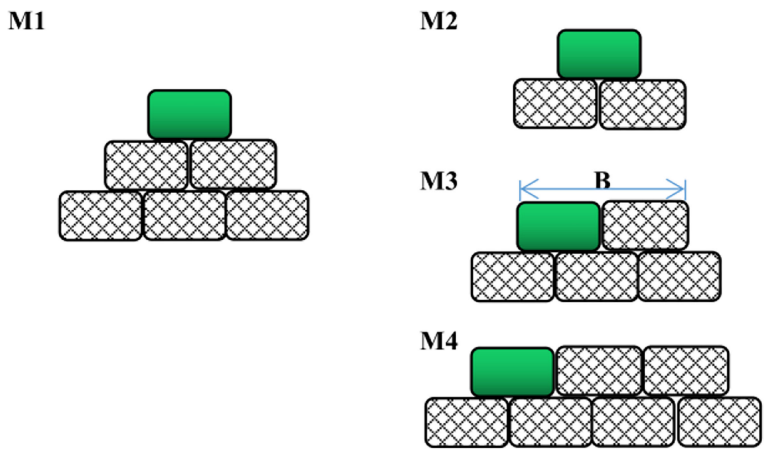

FIGURE 2
Oyster reef type.

10.3389/fmars.2022.1096497

FIGURE 3
M1 physical model.

TABLE 1 Incident wave parameters.

Wave code	Model types	Incident wave heightH_i/m	Water depth D/m	Peak period of spectra$T$/s
IR01	M1	0.033, 0.038, 0.043	0.26	1
IR02			0.27	
IR03			0.28	
IR04			0.3	
IR05			0.032	
IR06			0.26	1.5
IR07			0.27	
IR08			0.28	
IR09			0.3	
IR10			0.032	
IR11	M2	0.043	0.27	1
IR12			0.3	
IR13			0.27	1.5
IR14			0.3	
IR15	M3	0.043	0.27	1
IR16			0.3	
IR17			0.27	1.5
IR18			0.3	
IR19	M4	0.043	0.27	1
IR20			0.3	
IR21			0.27	1.5
IR22			0.3	

The commonly used JONSWAP spectra is adopted as the incident wave, and the incident spectrum is simulated according to the following equations:

$$S(f) = \beta_J H_{1/3}^2 T_{1/3}^{-4} f^{-5} \exp\left[-1.25(T_P f)^{-4}\right] \cdot \gamma^{\exp\left[-(T_P f-1)^2/2\sigma^2\right]}$$
$$\beta_J \approx \frac{0.06238}{0.230+0.0336\gamma-0.185(1.9+\gamma)^{-1}} \times [1.094 - 0.01915 \ln \gamma]$$
$$T_P \approx \frac{T_{H1/3}}{1.0-0.132(\gamma+0.2)^{-0.559}}$$
$$\sigma = \begin{cases} 0.07 & f \le f_P \\ 0.09 & f > f_P \end{cases} \quad (1)$$

where $S(f)$ is the spectra density function, reflecting the wave energy at the corresponding frequency. f is the frequency of wave component. T is the peak period of spectra, and γ is the peak enhancement factor. Only the case of $\gamma = 3.3$ is studied, which is close to the actual wave spectrum. σ is the spectral shape parameter, which controls the skewness of the spectrum. β_J is defined as a function of spectrum bandwidths. $H_{1/3}$ and $T_{H1/3}$ are the effective wave height and the corresponding effective period, respectively.

2.4 Data analysis method

2.4.1 Energy spectral analysis

Through Fourier spectrum analysis, the distribution of wave energy in the frequency domain can be clearly seen. This method is relatively mature and has been widely used. The fast Fourier transform (FFT) is used to calculate the spectrum of the wave, and then, the spectrum is smoothed by the Hanning window with a smooth degree of 6. Abroug et al. (2020) summarized the methods of previous researchers on wave spectrum partitioning. Through flume experiments, the wave energy spectrum of different spectral pattern, including P-M spectrum, J spectrum with $\gamma = 3.3$ and 7, were divided into four regions according to the proportion of energy in each frequency, namely, the spectral peak region E1, the transfer region E2, the high frequency region E3, the low frequency region E4. The partition is shown in Figure 4.

2.4.2 Wavelet-based bispectrum analysis

The continuous wavelet transforms of a time series x(t) is defined as:

$$WT(a,\tau) = \int_{-\infty}^{+\infty} x(t)\psi_{a,\tau}^{*}(t)dt \quad (2)$$

where the asterisk (*) represents the complex conjugate operation. And $\psi_{a,\tau}$ is generally called the analytic wavelet or the continuous wavelet, which represents family wavelets obtained from the mother wavelet function $\psi(t)$ by translating in time, τ, and dilation with scale, a. The scale a can be interpreted as the reciprocal of frequency f, i.e. $f = 1/a$. Thus, the expression for $\psi_{a,\tau}^{*}$ can be defined as:

$$\psi_{a,\tau}^{*}(t) = |a|^{-0.5}\psi\left(\frac{t-\tau}{a}\right) \quad (3)$$

When analyzing data related to water waves, the Morlet wavelet is usually chosen as the mother wavelet (Liu, 2000a; Liu, 2000b). The wavelet is a plane wave modulated by the Gaussian envelope, with good local properties in both time and frequency domain, and is defined as:

$$\psi(t) = \pi^{-1/4}\exp\left(-\frac{t^2}{2}\right)\exp(i\omega_0 t) \quad (4)$$

where $\omega_0$is the peak frequency of the wavelet, which needs to be greater than 6.0 at least to meet the condition of the wavelet transform.

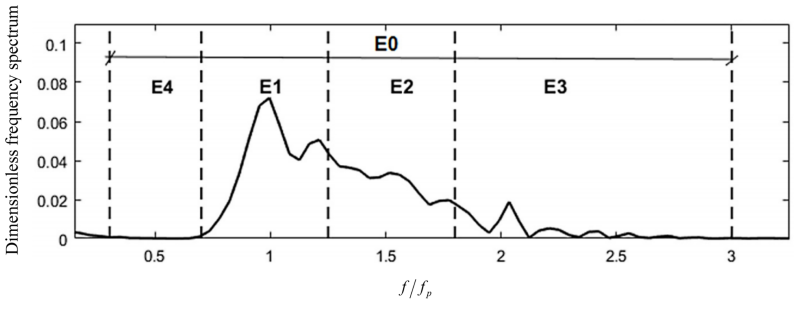

$$\begin{cases} E1: 0.7f_p < f < 1.1f_p \\ E2: 1.1f_p < f < 1.45f_p \\ E3: 1.45f_p < f < 3f_p \\ E4: 0.2f_p < f < 0.7f_p \end{cases}$$

FIGURE 4
Energy spectrum partition proposed by Abroug et al. (2020).

The wavelet-based bispectrum is defined as:

$$B(f_1,f_2) = \int_T WT(f_1,\tau)WT(f_2,\tau)WT^*(f,\tau)d\tau \quad (5)$$

where f_1 and $f_2$must satisfy the resonant triad, that is, the correlation in Eq. (6):

$$\begin{aligned} f &= f_1 \pm f_2 \\ k &= k_1 \pm k_2 \end{aligned} \quad (6)$$

The meaning of f and k is that the wave component (f, k) is generated by the sum frequency or difference frequency of the waves (f_1, k_1) and (f_2, k_2). If f and k satisfy the linear dispersion relationship, resonance interaction occurs, accompanied by intense energy transfer.

To directly measure the degree of nonlinear phase coupling between the wave components, the dimensionless wavelet bispectrum, also called wavelet bicoherence, is expressed as:

$$b(f_1,f_2) = \frac{|B(f_1,f_2)|}{\int_T |WT(f_1,\tau)WT(f_2,\tau)|dt \int_T |WT(f_1,\tau)|dt} \quad (7)$$

The value of $b(f_1, f_2)$ is between 0 and 1 and represents the coupling degree between any two frequencies f_1 and f_2 under the triad interaction. $b = 1$ denotes that the three wave components are completely correlated, that is, the energy of f is transmitted completely through the nonlinear interaction between f_1 and f_2. $b = 0$ indicates no interaction between the three wave components, and the wave with a frequency of f is completely randomly generated. The imaginary part of $b(f_1, f_2)$ dominates the energy transfer. For example, a positive value of imaginary part indicates the energy will transfer from f_1 and f_2 to their sum frequency $f_1 + f_2 = f$, while a negative value denotes energy transferred in an opposite direction. In addition, the absolute value of the imaginary part also indicates the degree of waveform asymmetry.

It is convenient to introduce the summed bicoherence b, which shows the distribution of nonlinear interaction intensity. To measure the distribution of phase coupling, the summed bicoherence b(f) is introduced as follows:

$$b(f) = \frac{1}{l(f)}\sum_{i=1}^{l(f)} b^2(f_1,f_2) \quad (8)$$

where l(f) is the number of frequencies, and b(f) denotes the nonlinear strength.

3 Results and discussion

3.1 Energy spectral analysis

3.1.1 Variation of the wave surface elevation and spectrum along the way

After propagating through the oyster reefs, part of the frequency of the incident waves is converted into locked waves and released as free waves, due to the complex three-dimensional structure of the oyster reefs and the height changes along the way. At the same time, affected by diffraction, the wave evolution process is complicated, and the energy of each frequency will change, which can be studied by spectral analysis. To investigate the influence of the oyster reefs on wave energy, the water depth D = 0.27 m, which are similar to the height d of the three-layer oyster reefs M1 (0.272 m), the incident wave height H_i = 0.043 m and the period T = 1 s are selected as the representative conditions to analyze the change of measured water surface elevations (η) before and after the oyster reefs, which are shown in Figure 5. As can be seen, after the wave propagates over the oyster reefs, the wave height decreases greatly (about 40%), indicating that part of wave energy is consumed during passing through the reef. At the same time, the secondary peaks and valleys are observed after the oyster reefs, and the wave surface shape became more irregular, indicating that part of the wave energy was converted from low frequency to high frequency, resulting in locked higher harmonics and free harmonics. This is consistent with the phenomenon observed by Beji and Battjes (1993), and Brossard et al. (2009) that waves propagate on submerged breakwaters.

In the process of wave propagation, the fluctuation of water surface can be observed, but the composition of wave components and the distribution of energy are the main factors affecting the change of wave in the process of propagation. After passes through the oyster reefs, the energy of waves at each frequency will change, which can be studied by spectral analysis. The same condition as Figure 5 is selected to analyze the energy spectrum changes before and after the oyster reefs model, as shown in Figure 6.

Figure 6 indicates that after the wave propagates through the oyster reefs, the energy transfer significantly from the primary to the higher harmonics because of the nonlinear interactions among wave components. In terms of spectrum shape, the incident spectrum is basically consistent with the theoretical spectral shape of the J spectrum, while the transmission spectrum shows three peaks, located at the primary, second and third harmonics. The energy in the E1 and E2 regions of the transmission spectrum is considerably lower than that of the incident spectrum, and the spectral peak energy is reduced by approximately 75%. In the high frequency region E3, the energy of transmitted wave near the secondary harmonic (2Hz) is substantially higher than that of the incident wave. There is basically no higher harmonics energy greater than 2.5Hz in the incident wave, while there is some higher harmonics energy in the transmitted wave. In the low frequency region E4, there is basically no energy in both the incident and transmitted waves, showing that the oyster reefs will not generate low frequency waves. In general, when the wave propagates through the oyster reefs, the energy of primary harmonic is greatly reduced and transfer to higher harmonics, resulting in the increase of higher harmonics energy, which is consistent with the conclusions of previous research on submerged breakwaters (Buccino and Calabrese, 2007).

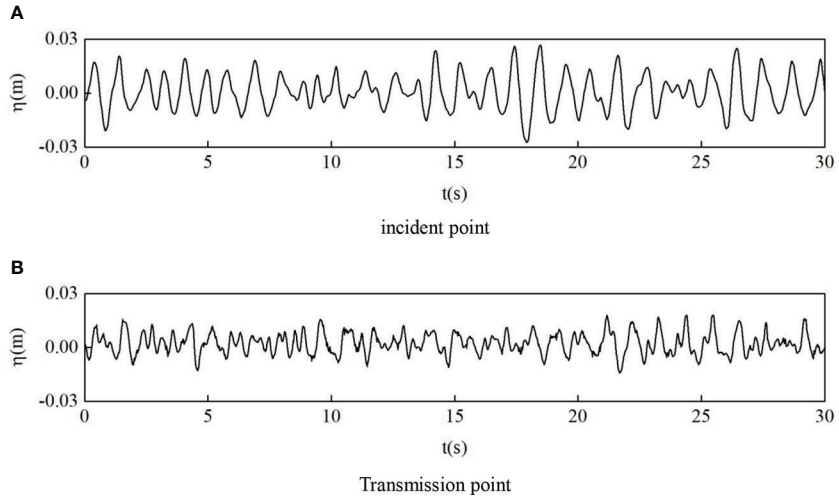

FIGURE 5
The measured water elevations **(A)** incident point **(B)** transmission point.

Then, under the same water depth and incident wave height, the variation in the energy spectrum after the oyster reefs is analyzed, and the results are shown in Figure 7. As can be seen from the figure, when T = 1 s, the energy spectrum presents an obvious trimodal pattern, with the three peaks located at the primary harmonic (1Hz), the second harmonic (2Hz) and the third harmonic (3Hz) respectively. However, previous studies mostly observed the bimodal shape of the energy spectrum (Buccino and Calabrese, 2007). When T = 1.5 s, the spectrum shows a weak trimodal pattern, and the overall energy is considerably greater than T = 1 s.

With increasing distance x, the energy of the spectral peak region E1 changes greatly. When T = 1 s, the energy in E1 shows a law of decreasing, rising and then decreasing. When T = 1.5 s, the pattern is a rising, falling and then rising. The energy in the transfer region E2 and the high frequency region E3 is little fluctuation. When T = 1 s, the spectrum of high frequency region E3 presents more burrs compared to T = 1.5 s,

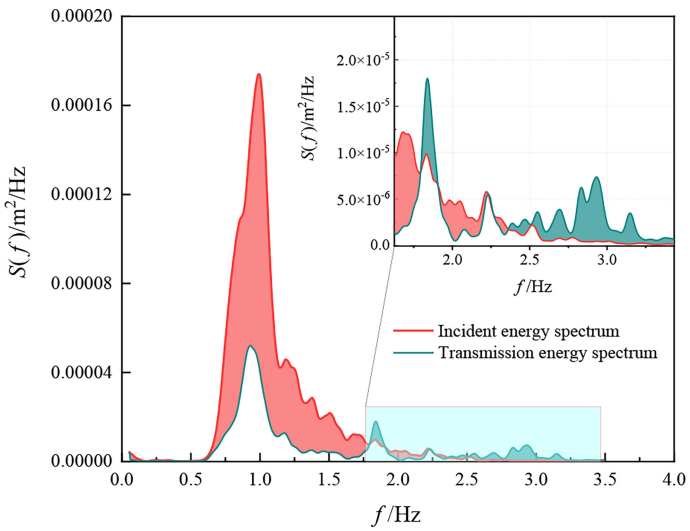

FIGURE 6
Comparison of incident and transmission spectra (M1, D = 0.27 m, H_i = 0.043 m, T = 1 s).

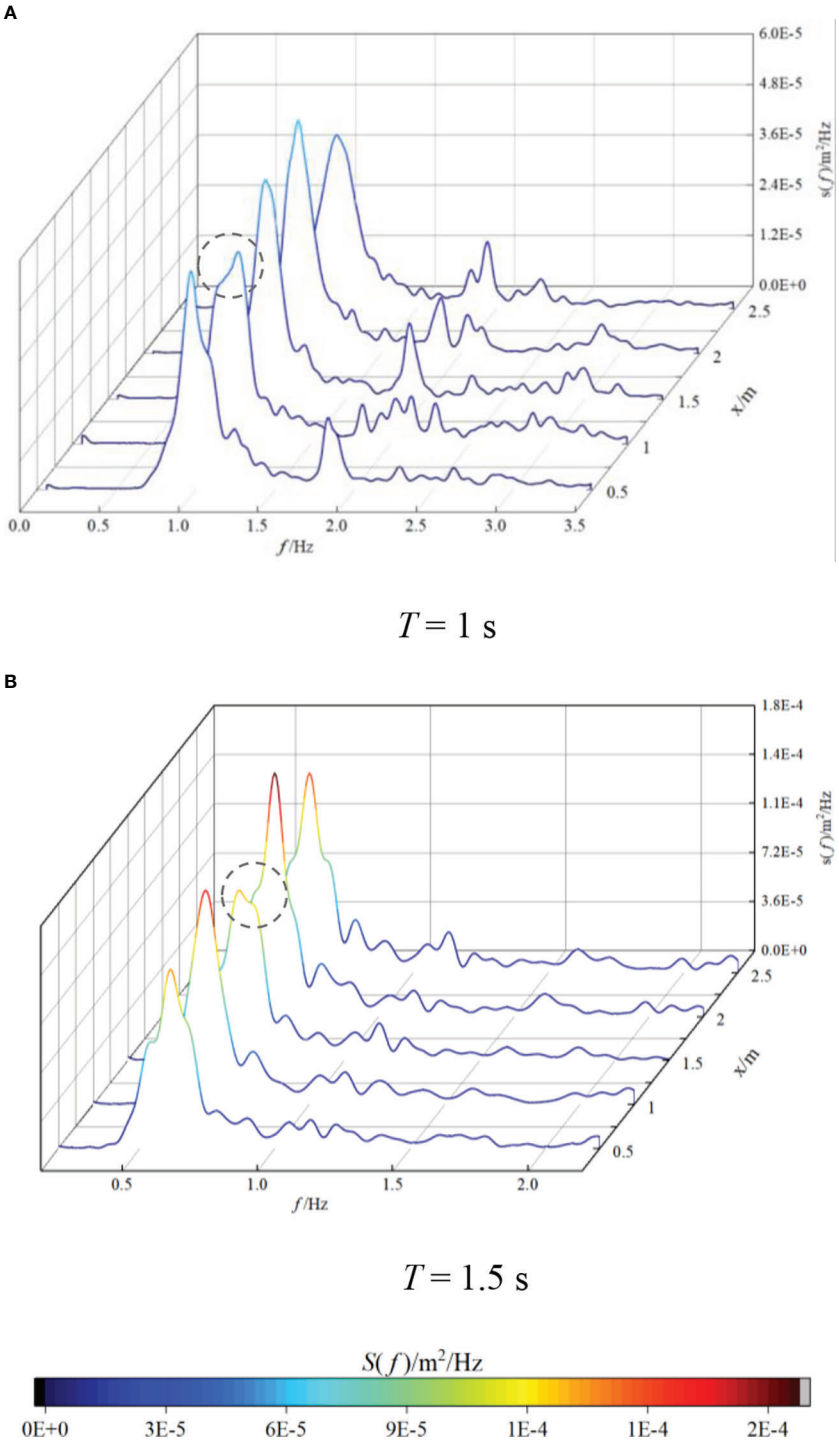

FIGURE 7
Comparison of wave energy spectra at different propagation distances (M1, D = 0.27 m, H_i = 0.043 m) **(A)** T = 1 s **(B)** T = 1.5 s.

indicating that the bound wave is converted into a free wave and then released is at a faster speed in the short-period wave, which is consistent with the research results from Chen et al. (2018).

In addition, at some positions, a unique phenomenon of energy loss may occur near the dominant frequency (in the dashed circle), which may due to the fact that the high-frequency waves are broken by the focusing effect after diffraction, and the

gas is rapidly exchanged, resulting in turbulent dissipation. The location of wave focusing is affected by the period T. The smaller the period is, the closer the location is to the oyster reefs.

3.1.2 Influence of water depth on the wave energy spectrum

To investigate the influence of water depth D on the wave spectrum, the energy spectrum at x = 1.5 m after three-layer oyster reefs M1 is calculated under water depth D = 0.26 m – 0.32 m, incident wave height H_i = 0.043 m, and period T = 1 s. The results are shown in Figure 8.

As can be seen from the figure, with increasing water depth, the energy of different frequencies generally increases, especially in the primary and secondary harmonics. When the water depth is small (D = 0.26 m and D = 0.27 m), with the model non-submerged, a large number of locked waves cannot be released due to the reflection of the oyster reefs. Thus, no increase in energy is observed in the high frequency region E3. At large water depths (D > 0.27 m), the model is submerged, and more locked waves are released as free waves, showing an increase of energy in the high frequency region E3.

3.1.3 Influence of top width on wave energy spectrum

Because of the three-dimensional structure of the oyster reefs, the top width B may be an important factor affecting the distribution of wave height. To investigate the influence of the top width on nonlinearity, the relationship between the energy spectrum and relative top width B/d is analyzed under water depth D = 0.27 m, incident wave height H_i = 0.043 m, period T = 1 s, and x = 1.5 m behind the oyster reefs. The results are presented in Figure 9.

As can be shown from the figure, with increasing relative top width B/d, the energy of the frequency near the primary harmonic decreases, while the energy near the secondary harmonic increases. This is because when the top width increases, the length of the shoaling region increases, leading to a gradually increase of triad nonlinear interactions in the shoaling process. Some locked higher harmonics are continuously released, resulting in a considerable increase in high-frequency energy. When the relative top width up to 2.56 (M4), the energy of higher harmonic is obviously larger compared to the other two smaller top width (M2, M3).

Since the spectral peak region E1 concentrates the main energy of the waves, the total energy of the wave spectrum will be lower after propagating through the wider oyster reefs, indicating a better energy dissipation effect. Therefore, when the oyster reefs are arranged in the ecological restoration project, the wider oyster reefs should be used as much as possible to take into account the effect of wave dissipation.

3.2 Nonlinear analysis of the bispectrum based on the continuous wavelet transform

As discussed in the spectral analysis, the energy transfer in the nonlinear interactions among wave components can be clearly seen. Nevertheless, which part of the harmonics participated in the triad interactions is unclear. Furthermore, the intensity of coupling between wave components and the

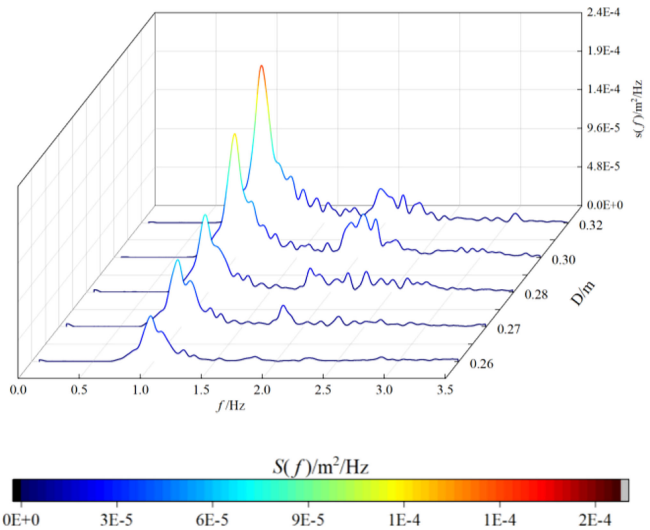

FIGURE 8
Comparison of wave energy spectra under different water depths (M1, H_i = 0.043 m, T = 1 s, x = 1.5 m).

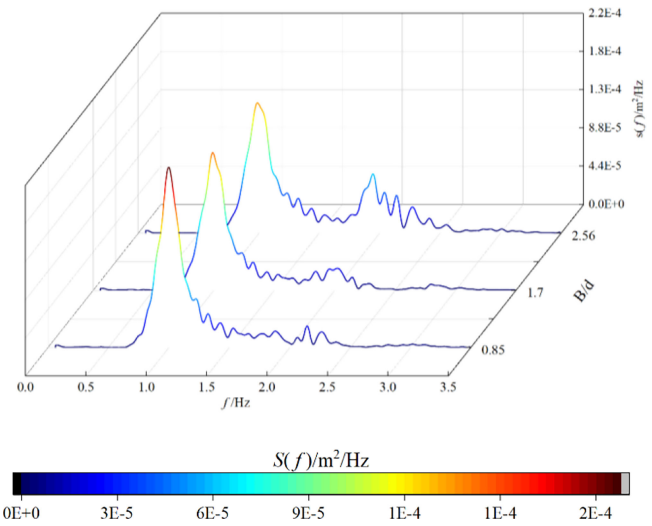

FIGURE 9
Comparison of the energy spectrum distribution under different top widths (D = 0.27 m, H_i = 0.043 m, T = 1 s, x = 1.5 m).

influencing factors are also worth discussing. Therefore, the triad interaction, to investigate where the energy comes from and what components it is transmitted to, is analyzed by the wavelet-based bicoherence method.

3.2.1 Viaration of wavelet-based bispectrum along the way

Figure 10 shows the calculation results of the bispectrum of the M1 (three-layer oyster reefs) model at the incident point and along x = 0.5 m, x = 1 m, and x = 2 m, under period T = 1.5 m, incident wave height H_i = 0.033 – 0.043 m and water depth D = 0.28 m. The interaction between different wave components can be clearly seen by the analysis of the bispectrum.

It can be seen from Figure 10 that both the incident wave height H_i and the distance x affect the bispectrum. As the Figures 10A–C show, at the incident point, the wave is not affected by the oyster reefs, only the primary wave (0.67Hz) and a few low frequency waves components participate in the weak interactions, and the phase coupling degree at this position is almost identical at different wave heights.

According to Figures 10D-F, at x = 0.5 m, a large number of bound harmonics are released at this point, the components involved in the nonlinear interactions are the most, and the coupling degree is the largest near the primary harmonic. As the incident wave height H_i increases from 0.033 m to 0.043 m, the value of bicoherence between the primary harmonics b(0.67, 0.67) increases from 0.65 to 0.68, and b(1.34, 0.67) between the primary and secondary harmonics increases from 0.63 to 0.66. It follows that the coupling intensity of the triad interactions keeps increasing with a slight magnitude. The value of b(0.67, 0.67) and b(1.34, 0.67) are both high, indicating that the increase in the higher harmonics of $2f_p$ and $3f_p$ (f_p is the frequency of spectral peak) results from the self-coupling of primary harmonics and the phase coupling between the primary and secondary harmonics, respectively, which is consistent with the findings of Elgar and Guza (1985). The oyster reefs have a substantial effect on primary harmonic (0.67Hz) of the wave, the energy of which transfer to the higher harmonics through the triad interactions. Therefore, after propagating through the oyster reefs, the energy of primary harmonic reduces significantly, while the energy of second and third harmonics increases, which corresponds to the trimodal pattern of the transmitted wave spectrum in Figure 6.

According to Figures 10 G–I, at x = 1 m, the number of frequencies participating in nonlinear interactions decreases, and the coupling degrees of the primary and secondary harmonics are both large. The value of bicoherence b(0.67, 0.67) = 0.41, b(1.34, 0.67) = -0.37, which is greatly weakened compared with the value at x = 0.5 m. As shown, with increasing distance, the coupling degree between different frequencies is weakened, that is, the intensity of the triad interactions decreases. The coupling value of the high-frequency changes from positive to negative, which means that energy transfer in an opposite direction, that is, energy transferred from the high frequency to the low frequency waves. At this position, not only is the low frequency energy transferred to the high frequency but also vice versa, and the energy transfer between the high and low frequencies is relatively balanced. Therefore, the overall variation in the energy spectrum is not great, as shown in Figure 7.

According to Figures 10J-L, at x = 2 m, the frequency with the strongest nonlinear interactions is transferred to the

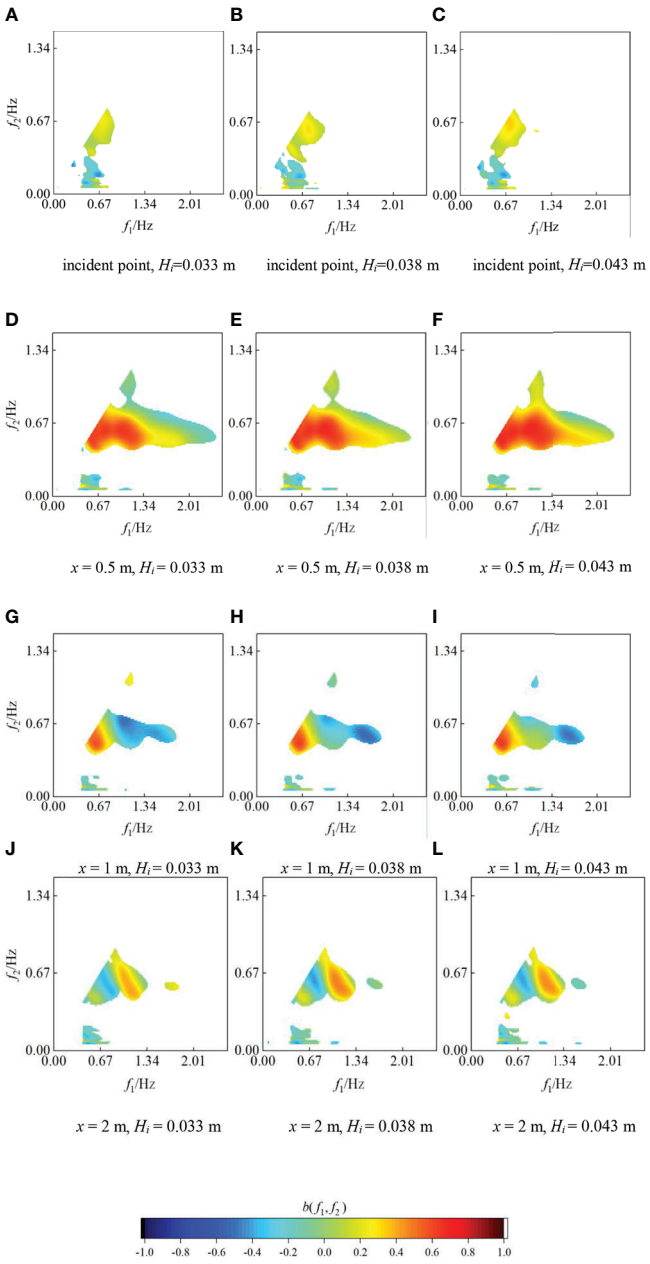

FIGURE 10
Changes in the wavelet-based bispectrum under different incident wave heights (M1, D = 0.28 m, T = 1.5 s) **(A)** incident point, H_i=0.033 m **(B)** incident point, H_i=0.038 m **(C)** incident point, H_i=0.043 m **(D)** x = 0.5 m, H_i = 0.033 m **(E)** x = 0.5 m, H_i = 0.038 m **(F)** x = 0.5 m, H_i = 0.043 m **(G)** x = 1 m, H_i = 0.033 m **(H)** x = 1 m, H_i = 0.038 m **(I)** x = 1 m, H_i= 0.043 m **(J)** x = 2 m, H_i = 0.033 m **(K)** x = 2 m, H_i = 0.038 m **(L)** x = 2 m, H_i= 0.043 m.

secondary harmonic. The value of bicoherence b(0.67, 0.67) = -0.16, b(1.34, 0.67) = 0.31. With increasing distance x, the coupling degree of the primary harmonics decreases continuously, becoming negative and approaching 0 when x = 2 m. This result indicates that when the wave propagates for a long distance (x > 2 m), the triad interactions basically no longer occur in the primary harmonic, and only a small part of the secondary harmonic energy transfer to higher harmonics, so the energy spectrum basically no longer changes.

The above analysis shows that the area with the strongest nonlinear interaction is near oyster reefs (x = 0.5 m). As the distance increases, less wave modes involved in the nonlinear interaction, and the coupling intensity decreases accordingly. After x = 2 m, the triad coupling weakens to a minor degree, and

the energy spectrum basically does not change. This result further indicates that it is a gradual evolution process for bound higher harmonics releasing into free waves, which is also consistent with previous conclusions of Dong et al. (2009).

To intuitively show the nonlinear interactions intensity of wave components at different frequencies, the summed bicoherence b under the same conditions is further provided. The results are shown in Figure 11.

It can be clearly demonstrated that with increasing distance, the summed bicoherence at each frequency decreases continuously, which suggests that the nonlinear interaction between different frequencies gradually weakens. The nonlinear phase couple at high frequency near the model (x = 0.5 m) is strongest, which proves the previous conclusion that the oyster reefs cause the energy transfer from the primary to higher harmonics. The energy transfer between high and low frequencies is basically balanced far from oyster reefs (x = 2 m), which is consistent with the results mentioned above. Comparing the values of summed bicoherence corresponding to different H_i in Figures 10A, B, the summed bicoherence of different incident wave heights shows basically the same change, indicating that the incident wave height has little effect on the nonlinear intensity.

It has been noted that the oyster reefs mainly affect the wave energy of the primary harmonic. Under the triad nonlinear interactions, the energy dissipation may increase in the process of energy transfer from the primary to higher harmonics, which may explain the mechanism of wave dissipation in oyster reefs to a certain extent, that is, wave energy is dissipated by the energy transfer between different frequencies.

3.2.2 Influence of water depth on the nonlinear interaction

To investigate the influence of the oyster reefs on wave nonlinear interaction under different water depths, the wavelet-based bispectrum at positions of x = 0.5 m and 1 m is given under period T = 1.5 s, incident wave height H_i = 0.043 m, and water depths D = 0.26 m, 0.28 m and 0.3 m, as shown in Figure 12.

From Figure 12, as the water depth D increases from 0.26 m to 0.3 m, the model switches from emerged to submerged, and the bispectrum at different positions changes significantly. The number of wave modes involved in the coupling process increases first and then decreases. The coupling intensity between the frequencies generally decreases.

At x = 0.5 m, near the oyster reefs, a large number of frequencies involved in the triad interactions with strong couplings. The value of bicoherence of the primary harmonics b(0.67, 0.67) decreases gradually with increasing water depth D. For example, when D = 0.26 m, 0.28 m and 0.3 m, b(0.67, 0.67) is 0.66, 0.64 and 0.51 respectively, indicating that the nonlinear intensity between the primary harmonics decreases with increasing water depth. When D = 0.26 m, the number of frequencies involved in the nonlinear interactions is substantially lower than that at other water depths. This is because the bound waves cannot be released by the reflection of the oyster reefs, resulting in a low energy of secondary harmonic, which is consistent with the results of the energy spectrum in Figure 8.

At x = 1 m, b(0.67, 0.67) is 0.58, 0.47, and 0.35 with increasing water depth, and the coupling degree also decreases gradually. The coupling value at high frequency changes from -0.17 to -0.4, showing an energy transfer in the opposite direction.

Notably, with increasing water depth, the oyster reefs changing from nonsubmerged to submerged, the degree of phase coupling between the primary harmonics and between the primary and secondary harmonics decreases, which means the energy transferred between different frequencies decreases. As a result, the energy of both primary and the secondary harmonics

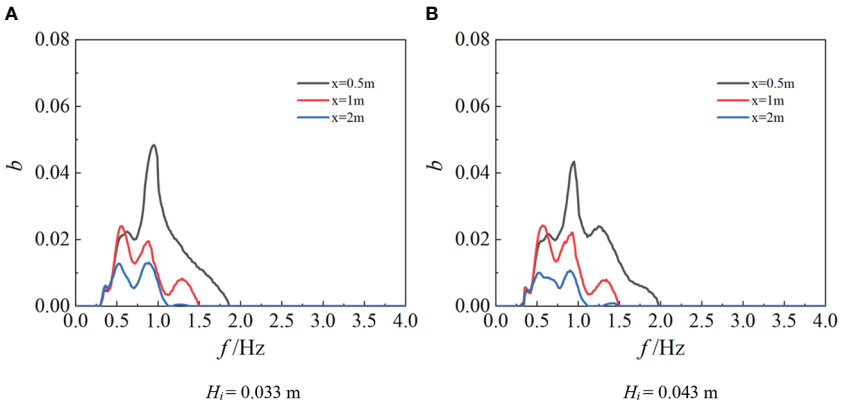

FIGURE 11
Comparison of summed bicoherence along the way (M1, D = 0.28 m, T = 1.5 s) **(A)** H_i= 0.033 m **(B)** H_i= 0.043 m.

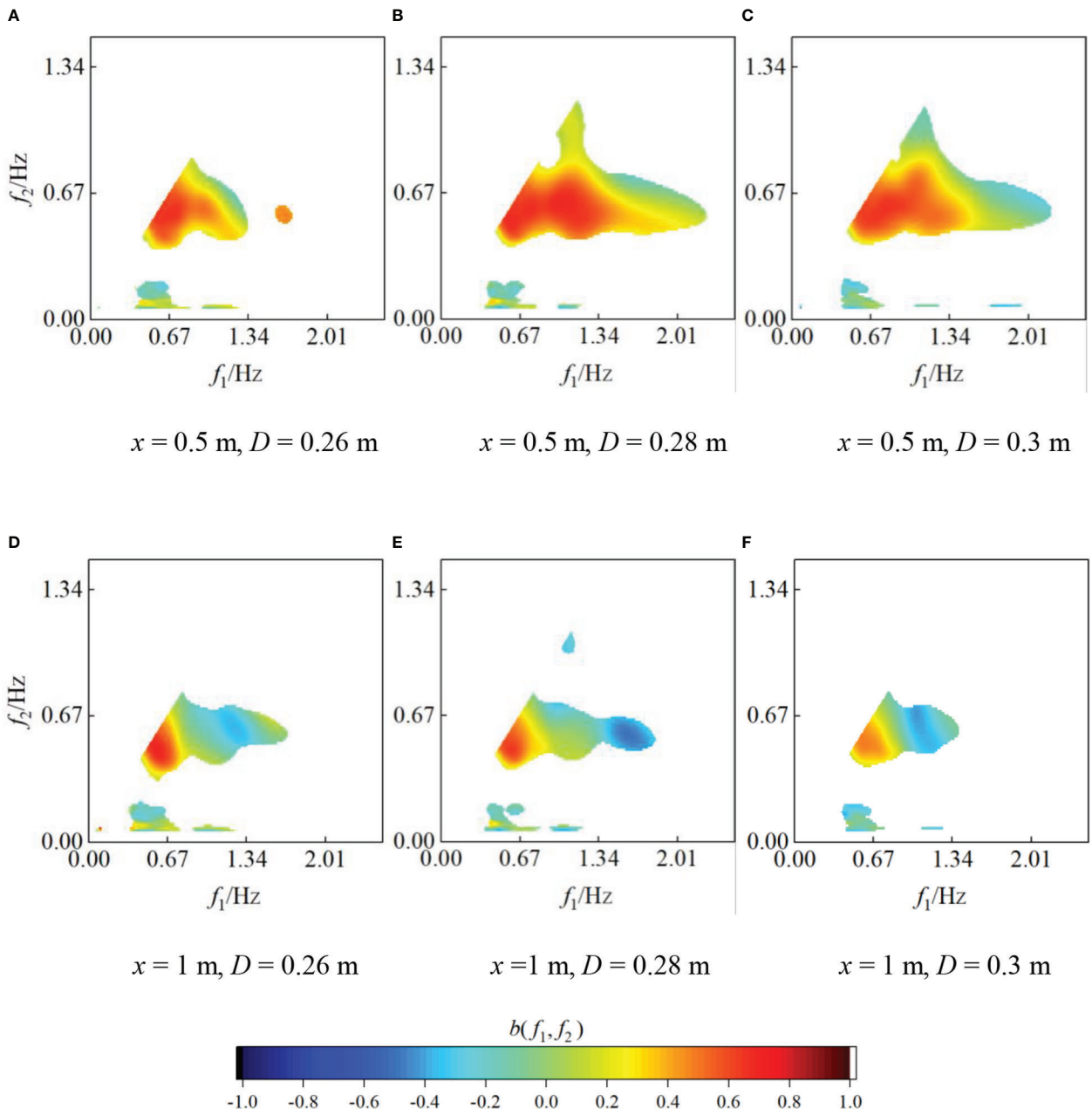

FIGURE 12
Changes in the wavelet-based bispectrum under different water depths (M1, H_i = 0.043 m, T = 1.5 s) **(A)** x = 0.5 m, D = 0.26 m **(B)** x = 0.5 m, D = 0.28 m **(C)** x = 0.5 m, D = 0.3 m **(D)** x = 1 m, D = 0.26 m **(E)** x =1 m, D = 0.28 m **(F)** x = 1 m, D = 0.3 m.

increase with increasing water depth, as exhibited in Figure 8. Therefore, in coastal ecological restoration projects, to reduce the wave energy, oyster reefs could be designed as nonsubmerged.

The influence of water depth on the summed bicoherence b is further studied, as shown in Figure 13. According to the Figure, with increasing water depth, the value of summed bicoherence first increases and then decreases, reaching a maximum at D = 0.28 m. At the distance of x = 0.5 m, more locked waves are released in the nonsubmerged (D > 0.27 m) oyster reefs, so frequency mode related to the strongest nonlinear phase couple shifts to higher frequencies. At x = 1 m, the summed bicoherence of the primary frequency is essentially unchanged. When D = 0.28 m, the value of summed bicoherence near the secondary harmonic is the highest, which is due to the large intensity of the energy reverse transmission.

3.3.3 Influence of top width on the nonlinear interaction

As described in Section 3.1.3, the top width impacts greatly on the energy spectrum. To further investigate the energy transfer characteristics under different top widths, the wave bispectrum of M2-M4 models at x = 0.5 m is analyzed. The results are presented in Figure 14. It can be seen that the relative top width B/d has a great influence on the bispectrum at the primary and secondary harmonics, and the influence differs between periods.

At T = 1 s, with increasing the top width, the wave components participating in the nonlinear interactions increase, and the coupling intensity between the primary harmonics decreases. Energy transfer in the opposite direction near the frequency of 1.5Hz and the coupling intensity decreases continuously, while the coupling value at 2Hz is positive and continuously strengthens. This is because as the top width increases, the times of the water shallowing and reverse-shallowing increases, the free wave is relocked and then rereleased to a higher frequency. As the energy locked lower than the energy released to high-frequency waves, the energy of high frequency (2Hz) increases.

At T = 1.5 s, with increasing top width, the wave modes involved in phase coupling process decrease. The coupling intensity between the primary harmonics is basically unchanged, while the intensity of the higher harmonics is weakened and becomes negative. For example, when B/d = 2.56, b(1.34, 0.67) = -0.21. The phenomenon being different from that when T = 1 s is because when the period is longer, that is, the wave steepness is smaller, the free wave releases at a slower speed, and the energy locked is higher than the energy released into the free wave of high-frequency. Therefore, with increasing top width, almost all the free waves released are relocked by the oyster reefs, which means that the energy transferred to the secondary harmonic is returned back to the primary harmonic, resulting in almost no change in the coupling intensity of the primary harmonics.

Figure 15 shows the influence of the top width on the summed bicoherence variation under different periods. When T = 1 s, with increasing top width, the value of b at the primary frequency decreases and the peak shifts to the primary frequency, while the b between 1.5Hz and 2Hz increases gradually. When T = 1.5 s and B/d< 1.7, the b of the dominant frequency almost constant, and the peak appears at 1.5Hz, and the peak value decreases by approximately 60% as B/d increases from 1.7 to 2.56. Notably, the decrease of b is caused by free waves locked rather than the energy reverse transmission.

4 Discussion

In addition, at some positions, a unique phenomenon of energy loss may occur near the dominant frequency (in the dashed circle of Figure 7), which may due to the fact that the high-frequency waves are broken by the focusing effect after diffraction, and the gas is rapidly exchanged, resulting in turbulent dissipation. The location of wave focusing is affected by the period T. The smaller the period is, the closer the location is to the oyster reefs.

After the oyster reefs, the primary harmonic energy generally presents a process of decreasing, and the smaller the water depth and the larger the top width, the greater the reduction of the primary harmonic energy. The high frequency energy shows an increases trend after the oyster reefs, and the smaller the water depth and the larger the top width, the smaller the increase of the high frequency energy. It can be seen that the wave dissipation effect of oyster reefs is partly due to friction dissipation, which reduces the primary harmonic energy behind the reefs rapidly. The other part is due to the attenuation of wave energy accelerated by the conversion

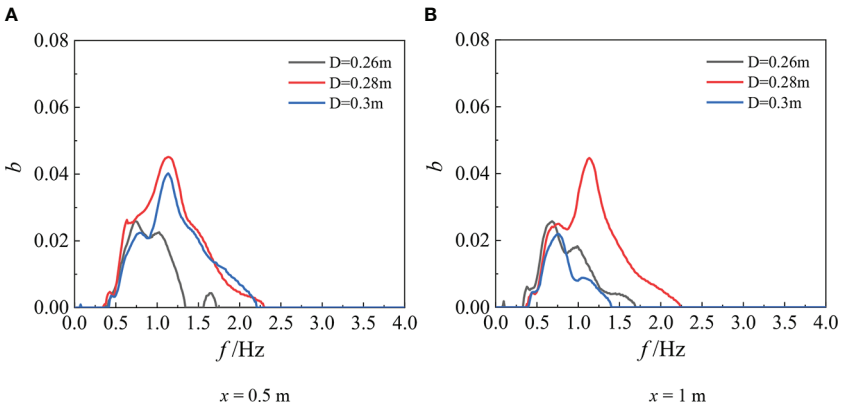

FIGURE 13
Comparison of summed bicoherence under different water depths (M1, H_i = 0.043 m, T = 1.5 s) **(A)** x = 0.5 m **(B)** x = 1 m.

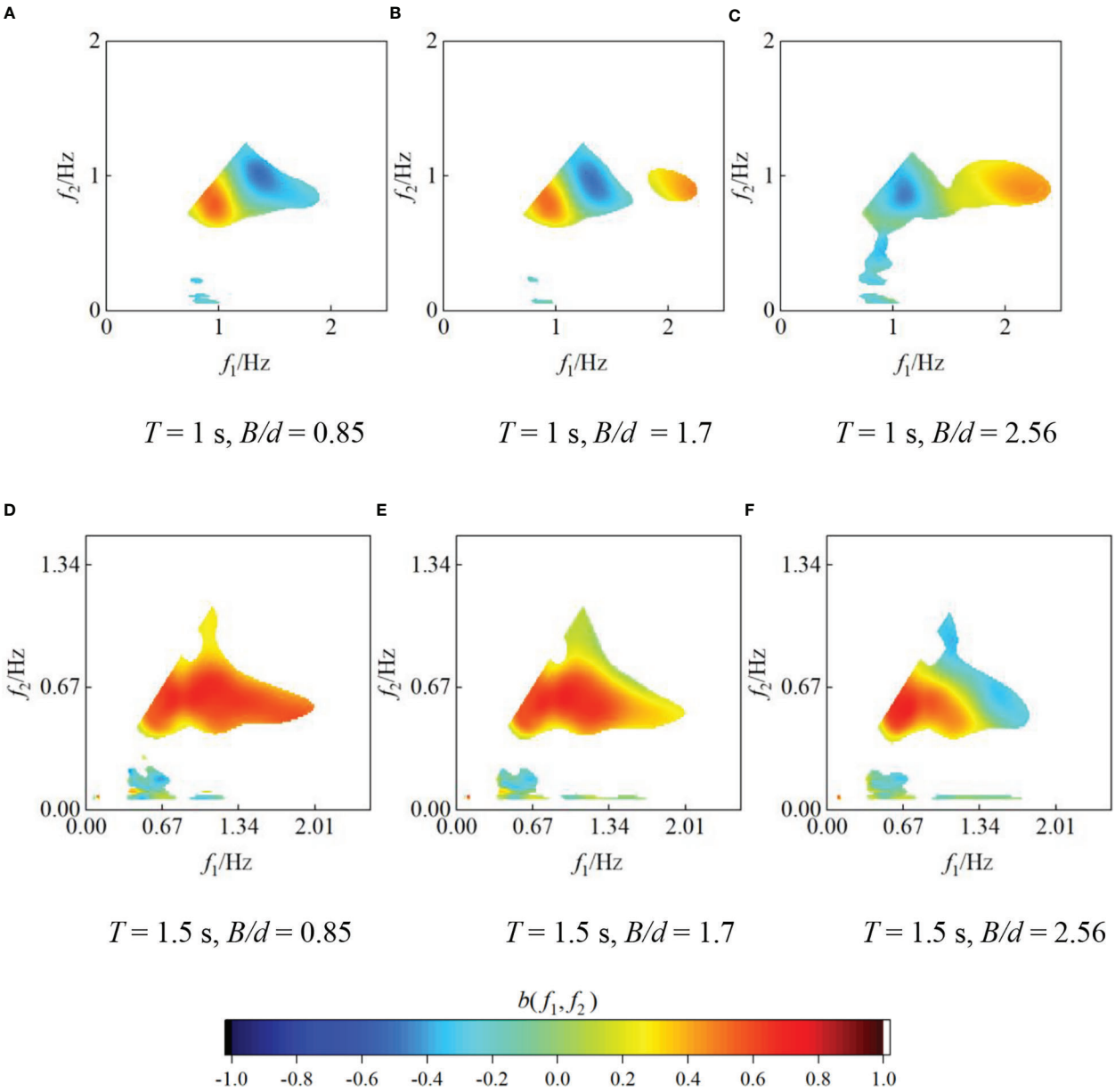

FIGURE 14
Wavelet-based bispectrum variation under different top widths (H_i = 0.043m, D = 0.27m, x = 0.5m) **(A)** T = 1 s, B/d = 0.85 **(B)** T = 1 s, B/d = 1.7 **(C)** T = 1 s, B/d = 2.56 **(D)** T = 1.5 s, B/d = 0.85 **(E)** T = 1.5 s, B/d = 1.7 **(F)** T = 1.5 s, B/d = 2.56.

of wave energy from low frequency component to high frequency component, which is consistent with the conclusion of submerged breakwaters (Chen et al., 2010).

Since the primary frequency E1 region concentrates the main energy of the wave, according to the experiment results, the total energy of the wave spectrum will be lower after passing through the oyster reefs with smaller water depth and larger top width, indicating a better energy dissipation effect. Therefore, in the ecological restoration project, to reduce the wave energy, oyster reefs are recommended to be designed as nonsubmerged, and the wider oyster reef should be used. However, it is also noted that the influence of top width on energy is much smaller than that of water depth, which confirms the previous view that the relative submerged depth is the most important parameter affecting the wave transmission coefficient of the submerged breakwaters (Seabrook and Hall, 1998). In engineering practice, increasing the top width of oyster reefs will increase the project cost. Therefore, the relationship between wave dissipation effect and economic investment should be considered comprehensively to design the appropriate top width.

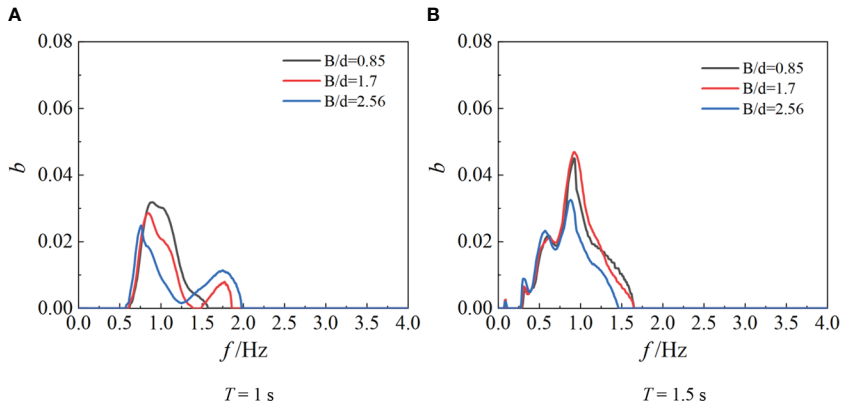

FIGURE 15
Comparison of summed bicoherence under different top widths (H_i = 0.043 m, D = 0.27 m, x = 0.5 m) **(A)** T = 1 s **(B)** T = 1.5 s.

The imaginary part of bispectrum is used to illustrate the phase coupling between wave components and the energy transfer caused by nonlinear wave-wave interaction. The nonlinear interaction is strongest in the area near the oyster reef (x = 0.5 m), where the secondary and third harmonics are generated. The amplitude of third harmonic is small, but it can be seen from the spectrum obviously (Figures 6, 7). As the distance increases, less wave modes involved in the nonlinear interaction, and the coupling intensity decreases accordingly. After x = 2 m, the triad coupling weakens to a minor degree, and the energy spectrum basically does not change. This result further indicates that it is a gradual evolution process for bound higher harmonics releasing into free waves, which is also consistent with previous conclusions of Dong et al. (2009).

At present, the success rate of coastal ecological projects is low, and the expected role of wave consumption is often unable to play in ecological projects (Lewis, 2009). For example, in coastal ecological projects focusing on mangrove restoration, the mortality rate of mangrove plants is high, which makes it almost impossible to attenuate wave. This result is partly due to the coastal hydrodynamic conditions (Hurst et al., 2015), including wave energy being too high and the sediment movement caused by wave nonlinearity being too strong (Constance et al., 2021). Based on the significant influence of oyster reefs on wave energy and nonlinear characteristics, if the oyster reefs could be arranged in front of immature mangroves to form a coastal ecological restoration system of "oyster reefs + mangroves", oyster reefs could dissipate wave energy before mangroves grow up steadily, improving the survival rate and expanding the suitable growth area of mangroves. Meanwhile, mangroves can degrade and purify the biological wastewater produced by oyster reefs (Chen et al., 2011). Finally, the combination system can improve the energy dissipation effect during storm surge (You, 2022). The combination of oyster reefs and mangroves can not only play its role in disaster reduction but also improve ecological benefits, which may have application potentiality in coastal ecological restoration projects.

After arriving at the reef, the oyster larvae will cling to the reef permanently, allowing the reef to expand continuously. Only the static or initial state of oyster reefs, rather than the dynamic growth, is considered in the experiment. The interaction and feedback mechanism between the hydrodynamic characteristics of waves and the growth process of oyster reefs is the direction of future research.

5 Conclusion

Physical experiments are carried out to study the energy transfer process and nonlinear triad interactions after waves propagating over the artificial bag oyster reefs, based on Fourier spectral and wavelet bispectral analysis.

The oyster reefs mainly affect primary harmonic energy, which transfer to higher harmonics by triad nonlinear interactions. The transmission spectrum presents three peaks at primary, second and third harmonics. The energy increase in $2f_p$ and $3f_p$ results from the phase coupling between the primary and secondary harmonics. The nonlinear interaction is strongest near the oyster reefs, and is weakened with increasing of distance.

With increasing water depth, the energy of both the primary and secondary harmonics increases. This is because the energy transferred between different frequencies decreases with the nonlinear coupling decreases. An increase in the top width leads to a decrease of the primary harmonic energy and an increase of the secondary harmonic energy, which is due to the increase of the shoaling region length, resulting in the enhancement of triad nonlinear interactions and the increase of high-frequency free waves released.

However, the influence of top width on energy is far less than that of water depth. Therefore, in the coastal restoration projects, taken

wave dissipation into consideration, it is recommended that keep the oyster reefs nonsubmerged. However, for the top width of oyster reefs, it is necessary to be designed reasonably by considering both the project cost and the influence on wave energy dissipation effect.

Data availability statement

The original contributions presented in the study are included in the article/supplementary material. Further inquiries can be directed to the corresponding author.

Author contributions

BJ contributed to the experimental design and data analysis. HZ contributed to the paper writing. TY conceived the study. YS provided funding and participated in the experiment. CF and FC contributed to the discussion and paper writing. WL contributes to data computation and analysis. All authors contributed to the article and approved the submitted version.

Funding

This study was supported by National Key R&D Program of China (Grant No. 2022YFC3106100) and the National Natural Science Foundation of China (Grant No. 42188102, 51509038, 51709048).

Acknowledgments

The authors would like to thank Fujian Hydrodynamic Research Center for their technical support.

Conflict of interest

The authors declare that the research was conducted in the absence of any commercial or financial relationships that could be construed as a potential conflict of interest.

Publisher's note

All claims expressed in this article are solely those of the authors and do not necessarily represent those of their affiliated organizations, or those of the publisher, the editors and the reviewers. Any product that may be evaluated in this article, or claim that may be made by its manufacturer, is not guaranteed or endorsed by the publisher.

References

Abroug, I., Abcha, N., Dutykh, D., Jarno-Druaux, A., and Marin, F. (2020). Experimental and numerical study of the propagation of focused wave groups in the nearshore zone. *Phys. Lett. A.* 384 (6), 126144. doi: 10.1016/j.physleta.2019.126144

Allen, R. J. (2013). *Physical modeling of wave transmission for submerged and emergent breakwaters used in living shorelines. [Dissertation]* (Mobile AL: University of South Alabama).

Beji, S., and Battjes, J. A. (1993). Experimental investigation of wave propagation over a bar. *Coast. Engineering.* 19 (1-2), 151–162. doi: 10.1016/0378-3839(93)90022-z

Beji, S., and Nadaoka, K. (1999). A spectral model for unidirectional nonlinear wave propagation over arbitrary depths. *Coast. Engineering.* 36 (1), 1–16. doi: 10.1016/S0378-3839(98)00046-5

Bian, F., Huang, Z., and Ju, L. (2020). Physical model test study on wave dissipation performance of submerged breakwater with different structural forms. *Port & Waterway Engineering* 08 (36), 41-58. doi: 10.16233/j.cnki.issn1002-4972.20200804.014

Brossard, J., Perret, G., Blonce, L., and Diedhiou, A. (2009). Higher harmonics induced by a submerged horizontal plate and a submerged rectangular step in a wave flume. *Coast. Engineering.* 56 (1), 11–22. doi: 10.1016/j.coastaleng.2008.06.002

Buccino, M., and Calabrese, M. (2007). Conceptual approach for prediction of wave transmission at low-crested breakwaters. *J. Waterway, Port, Coast, Ocean Eng.* 133, 213–224. doi: 10.1061/(ASCE)0733-950X(2007)133:3(213

Carter, J., Fenical, S., Harter, C., and Todd, J. (2017). *CFD modeling for the analysis of living shoreline structure performance, coastal structures and solutions to coastal disasters 2015: Resilient coastal communities* (Reston, VA: American Society of Civil Engineers), 442–450.

Chauvin, J. M. (2018). *Wave attenuation by constructed oyster reef breakwaters. [Master's thesis]* (Louisiana State University). doi: 10.31390/gradschool_theses.4752

Chen, J., Jiang, C., Hu, S., and Huang, W. (2010). Numerical study on the characteristics of flow field and wave propagation near submerged breakwater on slope. *Acta Oceanologica Sinica.* 29 (1), 88–99. doi: 10.1007/s13131-010-0011-5

Chen, Z., Li, S., Zhou, Q., Hong, M., Zhang, J., Li, C., et al. (2011). Analysis of water quality change after aquaculture wastewater entering mangrove. *Anhui Agric. Sci.* 10, 6039–6040. doi: 10.13989/j.cnki.0517-6611.2011.10.059

Chen, H., Tang, X., Zhang, R., and Gao, J.. (2018). Effect of bottom slope on the nonlinear triad interactions in shallow water. *Ocean Dynamics.* 68 (4), 469–483. doi: 10.1007/s10236-018-1143-y

Chowdhury, M. S. N., Walles, B., Sharifuzzaman, S. M., Hossain, M. S., Ysebaert, T., Smaal, A. C., et al. (2019). Oyster breakwater reefs promote adjacent mudflat stability and salt marsh growth in a monsoon dominated subtropical coast. *Sci. Rep.* 9 (1), 8549. doi: 10.1038/s41598-019-44925-6

Chung, J., and Powers, E. J. (1998). "The statistics of wavelet-based bicoherence," in Proceedings of the IEEE-SP International Symposium on Time-Frequency and Time-Scale Analysis (Pittsburgh, PA, USA: IEEE). 141–144.

Constance, A., Haverkamp, P. J., Bunbury, N., and Schaepman-Strub, G. (2021). Extent change of protected mangrove forest and its relation to wave power exposure on aldabra atoll. *Global Ecol. Conserv.* 27, e01564. doi: 10.1016/j.gecco.2021.e01564

Daemen, I. F. R. (1991). *Wave transmission at low-crested breakwater. [Dissertation]* (Dell: Delft University of Technology).

D'angermound, K., Meer, J. W., and Jong, R. J. (1996). "Wave transmission at low-crested structures," in *Proceedings of the 25th International Conference on Coastal Engineering*, (New York, NY, USA: ASCE). 2418–2427.

De Paiva, J. N. S., Walles, B., Ysebaert, T., and Bouma, T. J. (2018). Understanding the conditionality of ecosystem services: the effect of tidal flat morphology and oyster reef characteristics on sediment stabilization by oyster reefs. *Ecol. Engineering.* 112, 89–95. doi: 10.1016/j.ecoleng.2017.12.020

De Wit, F., Tissier, M., and Reniers, A.. (2020). The relationship between sea-swell bound wave height and wave shape. *J. Mar. Sci. Engineering.* 8 (9), 643. doi: 10.3390/jmse8090643

Doering, J. C., and Bowen, A. J. (1995). Parameterization of orbital velocity asymmetries of shoaling and breaking waves using bispectral analysis. *Coast. Engineering.* 26 (1–2), 15–33. doi: 10.1016/0378-3839(95)00007-X

Dong, G., Ma, Y., Perlin, M., Ma, Y., Yu, B., and Wang, G.. (2009). Experimental study of long wave generation on sloping bottoms. *Coast. Engineering.* 56 (1), 82–89. doi: 10.1016/j.coastaleng.2008.10.002

Dong, G., Ma, Y., Perlin, M., Ma, X., Yu, B., and Xu, J. (2008). Experimental study of wave-wave nonlinear interactions using the wavelet-based bicoherence. *Coast. Engineering.* 55 (9), 741–752. doi: 10.1016/j.coastaleng.2008.02.015

Drake, T. G., and Calantoni, J. (2001). Discrete particle model for sheet flow sediment transport in the nearshore. *J. Geophys. Res-Oceans* 106 (C9), 19859–19868. doi: 10.1029/2000JC000611

Eldeberky, Y., and Battjes, Y. (1996). Spectral modeling of wave breaking: Application to Boussinesq equations. *J. Geophys. Res-Oceans* 101 (C1), 1253–1264. doi: 10.1029/95JC03219

Elgar, S., and Guza, R. T. (1985). Observations of bispectra of shoaling surface gravity-waves. *J. Fluid Mechanics.* 161, 425–448. doi: 10.1017/S0022112085003007

Elsayed, M. A. K. (2006). A novel technique in analyzing non-linear wave-wave interaction. *Ocean engineering.* 33 (2), 168–180. doi: 10.1016/j.oceaneng.2005.04.010

IPCC. (2014). "Climate change 2014: Impacts, adaptation, and vulnerability. part b: Regional aspects," in *Contribution of working group II to the fifth assessment report of the intergovernmental panel on climate change* (U K and New York. (USA: Cambridge University Press).

Hurst, T. A., Pope, A. J., and Quinn, G. P. (2015). Exposure mediates transitions between bare and vegetated states in temperate mangrove ecosystems. *Mar. Ecol. Prog. Ser.* 533, 121–134. doi: 10.3354/meps11364

Jiang, W., Shi, W., Li, N., Fan, R., Zhang, W., Quan, W., et al. (2022). Oyster and barnacle recruitment dynamics on and near a natural reef in China: Implications for oyster reef restoration. *Front. Mar. Science.* 9. doi: 10.3389/fmars.2022.905373

Kennish, M. J. (2002). Environmental threats and environmental future of estuaries. *Environ. Conserv.* 29, 78–107. doi: 10.1017/S0376892902000061

Kibler, K. M., Kitsikoudis, V., Donnelly, M., Spiering, D. W., and Walters, L. (2019). Flow–vegetation interaction in a living shoreline restoration and potential effect to mangrove recruitment. *Sustainability.* 11, 3215. doi: 10.3390/su11113215

Larsen, Y., and Hanssen, A. (2000). "Wavelet-polyspectra: principles and properties. signal processing X theories and applications," in *Proceedings of EUSIPCO 2000, Tenth European Signal Processing Conference*. (Tampere, Finland: IEEE). 797–800.

Lewis, R. R. (2009). Chapter 24 - methods and criteria for successful mangrove forest restoration. *Coast. Wetlands: integrated ecosystem approach.*, 787–800. doi: 10.1016/B978-0-444-63893-9.00024-1

Lipcius, R. N., Zhang, Y., Zhou, J., Shaw, L., and Shi, J.. (2021). Modeling oyster reef restoration: Larval supply and reef geometry jointly determine population resilience and performance. *Front. Mar. Science.* 8. doi: 10.3389/fmars.2021.677640

Liu, P. C. (2000a). Is the wind wave frequency spectrum outdated. *Ocean engineering.* 27 (5), 577–588. doi: 10.1016/S0029-8018(98)00074-2

Liu, P. C. (2000b). Wave grouping characteristics in nearshore great lakes. *Ocean engineering.* 27 (11), 1221–1230. doi: 10.1016/S0029-8018(99)00042-6

Ma, Y. (2010). *Study on wave nonlinearity based on continuous wavelet transform. [Dissertation]* (Dalian: Dalian University of Technology).

Ma, Y., Dong, G., Perlin, M., Ma, X., Wang, G., and Xu, J. (2010). Laboratory observations of wave evolution, modulation and blocking due to spatially varying opposing currents. *J. Fluid Mechanics.* 661, 108–129. doi: 10.1017/S0022112010002880

Ma, Y., Ma, X., and Dong, G. (2015). Variations of statistics for random waves propagating over a bar. *J. Mar. Sci. Tech.* 23 (6), 864–869. doi: 10.6119/JMST-015-0610-3

Manis, J. E., Garvis, S. K., Jachec, S. M., and Walters, L. J. (2015). Wave attenuation experiments over living shorelines over time: a wave tank study to assess recreational boating pressures. *J. Coast. Conserv.* 19, 1–11. doi: 10.1007/s11852-014-0349-5

Morris, R. L., Bilkovic, D. M., Boswell, M. K., Bushek, D., Cebrian, J., Goff, J., et al. (2019). The application of oyster reefs in shoreline protection: are we over engineering for an ecosystem engineer? *J. Appl. Ecology.* 56, 1703–1711. doi: 10.1111/1365-2664.13390

Muchebve, E., Nakamura, Y., Suzuki, T., and Kamiya, H.. (2016). Analysis of the dynamic characteristics of seawater intrusion using partial wavelet coherence: a case study at nakaura Watergate, Japan. *Stochastic Environ. Res. Risk Assessment.* 30 (8), 2143–2154. doi: 10.1007/s00477-016-1336-1

National Research Council (2007). "Chapter 4 Mitigating eroding sheltered shorelines: A trade-off in ecosystem services," in: Mitigating shore erosion along sheltered coasts. *Natl. Academies Press* 92-97.

Newman, J., Pidde, A., and Stefanovska, A. (2021). Defining the wavelet bispectrum. *Appl. Comput. Harmonic Analysis.* 51, 171–224. doi: 10.1016/j.acha.2020.10.005

Nielsen, P. (1992). *Coastal bottom boundary layers and sediment transport* (Singapore: Mainland Press).

Nielsen, P., and Callaghan, D. P. (2003). Shear stress and sediment transport calculations for sheet flow under waves. *Coast. Engineering.* 47, 347–354. doi: 10.1016/S0378-3839(02)00141-2

Ohyama, T., and Nadaoka, K. (1994). Transformation of a nonlinear-wave train passing over a submerged shelf without breaking. *Coast. Engineering.* 24, 1–22. doi: 10.1016/0378-3839(94)90024-8

Peng, Z., Zou, Q., Reeve, D., and Wang, B. (2009). Parameterisation and transformation of wave asymmetries over a low-crested breakwater. *Coast. Engineering.* 56 (11-12), 1123–1132. doi: 10.1016/j.coastaleng.2009.08.005

Rambabu, A. C., and Mani, J. S. (2005). Numerical prediction of performance of submerged breakwaters. *Ocean Engineering.* 32 (10), 1235–1246. doi: 10.1016/j.oceaneng.2004.10.023

Saleh, F., and Weinstein, M. P. (2016). The role of nature-based infrastructure (NBI) in coastal resiliency planning: A literature review. *J. Environ. Manage.* 183 (PT.3), 1088–1098. doi: 10.1016/j.jenvman.2016.09.077

Saprykina, Y., Kuznetsov, S., Andreeva, N., and Shtremel, M. N.. (2013). Scenarios of nonlinear wave transformation in the coastal zone. *Oceanology.* 53 (4), 422–431. doi: 10.1134/S0001437013040103

Spalding, M. D., Ruffo, S., Lacambra, C., Meliane, I., Hale, L. Z., Shepard, C. C., et al. (2014). The role of ecosystems in coastal protection: Adapting to climate change and coastal hazards. *Ocean Coast. Manage.* 90, 50–57. doi: 10.1016/j.ocecoaman.2013.09.007

Spiering, D., Kibler, K. M., and Kitsikoudis, V. (2018). "Hydrodynamic change following living shoreline restoration based on a before-After-Control-Impact experiment," in *World environmental and water resources congress 2018* (Minnesota, USA: Hydraulics and Waterways, Water Distribution Systems Analysis and Smart Water. Minneapolis), 54–64.

Seabrook, S. R., and Hall, K. R. (1998). Wave transmission at submerged rubblemound breakwater; in *Proceedings of the 26th International Conference on Coastal Engineering* . (New York, NY, USA: ASCE). 2000–2013.

Styles, R. (2015). Flow and turbulence over an oyster reef. *J. Coast. Res.* 31, 978–985. doi: 10.2112/JCOASTRES-D-14-00115.1

Van Milligen, B. P., Sanchez, E., Estrada, T., Hidalgo, C., Branas, B., Carreras, B., et al. (1995). Wavelet bicoherence: A new turbulence analysis tool. *Phys. Plasmas.* 8, 3 017–3 032. doi: 10.1063/1.871199

Wang, X., Feng, J., Lin, C., Liu, H., Chen, M., Zhang, Y., et al. (2022). Structural and functional improvements of coastal ecosystem based on artificial oyster reef construction in the bohai Sea, China. *Front. Mar. Science.* 9. doi: 10.3389/fmars.2022.829557

Whitman, E. R., and Reidenbach, M. A. (2012). Benthic flow environments affect recruitment of crassostrea virginica larvae to an intertidal oyster reef. *Mar. Ecol. Prog. Series.* 463, 177–191. doi: 10.3354/meps09882

Wiberg, P. L., Taube, S. R., Ferguson, A. E., Kremer, M. R., Reidenbach, M. A., et al. (2019). Wave attenuation by oyster reefs in shallow coastal bays. *Estuaries Coasts.* 42 (2), 331–347. doi: 10.1007/s12237-018-0463-y

You, T. (2022). *Experimental study on wave evolution characteristics in oyster reef-mangrove wave dissipation system. [Master's thesis]* (Fuzhou: Fuzhou University).

Young, I. R., and Eldeberky, Y. (1998). Observations of triad coupling of finite depth wind waves. *Coast. Eng.* 33 (2), 137–154. doi: 10.1016/S0378-3839(98)00006-4

Yu, B. (2013). *Experimental study on low-frequency waves. [Dissertation]* (Dalian: Dalian University of Technology).

Zanuttigh, B., and Martinelli, L. (2018). Transmission of wave energy at permeable low crested structures. *Coast. Engineering.* 55 (12), 1135–1147. doi: 10.1016/j.coastaleng.2008.05.005

frontiers | Frontiers in Marine Science

TYPE Original Research
PUBLISHED 12 January 2023
DOI 10.3389/fmars.2022.1089331

OPEN ACCESS

EDITED BY
Qiuying Han,
Hainan Tropical Ocean University, China

REVIEWED BY
Peng Zhang,
Guangdong Ocean University, China
Zhenming Lv,
Zhejiang Ocean University, China

*CORRESPONDENCE
Qiang Su
sqiang@ucas.ac.cn

SPECIALTY SECTION
This article was submitted to Coastal Ocean Processes, a section of the journal Frontiers in Marine Science

RECEIVED 04 November 2022
ACCEPTED 15 December 2022
PUBLISHED 12 January 2023

CITATION
Gao J and Su Q (2023) The relationship between inorganic nutrients and diversity of dinoflagellate cysts: An evaluation from the perspective of species abundance distribution.
Front. Mar. Sci. 9:1089331.
doi: 10.3389/fmars.2022.1089331

The relationship between inorganic nutrients and diversity of dinoflagellate cysts: An evaluation from the perspective of species abundance distribution

Junfeng Gao and Qiang Su*

College of Earth and Planetary Sciences (CEPS), University of Chinese Academy of Sciences (UCAS), Beijing, China

The relationships between the inorganic nutrients and diversity of dinoflagellate cysts (the N-Dc relationships) are one of the most central issues in coastal ecology. It is not only an important pathway to explore the ecological processes of plankton, but also a key element for assessing eutrophication in marine ecosystems. Although the N-Dc relationships have been studied for many years, they have remained controversial, which may be attributed to (1) using samples collected from a single source (2) considering an insufficient range of nutrient concentrations (3) rarely taking into account species abundance distributions (SAD) that could better represent diversity. In this study, the N-Dc relationships are evaluated according to a compiled dataset, which cover the wide range of nutrient concentrations. Species diversity of cysts are estimated by four common diversity metrics and a new SAD parameter. Results show that all diversity metrics are negative with nutrients, which supports that low diversity of cysts could be considered as a signal of eutrophication. Additionally, this study finds a new pattern that SAD of cysts (N_r/N_1, N_r and N_1 is the abundance of the r-th and the first species in descending order) with decreasing nutrients appears to gradually approach 1: 1/2: 1/3.... In the future, if this pattern can be verified by more investigations, understanding the negative N-Dc relationships is more likely to provide new direction for assessing and managing eutrophication in coastal ecosystem, and even for exploring the general mechanisms determining diversity.

KEYWORDS

dinoflagellate cysts, inorganic nutrients, coastal ecosystem, species abundance distribution, fractal model, Zipf's law

Introduction

The dinoflagellate is an important component of the food chain in the coastal ecosystem (Penaud et al., 2018; Rodrigues et al., 2019; Keskes et al., 2020). It can not only use inorganic nutrients for primary production, but also produces harmful algal blooms in eutrophic waters (Liu et al., 2012; Price et al., 2017; Rodrigues et al., 2022). Thus, understanding the relationships between marine dinoflagellate and inorganic nutrients is highly valuable in exploring the ecological processes of plankton and environmental changes of the coastal ecosystems (Baula et al., 2011; Price et al., 2017; Gurdebeke et al., 2018; Rodrigues et al., 2022).

Many dinoflagellates produce the resting cyst that settles on the sediment bottom (Ellegaard et al., 2017; Gurdebeke et al., 2018). Previous studies suggested that species diversity of cysts could characterize diversity of living dinoflagellates, and even could reflect the nutrient status of waters (Dale, 2009; Gurdebeke et al., 2018; Rodrigues et al., 2022). For example, Marret and Zonneveld (Marret and Zonneveld, 2003) encoded information about diversity of dinoflagellates according to diversity of cysts. Sangiorgi and Donders (Sangiorgi and Donders, 2004) used diversity of cysts to explore the history and trends of eutrophication in coastal ecosystem. Thus, understanding the relationships between nutrients and diversity of cysts is one of the keys to study how diversity of dinoflagellates responds to nutrient conditions (Dale, 2009; Gurdebeke et al., 2018; Rodrigues et al., 2022), which will help to maintain the safe and sustainable management of coastal waters (Price et al., 2017; Penaud et al., 2018; Keskes et al., 2020; Rodrigues et al., 2022).

Although the relationships between main nutrients (such as NO_3 and PO_4) and diversity of cysts (hereafter referred to as the N-Dc relationships) have been discussed for many years (Pospelova et al., 2002; Ellegaard et al., 2017; Gurdebeke et al., 2018), they has remained controversial (Ellegaard et al., 2017; Price et al., 2017; Rodrigues et al., 2022). Most studies showed that the N-Dc relationships were negative (Tsirtsis and Karydis, 1998; Wang et al., 2004; Rodrigues et al., 2019; Keskes et al., 2020), which indicated that the diversity of cysts could be used as an indicator of eutrophication (Penaud et al., 2018; Rodrigues et al., 2019; Keskes et al., 2020). However, some studies suggested that their relationships were not always negative (Liu et al., 2012; Price et al., 2017; Rodrigues et al., 2022). For example, Rodrigues et al. (Rodrigues et al., 2022) found that the diversity of cysts was highest in highly eutrophicated condition followed by medium and low eutrophicated condition. Price et al. (Price et al., 2017) investigated the effect of nutrients on dinoflagellate cysts assemblages across estuaries of the Northwest Atlantic, and indicated that the N-Dc relationships were not very significant.

These inconsistent findings may be attributed to the following reasons. (1) Most studies sampled from a single water or cruise, which made their investigations potentially unrepresentative (Baula et al., 2011; Liu et al., 2012; Rodrigues et al., 2022). (2) The range of nutrient concentrations in some studies might be insufficient to present the complete N-Dc relationships (Baula et al., 2011; Price et al., 2017). (3) Only species richness or Shannon - Wiener index was used as diversity metric (Chen et al., 2011; Liu et al., 2012), which could not reflect other aspects of diversity, such as evenness and dominance. (4) Although species abundance distribution (SAD), as an important diversity surrogate, had been widely used to study the relationships between nutrients and diversity in terrestrial ecosystem (Arellano et al., 2017; Villa et al., 2019; Feng et al., 2021), few studies of the N-Dc relationships considered SAD of cysts (Penaud et al., 2018; Rodrigues et al., 2019; Keskes et al., 2020). Thus, there is still a need for the analysis that take into account the wide range of nutrient concentrations and multiple aspects of diversity, especially SAD (Dale, 2009; Gurdebeke et al., 2018; Rodrigues et al., 2022).

The main purpose of this study is to seek a more comprehensive understanding of how diversity of cysts responds to changing nutrient condition. To this end, 602 quantitative samples of marine dinoflagellate cysts that are compiled from six datasets (Marret and Zonneveld, 2003; Orlova et al., 2004; Wang et al., 2004; Esper and Zonneveld, 2007; Vásquez-Bedoya et al., 2008; Bouimetarhan et al., 2009) are used to explore the N-Dc relationships. PO_4 and NO_3 are used as representatives of inorganic nutrients, which are considered to be the main contributing nutrient of eutrophication in coastal waters (Elser et al., 2007). The diversity of cysts are estimated by four common metrics of diversity (Pielou, 1975) and a new SAD parameter (Su, 2016).

Methods

The diversity of cysts are measured by Species richness (S), Shannon's index (H'), Simpson's index (D) and Pielou's evenness (J) (Pielou, 1975), which are the most common metrics in the studies of species diversity (Baula et al., 2011; Liu et al., 2012; Price et al., 2017; Rodrigues et al., 2022). Additionally, a new SAD parameter is also calculated as the diversity surrogate.

Diversity metrics

H', D and J are calculated based on the cyst taxon composition and their abundances, they can be expressed as:

$$H' = -\sum_{i=1}^{S} p_i \ln p_i \quad (1)$$

$$D = 1 - \sum_{i=1}^{S} p_i^2 \quad (2)$$

$$J = \frac{H'}{\ln S} \quad (3)$$

where p_i is the relative abundance of the i-th species (i = 1, 2, 3, …S). As diversity increases, H' and J increase and D decreases.

The SAD parameter

The parameter p is generated from a new fractal model of SAD (Su, 2016). According to the fractal hypothesis (when K more species appear at each step of the accumulation process, their abundance are k times less abundant and $K = k^d$, where d is a fractal dimension (Su, 2016)), SAD is

$$\frac{N_r}{N_1} = r^{-p} \quad (4)$$

where r (= 1, 2, 3,… S) is the rank of species sorted down by species abundance; N_r and N_1 are the abundance of the r-th and the first species in descending order; p (= 1/d) is the fractal parameter that determines SAD. The lower p, the higher species diversity. For example, when p = 1 and S = 3, N_r/N_1 is 1: 1/2: 1/3; when p = 3 and S = 3, N_r/N_1 is 1: 1/8: 1/27.

Let $F_r = \ln(N_r/N_1)$ and $D_r = \ln(r)$. By minimizing the sum of squared error ($\sum_{r=1}^{S}(-pD_r - F_r)^2$) p can be calculated as (Su, 2016)

$$p = \frac{-\sum_{r=1}^{S} D_r F_r}{\sum_{r=1}^{S} D_r^2} \quad (5)$$

The goodness of fit is estimated by the coefficient of determination (R^2), which denotes how well the fractal model (*Eq.* 4) fits the samples of dinoflagellate cysts. R^2 is closer to 1, the goodness of fit is better.

Datasets

602 quantitative samples of dinoflagellate cysts are compiled from six published datasets, which are taken from modern sediments in coastal and outer ocean areas (Marret and Zonneveld, 2003; Orlova et al., 2004; Wang et al., 2004; Esper and Zonneveld, 2007; Vásquez-Bedoya et al., 2008; Bouimetarhan et al., 2009). These datasets are selected because (1) the sedimented cysts offer more comprehensive sample coverage, which is seldom attainable from living dinoflagellates records (Dale, 2009); (2) they contain the abundance of each species, by which SAD of cysts can be calculated; (3) there are NO_3 and PO_4 records matched with these datasets (Zonneveld et al., 2013); (4) the N-Dc relationships can be evaluated over a wider range (51.2°N-69.3°S); (5) they can give the comparable results, as these datasets have been standardized by excluding the samples that contained less than 50 individual numbers and 3 species numbers (Zonneveld et al., 2013); (6) the published datasets are easy to recheck. More background information of these datasets are given in the Table 1 of Supplementary Files and the corresponding literatures (Marret and Zonneveld, 2003; Orlova et al., 2004; Wang et al., 2004; Esper and Zonneveld, 2007; Vásquez-Bedoya et al., 2008; Bouimetarhan et al., 2009).

The relationship between nutrient concentrations and species diversity

S, *H'*, *D* and *J* are calculated by the vegan packages (Oksanen et al., 2020). The fractal *p* are calculated by *Eq.* 5. The frequency distribution patterns of each diversity metric are established using the histogram of 8 bins. Nutrient concentrations are divided equally into 50 segments, and all diversity metrics are standardized by taking the average of each segment. General linear regressions are used to fit the relationships between nutrient concentrations and each diversity metric, and the directions of the N-Dc relationships are marked by the slops of regressions (m). The relationships between nutrient concentrations and p are also fitted by non-linear regressions. All statistical analyses in this paper are performed in R ver. 4.0.4 (www.r-project.org), and code can be archived in figshare (Gao and Su, 2022).

Results

The analytical results of the compiled dataset show that PO_4 ranges from 0.08 ± 0.00 to 2.08 ± 0.01 µmol/L and NO_3 ranges from 0.35 ± 0.16 to 30.31 ± 0.00 µmol/L. The ranges of *S*, *H'*, *D*, *J* and *p* after segmenting PO_4 are from 3.00 ± 0.00 to 20.66 ± 7.57, 0.22 ± 0.00 to 1.98 ± 0.47, 0.22 ± 0.00 to 0.91 ± 0.13, 0.13 ± 0.00 to 0.82 ± 0.07 and 1.31 ± 0.00 to 4.16 ± 0.21, respectively. Their ranges after segmenting NO_3 are from 3.00 ± 0.00 to 19.86 ± 4.37, 0.09 ± 0.00 to 1.96 ± 0.35, 0.22 ± 0.00 to 0.97 ± 0.10, 0.05 ± 0.00 to 0.74 ± 0.08 and 1.32 ± 0.00 to 4.77 ± 0.19, respectively. The relationships between diversity metrics and two inorganic nutrients show the similar patterns (Figures 1, 2). *S*, *H'* and *J* are negative with PO_4 and NO_3 (PO_4: m_S = -5.97, $m_{H'}$ = -0.69, m_J = -0.15; NO_3: m_S = -0.44, $m_{H'}$ = -0.05, m_J = -0.01). *D* and *p* are positive with PO_4 and NO_3 (PO_4: m_D = 0.24, m_p = 0.74; NO_3: m_D = 0.02, m_p = 0.05). Their relationships are all significant (P< 0.01, Table 1). The non-liner regression also shows that *p* decrease pronouncedly with decreasing PO_4 and NO_3 (PO_4: R^2 = 0.47, P< 0.01; NO_3: R^2 = 0.48, P< 0.01; please see the legend of Figure 2 for the fitting formula).

The average values of *S*, *H'*, *D*, *J* and *p* are 13.75 ± 5.37, 1.60 ± 0.55, 0.34 ± 0.19, 0.63 ± 0.16 and 1.73 ± 0.62, and their median values are 14, 1.70, 0.28, 0.66 and 1.58, respectively. The percentage distributions of diversity metrics show that the

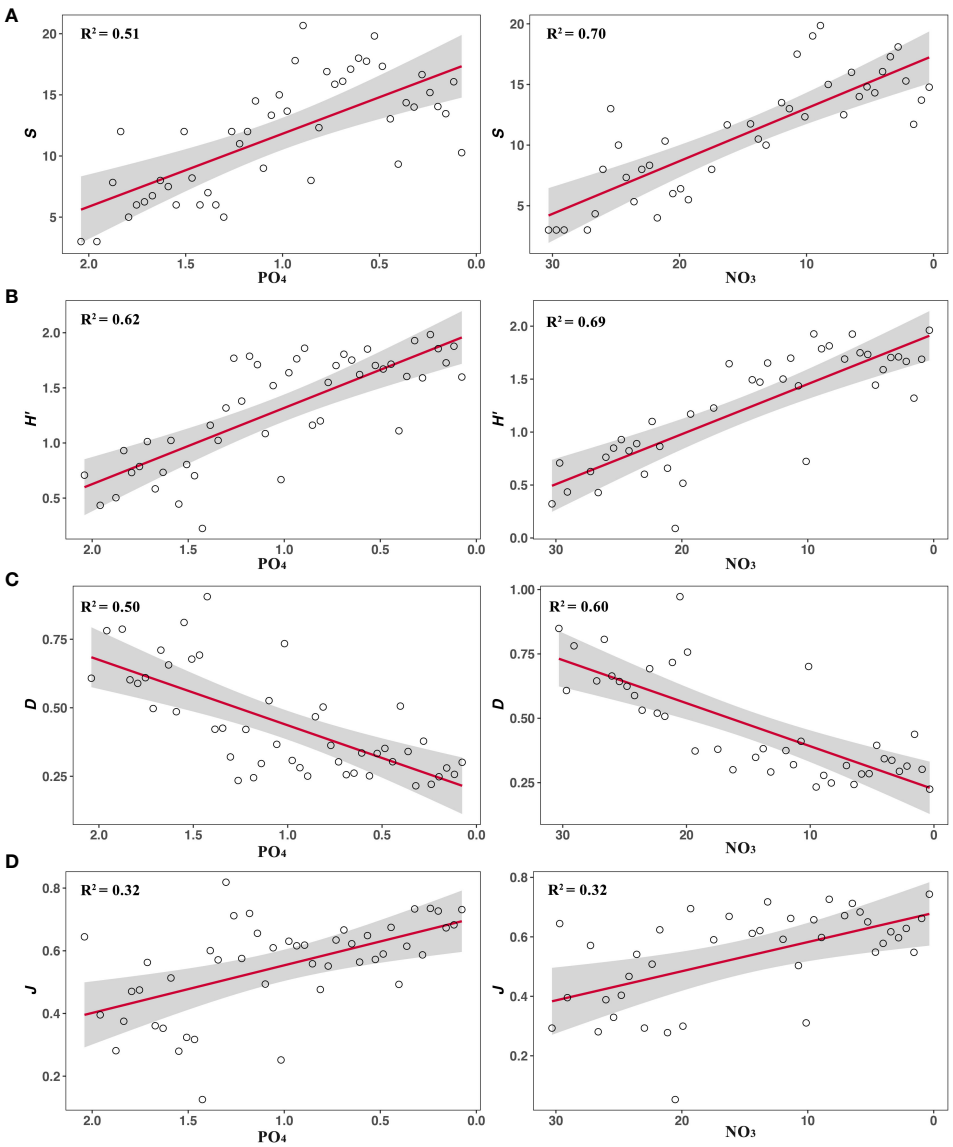

FIGURE 1
The N-Dc relationships are measured by **(A)** Species Richness (*S*), **(B)** Shannon's index (*H'*), **(C)** Simpson's index (*D*), **(D)** Pielou's evenness (*J*). All metrics show the similar patterns with changes in PO_4 and NO_3. The red line represents the regression result and the gray shading represents the 95% confidence limits.

interval with the highest percentage of *S*, *H'*, *D* and *J* are (12.50 16.07], (1.73, 2.11], (0.19, 0.32] and (0.68, 0.80], and they account for 26.08%, 29.90%, 35.04% and 33.55%, respectively (please see Figure 1 of Supplemental Files). [1.03 1.71) is the interval with the highest percentage of *p*, accounting for 55.48% (Figure 3). It is rare that *p* is far greater than 1 or very near 0. R^2 of the fractal model to the samples of dinoflagellate cysts is from 0.3 to 1 (please see Table 2 of Supplemental Files). R^2 of over 82% samples are above 0.8.

Discussion

With increasing urbanization and growth of agriculture, inorganic nutrient discharge has become a major problem in most coastal regions (Liu et al., 2012; Price et al., 2017; Rodrigues et al., 2022). Dinoflagellate is one of the most sensitive plankton to the nutrition condition (Ellegaard et al., 2017; Gurdebeke et al., 2018), and the diversity of dinoflagellate cysts are usually used for describing their responses (Baula et al., 2011; Price et al.,

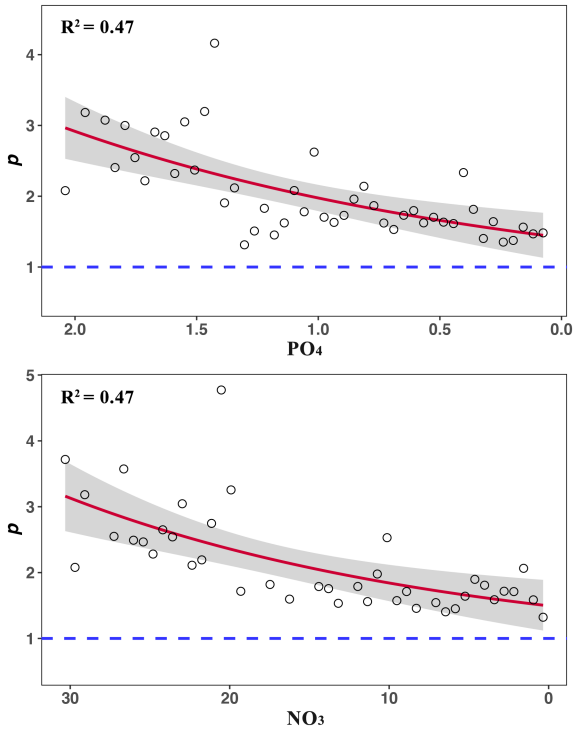

FIGURE 2
The relationships between nutrient concentrations (μmol/L) and fractal *p*. The red line represents the result of non-line regression and the gray shading represents the 95% confidence limits (PO_4: $y = 0.81e^{0.52x} + 0.61$, $R^2 = 0.47$, $P< 0.01$; NO_3: $y = 0.72e^{0.04x}+0.77$, $R^2 = 0.47$, $P< 0.01$).

TABLE 1 The liner regressions between nutrient concentrations and diversity metrics.

Nutrients	Diversity metric	Slop (*m*)	R^2	*P*
PO_4	*S*	-5.97	0.51	<0.01
	H'	-0.69	0.62	<0.01
	D	0.24	0.50	<0.01
	J	-0.15	0.32	<0.01
	p	0.74	0.45	<0.01
NO_3	*S*	-0.44	0.70	<0.01
	H'	-0.05	0.69	<0.01
	D	0.02	0.60	<0.01
	J	-0.01	0.32	<0.01
	p	0.05	0.45	<0.01

All diversity metrics show the similar patterns with changes in PO_4 and NO_3, and they present the significantly negative N-Dc relationships.

2017). Thus, understanding the relationships between nutrients and diversity of cysts (the N-Dc relationships) will help to develop information crucial for the identification of eutrophication in the coastal ecosystem (Penaud et al., 2018; Rodrigues et al., 2019; Keskes et al., 2020). However, although many studies have surrounded the N-Dc relationships over decades (Pospelova et al., 2002; Ellegaard et al., 2017; Gurdebeke et al., 2018), a further analysis is still needed, because (1) the samples of some studies were collected from a single source; (2) the ranges of nutrient concentrations might be

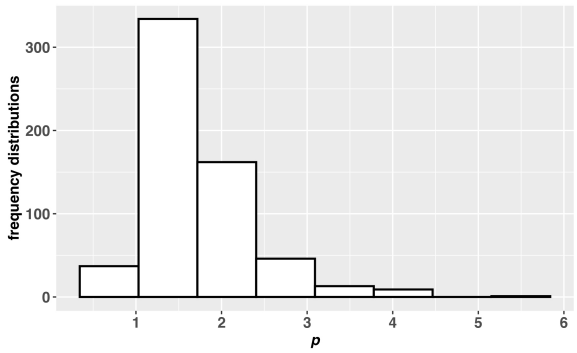

FIGURE 3
The frequency distribution of the fractal *p*. The interval with the highest percentage of *p* is [1.03 1.71) and its percentage is 55.58%.

insufficient; (3) SAD was rarely considered (Ellegaard et al., 2017; Price et al., 2017; Rodrigues et al., 2022). The biggest difference of this study is that the N-Dc relationships are evaluated by multiple aspects of diversity (including SAD) over a wide range of nutrient concentrations according to the compiled dataset (Marret and Zonneveld, 2003; Orlova et al., 2004; Wang et al., 2004; Esper and Zonneveld, 2007; Vásquez-Bedoya et al., 2008; Bouimetarhan et al., 2009).

In this study, all diversity metrics show the similar patterns with changes in PO_4 and NO_3 (Figures 1, 2). *S*, *H'* and *J* significantly decrease with nutrients (Figure 1). *D* and *p* significantly increase with nutrients (Figures 1, 2). The lower *D* and *p*, the higher species diversity (Pielou, 1975; Su, 2016). Thus, all five metrics are negative with nutrient concentrations. These results echo most of the empirical studies, noting that diversity of cysts was usually negative with nutrients, and it could be considered as an ecological indicator of eutrophication (Tsirtsis and Karydis, 1998; Wang et al., 2004; Rodrigues et al., 2019; Keskes et al., 2020). However, they are inconsistent with the expectation of traditional theories, noting that the link between nutrients and diversity of phytoplankton is considered as the effect of nutrient enrichment on productivity or biomass, and then their relationships will be unimodal (Bedford et al., 1999; Irigoien et al., 2004; Adjou et al., 2012).

Such contradictions between the empirical investigations and the theoretical expectations are apparently worth discussing. Firstly, the negative N-Dc relationships similar to this study have been frequently observed (Wang et al., 2004; Rodrigues et al., 2019; Keskes et al., 2020). For example, Wang et al. (Wang et al., 2004) found that diversity of cysts in Daya Bay dramatically declined when the marine system enriched with nutrients. Keskes et al. (Keskes et al., 2020) suggested cyst diversity of South-Western Mediterranean were lower in the water with higher nutrients. Secondly, the decrease in diversity of cysts has been widely used as warning signs of eutrophication (Tsirtsis and Karydis, 1998; Wang et al., 2004; Rodrigues et al., 2019), which is based entirely on the negative N-Dc relationships. For example, Baula et al. (Baula et al., 2011) have used *S* of cysts to reflect the changes in nutrients caused by maricultural activities. Keskes et al. (Keskes et al., 2020) have evaluated the eutrophication in coastal ecosystem using to *H'* of cysts. Pospelova et al. (Pospelova et al., 2002; Pospelova et al., 2005) used *S* and Fisher's α of cysts as indicators of environmental conditions in estuarine systems. Finally, some studies have shown the very weak relationships between diversity and biomass (Currie and Fritz, 1993; Gough et al., 1994; Bedford et al., 1999; Enquist and Niklas, 2001; Currie et al., 2004), which indicates that species diversity may not be determined by the effect of nutrient enrichment on productivity or biomass. Accordingly, the negative N-Dc relationships repeatedly found by empirical investigations imply the possibility that traditional theories of the relationships between nutrients and phytoplankton diversity are still need to be further discussed, or at least the links of diversity with productivity (or biomass) are need to be carefully reconsidered (Currie et al., 2004; Brown, 2014).

Although the negative N-Dc relationships have been supported by many studies (Wang et al., 2004; Rodrigues et al., 2019; Keskes et al., 2020), the explanations for their intrinsic causes were rarely concerned (Liu et al., 2012; Price et al., 2017; Rodrigues et al., 2022). Previous studies mostly focused on the application of diversity as the indicator of eutrophication (Baula et al., 2011; Rodrigues et al., 2022; Shen et al., 2023), such as the comparison of usefulness between diversity and other ecological indicators for assessing eutrophication (Kitsiou and Karydis, 2011; Garmendia et al., 2013) and the evaluation of the efficiency of different diversity metrics to describe trophic levels (Tsirtsis and Karydis, 1998; Danilov and Ekelund, 2001; Spatharis and Tsirtsis, 2010). Actually, it is interesting to note that the negative relationships between nutrients and diversity have also been found in many taxa of marine and terrestrial systems (Morris, 1991; Vitousek,

1994; Elser et al., 2009; Cleland and Harpole, 2010; Kitsiou and Karydis, 2011). For example, Borer et al. (Borer et al., 2014) have manipulated a factorial experiment on herbaceous plants and found that nutrient addition caused declines in diversity. Soons et al. (Soons et al., 2017) compared effects of NO_3 and PO_4 on diversity of terrestrial ecosystems, and they suggested that nutrients enrichment had widespread and strong negative effects on plant diversity. Therefore, it seems reasonable to speculate that such negative relationships may be caused by some general concepts of ecology, such as resource competition or allometric scaling laws (West et al., 1997; Adjou et al., 2012; Borer et al., 2014). If this speculation holds true, the analysis of the N-Dc relationships according to these concepts will be useful to understand the mechanisms determining species diversity.

The frequency distributions of diversity show that the interval with the highest percentage of p is [1.03 1.71), and its average and median value are 1.73 ± 0.62 and 1.58, respectively. In previous studies, Su (Su, 2018) found very similar results using eight datasets that represented bird, mammal, insect, plant and plankton taxa. His study showed that the interval with the highest percentage of p mostly appeared close to 1, and the average and median value for all taxa were 1.11 ± 0.00 and 1.03, respectively (Su, 2018). Although dinoflagellate cysts and other taxa are from very different ecosystems, their frequency distributions of p all aggregate around 1 [Figure 3 and (Su, 2018)]. According to *Eq.* 4, when p approaches 1, SAD (N_r/N_1) will be 1: 1/2: 1/3… that is consistent with Zipf's law (Zipf, 1949). Accordingly, diversity of dinoflagellate cysts, as many other taxa, is more likely to appear 1: 1/2: 1/3…, which means that there may be a similar mechanism that structures SAD in the community.

To elucidate this pattern, Su (Su, 2018) proposed two hypotheses (hereafter called the entropy hypothesis). H_1: The total energy (E_T) in a community was finite; H_2: Species diversity was determined by the entropy that increased with the energy transformation. According to H_1, N_T/N_1 (N_T is the total abundance in a community) is finite, as N_T is usually equivalent to E_T (Su, 2018). The finiteness of N_T/N_1 determines that p ought to be higher than 1 ($N_T/N_1 = \sum_{r=1}^{\infty} r^{-p}$ converges only when $p > 1$) (Su, 2018). Since a lower p represents a higher species diversity, $p = 1$ (N_r/N_1 is 1: 1/2: 1/3…) will be the theoretical maximum of diversity presented by the fractal model (Su, 2016). On the one hand, the p distribution of dinoflagellate cysts mostly appears close to 1 (Figure 3). On the other hand, the nonlinear regressions of the relationships between nutrients and p tend to be flat and do not exceed 1 (Figure 2). Thus, this study supposes that diversity of cysts with decreasing nutrients is more likely to approach the maximum 1: 1/2: 1/3….

The frequency distributions of *S, H', D* and *J* also indicate that they are mainly aggregated in the particular intervals that are (12.50 16.07], (1.73, 2.11], (0.19, 0.32] and (0.68, 0.80]. However, previous studies rarely focused on the frequency distributions of these metrics, and almost none of them proposed that these intervals had any particular significance of ecology (Liu et al., 2012; Price et al., 2017; Rodrigues et al., 2022). Thus, it is hard to conclude that *S*, *H'*, *D* and *J* with decreasing nutrient concentrations will converge to an extreme value similar to p. This is the difference between the N-Dc relationships presented by p and the other metrics, noting that $p = 1$ is the special case of the fractal model (Su, 2018), while such particular values for other metrics have not been demonstrated by previous studies (Liu et al., 2012; Price et al., 2017; Rodrigues et al., 2022).

Finally, when the samples of cysts are used to explore the relationships between nutrients and diversity of dinoflagellates, there are some influences that are not taken into account by this study. (1) The cyst-producing species include autotrophs, heterotrophs and mixotrophs (Baula et al., 2011; Price et al., 2017). (2) Diversity of dinoflagellates are also affected by other factors including, sea surface salinity, temperature and coastal upwelling events (Dale, 2009; Chen et al., 2011). (3) The cysts record at some site usually represents 30-40% of the species included in local plankton (Pospelova et al., 2002; Dale, 2009). Thus, the results and conclusions of this study may be affected by these points. Additionally, some other algas (such as diatoms) were also frequently used as indictor of eutrophication (Kitsiou and Karydis, 2011; Blanco et al., 2012). In the future, it is very necessary to further test and verify the negative relationships between nutrients and diversity (especially the maximum 1: 1/2: 1/3…) using the dinoflagellate and other algae samples.

Conclusion

This study suggests that the relationships between inorganic nutrient concentrations and diversity of dinoflagellate cysts (including richness, dominance, evenness and SAD) are negative over a wide range of nutrient concentrations (Table 1 and Figures 1, 2). This is consistent with the most previous empirical studies, which further supports that low diversity indices could be considered as a signal of eutrophication (Tsirtsis and Karydis, 1998; Wang et al., 2004; Rodrigues et al., 2019; Keskes et al., 2020). Different from previous studies of dinoflagellate cysts, this study finds a new pattern of the N-Dc relationship that diversity of cysts with decreasing nutrient concentrations appear to gradually approach the maximum 1: 1/2: 1/3…. This is a general SAD presented by fractal model that is supported by many taxa (Su, 2018). Thus, if this new pattern can be verified by more investigations, maintaining diversity at nearly this maximum value can be one of the goals of coastal management. Additionally, analyzing the N-Dc relationship

according to their intrinsic mechanism is expected to help quantitative identification of the quality of the coastal environment and even understand the general mechanisms determining diversity.

Data availability statement

The datasets presented in this study can be found in online repositories. The names of the repository/repositories and accession number(s) can be found in the article/Supplementary Material. The code supporting the results in the paper have been archived in Figshare (https://doi.org/10.6084/m9.figshare.21437694.v2).

Author contributions

QS conceived, designed this study. JG developed the mathematical models and performed statistical analyses. JG and QS wrote the manuscript. All authors contributed to the article and approved the submitted version.

Funding

This work was supported by the National Natural Science Foundation of China (Grant Nos. 42071137 and 41676113). The funders had no role in study design, data collection and analysis, decision to publish, or preparation of the manuscript.

Conflict of interest

The authors declare that the research was conducted in the absence of any commercial or financial relationships that could be construed as a potential conflict of interest.

Publisher's note

All claims expressed in this article are solely those of the authors and do not necessarily represent those of their affiliated organizations, or those of the publisher, the editors and the reviewers. Any product that may be evaluated in this article, or claim that may be made by its manufacturer, is not guaranteed or endorsed by the publisher.

Supplementary material

The Supplementary Material for this article can be found online at: https://www.frontiersin.org/articles/10.3389/fmars.2022.1089331/full#supplementary-material

References

Adjou, M., Bendtsen, J., and Richardson, K. (2012). Modeling the influence from ocean transport, mixing and grazing on phytoplankton diversity. *Ecol. Model.* 225, 19–27. doi: 10.1016/j.ecolmodel.2011.11.005

Arellano, G., Umaña, M. N., Macía, M. J., Loza, M. I., Fuentes, A., Cala, V., et al. (2017). The role of niche overlap, environmental heterogeneity, landscape roughness and productivity in shaping species abundance distributions along the Amazon–Andes gradient. *Global Ecol. Biogeogr* 26 (2), 191–202. doi: 10.1111/geb.12531

Baula, I. U., Azanza, R. V., Fukuyo, Y., and Siringan, F. P. (2011). Dinoflagellate cyst composition, abundance and horizontal distribution in bolinao, pangasinan, northern Philippines. *Harmful Algae* 11, 33–44. doi: 10.1016/j.hal.2011.07.002

Bedford, B. L., Walbridge, M. R., and Aldous, A. (1999). Patterns in nutrient availability and plant diversity of temperate north American wetlands. *Ecology* 80 (7), 2151–2169. doi: 10.1890/0012-9658(1999)080[2151:PINAAP]2.0.CO;2

Blanco, S., Cejudo-Figueiras, C., Tudesque, L., Bécares, E., Hoffmann, L., and Ector, L. (2012). Are diatom diversity indices reliable monitoring metrics? *Hydrobiologia* 695 (1), 199–206. doi: 10.1007/s10750-012-1113-1

Borer, E. T., Seabloom, E. W., Gruner, D. S., Harpole, W. S., Hillebrand, H., Lind, E. M., et al. (2014). Herbivores and nutrients control grassland plant diversity *via* light limitation. *Nature* 508 (7497), 517–520. doi: 10.1038/nature13144

Bouimetarhan, I., Marret, F., Dupont, L., and Zonneveld, K. (2009). Dinoflagellate cyst distribution in marine surface sediments off West Africa (17–6 n) in relation to sea-surface conditions, freshwater input and seasonal coastal upwelling. *Mar. Micropaleontol* 71 (3-4), 113–130. doi: 10.1016/j.marmicro.2009.02.001

Brown, J. H. (2014). Why are there so many species in the tropics? *J. biogeogr* 41 (1), 8–22. doi: 10.1111/jbi.12228

Chen, B., Irwin, A. J., and Finkel, Z. V. (2011). Biogeographic distribution of diversity and size-structure of organic-walled dinoflagellate cysts. *Mar. Ecol. Prog. Ser.* 425, 35–45. doi: 10.3354/meps08985

Cleland, E. E., and Harpole, W. S. (2010). Nitrogen enrichment and plant communities. *Ann. New York Acad. Sci.* 1195 (1), 46–61. doi: 10.1111/j.1749-6632.2010.05458.x

Currie, D. J., and Fritz, J. T. (1993). Global patterns of animal abundance and species energy use. *Oikos* 67, 56–68. doi: 10.2307/3545095

Currie, D., Mittelbach, G., Cornell, H., Field, R., Guégan, J.-F., Hawkins, B., et al. (2004). Predictions and tests of climate-based hypotheses broad-scale variation in taxonomic richness. *Ecol. Lett.* 7, 1121–1134. doi: 10.1111/j.1461-0248.2004.00671.x

Dale, B. (2009). Eutrophication signals in the sedimentary record of dinoflagellate cysts in coastal waters. *J. Sea Res.* 61 (1-2), 103–113. doi: 10.1016/j.seares.2008.06.007

Danilov, R. A., and Ekelund, N. G. A. (2001). Comparative studies on the usefulness of seven ecological indices for the marine coastal monitoring close to the shore on the Swedish East coast. *Environ. Monit. Assess.* 66 (3), 265–279. doi: 10.1023/A:1006364317956

Ellegaard, M., Dale, B., Mertens, K. N., Pospelova, V., and Ribeiro, S. (2017). "Dinoflagellate cysts as proxies for Holocene environmental change in estuaries: Diversity, abundance and morphology," in *Applications of paleoenvironmental techniques in estuarine studies*. Eds. K. Weckström, K. M. Saunders, P. A. Gell and C. G. Skilbeck (Dordrecht: Springer Netherlands), 295–312.

Elser, J. J., Bracken, M. E. S., Cleland, E. E., Gruner, D. S., Harpole, W. S., Hillebrand, H., et al. (2007). Global analysis of nitrogen and phosphorus limitation of primary producers in freshwater, marine and terrestrial ecosystems. *Ecol. Lett.* 10 (12), 1135–1142. doi: 10.1111/j.1461-0248.2007.01113.x

Elser, J. J., Kyle, M., Steger, L., Nydick, K. R., and Baron, J. S. (2009). Nutrient availability and phytoplankton nutrient limitation across a gradient of atmospheric nitrogen deposition. *Ecology* 90 (11), 3062–3073. doi: 10.1890/08-1742.1

Enquist, B. J., and Niklas, K. J. (2001). Invariant scaling relations across tree-dominated communities. *Nature* 410 (6829), 655–660. doi: 10.1038/35070500

Esper, O., and Zonneveld, K. A. (2007). The potential of organic-walled dinoflagellate cysts for the reconstruction of past sea-surface conditions in the southern ocean. *Mar. Micropaleontol* 65 (3-4), 185–212. doi: 10.1016/j.marmicro.2007.07.002

Feng, G., Huang, J., Xu, Y., Li, J., and Zang, R. (2021). Disentangling environmental effects on the tree species abundance distribution and richness in a subtropical forest. *Front. Plant Sci.* 12. doi: 10.3389/fpls.2021.622043

Gao, J., and Su, Q. (2022). The relationship between diversity and nutrient concentrations. doi: 10.6084/m9.figshare.21437694.v2

Garmendia, M., Borja, Á., Franco, J., and Revilla, M. (2013). Phytoplankton composition indicators for the assessment of eutrophication in marine waters: Present state and challenges within the European directives. *Mar. pollut. Bull.* 66 (1-2), 7–16. doi: 10.1016/j.marpolbul.2012.10.005

Gough, L., Grace, J. B., and Taylor, K. L. (1994). The relationship between species richness and community biomass: the importance of environmental variables. *Oikos* 70 (2), 271–279. doi: 10.2307/3545638

Gurdebeke, P. R., Pospelova, V., Mertens, K. N., Dallimore, A., Chana, J., and Louwye, S. (2018). Diversity and distribution of dinoflagellate cysts in surface sediments from fjords of western Vancouver island (British Columbia, Canada). *Mar. Micropaleontol* 143, 12–29. doi: 10.1016/j.marmicro.2018.07.005

Irigoien, X., Huisman, J., and Harris, R. P. (2004). Global biodiversity patterns of marine phytoplankton and zooplankton. *Nature* 429 (6994), 863–867. doi: 10.1038/nature02593

Keskes, F. A., Ayadi, N., Atoui, A., Mahfoudi, M., Abdennadher, M., Walha, L. D., et al. (2020). Dinoflagellates encystment with emphasis on blooms in boughrara lagoon (South-Western mediterranean): Combined effects of trace metal concentration and environmental context. *Estuarine Coast. Shelf Sci.* 237, 106648. doi: 10.1016/j.ecss.2020.106648

Kitsiou, D., and Karydis, M. (2011). Coastal marine eutrophication assessment: a review on data analysis. *Environ. Int.* 37 (4), 778–801. doi: 10.1016/j.envint.2011.02.004

Liu, D., Shi, Y., Di, B., Sun, Q., Wang, Y., Dong, Z., et al. (2012). The impact of different pollution sources on modern dinoflagellate cysts in sishili bay, yellow Sea, China. *Mar. Micropaleontol* 84, 1–13. doi: 10.1016/j.marmicro.2011.11.001

Marret, F., and Zonneveld, K. A. (2003). Atlas of modern organic-walled dinoflagellate cyst distribution. *Rev. Palaeobotany Palynology* 125 (1-2), 1–200. doi: 10.1016/S0034-6667(02)00229-4

Morris, J. T. (1991). *Effects of nitrogen loading on wetland ecosystems with particular reference to atmospheric deposition* (San Mateo, California: Annual Reviews).

Oksanen, J., Blanchet, F. G., Friendly, M., Kindt, R., Legendre, P., McGlinn, D., et al. (2020) *Vegan: Community ecology package. r package version 2.5-6. 2019*. Available at: https://scholar.google.com/scholar?cluster=11712188988930644900&hl=en&oi=scholarr.

Orlova, T. Y., Morozova, T. V., Gribble, K. E., Kulis, D. M., and Anderson, D. M. (2004). Dinoflagellate cysts in recent marine sediments from the east coast of Russia. *Botanica Marina* 47 (3), 184–201. doi: 10.1515/BOT.2004.019

Penaud, A., Hardy, W., Lambert, C., Marret, F., Masure, E., Servais, T., et al. (2018). Dinoflagellate fossils: Geological and biological applications. *Rev. Micropaléontologie* 61 (3-4), 235–254. doi: 10.1016/j.revmic.2018.09.003

Pielou, E. (1975). *Ecological diversity* (New York: Wiley).

Pospelova, V., Chmura, G. L., Boothman, W. S., and Latimer, J. S. (2002). Dinoflagellate cyst records and human disturbance in two neighboring estuaries, new Bedford harbor and apponagansett bay, Massachusetts (USA). *Sci. Total Environ.* 298 (1-3), 81–102. doi: 10.1016/S0048-9697(02)00195-X

Pospelova, V., Chmura, G. L., Boothman, W. S., and Latimer, J. S. (2005). Spatial distribution of modern dinoflagellate cysts in polluted estuarine sediments from buzzards bay (Massachusetts, USA) embayments. *Mar. Ecol. Prog. Ser.* 292, 23–40. doi: 10.3354/meps292023

Price, A. M., Coffin, M. R., Pospelova, V., Latimer, J. S., and Chmura, G. L. (2017). Effect of nutrient pollution on dinoflagellate cyst assemblages across estuaries of the NW Atlantic. *Mar. Pollut. Bull.* 121 (1-2), 339–351. doi: 10.1016/j.marpolbul.2017.06.024

Rodrigues, R., Patil, J., and Anil, A. (2022). Dinoflagellates cyst assemblage concerning trophic index for eutrophication from major ports along the west coast of India. *Mar. Pollut. Bull.* 176, 113423. doi: 10.1016/j.marpolbul.2022.113423

Rodrigues, R., Patil, J., Sathish, K., and Anil, A. (2019). Dinoflagellate planktonic-motile-stage and benthic-cyst assemblages from a monsoon-influenced tropical harbour: Elucidating the role of environmental conditions. *Estuarine Coast. Shelf Sci.* 226, 106253. doi: 10.1016/j.ecss.2019.106253

Sangiorgi, F., and Donders, T. H. (2004). Reconstructing 150 years of eutrophication in the north-western Adriatic Sea (Italy) using dinoflagellate cysts, pollen and spores. *Estuarine Coast. Shelf Sci.* 60 (1), 69–79. doi: 10.1016/j.ecss.2003.12.001

Shen, P.-P., Li, Y., Tang, Y.-N., Song, Q.-S., and Xue, Y. (2023). Sedimentary dinoflagellate cyst records of human-induced environmental changes in daya bay, the northern south China Sea. *J. Mar. Syst.* 237, 103823. doi: 10.1016/j.jmarsys.2022.103823

Soons, M. B., Hefting, M. M., Dorland, E., Lamers, L. P., Versteeg, C., and Bobbink, R. (2017). Nitrogen effects on plant species richness in herbaceous communities are more widespread and stronger than those of phosphorus. *Biol. Conserv.* 212, 390–397. doi: 10.1016/j.biocon.2016.12.006

Spatharis, S., and Tsirtsis, G. (2010). Ecological quality scales based on phytoplankton for the implementation of water framework directive in the Eastern Mediterranean. *Ecol. Indic.* 10 (4), 840–847. doi: 10.1016/j.ecolind.2010.01.005

Su, Q. (2016). Analyzing fractal property of species abundance distribution and diversity indexes. *J. Theor. Biol.* 392, 107–112. doi: 10.1016/j.jtbi.2015.12.010

Su, Q. (2018). A general pattern of the species abundance distribution. *PeerJ* 6, 1–11. doi: 10.7717/peerj.5928

Tsirtsis, G., and Karydis, M. (1998). Evaluation of phytoplankton community indices for detecting eutrophic trends in the marine environment. *Environ. Monit. Assess.* 50 (3), 255–269. doi: 10.1023/A:1005883015373

Vásquez-Bedoya, L., Radi, T., Ruiz-Fernández, A., De Vernal, A., Machain-Castillo, M., Kielt, J., et al. (2008). Organic-walled dinoflagellate cysts and benthic foraminifera in coastal sediments of the last century from the gulf of tehuantepec, south pacific coast of Mexico. *Mar. Micropaleontol* 68 (1-2), 49–65. doi: 10.1016/j.marmicro.2008.03.002

Villa, P. M., Martins, S. V., Rodrigues, A. C., Safar, N. V. H., Bonilla, M. A. C., and Ali, A. (2019). Testing species abundance distribution models in tropical forest successions: implications for fine-scale passive restoration. *Ecol. Eng.* 135, 28–35. doi: 10.1016/j.ecoleng.2019.05.015

Vitousek, P. M. (1994). Beyond global warming: ecology and global change. *Ecology* 75 (7), 1861–1876. doi: 10.2307/1941591

Wang, Z., Matsuoka, K., Qi, Y., Chen, J., and Lu, S. (2004). Dinoflagellate cyst records in recent sediments from daya bay, south China Sea. *Phycol Res.* 52 (4), 396–407. doi: 10.1111/j.1440-183.2004.00357.x

West, G. B., Brown, J. H., and Enquist, B. J. (1997). A general model for the origin of allometric scaling laws in biology. *Science* 276 (5309), 122–126. doi: 10.1126/science.276.5309.122

Zonneveld, K. A., Marret, F., Versteegh, G. J., Bogus, K., Bonnet, S., Bouimetarhan, I., et al. (2013). Atlas of modern dinoflagellate cyst distribution based on 2405 data points. *Rev. Palaeobotany Palynology* 191, 1–197. doi: 10.1016/j.revpalbo.2012.08.003

frontiers | Frontiers in Marine Science

TYPE Original Research
PUBLISHED 16 January 2023
DOI 10.3389/fmars.2022.1096307

OPEN ACCESS

EDITED BY
Qiuying Han,
Hainan Tropical Ocean University, China

REVIEWED BY
Peidong Zhang,
Ocean University of China, China
Le-Zheng Qin,
Hainan University, China

*CORRESPONDENCE
Kirk Cammarata
Kirk.Cammarata@tamucc.edu

SPECIALTY SECTION
This article was submitted to Coastal Ocean Processes, a section of the journal Frontiers in Marine Science

RECEIVED 12 November 2022
ACCEPTED 19 December 2022
PUBLISHED 16 January 2023

CITATION
Huang C, Piñón C, Mehrubeoglu M and Cammarata K (2023) Image analysis reveals environmental influences on the seagrass-epiphyte dynamic relationship for *Thalassia testudinum* in the northwestern Gulf of Mexico.
Front. Mar. Sci. 9:1096307.
doi: 10.3389/fmars.2022.1096307

Image analysis reveals environmental influences on the seagrass-epiphyte dynamic relationship for *Thalassia testudinum* in the northwestern Gulf of Mexico

Chi Huang[1], Carissa Piñón[1], Mehrube Mehrubeoglu[2] and Kirk Cammarata[1]*

[1]Department of Life Sciences, Texas A&M University-Corpus Christi, Corpus Christi, TX, United States, [2]Department of Engineering, Texas A&M University-Corpus Christi, Corpus Christi, TX, United States

Spatiotemporal patterns in seagrass-epiphyte dynamics for *Thalassia testudinum* in the northwestern Gulf of Mexico were evaluated through biomass measurements and scanned-image based metrics to investigate the potentially harmful impact of excessive epiphyte accumulations on seagrass condition. Image analysis with Spectral Angle Mapper algorithms distinguished epiphyte and uncovered seagrass leaf pixels to generate a normalized metric of leaf area coverage (epiphyte pixels/total leaf pixels). Imaging metrics were compared to biomass-based metrics seasonally, among three locations with different environmental conditions (depth, salinity, temperature and nutrient levels inferred from sediment porewater measurements) near Redfish Bay, Texas, USA. Image analysis, in conjunction with biomass measures, provides enhanced insight into the seagrass-epiphyte dynamic relationship and how it varies with environmental conditions. Compared with the biomass and morphological measures, image analysis may be more informative as an indicator of environmental changes. Variation in linear regressions of epiphyte biomass *vs.* epiphyte area (pixels) suggested changes in the thickness and/or density of accumulated epiphytes across environmental contexts and seasons. Two different epiphyte colonization patterns were presented based on the correlation between the normalized metrics of epiphyte load and epiphyte leaf coverage. The epiphyte load was highest at low temperatures and locations with elevated DIN:P ratio in sediment porewater.

Conversely, the mean leaf coverage by epiphytes stayed relatively constant (± 10%) across seasons but differed by location (25% ~55% in this case), suggesting that leaf growth in this study is regulated to maintain the proportion of uncolonized leaf surface and that epiphyte coverage plays a role in its regulation.

KEYWORDS

epiphyte-seagrass dynamics, image analysis, *Thalassia testudinum*, environmental conditions, epiphyte abundance, seagrass, nutrients, indicator

1 Introduction

As major primary producers, seagrasses rank high in their nutrient cycling ability and their economic value per hectare (Costanza et al., 1997; Dewsbury et al., 2016). Seagrass beds enhance biodiversity and provide ideal habitat and abundant food sources for marine organisms in different life stages, including commercially important species (Wolaver et al., 1980; Heck et al., 1997; Orth et al., 2006a; van Katwijk et al., 2016). The roles of nutrient filtration and blue carbon storage by seagrass beds further demonstrate the importance of seagrasses in coastal ecosystems (Hemminga and Duarte, 2000; Greiner et al., 2013). Seagrass reintroduction has been shown to enhance ecosystem functions worldwide, including habitat improvement and fisheries recoveries (Orth et al., 2006b; Bell et al., 2008; Greening et al., 2011; Bell et al., 2014; Katwijk et al., 2016). One of the most critical components of the seagrass ecosystem is epiphytes, which include large amounts of microorganisms, algae, and invertebrates attaching and growing on the surface of seagrass leaves (Humm, 1964; Corlett and Jones, 2007; Michael et al., 2008; Frankovich et al., 2009). The epiphytic algae provide primary food resources for the invertebrates in seagrass meadows (Kitting et al., 1984; Nielsen and Lethbridge, 1989). However, the seagrasses are not only just simple substrata for epiphytes (Pinckney and Micheli, 1998). Recent work (Crump et al., 2018) has dramatically illuminated the complex biochemical interactions between epiphytes and their hosts. In a successional pattern, diatoms and other microorganisms attach directly to the seagrass leaves, followed by a variety of red, green, and brown algae, some filamentous and some coralline (Corlett and Jones, 2007). Each of these epiphytes provides additional surfaces which can be utilized for secondary colonization by other algae. A significant component of the epiphytic biofilm is comprised of invertebrates, some of which consume the epiphytic algae and some just take advantage of the substrate (Moncreiff et al., 1992; Heck and Valentine, 2006; Peterson et al., 2007; Whalen et al., 2013).

Although seagrass epiphytes play an essential role in the primary production of the seagrass ecosystem, excessive accumulations of epiphytes compete with seagrass for light, nutrients and oxygen (Sand-Jensen, 1977; Duarte, 1995; Noisette et al., 2020; Brodersen and Kühl, 2022). Light attenuation is the primary driver limiting seagrass growth by decreasing photosynthesis and oxygen diffusion into roots (Lee and Dunton, 2000; Koch and Erskine, 2001; Ralph et al., 2007; O'Brien et al., 2018). Eutrophication stress enhances the growth of epiphytic algae to reduce light availability, with adverse effects on photosynthesis (Dennison and Alberte, 1982; Bulthuis and Woelkerling, 1983; Lee and Dunton, 1997; Ow et al., 2020), nutrient uptake processes (McGlathery, 2001; Armitage et al., 2005; Noisette et al., 2020) and species diversity in seagrass meadows (Moore and Wetzel, 2000; Peterson et al., 2007). More epiphyte biomass and less light availability were found along a gradient of external nitrogen loading, and epiphyte accumulation was limited by available nitrogen and phosphorus concentration (Wright et al., 1995; Johnson et al., 2006). Grazers exert top-down control of epiphytes, impacting seagrass productivity (Heck and Valentine, 2006). Nutrition content or algal chemical defenses affect feeding preferences and can deter grazing (Nielsen and Lethbridge, 1989; Crump et al., 2018). Such loss of top-down control increases epiphyte abundance and reduces the light required for seagrass growth.

Hence, understanding the epiphyte-seagrass dynamics under multiple biotic and abiotic factors may illuminate the influence of environmental conditions on the health of seagrass ecosystems. However, it has been argued that epiphyte abundance and composition are limited in predicting seagrass loss and thus has limited utility as an environmental indicator of nutrients (Worm and Sommer, 2000; Cambridge et al., 2007; Fourqurean et al., 2010). These complex epiphyte communities are spatiotemporally dynamic (Whalen et al., 2013). Epiphyte community structure on *Thalassia testudinum* at Grand Cayman (Corlett and Jones, 2007) was different from that for Florida Bay (Frankovich et al., 2009). Additional variation with seasons and environmental conditions have been noted for epiphytic algae and invertebrates (Novak, 1982; Borum, 1985; Armitage et al., 2005; Hasegawa et al., 2007; Peterson et al., 2007; Whalen et al., 2013). Multiple studies of nutrient impacts on

seagrass response showed that nutrient levels alone could affect the growth of seagrass and associated epiphytes, but the effects were highly variable between studies (Frankovich and Fourqurean, 1997; Moore and Wetzel, 2000; Worm and Sommer, 2000; Armitage et al., 2005; Johnson et al., 2006). However, none of these studies teased apart relationships for seagrass leaves in the growth *vs.* dying phases, and the methods employed were spatiotemporally limited.

The dominant methods to monitor the response of seagrass growth and epiphyte accumulation focus on biomass, including dry weight biomass, ash-free dry weight biomass, or chlorophyll *a* and b, and other pigments (Heijs, 1984; Pinckney and Micheli, 1998; Armitage et al., 2006; Peterson et al., 2007; Smith et al., 2018). The epiphytes are typically scraped gently from seagrass for biomass analysis (Libes, 1986; Ray et al., 2014) but weak acid or chelators can also be used to more effectively remove organisms (Zimba and Hopson, 1997) However, the traditional biomass measures fail to provide detailed information on the complex relationship between epiphytes and seagrass because high-resolution spatiotemporal leaf coverage information is lost. Since an individual seagrass leaf may persist for months, the morphological and physiological states of the leaf and epiphytes provide a temporally integrated record of any environmental conditions which impact their relationship. Nevertheless, traditional dry weight biomass metrics present single values that represent variable periods exceeding a month. Previous studies using biomass measurements recognized, but did not fully capture the dynamic spatiotemporal information of epiphyte distribution on the seagrass leaves (Bulthuis and Woelkerling, 1983; Borum, 1987; Biber et al., 2004; Atmaja et al., 2021) because of temporally-limited sampling and the spatial limitations of the biomass measures.

A novel imaging-based technology was developed (Huang, 2020) to obtain more detailed spatiotemporal analysis of the dynamic epiphyte-seagrass relationship. Many plant studies, such as the evaluation of algal communities' recruitment and composition shifts, diagnosis of injured seagrass leaves, bacterial aggregation on leaf surfaces, and shoot biomass estimation, have been investigated *via* image analyses (Monier and Lindow, 2004; Boese et al., 2008; Fikes and Lehman, 2008; Golzarian et al., 2011; Aoki et al., 2022). Spatial patterns of seagrasses' photosynthetic efficiency were obtained by Imaging-PAM fluorometry (Ralph et al., 2005). A machine-learning approach (Pattern Recognition Software) was trained with specific features, such as the images' color, brightness, and texture, and subsequently used for feature identification (Shamir et al., 2010). Geographic Information System (GIS) technology has been applied in terrestrial epiphyte ecology research based on image analysis (Bader et al., 2000). A novel epiphyte fluorescence imaging measurement was used to measure photosynthetic accessory pigments as a proxy for epiphyte abundance (Ray et al., 2014). The widespread availability of public resources for image analysis makes these methodologies particularly attractive for seagrass and epiphyte analyses.

This study aims to characterize spatiotemporal epiphyte accumulation patterns on *Thalassia. testudinum*, a prevalent climax seagrass species in the northwestern Gulf of Mexico, and delineate the shifts in seagrass and epiphyte growth under different environmental conditions through a an accessible, scanner-based imaging method (Huang, 2020). This approach provides highly informative metrics of epiphyte accumulation profiles and seagrass morphological responses to interpret changing seagrass-epiphyte dynamics under several different environmental conditions. The spatiotemporal epiphyte accumulation patterns, along with environmental condition information such as water temperature, salinity, sediment porewater nutrient levels, and depth, were correlated to evaluate their influences on seagrass-epiphyte interactions and to test the hypothesis that image-analysis methodology can capture the corresponding spatiotemporal shifts in both seagrass morphology and epiphyte communities.

2 Materials and methods

2.1 Study sites

The seagrass study sites were located near the Redfish Bay State Scientific Area in Aransas Pass, Texas, USA (Figure 1). The study location is bounded by the City of Aransas Pass Wastewater Treatment Plant on the northwest, the Intracoastal Waterway (ICWW) to the southeast, and centered around the ICW RV Park. Three study areas were selected based on perceived differences in epiphyte communities on the monotypic *Thalassia testudinum* beds in areas with different exposures to nutrient sources (Figure 1; Table 1). The WWTP area received direct discharge of treated wastewater effluent (WWTP; Shallow: N 97.14861, W -27.88485; Medium: N 97.14790, W -27.88467; Deep: N 97.14761, W -27.88435). There were additional possible impacts from a fish cleaning station and associated feeding and roosting of pelicans. The "Control" area received indirect discharge of treated wastewater effluent that was additionally polished by wetlands ("Control"; Shallow: N 97.15044, W -27.88053; Deep: N 97.15002, W -27.88021). Both WWTP and "Control" areas were near mangrove stands as well. A third site called CI was near the "Control" area, but distal to the wetland. It had additional potential impacts from an adjacent subtidal oyster bed and the ICWW channel (CI; N 097.15044, W -27.88485) Site CI is impacted by boat and barge wake that washes over the shallow oyster reef. It is the most shallow site, with visibly higher epiphyte accumulations. All sampling

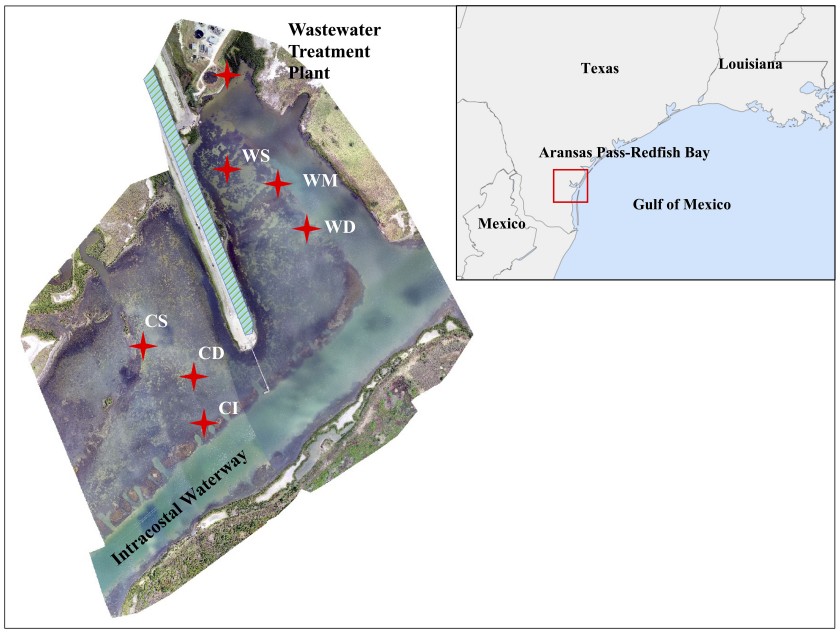

FIGURE 1
Aransas Pass-Redfish Bay sampling area, USA, showing sampling sites. The "Control" area includes shallow (CS, 58.1±13.1 *cm*) and deep (CD, 82.3 ±13.4 *cm*) sites. The "WWTP" sites include shallow (WS, 67.2±17.8 *cm*), medium (WM, 79.3±16.6 cm), and deep (WD, 93.2±16.5 *cm*) sites. The CI (47.2 ±11.9 *cm*) site adjacent to the ICWW channel is also shown. The average depth ± standard deviation for each sampling site is shown in parentheses. (Aerial imagery of study area courtesy of Dr. Hua Zhang at Texas A&M University-Corpus Christi).

stations are primarily sandy mud sediment, but the CI site additionally has an abundance of embedded oyster shell. Each site was expected to differ primarily by nutrient conditions, and preliminary observations suggested differences in the epiphyte communities.

2.2 Measurement of environmental conditions

Field conditions (depth, salinity, temperature, and general observations of wind, weather, etc.) were recorded at each visit to

TABLE 1 Season data for locations-times two-way ANOVA designated by sampling date and corresponding water temperature.

Sampling Location	Season	Sampling Date	Mean Water Temperature (°C)
"Control" area and CI site	2019 Summer	2019-07-31	31.47 (±0.42)
"WWTP" area	2019 Summer	2019-08-09	29.57 (±0.68)
"Control" area and CI site	2019 Autumn	2019-08-30	30.92 (±0.68)
"WWTP" area	2019 Autumn	2019-09-11	30.27 (±0.25)
"Control" area and CI site	2019 Autumn	2019-09-25	31.40 (±0.50)
"WWTP" area	2019 Autumn	2019-10-09	29.31 (±0.24)
"Control" area and CI site	2019 Winter	2019-11-20	22.13 (±0.22)
"WWTP" area	2019 Winter	2019-12-18	16.27 (±0.44)
"Control" area and CI site	2019 Winter	2020-01-17	23.00 (±0.00)
"WWTP" area	2019 Winter	2020-02-22	17.57 (±0.41)
"Control" area and CI site	2020 Spring	2020-04-30	24.37 (±0.48)
"WWTP" area	2020 Spring	2020-04-19	23.00 (±0.00)

Values of water temperature are means (±SE).

each sampling site to provide contextual information on factors that may affect seagrass condition and epiphyte. Depth was measured with a calibrated PVC pole. Salinity was measured using a refractometer (VEE GEE, STX-3), under standard conditions in the laboratory, on 50 mL water samples collected at seagrass canopy depth, without headspace. The temperature of the water column near the seagrass canopy height was measured with a calibrated thermometer.

Sediment for porewater analysis was sampled in May 2020 in triplicate from the six sampling sites (Figure 1) using a 10 cm inner diameter PVC corer inserted to a depth of 20 cm. Sediments from a zone of 5-15 cm depth, which represents the root zone of the seagrass, was collected from the cores and centrifuged at 5000g for 20 minutes at 4°C for porewater extraction. After centrifugation, supernatants were filtered through VWR glass microfiber filters, grade 696 (particle retention: 1.2µm). The filtrates were stored at -25°C and shipped frozen for nutrient analyses at the University of California-Davis (UC Davis) Analytical Lab (Davis, CA, USA). Nutrient analyses included ammonium (NH_4^+), Nitrate (NO_3^-), total dissolved inorganic nitrogen (DIN), and phosphate (PO_4^{3-}). The nutrient levels of sediment porewater measured at this single time are considered to be an indicator of long-term relative nutrient exposure at each site.

2.3 Seagrass and epiphyte sampling and processing

The epiphyte-seagrass dynamics were quantified by biomass measurements and image-based metrics (Huang, 2020). Shoots of *Thalassia testudinum* were collected monthly or bimonthly at the six sampling locations from 2019 summer to 2020 spring. Regular sampling (at least bimonthly) across different seasons was necessary to capture the morphological response of seagrass in relation to accumulation patterns of epiphytes. The volume and time requirements of seagrass processing work necessitated that sampling in the "Control" and WWTP areas be staggered at approximately two- to three-week intervals. Three rings made of 7.6 cm diameter PVC pipe were placed haphazardly for triplicate replication of seagrass samples. Seagrass shoots located inside the ring (an area of approximately 45 cm^2) were harvested with all leaves intact to equitably represent the morphological variation in seagrass growth and epiphyte accumulation. Collected seagrass shoots. placed into bottles without water to minimize disruption of the epiphytes, were stored dark and cold (4°C) at the lab, and imaged within 72 h.

For analyses, seagrass shoots were gently rinsed with deionized water, and the green portion of each individual leaf was measured for length and width and arranged on a fluid mount tray (Epson, Carson, CA) for imaging. As needed, microscope slides were used to weigh down twisted seagrass leaves to lie flat. Leaf images were captured by the Epson Perfection V-750 Pro color flatbed scanner (Epson, Carson, CA) using 24-bit color scanning at 1200 dpi resolution. After scanning, epiphytes were removed from each seagrass blade by scraping with a microscope slide. Epiphytes were quantitatively transferred to a pre-weighed empty aluminum dish. The epiphytes and epiphyte-free seagrass were dried to constant weight at 60°C to measure the biomass of each individual leaf.

2.4 Image analysis

Scanned seagrass leaf images (TIFF files) were analyzed to characterize the total leaf area, the epiphyte covered area and the uncovered leaf area (Huang, 2020). The pixels of seagrass and epiphytes on the images were classified using the spectral angle mapper (SAM) algorithm in ENVI 5.0 (L3 Harris Technologies, Niles, Ohio). Each image pixel was interpreted by a vector consisting of three hues of the light spectrum (Red band, Green band, and Blue band). The SAM algorithm distinguished the uncolonized seagrass leaf and epiphyte-covered areas based on a spectral angle between the vectors of targeted pixels and reference pixels in three-dimensional coordinates. The assignment of each pixel as seagrass or epiphyte was made using a threshold of spectral angle (< 2.3°). 482 reference pixels of seagrass, which had visually different colors due to variable growing conditions, were selected for establishing the seagrass spectral library. The epiphyte spectral library contained 843 reference pixels of epiphytes from variously colored groups of epiphytes. Finally, 2061 scanned images of each seagrass blade were analyzed *via* the seagrass and epiphyte spectral libraries.

Normalized and un-normalized biomass and image-derived metrics were evaluated. Correlations between epiphyte biomass vs. epiphyte covered area (number of epiphyte pixels), and between epiphyte load (epiphyte biomass/seagrass biomass) *vs.* leaf coverage % by epiphyte (epiphyte pixels/pixels of whole blade) were quantified by several regression models, including the linear, quadratic, power law, and the exponential models (Fong and Harwell, 1994). The best model was then selected, given the goodness of fits, such as linearity, R^2 value, the Akaike Information Criterion correction (AICc), and the intrinsic biological meaning (Johnson and Omland, 2004). The regression analyses were drawn from samples within different environmental contexts or sampling times to demonstrate their site- and seasonal- patterns *via* R version 3.6.2.

2.5 Carbon and nitrogen content and stable isotope analysis

Stable isotope analyses were performed (separately) for seagrass and epiphytes to inform the physiology and status of

T. testudinum and its epiphytes under the different environmental conditions at each sampling site. Four shoots of *T. testudinum* were collected from each of the 6 sampling sites in June 2020. The seagrass and epiphytes were processed separately as described above to obtain dried samples, which were then ground using a mortar and pestle. Leaf and epiphyte tissue content (total carbon and total nitrogen) and stable isotope ratios ($\delta^{13}C$, $\delta^{15}N$) were analyzed at the UC Davis Stable Isotope Facility (Davis, CA, USA). The mean standard deviation for reference material replicates was ±0.03 ‰ for $\delta^{15}N$ and ±0.04 ‰ for $\delta^{13}C$, and the mean absolute accuracy for calibrated reference materials was within ±0.05 ‰ for $\delta^{15}N$ and ±0.04 ‰ for $\delta^{13}C$.

2.6 Statistical methods for analysis of variance

The spatiotemporal variance of salinity, nutrient level of sediment porewater, and water temperature were tested using analysis of variance (ANOVA). Comparisons of the epiphyte-seagrass dynamics across environmental contexts from July 2019 to April 2020 were analyzed using two-way ANOVA followed by Tukey's honest significant difference. The different sampling times in the "Control" area, "WWTP" area and CI site precluded the use of ANOVA for statistical comparisons between sampling locations across six sampling times. Instead, data were reallocated to four seasons based on the sampling date and average water temperature (Table 1) to facilitate environmental comparisons. Seagrass growth response was inferred from the mean seagrass leaf biomass and mean seagrass leaf area (number of covered and uncovered leaf pixels), and the epiphyte accumulation was determined by epiphyte biomass per leaf and epiphyte covered leaf area (number of epiphyte pixels). The normalized expressions of epiphyte metrics relative to the host seagrass leaves, such as epiphyte load (epiphyte biomass/seagrass biomass) and image-derived % cover (epiphyte pixels/pixels of whole blade), were used to further understand the seagrass-epiphyte dynamic relationship spatiotemporally. A mixed model (Fixed × Random) nested ANOVA was performed to evaluate the significance of differences in epiphyte-seagrass dynamics among sites of different depths in the "Control" and "WWTP" areas separately. Variables were grouped by sampling times (random factor) nested in different 'depth' sites. Differences in the C and N content and the C and N isotope composition were compared between the sampling locations. All comparisons were analyzed using ANVOA, with significant differences between specific groups assessed using Tukey *post-hoc* test separately. All analyses were conducted *via* R version 3.6.2. with a false discovery probability of $p = 0.1$ through the "Westfall" and "Shaffer" procedures for multiple comparisons of balanced and unbalanced data, respectively (Shaffer, 1986; Westfall, 1997).

3 Results

3.1 Classification outputs of seagrass and epiphyte image analyses

A true color image of an epiphyte-covered seagrass leaf and the classified outputs derived from the seagrass and the epiphyte spectral libraries are shown in Figure 2. It takes around 15 seconds to classify a scanning image of an individual seagrass leaf. The seagrass-classified images showed 482 uncovered leaf spectral classes with different colors, including growing areas and senescing or injured areas, which presented different levels of green and yellow or brown, respectively. The epiphyte-classified images contained 843 spectral classes of variable epiphytic groups distinguished by different colors. Due to natural variation and errors of visually estimated differences

FIGURE 2
An example of seagrass blade color scans **(A)** and ENVI classification of seagrass and epiphyte (**B**, **C**, respectively). The black area represents the scanning background in image **A**, and the black areas in images **(B, C)** are the unclassified pixels using a particular spectral library. **(A)** original scanned blade; **(B)** seagrass classified Image (ENVI); **(C)** epiphyte classified image (ENVI). Images lightened by 35%.

during spectral library establishment, numerous spectral classes might characterize identical features.

3.2 Comparison of metrics for seagrass and epiphytes across all study sites

Comparison of mean values of biomass- and imaging-based metrics across all study sites for the entire study period (Figure 3) revealed similar site to site patterns (ordination) of variation. Both epiphyte metrics, biomass load and % coverage, were normalized to the amount of seagrass substrate. Although there were no significant differences in epiphyte accumulation between the WWTP and the "Control" areas, site CI exhibited significantly higher values for both biomass and imaging metrics ($p < 0.05$). Thus, both biomass- and imaging-based metrics revealed greater relative epiphyte accumulation at CI site. Leaf biomass and blade areas did not significantly differ among the CI, the CS, and the CD site across sampling times. Conversely, there was significantly lower leaf biomass at the WS site than at the WM and the WD site, respectively (Figures 3A, B; $p < 0.05$).

3.3 Environmental conditions and site comparisons

Water temperatures ranged from 16 to 32 °C and were stable in summer and early autumn (29.17~32.00 °C from July to October) (Table 1). Temperatures dropped in November and fluctuated through winter, with an average temperature of 20.75 °C. In April, the mean temperature warmed to 24.00 °C (Table 1).

Salinity levels ranged from 25 – 37 and differed significantly with seasonal change (highest in summer) ($df = 3$, $F = 31.68$, $P < 0.05$), but there was no significant difference in the mean salinity among the "Control" area, CI site, and "WWTP" area (Table S1). However, the transition from Autumn to Winter (Table 1) was accompanied by a decrease in salinity by about 8, as well as a decrease in temperature by 9-13 °C.

The depths of the study sites varied from 29 cm to 125 cm over the course of the study, with mean values ranging from 47.2 cm to 93.2 cm. The relationship of the seagrass and epiphyte metrics to variation in average depth of study sites showed only weak correlations (Figure S1; $R^2 = 0.31, 0.22$). Likewise, with the exception of pixels of leaf area, only weak correlations were

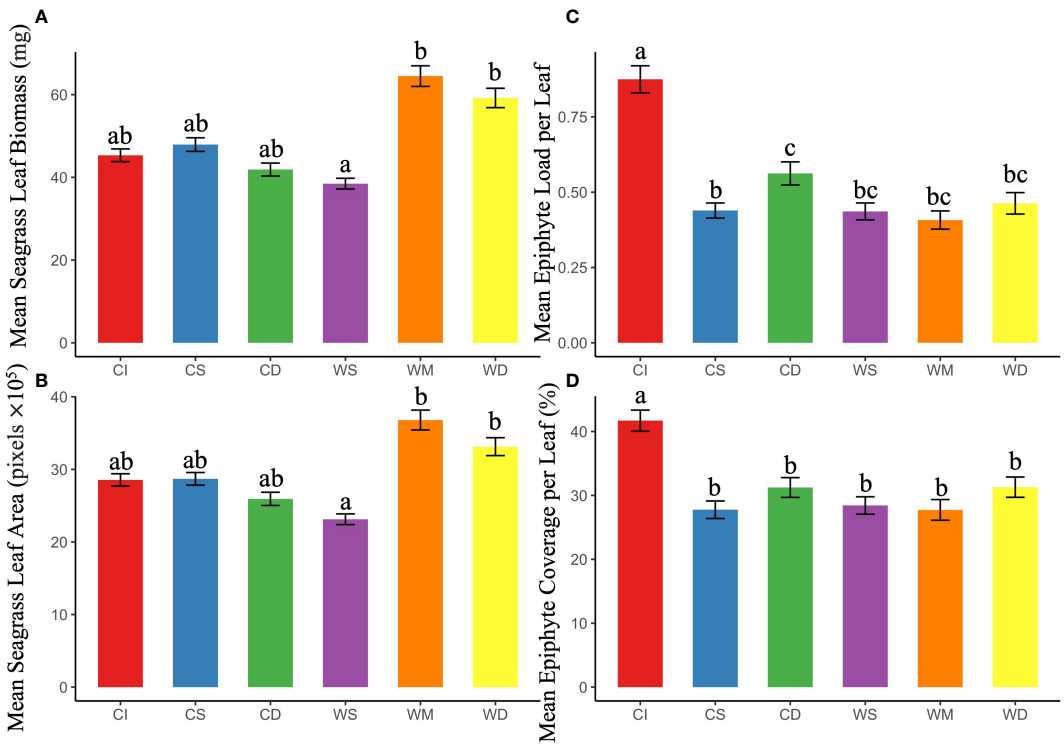

FIGURE 3
Average (+/-SE) metrics of seagrass growth **(A)** leaf biomass and **(B)** blade area, and metrics of epiphyte-seagrass dynamics **(C)** epiphyte load and **(D)** epiphyte coverage (%) of leaf and **(C)** epiphyte load at different sampling locations "Control" area, WWTP area, and CI site. For each panel, bars showing the different letters differ significantly from each other at $p < 0.05$ using Tukey's pairwise test.

observed for seagrass and epiphyte metrics with mean temperature and mean salinity (Figures S2 and S3 respectively). Divergence of the correlations of leaf area and leaf biomass metrics, with temperature and salinity indicated greater variability in the biomass data. Thus, mean depth, temperature or salinity differences do not appear to play a major role in the biomass observations.

The different potential environmental influences on each site from direct vs polished wastewater effluent, a shipping channel or oyster beds prompted an examination of relative nutrient levels. Sediment porewater nutrient levels were taken to be indicators of long-term nutrient exposure history at each site. Table 2 shows the results obtained from a measurement in May 2020. The average concentrations of nitrate (NO_3^-) and ammonium (NH_4^+) from the CI site sediment porewater were nearly 1.5 times higher than from the "Control" area. However, these differences were not significant among the three locations. The average concentration of phosphate (PO_4^{3-}) at the "WWTP" area was more than two times higher than at "Control" and CI sites ($df = 2$, $F = 8.369$, $P < 0.05$), which was significant (Table 2). The total dissolved inorganic nitrogen (DIN = NH_4^+ + NO_3^-) (45.01~68.55 µmole/L) differed among the three sampling locations but was not significant. However, ratios of DIN:P (NH_4^+ + NO_3^-: PO_4^{3-}), varied significantly from 7.82 in the "WWTP" area to 154.55 at the CI site ($df = 2$, $F = 11.93$, $P < 0.05$) (Table 2).

The tissue C and N content and stable isotope ratios were examined (Figure 4) to describe the status of epiphytes and seagrass at the environmentally unique sites. The carbon and nitrogen concentrations of seagrass were significantly higher than in corresponding epiphyte samples (Figure 4, ANOVA, $p < 0.05$). The C concentration of seagrass for the CI site was significantly higher than at the WWTP or "Control" areas. In contrast, the epiphyte C concentration was highest in the "Control" area. The N concentration of seagrass was not significantly different among the 3 locations, but the CI site had the lowest N concentration for the epiphytes. Epiphytes from the WWTP area had the lowest C/N ratio (Figure 4, ANOVA, $p < 0.05$), while seagrass did not show a significant difference in the C/N ratio among the three sampling locations.

The isotopic composition analysis of carbon ($\delta^{13}C$) demonstrated the greatest depletion of ^{13}C for epiphytes at the WWTP area, whereas for seagrass, the depletion of ^{13}C was greatest at the CI site (Figure 4, ANOVA, $p < 0.05$). For $\delta^{15}N$ analysis, the $\delta^{15}N$ values of epiphytes were significantly enriched compared to their seagrass hosts. Although there was no

TABLE 2 Average concentration (µmole/L) of ammonium, nitrate, total DIN, phosphate, and DIN:P ratio of sediment porewater (+/-SD) from the "Control" area (n = 6), CI site (n = 3), and "WWTP" area (n = 9).

Location	NH_4^+	NO_3^-	DIN	PO_4^{3-}	DIN: P
"Control"	44.21 (±2.12)	0.80 (±0.05)	**45.01 (±2.12)**	**0.62 (±0.13) A**	**73.54 (±37.62) A**
CI	67.60 (±5.24)	0.96 (±0.28)	**68.55 (±5.27)**	**0.59 (±0.12) A**	**154.55 (±89.88) A**
"WWTP"	54.97 (±2.15)	0.87 (±0.12)	**55.84 (±2.14)**	**1.49 (±0.64) B**	**39.32 (±10.43) B**

Different letters (A and B) display statistically significant differences (Tukey *post-hoc* HSD test, P < 0.05).

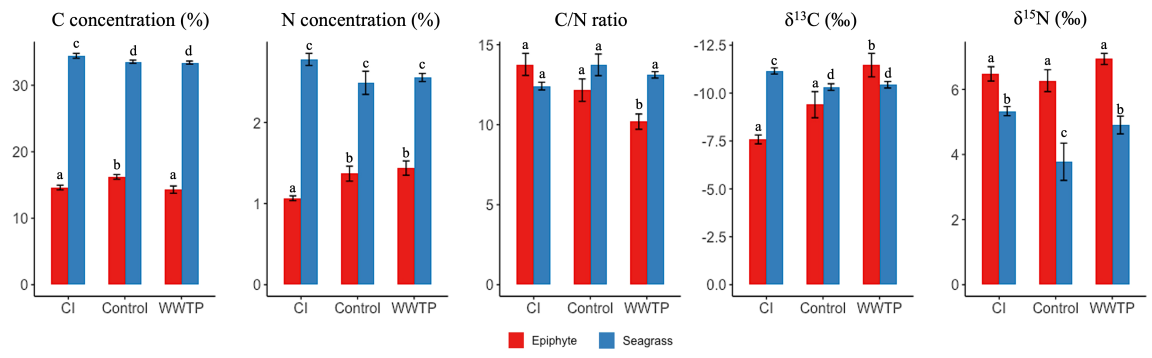

FIGURE 4
Mean (+/- SE) of the concentration of carbon (C), the concentration of nitrogen (N), the C/N ratio, the $\delta^{13}C$, and the $\delta^{15}N$ of T. testudinum and related epiphytes among three sampling locations. Epiphyte and seagrass are shown in red and blue, respectively. For each panel, bars showing the different letters differ significantly from each other at p < 0.1 using Tukey's pairwise test.

significant difference in the $\delta^{15}N$ values of epiphytes among the three sampling locations, seagrass at the "Control" area was lighter than seagrass from the CI and WWTP sites (Figure 4 ANOVA, $p < 0.1$).

3.4 Comparative metrics for the epiphyte-seagrass relationship

Comparisons of the different measures of epiphyte accumulation were made across different seasonal environmental influences. Linear regression between dried biomass of epiphyte per seagrass leaf and the numbers of identified epiphyte pixels per leaf revealed unique accumulation patterns by different sampling locations and seasons. The proportion of variation explained by linear regression ranged from 0.67 to 0.94, and there was a marked and consistent increase in the slope of the regression line, from all sampling areas (environmental contexts), with seasonal progression from summer through winter (Table 3). The different slopes demonstrate a seasonally changing relationship between epiphyte biomass and epiphyte coverage of the leaf. As an example, linear regression of the data from the "Control" area, July 31, 2019, had an R^2 of 0.81 and a slope of 0.017, representing that there was 0.017 µg epiphyte biomass per identified epiphyte pixel. Epiphyte accumulation gradually increased to 0.0559 µg per epiphyte pixel through winter into spring (Table 3). Similarly, epiphyte accumulation in the "WWTP" area increased from 0.014 µg to 0.033 µg over the same period (but with a peak at 0.0675 µg in February). At the CI site, epiphytes increased from 0.024 µg to 0.0434 µg over the same period (but with a peak at 0.0709 µg in February).

Expression of epiphyte metrics relative to the host seagrass leaves is another approach to represent the epiphyte-seagrass dynamic relationship. The epiphyte load (epiphyte biomass/seagrass biomass) and the image-derived % epiphyte coverage were correlated and revealed seasonal changes in the seagrass-epiphyte relationship (Figures 5–7). Potential regression models were applied across six sampling times for the three locations. Two scenarios emerged to describe the relationship between epiphyte load (Y) and epiphyte coverage of the leaf (X) under variable environmental conditions. Analyses of this relationship in the "WWTP" area (Figure 5) showed a strong linear regression (Scenario 1) from August through December 2019. However, the exponential-rise model (Scenario 2) was the best-fitted model in February and April 2020 based on the AICc values (Figure 5). In the "Control" area and CI site, the exponential model was generated during August (Figures 6, 7) and was also presented at the CI site in April 2020 (Figure 6). The linear relationship between epiphyte load and epiphyte coverage held under most environmental circumstances, except August samplings from "Control" and CI; and April sampling from "WWTP" and CI (Figures 5–7). Different slope values revealed different accumulation rates of epiphyte biomass relative to epiphyte coverage. The slopes of this relationship varied from 0.75 to 3.43, with a progressive increase from August to December and with the highest values observed during winter or spring, when the coolest observed water temperatures prevailed (Table 1).

TABLE 3 Slope of regression of epiphyte accumulation on epiphyte covered area for "Control" area, "WWTP" area, and CI site.

Sampling Date	"Control" area	CI Site	"WWTP" area
07-31-2019	0.0170 (R^2 = 0.81)	0.0240 (R^2 = 0.70)	
08-09-2019			0.0140 (R^2 = 0.73)
08-30-2019	0.0253 (R^2 = 0.87)	0.0259 (R^2 = 0.86)	
09-11-2019			0.0178 (R^2 = 0.76)
09-25-2019	0.0242 (R^2 = 0.91)	0.0378 (R^2 = 0.87)	
10-09-2019			0.01534 (R^2 = 0.86)
11-20-2019	0.0275 (R^2 = 0.88)	0.0437 (R^2 = 0.95)	
12-18-2019			0.0311 (R^2 = 0.73)
01-17-2020	0.0318 (R^2 = 0.68)	0.0709 (R^2 = 0.86)	
02-22-2020			0.0675 (R^2 = 0.87)
04-19-2020			0.0332 (R^2 = 0.71)
04-30-2020	0.0559 (R^2 = 0.67)	0.0434 (R^2 = 0.84)	

The epiphyte biomass per identified epiphyte pixel was determined by the slope of linear regression. R^2 for the linear regressions are given in parentheses.

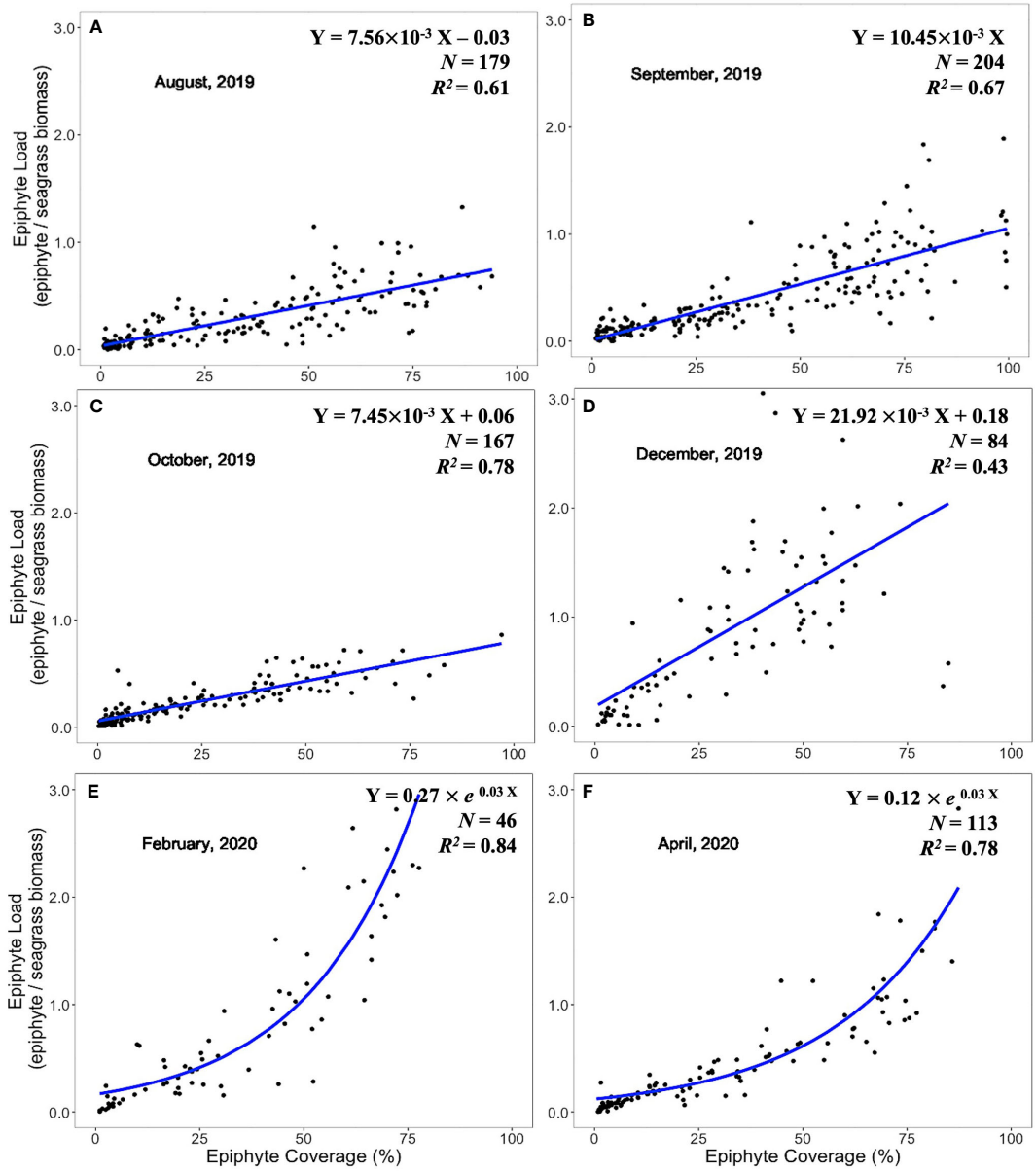

FIGURE 5
Linear and exponential accumulation scenarios 1 and 2, respectively, in "WWTP" area. Graphs **(A–F)** showed the best fitted regression of the relationship between epiphyte load and epiphyte coverage from August 2019 to April 2020.

3.5 Spatial and temporal comparisons of seagrass growth and epiphyte accumulation patterns

The observed changes in seagrass-normalized epiphyte accumulation could be due to changes in epiphyte growth, seagrass growth, or a combination of both. Figures 8–11 present different aspects of each possibility. Because sampling events at different sites did not occur simultaneously, measures were grouped by season for comparisons (Table 1). Seagrass leaf biomass and imaged seagrass leaf area presented similar seasonal patterns in general, where the high levels in Summer or Autumn declined in the transition through Winter and Spring (Figures 8–11). There were no significant differences in the seagrass leaf biomass and blade area between the "Control" area and the CI site from summer to spring (Figure 8, Table 4). The leaf biomass in the WWTP area was significantly higher than at the "Control" area and the CI site in the summer ($df = 2$, $F = 8.10$, $p < 0.05$) and

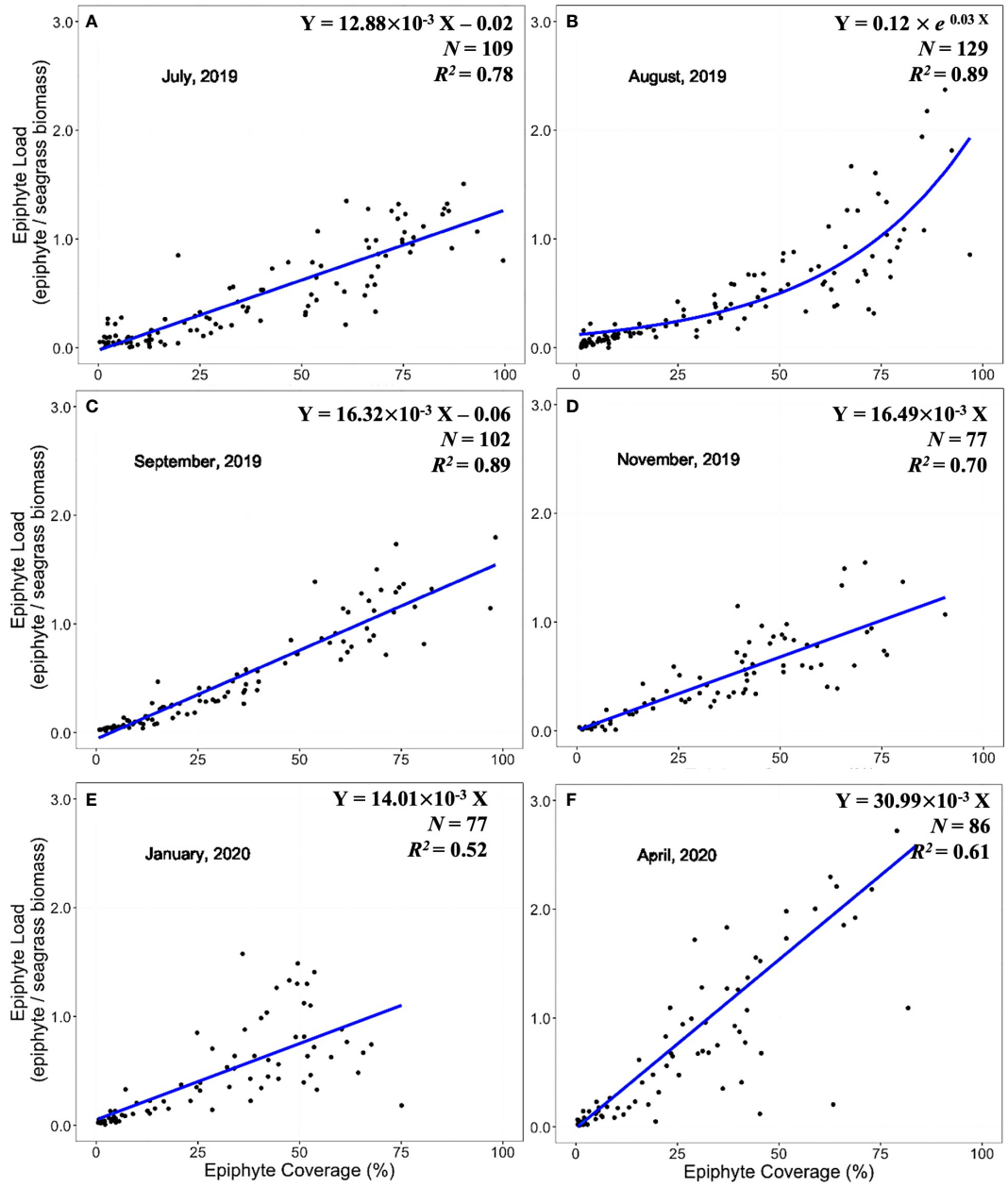

FIGURE 6
Linear and exponential accumulation scenarios 1 and 2, respectively, in "Control" area. Graphs **(A-F)** showed the best fitted regression of the relationship between epiphyte load and epiphyte coverage from July 2019 to April 2020.

autumn (df = 2, F = 10.06, $p < 0.05$), but it decreased strikingly and exhibited significantly lower value than the other two locations in the winter (df = 2, F = 3.40, $p < 0.05$) (Figure 8). In the spring, there was no significant difference in the leaf biomass among the three locations (Table 4).

The blade area also did not exhibit a significant difference between the "Control" area and the CI site from summer to spring (Figure 9; Table S2). In the "Control" area (df = 3, F = 5.95, $p < 0.05$) and the CI site (df = 3, F = 16.50, $p < 0.05$), the blade areas were both significantly higher in the summer and autumn than in the winter and spring (Figure 9). The blade area from the "WWTP" area was significantly higher than from the "Control" area and the CI site in the autumn (df = 3, F = 11.60, $p < 0.05$). A sharp decrease in average blade area from the "WWTP" area was observed in the transition to winter when the blade area was significantly lower than at the other two

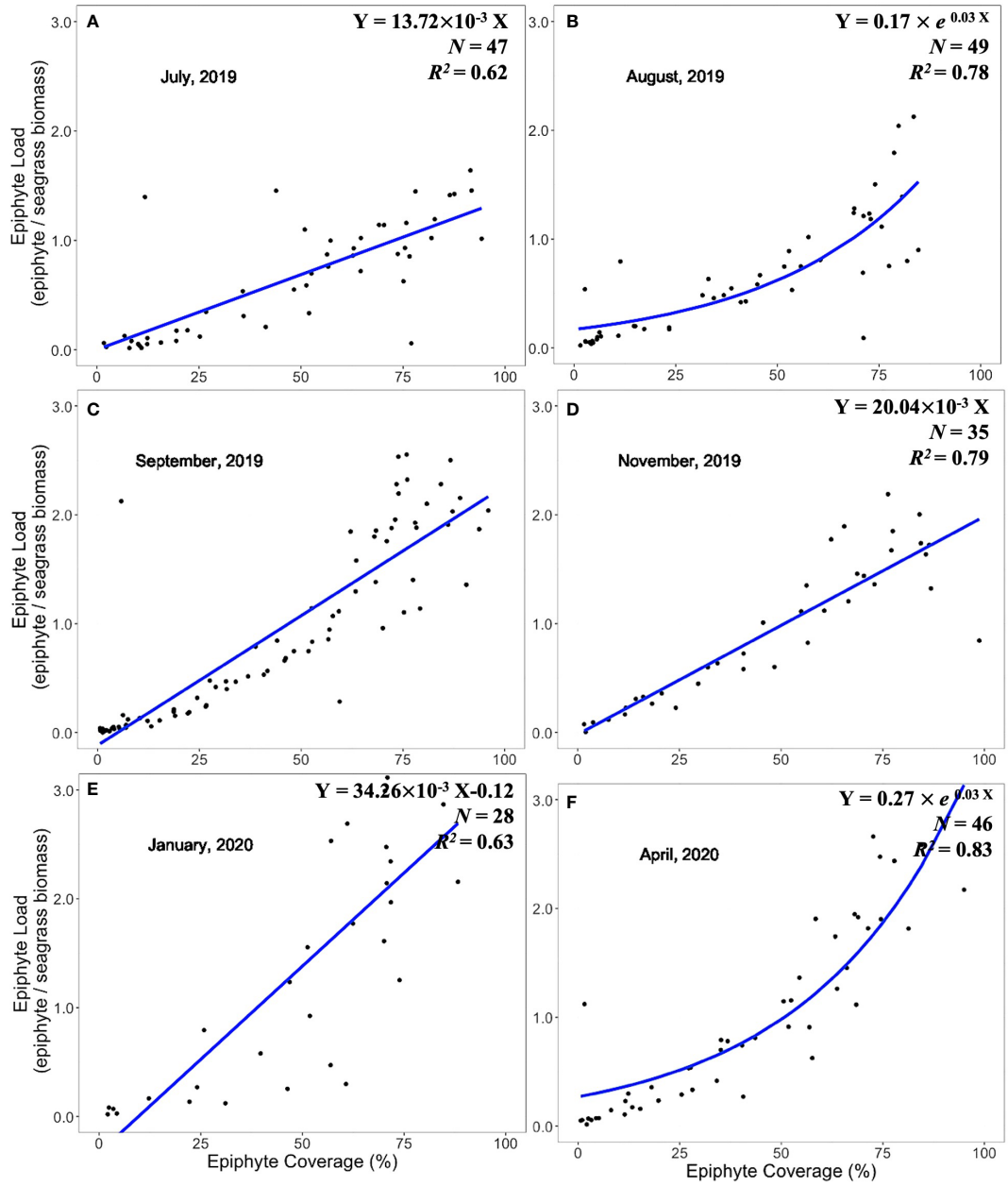

FIGURE 7
Linear and exponential accumulation scenarios 1 and 2, respectively, at CI site. Graphs **(A-F)** showed the best fitted regression of the relationship between epiphyte load and epiphyte coverage from July 2019 to April 2020.

locations. Generally, the seasonal changes of leaf biomass and blade area among three sites with different environmental conditions were similar, with high values in summer and autumn which significantly decreased in winter and stayed low through April (Table S2).

Seasonally aggregated observations of epiphyte accumulations expressed as epiphyte load and epiphyte coverage of leaves showed different patterns by season and site (Figures 10, 11). Epiphyte loads (epiphyte biomass relative to seagrass biomass) presented an inverse temporal pattern compared to seagrass growth. There were significant differences in epiphyte load among the three sampling locations (Figure 10; Table 4). Epiphyte loads at the CI site were significantly higher than at the "Control" area and "WWTP" area in all seasons (df = 2, F = 70.64, p < 0.05). Opposite to the seagrass growth pattern, the epiphyte load pattern increased significantly (df = 2, F = 25.89, P < 0.05) in the winter (Figure 10), except for the

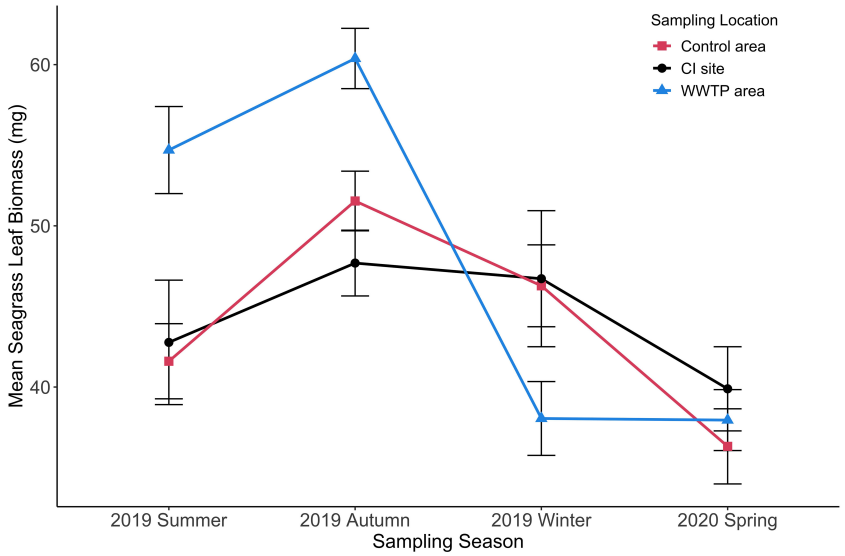

FIGURE 8
Mean seagrass leaf biomass (+/-SE) for three sampling locations from summer to spring. (n = 2062).

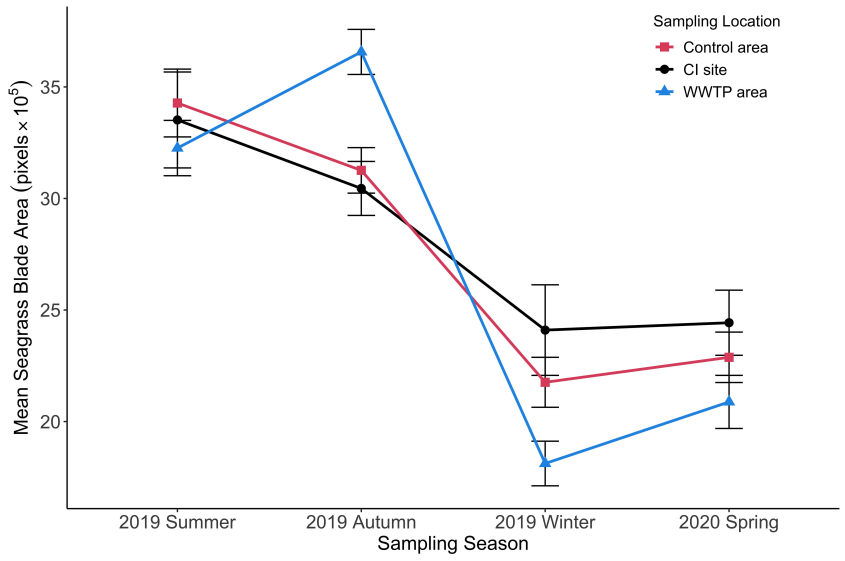

FIGURE 9
Mean seagrass blade area (+/-SE) for three sampling locations from summer to spring. (n = 2055).

"Control" area, where epiphyte load did not change significantly in winter but was instead highest in the spring. On the contrary, the epiphyte load in the "WWTP" area decreased from winter to spring and was significantly lower than in the other two locations in the spring ($df = 2$, $F = 8.03$, $p < 0.05$). Overall, epiphyte loads exhibited seasonal changes inverse to the seagrass growth. The CI site had the greatest epiphyte/seagrass biomass ratio, whereas the "WWTP" area had the lowest values except in the winter.

Epiphyte coverage (Figure 11) did not show a significant seasonal change but was affected by the environments of the

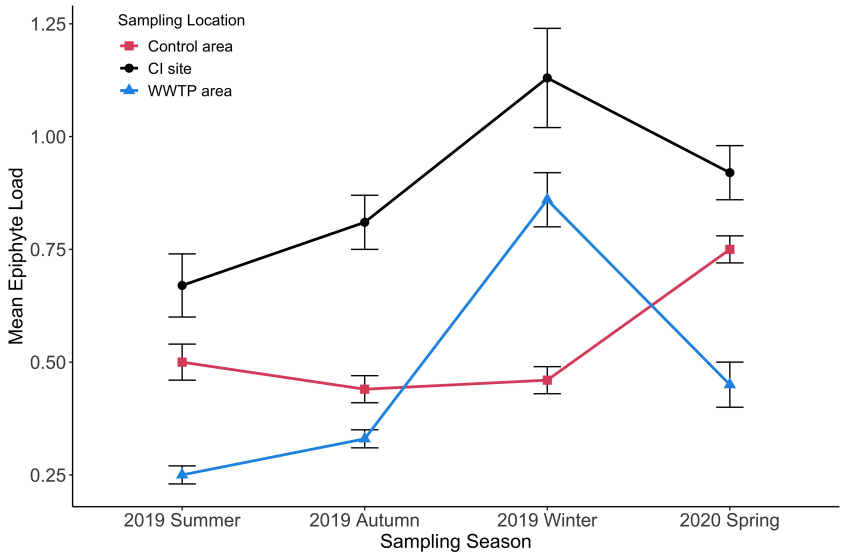

FIGURE 10
Mean epiphyte load (+/-SE) for three sampling locations from summer to spring. (n = 1833).

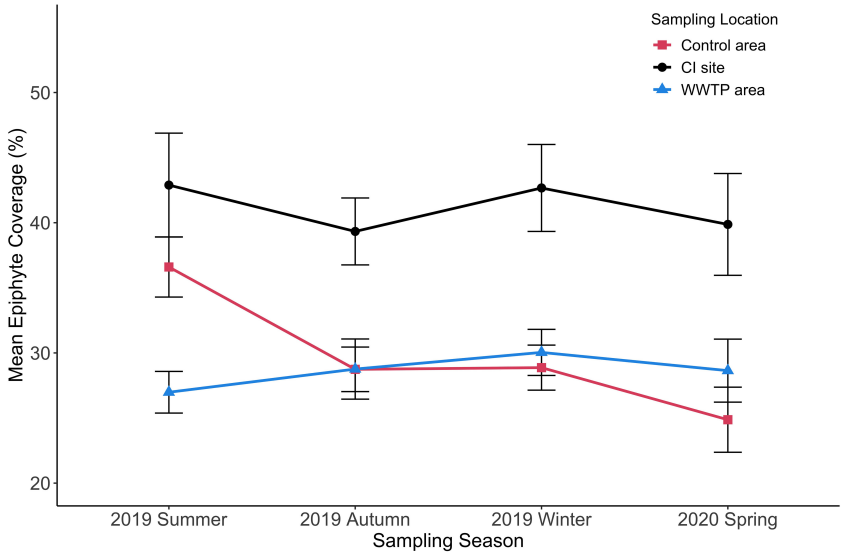

FIGURE 11
Mean epiphyte coverage (+/-SE) for three sampling locations from 2019 summer to 2020 spring. (n = 2001).

three sampling locations. Across sampling periods, epiphyte coverage was highest at the CI site. This difference was significant in all seasons (Table 4). The epiphyte coverage in the "Control" area was significantly higher than in the WWTP area in the summer (df = 2, F = 10.21, p < 0.05) and then there were no significant differences in epiphyte coverage from autumn to spring. Even though the seasonal pattern of epiphyte coverage was not similar to that for epiphyte load, these two indicators both ordinated the CI site as highest across all seasons (Figure 11, Table S2). The relative consistency in epiphyte coverage across seasons (CI varied from ~40 – 45%; WWTP varied from ~25 – 30%; Control varied from ~25 – 35%) highlights a unique aspect of the complicated epiphyte-seagrass relationship that is not readily apparent from biomass measurements.

TABLE 4 Two-way ANOVA for Thalassia testudinum leaf biomass (g) and blade area (pixels), epiphyte load, and epiphyte coverage (%) variables.

Source	*df*	*F*	*P*
A. Seagrass leaf biomass			
Location	2	0.16	0.86
Season	3	29.32	< **0.0001**
Location × Season	6	7.79	< **0.0001**
B. Seagrass blade area			
Location	2	0.49	0.62
Season	3	86.42	< **0.0001**
Location × Season	6	5.13	< **0.0001**
C. Epiphyte load			
Location	2	45.55	< **0.0001**
Season	3	35.24	< **0.0001**
Location × Season	6	12.79	< **0.0001**
D. Epiphyte coverage			
Location	2	23.49	**<0.0001**
Season	3	1.45	0.22
Location × Season	6	2.42	**0.02**

Independent variables are T. testudinum sampling season and sampling locations. df, degrees of freedom. Values significant at the 0.05 level are shown in bold.

4 Discussion

This study measured epiphyte accumulation patterns *via* image analysis to quantitatively distinguish the uncovered leaf areas from those colonized by diverse epiphytes. Comparisons to biomass-based epiphyte accumulation metrics among sites of different environmental influences revealed different response patterns and insight into the spatiotemporal dynamics of the epiphyte-seagrass relationship. Both types of metrics were correlated for both seagrasses and epiphytes, but the latter relationship varied between linear and exponential with site- and season-dependent patterns. The two modes of correlation (linear *vs.* exponential) can be explained by the super-imposition of seasonal leaf growth patterns of the seagrass host, and successional epiphyte growth (new layers), filamentous growth, and/or community compositional changes towards denser (e.g., calcareous) epiphytes. The mean % leaf coverage by epiphytes varied in a narrow range (± 10%) across seasons, in contrast to the strong and opposing seasonal variations observed for biomass metrics of seagrasses and epiphytes. Importantly, the relatively consistent leaf coverage metric ordinated the major site difference of greatest epiphyte accumulation at CI irrespective of the season. Compared to image-based % leaf cover, the seagrass and epiphyte biomass metrics showed greater variability compounded by the large and opposing seasonal growth changes. These results suggest that leaf growth is regulated to maintain the proportion of uncolonized leaf surface (Fong and Harwell, 1994; Biber et al., 2004).

The observed spatiotemporal variability of seagrass growth and epiphyte accumulation suggested that multiple environmental variables affect the seagrass-epiphyte relationship with complex dynamics. Environmental variables compared included water temperature, depth, salinity and sediment porewater nutrients. Decreasing seasonal temperatures were correlated with diminished seagrass leaf biomass, and an increased slope of epiphyte accumulation at all sites. Porewater nutrients exhibited significant site differences in phosphate and the DIN/phosphate ratio. Phosphate was most enriched in the porewater at the WWTP area, where the highest maximum seagrass biomasses were found. In contrast, the greatest porewater DIN/phosphate ratio, observed at the CI site, corresponded to the greatest epiphyte accumulations. Porewater at the Control site had lower but nonsignificant DIN compared to the CI site, but a significantly different DIN/phosphate ratio that was between those of WWTP and CI, much like the epiphyte load metric in that area.

The explanation most consistent with all observations is that seagrass growth correlated with porewater phosphate levels, and was negatively impacted by low temperatures, whereas the epiphyte community accumulation as a whole is correlated with the DIN/phosphate ratio and relatively unaffected by the winter temperatures observed here. This explains a high slope

and exponential accumulation of epiphyte biomass in the winter. But this epiphyte accumulation pattern was also observed in late summer at "Control" and CI sites. This could be explained by highly active levels of both seagrass leaf and epiphyte growth, with successional secondary colonization occurring to a high degree in the warm waters. Two major unknowns that require further definition are the knowledge of how the epiphyte community changes and what role invertebrate or fish grazers play in controlling the epiphyte accumulation and community composition at these sites. Our unpublished fluorescence and 18S and COI metabarcoding data suggest that the algal epiphyte communities differ in the proportions of green and red algae, and that there are greater relative abundances of invertebrates at the Control and CI compared to WWTP.

4.1 Comparative metrics for epiphyte accumulation and epiphyte-seagrass relationship

The seasonal shift in seagrass-epiphyte dynamics evaluated by image analysis in this study is consistent with previous studies on multiple seagrass species, (Bulthuis and Woelkerling, 1983; Lee and Dunton, 1996; Moore and Wetzel, 2000; Hasegawa et al., 2007). Image analysis has the potential to unlock a wealth of knowledge regarding the seagrass-epiphyte dynamic relationship if it can be applied to detect changing epiphyte community composition with environmental conditions.

For all three sampling locations, the slopes of linear regressions of epiphyte biomass *vs.* epiphyte pixels changed in a consistent seasonal pattern where the slope increased with progression from autumn through winter. The observation of increased epiphyte biomass per unit of epiphyte-covered area is consistent with continued epiphyte growth despite observed decreases in seagrass leaf growth and production during winter and early spring (Figures 5–7). Cooler water temperatures (and perhaps shorter days/lower light levels) may be critical environmental factors diminishing leaf growth (Zieman, 1975; Marbà et al., 1994; Zieman et al., 1999; Koch and Erskine, 2001; Kim et al., 2020). However, these observations could also be partly explained by shifts in the epiphyte community composition that increase biofilm "thickness" and/or density of the epiphyte biofilm per unit area of leaf coverage as previously observed (Corlett and Jones, 2007; Giovannetti et al., 2010). The epiphyte biofilms in this study varied from 14 – 70 ng biomass per pixel. The highest epiphyte biomass per epiphyte area (pixels) was observed at the CI site (Table S2), which had significantly highest DIN/Phosphate ratio as well as unique influences from proximity to oysters and hydrodynamic disturbance from boat traffic in the ICWW.

Changes in the relationship between epiphyte load and epiphyte coverage are attributed to two types of epiphyte-seagrass dynamics under different seasonal conditions (Figures 5–7). In the first accumulation scenario (typical of most samples from August – December), the strong linear relationship between epiphyte load and epiphyte coverage implied that primary epiphyte colonization on the available seagrass leaf surface was dominant due to the growth of new leaf surface (Table 3).

In the second epiphyte accumulation phase, indicated by fitting exponential regressions of epiphyte load with epiphyte coverage for several specific sites and times, the model clearly demonstrates a strong tendency for accumulation of epiphyte biomass more rapidly than the expansion of epiphyte coverage. Epiphyte coverage of leaves saturates if leaf growth slows relative to the primary colonization rate. Existing epiphytes continue to grow in size, thickness and/or density (e.g., calcareous) in an orderly succession with three or more layers (Willcocks, 1982; Kitting et al., 1984; Corlett and Jones, 2007; Saha et al., 2019). On older leaves where growth has slowed, stopped, or even reversed (senescence), epiphyte biomass accumulates *via* further secondary colonization and growth contributed by filamentous algae and invertebrates (Novak, 1982; Armitage et al., 2006; Whalen et al., 2013), while the underlying primary coralline algae eventually die (Borum, 1987). It is not uncommon for epiphyte biomass to exceed seagrass biomass (Figures 5–7; Kitting et al., 1984; Moncreiff et al., 1992). A community shift to a greater abundance of filamentous algae and/or heavier calcareous epiphytes, such as serpulid worms, would potentially increase both biomass and biological diversity.

While previous reports suggested a higher biomass accumulation rate of epiphytes on seagrass leaves in the summer (Heijs, 1984; Hasegawa et al., 2007), our observations noted a reverse seasonal pattern of maximum epiphyte accumulation, relative to seagrass growth, in the winter and spring seasons, coinciding with most observations of exponential correlations. The exceptions of the August exponential correlations at the "Control" and CI sites suggests that there are multiple environmental scenarios that can produce a similar physiological outcome. Shading is not the only impact of epiphyte biofilms. Availability of O_2, CO_2, or other gasses might be linked to localized necrosis or the initiation of leaf senescence to avoid excessive consumption of stored plant reserves. The recent works of Brodersen (Brodersen et al., 2015; Brodersen et al., 2020) have expanded on old ideas (Sand-Jensen, 1977) about epiphyte biofilms altering gas exchange and leaf physiology. Such measurements, alongside transcriptomic profiling (Crump et al., 2018) are likely to reveal underlying physiological regulatory mechanisms unique to seagrasses.

For the shift from the first to second accumulation scenarios of epiphytes, it is unclear whether the leaf stops growing due to environmental factors, allowing epiphytes to accumulate exponentially, or if the epiphytes outgrow the seagrass and reduce light to the point of reducing seagrass leaf growth. The

two patterns may also occur simultaneously on different parts of the same long leaf, which could be further investigated with the imaging approach. However, even with the heaviest epiphyte accumulations, coverage only rarely reaches 100% (on senescing leaves), and the basal 5 cm of *Thalassia testudinum* leaves (near the leaf sheath) is usually not visibly covered by epiphytes. This two-phase epiphyte accumulation may imply an existing threshold or trigger point for the balance between leaf growth response to epiphyte shading and leaf senescence. Accordingly, environmental effects on seagrasses and epiphytes are considered separately below.

4.2 Environmental effects on seagrass growth

The seasonal growth pattern of *T. testudinum* at all locations, maximum in the summer and early autumn followed by a decline through winter or early spring (Figures 8, 9), is widely observed (Herzka and Dunton, 1997; Fourqurean et al., 2001) and may be initiated by low temperature and/or salinity (Fernández-Torquemada and Sánchez-Lizaso, 2005), with the former most likely in this study (Tables 1, 3; Figures S2, S3). Slow recovery of leaf area in April is consistent with photosynthesis rates at sub-optimal water temperature (23° C) (Herzka and Dunton, 1997; Campbell et al., 2006; Collier and Waycott, 2014; Rasmusson et al., 2020). Decreasing temperatures and salinity may have initiated the significant decline of leaf biomass and leaf area in winter and early spring (Tables 1, 3; Figures S2 and S3). Seagrass biomass was only weakly correlated with depth and salinity, but seagrass leaf area did show correlation with both temperature and salinity. The variability in thickness of seagrass blades might cause the inconsistence between the leaf biomass and areas.

Sediment porewater nutrients were measured during May under the assumption that the porewater nutrient differences would reflect the long-term exposure history to water column nutrients. Seagrass biomass and leaf area were significantly higher at two of three WWTP sites during warmer water summer and autumn periods (Figures 8, 9), which correlated with the significantly greatest porewater phosphate levels at WWTP. There were no corresponding significant increases in DIN, or DIN/phosphate ratio at the WWTP site (Table 2). Likewise N content and C:N ratios did not differ significantly in seagrasses from any of the study sites (Figure 4), suggesting that all three sampling locations are replete with N (Duarte et al., 2018).

Observed differences in seagrass stable isotope ratios showed ^{13}C significantly more depleted at CI, and ^{15}N significantly less enriched at "Control". The most negative $\delta^{13}C$ values of seagrass leaves at the CI site (Figure 4), could be explained by the seagrass leaves having low light and CO_2 availability due to coverage by the greatest accumulation of epiphytes (Grice et al., 1996; Lapointe et al., 2020; Premarathne et al., 2021). Carbon-limited photosynthesis would increase discrimination against ^{13}C compared to "Control" and WWTP seagrasses. It suggests that the influence of light and/or CO_2 availability caused by high epiphyte accumulations might be an important factor controlling seagrass productivity in this study. However, conditions that seem inconsistent with differential light and/or CO_2 limitation are CI having the shallowest depth, as well as hydrodynamic turbulence from nearby boat traffic. The lower $\delta^{15}N$ value of *T. testudinum* in the "Control" area compared to the WWTP area (and CI) might reflect the influence of the wetland used to polish the treated wastewater there. The WWTP site receives treated wastewater unpolished by wetlands, but also potential influence from a fish cleaning station and associated bird roosting.

4.3 Environmental effects on epiphyte accumulation patterns

Unlike the seasonal pattern of seagrass growth, the epiphyte load, relative to the seagrass host, presented an opposite seasonal pattern. The epiphyte load in the "WWTP" area and the CI site followed a similar seasonal pattern, with the maximum in winter and low relative epiphyte accumulation in summer (Figure 10). The increased epiphyte load from summer to winter is consistent with previous reports of epiphyte accumulation on *Cymodocea nodosa* and *Zostera marina* (Nelson and Waaland, 1997; Reyes and Sansón, 2001). Seasonal seagrass growth condition has been suggested as the primary factor controlling the temporal epiphyte accumulation pattern (Momota and Nakaoka, 2018; Bračun et al., 2021). A faster leaf turnover rate may drive a lower epiphyte load in the summer than in the winter (Duarte and Sand-Jensen, 1990; Peterson et al., 2007), which causes a shorter period for epiphyte accumulation on the available leaf surface. However, our observation of exponential epiphyte accumulation in August suggests that the lifetime of the leaf is still sufficiently long enough to be overtaken by excessive epiphyte growth. Here, "excessive growth" might be somewhat arbitrarily defined as an epiphyte/seagrass biomass ratio > 1, but this value approximates the point of deviation from a linear accumulation response (See Figures 5–7).

Epiphyte colonization may be secondarily controlled by environmental conditions such as the DIN/phosphate ratio in this study (Biber et al., 2004). Despite the acute decline of seagrass leaf area in the winter and spring, epiphytes appear to secondarily colonize on top of the basal layers of diatoms and coralline red algae to initiate an exponential accumulation phase (Armitage et al., 2006; Corlett and Jones, 2007; Whalen et al., 2013). Community succession patterns and compositional changes would impact the per-pixel biomass values. Notably, the average % epiphyte coverage metric (Figure 11) showed relatively little seasonal fluctuation compared to the epiphyte load metric (Figure 10). It would be

informative to distinguish and quantify changes in epiphyte community composition by combining image analysis, pigment analysis and molecular taxonomy.

Site to site differences in biotic and abiotic factors, especially temperature, nutrients, and grazer densities, also play essential roles in epiphyte accumulation. (Thom et al., 1995; Nelson and Waaland, 1997; Wear et al., 1999; Frankovich and Zieman, 2005; Whalen et al., 2013; Ruesink, 2016). Some epiphytic algae on *T. testudinum* tolerate low temperature but decline rapidly over 30 (Biber et al., 2004). Summer water temperatures possibly drive seasonal epiphyte community composition changes (Stanca and Parsons, 2021). Our observation that epiphyte coverage ordinated higher at CI site across all seasons indicates that environmental factors playing a major role in these site-to-site differences are consistent.

Oyster impacts on porewater nutrients (Booth and Heck, 2009; Wagner et al., 2015), hydrodynamics (Booth and Heck, 2009; Smith et al., 2009) and epiphyte community composition and relative abundances (Frankovich and Fourqurean, 1997; Smith et al., 2018), may provide the consistent forcing observed at CI. The significantly highest DIN/phosphate ratio of the sediment porewater suggests long-term greater nutrient exposure, and nutrient effects on epiphytes have been explored extensively (Frankovich and Zieman, 2005; Johnson et al., 2006; Frankovich et al., 2009; Nelson, 2017). But temporal shifts in top-down grazer control have been noted (Whalen et al., 2013), and 18S sequence abundance actually suggests a greater epiphytic animal abundance at CI (unpublished observations), Thus relatively less effective grazer control of epiphyte accumulation at CI seems incongruous as the major explanation for this site's consistently greater epiphyte accumulation. On the other hand, hydrodynamic wave effects from proximity to the ICWW (Schanz et al., 2002) could disrupt grazing pressure across seasons.

Although the nitrogen sources for seagrass differ among the three locations, the similarity of $\delta^{15}N$ of epiphytes did not reveal any such differences. Porewater nutrient differences may be more indicative of past nutrient history (e.g., untreated wastewater spill) as opposed to recent conditions affecting epiphytes. Thus increased epiphyte load and coverage at CI seems likely due to the influence of nutrient levels and hydrodynamics, on the epiphyte community composition and abundance (Armitage et al., 2005). The greater degree of carbon isotope discrimination by epiphytes ($-12.46 < \delta^{13}C < -10.82$) at the WWTP area than at other locations ($-7.35 < \delta^{13}C < -7.82$) might derive from different epiphytic communities (algae and animals) among the three locations (Smit et al., 2005), especially the presence of invertebrates. The seagrass host can also produce secondary compounds that influence microbial, algal and animal epibiota (Harrison, 1982; Harrison and Durance, 1985; Crump et al., 2018).

While nutrient enrichment at the "WWTP" area was expected to promote seagrass and epiphyte growth (Borum, 1985; Lee et al., 2007; Baggett et al., 2010), such effects were not observed on any consistent basis in comparison to nearby sites receiving only polished wastewater or under influence from oyster habitat. Future studies would benefit from monitoring grazers, epiphyte community change, and seasonal water column nutrient levels to improve understanding of the seagrass-epiphyte relationship.

This study demonstrated the utility of the image analysis approach to understand the seagrass-epiphyte dynamic relationship and the impact of environmental stressors on this relationship. The emerging interpretation from these results is that epiphyte community change from environmental factors impacts both biomass and imaging measures in sometimes different ways that provide complementary insights. Specifically, the relationship between epiphyte biomass accumulation and epiphyte coverage of the leaf provides insight into the morphology of the epiphyte biofilm in ways that impact the seagrass host such as light attenuation and gas exchange (Sand-Jensen, 1977; Brodersen et al., 2015). It is worth examining more closely to understand the significance of the epiphyte composition and colonization pattern in conjunction with seagrass physiology. However, evaluation of the image analysis method shows that classification discrepancies still exist (Huang, 2020), and a major challenge is accurate classification of diverse epiphyte constituents through refinement of epiphyte and seagrass reference spectra. An advanced image-analysis tool should be able to define the spatiotemporal changes in epiphyte communities and improve efficiency through deep learning with neural networks (Mehrubeoglu et al., 2021).

Data availability statement

The raw data supporting the conclusions of this article will be made available by the authors, without undue reservation.

Author contributions

KC, CH, and CP designed the experiment; CH, CP, and KC sampled and processed the seagrasses and epiphytes; CH and KC performed the data analyses; CH, MM, and KC performed the validation of imaging analysis; CH and KC prepared the manuscript. All authors contributed to the article and approved the submitted version.

Funding

The image analysis development and seagrass sampling were supported by a Texas A&M University-Corpus Christi Research

Enhancement Award to KC. Funding for the nutrient measurement and the stable isotope analyses were from the Millicent Quammen Memorial Research Award, Texas A&M University-Corpus Christi to CH, and the Research and Innovation Award, Texas A&M University-Corpus Christi to CH. The open access publication fee was paid by the Open Access Publication Fund administered by the Mary and Jeff Bell Library at Texas A&M University-Corpus Christi.

Conflict of interest

The authors declare that the research was conducted in the absence of any commercial or financial relationships that could be construed as a potential conflict of interest.

Publisher's note

Supplementary material

The Supplementary Material for this article can be found online at: https://www.frontiersin.org/articles/10.3389/fmars.2022.1096307/full#supplementary-material

References

Aoki, L. R., Rappazzo, B., Beatty, D. S., Domke, L. K., Eckert, G. L., Eisenlord, M. E., et al. (2022). Disease surveillance by artificial intelligence links eelgrass wasting disease to ocean warming across latitudes. *Limnol. Oceanogr.* 67, 1577–1589. doi: 10.1002/lno.12152

Armitage, A. R., Frankovich, T. A., and Fourqurean, J. W. (2006). Variable responses within epiphytic and benthic microalgal communities to nutrient enrichment. *Hydrobiologia* 569, 423–435. doi: 10.1007/s10750-006-0146-8

Armitage, A. R., Frankovich, T. A., Heck, K. L., and Fourqurean, J. W. (2005). Experimental nutrient enrichment causes complex changes in seagrass, microalgae, and macroalgae community structure in Florida bay. *Estuaries* 28, 422–434. doi: 10.1007/BF02693924

Atmaja, P. S. P., Bengen, D. G., and Madduppa, H. H. (2021). The second skin of seagrass leaves: A comparison of microalgae epiphytic communities between two different species across two seagrass meadows in lesser sunda islands. *Trop. Life Sci. Res.* 32, 97. doi: 10.21315/tlsr2021.32.2.7

Bader, M., van Dunné, H. J. F., and Stuiver, H. J. (2000). Epiphyte distribution in a secondary cloud forest vegetation; a case study of the application of GIS in epiphyte ecology. *Ecotropica* 6, 181–195.

Baggett, L. P., Heck, K. L.Jr., Frankovich, T., Armitage, A. R., and Fourqurean, J. W. (2010). Nutrient enrichment, grazer identity, and their effects on epiphytic algal assemblages: field experiments in subtropical turtlegrass thalassia testudinum meadows. *Mar. Ecol. Prog. Ser.* 406, 33–45. doi: 10.3354/meps08533

Bell, S. S., Fonseca, M. S., and Kenworthy, W. J. (2008). Dynamics of a subtropical seagrass landscape: links between disturbance and mobile seed banks. *Landscape Ecol.* 23, 67–74. doi: 10.1007/s10980-007-9137-z

Bell, S. S., Middlebrooks, M. L., and Hall, M. O. (2014). The value of long-term assessment of restoration: Support from a seagrass investigation. *Restor. Ecol.* 22, 304–310. doi: 10.1111/rec.12087

Biber, P. D., Harwell, M. A., and Cropper, W. P. (2004). Modeling the dynamics of three functional groups of macroalgae in tropical seagrass habitats. *Ecol. Model.* 175, 25–54. doi: 10.1016/j.ecolmodel.2003.10.003

Boese, B. L., Clinton, P. J., Dennis, D., Golden, R. C., and Kim, B. (2008). Digital image analysis of zostera marina leaf injury. *Aquat. Bot.* 88, 87–90. doi: 10.1016/j.aquabot.2007.08.016

Booth, D. M., and Heck, K. (2009). Effects of the American oyster crassostrea virginica on growth rates of the seagrass halodule wrightii. *Mar. Ecol. Prog. Ser.* 389, 117–126. doi: 10.3354/meps08163

Borum, J. (1985). Development of epiphytic communities on eelgrass (*Zostera marina*) along a nutrient gradient in a Danish estuary. *Mar. Biol.* 87, 211–218. doi: 10.1007/BF00539431

Borum, J. (1987). Dynamics of epiphyton on eelgrass (*Zostera marina* l.) leaves: Relative roles of algal growth, herbivory, and substratum turnover. *Limnol. Oceanogr.* 32, 986–992. doi: 10.4319/lo.1987.32.4.0986

Bračun, S., Wagner, M., and Koblmüller, S. (2021). Spatio-temporal occurrence patterns of epibiota along the leaves of the seagrass cymodocea nodosa in the northern Adriatic Sea. *Mar. Biol. Res.* 17, 592–602. doi: 10.1080/17451000.2021.2015389

Brodersen, K. E., and Kühl, M. (2022). Effects of epiphytes on the seagrass phyllosphere. *Front. Mar. Sci.* 9. doi: 10.3389/fmars.2022.821614

Brodersen, K., Kühl, M., Trampe, E., and Koren, K. (2020). Imaging O2 dynamics and microenvironments in the seagrass leaf phyllosphere with magnetic optical sensor nanoparticles. *Plant J.* 104, 1504–1519. doi: 10.1111/tpj.15017

Brodersen, K. E., Lichtenberg, M., Paz, L.-C., and Kühl, M. (2015). Epiphyte-cover on seagrass (Zostera marina l.) leaves impedes plant performance and radial O2 loss from the below-ground tissue. *Front. Mar. Sci.* 2, 58.

Bulthuis, D. A., and Woelkerling, W. (1983). Biomass accumulation and shading effects of epiphytes on leaves of the seagrass, heterozostera tasmanica, in Victoria, Australia. *Aquat. Bot.* 16, 137–148. doi: 10.1016/0304-3770(83)90089-X

Cambridge, M. L., How, J. R., Lavery, P. S., and Vanderklift, M. A. (2007). Retrospective analysis of epiphyte assemblages in relation to seagrass loss in a eutrophic coastal embayment. *Mar. Ecol. Prog. Ser.* 346, 97–107. doi: 10.3354/meps06993

Campbell, S. J., McKenzie, L. J., and Kerville, S. P. (2006). Photosynthetic responses of seven tropical seagrasses to elevated seawater temperature. *J. Exp. Mar. Biol. Ecol.* 330, 455–468. doi: 10.1016/j.jembe.2005.09.017

Collier, C. J., and Waycott, M. (2014). Temperature extremes reduce seagrass growth and induce mortality. *Mar. pollut. Bull.* 83, 483–490. doi: 10.1016/j.marpolbul.2014.03.050

Corlett, H., and Jones, B. (2007). Epiphyte communities on *Thalassia testudinum* from grand Cayman, British West indies: Their composition, structure, and contribution to lagoonal sediments. *Sedimentary Geol.* 194, 245–262. doi: 10.1016/j.sedgeo.2006.06.010

Costanza, R., d'Arge, R., de Groot, R., Farber, S., Grasso, M., Hannon, B., et al. (1997). The value of the world's ecosystem services and natural capital. *Nature* 387, 253–260. doi: 10.1038/387253a0

Crump, B. C., Wojahn, J. M., Tomas, F., and Mueller, R. S. (2018). Metatranscriptomics and amplicon sequencing reveal mutualisms in seagrass microbiomes. *Front. Microbiol.* 9, 388. doi: 10.3389/fmicb.2018.00388

Dennison, W. C., and Alberte, R. S. (1982). Photosynthetic responses of zostera marina l. (Eelgrass) to in situ manipulations of light intensity. *Oecologia* 55, 137–144. doi: 10.1007/BF00384478

Dewsbury, B. M., Bhat, M., and Fourqurean, J. W. (2016). A review of seagrass economic valuations: gaps and progress in valuation approaches. *Ecosystem Serv.* 18, 68–77. doi: 10.1016/j.ecoser.2016.02.010

Duarte, C. M. (1995). Submerged aquatic vegetation in relation to different nutrient regimes. *Ophelia* 41, 87–112. doi: 10.1080/00785236.1995.10422039

Duarte, C. M., Delgado-Huertas, A., Anton, A., Carrillo-de-Albornoz, P., López-Sandoval, D. C., Agustí, S., et al. (2018). Stable isotope (δ13C, δ15N, δ18O, δD)

composition and nutrient concentration of red Sea primary producers. *Front. Mar. Sci.* 5. doi: 10.3389/fmars.2018.00298

Duarte, C., and Sand-Jensen, K. (1990). Seagrass colonization: biomass development and shoot demography in *Cymodocea nodosa* patches. *Mar. Ecol. Prog. Ser.* 67, 97–103. doi: 10.3354/meps067097

Fikes, R. L., and Lehman, R. L. (2008). Small-scale recruitment of flora to a newly developed tidal inlet in the Northwest gulf of Mexico. *Gulf Mexico Sci.* 26, 130-132. doi: 10.18785/goms.2602.05

Fernández-Torquemada, Y., and Sánchez-Lizaso, J. L. (2005). Effects of salinity on leaf growth and survival of the Mediterranean seagrass posidonia oceanica (L.) delile. *J. Exp. Mar. Biol. Ecol.* 320, 57–63. doi: 10.1016/j.jembe.2004.12.019

Fong, P., and Harwell, M. A. (1994). Modeling seagrass communities in tropical and subtropical bays and estuaries: a mathematical model synthesis of current hypotheses. *Bull. Mar. Sci.* 54, 757–781.

Fourqurean, J. W., Muth, M. F., and Boyer, J. N. (2010). Epiphyte loads on seagrasses and microphytobenthos abundance are not reliable indicators of nutrient availability in oligotrophic coastal ecosystems. *Mar. pollut. Bull.* 60, 971–983. doi: 10.1016/j.marpolbul.2010.03.003

Fourqurean, J. W., Willsie, A., Rose, C. D., and Rutten, L. M. (2001). Spatial and temporal pattern in seagrass community composition and productivity in south Florida. *Mar. Biol.* 138, 341–354. doi: 10.1007/s002270000448

Frankovich, T. A., Armitage, A. R., Wachnicka, A. H., Gaiser, E. E., and Fourqurean, J. W. (2009). Nutrient effects on seagrass epiphyte community structure in Florida bay. *J. Phycol.* 45, 1010–1020. doi: 10.1111/j.1529-8817.2009.00745.x

Frankovich, T. A., and Fourqurean, J. W. (1997). Seagrass epiphyte loads along a nutrient availability gradient, Florida bay, USA. *Mar. Ecol. Prog. Ser.* 159, 37–50. doi: 10.3354/meps159037

Frankovich, T. A., and Zieman, J. C. (2005). A temporal investigation of grazer dynamics, nutrients, seagrass leaf productivity, and epiphyte standing stock. *Estuaries* 28, 41–52. doi: 10.1007/BF02732752

Giovannetti, E., Montefalcone, M., Morri, C., Bianchi, C. N., and Albertelli, G. (2010). Early warning response of *Posidonia oceanica* epiphyte community to environmental alterations (Ligurian Sea, NW Mediterranean). *Mar. pollut. Bull.* 60, 1031–1039. doi: 10.1016/j.marpolbul.2010.01.024

Golzarian, M. R., Frick, R. A., Rajendran, K., Berger, B., Roy, S., Tester, M., et al. (2011). Accurate inference of shoot biomass from high-throughput images of cereal plants. *Plant Methods* 7, 1–11. doi: 10.1186/1746-4811-7-2

Greening, H. S., Cross, L. M., and Sherwood, E. T. (2011). A multiscale approach to seagrass recovery in Tampa bay, Florida. *Ecol. Restor.* 29, 82–93. doi: 10.3368/er.29.1-2.82

Greiner, J. T., McGlathery, K. J., Gunnell, J., and McKee, B. A. (2013). Seagrass restoration enhances "Blue carbon" sequestration in coastal waters. *PloS One* 8, null. doi: 10.1371/journal.pone.0072469

Grice, A. M., Loneragan, N. R., and Dennison, W. C. (1996). Light intensity and the interactions between physiology, morphology and stable isotope ratios in five species of seagrass. *J. Exp. Mar. Biol. Ecol.* 195, 91–110. doi: 10.1016/0022-0981(95)00096-8

Harrison, P. G. (1982). Control of microbial growth and of amphipod grazing by water-soluble compounds from leaves of zostera marina. *Mar. Biol.* 67, 225–230. doi: 10.1007/BF00401288

Harrison, P. G., and Durance, C. D. (1985). Reductions in photosynthetic carbon uptake in epiphytic diatoms by water-soluble extracts of leaves of *Zostera marina*. *Mar. Biol. (Berl.)* 90, 117–119. doi: 10.1007/BF00428222

Hasegawa, N., Hori, M., and Mukai, H. (2007). Seasonal shifts in seagrass bed primary producers in a cold-temperate estuary: Dynamics of eelgrass *Zostera marina* and associated epiphytic algae. *Aquat. Bot.* 86, 337–345. doi: 10.1016/j.aquabot.2006.12.002

Heck, K.L., Nadeau, D. A., and Thomas, R. (1997). The nursery role of seagrass beds. *Gulf Mexico Sci.* 15, 8. doi: 10.18785/goms.1501.08

Heck, K. L.Jr., and Valentine, J. F. (2006). Plant–herbivore interactions in seagrass meadows. *J. Exp. Mar. Biol. Ecol.* 330, 420–436. doi: 10.1016/j.jembe.2005.12.044

Heijs, F. M. L. (1984). Annual biomass and production of epiphytes in three monospecific seagrass communities of *Thalassia hemprichii* (Ehrenb.) aschers. *Aquat. Bot.* 20, 195–218. doi: 10.1016/0304-3770(84)90087-1

Hemminga, M. A., and Duarte, C. M. (2000). *Seagrass ecology* (Edinburgh Building, Cambridge CB2 2RU, UK: Cambridge University Press) 256-276.

Herzka, S., and Dunton, K. (1997). Seasonal photosynthetic patterns of the seagrass *Thalassia testudinum* in the western gulf of Mexico. *Mar. Ecol. Prog. Ser.* 152, 103–117. doi: 10.3354/meps152103

Huang, C. (2020) *Image analysis of epiphyte-seagrass dynamics on thalassia testudinum from different environmental conditions*. Available at: https://tamucc-ir.tdl.org/handle/1969.6/89696 (Accessed November 7, 2022).

Humm, H. J. (1964). Epiphytes of the sea grass, *Thalassia testudinum*, in Florida. *Bull. Mar. Sci.* 14, 306–341.

Johnson, M. W., Heck, K. L., and Fourqurean, J. W. (2006). Nutrient content of seagrasses and epiphytes in the northern gulf of Mexico: Evidence of phosphorus and nitrogen limitation. *Aquat. Bot.* 85, 103–111. doi: 10.1016/j.aquabot.2006.02.003

Johnson, J. B., and Omland, K. S. (2004). Model selection in ecology and evolution. *Trends Ecol. Evol.* 19, 101–108. doi: 10.1016/j.tree.2003.10.013

Katwijk, M. M., Thorhaug, A., Marbà, N., Orth, R. J., Duarte, C. M., Kendrick, G. A., et al. (2016). Global analysis of seagrass restoration: the importance of large-scale planting. *J. Appl. Ecol.* 53, 567–578. doi: 10.1111/1365-2664.12562

Kim, M., Qin, L.-Z., Kim, S. H., Song, H.-J., Kim, Y. K., and Lee, K.-S. (2020). Influence of water temperature anomalies on the growth of zostera marina plants held under high and low irradiance levels. *Estuaries Coasts* 43, 463–476. doi: 10.1007/s12237-019-00578-2

Kitting, C. L., Fry, B., and Morgan, M. D. (1984). Detection of inconspicuous epiphytic algae supporting food webs in seagrass meadows. *Oecologia* 62, 145–149. doi: 10.1007/BF00379006

Koch, M. S., and Erskine, J. M. (2001). Sulfide as a phytotoxin to the tropical seagrass *Thalassia testudinum:* interactions with light, salinity and temperature. *J. Exp. Mar. Biol. Ecol.* 266, 81–95. doi: 10.1016/S0022-0981(01)00339-2

Lapointe, B. E., Herren, L. W., Brewton, R. A., and Alderman, P. K. (2020). Nutrient over-enrichment and light limitation of seagrass communities in the Indian river lagoon, an urbanized subtropical estuary. *Sci. Total Environ.* 699, 134068. doi: 10.1016/j.scitotenv.2019.134068

Lee, K.-S., and Dunton, K. H. (1996). Production and carbon reserve dynamics of the seagrass *Thalassia testudinum* in corpus Christi bay, Texas, USA. *Mar. Ecol. Prog. Ser.* 143, 201–210. doi: 10.3354/meps143201

Lee, K.-S., and Dunton, K. H. (1997). Effect of *in situ* light reduction on the maintenance, growth and partitioning of carbon resources in *Thalassia testudinum* banks ex könig. *J. Exp. Mar. Biol. Ecol.* 210, 53–73. doi: 10.1016/S0022-0981(96)02720-7

Lee, K.-S., and Dunton, K. H. (2000). Effects of nitrogen enrichment on biomass allocation, growth, and leaf morphology of the seagrass *Thalassia testudinum*. *Mar. Ecol. Prog. Ser.* 196, 39–48. doi: 10.3354/meps196039

Lee, K.-S., Park, S. R., and Kim, Y. K. (2007). Effects of irradiance, temperature, and nutrients on growth dynamics of seagrasses: A review. *J. Exp. Mar. Biol. Ecol.* 350, 144–175. doi: 10.1016/j.jembe.2007.06.016

Libes, M. (1986). Productivity-irradiance relationship of posidonia oceanica and its epiphytes. *Aquat. Bot.* 26, 285–306. doi: 10.1016/0304-3770(86)90028-8

Marbà, N., Gallegos, M. E., Merino, M., and Duarte, C. M. (1994). Vertical growth of *Thalassia testudinum*: seasonal and interannual variability. *Aquat. Bot.* 47, 1–11. doi: 10.1016/0304-3770(94)90043-4

McGlathery, K. J. (2001). Macroalgal blooms contribute to the decline of seagrass in nutrient-enriched coastal waters. *J. Phycol.* 37, 453–456. doi: 10.1046/j.1529-8817.2001.037004453.x

Mehrubeoglu, M., Vargas, I., Huang, C., and Cammarata, K. (2021). "Segmentation of seagrass blade images using deep learning," in *Real-time image processing and deep learning 2021* (SPIE; Bellingham, Washington USA) 11736, 26–38. doi: 10.1117/12.2587057

Michael, T. S., Shin, H. W., Hanna, R., and Spafford, D. C. (2008). A review of epiphyte community development: surface interactions and settlement on seagrass. *J. Environ. Biol.* 29, 629–638.

Momota, K., and Nakaoka, M. (2018). Seasonal change in spatial variability of eelgrass epifaunal community in relation to gradients of abiotic and biotic factors. *Mar. Ecol.* 39, e12522. doi: 10.1111/maec.12522

Moncreiff, C., Sullivan, M., and Daehnick, A. (1992). Primary production dynamics in seagrass beds of Mississippi sound: the contributions of seagrass epiphytic algae, sand microflora, and phytoplankton. *Mar. Ecol. Prog. Ser.* 87, 161–171. doi: 10.3354/meps087161

Monier, J.-M., and Lindow, S. E. (2004). Frequency, size, and localization of bacterial aggregates on bean leaf surfaces. *Appl. Environ. Microbiol.* 70, 346–355. doi: 10.1128/AEM.70.1.346-355.2004

Moore, K. A., and Wetzel, R. L. (2000). Seasonal variations in eelgrass (*Zostera marina* l.) responses to nutrient enrichment and reduced light availability in experimental ecosystems. *J. Exp. Mar. Biol. Ecol.* 244, 1–28. doi: 10.1016/S0022-0981(99)00135-5

Nelson, W. G. (2017). Development of an epiphyte indicator of nutrient enrichment: Threshold values for seagrass epiphyte load. *Ecol. Indic.* 74, 343–356. doi: 10.1016/j.ecolind.2016.11.035

Nelson, T. A., and Waaland, J. R. (1997). Seasonality of eelgrass, epiphyte, and grazer biomass and productivity in subtidal eelgrass meadows subjected to moderate tidal amplitude. *Aquat. Bot.* 56, 51–74. doi: 10.1016/S0304-3770(96)01094-7

Nielsen, J., and Lethbridge, R. (1989). Feeding and the epiphyte food resources of gastropods living on leaves of the seagrass *Amphibolis griffithii* in south-western Australia. *J. Malacol. Soc. Aust.* 10, 47–58. doi: 10.1080/00852988.1989.10674005

Noisette, F., Depetris, A., Kühl, M., and Brodersen, K. E. (2020). Flow and epiphyte growth effects on the thermal, optical and chemical microenvironment in the leaf phyllosphere of seagrass (*Zostera marina*). *J. R. Soc. Interface* 17, 20200485. doi: 10.1098/rsif.2020.0485

Novak, R. (1982). Spatial and seasonal distribution of the meiofauna in the seagrass. *posidonia oceanica Netherlands J. Sea Res.* 16, 380–388. doi: 10.1016/0077-7579(82)90044-8

O'Brien, K. R., Adams, M. P., Ferguson, A. J., Samper-Villarreal, J., Maxwell, P. S., Baird, M. E., et al. (2018). "Seagrass resistance to light deprivation: implications for resilience," in *Seagrasses of Australia* (Australia: Springer), 287–311. doi: 10.1007/978-3-319-71354-0

Orth, R. J., Carruthers, T. J. B., Dennison, W. C., Duarte, C. M., Fourqurean, J. W., Heck, K. L., et al. (2006a). A global crisis for seagrass ecosystems. *BioScience* 56, 987–996. doi: 10.1641/0006-3568(2006)56[987:AGCFSE]2.0.CO;2

Orth, R. J., Luckenbach, M. L., Marion, S. R., Moore, K. A., and Wilcox, D. J. (2006b). Seagrass recovery in the Delmarva coastal bays, USA. *Aquat. Bot.* 84, 26–36. doi: 10.1016/j.aquabot.2005.07.007

Ow, Y. X., Ng, K. J., Lai, S., Yaakub, S. M., and Todd, P. (2020). Contribution of epiphyte load to light attenuation on seagrass leaves is small but critical in turbid waters. *Mar. Freshw. Res.* 71, 929–934. doi: 10.1071/MF19178

Peterson, B. J., Frankovich, T. A., and Zieman, J. C. (2007). Response of seagrass epiphyte loading to field manipulations of fertilization, gastropod grazing and leaf turnover rates. *J. Exp. Mar. Biol. Ecol.* 349, 61–72. doi: 10.1016/j.jembe.2007.04.012

Pinckney, J. L., and Micheli, F. (1998). Microalgae on seagrass mimics: does epiphyte community structure differ from live seagrasses? *J. Exp. Mar. Biol. Ecol.* 221, 59–70. doi: 10.1016/S0022-0981(97)00115-9

Premarathne, C., Jiang, Z., He, J., Fang, Y., Chen, Q., Cui, L., et al. (2021). Low light availability reduces the subsurface sediment carbon content in halophila beccarii from the south China Sea. *Front. Plant Sci.* 12. doi: 10.3389/fpls.2021.664060

Ralph, P. J., Durako, M. J., Enríquez, S., Collier, C. J., and Doblin, M. A. (2007). Impact of light limitation on seagrasses. *J. Exp. Mar. Biol. Ecol.* 350, 176–193. doi: 10.1016/j.jembe.2007.06.017

Ralph, P. J., Macinnis-Ng, C. M. O., and Frankart, C. (2005). Fluorescence imaging application: effect of leaf age on seagrass photokinetics. *Aquat. Bot.* 81, 69–84. doi: 10.1016/j.aquabot.2004.11.003

Rasmusson, L. M., Buapet, P., George, R., Gullström, M., Gunnarsson, P. C., and Björk, M. (2020). Effects of temperature and hypoxia on respiration, photorespiration, and photosynthesis of seagrass leaves from contrasting temperature regimes. *ICES J. Mar. Sci.* 77, 2056–2065. doi: 10.1093/icesjms/fsaa093

Ray, B. R., Johnson, M. W., Cammarata, K., and Smee, D. L. (2014). Changes in seagrass species composition in northwestern gulf of Mexico estuaries: effects on associated seagrass fauna. *PloS One* 9, e107751. doi: 10.1371/journal.pone.0107751

Reyes, J., and Sansón, M. (2001). Biomass and production of the epiphytes on the leaves of cymodocea nodosa in the canary islands. *Botanica Marina* 44 (4). doi: 10.1515/BOT.2001.039

Ruesink, J. L. (2016). Epiphyte load and seagrass performance are decoupled in an estuary with low eutrophication risk. *J. Exp. Mar. Biol. Ecol.* 481, 1–8. doi: 10.1016/j.jembe.2016.03.022

Saha, M., Berdalet, E., Carotenuto, Y., Fink, P., Harder, T., John, U., et al. (2019). Using chemical language to shape future marine health. *Front. Ecol. Environ.* 17, 530–537. doi: 10.1002/fee.2113

Sand-Jensen, K. (1977). Effect of epiphytes on eelgrass photosynthesis. *Aquat. Bot.* 3, 55–63. doi: 10.1016/0304-3770(77)90004-3

Schanz, A., Polte, P., and Asmus, H. (2002). Cascading effects of hydrodynamics on an epiphyte–grazer system in intertidal seagrass beds of the wadden Sea. *Mar. Biol.* 141, 287–297. doi: 10.1007/s00227-002-0823-8

Shaffer, J. P. (1986). Modified sequentially rejective multiple test procedures. *J. Am. Stat. Assoc.* 81, 826–831. doi: 10.1080/01621459.1986.10478341

Shamir, L., Delaney, J. D., Orlov, N., Eckley, D. M., and Goldberg, I. G. (2010). Pattern recognition software and techniques for biological image analysis. *PloS Comput. Biol.* 6, 1-10. doi: 10.1371/journal.pcbi.1000974

Smit, A. J., Brearley, A., Hyndes, G. A., Lavery, P. S., and Walker, D. I. (2005). Carbon and nitrogen stable isotope analysis of an amphibolis griffithii seagrass bed. *Estuarine Coast. Shelf Sci.* 65, 545–556. doi: 10.1016/j.ecss.2005.07.002

Smith, C. S., Ito, M., Namba, M., and Nakaoka, M. (2018). Oyster aquaculture impacts *Zostera marina* epibiont community composition in akkeshi-ko estuary, Japan. *PloS One* 13, e0197753. doi: 10.1371/journal.pone.0197753

Smith, K. A., North, E. W., Shi, F., Chen, S.-N., Hood, R. R., Koch, E. W., et al. (2009). Modeling the effects of oyster reefs and breakwaters on seagrass growth. *Estuaries Coasts* 32, 748–757. doi: 10.1007/s12237-009-9170-z

Stanca, E., and Parsons, M. L. (2021). Examining the dynamic nature of epiphytic microalgae in the Florida keys: What factors influence community composition? *J. Exp. Mar. Biol. Ecol.* 538, 151538. doi: 10.1016/j.jembe.2021.151538

Thom, R., Miller, B., and Kennedy, M. (1995). Temporal patterns of grazers and vegetation in a temperate seagrass system. *Aquat. Bot.* 50, 201–205. doi: 10.1016/0304-3770(95)00449-A

Wagner, S., Jaffé, R., Cawley, K., Dittmar, T., and Stubbins, A. (2015). Associations between the molecular and optical properties of dissolved organic matter in the Florida Everglades, a model coastal wetland system. *Front. Chem.* 3, 66. doi: 10.3389/fchem.2015.00066

Wear, D. J., Sullivan, M. J., Moore, A. D., and Millie, D. F. (1999). Effects of water-column enrichment on the production dynamics of three seagrass species and their epiphytic algae. *Mar. Ecol. Prog. Ser.* 179, 201–213. doi: 10.3354/meps179201

Westfall, P. H. (1997). Multiple testing of general contrasts using logical constraints and correlations. *J. Am. Stat. Assoc.* 92, 299–306. doi: 10.1080/01621459.1997.10473627

Whalen, M. A., Duffy, J. E., and Grace, J. B. (2013). Temporal shifts in top-down vs. bottom-up control of epiphytic algae in a seagrass ecosystem. *Ecology* 94, 510–520. doi: 10.1890/12-0156.1

Willcocks, P. A. (1982). Colonization and distribution of the red algal epiphytes melobesia mediocris and smithora naiadum on the seagrass. *Phyllospadix torreyi. Aquat. Bot.* 12, 365–373. doi: 10.1016/0304-3770(82)90028-6

Wolaver, T. G., Wetzel, R. L., Zieman, J. C., and Webb, K. L. (1980). "Nutrient interactions between salt marsh, mudflats, and estuarine water," in *Estuarine perspectives* (Elsevier), 123–133. doi: 10.1016/C2013-0-10959-2

Worm, B., and Sommer, U. (2000). Rapid direct and indirect effects of a single nutrient pulse in a seaweed-epiphyte-grazer system. *Mar. Ecol. Prog. Ser.* 202, 283–288. doi: 10.3354/meps202283

Wright, A., Bohrer, T., Hauxwell, J., and Valiela, I. (1995). Growth of epiphytes on *Zostera marina* in estuaries subject to different nutrient loading. *Biol. Bull.* 189, 261–261. doi: 10.1086/BBLv189n2p261

Zieman, J. C. (1975). Seasonal variation of turtle grass, *Thalassia testudinum* könig, with reference to temperature and salinity effects. *Aquat. Bot.* 1, 107–123. doi: 10.1016/0304-3770(75)90016-9

Zieman, J. C., Fourqurean, J. W., and Frankovich, T. A. (1999). Seagrass die-off in Florida bay: Long-term trends in abundance and growth of turtle grass. *Thalassia testudinum Estuaries* 22, 460–470. doi: 10.2307/1353211

Zimba, P. V., and Hopson, M. S. (1997). Quantification of epiphyte removal efficiency from submersed aquatic plants. *Aquat. Bot.* 58, 173–179. doi: 10.1016/S0304-3770(97)00002-8

frontiers | Frontiers in Marine Science

TYPE Original Research
PUBLISHED 24 January 2023
DOI 10.3389/fmars.2023.1121731

OPEN ACCESS

EDITED BY
Hui Zhao,
Guangdong Ocean University, China

REVIEWED BY
Chunhua Qiu,
Sun Yat-sen University, China
Lixiao Xu,
Ocean University of China, China

*CORRESPONDENCE
Yu Liu
liuyuhk@zjou.edu.cn

SPECIALTY SECTION
This article was submitted to Coastal Ocean Processes, a section of the journal Frontiers in Marine Science

RECEIVED 12 December 2022
ACCEPTED 11 January 2023
PUBLISHED 24 January 2023

CITATION
Sun W, An M, Liu J, Liu J, Yang J, Tan W, Sian KTCLK, Ji J, Liu Y and Dong C (2023) Comparative analysis of four types of mesoscale eddies in the North Pacific Subtropical Countercurrent region - part II seasonal variation. *Front. Mar. Sci.* 10:1121731. doi: 10.3389/fmars.2023.1121731

Comparative analysis of four types of mesoscale eddies in the North Pacific Subtropical Countercurrent region - part II seasonal variation

Wenjin Sun[1,2,3,4], Mengxuan An[1], Jishan Liu[1], Jie Liu[1], Jingsong Yang[2,3], Wei Tan[5], Kenny T. C. Lim Kam Sian[6], Jinlin Ji[1,2], Yu Liu[2,7]* and Changming Dong[1,2]

[1]School of Marine Sciences, Nanjing University of Information Science and Technology, Nanjing, China, [2]Southern Marine Science and Engineering Guangdong Laboratory (Zhuhai), Zhuhai, China, [3]State Key Laboratory of Satellite Ocean Environment Dynamics, Second Institute of Oceanography, Ministry of Natural Resources, Hangzhou, China, [4]GEOMAR Helmholtz Centre for Ocean Research Kiel, Kiel, Germany, [5]College of Ocean Science and Engineering, Shandong University of Science and Technology, Qingdao, China, [6]School of Atmospheric Science and Remote Sensing, Wuxi University, Wuxi, China, [7]Marine Science and Technology College, Zhejiang Ocean University, Zhoushan, China

The North Pacific Subtropical Countercurrent area (STCC) is high in mesoscale eddy activities. According to the rotation direction of the eddy flow field and the sign of temperature anomaly within the eddy, they can be divided into four categories: cyclonic cold-core eddy (CCE), anticyclonic warm-core eddy (AWE), cyclonic warm-core eddy (CWE) and anticyclonic cold-core eddy (ACE). CCE and AWE are called normal eddies, and CWE and ACE are named abnormal eddies. Based on the OFES data and vector geometry automatic detection method, we find that at the sea surface, the maximum monthly number of the CCE, AWE, CWE, and ACE occurs in December (765.70 ± 52.05), January (688.20 ± 82.53), August (373.40 ± 43.09) and August (533.00 ± 56.92), respectively. The number of normal eddies is more in winter and spring, and less in summer and autumn, while abnormal eddies have the opposite distribution. The maximum rotation velocity of the four types of eddies appears in June (11.71 ± 0.75 cm/s), June (12.24 ± 0.86 cm/s), May (10.63 ± 0.99 cm/s) and June (9.97 ± 0.91 cm/s), which is fast in winter and spring. The moving speed of the four types of eddies is almost similar (about 10 ~ 11 cm/s). The amplitude of normal and abnormal eddies is both high in summer and autumn, and low in winter and spring, with larger amplitudes in normal than abnormal eddies. The eccentricity (defined as the eccentricity of the ellipse obtained by fitting the eddy boundary) of the four types of eddies is also close to each other, and their variation ranges from 0.7 to 0.8, with no apparent seasonal variation. The vertical penetration depth, which has no significant seasonal difference, is 675.13 ± 67.50 m in cyclonic eddies (CCE and CWE), which is deeper than that 622.32 ± 81.85 m in anticyclonic eddies (ACE and AWE). In addition, increasing the defined temperature threshold for abnormal eddies can significantly reduce their numbers but does not change their seasonal variation trend.

KEYWORDS

abnormal eddy, mesoscale eddy, seasonal variation, STCC region, OFES data

1 Introduction

Satellite observations show that mesoscale eddies are almost ubiquitous in the global oceans (Chelton et al., 2007; Chelton et al., 2011; Ma and Wang, 2014; Wang et al., 2015; Chen and Han, 2019; Dong et al., 2022). The lifespan of these mesoscale eddies is from several weeks to months, and the eddy diameter is O(100 km). Mesoscale eddies are strongly nonlinear and have significant effects on physical quantities in the ocean and the atmospheric bottom boundary layer. Mesoscale eddies can transport material and energy through their horizontal movement (Dong et al., 2014), rotation (He et al., 2018) and asymmetric flow field structure (Qiu et al., 2022). Eddy-induced zonal mass transport is comparable in magnitude to the large-scale wind- and thermohaline-driven circulation (Zhang et al., 2014a). Therefore they play a crucial role in the redistribution of heat and freshwater (Chen et al., 2012; Gaube et al., 2015; Xu et al., 2016; Dong et al., 2017; Lin et al., 2019; Xu et al., 2019; Dai et al., 2020; Ding et al., 2021a).

Mesoscale eddies also affect biological productivity in the upper ocean (Xian et al., 2012; McGillicuddy, 2016; Wang et al., 2018; He et al., 2019; Patel et al., 2020; Geng et al., 2021). In the south Indian Ocean, anticyclonic eddies (AEs) can induce a positive chlorophyll anomaly within the eddy (Gaube et al., 2013). Besides, cyclonic eddies (CEs) usually cause the upper mixed layer depth to become shallow, while AEs can cause the deepening of the upper mixed layer (Sun et al., 2017; Gaube et al., 2019; Ding et al., 2021b). Using satellite data from 2006 ~ 2009 in the Kuroshio Extension region, Ma et al. (2015) demonstrated that CEs-induced (AEs-induced) surface winds speed decelerate (accelerate) and reduce (increase) latent and sensible heat fluxes, water vapor content, cloud liquid water, and rain rate.

According to the rotation direction of the eddy surface flow field, mesoscale eddies are usually divided into CEs (with a counterclockwise rotation flow field) and AEs (with a clockwise rotation flow field). Synthetic analysis of large samples found that CEs are usually associated with a cold eddy core, while the AEs usually have a warm eddy core (Qiu and Chen, 2004; Meijers et al., 2007; Wang et al., 2012; Zhang et al., 2014b; Yang et al., 2015; Amores et al., 2016; Treguier et al., 2017). Therefore, CEs are also called cyclonic cold-core eddies (CCEs), and AEs are also named anticyclonic warm-core eddies (AWEs). However, recent studies have pointed out the existence of CEs with a warm eddy core (CWEs) and AEs with a cold eddy core (ACEs) (Itoh and Yasuda, 2010; Ji et al., 2016; Ni et al., 2021; An et al., 2022; Sun et al., 2022). In order to distinguish these eddies from the traditional CCEs and AWEs, these eddies are named abnormal eddies (Sun et al., 2019).

Using different definitions and identification methods, the proportion of abnormal eddies is from about 10% (Sun et al., 2019) to 20% (Ni et al., 2021) and even as high as 1/3 (Liu et al., 2021). Sun et al. (2019) pointed out that abnormal eddies are widespread in the North Pacific Ocean and have significant regional differences. The CWEs are concentrated in the northwest and southeast of the North Pacific Ocean. At the same time, the ACEs are also widely distributed in the northeast area in addition to these above two regions. The monthly distribution of the abnormal eddy numbers shows they are more numerous in summer than in winter.

Ni et al. (2021) pointed out that CWEs account for 19% of the global CEs, and AWEs account for 22% of the total AEs. The proportion of abnormal eddies is higher in tropical and boundary current regions. Besides, they have a noticeable seasonal difference in extratropical oceans area caused by the seasonal difference in the mixed layer depth. Combining the global Archiving, Validation, and Interpretation of Satellite Oceanographic (AVISO) and Advanced Very High-Resolution Radiometer (AVHRR) data from 1996 to 2015 and an artificial intelligence identification algorithm, Liu et al. (2021) found that abnormal eddies account for one-third of the total mesoscale eddies. Abnormal eddies showed a decreasing trend year by year in the global ocean, which is consistent with the results of Sun et al. (2019) in the North Pacific Ocean. They pointed out that there is a good correlation between the change in the number of abnormal eddies and the sea surface temperature gradient induced by global warming. The correlation coefficient between the two can reach 0.68, significant at 90% confidence level.

An et al. (2022, hereafter known as Part I) discussed the spatial characteristics of the four types of eddies in the STCC region based on the OFES data from 2008 to 2017. They found that the proportion of the four eddy types is 35.60, 32.08, 12.95, and 19.37% at the sea surface, respectively. From the vertical distribution, abnormal eddies are mainly distributed in the oceanic upper layer. There is no significant difference in eddy radius (about 70 ~ 80 km) and amplitude (3 ~ 6 cm) for the four types of eddies. These mesoscale eddies generally move westward at about 3 ~ 5 km per day. Part I provides a reference to comprehensively understand the spatial characteristics of mesoscale eddies in the STCC area.

The STCC area is located in the East-Asian monsoon region, and its eddy kinetic energy (EKE) shows a prominent annual cycle (Qiu, 1999; Kang et al., 2010; Qiu and Chen, 2010; Qiu et al., 2014). Therefore, this region's mesoscale eddies characteristics may have obvious seasonal variation. Following Part I, this study systematically explores the seasonal variation of the four mesoscale eddy types. The findings are useful for getting a more comprehensive understanding of mesoscale eddy characteristics in the STCC region.

The rest of the study is organized as follows. Section 2 introduces the OFES data, the automatic eddy detection method, and the definition of the four types of mesoscale eddies. Section 3 analyzes the seasonal variations of the four types of mesoscale eddies in detail, including eddy number, radius, rotation velocity, horizontal movement velocity, nonlinearity, amplitude, eccentricity, and penetration depth. The eddy anomaly ratio (the ratio of the abnormal eddy existence duration to that of the eddy lifespan) and the influence of different temperature thresholds value on abnormal eddy numbers are discussed in Section 4. Finally, the main conclusions of this study are summarized in Section 5.

2 Data and methods

2.1 OFES data

This study explores the seasonal variation of the mesoscale eddies in the STCC region (16°N ~ 27°N, 115°E ~ 160°W) based on the OFES data (OGCM for the Earth Simulator), which extends from January 2008 to December 2017. The horizontal resolution of this data is 1/10° × 1/10° and is vertically divided into 54 uneven layers. The minimum depth at the upper-most layer is 2.5 m, and the

maximum depth is 6,300 m. The time resolution of this data is three days. It can be downloaded from the Asia-Pacific Data Research Center of the University of Hawaii (http://apdrc.soest.hawaii.edu/las_ofes).

We use 3-day snapshots of sea surface height (η), three-dimensional zonal velocity (U), meridional velocity (V), and temperature (T) in this study. The OFES data are first passed through a high-pass space filter of 3° × 3° to obtain the sea surface height (η'), velocity (U' and V'), and temperature (T') anomalies. The spatial resolution of the OFES data is higher than common satellite data (generally only 0.25° × 0.25°, such as AVISO data, Pujol et al., 2016), and it contains three-dimensional variables. Thus the OFES data is more suitable than satellite data for mesoscale eddies studies. In addition, the OFES data does not adopt an assimilation scheme. Therefore its dynamic process is self-consistent and can be used for numerical diagnosis of thermodynamic or dynamic processes. Many previous works used this data for mesoscale eddy and other mesoscale process research (Taguchi et al., 2010; Zhang et al., 2017; Ji et al., 2018; Sun et al., 2022; Wang et al., 2022). For more information about the OFES data, please refer to Sasaki et al. (2008).

2.2 Two-dimensional eddy detection method

The automatic eddy detection algorithm is essential for extensive sample analysis studies. Predecessors have proposed a variety of automatic eddy identification methods, such as the Okubo-Weiss parameter method (Okubo, 1970; Weiss, 1991), the Winding-Angle method (Sadarjoen and Post, 2000), and the Sea Surface Height Topological method (Chelton et al., 2011). Among these methods, the Okubo-Weiss parameter method is the easiest to implement, but its accuracy is relatively low. Winding-Angle method has a high accuracy of eddy identification but with low computational efficiency. The altimeter sampling ability limits the Sea Surface Height Topological method, resulting in a lower successful identification (Tang et al., 2019).

This study adopts a vector geometry automatic detection method based on the geometric characteristics of mesoscale eddies (Nencioli et al., 2010). This method has already been applied to multiple data sources and complex flow fields (Dong et al., 2009; Aguiar et al., 2013; Lin et al., 2015; Sun et al., 2018; Yang et al., 2020; Sun et al., 2021a; Sun et al., 2021b; Qiu et al., 2022). Recently research has shown that the vector geometry method has more advantages than the Sea Surface Height Topology approach in terms of correct eddy identification rate and detection efficiency (You et al., 2022). The specific operations of this method are summarized as follows:

Firstly, based on the two-dimensional flow field data and the rotation characteristics of the eddy velocity field, the eddy center point is defined as a point meeting the following four constraints.

1~2) In the east-west (north-south) direction across the eddy center, the meridional (zonal) velocity component V' (U') has an opposite sign on the left and right (upper and lower) sides of the eddy center, and its size gradually increases with the distance from the eddy center.

3) The velocity at the eddy center point has the minimum value among the local area around the eddy center.

4) The velocity vector rotates clockwise or counterclockwise around the eddy center, and the rotation direction remains unchanged.

After the eddy center is determined, the outermost closed streamline of the local stream function around the eddy center is extracted as the eddy boundary. The eddy radius is then calculated as the radius of a circle which gives a circle area equivalent to the polygonal area enclosed by the eddy boundary.

2.3 Two-dimensional eddy tracking algorithm

Mesoscale eddy is a "living" marine phenomenon that goes through different life stages, from formation to decay (Liu et al., 2012). This study uses a similar method following Doglioli et al. (2007) and Chaigneau et al. (2008) to track the mesoscale eddies' trajectory. The tracking steps are as follows:

1) The search area (S_1) and extended search area (S_2) with a radius of 1.2° and 1.8° are defined, with the eddy center as the circle center. The search area's size selection depends on the background field's current velocity and the data's spatiotemporal resolution. On the one hand, the center of the mesoscale eddy is required not to move out of S_1 at the next time step. On the other hand, S_1 should not be too large. Otherwise, two distinct eddies will be incorrectly identified as the same eddy. The radius of S_2 is generally set as 1.5 times that of S_1.

2) If an arbitrary eddy (the current eddy hereafter) is successfully detected at the time step t, then we search for an eddy with the same polarity as the current eddy in the search area S_1 at time step t+1. If more than one eddy meets the requirement, the eddy closest to the current eddy center is selected as the continuation of the current eddy. If no eddy is successfully identified at the time step t+1, we search again using the extended search area S_2 at the time step t+2. If still no eddy with the same polarity is found, then the current eddy is considered decayed, and its lifespan is defined as the time interval from the time step of the first successful detection to the time step t. After the automatic eddy detection and tracking, a dataset containing eddy radius, polarity, boundary, lifespan, and the moving path is obtained.

2.4 Three-dimensional eddy detection algorithm

Based on the two-dimensional eddy detection results (subsection 2.3), three-dimensional eddy detection is carried out layer by layer from the sea surface down to the bottom layer (Dong et al., 2012; Lin et al., 2015). The specific steps are summarized as follows:

According to the eddy information at the sea surface (N_1 , current layer): eddy center position $P_1(x_1,y_1)$, occurrence time (t_1), eddy radius (R_1) , and eddy polarity (cyclonic/anticyclonic), we search for the eddy center at time (t_1) with the same polarity within the area S_3 in the next layer (search layer). S_3 is a circular area, with $P_1(x_1,y_1)$ as the center and $0.25R_1$ as the radius. If no eddy center satisfies the conditions in the next layer, the eddy penetration depth is equal to the depth of the current layer. If only one eddy center meeting the conditions is found in the next layer, it is regarded as the vertical extension of the current eddy. The eddy central point position $P_2(x_2, y_2)$, radius (R_2) and other information in the second layer are extracted. Then, the second layer is used as the current layer, and the third layer is the search layer, thus continuing the search process until no eddy can be found or the search reaches the bottom boundary. If more than one eddy satisfies the conditions in the search layer, then the one with the nearest eddy center is taken as the vertical extension of the current eddy. Using this method, the eddy vertical penetration depth is slightly shallower than the realistic value. The difference depends on the interval between the two layers in the vertical direction. In this study, we consider it as a small amount and do not discuss this difference.

2.5 Eddy classification

Eddies are classified into four types according to the combination of the rotation direction (clockwise or counterclockwise) of the eddy flow fields and the signs of the temperature anomaly (warm or cold) within the eddy. They are cyclonic cold-core eddy (CCE, with a counterclockwise rotating flow field and a negative temperature anomaly); cyclonic warm-core eddy (CWE, with a counterclockwise rotating flow field and a positive temperature anomaly); anticyclonic cold-core eddy (ACE, with a clockwise rotating flow field and a negative temperature anomaly), and anticyclonic warm-core eddy (AWE, with a clockwise rotating flow field and a positive temperature anomaly). CCEs and AWEs are also known as normal eddies because they satisfied traditional mesoscale eddies definition, while CWEs and ACEs are known as abnormal eddies (Sun et al., 2019).

There are two ways to define temperature anomaly. One is the average temperature anomaly within the eddy ($T_1 = \frac{1}{N}\sum_{i=1}^{N} T'$), where T' is the temperature deviation from the background field and N represents the number of grid points within the eddy (Sun et al., 2022). The other one is the difference between the average temperature anomaly within the eddy (T') and the eddy background field ($T_2 = \frac{1}{M}\sum_{i=1}^{M} T'$). Where M represents the number of grid points within the eddy background field, usually defined as the annular area from the eddy boundary to 1.5 times the eddy radius (Sun et al., 2019).

The method in Part I is also used here to determine the eddy temperature anomaly. That is, the first definition method is adopted. Considering that the time scale of mesoscale eddies is several weeks to months, eddies with a lifespan shorter than 30 days are removed to increase the results' robustness. This study focuses on eddies' seasonal variation, concentrated in the oceanic upper layer. Therefore, although the maximum depth of the OFES data is 6,300 m, we only focus on the oceanic upper layer shallower than 1,000 m.

3 Eddy seasonal variations

The STCC region (16°N ~ 27°N, 115°E ~ 160°W) is affected by the East-Asian monsoon and has obvious seasonal variations. Part I of the study discusses the three-dimensional spatial distribution of mesoscale eddies from 2008 to 2017. The present study focuses on the seasonal variations of the eddy number, radius, rotation velocity, horizontal moving velocity, nonlinearity, amplitude, eccentricity, and vertical penetration depth.

3.1 Eddy number

Previous studies have shown that the temporal variability of sea surface temperature (SST) gradient on a seasonal scale is closely related to the number of eddies generated (Liu et al., 2012). The larger SST gradient generates more eddies in the early spring than in summer. To verify this result, Figure 1 shows the monthly distribution of multi-year average (2008 ~ 2017) eddy numbers at the sea surface (Figures 1A, B) and 1,000 m (Figures 1C, D). At the sea surface, the multi-year average monthly number of CCEs, AWEs, CWEs, and ACEs are 631.34 ± 100.11, 568.37 ± 97.90, 229.62 ± 98.36, and 343.31 ± 128.81, respectively. The largest number of the four types of eddies (hereafter, the order of the four types of eddies is CCEs, AWEs, CWEs, and ACEs) appears in December (765.70 ± 52.05), January (688.20 ± 82.53), August (373.40 ± 43.09), and August (533.00 ± 56.92). Accordingly, the four types of eddies reach the minimum number in April, April, February and February, and the corresponding values are 529.00 ± 29.92, 440.30 ± 32.28, 112.20 ± 22.51 and 151.00 ± 28.41, respectively. The result indicates that the number of normal eddies, whether average value, maximum or minimum, is far greater than abnormal eddies.

Normal eddies at the sea surface are more in winter and spring, and less in summer and autumn (Figure 1A). Unlike normal eddies, the number of abnormal eddies is higher in summer and autumn, and less in spring and winter (Figure 1B). The mechanism causing this difference may be that the wind stress curl in the STCC region, pointed out by Ni et al. (2021), is stronger in winter than in summer. Therefore, the eddies generated by the wind stress curl are more normal eddies, while the abnormal eddies occur more in summer when the wind stress curl is weak. Of course, there are other mechanisms for eddy generation in the STCC region (such as flow instability and the interaction between flow field and topography), but this is beyond the scope of this paper, and we will further discuss it in future studies. In addition, CCEs are generally slightly more than AWEs, which is consistent with the result of Tang et al. (2019).

At 1,000 m, the multi-year monthly average number of CCEs, AWEs, CWEs, and ACEs are 1,192.38 ± 163.66, 1,133.62 ± 146.50, 28.50 ± 19.46 and 39.46 ± 21.14, respectively. Their maximum values all appear in December, with corresponding values of 1,272.40 ± 378.98, 1,202.10 ± 337.32, 38.80 ± 46.08, and 52.40 ± 50.52. Accordingly, the minimum is in February (1,061.40 ± 63.11), February (1,009.40 ± 73.01), April (21.60 ± 11.54), and February (31.60 ± 15.58). Comparing Figures 1C, D with Figures 1A, B, it can be concluded that eddy numbers at 1,000 m do not vary with seasons.

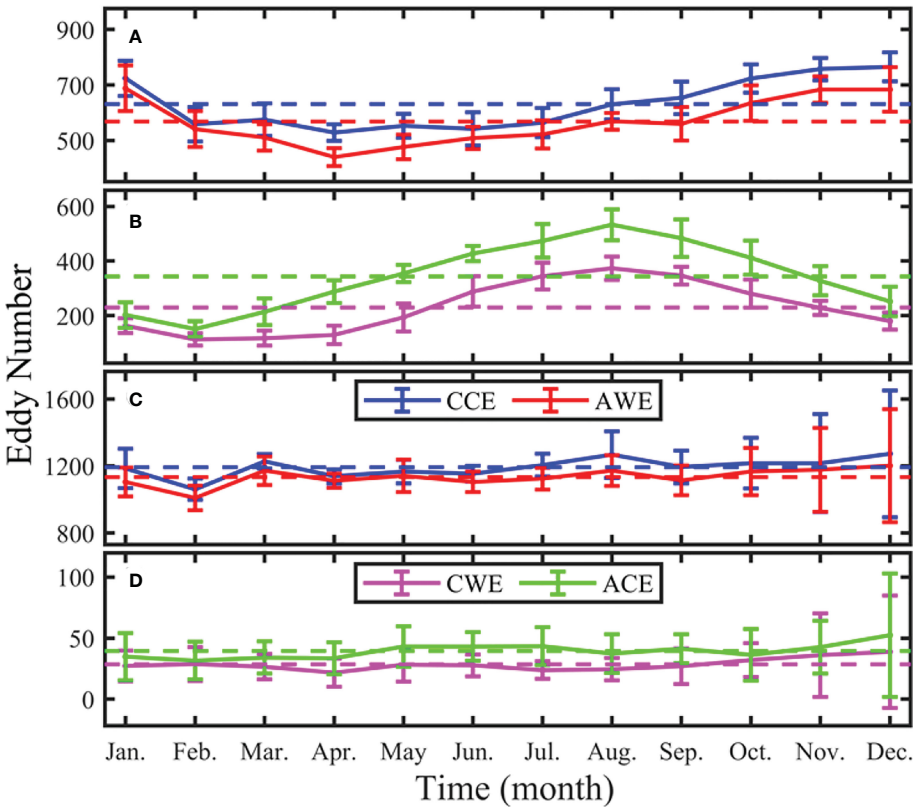

FIGURE 1
Monthly distribution of multi-year (2008 ~ 2017) average eddy number at the sea surface **(A, B)** and 1,000 m **(C, D)** in the STCC region. Blue, red, pink, and green curves represent cyclonic cold-core eddy, anticyclonic warm-core eddy, cyclonic warm-core eddy, and anticyclonic cold-core eddy, respectively. The bar represents the standard deviation, and the dotted line represents the multi-year average value.

Whether at the sea surface or 1,000 m, the number of CCEs is generally higher than that of AWEs, while the number of ACEs is generally higher than that of CWEs, and the number of normal eddies is greater than that of abnormal eddies. Hence, the multi-year monthly average eddy number has an apparent seasonal variation at the sea surface, but there is no seasonal variation in the eddy numbers at 1,000 m.

3.2 Eddy radius

Figure 2 shows the monthly distribution of the four types of mesoscale eddies radii at the sea surface (Figures 2A, B) and 1,000 m (Figures 2C, D). At the sea surface, the multi-year average monthly radii of CCEs, AWEs, CWEs, and ACEs are 79.19 ± 2.95, 83.28 ± 3.47, 73.23 ± 4.45, and 79.37 ± 3.48 km, respectively. The maximum monthly average radii of the four eddy types occur in February, January, June, and July, and their corresponding values are 81.29 ± 1.85, 85.07 ± 3.97, 76.60 ± 3.68, and 81.48 ± 3.20 km. Accordingly, the minimum values appear in June (77.13 ± 3.46 km), June (81.45 ± 2.45 km), December (70.84 ± 2.06 km), and December (77.65 ± 4.58 km). That is, the maximum of the multi-year monthly average radius of the normal eddies (CCEs and AWEs) appears in winter (February, January), and the minimum appears in summer (June, July). However, the opposite is observed in abnormal eddies. Besides, there is no apparent difference between the multi-year monthly average radii of the four eddy types, which are all about 80 km.

At 1,000 m, the multi-year monthly average radii of the four eddy types are 68.32 ± 2.20, 70.34 ± 2.68, 48.06 ± 7.17, and 51.14 ± 7.28 km. The maximum multi-year monthly average radii occur in October, January, September, and December, with corresponding values of 69.43 ± 2.12, 71.79 ± 3.21, 52.69 ± 7.30, and 54.81 ± 6.01 km. Accordingly, the minimum value is in January, August, June, and June, and their corresponding values are 67.31 ± 1.64, 68.67 ± 2.67, 43.00 ± 4.58, and 48.07 ± 6.67 km, respectively.

In Figure 2, the radius of the four types of eddies has no obvious variation with the month, either at the surface or at 1,000 m. This characteristic is consistent with the result of Tang et al. (2019), based on AVISO data in the STCC area. At the sea surface and 1,000 m, the average radius of AEs (ACEs and AWEs) is slightly larger than that of CEs (CWEs and CCEs), except in September (Figure 2D). By comparing Figures 2A, B with Figures 2C, D, the eddy radius at the sea surface is larger than that at 1,000 m.

3.3 Eddy rotation velocity

Eddy rotation velocity embodies its ability to encircle its internal seawater and is an important influencing factor of eddy nonlinearity. In this study, the eddy rotation velocity is defined as the average value

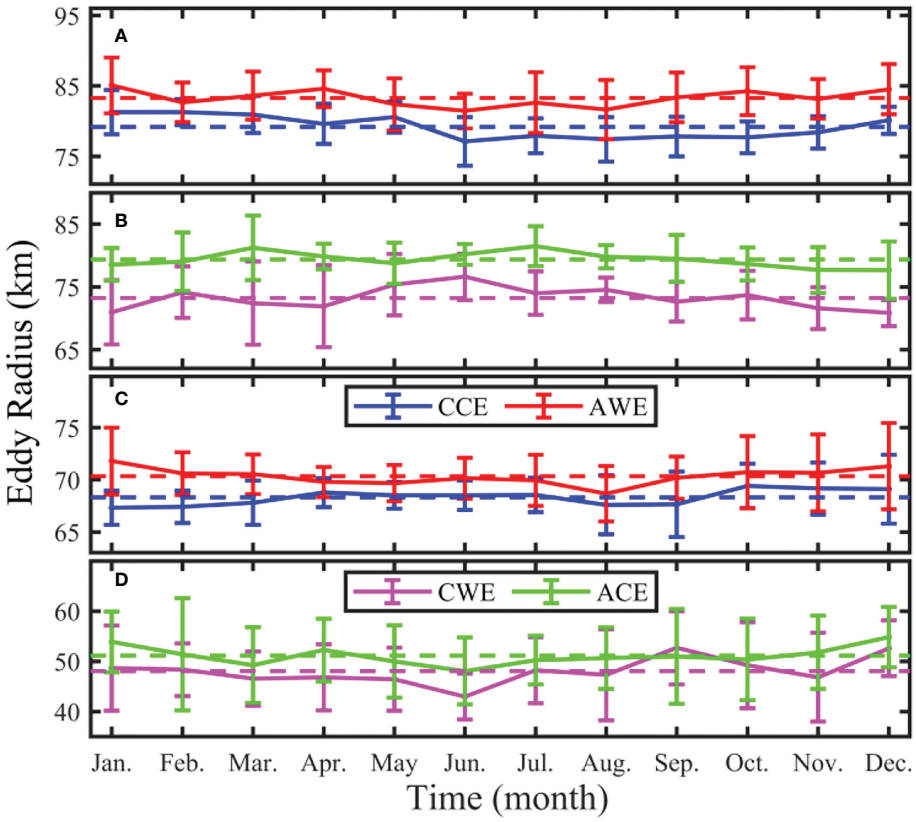

FIGURE 2
Monthly distribution of multi-year (2008 ~ 2017) average eddy radius at the sea surface **(A, B)** and 1,000 m **(C, D)** in the STCC area. Blue, red, pink, and green curves represent cyclonic cold-core eddy, anticyclonic warm-core eddy, cyclonic warm-core eddy, and anticyclonic cold-core eddy, respectively. The bar represents the standard deviation, and the dotted line represents the multi-year average value.

of the flow velocity within the eddy ($U_R = \frac{1}{N}\sum_{i=1}^{N}\sqrt{U_i'2 + V_i'2}$), where N represents the total number of grid point within the eddy. At the sea surface, the monthly distribution of the multi-year average rotation velocity of the four types of eddies shows large values in summer and small values in winter (Figures 3A, B). Their average values are 10.59 ± 1.05, 10.53 ± 1.36, 8.93 ± 1.50, 8.96 ± 1.13 cm/s, respectively. It can be seen that the normal eddy's rotation velocity is greater than that of the abnormal eddy. The maximum eddy rotation velocity of the four types of eddies occurs in June, June, May, June, and their corresponding values are 11.71 ± 0.75, 12.24 ± 0.86, 10.63 ± 0.99, and 9.97 ± 0.91 cm/s, respectively. Accordingly, the minimum rotation velocity is 9.47 ± 0.65, 9.02 ± 0.73, 7.44 ± 0.83, and 7.84 ± 0.71 cm/s, appearing in December, December, November, and December, respectively. At the sea surface, the eddy rotation velocity in summer is significantly higher than in winter. The normal eddy rotation velocity is faster than that of the abnormal eddy.

In contrast, at 1,000 m, the multi-year monthly average rotation velocity of the four types of eddies slightly varies with time (Figures 3C, D). The rotation velocity of the four eddy types is 1.61 ± 0.12, 1.76 ± 0.16, 1.15 ± 0.39, and 1.06 ± 0.28 cm/s, respectively. Their maximum values appear in October (1.65 ± 0.64 cm/s), October (1.86 ± 0.56 cm/s), July (1.35 ± 1.59 cm/s), and November (1.26 ± 1.11 cm/s), respectively. Accordingly, it reaches its minimum in August, April, May, and May, with 1.59 ± 0.47, 1.68 ± 0.51, 0.99 ± 1.50, and 0.92 ± 1.25 cm/s. The eddy rotation velocity at the sea surface is larger by about 4 ~ 5 times than that at 1,000 m. The average rotation velocity of normal eddies is larger than that of abnormal eddies at both the surface and 1,000 m.

3.4 Eddy horizontal movement velocity

Eddy horizontal moving velocity is another crucial factor determining its heat and freshwater transport capacity. The horizontal moving velocity ($U_H = \frac{L}{\Delta t}$) is defined as the ratio of the eddy center moving distance ($L = \sqrt{(x_2 - x_1)^2 + (y_2 - y_1)^2}$) to the temporal resolution of the OFES data Δt , where (x_1,y_1) and (x_2,y_2) represent the spatial position of the eddy center at two adjacent time steps. From Figure 4, the eddy horizontal moving velocity at the sea surface and 1,000 m show no noticeable seasonal variations. The eddy horizontal moving velocity at the sea surface is about 1.7 ~ 2.0 times at 1,000 m.

At the sea surface, the multi-year monthly average horizontal moving velocities of the four eddy types are 10.31 ± 0.67, 10.66 ± 0.83, 10.27 ± 0.81, and 10.66 ± 0.81 cm/s, respectively. The maximum horizontal moving velocity appears in July, May, March, and June, and their corresponding values are 10.85 ± 0.73, 11.59 ± 0.71, 11.09 ± 0.74, and 11.04 ± 0.67 cm/s. The minimum values are reached in December, January, December, and September, and the corresponding values are 9.96 ± 0.49, 9.82 ± 0.60, 9.60 ± 0.76, 10.15 ± 0.65 cm/s, respectively.

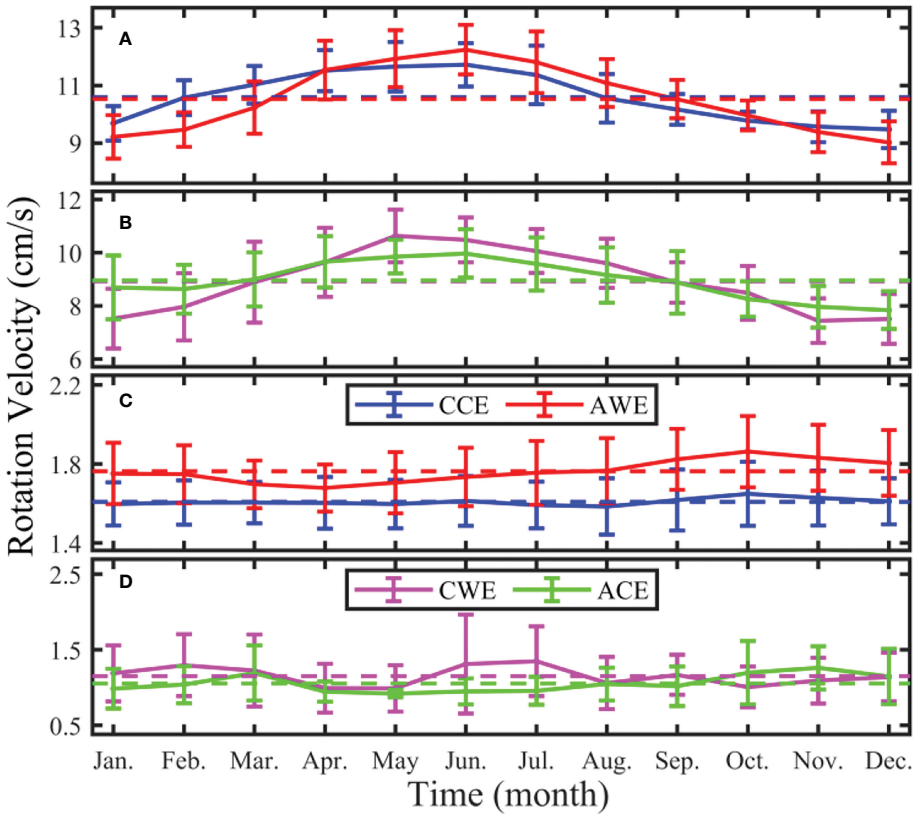

FIGURE 3
Monthly distribution of multi-year (2008 ~ 2017) average eddy rotation velocity at the sea surface **(A, B)** and 1,000 m **(C, D)** in the STCC area. Blue, red, pink, and green curves represent cyclonic cold-core eddy, anticyclonic warm-core eddy, cyclonic warm-core eddy, and anticyclonic cold-core eddy, respectively. The bar line represents the standard deviation, and the dotted line represents the multi-year average value.

The eddy horizontal moving velocity (average, maximum or minimum) at 1,000 m is about half of that at the sea surface. Accordingly, at 1,000 m, the average horizontal moving velocity of four types of eddies are 5.54 ± 0.34, 5.74 ± 0.45, 6.36 ± 3.92, and 6.28 ± 3.12 cm/s, respectively. The maximum moving velocities appear in November, December, April, and January, and their corresponding values are 5.81 ± 0.41, 6.21 ± 0.49, 9.75 ± 11.28, and 9.19 ± 9.08 cm/s. The minimum values appear in June, July, June, and June with 5.25 ± 0.28, 5.25 ± 0.30, 5.33 ± 2.32, and 4.70 ± 0.40 cm/s, respectively.

3.5 Eddy nonlinearity

Following Chelton et al. (2011) and Part I, the eddy nonlinearity is defined as $R_{NL} = \frac{U_R}{U_H}$, where U_R and U_H are the eddy rotation velocity and the horizontal moving velocity, respectively. When the eddy nonlinearity is greater than 1.0, an eddy can entrap material and transport them horizontally. Figure 3 illustrates that the eddy rotation velocity at the sea surface is large in summer and autumn, and small in winter and spring. There are discernable seasonal variations at 1,000 m. Correspondingly, Figure 4 shows that the eddy horizontal moving velocity does not vary with seasons at the sea surface and 1,000 m. The eddy nonlinearity shown in Figure 5 at the sea surface is large in summer and autumn, and small in winter and spring, indicating that the eddy rotation velocity plays a dominant role in the seasonal variation of the eddy nonlinearity.

At the sea surface layer, the average nonlinearity of CCEs, AWEs, CWEs, and ACEs are 1.41 ± 0.13, 1.40 ± 0.15, 1.20 ± 0.20, and 1.16 ± 0.16, respectively. Except for CWEs, eddy nonlinearity in November is slightly less than 1.0, while in other months, they are all greater than 1.0 (Figures 5A, B). The nonlinearity of the four eddy types reaches the maximum value in May, June, May, and June, and the corresponding values are 1.56 ± 0.09, 1.59 ± 0.12, 1.44 ± 0.127 ± 0.14, and 1.27 ± 0.14, respectively. Accordingly, it reaches the minimum in November, December, November, and December, and the corresponding values are 1.28 ± 0.08, 1.25 ± 0.10, 0.98 ± 0.10, and 1.01 ± 0.13, respectively. In a word, the eddy nonlinearity is maximum in summer and minimum in winter.

Accordingly, there is no seasonal variation in eddy nonlinearity at 1,000 m. The variation of eddy nonlinearity is small, ranging from 0.17 to 0.36 (Figures 5C, D). The average nonlinearity of the four types of eddies is 0.31 ± 0.02, 0.34 ± 0.03, 0.21 ± 0.08, 0.20 ± 0.05, which is far less than 1.0. At 1,000 m, the nonlinearity of the four types of eddies reaches the maximum in October, October, July, and November, respectively, and the corresponding values are 0.32 ± 0.13, 0.36 ± 0.13, 0.26 ± 0.13, and 0.23 ± 0.13. Accordingly, the eddy nonlinearity reaches its minimum in December, April, April, and May, with 0.31 ± 0.13, 0.32 ± 0.13, 0.17 ± 0.13, and 0.17 ± 0.13, respectively. The eddy nonlinearity at the sea surface is about 4 ~ 5 times greater than that at 1,000 m. It can be inferred that the eddy-induced heat and freshwater transports are mainly concentrated in the oceanic upper layer.

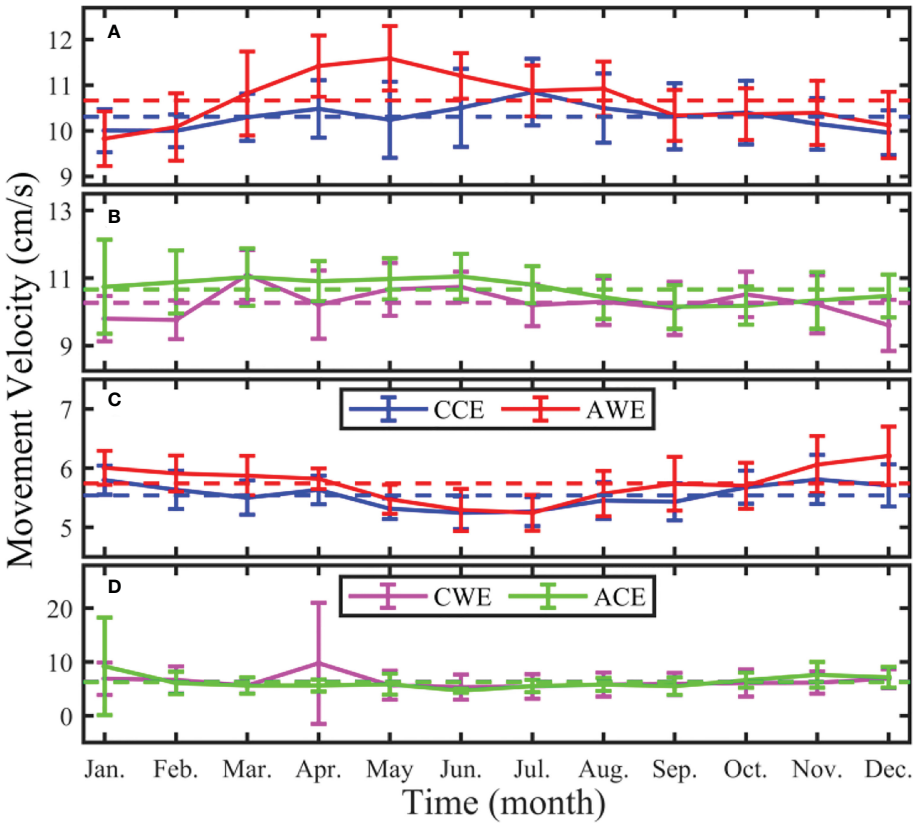

FIGURE 4
Monthly distribution of multi-year (2008 ~ 2017) average eddy horizontal moving velocity at the sea surface **(A, B)** and 1,000 m **(C, D)** in the STCC area. Blue, red, pink, and green curves represent cyclonic cold-core eddy, anticyclonic warm-core eddy, cyclonic warm-core eddy, and anticyclonic cold-core eddy, respectively. The bar line represents the standard deviation, and the dotted line represents the multi-year average value.

3.6 Eddy amplitude

Following Part I, the sea surface height abnormal (SSHA) data is obtained by using a high-pass filter on the OFES data. Then the absolute of the extreme SSHA value within the eddy (the minimum value for CEs and the maximum value for AEs) is taken as the eddy amplitude. Figures 6A, B show the multi-year monthly average eddy amplitude distribution for normal and abnormal eddies, respectively. The amplitude of four types of eddies are 3.73 ± 0.35, 3.62 ± 0.33, 3.33 ± 0.57, and 3.30 ± 0.42 cm, respectively. The amplitude of the CCEs is larger than that of AWEs from February to July, and is smaller in other months (Figure 6A).

For abnormal eddies, the amplitude of CWEs is very close to that of ACEs except in May and June (Figure 6B). The maximum amplitude of the four types of eddies appear in May, June, May, and July, respectively, and the corresponding values are 3.97 ± 0.31, 3.87 ± 0.38, 3.67 ± 0.70, 3.49 ± 0.30 cm. The minimum amplitude all appear in December, and their corresponding values are 3.45 ± 0.25, 3.41 ± 0.31, 3.02 ± 0.55, and 2.99 ± 0.46 cm, respectively. By comparing Figures 6A, B, the amplitude of normal and abnormal eddies has the same change trend, but the size of the former is larger than that of the latter.

3.7 Eddy eccentricity

Using the same definition as in Part I, eddy eccentricity, which represents the flatness of the eddy shape, is obtained by fitting the eddy boundary. At the sea surface, the average eccentricity of four types of eddies are 0.79 ± 0.02, 0.78 ± 0.02, 0.78 ± 0.04, and 0.76 ± 0.03 (Figure 7A). The maximum eccentricity appear in September (0.80 ± 0.02), July (0.79 ± 0.02), May (0.79 ± 0.03), and June (0.77 ± 0.03), respectively, and the minimum in April (0.78 ± 0.02), February (0.77 ± 0.02), January (0.76 ± 0.05), and March (0.74 ± 0.04).

At 1,000 m, the average eccentricity of the four types of eddy are 0.79 ± 0.01, 0.78 ± 0.01, 0.76 ± 0.11, and 0.76 ± 0.09, respectively (Figure 7B). The maximum eccentricity of the four eddy types appear in September (0.78 ± 0.01), October (0.78 ± 0.01), January (0.74 ± 0.11), and September (0.74 ± 0.09), respectively. Correspondingly, the minimum eccentricity appear in September (0.78 ± 0.01), October (0.78 ± 0.01), January (0.74 ± 0.11), and September (0.74 ± 0.09).

The eddy eccentricity of CEs (CWEs and CCEs) is greater than that of AEs (AWEs and ACEs) at the sea surface, indicating that the shape of AEs is more regular than that of CEs. The eccentricity of abnormal eddies at 1,000 m is larger than that at the sea surface. Besides, the eddy eccentricity of the normal eddies at 1,000 m is smaller than that at the sea surface. Similarly to that at the sea surface, the eddy eccentricity at 1,000 m shows no seasonal variation.

3.8 Eddy penetration depth

The eddy vertical penetration depth depends on the eddy's energy and the stratification of ambient water. In the vertical direction, part

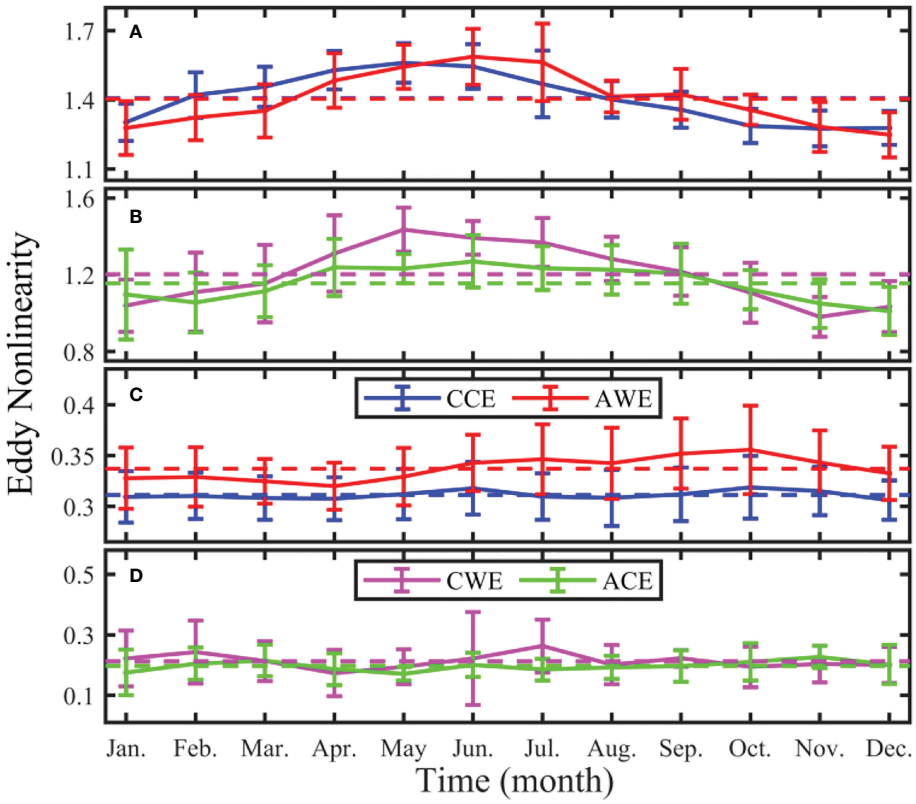

FIGURE 5
Monthly distribution of multi-year (2008 ~ 2017) average eddy nonlinearity at the sea surface **(A, B)** and 1,000 m **(C, D)** in the STCC area. Blue, red, pink, and green curves represent cyclonic cold-core eddy, anticyclonic warm-core eddy, cyclonic warm-core eddy, and anticyclonic cold-core eddy, respectively. The bar line represents the standard deviation, and the dotted line represents the multi-year average value.

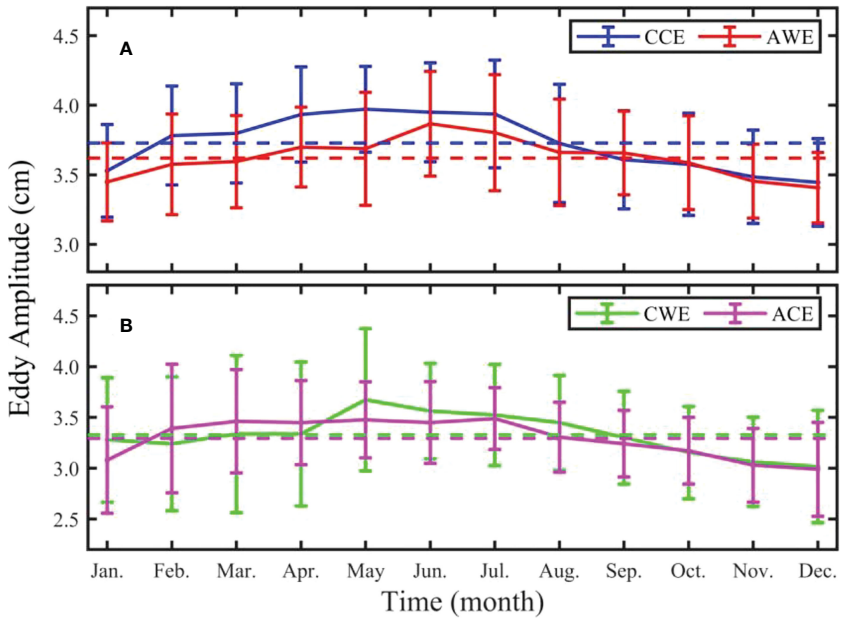

FIGURE 6
Monthly distribution of multi-year (2008 ~ 2017) average eddy amplitude at the sea surface **(A, B)** in the STCC area. Blue, red, pink, and green curves represent cyclonic cold-core eddy, anticyclonic warm-core eddy, cyclonic warm-core eddy, and anticyclonic cold-core eddy, respectively. The vertical line represents the standard deviation, and the dotted line represents the multi-year average value.

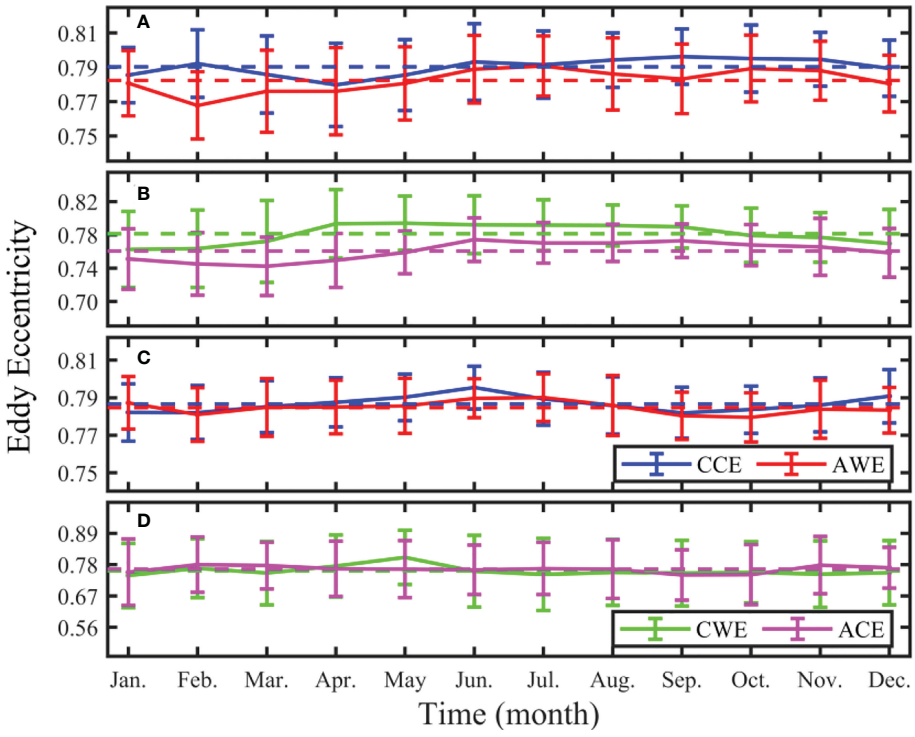

FIGURE 7
Monthly distribution of multi-year (2008 ~ 2017) average eddy eccentricity at the sea surface **(A, B)** and 1,000 m **(C, D)** in the STCC area. Blue, red, pink, and green curves represent cyclonic cold-core eddy, anticyclonic warm-core eddy, cyclonic warm-core eddy, and anticyclonic cold-core eddy, respectively. The vertical line represents the standard deviation, and the dotted line represents the multi-year average value.

of the eddy is normal in some layers and abnormal in other layers (Part I). Thus, the four eddy categories cannot be used when discussing the eddy penetration depth. Therefore, according to the rotation direction of the eddy flow field at the sea surface, only two types of eddies are considered: CEs and AEs.

The average penetration depth of CEs is 675.13 ± 67.50 m, with the maximum value in May (698.24 ± 55.79 m) and the minimum in July (635.86 ± 59.16 m, Figure 8A). The average penetration depth of AEs is 622.32 ± 81.85 m, with the maximum value in April (648.81 ± 67.24 m) and the minimum in August (595.25 ± 96.80 m). That is, the penetration depth of CEs is always deeper than that of AEs. There is no apparent seasonal variation in these two categories of eddies.

Stratification is an important parameter to measure the vertical stability of seawater. Vertical penetration of eddy needs to overcome the blocking effect of stratification. In order to explain the monthly variation of eddy penetration depth, Figure 8B shows the monthly variation of the integrated stratification from 1,000 m to the sea surface. The integrated stratification over the upper 1,000 m has a seasonal pattern, greater in summer and autumn than in winter and spring. Its multi-year monthly average value is 1.89 ± 0.03 m/s^2, the maximum value appears in August (1.96 ± 0.02 m/s^2), and the minimum value appears in February (1.84 ± 0.03 m/s^2).

Correspondingly, the multi-year monthly average EKE is characterized by a high-value distribution in spring and summer, and low values in autumn and winter (Figure 8C), similar to the vertically-integrated stratification distribution. The multi-year monthly average EKE is 80.99 ± 0.02 cm^2/s^2, the maximum value appears in May (94.55 ± 7.31 cm^2/s^2), and the minimum value appears in December (67.88 ± 4.95 cm^2/s^2). The integrated stratification and the EKE have a similar trend, and their combined effects show almost no seasonal variations in eddy penetration depth.

4 Discussion

4.1 Eddy anomaly ratio

During the lifespan of an eddy, some eddies can convert from one eddy type to another. At present, the known mechanisms for a normal eddy changing into an abnormal eddy include 1) at the eddy decay period, due to the instability of its structure, the radius of the normal eddy suddenly increases and wraps around the surrounding water to form an abnormal eddy; 2) through eddy-eddy interaction to form an abnormal eddy (Sun et al., 2019). Therefore, the ratio of the survival time of abnormal eddies to the overall eddy lifespan is an interesting topic. Figure 9 shows the statistical histogram (Figures 9A, C) and cumulative frequency distribution (Figures 9B, D) of the anomaly ratio γ_2 at the sea surface (Figures 9A, B) and 1,000 m (Figures 9C, D). The horizontal axis (γ_2) indicates the ratio of the abnormal eddy existence duration to that of the eddy lifespan. For example, suppose a CE has a lifespan of 60 days, including 12 and 15 discontinuous days as a CWE and the remaining 33 days as a CCE. In that case, the anomaly ratio is 0.2 and 0.25, respectively, located within the bins of 0.1 ~ 0.2 and 0.2 ~ 0.3 in Figure 9A. The vertical axis γ_1 ($\gamma_1 = \frac{N_1}{N_2} \times 100\,\%$) in Figures 9A, C means the percentage of the

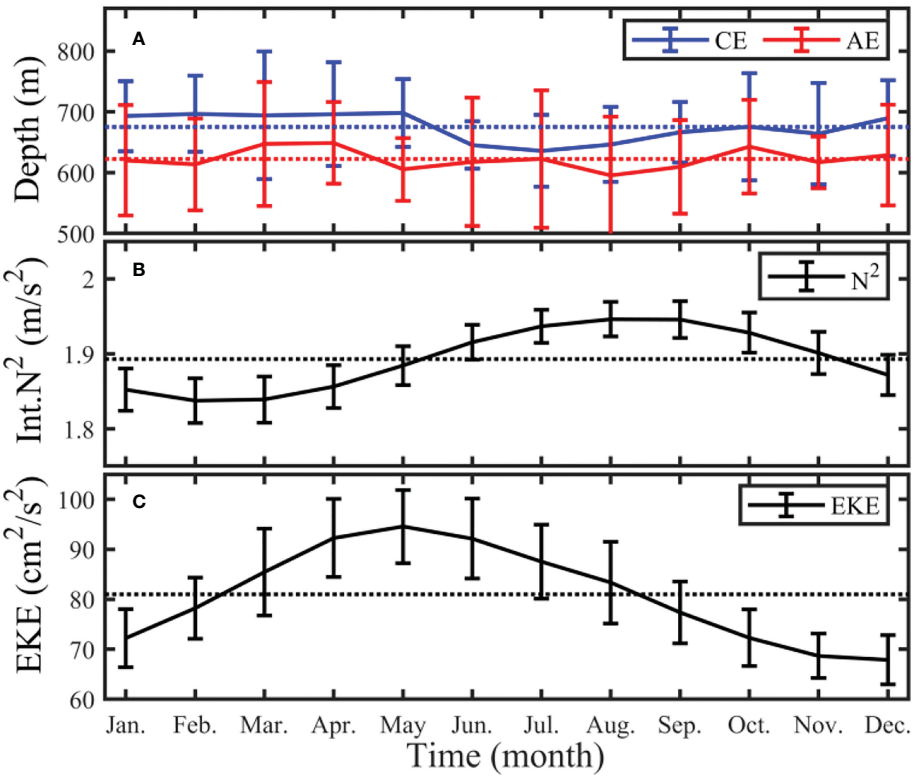

FIGURE 8
Monthly distribution of multi-year (2008 ~ 2017) average eddy penetration depths **(A)**, integrated stratification **(B)**, and eddy kinetic energy **(C)** in the STCC area. Blue and curves represent cyclonic eddy and anticyclonic eddy, respectively. The corresponding vertical lines on each curve represent the standard deviation, and the dotted line represents the multi-year average value.

eddy numbers (N_1) in the corresponding section of the horizontal axis to the total eddy numbers (N_2) with the same polarity.

From Figure 9A, the number of CWEs decreases with the increase in anomaly ratio, except in the interval of 0.9 ~ 1.0. The highest ratio γ_1 of CWEs appears in the 0.0 ~ 0.1 bin, accounting for 13.47% of the total CEs. About 48.84% of the CWEs exist for less than half of the overall CEs lifespan (Figure 9B). Only 5.69% of CWEs have an anomaly ratio γ_2 that exceeds 90% of the CEs lifespan. Accordingly, the highest proportion of ACEs appears in the range of 0.0 ~ 0.1, reaching 11.09% of the total AEs. About 45.54% of the ACEs are less than half of the overall AEs lifespan. Only 8.64% of the AEs have an anomaly ratio γ_2 exceeding 90% of their lifespan.

From Figure 9B, the proportion of ACEs is always more than that of CWEs within the cumulative frequency of less than 0.7. In contrast, the proportion of CWEs within a cumulative frequency between 0.7 and 1.0 is more than that of ACEs. There are 1,393 (30.47%) CCEs and 1,099 (24.04%) AWEs, which are normal eddies throughout their lifespan (Figure 9B).

The abnormal eddies are mainly concentrated in the oceanic upper layer. The number of ACEs in each interval bin is more than that of CWEs at 1,000 m (Figure 9C). This result is more clearly shown in the cumulative frequency distribution in Figure 9D. At 1,000 m, the proportion of abnormal eddies is smaller than that at the sea surface, and the cumulative frequency of CWEs and ACEs are 14.06% and 18.19%, respectively. This feature is consistent with the results of Sun et al. (2021a) in the South China Sea.

4.2 Influence of different definitions of abnormal eddy

Abnormal eddies have several definitions. Sun et al. (2019) proposed a rigorous definition of an abnormal eddy. In addition to the conditions already used in this study, the anomalous temperature within an abnormal eddy is 0.1°C higher (for CWE) or lower (for ACE) than the surrounding background field temperature. This condition (set the temperature threshold as 0.1°C) can make the abnormal eddies more robust and eliminate some weak eddies. On the other hand, it leads to a significant reduction in abnormal eddy numbers. The research in the North Pacific Ocean pointed out that the proportion of abnormal eddies is about 10% (Sun et al., 2019), far less than the results pointed out by Ni et al. (2021), which accounted for about 20%, and that of Liu et al. (2021), which accounted for about 1/3.

Figure 10 shows the multi-year monthly average eddy number distribution under the temperature thresholds of 0.025 (solid line) and 0.05°C (dotted line). It can be seen that when the temperature threshold is set to 0.025°C (0.05°C), the number of CCEs is less in summer and autumn, and more in winter and spring. Accordingly, the multi-year monthly average CCEs is 522.39 ± 48.84 (419.06 ± 46.57), the maximum value is 684.70 ± 47.25 (591.30 ± 55.64), which appears in December (January), and the minimum value is 406.50 ± 45.92 (279.10 ± 35.90) appearing in July (July). AWEs are less in summer and autumn, and more in winter and spring. The average number of AWEs is 454.59 ± 51.26 (355.56 ± 48.85), the maximum

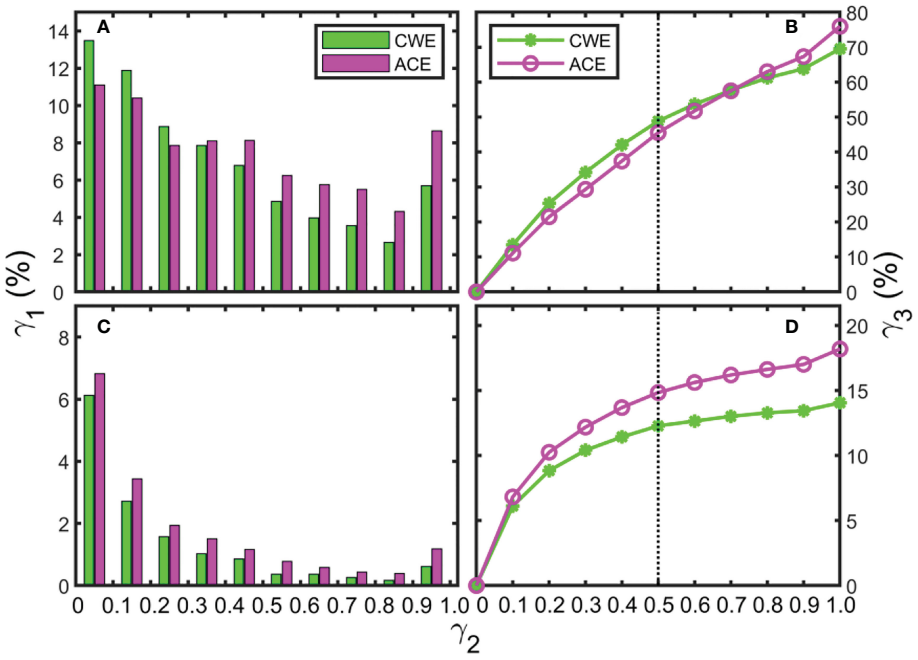

FIGURE 9
Statistical histogram of the anomaly ratio, which is the time length during which an eddy is abnormal to the overall eddy lifespan **(A, C)**, and the corresponding cumulative frequency **(B, D)** at the sea surface layer **(A, B)** and 1,000 m **(C, D)** in the STCC area. Green and magenta indicate cyclonic cold-core eddy and anticyclonic warm-core eddy, respectively.

number is 625.40 ± 80.10 (556.60 ± 75.00), which appears in January (January), and the minimum number is 368.20 ± 45.67 (240.10 ± 53.41) appearing in July (September).

The average number of CWEs is 138.48 ± 29.02 (81.97 ± 22.14), the maximum is 205.40 ± 32.89 (114.60 ± 26.00) in August (July), and the minimum is 77.30 ± 22.21 (52.60 ± 19.93), which occurs in February (April) (Figure 10B). ACEs are more in summer and autumn, and less in winter and spring. The average number of ACEs is 229.47 ± 39.14 (141.95 ± 30.34), the maximum value is 327.60 ± 42.69 (182.70 ± 38.34), which appears in August (August),

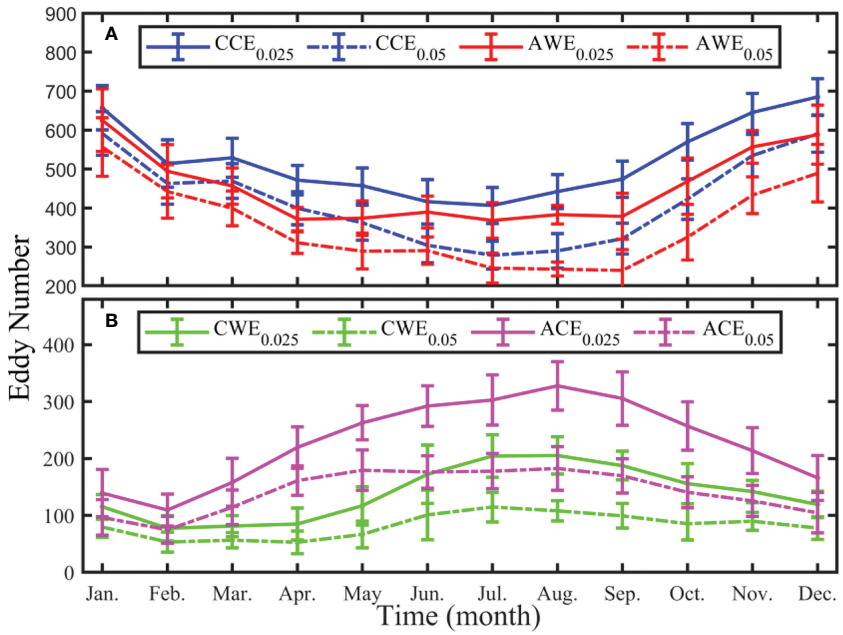

FIGURE 10
Monthly distribution of multi-year (2008 ~ 2017) average eddy number under different temperature threshold conditions (0.025 and 0.05°C) in the STCC area. **(A)** Cyclonic cold-core and anticyclonic warm-core eddy, and **(B)** cyclonic warm-core and anticyclonic cold-core eddy.

the minimum value is 109.50 ± 27.98 (74.70 ± 23.60), appears in February (February) (Figure 10B). From Figure 10, when the temperature threshold increases from 0.025 to 0.05°C, the number of eddies shows a decreasing trend, but the variation trend of the eddy number does not change.

The seasonal variation of normal and abnormal eddies presents opposite trends, consistent with the results in the main text. Under different temperature thresholds, the monthly average number of CCEs is always more than that of AWEs, while the CWE is always less than that of ACE. In order to verify the reliability of the results, we also use temperature thresholds of 0.075 and 0.1°C (Figures not shown). As the temperature threshold value increases, the number of the four types of eddies further decreases, but the seasonal variation trend remains unchanged.

5 Conclusions

Previous studies pointed out that the STCC area has abundant mesoscale eddy activities (Liu et al., 2012; Tang et al., 2019). Based on the OFES data and vector geometry automatic detection method, the seasonal variation of various characteristics for four types of mesoscale eddies is studied in detail. Following Part I, according to the rotation direction of the eddy flow field and the sign of anomalous temperature within the eddy, they can be divided into four categories: CCE, AWE, CWE, and ACE. We draw the following conclusions from this study:

1) At the sea surface, there are significant seasonal variations for four types of eddies number, rotation velocity, nonlinearity, and amplitude. Specifically, the normal eddies in winter and spring are more than in summer and autumn, while the abnormal eddies show the opposite distribution. The rotation velocity of the four types of eddies is faster in summer and autumn than in winter and spring, making the nonlinearity of eddies in summer and autumn stronger than in winter and spring. The amplitude of the four types of eddies is strong in summer and autumn, weak in winter and spring, and the amplitude of the normal eddy is larger than that of the abnormal eddy.
2) There is no significant seasonal difference in eddy radius, horizontal velocity, eccentricity, and vertical penetration depth of the four types of eddies at the sea surface.
3) At 1,000 m, there is no seasonal variation in each characteristic of the four types of eddies.
4) It is a common phenomenon that the abnormal eddy alternates between a normal and an abnormal eddy during its overall lifespan. Only 30.47% (24.04%) of cyclonic (anticyclonic) eddies belong to the normal eddy in the overall eddy lifespan.
5) Increasing the defined temperature threshold value of abnormal eddies can significantly reduce the eddy numbers but the seasonal trend of abnormal eddies does not change.

Data availability statement

The original contributions presented in the study are included in the article/supplementary material. Further inquiries can be directed to the corresponding author.

Author contributions

WS, YL, MA, JSL and JL conceived and designed the experiments. WS, YL and MA performed the experiments. MA, JSL, and JL analyzed the data. WS, YL and MA drafted the original manuscript. WS, YL, JY, KL, WT, JJ and CD revised and edited the manuscript. All authors contributed to the article and approved the submitted version.

Funding

This study was supported by the National Natural Science Foundation of China under contract Nos. 41906008, 42192562; the China Scholarship Council under contract No. 202008320195; the Open Fund of State Key Laboratory of Satellite Ocean Environment Dynamics, Second Institute of Oceanography, MNR under contract No. QNHX2231; and the Innovation Group Project of Southern Marine Science and Engineering Guangdong Laboratory (Zhuhai) under contract No. 311020004.

Acknowledgments

The OFES simulation was conducted on the Earth Simulator under the support of JAMSTEC. This data is downloaded from http://apdrc.soest.hawaii.edu/(Data doi: https://doi.org/10.17596/0002029). We thank the editor (Prof. Zhao Hui) and two reviewers for their constructive comments and helpful suggestions on an earlier manuscript version.

Conflict of interest

The authors declare that the research was conducted in the absence of any commercial or financial relationships that could be construed as a potential conflict of interest.

Publisher's note

References

Aguiar, A. C. B., Peliz, Á., and Carton, X. (2013). A census of meddies in a long-term high-resolution simulation. *Prog. Oceanogr.* 116 (9), 80–94. doi: 10.1016/j.pocean.2013.06.016

Amores, A., Melnichenko, O., and Maximenko, N. (2016). Coherent mesoscale eddies in the north Atlantic subtropical gyre: 3D structure and transport with application to the salinity maximum. *J. Geophys. Res.* 122, 23–41. doi: 10.1002/2016JC012256

An, M., Liu, J., Liu, J., Sun, W., Yang, J., Tan, W., et al. (2022). Comparative analysis of four types of mesoscale eddies in the north pacific subtropical countercurrent region – part I spatial characteristics. *Front. Mar. Sci.* 9. doi: 10.3389/fmars.2022.1004300

Chaigneau, A., Gizolme, A., and Grados, C. (2008). Mesoscale eddies off Peru in altimeter records: Identification algorithms and eddy spatio-temporal patterns. *Prog. Oceanogr.* 79 (2), 106–119. doi: 10.1016/j.pocean.2008.10.013

Chelton, D. B., Schlax, M. G., and Samelson, R. M. (2011). Global observations of nonlinear mesoscale eddies. *Prog. Oceanogr.* 91 (2), 167–216. doi: 10.1016/j.pocean.2011.01.002

Chelton, D. B., Schlax, M. G., Samelson, R. M., and De Szoeke, R. A. (2007). Global observations of large oceanic eddies. *Geophys. Res. Lett.* 34 (L15606), 87–101. doi: 10.1029/2007GL030812

Chen, G., Gan, J., Xie, Q., Chu, X., Wang, D., and Hou, Y. (2012). Eddy heat and salt transports in the south China Sea and their seasonal modulations. *J. Geophys. Res.* 117 (C05021), 78–91. doi: 10.1029/2011JC007724

Chen, G., and Han, G. (2019). Contrasting short-lived with long-lived mesoscale eddies in the global ocean. *J. Geophys. Res.* 124 (5), 3149–3167. doi: 10.1029/2019JC014983

Dai, J., Wang, H., Zhang, W., An, Y., and Zhang, R. (2020). Observed spatiotemporal variation of three-dimensional structure and heat/salt transport of anticyclonic mesoscale eddy in Northwest pacific. *J. Oceanol. Limnol.* 38 (6), 1654–1675. doi: 10.1007/s00343-019-9148-z

Ding, R., Xuan, J., Zhang, T., Zhou, L., Zhou, F., Meng, Q., et al. (2021a). Eddy-induced heat transport in the south China Sea. *J. Phys. Oceanogr.* 51, 2327–2348. doi: 10.1175/JPO-D-20-0206.1

Ding, Y., Xu, L., and Zhang, Y. (2021b). Impact of anticyclonic eddies under stormy weather on the mixed layer variability in april south of the kuroshio extension. *J. Geophys. Res.* 126, e2020JC016739. doi: 10.1029/2020JC016739

Doglioli, A. M., Blanke, B., Speich, S., and Lapeyre, G. (2007). Tracking coherent structures in a regional ocean model with wavelet analysis: Application to cape basin eddies. *J. Geophys. Res.* 112, C5043. doi: 10.1029/2006JC003952

Dong, C., Lin, X., Liu, Y., Nencioli, F., Chao, Y., Guan, Y., et al. (2012). Three-dimensional oceanic eddy analysis in the southern California bight from a numerical product. *J. Geophys. Res.* 117, C00H14, 92–99. doi: 10.1029/2011JC007354

Dong, C., Liu, L., Nencioli, F., Bethel, B. J., Liu, Y., Xu, G., et al. (2022). The near-global ocean mesoscale eddy atmospheric-oceanic-biological interaction observational dataset. *Sci. Data.* 9 (1). doi: 10.1038/s41597-022-01550-9

Dong, C., Mcwilliams, J. C., Liu, Y., and Chen, D. (2014). Global heat and salt transports by eddy movement. *Nat. Commun.* 5 (2), 1–6. doi: 10.1038/ncomms4294

Dong, D., Peter, B., Chang, P., Florian, S., Yang, X., Yan, J., et al. (2017). Mesoscale eddies in the northwestern pacific ocean: Three-dimensional eddy structures and heat/salt transports. *J. Geophys. Res.* 122, 9795–9813. doi: 10.1002/2017JC013303

Dong, C., Timothy, M., Francesco, N., Jiang, S., Yusuke, U., Mcwilliams, J. C., et al. (2009). An oceanic cyclonic eddy on the lee side of Lanai island, Hawaii. *J. Geophys. Res.* 114, C10008. doi: 10.1029/2009JC005346

Gaube, P., Chelton, D. B., Samelson, R. M., Schlax, M. G., and O Neill, L. W. (2015). Satellite observations of mesoscale eddy-induced ekman pumping. *J. Phys. Oceanogr.* 45 (1), 104–132. doi: 10.1175/JPO-D-14-0032.1

Gaube, P., Chelton, D. B., Strutton, P. G., and Behrenfeld, M. J. (2013). Satellite observations of chlorophyll, phytoplankton biomass, and ekman pumping in nonlinear mesoscale eddies. *J. Geophys. Res.* 118 (12), 6349–6370. doi: 10.1002/2013JC009027

Gaube, P., J., M. D., and Moulin, A. J. (2019). Mesoscale eddies modulate mixed layer depth globally. *Geophys. Res. Lett.* 46 (3), 1505–1512. doi: 10.1029/2018GL080006

Geng, B., Xiu, P., Liu, N., He, X., and Chai, F. (2021). Biological response to the interaction of a mesoscale eddy and the river plume in the northern south China Sea. *J. Geophys. Res.* 126 (9), e2021J–e17244J. doi: 10.1029/2021JC017244

He, Q., Zhan, H., Cai, S., He, Y., Huang, G., and Zhan, W. (2018). A new assessment of mesoscale eddies in the south China Sea: Surface features, three-dimensional structures, and thermohaline transports. *J. Geophys. Res.* 123, 4906–4929. doi: 10.1029/2018JC014054

He, Q., Zhan, H., Xu, J., Cai, S., Zhan, W., Zhou, L., et al. (2019). Eddy-induced chlorophyll anomalies in the western south China Sea. *J. Geophys. Res.* 124 (12), 9487–9506. doi: 10.1029/2019JC015371

Itoh, S., and Yasuda, I. (2010). Water mass structure of warm and cold anticyclonic eddies in the western boundary region of the subarctic north pacific. *J. Phys. Oceanogr.* 40 (12), 2624–2642. doi: 10.1175/2010JPO4475.1

Ji, J., Dong, C., Zhang, B., and Liu, Y. (2016). Oceanic eddy statistical comparison using multiple observational data in the kuroshio extension region. *Acta Oceanol. Sin.* 36 (3), 1–7. doi: 10.1007/s13131-016-0882-1

Ji, J., Dong, C., Zhang, B., Liu, Y., Zou, B., Gregory, P. K., et al. (2018). An oceanic eddy characteristics and generation mechanisms in the kuroshio extension region. *J. Geophys. Res.* 123, 2018J–2123J. doi: 10.1029/2018JC014196

Kang, L., Wang, F., and Chen, Y. L. (2010). Eddy generation and evolution in the north pacific subtropical countercurrent (NPSC) zone. *Chin. J. Oceanology Limnol.* 28 (5), 968–973. doi: 10.1007/s00343-010-9010-9

Lin, X., Dong, C., Chen, D., Liu, Y., Yang, J., Zou, B., et al. (2015). Three-dimensional properties of mesoscale eddies in the south China Sea based on eddy-resolving model output. *Deep Sea Res.* 99, 46–64. doi: 10.1016/j.dsr.2015.01.007

Lin, X., Qiu, Y., and Sun, D. (2019). Thermohaline structures and heat/freshwater transports of mesoscale eddies in the bay of Bengal observed by argo and satellite data. *Remote Sens.* 11 (24) 2989. doi: 10.3390/rs11242989

Liu, Y., Dong, C., Guan, Y., Chen, D., Mcwilliams, J., and Nencioli, F. (2012). Eddy analysis in the subtropical zonal band of the north pacific ocean. *Deep Sea Res.* 68 (5), 54–67. doi: 10.1016/j.dsr.2012.06.001

Liu, Y., Zheng, Q., and Li, X. (2021). Characteristics of global ocean abnormal mesoscale eddies derived from the fusion of sea surface height and temperature data by deep learning. *Geophys. Res. Lett.* 48 (17), e2021GL094772. doi: 10.1029/2021GL094772

Ma, L., and Wang, Q. (2014). Mean properties of mesoscale eddies in the kuroshio recirculation region. *Chin. J. Oceanol. Limn.* 32 (3), 681–702. doi: 10.1007/s00343-014-3029-2

Ma, J., Xu, H., Dong, C., Lin, P., and Liu, Y. (2015). Atmospheric responses to oceanic eddies in the kuroshio extension based on composite analyses. *J. Geophys. Res.* 120 (13), 6313–6330. doi: 10.1002/2014JD022930

McGillicuddy, D. J.Jr. (2016). Mechanisms of physical-biological-biogeochemical interaction at the oceanic mesoscale. *Ann. Rev. Mar. Sci.* 8 (1), 125. doi: 10.1146/annurev-marine-010814-015606

Meijers, A. J., Bindoff, N. L., and Roberts, J. L. (2007). On the total, mean, and eddy heat and freshwater transports in the southern hemisphere of a global ocean model. *J. Phys. Oceanogr.* 37 (2), 277–295. doi: 10.1175/JPO3012.1

Nencioli, F., Dong, C., Dickey, T., Washburn, L., and Mcwilliams, J. C. (2010). A vector geometry-based eddy detection algorithm and its application to a high-resolution numerical model product and high-frequency radar surface velocities in the southern California bight. *J. Atmos. Oceanic Technol.* 27 (27), 564–579. doi: 10.1175/2009JTECHO725.1

Ni, Q., Zhai, X., Jiang, X., and Chen, D. (2021). Abundant cold anticyclonic eddies and warm cyclonic eddies in the global ocean. *J. Phys. Oceanogr.* 51 (9), 2793–2806. doi: 10.1175/JPO-D-21-0010.1

Okubo, A. (1970). Horizontal dispersion of floatable particles in the vicinity of velocity singularities such as convergences. *Deep Sea Res.* 17, 445–454. doi: 10.1016/0011-7471(70)90059-8

Patel, R. S., Llort, J., Strutton, P. G., Phillips, H. E., Moreau, S., Conde Pardo, P., et al. (2020). The biogeochemical structure of southern ocean mesoscale eddies. *J. Geophys. Res.* 125 (8). doi: 10.1029/2020JC016115

Pujol, M. I., Faugère, Y., Taburet, G., Dupuy, S., Pelloquin, C., Ablain, M., et al. (2016). DUACS DT2014: The new multi-mission altimeter dataset reprocessed over 20 years. *Ocean Sci. Discuss.* 6 (1), 1–48. doi: 10.5194/os-2015-110

Qiu, B. (1999). Seasonal eddy field modulation of the north pacific subtropical countercurrent: TOPEX/Poseidon observations and theory. *J. Phys. Oceanogr.* 29 (10), 2471–2486. doi: 10.1175/1520-0485(1999)029<2471:SEFMOT>2.0.CO;2

Qiu, B., and Chen, S. (2004). Eddy-induced heat transport in the subtropical north pacific from argo, TMI, and altimetry measurements. *J. Phys. Oceanogr.* 35 (4), 458–473. doi: 10.1175/JPO2696.1

Qiu, B., and Chen, S. (2010). Interannual variability of the north pacific subtropical countercurrent and its associated mesoscale eddy field. *J. Phys. Oceanogr.* 40, 213–225. doi: 10.1175/2009JPO4285.1

Qiu, B., Chen, S., Klein, P., Sasaki, H., and Sasai, Y. (2014). Seasonal mesoscale and submesoscale eddy variability along the north pacific subtropical countercurrent. *J. Phys. Oceanogr.* 44 (12), 3079–3098. doi: 10.1175/JPO-D-14-0071.1

Qiu, C., Yi, Z., Su, D., Wu, Z., Liu, H., Lin, P., et al. (2022). Cross-slope heat and salt transport induced by slope intrusion eddy's horizontal asymmetry in the northern south China Sea. *J. Geophys. Res.* 127 (9). doi: 10.1029/2022JC018406

Sadarjoen, I. A., and Post, F. H. (2000). Detection, quantification, and tracking of vortices using streamline geometry. *Comput. Graphics.* 24 (3), 333–341. doi: 10.1016/S0097-8493(00)00029-7

Sasaki, H., Nonaka, M., Masumoto, Y., Sasai, Y., Uehara, H., and Sakuma, H. (2008). "An eddy-resolving hind cast simulation of the quasi-global ocean from 1950 to 2003 on the earth simulator," in *High resolution numerical modelling of the atmosphere and ocean*. Eds. K. Hamilton and W. Ohfuchi (New York: Springer), 157–185.

Sun, W., An, M., Liu, J., Liu, J., Yang, J., Tan, W., et al. (2022). Comparative analysis of four types of mesoscale eddies in the kuroshio-oyashio extension region. *Front. Mar. Sci.* 9. doi: 10.3389/fmars.2022.984244

Sun, W., Dong, C., Tan, W., and He, Y. (2019). Statistical characteristics of cyclonic warm-core eddies and anticyclonic cold-core eddies in the north pacific based on remote sensing data. *Remote Sens.* 11 (2), 208. doi: 10.3390/rs11020208

Sun, W., Dong, C., Tan, W., Liu, Y., He, Y., and Wang, J. (2018). Vertical structure anomalies of oceanic eddies and eddy-induced transports in the south China Sea. *Remote Sens.* 10, 795. doi: 10.3390/rs10050795

Sun, W., Dong, C., Wang, R., Liu, Y., and Yu, K. (2017). Vertical structure anomalies of oceanic eddies in the kuroshio extension region. *J. Geophys. Res.* 122 (2), 1476–1496. doi: 10.1002/2016JC012226

Sun, W., Liu, Y., Chen, G., Tan, W., Lin, X., Guan, Y., et al. (2021a). Three-dimensional properties of mesoscale cyclonic warm-core and anticyclonic cold-core eddies in the south China Sea. *Acta Oceanol. Sin.* 40 (10), 17–29. doi: 10.1007/s13131-021-1770-x

Sun, W., Yang, J., Tan, W., Liu, Y., Zhao, B., He, Y., et al. (2021b). Eddy diffusivity and coherent mesoscale eddy analysis in the southern ocean. *Acta Oceanol. Sin.* 40 (10), 1–16. doi: 10.1007/s13131-021-1881-4

Taguchi, B., Qiu, B., Nonaka, M., Sasaki, H., Xie, S., and Schneider, N. (2010). Decadal variability of the kuroshio extension: Mesoscale eddies and recirculations. *Ocean Dynam.* 60 (3), 673–691. doi: 10.1007/s10236-010-0295-1

Tang, B., Hou, Y., Yin, Y., and Po, H. (2019). Statistical characteristics of mesoscale eddies and the distribution in the north pacific subtropical countercurrent (in Chinese). *Oceanol. Limnol. Sin.* 50 (5), 937–947. doi: 10.11693/hyhz20190300050

Treguier, A. M., Lique, C., Deshayes, J., and Molines, J. M. (2017). The north Atlantic eddy heat transport and its relation with the vertical tilting of the gulf stream axis. *J. Phys. Oceanogr.* 47 (6), 1281–1289. doi: 10.1175/JPO-D-16-0172.1

Wang, X., Li, W., Qi, Y., and Han, G. (2012). Heat, salt and volume transports by eddies in the vicinity of the Luzon strait. *Deep Sea Res.* 61, 21–33. doi: 10.1016/j.dsr.2011.11.006

Wang, Z., Li, Q., Sun, L., Li, S., Yang, Y., and Liu, S. (2015). The most typical shape of oceanic mesoscale eddies from global satellite sea level observations. *Front. Earth Sci.* 9 (2), 202–208. doi: 10.1007/s11707-014-0478-z

Wang, Y., Zhang, H., Chai, F., and Yuan, Y. (2018). Impact of mesoscale eddies on chlorophyll variability off the coast of Chile. *PloS One* 13 (9), e203598. doi: 10.1371/journal.pone.0203598

Wang, Q., Zhang, B., Zeng, L., He, Y., Wu, Z., and Chen, J. (2022). Properties and drivers of marine heat waves in the northern south China Sea. *J. Phys. Oceanogr.* 52 (5), 917–927. doi: 10.1175/JPO-D-21-0236.1

Weiss, J. (1991). The dynamics of enstrophy transfer in two-dimensional hydrodynamics. *Physica D.* 48, 273–294. doi: 10.1016/0167-2789(91)90088-Q

Xian, T., Sun, L., Yang, Y., and Fu, Y. (2012). Monsoon and eddy forcing of chlorophyll-a variation in the northeast south China Sea. *Int. J. Remote Sens.* 33 (23), 7431–7443. doi: 10.1080/01431161.2012.685970

Xu, G., Dong, C., Liu, Y., Gaube, P., and Yang, J. (2019). Chlorophyll rings around ocean eddies in the north pacific. *Sci. Rep.* 9 2019. doi: 10.1038/s41598-018-38457-8

Xu, L., Li, P., Xie, S. P., Liu, Q., Liu, C., and Gao, W. (2016). Observing mesoscale eddy effects on mode-water subduction and transport in the north pacific. *Nat. Commun.* 7, 10505. doi: 10.1038/ncomms10505

Yang, X., Xu, G., Liu, Y., Sun, W., Xia, C., and Dong, C. (2020). Multi-source data analysis of mesoscale eddies and their effects on surface chlorophyll in the bay of Bengal. *Remote Sens.* 12 (21) 3485. doi: 10.3390/rs12213485

Yang, G., Yu, W., Yuan, Y., Zhao, X., Wang, F., Chen, G., et al. (2015). Characteristics, vertical structures, and heat/salt transports of mesoscale eddies in the southeastern tropical Indian ocean. *J. Geophys. Res.* 120 (10), 6733–6750. doi: 10.1002/2015JC011130

You, Z., Liu, L., Bethel, B. J., and Dong, C. (2022). Feature comparison of two mesoscale eddy datasets based on satellite altimeter data. *Remote Sens.* 14 (1), 116. doi: 10.3390/rs14010116

Zhang, Z., Wang, W., and Qiu, B. (2014a). Oceanic mass transport by mesoscale eddies. *Science* 345 (6194), 322–324. doi: 10.1126/science.1252418

Zhang, Z., Zhao, W., Qiu, B., and Tian, J. (2017). Anticyclonic eddy sheddings from kuroshio loop and the accompanying cyclonic eddy in the northeastern south China Sea. *J. Phys. Oceanogr.* 47 (6), 1243–1259. doi: 10.1175/JPO-D-16-0185.1

Zhang, Z., Zhong, Y., Tian, J., Yang, Q., and Zhao, W. (2014b). Estimation of eddy heat transport in the global ocean from argo data. *Acta Oceanol. Sin.* 33 (1), 42–47. doi: 10.1007/s13131-014-0421-x

frontiers | Frontiers in Marine Science

TYPE Original Research
PUBLISHED 03 February 2023
DOI 10.3389/fmars.2023.1015323

OPEN ACCESS

EDITED BY
Zhan Hu,
Sun Yat-sen University, Zhuhai Campus, China

REVIEWED BY
Peidong Zhang,
Ocean University of China, China
Dilip Kumar Jha,
National Institute of Ocean Technology, India

*CORRESPONDENCE
Qiuying Han
hanqiuying0312@sina.com

SPECIALTY SECTION
This article was submitted to Coastal Ocean Processes, a section of the journal Frontiers in Marine Science

RECEIVED 09 August 2022
ACCEPTED 17 January 2023
PUBLISHED 03 February 2023

CITATION
Han Q, Qiu C, Zeng W, Chen Y, Zhao M, Shi Y and Zheng F (2023) Effect of DIN and DON sources on the nitrogen uptake of the seagrass *Zostera japonica* and the macroalgae *Ulva pertusa* previously grown in different light levels. *Front. Mar. Sci.* 10:1015323. doi: 10.3389/fmars.2023.1015323

Effect of DIN and DON sources on the nitrogen uptake of the seagrass *Zostera japonica* and the macroalgae *Ulva pertusa* previously grown in different light levels

Qiuying Han[1]*, Chongyu Qiu[1], Wenxuan Zeng[1], Yu Chen[2], Muqiu Zhao[1], Yunfeng Shi[1] and Fengying Zheng[2]

[1]Key Laboratory for Coastal Marine Eco-Environment Process and Carbon Sink of Hainan province/ Yazhou Bay Innovation Institute/Key Laboratory of Utilization and Conservation for Tropical Marine Bioresources of Ministry of Education/Modern Marine Ranching Engineering Research Center of Hainan, Hainan Tropical Ocean University, Sanya, China, [2]Marine College, Shandong University, Weihai, Shandong, China

This study quantified the absorption ability of the seagrass *Zostera japonica* and the macroalgae *Ulva pertusa* for dissolved inorganic nitrogen (DIN) (ammonium and nitrate) and dissolved organic nitrogen (DON) (urea and glycine) under different light conditions. The plants were cultured in filtered seawater (31‰, 25°C) for 2 weeks under three light levels. Macroalgae and the above- and belowground parts of seagrasses were separately placed into four different manmade seawater solutions with DIN (ammonium and nitrate) and DON (urea and glycine) stable isotopes for 1 h. The results showed that macroalgae had higher absorption rates for ammonium and nitrate after higher light (14.67 ± 2.50 and 1.29 ± 0.16 mg^{-1} dry weight (DW) h^{-1}) than after lower light (4.52 ± 0.95 and 0.18 ± 0.12 mg^{-1} DW h^{-1}) treatments. Compared to the belowground seagrass portions that had previously been grown in high and low light conditions, the seagrass leaves assimilated ammonium more quickly. *Z. japonica* preferred glycine to nitrate and urea after the high- and low-light treatments; that is, the absorption rates of the belowground seagrass parts for glycine were 14.71 ± 1.85 and 6.38 ± 0.52 mg^{-1} DW h^{-1} after the high- and low-light treatments, respectively, which were higher than those of ammonium, nitrate, and urea. The absorption rates of algae were lower than those for ammonium previously grown under medium- and low-light treatments. These results indicate that light reduction can impact the assimilation of DIN by *Z. japonica* and *U. pertusa*, and both have the ability to directly assimilate DON. This study provides information that could help reduce the negative effects of eutrophication on macroalgae and seagrasses in order to protect seagrass meadows.

KEYWORDS

species competition, light reduction, organic nitrogen, inorganic nitrogen, macroalgal blooms, seagrasses

1 Introduction

Seagrasses provide important ecological services, including altering nutrient cycling; producing organic carbon; enhancing biodiversity and food sources; supporting critical habitats for economic animals such as nereids, sipunculids, shellfish, shrimps, crabs, and fish; and stabilizing sediments in coastal areas (Costanza et al., 1997; Hemminga and Duarte, 2000; Beck et al., 2001; Orth et al., 2006; Huang et al., 2017). In recent years, land-derived nitrogen loading, largely from anthropogenic origin, has increased the eutrophication in coastal areas, resulting in a decline in seagrass meadows (Valiela et al., 1992; Duarte, 1995; Orth et al., 2006). More than half of the seagrass areas are reduced when land-derived nitrogen loads exceed 100 kg N ha^{-1} $year^{-1}$ (Valiela and Cole, 2002). Seagrasses serve as one of the sensitive indicators of nutrient pollution (Bricker et al., 2003). The nutrient concentrations in the environment may alter the competitive advantage of seagrasses and macroalgae. Seagrasses can absorb nutrients from seawater and sediments in oligotrophic environments, although they have lower nutrient absorption rates than macroalgae (Harvens et al., 2001; Han and Liu, 2014). Eutrophication may result in fast-growing macroalgal blooms (Duarte, 1995; Harvens et al., 2001), which often aggravate the decline of seagrasses in temperate estuaries (Valiela et al., 1997; Hauxwell et al., 2001; McGlathery, 2001; Burkholder et al., 2007) by promoting light reduction and increasing nutrient turnover in ecosystems, thereby altering the absorption ability of seagrasses for nitrogen (Han and Liu, 2014 and references therein; Han et al., 2016).

Nutrients are some of the major environmental factors that control the primary production of seagrasses (Harvens et al., 2001; Leoni et al., 2008). Sea nitrogen is composed of dissolved inorganic nitrogen (DIN), dissolved organic nitrogen (DON), and particulate organic nitrogen (PON) (Gruber, 2004; Zhang et al., 2021). Wastewater from aquaculture releases some inorganic and organic nutrients from uneaten feed and from feces of farmed animals (Holmer et al., 2008; Herbeck et al., 2013). DIN, such as ammonium and nitrate, is considered an important nitrogen source for seagrass and macroalgal assimilation (Valiela et al., 1997; Lee and Dunton, 1999; van Alstyne, 2008; Fan et al., 2014; Alexandre et al., 2015). Some seagrass species, such as *Zostera noltii*, can absorb more nitrate when ammonium is absent (Alexandre et al., 2011). Ammonium can be toxic to seagrasses because its accumulation can increase protein breakdown (van Katwijk et al., 1997). DON constitutes a large part of the total dissolved nitrogen pool in coastal areas (Tyler et al., 2005; Wang, 2015 and references therein). Urea and dissolved free amino acids are important nitrogen sources for autotrophic organisms (Bronk, 2002). The hydrolysis of seagrass leaf litter drives the rapid release of DON during the early phase of decomposition (Wang et al., 2014; Delgado et al., 2017; Prasad et al., 2019). To date, there have been few studies on the DON absorption of seagrasses (Vonk et al., 2008; van England et al., 2011; Alexandre et al., 2015). Some seagrasses (e.g., *Cymodocea nodosa* and *Z. noltii*) can absorb nitrogen from small organic substrates (van England et al., 2011). Alexandre et al. (2015) found that DON was a complementary nitrogen source to DIN, although *Zostera marina* preferred DON to nitrate. The macroalgal uptake of DIN in coastal waters is also well known (Valiela et al., 1997; van Alstyne, 2008; Fan et al., 2014). The macroalgal absorption of DON compounds is still not as well understood as that of DIN (Tyler et al., 2005; Xu, 2020; Zhang et al., 2021b). Phytoplankton and detritus supported by DIN are defined as PON (Zhang et al., 2021a), which could be difficult for seagrasses and macroalgae to directly absorb.

Light reduction from eutrophication and extreme climatic events such as hurricanes and tsunamis, resulting in pulsed turbidity, has been considered as the primary factor that leads to seagrass decline (Cambridge et al., 1986; Walker and McComb, 1992; Preen and Marsh, 1995). Light reduction may increase the mortality of seagrasses and decrease their growth and coverage (Preen and Marsh, 1995; Collier et al., 2007; Collier et al., 2011) by contracting respiratory and growth requirements with a combination of photosynthetic carbon fixation and reallocation of reserves (Ralph et al., 2007). Thin macroalgae (e.g., *Ulva* sp.) have lower light requirements than seagrasses; therefore, macroalgae can use more incidental light compared to seagrasses (Duarte, 1995). The growth superiority of the two communities may depend on irradiance (Moore and Wetezl, 2000), nutrient quantity (Lapointe et al., 1994) and type.

Limited light may have negative effects on the nitrogen absorption of seagrasses (Touchette et al., 2003). Because plants may have a relatively fixed cell quota for proteins, lipids, and carbohydrates (Hedges et al., 2002), they tend to absorb different elements with relatively fixed ratios (Gruber, 2004). Energy is consumed when plants assimilate nitrogen (Touchette et al., 2003). The metabolism of nitrogen in plants is strongly linked to the photosynthetic fixation of carbon (Turpin, 1991 and references therein) because nitrogen and carbon are needed to build living organic tissues (Griffiths, et al., 2020). Nitrogen assimilation requires carbon in the respiratory pathway (Leoni et al., 2008). The synthesis of amino acids by seagrasses requires more carbon in comparison with their carbon fixation capacity under conditions of nitrogen enrichment (Turpin, 1991 and references therein; Brun et al., 2002), which will result in a lower carbohydrate content, leading to an internal carbon limit (Touchette et al., 2003; Inverse et al., 2004). Macroalgal blooms resulting from eutrophication may lead to light reduction and may impact the nitrogen cycle in seagrass ecosystems (Han and Liu, 2014; Moreira-Saporiti et al., 2021), thus altering the ability of seagrasses to absorb inorganic and organic forms of nitrogen.

Zostera japonica, one of the dominant seagrass species in the Shandong coast of China, such as Swan Lake, has shown a decreasing trend, although it invaded and expanded along the Pacific Northwest coast (Ruesink et al., 2010; Han et al., 2017). The high nutrient and organic matter loads originating from benthos aquaculture and wastewater discharge could have contributed to the decline of *Z. japonica* in Shandong coast (Zhang et al., 2014; Han et al., 2017). In some areas along the Shandong coast, macroalgal mats (e. g., *Ulva pertusa*) have replaced the seagrass meadows (Zhang et al., 2014). Moreover, macroalgal mats cover the seagrass meadows during extended algal blooms every summer from June to July in Swan Lake, Shandong (Han et al., 2016). Until now, there have only been a few studies on how macroalgal blooms induce light attenuation and how they impact the capability of seagrasses and macroalgae to absorb DIN and DON.

The overall aim of this study was to compare the ability of seagrasses and green algae to absorb DIN and DON after light

stress. Our hypotheses were as follows: firstly, plants require different amounts of energy for the two nitrogen forms (DIN and DON), and the nitrogen absorption ability of plants is lower because of the small amount of energy left for assimilation at lower light levels. Secondly, the light availability and the amount of energy required for nutrient uptake differ between seagrass and macroalgal species. Our results could provide information for environment managers regarding the control of nutrient inputs by intensive human activities and the reduction of the negative effects of macroalgae when macroalgal blooms result in more DIN and DON released into coastal eutrophication ecosystems in early low-light stress.

2 Materials and methods

2.1 Experimental design

Z. japonica and *U. pertusa* were collected from Swan Lake, whichis located in Rongcheng City, Shandong Province, China (37.3382° N–37.3588° N, 122.5551° E–122.5793° E), and were exposed for 2 weeks to three light levels: high light (HL 160 mol photons m^{-2} s^{-1}), medium light (ML, 40% HL), and low light (LL, 10% HL). The seagrasses and macroalgae were collected in June when the daylight is longer than the dark, so light was set up with a photoperiod of 18-h light and 6-h dark. Light intensity was measured using an underwater fluorometer (DIVING-PAM, WALZ company, Germany). Round macroalgae (wet weight, 2 g) were placed in PVC cylinders with muddy sand (diameter, 11 cm; height, 10 cm). On top of the cylinders were nets with large holes to maintain sufficient light and to keep the plants inside. *Z. japonica* propagules (one apical shoot plus the first lateral shoot, and respective internodes; wet biomass, 11.35 ± 0.52) were buried in the same PVC cylinders as mentioned above. The cylinders were filled with muddy sand. The depth of the sediment cover of the propagules was 1.5 cm. A total of 75 macroalgae and seagrasses were cultivated. There were 25 macroalgal replicates and 25 seagrass replicates for each light treatment in three different tanks. The PVC cylinders were submerged in aerated and filtered seawater (31‰). The seawater flowed slowly and was changed once every 2 days. The temperature was maintained at 25° using constant temperature system in the climate laboratory. The temperature and salinity of the seawater were measured using a YSI 30 portable meter (YSI, Yellow Springs, OH, USA).

2.2 Stable nitrogen isotope treatments and plant measurements

After 2 weeks, the seagrasses and algae were separately divided into five groups for each light treatment, with five replicates for each group. In one group, the dry biomass of the macroalgae was weighed. The leaf length, width, rhizome node diameter, node length, and root length of seagrasses were measured, and the above- and belowground dry biomass was weighed. The total dry biomass was also calculated. Finally, the N content and δ^{15}N‰ of the macroalgae and the aboveground (leaves) and belowground (roots with rhizomes) parts of seagrasses were measured using IRMS (MAT253; Thermo Fisher, Waltham, MA, USA) (n = 5).

Four different artificial seawater solutions with DIN and DON stable isotopes (Sigma-Aldrich, St. Louis, MO, USA) were prepared. The DIN solution contained ammonium (ammonium chloride, 10 µmol/L) and nitrate (sodium nitrate, 10 µmol/L), while the DON solution contained urea (10 µmol/L) and glycine (1 µmol/L). The glycine concentration is lower than that of DIN and urea in natural environments; therefore, the concentration of the glycine solution was lower than that of ammonium, nitrate, and urea. In the other four plant groups, the macroalgae and the above- and belowground parts of seagrasses were separately placed in the above-mentioned solutions. Each plant tissue was cultured in a container with 1 L stable nitrogen isotope solution, for a total of 180 treatments [three light treatments × four nitrogen solutions × three plant tissues (macroalgae and aboveground and belowground parts of seagrasses) × five replicates]. The seagrasses and macroalgae were incubated for 2–3 h in stable nitrogen isotope solutions in order to study their absorption ability (van England et al., 2011). Our preliminary experiments indicated that 1 h was sufficient for the absorption of DIN and DON stable isotopes by *Z. japonica* and *U. pertusa*. Therefore, in this study, 1 h was taken as the absorption time for plant tissues (macroalgae, aboveground parts and belowground parts of seagrasses) to absorb stable nitrogen isotopes. The temperature was maintained at 25°C. Lastly, the δ^{15}N‰ values of macroalgae and the above- and belowground parts of seagrasses were measured using IRMS (MAT253; Thermo Fisher) (n = 5).

2.3 Data calculation

δ^{15}N‰, which can be used to compare the amount of nitrogen absorbed by plants or plant tissues, was calculated as follows:

$$\delta^{15}N\,‰ = \left(R_{sample} - R_{standard}\right)/R_{standard} * 1{,}000 \quad (1)$$

In Equation 1, $R_{standard}$ and R_{sample} denote the $^{15}N/^{14}N$ of the standard and the sample, respectively. Nitrogen in air was used as the analysis standard for stable nitrogen isotopes.

Isotope excess (E_{sample}) was calculated as the difference between the isotope fraction in the sample (F_{sample}) and the natural abundance (i.e., initial isotope fraction, F_{nat}) (van England et al., 2011), as follows:

$$E_{sample} = F_{sample} - F_{nat} \quad (2)$$

The specific uptake rate of ^{15}N, V_{sample} [in micromoles ^{15}N per milligram dry weight (DW) per hour], was calculated using the following equation:

$$V_{sample} = POM \text{ x } E_{sample}/(time \times dry\ weight) \quad (3)$$

where POM is the value of the stable nitrogen isotope in the plant tissue (in micromoles ^{15}N) (van England et al., 2011). Correction of varying substrate concentrations was accomplished by dividing V_{sample} by the substrate concentration (nitrogen added, N_{added}) and multiplying by 100 to convert to % $(mg\ DW)^{-1}\ h^{-1}$.

$$\%\,V_{sample} = 100 \text{ x } V_{sample}/N_{added} \quad (4)$$

$\%V_{sample}$ can be used to compare the nitrogen uptake rates of the different plants or plant tissues.

2.4 Statistical analysis

For the effects of light treatments on macroalgal dry biomass, seagrass leaf length, leaf width, rhizome node diameter, node and root lengths, total dry biomass, and above- and belowground dry biomass, the $\delta^{15}N$ values of plants were analyzed using one-way ANOVA and *post-hoc* tests. The light and nitrogen effects on the $\%V_{sample}$ of algae and the above- and belowground components of seagrasses were separately analyzed using two-way ANOVA and *post-hoc* tests. Differences in the $\%V_{sample}$ values among groups (light × nitrogen × plant tissues) were analyzed using three-way ANOVA and *post-hoc* tests. When ANOVA was significant ($p < 0.05$), Tukey's test was applied to determine which treatments were significantly different.

3 Results

3.1 Physiological and morphological parameters of algae and seagrasses

The N% and $\delta^{15}N$‰ of algae after light treatment were not significantly different (Table 1). The dry biomass of *U. pertusa* after HL treatment was significantly higher than that after ML and LL treatments ($p < 0.01$) (Table 1). The highest (0.32 ± 0.05 g) and the lowest (0.25 ± 0.05 g) values were recorded for the HL and ML treatments, respectively (Table 1).

The total dry biomass of *Z. japonica* in the HL treatment was significantly higher than that in the lower light treatments ($p < 0.05$) (Table 2). The highest and the lowest total dry biomass values in the HL and LL treatments were 2.14 ± 0.39 and 1.19 ± 0.23 mg, respectively (Table 2). The belowground dry biomass of *Z. japonica* was significantly different after the three light treatments ($p < 0.05$) (Table 2). The highest (1.04 ± 0.17 mg) and the lowest (0.55 ± 0.13 mg) belowground dry biomass values were found in the HL and LL treatments, respectively (Table 2).

The leaf length, width, and rhizome diameter of the seagrasses showed significant differences after the three light treatments ($p < 0.05$) (Table 2). The highest (6.17 ± 0.81 mg) and the lowest (3.36 ± 0.69 mg) values for seagrass leaf length were recorded in the HL and LL treatments, respectively (Table 2), while the highest (0.96 ± 0.14 mm) and the lowest (0.77 ± 0.09 mm) values for seagrass leaf width were found in the HL and ML treatments, respectively (Table 2). On the other hand, the highest (1.07 ± 0.12 mm) and the lowest (0.96 ± 0.07 mm) values for seagrass rhizome diameter were recorded in the HL and LL treatments, respectively (Table 2). The rhizome node and root lengths of seagrasses did not differ significantly among the three light treatments (Table 2).

TABLE 1 Content of nitrogen, $\delta^{15}N$, and dry biomass of *Ulva pertusa* after light treatments.

	High light	Medium light	Low light
N (%dry biomass)	4.81 ± 0.59	4.69 ± 0.49	5.37 ± 0.57
$\delta^{15}N$‰	6.49 ± 0.35	6.8 ± 0.36	7.05 ± 1.18
Dry biomass (g)	0.32 ± 0.05a	0.25 ± 0.05b	0.27 ± 0.07b

Lowercase letters indicate that there were differences between the two data points for each line after different light treatments. The same letters indicate no significant differences in the same line.

TABLE 2 Biomass and morphological parameters of *Zostera japonica* after different light treatments.

	High light	Medium light	Low light
Total dry biomass (mg)	2.14 ± 0.39a	1.38 ± 0.24b	1.19 ± 0.23b
Aboveground dry biomass (mg)	1.10 ± 0.29a	0.73 ± 0.17ab	0.64 ± 0.13b
Belowground dry biomass (mg)	1.04 ± 0.17a	0.65 ± 0.15b	0.55 ± 0.13b
N (% aboveground dry biomass)	2.17 ± 0.08	2.08 ± 0.09	2.11 ± 0.21
N (% belowground dry biomass)	1.33 ± 0.11	1.32 ± 0.08	1.29 ± 0.07
Leaf length (cm)	6.17 ± 0.81a	4.98 ± 0.59b	3.36 ± 0.69c
Leaf width (mm)	0.96 ± 0.14a	0.77 ± 0.09b	0.79 ± 0.08b
Rhizome diameter (mm)	1.07 ± 0.12a	1.00 ± 0.09b	0.96 ± 0.07b
Node length (mm)	3.28 ± 0.94	3.69 ± 0.33	3.72 ± 0.29
Root length (cm)	2.02 ± 0.24	1.96 ± 0.18	2.31 ± 0.40

Lowercase letters indicate differences between the two data points for each line after different light treatments. The same letters indicate no significant differences in the same line.

The $\delta^{15}N$ values of algae after the absorption of ammonium by plant tissues were significantly higher than those of the other three nutrients and natural groups after each light treatment ($p < 0.01$) (Figure 1). The highest (97.26 ± 30.84‰) and the lowest (35.65 ± 9.15‰) $\delta^{15}N$ values of algae after ammonium absorption were found after HL and LL treatments, respectively (Figure 1).

The $\delta^{15}N$ values of the aboveground seagrass tissues after the absorption of ammonium were significantly higher than those of the natural groups and other three nutrients previously grown under each light treatment ($p < 0.01$) (Figure 2A). The $\delta^{15}N$ values of the aboveground seagrass tissues after ammonium absorption were 62.99 ± 15.94‰, 91.95 ± 34.38‰, and 74.14 ± 22.49‰ after the HL, ML, and LL treatments, respectively (Figure 2A). The $\delta^{15}N$ value of seagrass belowground tissues after nutrient absorption was significantly different after each light treatment (Figure 2B, $p<0.05$). The highest δ15N values of seagrass belowground tissues after ammonium absorption appeared after HL (67.90±10.49‰), ML (128.37±38.74‰) and LL (64.66±22.06‰) treatments (Figure 2B).

3.2 $\%V_{sample}$ value of alagae and seagrasses

Both nitrogen and light significantly impacted the $\%V_{sample}$ values of algae ($p < 0.001$) (Figure 3A and Table 3). The highest absorption rates of algae for ammonium (14.67 ± 2.50 mg^{-1} DW h^{-1}), nitrate (1.29 ± 0.16 mg^{-1} DW h^{-1}), and urea (1.67 ± 0.65 mg^{-1} DW h^{-1}) were found after HL treatment (Figure 3A). The lowest $\%V_{sample}$ values of algae for ammonium (4.52 ± 0.95 mg^{-1} DW h^{-1}) and nitrate (0.18 ± 0.12 mg^{-1} DW h^{-1}) occurred after LL

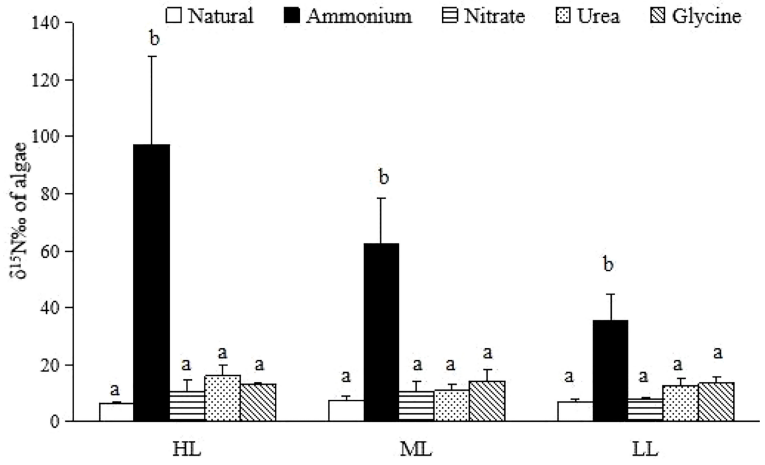

FIGURE 1
The $\delta^{15}N$ value of *U. pertusa*. The different letters indicated significant differences in the same light treatment..

treatment (Figure 3A). The lowest $\%V_{sample}$ value of algae for urea was 0.58 ± 0.41 mg^{-1} DW h^{-1}, which was found after ML treatment (Figure 3A).

Nitrogen had significant effects on the $\%V_{sample}$ values of the aboveground seagrass parts ($p < 0.001$) (Figure 3B and Table 3). The $\%V_{sample}$ values of the aboveground seagrass parts for ammonium were higher than those for glycine after all light treatments (Figure 3B). The highest ammonium absorption rates of the aboveground seagrasses were 8.27 ± 1.97, 9.93 ± 2.42, and 9.70 ± 2.12 mg^{-1} DW h^{-1} after HL, ML, and LL treatments, respectively (Figure 3B). For glycine, the highest absorption rates of the aboveground seagrasses were 3.92 ± 1.11, 3.35 ± 1.99, and 5.32 ± 0.27 mg^{-1} DW h^{-1} after HL, ML, and LL treatments, respectively (Figure 3B).

Light and nitrogen significantly impacted the $\%V_{sample}$ values of the belowground seagrass parts ($p < 0.001$) (Figure 3C and Table 3). After HL, ML, and LL treatments, the $\%V_{sample}$ values of the belowground seagrass parts for ammonium were 4.56 ± 0.04, 11.97 ± 1.89, and 3.87 ± 1.16 mg^{-1} DW h^{-1}, respectively, while those for glycine were 14.71 ± 1.85, 3.98 ± 0.20, and 6.38 ± 0.52 mg^{-1} DW h^{-1}, respectively (Figure 3C).

Nitrogen also altered the $\%V_{sample}$ values of algae and the above- and belowground seagrass parts under different light pressures ($p < 0.001$) (Table 4). The $\%V_{sample}$ values of algae for ammonium were higher than those of seagrass leaves after HL treatment, but were lower than those of seagrass leaves after LL treatments (Figure 3). For ammonium, the $\%V_{sample}$ values of the aboveground seagrass parts were higher than those of the belowground parts after HL and LL treatments (Figure 3). For nitrite, the $\%V_{sample}$ values of the belowground seagrass parts were higher than those of the aboveground seagrass parts and algae after all light treatments (Figure 3). The $\%V_{sample}$ values of algae for nitrate after LL treatments were lower than those of the aboveground seagrass parts, while these values in the belowground seagrass parts for urea after all treatments were higher than those in the aboveground seagrass parts (Figure 3). For glycine, the $\%V_{sample}$ values of algae were higher than those of seagrass leaves after all light treatments, while these values in the belowground seagrass parts were higher than those of the aboveground seagrass parts after HL treatment (Figure 3).

The three-way ANOVA (light × nitrogen × plant tissues) illustrated the significant effects of nitrogen type on the ability of plant tissues (algae and the above- and belowground parts of

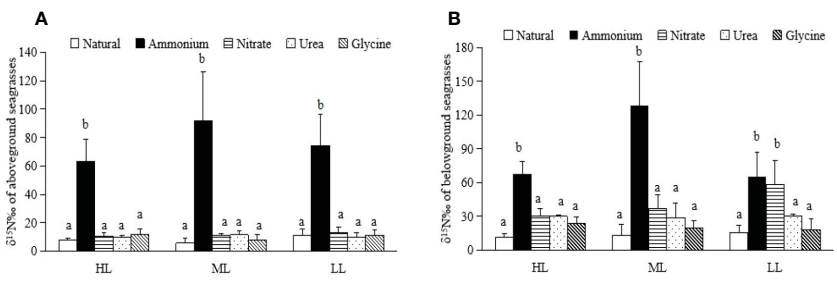

FIGURE 2
$\delta^{15}N$ values in the aboveground and belowground tissues of *Zostera japonica*. **(A)** Aboveground seagrasses. **(B)** Belowground seagrasses.

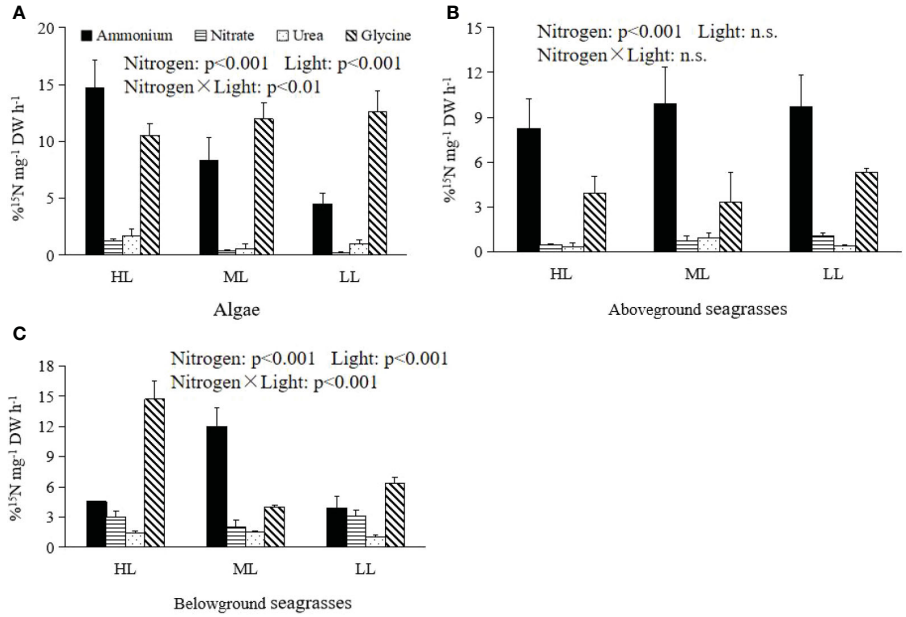

FIGURE 3
The N absorption rates between algae and the aboveground and belowground parts of seagrasses for the different N sources afterlight treatments. **(A)** Algae. **(B)** Aboveground seagrasses. **(C)** Belowground seagrasses.

seagrasses) to absorb nitrogen and showed that light and the nitrogen type altered the absorption ability of algae and seagrasses for nitrogen (Table 4).

4 Discussion

This study showed that the dry weight of *U. pertusa* after HL treatment was significantly higher than that after lower light treatments (Table 1), which is similar to the results of van Alstyne (2008) and Schmid et al. (2021), who found that macroalgae showed a higher growth rate under higher light than under lower light conditions. Macroalgae have evolved physiological responses to light reduction, driving photosynthesis (Takahashi and Murata, 2008; Esteban et al., 2015), thereby impacting algal biomass. The physiological responses of algae to stress can increase amino acids or reduce sugars at the cellular level (Sharma et al., 2016). High light intensity increases the concentrations of β-carotene and zeaxanthin in marine macroalgae (Xie et al., 2020), resulting in an increase in storage lipids in some algae (Khotimchenko and Yakovleva, 2005). However, some macroalgae showed lower chlorophyll a (Chl-a) and pigment composition under higher light conditions (see, for example, Esteban et al., 2015; Schmid et al., 2021). *Ulva fenestra* exhibited higher concentrations of lipids and higher proportions of polyunsaturated fatty acids in low-light habitats than in moderate-light conditions (Hotimchenko, 2002). *Ulva lactuca* grown under high-light conditions had lower nitrogen, carbon, pigment, and dimethylsulfoniopropionate concentrations relative to algae in low light (van Alstyne 2008). This could be due to the physiological responses and resource allocation of macroalgae to light reduction being species-specific.

Light availability is the main factor limiting the growth and distribution of seagrasses compared with all other factors (Dennison et al., 1993; Lee et al., 2007). Seagrasses show physiological and morphological responses to light reduction depending on localized environmental conditions and timescales (Bertelli and Unsworth, 2018; Kim et al., 2019; Zhang et al., 2020). The responses of seagrasses to light reduction also include biomass decrease (Holmer and Laursen, 2002) and growth reduction (Rruiz and Romero, 2001). The total dry biomass and belowground biomass of *Z. japonica* in the HL treatment were significantly higher than those in the lower light treatments in this study (Table 2), which is in

TABLE 3 Analysis of variance of the effects of light and nitrogen on the $\%V_{sample}$ values of plant tissues.

	Macroalgae			Aboveground seagrass parts			Belowground seagrass parts		
	df	*F*	*p*	*df*	*F*	*p*	*df*	*F*	*p*
Nitrogen	3	188.38	<0.001	3	91.06	<0.01	3	121.46	<0.001
Light	2	12.57	<0.001	2	1.38	n.s.	2	19.66	<0.001
Nitrogen × light	6	14.34	<0.001	6	0.77	n.s.	6	57.45	<0.001

n.s., no significant differences.

TABLE 4 Analysis of variance of the three-factor model with the % V_{sample} of plants as the response variable and light, nitrogen, and plant tissues (algae and the aboveground and belowground seagrasses) and all possible interactions.

Source	*df*	*F*	*p*
Light	2	1.44	n.s.
Nitrogen	3	18.70	<0.001
Plant tissues	2	1.01	n.s.
Light × nitrogen	6	2.02	n.s.
Light × plant tissues	4	0.75	n.s.
Nitrogen × plant tissues	6	0.26	n.s.
Light × nitrogen × plant tissues	12	1.41	n.s.

n.s., no significant differences.

accordance with other reports on seagrass habitats (*Z. marina* and *C. nodosa*: Silva et al., 2013; Collier et al., 2016; *Z. muelleri*: Griffiths et al., 2020).

Exposure to low light may lead to carbonhydrate reduction in seagrasses (Hasler-Sheetal et al., 2016; Kumar et al., 2017). Smaller species are less resistant to light reduction (Collier et al., 2016), and the responses of seagrasses to light reduction are species-specific (Collier et al., 2007; Manassa et al., 2017; Statton et al., 2018). For example, the low light requirements of *Z. noltii*, *Posidonia oceanica*, *Thalassia testudinum*, *Halodule pinifolia*, and *Syringodium filiforme* for survival were 2%, 10%, 14%, 14%, and 24% of surface irradiance (SI), respectively (Leoni et al., 2008 and references therein). Our results showed that the rhizome diameters of the seagrasses in the HL treatment were significantly higher than those in the lower treatments (Table 2). The lower rhizome diameters of seagrasses demonstrate that carbon can be transported from belowground to the aboveground parts of seagrasses under low-light conditions due to disruption of the carbon fixation and energy metabolism (Griffiths et al., 2020). In this study, the leaf length and width were longer and thicker, respectively, in the HL treatment than in the ML and LL treatments (Table 2). A smaller area of seagrass leaves further limits photosynthesis. Our experiments prevented seagrasses from receiving nutrients and carbon *via* adjacent plants, as a result of isolating plant cultivation. This may be different from natural conditions, which should be considered in the future.

Light reduction and nitrogen availability can affect the physiological or biochemical properties of seaweeds by altering their carbon and nitrogen contents (Cruz-Rivera and Hay, 2003; Buapet et al., 2008). Although van Alstyne (2008) found that light and nitrate always independently affect the algal response, the absorption of nutrients by some algae is related to light and carbon metabolism (Dortch, 1990). The nitrogen concentrations in void tissues are often correlated with the DIN concentrations of seawater (Fujita et al., 1989; Björnsäter and Wheeler, 1990; Teichberg et al., 2010; Fan et al., 2014). In this study, it was found that the $\delta^{15}N$ values of the algal tissues after ammonium absorption were significantly higher than those of the other three nutrients and natural groups after each light treatment (Figure 1). The absorption rate of ammonium by algae is higher than that of nitrate because the uptake of ammonium into cells requires less energy than nitrate (Flynn, 1991).

During the macroalgal bloom and decay phases, *Ulva* sp. are an important source of DON in the aquatic environment (Tyler et l., 2001; Zhang et al., 2021). During the early period of macroalgal blooms, green macroalgae can take up DIN, thus lowering the DIN concentration in ambient seawater and effectively relieving eutrophication (Zhang and Wang, 2017). Subsequently, algae assimilate DIN into DON, continuously releasing DON into the ambient environment, or depositing it into sediments (Li et al., 2016). This explains the increase of the DON concentration in the culture environment, mainly because the DON produced by *Ulva* sp. was released into the ambient media (Sharp, 1977). Higher DON concentrations may increase the soluble sugar and protein contents of macroalgae (Xu, 2020). Tyler et al. (2005) found that *Gracilaria vermiculophylla* can assimilate urea and amino acids and that *U. lactuca* has higher uptake rates than *G. vermiculophylla*. The DON and ammonium from decomposed algae can be important nitrogen sources and take part in the nitrogen cycle in seagrass ecosystems, thereby further changing the biochemical cycle processes in the long term (Zhang et al., 2021b).

It is conceivable that the nitrogen uptake of seagrasses may change during or after macroalgal blooms. Macroalgal blooms lead to light limitations, which affect the functions of seagrass ecosystems, such as nutrient uptake. In this study, light reduction and the nitrogen type altered the absorption ability of seagrasses and algae for nitrogen (Figure 3). After light reduction, seagrass growth is limited, which may result in a reduction in the nutrient requirements for growth. The physiological responses of seagrasses to low irradiance include the increase in the nitrogen and amino acid contents in tissues (van Lent et al., 1995; Longstaff and Dennison, 1999; Leoni et al., 2008; McMahon et al., 2013). Nitrogen enrichment can promote the demand for energy and carbon skeletons from photosynthates to drive the assimilation of DIN (Inverse et al., 2004), affecting the productivity and survival of seagrasses, which may aggravate the deleterious effects of low light (Villazán et al., 2013). Our results showed that the aboveground parts of seagrasses had higher absorption ability for ammonium than for nitrate, urea, and glycine after all light treatments (Figure 3). Some seagrass species have increased affinity for ammonium over nitrate (Terrados and Williams, 1997; Lee and Dunton, 1999). The preferential uptake of ammonium by seagrasses may be due to the physiological demands associated with nitrate uptake (Nayar et al., 2018 and references therein). Furthermore, seagrass tissues require far less energy than nitrate to transform ammonium into organic nitrogen (Nayar et al., 2018). Sandoval-Gil et al. (2015) found that seagrass roots showed reduced capacity to absorb ammonium compared to leaves because of the very high availability of this nutrient in sediments. This is in agreement with our results, in which the absorption rates of ammonium by the aboveground parts of seagrasses were higher than those of the belowground parts after HL and LL treatments (Figure 3). Lee and Dunton (1999) found that ammonia is mostly absorbed by the rhizomes and roots of seagrasses. The belowground parts of seagrasses grow in sediments, where there is less oxygen concentration than in coastal waters; therefore, seagrass roots and

rhizomes may adapt to environments with less oxygen through evolved physiological responses. The substratum type can influence the leaf *versus* root nutrient uptake, and fine-grained sediments generally support a higher absorption rate of seagrasses for ammonium (Bulthuis et al., 1992). We recommend further research involving the combined effects of sediment types on the absorption ability of seagrasses for organic and inorganic nitrogen nutrients to lower the negative effects of eutrophication on seagrass ecosystems through a long-term investigation.

Sandoval-Gil et al. (2019) found that nitrate is mainly absorbed by seagrass leaves. This is contrary to our results, in which the absorption rates of nitrate by the belowground seagrass parts were significantly higher than those of seagrass leaves and macroalgae after all light treatments (Figure 3). Nitrate enrichment in sediments can stimulate the growth of seagrasses (Peralta et al., 2003), while water column nitrate enrichment may lead to the die-off of seagrasses (Leoni et al., 2008). Zimmerman et al. (1987) reported that most nitrogen assimilation occurs in the roots; however, limited light conditions interfere with the nitrogen assimilation in the roots because the root–rhizome system is photosynthesis-dependent (Pregnall et al., 1987). The nitrogen uptake rates of seagrass roots depend on the belowground biomass of seagrasses (Kraemer et al., 1997; Leoni et al., 2008). Some seagrass species (e.g., *Z. noltii*) can absorb more nitrate in the absence of ammonium (Alexandre et al., 2011). The assimilation of seagrasses into nitrate requires more energy because it involves an active transport system (Lepoint et al., 2002), which may aggravate the potentially harmful effects of nitrate enrichment, such as toxicity and metabolic costs (Burholder et al., 1992; Sandoval-Gil et al., 2015). Our results demonstrate that limited light use did not alter the absorption ability of the above- and belowground parts of seagrasses for nitrogen, especially nitrate.

When the nitrogen requirement is lower than the uptake, the absorbed nutrients may be reserved in the plant tissues as amino acids or proteins (Udy et al., 1999; Invers et al., 2004). The carbon requirements for synthesizing amino acids can exceed the carbon fixation capacity under nitrogen enrichment conditions. The results of this study showed that the absorption ability of seagrasses for glycine was significantly higher than that for nitrate and urea after HL and LL treatments (Figure 3), which is in agreement with Alexandre et al. (2015), who found that *Z. marina* showed preferential uptake of DON over nitrate and that DON was a complementary nitrogen source compared to DIN. Seagrass tissues can limit the use of nitrogen once they reach substrate saturation (Touchette and Burkholder, 2000). The lower concentration of glycine than nitrate and urea may have enhanced the uptake ratio of seagrasses to glycine in this study. The belowground parts of seagrasses had higher absorption rates for urea than the aboveground parts after all light treatments (Figure 3). The urea in coastal waters resulting from agricultural fertilizers, coastal aquaculture, domestic sewage, and industrial waste can be deposited in sediments (Li et al., 2015), thereby providing an organic nitrogen source for the roots and rhizomes of seagrasses. Organic nitrogen (e. g., amino acid nitrogen) can be mineralized and directly assimilated by plants and microbes (Dong et al., 2021). For example, some dinoflagellates can absorb urea and nitrate (Wang, 2015). Vonk et al. (2008) found that seagrasses may prefer organic nitrogen at low ambient nitrogen concentrations; however, several studies have shown that seagrasses more preferred absorbing DIN (Burkholder et al., 1992; Lee and Dunton, 1999; Sandoval-Gil et al., 2015). The DON uptake of seagrasses may be more widespread than is traditionally recognized (van England et al., 2011). Microorganisms can facilitate the assimilation of DON by mineralizing amino acids in the seagrass *Posidonia sinuosa*, which may promote the growth and productivity of seagrasses (Tarquinio et al., 2018). However, the microbial catabolism of amino acids can lead to exuded ammonium, which is harmful to plant tissues at extremely high concentrations (van Katwijk et al., 1997). The mechanisms by which microorganisms affect the uptake of DON by seagrasses require further research.

Under lower light conditions, seagrasses may need more energy for the absorption of organic nitrogen in order to reduce the negative effects of light limitation (Collier et al., 2010). A reduced photosynthetic carbon fixation under low light conditions leads to less carbon being transferred from the leaves to seagrass roots and rhizomes. This may explain our results where the assimilation of glycine by *Z. japonica* roots and rhizomes after HL treatment was higher than that of the lower treatment (Figure 3D). Processes that minimize the utilization of reserved carbon by reducing the organic nitrogen assimilation within seagrass roots and rhizomes may contribute to shading tolerance. Our results indicate that *Z. japonica* quickly responded to short-term light reduction due to changes in organic nitrogen metabolism processes. The internal assimilation to organic nitrogen and the transfer mechanism to carbon of seagrasses should be considered in the future.

5 Conclusion

The eutrophication problem is complex because it may change the primary producers and environmental variables through ecosystem self-organization. Overall, this study provides evidence that shading alters the absorption ability of macroalgae and seagrasses for inorganic and organic nitrogen, although it is also necessary to deeply understand the difference between the limited, highly artificial study and the non-linear, highly interactive responses in the seagrass meadows. Light reduction may alter the competition status between seagrasses and macroalgae through a change in their inorganic and organic absorption strategies. This difference should be well considered in future coastal management and seagrass protection. Regular seagrass monitoring, coupled with long-term studies to assess the effects of macroalgal bloom progression and duration on seagrass ecosystems, is required. Additional tests of the thresholds of the different nitrogen sources and their effects under different environmental, social, and economic contexts are also required.

Data availability statement

The original contributions presented in the study are included in the article/supplementary material. Further inquiries can be directed to the corresponding author.

Author contributions

QH and CQ: Conceptualization. QH and YC: Methodology. QH, WZ, and YC: Formal analysis. QH, CQ, and FZ: Writing—original draft preparation. QH, MZ, YS, and CQ: Writing—review and editing. All authors contributed to the article and approved the submitted version.

Funding

This research was supported by the projects ofthe National Natural Science Foundation of China (41730529) andthe High-Level Talented Person Project of the Natural ScienceFoundation of Hainan Province (420RC657).

Acknowledgments

We thank Laura M. Soissons for her support during the experiment design.

Conflict of interest

The authors declare that the research was conducted in the absence of any commercial or financial relationships that could be construed as a potential conflict of interest.

Publisher's note

References

Alexandre, A., Hill, P. W., Jones, D. L., and Santos, R. (2015). Dissolved organic nitrogen: A relevant, complementary source of nitrogen for the seagrass *Zostera marina*. *Limnology Oceanography* 60, 1477–1483. doi: 10.1002/lno.10084

Alexandre, A., Silva, J., Bouma, T. J., and Santos, R. (2011). Inorganic nitrogen uptake kinetics and whole-plant nitrogen budget in the seagrass *Zostera noltii*. *J. Exp. Mar. Biol. Ecology* 401, 7–12. doi: 10.1016/j.jembe.2011.03.008

Beck, M. W., Heck, K. L.Jr., Able, K. W., Childers, D. L., Eggleston, D. B., Gillanders, B. M., et al. (2001). The identification, conservation, and management of estuarine and marine nurseries for fish and invertebrates. *BioScience* 51, 633–641. doi: 10.1641/0006-3568(2001)051[0633:TICAMO]2.0.CO;2

Bertelli, C. M., and Unsworth, R. K. F. (2018). Light stress responses by the eelgrass, *Zostera marina* (L). *Front. Environ. Science* 6, 39. doi: 10.3389/fenvs.2018.00039

Björnsäter, B. R., and Wheeler, P. A. (1990). Effect of nitrogen and phosphorus supply on growth and tissue composition of *Ulva fenestrata* and *Enteromorpha intestinalis* (Ulvales, chlorophyta). *J. Phycology* 26, 603–611. doi: 10.1111/j.0022-3646.1990.00603.x

Bricker, S. B., Ferreira, J. G., and Simas, T. (2003). An integrated methodology for assessment of estuarine trophic status. *Ecol. Modelling* 169, 39–60. doi: 10.1016/S0304-3800(03)00199-6

Bronk, D. A. (2002). "Dynamics of organic nitrogen," in *Biogeochemistry of marine dissolved organic matter*. Eds. D. A. Hansell and C. A. Carlson (San Diego: Academic Press), 153–247.

Brun, F. G., Hernández, I., Vergara, J. J., Peralta, G., and Pérez-Lloérnz, J. L. (2002). Assessing the toxicity of ammonium pulses to the survival and growth of *Zostera noltii*. *Mar. Ecol. Progess Series* 225, 177–187. doi: 10.3354/meps225177

Buapet, P., Hiranpan, R., Ritchie, R. J., and Prathep, A. (2008). Effect of nutrient inputs on growth, chalorophyll, and tissue nutrient concentration of *Ulva reticulate* from a tropical habitat. *ScienceAsia* 34, 245–252. doi: 10.2306/scienceasia1513-1874.2008.34.245

Bulthuis, D. A., Axelrad, D. M., and Mickelson, M. J. (1992). Growth of the seagrass *Heterozostera tasmanica* limited by nitrogen in port phillip bay, Australia. *Mar. Ecol. Prog. Series* 89, 269–275. doi: 10.3354/meps089269

Burkholder, J. M., Noga, E. J., Hobbs, C. H., and Glasgow, Jr. H. B. (1992). New 'phantom' dinoflagellate is the causative agent of major estuarine fish kills. *Nature* 358, 407–410. doi: 10.1038/358407a0

Burkholder, J. M., Tomasko, D. A., and Touchette, B. W. (2007). Seagrasses and eutrophication. *J. Exp. Mar. Biol. Ecology* 350, 46–72. doi: 10.1016/j.jembe.2007.06.024

Cambridge, M. I., Chiffings, A. W., Brittain, C., Moore, L., and McComb, A. J. (1986). The loss of seagrass in Cockburn sound, Western australia. II. possible causes of seagrass decline. *Aquat. Botany* 24, 269–285. doi: 10.1016/0304-3770(86)90062-8

Collier, C. J., Adams, M. P., Langlois, L., Waycott, M., O'Brien, K. R., Maxwell, P. S., et al. (2016). Thresholds for morphological response to light reduction for four tropical seagrass species. *Ecol. Indicators* 67, 358–366. doi: 10.1016/j.ecolind.2016.02.050

Collier, C. J., Lavery, P. S., Masini, R. J., and Ralph, P. J. (2007). Morphological, growth and meadow characteristics of the seagrass *Posidonia sinuosa* along a depth-reltated gradient of light availability. *Mar. Ecol. Prog. Series* 337, 103–115. doi: 10.3354/meps337103

Collier, C. J., Prado, P., and Lavery, P. S. (2010). Carbon and nitrogen translocation in response to shading of the seagrass *Posidonia sinuosa*. *Aquat. Botany* 93, 47–54. doi: 10.1016/j.aquabot.2010.03.003

Collier, C. J., Uthicke, S., and Waycott, M. (2011). Thermal tolerance of two seagrass species at contrasting light levels: implications for future distribution in the great barrier reef. *Limnology Oceanography* 56, 2200–2210. doi: 10.4319/lo.2011.56.6.2200

Costanza, R., d'Arge, R., de Groot, R., Farber, S., Grasso, M., Hannon, B., et al. (1997). The value of the world's ecosystem services and natural capital. *Nature* 387, 253–260. doi: 10.1038/387253a0

Cruz-Rivera, E., and Hay, M. (2003). Prey nutritional quality interacts with chemical defenses to affect consumer feeding and fitness. *Ecol. Monographs* 73, 483–506. doi: 10.1890/0012-9615(2003)073[0483:PNQIWC]2.0.CO;2

Delgado, M., Carlos, M., Cintra-Buenrostro, E., and Fierro-Cabo, A. (2017). Decomposition and nitrogen dynamics of turtle grass (*Thalassia testudinum*) in a subtropical estuarine system. *Wetlands Ecol. Management* 25, 667–681. doi: 10.1007/s11273-017-9543-1

Dennison, W. C., Orth, R. J., Moore, K. A., Stevenson, J. C., Carter, V., Kollar, S., et al. (1993). Assessing water quality with submersed aquatic vegetation: habitat requirements as barometers of Chesapeake bay health. *Bioscience* 43, 86–94. doi: 10.2307/1311969

Dong, S. H., Lv, H. J., Zhou, F., Zhang, X. C., He, H. B., Zhang, X. D., et al. (2021). Variation of soil organic nitrogen fractions in maize field during growing season and its response to current year and long-term straw returning. *Chin. J. Ecology* 41, 73–80. doi: 10.13292/j.1000-4890.20220.1036

Dortch, Q. (1990). The interaction between ammonium and nitrate uptake in phytoplankton. *Mar. Ecol. Prog. Series* 61, 183–201. doi: 10.3354/meps061183

Duarte, C. M. (1995). Submerged aquatic vegetation in relation to different nutrient regimes. *Ophelia* 41, 87–112. doi: 10.1080/00785236.1995.10422039

Esteban, R., Barrutia, O., Artetxe, U., Fernandez-Marin, B., Hernandez, A., and Garcia-Plazaola, J. I. (2015). Internal and external factors affecting photosynthetic pigment composition in plants: a meta-analytical approach. *New Phytologist* 206, 268–280. doi: 10.1111/nph.13186

Fan, X., Xu, D., Wang, Y., Zhang, X., Cao, S., Mou, S., et al. (2014). The effect of nutrient concentrations, nutrient ratios and temperature on photosynthesis and nutrient uptake by *Ulva prolifera*: implications for the explosion in green tides. *J. Appl. Phycology* 26, 537–544. doi: 10.1007/s10811-013-0054-z

Flynn, K. J. (1991). Algal carbon-nitrogen metabolism: A biochemical basis for modeling the interaction between nitrate and ammonium uptake. *J. Plankton Res.* 13 (2), 373–387. doi: 10.1093/plankt/13.2.373

Fujita, R., Wheeler, P., and Edwards, R. L. (1989). Assessment of macroalgal nitrogen limitation in a seasonal upwelling region. *Mar. Ecol. Prog. Series* 53, 293–303. doi: 10.3354/meps053293

Griffiths, L. L., Melvin, S. D., Connolly, R. M., Pearson, R. M., and Brown, C. J. (2020). Metabolomic indicators for low-light stress in seagrass. *Ecol. Indicators* 114, 106316. doi: 10.1016/j.ecolind.2020.106316

Gruber, G. (2004). "The dynamics of the marine nitrogen cycle and its influence on atmospheric CO2 variations," in *The ocean carbon cycle and climate*. Eds. M. Follows and T. Oguz (Amstertam: LOS Press), 97–148.

Han, Q. Y., and Liu, D. Y. (2014). Macroalgae blooms and their effects on seagrass ecosystems. *J. Ocean Univ. China* 13, 791–798. doi: 10.1007/s11802-014-2471-2

Han, Q. Y., Soissons, L. M., Bouma, T. J., van Katwijk, M. M., and Liu, D. Y. (2016). Combined nutrient and macroalgae loads lead to response in seagrass indicator properties. *Mar. pollut. Bulletin* 106, 174–182. doi: 10.1016/j.marpolbul.2016.03.004

Han, Q. Y., Soissons, L. M., Liu, D. Y., van Katwijk, M. M., and Bouma, T. J. (2017). Individual and population indicators of *Zostera japonica* resond quickly to experimental addition of sediment-nutrient and organic matter. *Mar. pollut. Bulletin* 114, 201–209. doi: 10.1016/j.marpolbul.2016.08.084

Harvens, K. E., Hauxwell, J., Tyler, A. C., Thomas, S., McGlathery, K. J., Cebrián, J., et al. (2001). Complex interactions between autotrophs in shallow marine and freshwater ecosystems: implications for community responses to nutrient stress. *Environ. Pollution* 113, 95–107. doi: 10.1016/S0269-7491(00)00154-8

Hasler-SheEtal, H., Castorani, M. C. N., Glud, R. N., Canfield, D. E., and Holmer, M. (2016). Metabolomics reveals cryptic interactive effects of species interactions and environmental stress on nitrogen and sulfur metabolism in seagrass. *Environ. Sci. Technology* 50, 11602–11609. doi: 10.1021/acs.est.6b04647

Hauxwell, J., Cebrián, J., Furlong, C., and Valiela, I. (2001). Macroalgal canopies contribute to eelgrass (*Zostera marina*) decline in temperate estuarine ecosystems. *Ecology* 82, 1007–1022. doi: 10.1890/0012-9658(2001)082[1007:MCCTEZ]2.0.CO;2

Hedges, J. I., Baldock, J., Gelinas, Y., Lee, C., Person, M., and Wakeham, S. (2002). The biochemical and elemental compositions of marine plankton: A NMR perspective. *Mar. Chem.* 78, 47–63. doi: 10.1016/S0304-4203(02)00009-9

Hemminga, M., and Duarte, C. M. (2000). *Seagrass ecology* (Cambridge, United Kingdom: Cambridge University Press).

Herbeck, L. S., Unger, D., Wu, Y., and Jennerjahn, T. C. (2013). Effluent, nutrient and organic matter export from shrimp and fish ponds causing eutrophication in coastal and back-reef waters of NE hainan. *Continental Shelf Res.* 57, 92–104. doi: 10.1016/j.csr.2012.05.006

Holmer, M., Argyrou, M., Dalsgaard, T., Danovaro, R., Diaz-Almela, E., Duatre, C. M., et al. (2008). Effects of fish farm waste on *Posidonia oceanica* meadows: synthesis and provision of monitoring and management tools. *Mar. pollut. Bulletin* 56, 1618–1629. doi: 10.1016/j.marpolbul.2008.05.020

Holmer, M., and Laursen, L. (2002). Effect of shading of *Zostera marina* (eelgrass) on sulfur cycling in sediments with contrasting organic matter and sulfide pools. *J. Exp. Mar. Biol. Ecology* 270, 25–37. doi: 10.1016/S0022-0981(02)00015-1

Hotimchenko, S. (2002). Fatty acid composition of algae from habitats with varying amounts of illumination. *Russian J. Mar. Biol.* 28, 218–220. doi: 10.1023/A:1016861807103

Huang, G. S., Li, X. B., Tang, Y. J., Liu, J. L., Liu, N., Ke, X. R., et al. (2017). An experiment of the ecological breeding for aquatic economic animals in *Sonneratia apetala* artificial plantation. *J. Guangdong Univ. Education* 37 (3), 85–89. doi: 10.3969/j.issn.2095-3798.2017.03.013

Inverse, O., Kraemer, G. P., Pérez, M., and Romero, J. (2004). Effect of nitrogen addition on nitrogen metabolism and carbon reserves in the temperate seagrass *Posidonia oceanica*. *J. Exp. Mar. Biol. Ecology* 303, 97–114. doi: 10.1016/j.jembe.2003.11.005

Khotimchenko, S. V., and Yakovleva, I. M. (2005). Lipid composition of the red alga *Tichocarpus crinitus* exposed to different levels of photon irradiance. *Phytochemistry* 66, 73–79. doi: 10.1016/j.phytochem.2004.10.024

Kim, M., Pernice, M., Watson-Lazowski, A., Guagliardo, P., Kilburn, M. R., Larkum, A. W. D., et al. (2019). Effect of reduced irradiance on ^{13}C uptake, gene expression and protein activity of the seagrass *Zostera mulleri*. *Mar. Environ. Res.* 149, 80–89. doi: 10.1016/j.marenvres.2019.06.004

Kraemer, G. P., Mazzella, L., and Alberte, R. S. (1997). Nitrogen assimilation and partitioning in the Mediterranean seagrass *Posidonia oceanica*. *Mar. Ecology* 18, 287–300. doi: 10.1111/j.1439-0485.1997.tb00435.x

Kumar, M., Padula, M. P., Davey, P., Pernice, M., Jiang, Z., Sablok, G., et al. (2017). Proteome analysis reveals extensive light stress-response reprogramming in the seagrass *Zostera muelleri* (Alismatales, zosteraceae) metabolism. *Front. Plant Science* 7, 2023. doi: 10.3389/fpls.2016.02023

Lapointe, B. E., Tomasko, D. A., and Matzie, W. R. (1994). Eutrophication and trophic state classification of seagrass communities in the Florida keys. *Bull. Mar. Sci.* 54, 696–717. doi: 10.1515/botm.1994.37.3.277

Lee, K. S., and Dunton, K. H. (1999). Inorganic nitrogen acquisition in the seagrass *Thalassia testudinum*: development of a whole plant nitrogen budget. *Limnology Oceanography* 44, 1204–1215. doi: 10.4319/lo.1999.44.5.1204

Lee, K., Park, S. R., and Kim, Y. K. (2007). Effects of irradiance, temperature, and nutrients on growth dynamics of seagrasses: a review. *J. Exp. Mar. Biol. Ecology* 350, 144–175. doi: 10.1016/j.jembe.2007.06.016

Leoni, V., Vela, A., Pasqualini, V., Pergent-Martini, C., and Pergent, G. (2008). Effects of experimental modifications of light levels and nutrient concentrations on seagrass: a review. *Aquat. Conservation: Mar. Freshw. Ecosystems* 18, 202–220. doi: 10.1002/aqc.842

Lepoint, G., Millet, S., Dauby, P., Gobert, S., and Bouquegneau, J. M. (2002). Annual nitrogen budget of the seagrass *Posidonia oceanica* as determined by *in situ* uptake experiments. *Mar. Ecol. Prog. Series* 237, 87–96. doi: 10.3354/meps237087

Li, Z. L., Shi, X. Y., and Zhang, C. S. (2015). Distribution characteristics of urea and constitution of dissolved nitrogen in the bohai sea and huanghai sea in spring. *Environ. Science* 36, 3999–4004. doi: 10.13227/j.hjkx.2015.11.008

Li, H., Zhang, Y., Han, X., Shi, X., Rivkin, R. B., and Legendre, L. (2016). Growth responses of *Ulva prolifera* to inorganic and organic nutrients: implications for macroalgal blooms in the southern yellow Sea. *Sci. Rep.* 6, 26498. doi: 10.1038/srep26498

Longstaff, B. J., and Dennison, W. C. (1999). Seagrass survival during pulsed turbidity events: the effects of light deprivation on the seagrasses *Halodule pinfolia* and *Halophila ovalis*. *Aquat. Botany* 65, 105–121. doi: 10.1016/S0304-3770(99)00035-2

Manassa, R. P., Smith, T. M., Beardall, J., Keough, M. J., and Cook, P. L. M. (2017). Capacity of a temperate intertidal seagrass species to tolerate changing environmental conditions: significance of light and tidal exposure. *Ecol. Indicators* 81, 578–586. doi: 10.1016/j.ecolind.2017.04.056

McGlathery, K. (2001). Macroalgal blooms contribute to the decline of seagrass in nutrient-enriched coastal water. *J. Phycology* 37, 453–456. doi: 10.1046/j.1529-8817.2001.037004453.x

McMahon, K., Collier, C., and Lavery, P. S. (2013). Identifying robust bioindicators of light stress in seagrasses: a meta-analysis. *Ecol. Indicator* 30, 7–15. doi: 10.1016/j.ecolind.2013.01.030

Moore, K. A., and Wetzel, R. L. (2000). Seasonal variations in eelgrass (*Zostera marina* l.) response to nutrient enrichment and reduced light availability in experimental ecosystems. *J. Exp. Mar. Biol. Ecology* 244, 1–28. doi: 10.1016/S0022-0981(99)00135-5

Moreira-Saporiti, A., Hoeijmakers, D., Msuya, F. E., Reuter, H., and Teichberg, M. (2021). Seaweed farming pressure affects seagrass and benthic macroalgae dynamics in chwaka bay (Zanzibar, Tanzania). *Regional Environ. Change* 21, 1–12. doi: 10.1007/s10113-020-01742-2

Nayar, S., Loo, M. G. K., Tanner, J. E., Longmore, A. R., and Jenkins, G. P. (2018). Nitrogen acquisition and resource allocation strategies in temperate seagrass *Zostera nigricaulis*: uptake, assimilation and translocation processes. *Sci. Rep.* 8, 17151. doi: 10.1038/s41598-018-35549-3

Orth, R. J., Carruthers, T. J. B., Dennison, W. C., Duarte, C. M., Fourqurean, J. W., Heck, K. L., et al. (2006). A global crisis for seagrass ecosystems. *BioScience* 56, 987–996. doi: 10.1641/0006-3568(2006)56[987:AGCFSE]2.0.CO;2

Peralta, G., Bouma, T. J., van Soelen, J., Pérez-Lloréns, J. L., and Hernández, I. (2003). On the use of sediment fertilization for seagrass restoration: a mesocosm study on *Zostera marina* l. *Aquat. Botany* 75, 95–110. doi: 10.1016/S0304-3770(02)00168-7

Prasad, M. H. K., Ganguly, D., Paneerselvam, A., Ramesh, R., and Purvaja, R. (2019). Seagrass litter decomposition: an additional nutrient source to shallow coastal waters. *Environ. Monit. Assessment* 191, 5. doi: 10.1007/s10661-018-7127-z

Preen, A. R., and Marsh, H. (1995). Responses of dugongs to large-scale loss of seagrass from hervey bay, Queensland, Australia. *Wildlife Res.* 22, 507–519. doi: 10.1071/WR9950507

Pregnall, A. M., Smith, R. D., and Alberte, R. S. (1987). Glutamine synthetase activity and free amino acid pools of eelgrass (*Zostera marina* l.) roots. *J. Exp. Mar. Biol. Ecology* 106, 211–228. doi: 10.1016/0022-0981(87)90094-3

Ralph, P. J., Durako, M. J., Enriquez, S., Collier, C. J., and Doblin, M. A. (2007). Impact of light limitation on seagrasses. *J. Exp. Mar. Biol. Ecology* 350, 176–193. doi: 10.1016/j.jembe.2007.06.017

Rruiz, J. M., and Romero, J. (2001). Effects of *in situ* experimental shading on the mediterranean seagrass *Posidonia oceanica*. *Mar. Ecol. Prog. Series* 215, 107–120. doi: 10.3354/meps215107

Ruesink, J. L., Hong, J. S., Wisehart, L., Hacker, S. D., Dumbauld, B. R., Hessing-Hessing-Lewis, M., et al. (2010). Congener comparison of native (*Zostera marina*) and introduced (*Z. japonica*) eelgrass at multiple scales within a pacific Northwest estuary. *Biol. Invasions* 12, 1773–1789. doi: 10.1007/s10530-009-9588-z

Sandoval-Gil, J. M., Ávila-López, M. C., Camacho-Ibar, V. F., Hernández-López, J., Zertuche-González, J. A., and Cabello-Pasini, A. (2019). Regulation of nitrate uptake by the seagrass *Zostera marina* during upwelling. *Estuaries Coasts* 42, 731–742. doi: 10.1007/s12237-019-00523-3

Sandoval-Gil, J. M., Camacho-Ibar, V. F., Ávila-López, M. C., Hernández-López, J., Zertuche-González, J. A., and Cabello-Pasini, A. (2015). Dissolved inorganic nitrogen uptake kinetics and δ^{15}N of *Zostera marina* l. (eelgrass) in a coastal lagoon with oyster aquaculture and upwelling influence. *J. Exp. Mar. Biol. Ecology* 472, 1–13. doi: 10.1016/j.jembe.2015.06.018

Schmid, M., Guihéneuf, F., Nitschke, U., and Stengel, D. B. (2021). Acclimation potential and biochemical response of four temperate macroalgae to light and future seasonal temperature scenarios. *Algal Res.* 54, 102190. doi: 10.1016/j.algal.2021.102190

Sharma, S. K., Singh, G., Kumar, H., and Kataria, R. (2016). Effect of temperature on viscometric properties of aliphatic amino acids glycine/L-alanine/L-valine in aqueous solutions of tetraethylammonium iodide. *J. Mol. Liquids* 216, 516–525. doi: 10.1016/j.molliq.2016.01.053

Sharp, J. H. (1977). Excretion of organic matter by marine phytoplankton: do healthy cells do it? *Limnology Oceanography* 22, 381–399. doi: 10.4319/lo.1977.22.3.0381

Silva, J., Barrote, I., Costa, M. M., Albano, S., and Santos, R. (2013). *Physiological responses of* zostera marina *and* cymodocea nodosa *to light-limitation stress*. *PloS One* 8, e81058. doi: 10.1371/journal.pone.0081058

Statton, J., McMahon, K., Lavery, P., and Kendrick, G. A. (2018). Determining light stress response for a tropical multi-species seagrass assemblage. *Mar. pollut. Bulletin* 128, 508–518. doi: 10.1016/j.marpolbul.2018.01.060

Takahashi, S., and Murata, N. (2008). How do environmental stresses accelerate photoinhibition? *Trends Plant Science* 13, 178–182. doi: 10.1016/j.tplants.2008.01.005

Tarquinio, F., Bourgoure, J., Koenders, A., Laverock, B., Säwström, C., and Hyndes, G. A. (2018). Microorganisms facilitate uptake of dissolved organic nitrogen by seagrass leaves. *Multidiscip. J. Microbial Ecology* 12, 2796–2800. doi: 10.1038/s41396-018-0218-6

Teichberg, M., Fox, S. E., Olsen, Y. S., Valjma, I., Martinetto, P., Iribarne, O., et al. (2010). Eutrophication and macroalgal blooms in temperate and tropical coastal waters: nutrient enrichment experiments with ulva spp. *Global Change Biol.* 16, 2624–2637. doi: 10.1111/j.1365-2486.2009.02108.x

Terrados, J., and Williams, S. L. (1997). Leaf versus root nitrogen uptake by the surfgrass *Phyllospadix torreyi*. *Mar. Ecol. Prog. Series* 149, 267–277. doi: 10.3354/meps149267

Touchette, B. W., and Burkholder, J. M. (2000). Review of nitrogen and phosphorus metabolism in seagrasses. *J. Exp. Biol. Ecology* 250, 133–167. doi: 10.1016/S0022-0981(00)00195-7

Touchette, B. W., Burkholder, J. M., and Glasgow, H. B. (2003). Variations in eelgrass (*Zotera marina* l.) morphology and internal nutrient composition as influenced by increased temperature and water column nitrate. *Estuaries* 26, 142–155. doi: 10.1007/BF02691701

Turpin, D. H. (1991). Effects of inorganic n availability on algal photosynthesis and carbon metabolism. *J. Phycology* 27, 14–20. doi: 10.1111/j.0022-3646.1991.00014.x

Tyler, A. C., McGlathery, K. J., and Anderson, I. C. (2001). Macroalgae mediation of dissolved organic nitrogen fluxes in a temperate coastal lagoon. *Estuar. Coast. Shelf Science* 53, 155–168. doi: 10.1006/ecss.2001.0801

Tyler, A. C., McGlathery, K. J., and Macko, S. A. (2005). Uptake of urea and amino acids by the macroalgae *Ulva lactuca* (Chlorophyta) and *Gracilaria vermiculophylla* (Rhodophyta). *Mar. Ecol. Prog. Series* 294, 161–172. doi: 10.3354/meps294161

Udy, J. W., Dennison, W. C., Long, W. J. L., and McKenzie, L. J. (1999). Responses of seagrasses to nutrients in the great barrier reef, Australia. *Mar. Ecol. Prog. Series* 185, 257–271. doi: 10.3354/meps185257

Valiela, I., and Cole, M. L. (2002). Comparative evidence that salt marshes and mangroves may protect seagrass meadows from land-derived nitrogen loads. *Ecosystems* 5, 92–102. doi: 10.1007/s10021-001-0058-4

Valiela, I., Foreman, F., LaMontagne, M., Hersh, D., Costa, J., Peckol, P., et al. (1992). Couplings of watersheds and coastal waters: sources and consequences of nutrient enrichment in waquoit bay, Massachusetts. *Estuaries* 15, 443–457. doi: 10.2307/1352389

Valiela, I., McGlelland, J., Hauxwell, J., Behr, P. J., Hersh, D., and Foreman, K. (1997). Macroalgal blooms in shallow estuaries: controls and ecophysiological and ecosystem consequences. *Limnology Oceanography* 42, 1105–1118. doi: 10.4319/lo.1997.42.5_part_2.1105

van Alstyne, K. L. (2008). "Ecological and physiological roles of dimethylsulfoniopropionate (DMSP) and its products in marine macroalgae," in *Algal chemical ecology*. Ed. C. D. Amsler (Heidelberg: Springer), 173–194.

van England, T., Bouma, T. J., Morris, E. P., Brun, F. G., Peralta, G., Lara, M., et al. (2011). Potential uptake of dissolved organic matter by seagrasses and macroalgae. *Mar. Ecol. Prog. Series* 427, 71–81. doi: 10.3354/meps09054

van Katwijk, M. M., Vergeer, L. H. T., Schmitz, G. H. W., and Roelofd, J. G. M. (1997). Ammonium toxicity in eelgrass *Zostera marina*. *Mar. Ecol. Prog. Series* 157, 159–173. doi: 10.3354/meps157159

van Lent, F., Verschuure, J. M., and van Veghel, M. L. J. (1995). Comparative study on population of *Zostera marina* l. (eelgrass): *in situ* nitrogen enrichment and light manipulation. *J. Exp. Mar. Biol. Ecology* 185, 55–76. doi: 10.1016/0022-0981(94)00131-V

Villazán, B., Pedersen, M. F., Brun, F. G., and Vergara, J. J. (2013). Elevated ammonium concentrations and low light from a dangerous synergy for eelgrass *Zostera marina*. *Mar. Ecol. Prog. Series* 493, 141–154. doi: 10.3354/meps10517

Vonk, J. A., Middelburg, J. J., Stapel, J., and Bouma, T. J. (2008). Dissolved organic nitrogen uptake by seagrasses. *Limnology Oceanography* 53, 542–548. doi: 10.4319/lo.2008.53.2.0542

Walker, D. I., and McComb, A. J. (1992). Seagrass degradation in Australian coastal waters. *Mar. pollut. Bulletin* 25, 191–195. doi: 10.1016/0025-326X(92)90224-T

Wang, X. J. (2015). *Effects of urea on the growth of typical algae in East China Sea* (Qingdao, China: Master Thesis in University of Ocean University of China).

Wang, X., Chen, R. F., Cable, J. E., and Cherrier, J. (2014). Leaching and microbial degradation of dissolved organic matter from salt marsh plants and seagrasses. *Aquat. Sci.* 76, 595–609. doi: 10.1007/s00027-014-0357-4

Xie, X. J., Lu, X. P., Wang, L. P., He, L. W., and Wang, G. C. (2020). High light intensity increases the concentrations of β-carotene and zeaxanthin in marine red macroalgae. *Algae Res.* 47, 101852. doi: 10.1016/j.algal.2020.101852

Xu, R. S. (2020). *Effects of different of nitrogen sources on the growth and biochemical components of monostroma nitidium gametophytes* (Zhanjiang, China: Master Thesis in University of Guangdong Ocean University).

Zhang, T., and Wang, X. (2017). Release and microbial degradation of dissolved organic matter (DOM) from the macroalgae. *Ulva prolifera Mar. pollut. Bulletin* 125, 192–198. doi: 10.1016/j.marpolbul.2017.08.029

Zhang, P. Y., Xin, Y., Zhong, X. S., Yan, Z. W., Jin, Y. M., Yan, M. J., et al. (2021). Integrated effects of *Ulva prolifera* bloom and decay on nutrients inventory and cycling in marginal sea of China. *Chemosphere* 264, 128389. doi: 10.1016/j.chemosphere.2020.128389

Zhang, X., Zhou, Y., Adams, M. P., Wang, F., Xu, S. C., Wang, P. M., et al. (2020). Plant morphology and seed germination responses of seagrass (*Zostera japonica*) to water depth and light availability in ailian bay, northern China. *Mar. Environ. Res.* 162, 105082. doi: 10.1016/j.marenvres.2020.105082

Zhang, X. M., Zhou, Y., Liu, P., Wang, F., Lui, B. J., Liu, X. J., et al. (2014). Temporal pattern in the bloom-forming macroalgae *Chaetomorpha linum* and *Ulva pertusa* in seagrass beds, swan lake lagoon, north China. *Mar. pollut. Bulletin* 89, 229–238. doi: 10.1016/j.marpolbul.2014.09.054

Zimmerman, R. C., Smith, R. D., and Alberte, R. S. (1987). Is growth of eelgrass nitrogen limited? a numerical simulation of the effects of light and nitrogen on the growth dynamics of *Zostera marina*. *Mar. Ecol. Prog. Series* 41, 167–176. doi: 10.3354/meps041167

frontiers | Frontiers in Marine Science

TYPE Original Research
PUBLISHED 09 February 2023
DOI 10.3389/fmars.2023.1096896

OPEN ACCESS

EDITED BY
Lin Hui,
Ministry of Natural Resources, China

REVIEWED BY
Yang Ding,
Ocean University of China, China
Marta Rodrigues,
National Laboratory for Civil Engineering, Portugal

*CORRESPONDENCE
Guangjun Xu
gjxu_gdou@yeah.net
Dazhao Liu
lddz@163.com

SPECIALTY SECTION
This article was submitted to Coastal Ocean Processes, a section of the journal Frontiers in Marine Science

RECEIVED 12 November 2022
ACCEPTED 27 January 2023
PUBLISHED 09 February 2023

CITATION
Xu Y, Sun Y, Xu G and Liu D (2023) Simulation of red tide drift-diffusion process in the Pearl River Estuary and its response to the environment. *Front. Mar. Sci.* 10:1096896. doi: 10.3389/fmars.2023.1096896

Simulation of red tide drift-diffusion process in the Pearl River Estuary and its response to the environment

Yuanxing Xu[1], Yan Sun[2], Guangjun Xu[1,3]* and Dazhao Liu[1,4]*

[1]College of Electronic and Information Engineering, Guangdong Ocean University, Zhanjiang, China, [2]College of Chemistry and Environment, Guangdong Ocean University, Zhanjiang, China, [3]Southern Marine Science and Engineering Guangdong Laboratory (Zhuhai), Zhuhai, China, [4]Guangdong Engineering Technology Research Center for Ocean Remote Sensing and Information Technology, Zhanjiang, China

A particle tracking model for the Lingdingyang Bay of the Pearl River Estuary (PRE) was established based on the Delft3D model. The model was initialized with remote sensing images to simulate the red tide drift-diffusion process in this sea area in the autumn of 2020 and analyze its response to tides, winds and runoffs. The results show that this red tide occurred in the central sea area of the Lingdingyang Bay. The red tide drifted south with the ebb tide and north with flood tide. The red tide spread northward to the waters near Humen and southward to the western waters of Zhuhai. Through the control variable experiments, it is found that the red tide drift-diffusion process was mainly affected by tide and wind, with minimal influence from runoff. The tide expanded the scope of red tide diffusion, and the wind further changed the distribution of red tide. Under the influence of the northeast wind, the red tide gathered on both sides of Lingdingyang Bay. Comparison with the red tide drift-diffusion process in the sea area near Shenzhen Airport shows that the red tide near Neilingding Island easily diffused toward surrounding waters.

KEYWORDS

red tide, drift-diffusion process, Lingdingyang Bay, Delft3D, particle tracking

1 Introduction

Red tide is a marine ecological anomaly where some microalgae, protozoans, or bacteria proliferate explosively or accumulate to a particular level under certain environmental conditions, resulting in water color changes or causing harm to other marine organisms (Liu et al., 2013; Zohdi and Abbaspour, 2019). Red tide outbreak is characterized by sudden and quick development. It is hard to timely and accurately monitor a red tide outbreak using traditional red tide monitoring methods, such as ship-based sea investigation and onshore artificial observation.

Satellite remote sensing characterizes all-day, all-weather and global observation. It gives us high-frequency, regular, long-term, near-real-time, and rapid access to multi-scale and

multi-element information about the global ocean. Independent of geographical location and artificial conditions, satellite remote sensing has been widely used to analyze the temporal and spatial distribution of red tides. Chen et al. (2021) studied the occurrence and extinction characteristics of mixed dinoflagellate red tide in the sea area near Dongtou and Nanji Islands, southern Zhejiang, based on field investigation and the satellite Aqua data from Moderate Resolution Imaging Spectro Radiometer (MODIS). To carry out red tide monitoring, Li et al. (2020a) obtained total suspended matter concentration and red tide index through an inversion method based on remote sensing reflectance data from the Geo-stationary Ocean Color Imager (GOCI) data. Liu et al. (2022) used the high spatial resolution broad band optical satellite data from Chinese satellites GF-1 Wide Field of View (WFV), Haiyang 1D (HY-1D) Coastal Zone Imager (CZI), Sentinel-2 Multi-Spectral Instrument (MSI) and Landsat 8 Operational Land Imager (OLI) to detect fine-scale red tide. In addition, Unmanned Aerial Vehicle (UAV) images can also be used for red tide identification (Cheng et al., 2020; Li et al., 2022).

Satellite remote sensing has an evident advantage in red tide monitoring. However, as a tool that periodically obtains marine element information, satellite remote sensing cannot reflect the quick dynamic change process of the elements. In addition, optical sensors are limited by cloud-covered areas or bad weather, which will lead to the loss of some data. All of these are not conducive for red tide research. However, numerical simulation can make up for the deficiency of satellite remote sensing and field measured data, and fully reproduce the distribution of algae in waters, which is conducive to further explaining the physical processes and mechanisms related to red tide. More and more researchers have used physical models or coupled physical-ecosystem models to simulate the distribution of algae in different water environments indirectly or directly, analyzing their outbreak and maintenance mechanism, drift and diffusion, source and driving force in coastal oceans, bays, estuaries, lakes and other waters. Many researchers used particle tracking models to simulate the movement of red tide in coastal waters. Kuang et al. (2016) and Qin et al. (2017) tracked the red tide drift-diffusion using Fractional Brownian Motion (FBM) particle tracking method. Without considering the process of algae generation and extinction, Soto et al. (2018) and Nogueira et al. (2022) used Lagrangian particle tracking model to explore the bloom dynamics in coastal water. Zhang et al. (2021) used the Lagrangian particle tracking model combined with the biological characteristics to analyze the distribution of alien phytoplankton.

Some researchers established hydrodynamic models to study red tide. Qu et al. (2019) established a hydrodynamic model to simulate the freshwater path of the Yangtze River and explored the hydrodynamic mechanism of summer red tide outbreak in the waters near the Yangtze River Estuary. Weisberg et al. (2019) explained the source and transport mechanism of the red tide on the West Florida continental shelf in 2018 by combining the measured data and the circulation numerical model. Based on the remote sensing image of red tide, Zhao and Ghedira (2014) used the results of the Hybrid Coordinate Ocean Model (HYCOM) and retrieval of sea surface temperature data from remote sensing to prove that the Arabian gulf red tide broke out offshore in 2008-2009 and was transported to the nearshore through the bottom Ekman layer advection.

The coupled bio-physical models were used to study the germination, initiation, and development of red tide. Considering the physiological processes and physical activities of algae such as growth, death and their movement, Li et al. (2009) established a bio-physical model based on *in-situ* observations and Regional Ocean Modeling System (ROMS), to reproduce the hydrodynamics and the temporal and spatial distributions of cell concentration. Hayashi and Yanagi (2008) used an ecological model to analyze the changes in material cycle in the Yodo River Estuary of Japan and clarify the reasons for the changes in red tide species.

According to the Guangdong Marine Disasters Bulletin (Department of Natural Resources of Guangdong Province, 2013-2020), 16 red tide events occurred in the PRE sea area during 2013–2020, including seven events occurring in the Zhuhai sea area and nine occurring in the Shenzhen sea area. The main marine organisms causing the red tides included *Noctiluca scientillans* (4 events), *Akashiwo sanguinea* (3 events), *Heterosigma akashiwo* (4 events), *Cochlodinium geminatum* (4 events), and *Skeletonema costatum* (1 event), among which *Heterosigma akashiwo* and *Cochlodinium geminatum* are poisonous species. In addition, the *Heterosigma akashiwo* red tides occurred in spring and the *Cochlodinium geminatum* red tides in autumn. The outbreak of red tide is regional and seasonal, and the species of red tide algae are diverse. Red tide disasters statistics from the Guangdong Marine Disasters Bulletin 2020 show that in 2020, red tide occurred six times in total in the coastal waters of Guangdong Province, including four times in total recorded in the sea areas of the PRE. Both times the red tide impact areas were smaller compared to the previous five years. It is essential to pay more attention to red tide disasters and develop adequate red tide monitoring technologies for the Guangdong-Hong Kong-Macao Great Bay Area construction. In recent years, the red tide research in the PRE mainly focuses on the large-scale temporal and spatial distribution and the analysis of water environment characteristics during the red tide, lacking high-precision dynamic research (Lu and Gan, 2015; Li et al., 2019; Tian et al., 2020). Therefore, this paper establishes a red tide drift-diffusion model based on the remote sensing images obtained by the HY-1C and HY-1D satellites. The *Cochlodinium geminatum* red tide outbreak in the PRE in the autumn of 2020 is used as a case to analyze the temporal and spatial distribution characteristics of the red tide process, and explore its response to the environment, thus providing a solid reference for monitoring and forecasting red tides.

2 Data and methods

2.1 Study area

This study is conducted over the Lingdingyang Bay of the PRE, located in the middle and south of Guangdong Province and the north of the South China Sea. The estuary area is about 1900 km^2. The length from the estuary to the open shelf is about 60 km and the width is 10-60 km. Its bathymetry is complicated, and is characterized by two channels and three shoals. The runoff from the Pearl River, with large seasonal variations, flows into the Lingdingyang Bay through four estuaries at Humen, Jiaomen, Hongqili and Hengmen (Figure 1). The flood season from April to September accounts for 80% of the annual runoff. The tides at the PRE are irregular semi-diurnal tides, with a mean tidal range of less than 2 m and a maximum tidal range of up to 3 m. The PRE is located in a subtropical monsoon climate region, where the summer southwest monsoon occurs from May to

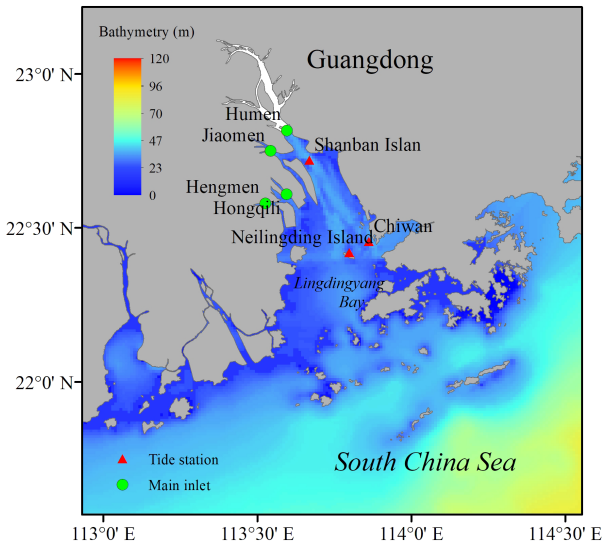

FIGURE 1
Study area and its bathymetric features.

August and the winter northeast monsoon occurs from October to March. April and September are transition months. The transition process from winter to summer monsoon is rapid, while the transition from summer to winter monsoon is slow.

With the construction of the Guangdong-Hong Kong-Macao Great Bay Area, the rapid development of industry and the continuous increase of population, pollutants from various sources enter the waters of the PRE through runoff, direct coastal discharge and atmospheric dry and wet deposition, which makes the water quality of the estuary deteriorate and water eutrophication. According to the 2020 offshore water quality monitoring information of Guangdong (Department of Ecology and Environment of Guangdong Province, http://gdee.gd.gov.cn/), dissolved inorganic nitrogen (DIN) and reactive phosphate exceeded the standard in most waters of the PRE in spring, summer and autumn, providing certain material conditions for the outbreak of red tide.

2.2 Remote sensing and processing

The coastal zone imagers (CZI) carried by Haiyang-1 C/D satellites (HY-1C/HY-1D) can identify red tides well. Since their launch, the satellites have detected red tides in areas such as the Liaodong Bay of the Bohai Sea, the Tianjin Binhai New Area of the East China Sea, and the Shenzhen sea area of the PRE (Liu et al., 2020). These satellites have become powerful tools for marine ecological environment monitoring. We use the HY-1C/HY-1D Rayleigh-corrected products to identify the red tide.

2.3 Numerical simulation

The Delft3D modeling system developed by Deltares, including Delft3D-FLOW (the hydrodynamic module), Delft3D-WAVE (the wave module), D-Water Quality (the far-field water quality module), D-WAQ PART (the mid-field water quality and particle tracking module), Delft3D-ECO (the ecological modeling module) and Delft3D-SED (the cohesive and non-cohesive sediment transport module), is capable of simulating flows, sediment transports, waves, water quality, morphological developments and ecology in coastal waters, rivers, estuaries and lakes (Deltares, 2018a).

Hydrodynamic flow is simulated with the FLOW module, which solves the unsteady shallow water equations in two (depth-averaged) or three dimensions (Deltares, 2018a). Many studies have shown that Delft3D has been shown to be robust and accurate in predicting near-shore flows (Chu, 2019; Seiler et al., 2020; Lapietra et al., 2022). D-WAQ PART is a random walk particle tracking model suitable for research application in a moderate scale range (200-15000m). It calculates the dynamic concentration distribution by tracking the paths of thousands of particles over time (Deltares, 2018b). The model can simulate salts, petroleum, temperature, and other conservative or simple decaying substances (Bigdeli et al., 2022; Li et al., 2022). In our research, simulation experiments of the hydrodynamic environment in the Lingdingyang Bay sea area of the PRE are carried out with the Delft3D-FLOW and the simulation of red tide drift-diffusion is conducted by coupling the D-WAQ PART.

2.4 Model establishment

2.4.1 Hydrodynamic numerical model

Three-dimensional tidal current models for the Lingdingyang Bay sea area of the PRE are established with nested. The outer domain covers the PRE and some waters outside the PRE (20.5°-23° N and 112.5°-115.5° E), with grids of 9225 and grid resolution of 700-5700 m (Figure 2A). The nested domain covers the Lingdingyang Bay (22° 10′-22°50′ N and 113°30′-114° E), with grids of 31009 and resolution of 200-500 m (Figure 2B). The bathymetry data is obtained from ETOPO1. In addition, the water depth data of Lingdingyang Bay is corrected with the high-accuracy electronic nautical chart drawn by

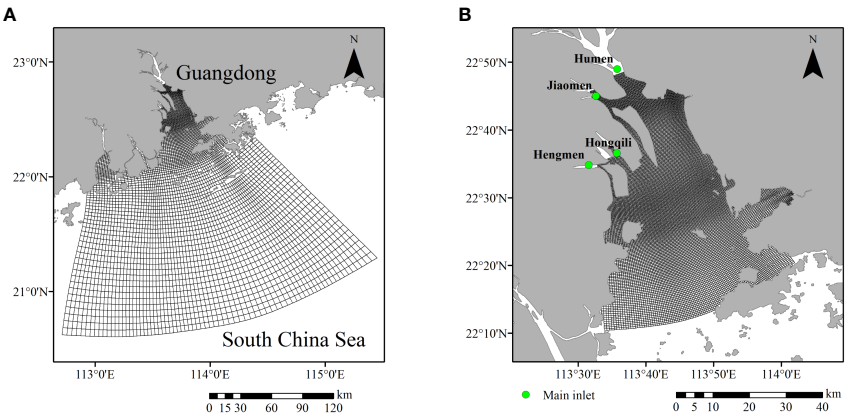

FIGURE 2
Model grids of **(A)** the PRE and some open waters; and **(B)** Lingdingyang Bay.

the China Navy Hydrographic Office. The tidal forcing is added to the open boundaries and imposed on the elevation and the barotropic velocities in the outer domain. It is derived from the harmonic constants of 8 main tidal components (M2, N2, S2, K2, K1, P1, O1, Q1) provided in the global tide model established by the Oregon State University (Egbert and Erofeeva, 2002). The river discharge boundaries include the estuaries at Humen, Jiaomen, Hongqili, and Hengmen. Owing to the lack of observed data at each outlet, the daily discharge data recorded at the Sanshui, Makou and Boluo gauge stations (https://zjhy.mot.gov.cn/zhuhangsj/) can be used to obtain appropriate river discharge boundaries. The total runoff data of each station in wet season: Humen accounts for 12.1%, Jiaomen accounts for 14%, Hongqili accounts for 13.2%, Hengmen accounts for 16.2%, and Modaomen accounts for 29.6% (Zhang and Li, 2010). However, because the river discharge boundaries in the model are located in the tidal reach, they are greatly affected by the tide in the dry season. The boundary flow rate at the cross-section of every outlet during dry season is replaced with the product of tidal current speed and cross-section area according to the model setting situations (Table 1). The nested interpolated values on the open boundary of the nested domain are from the water level data of the outer domain. The wind speed and direction are based on the daily meteorological data of Hong Kong International Airport released by the Hong Kong Observatory (https://www.hko.gov.hk/sc/index.html). Referring to relevant literature and calibration, the manning coefficient (0.016-0.02) is used as the roughness coefficient to calculate the bottom roughness. The eddy viscosity coefficient is set to 10 m^2/s and 1 m^2/s in the outer domain and nested domain, respectively (Deltares, 2008). The time step is 10 and 5 minutes in the outer domain and nested domain, respectively. A cold start is used for the model and the simulation period is from September 1, 2020 to December 1, 2020.

TABLE 1 Discharge at the eight outlets.

River outlet	Wet season(m^3/s)	Dry season(m^3/s)
Humen	1496	542
Jiaomen	1731	77
Hongqili	1632	43
Hengmen	2003	111

The runoff of the Pearl River decreases greatly in the dry season, and most of the water columns in the PRE are fully mixed (Lu and Gan, 2015). There is almost no salinity stratification in most areas, which results in weak barotropic flow. Therefore, the baroclinic effect driven by salinity is not considered in the models (Wang, 2014).

2.4.2 Particle tracking model

The particle drift-diffusion process is simulated with the PART particle tracking module, based on hydrodynamics simulation in the FLOW module, with the red tide drift-diffusion regarded as surface-layer water mass point motion (Li et al., 2022). The locations of particle release in the model (Figure 3B) are determined according to the red tide distribution captured by the HY-1C satellite (Figure 3A). Zone 1: sea area near Shenzhen Airport at the PRE; and Zone 2: sea area near the northwest of the Neilingding Island. Fifty-two instantaneous release points are set to represent red tides, with each point releasing 10,000 particles. The instantaneous release time is October 26, 2020, 04:00 (UTC+8:00). The simulation period is from October 25, 2020 to November 6, 2020. In this study, control variable experiments are used to compare the red tide drift-diffusion situations under different dynamic conditions (Table 2).

3 Results

3.1 Model validation

3.1.1 Hydrodynamic simulation validation

This paper uses the water level provided by the Guangzhou Port Authority (https://gwj.gz.gov.cn/) to validate the model's accuracy. The tide stations are located on Shanban Island, Neilingding Island, and Chiwan. As shown in Figure 4, the simulation results accurately reproduce the tide level variation of the PRE. The mean absolute error (MAE) and the root mean square error (RMSE) between the measurements and the simulations were computed for all three tide stations, to evaluate the goodness of fit of the numerical model. The

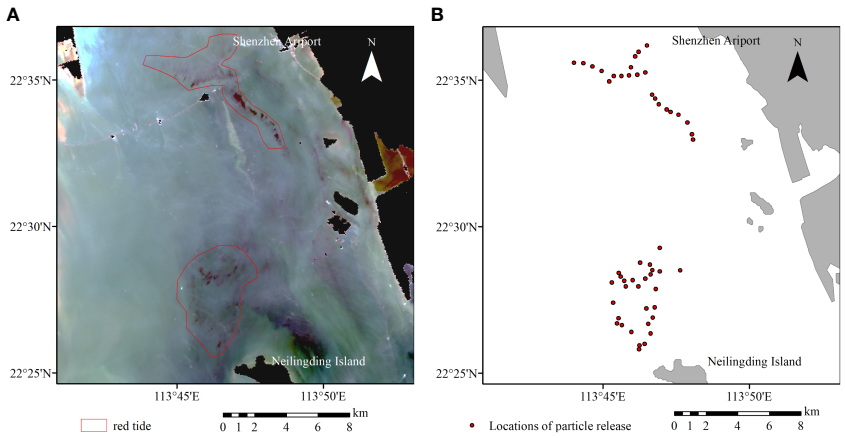

FIGURE 3
(A) True color composite image from the HY-1C satellite on 26 October, 2020. The red lines delineate areas where red tides occurred; **(B)** Locations of particle release in the model on 26 October, 2020. 10,000 particles are released at each point to represent the cloud particles of red tides.

MAE of water level of Shanban Island is 0.21 m and the RMSE is 0.23 m. The MAE of water level of Neilingding Island is 0.16 m and the RMSE is 0.19 m. The MAE of water level of Chiwan is 0.17 m and the RMSE is 0.21 m. The error is acceptable. In addition, the statistical method proposed by Willmott (1981) was adopted to evaluate the model simulation results. Model skill was calculated as follows:

$$Skill = 1 - \frac{\sum |X_{mod\,el} - X_{obs}|^2}{\sum (|X_{mod\,el} - \bar{X}_{obs}| + |X_{obs} - \bar{X}_{obs}|)^2} \quad (1)$$

The skill value represents the deviation between the measured value and the calculated value. The range of skill value is between 0 and 1. When skill is 1, the calculated value is completely consistent with the measured value. When skill is greater than 0.65, the calculated result of the model is excellent. When skill is between 0.65 and 0.5, the calculated result of the model is very good. When skill is between 0.5 and 0.2, the calculated result of the model is good. When skill is less than 0.2, the calculated result of the model is poor. The skill decreased toward zero as model diverged from observations. In general, the hydrodynamic model can be used for particle diffusion analysis (Table 3).

3.1.2 Comparison between particle drift-diffusion distribution and satellite observation

Figure 5A is true color composite image from the HY-1C satellites. The red lines show the red tide distribution (reddish-brown ribbons). The red tide drifted and diffused to the north and middle of Lingdingyang Bay at 3:25 on November 1. To assess the particle tracking model, the particle diffusion results at the corresponding time is extracted from the model. As shown in Figure 5A, the red tide distribution area contains 568 grids, while the simulation results show that the high concentration particles are mainly concentrated in the red tide distribution area, including 544 grids (Figure 5B). It can be seen that the simulated particle distribution is consistent with the observed red tide distribution. This also indicates that the model's flow field simulation is good. That is, the particle tracking model established relatively accurately simulates the red tide drift-diffusion process in Lingdingyang Bay in the autumn of 2020.

TABLE 2 List of experiments.

Experiment	Description	Tide	Runoff	Wind
1	Normal	✓	✓	✓
2	No tide		✓	✓
3	No runoff	✓		✓
4	No wind	✓	✓	

✓ means choosing some kind of force to drive the model.

3.2 Red tide drift-diffusion process

The features of red tide drift-diffusion are analyzed by extracting the particles cloud distribution at different time points within one tidal period, coupled with water level variation during red tide (Figure 6) from the particle tracking model.

Based on the remote sensing data, the instantaneous particle release time for the model was October 26, 2020, 04:00. The red tide started when Lingdingyang Bay was in a flood tide stage. During ebb tide (October 26, 6:00-14:00), the red tide moved southward. The red tide in the sea area near Shenzhen Airport moved southward to the sea area near the west of the Dachan Bay mouth. The red tide in the sea area near the northwest of Neilingding Island moved southward to the sea area near the west of the island, and part of the red tide moved to the sea area 11.3 km away from the island (Figures 7A, B). In the flood tide stage (October 26, 14:00-21:00), the red tide moved northward. The red tide in the sea area near Shenzhen Airport drifted away from the sea area west of the Dachan Bay mouth. The red tide in the sea area near the west and south of Neilingding Island moved northward to the sea area northwest of the island (Figure 7C).

From the particles cloud distribution (Figures 7D-F) at flood and ebb tides on November 1, it can be seen that the red tide moved

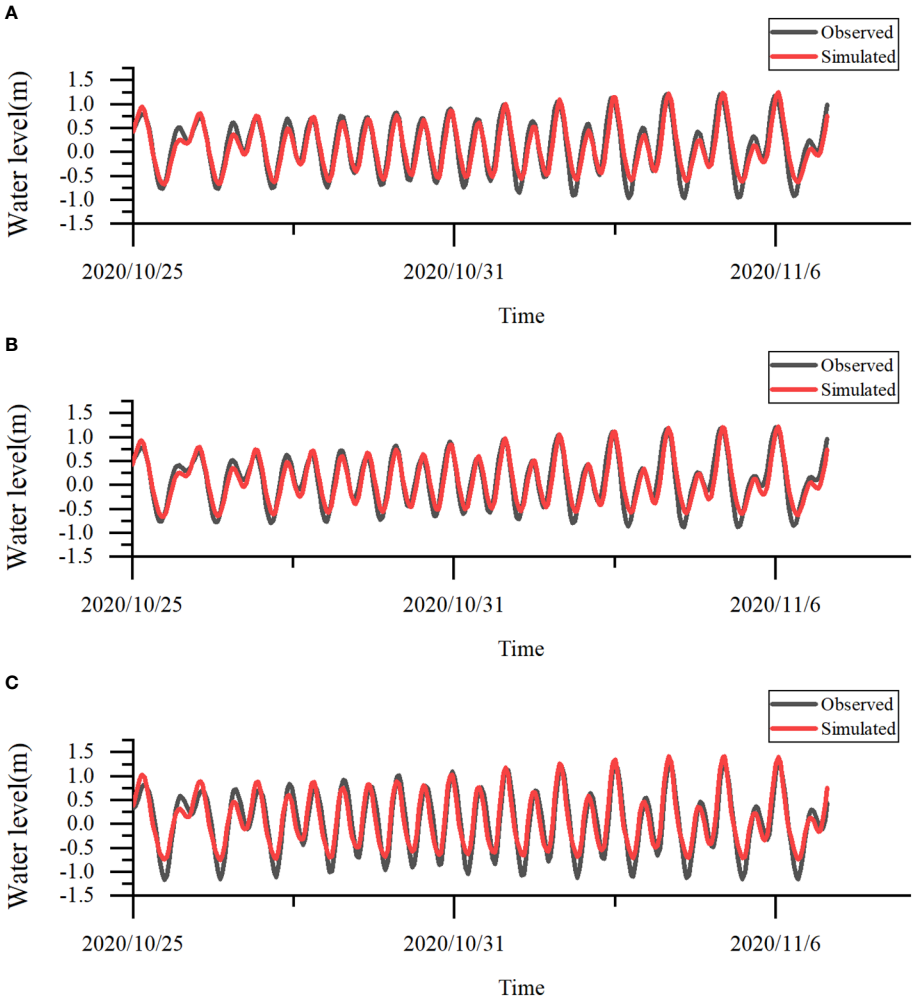

FIGURE 4
Water level validation at **(A)** Shanban Island; **(B)** Neilingding Island; and **(C)** Chiwan.

southward and northward under the effects of tides. Comparison with the particles cloud distribution on October 26 shows that the red tide in different zones merged into a large patch which was concentrated in the middle of Lingdingyang Bay. The red tide moved northward to the junction of Jiaomen and Humen and moved southward to the sea area near Zhuhai.

3.3 Red tide drift-diffusion control variable experiments

It can be seen from the distribution of particles cloud during a whole tidal period (Figures 7A-C), that the red tide moved north during flood tide and moved south during ebb tide. To discuss the influence of tides on the drift-diffusion of red tide, the distribution of particles cloud without tidal forcing was simulated by experiment 2. Compared with the no tide situation, it can be seen that under the influence of current, particles were distributed in a large area in the middle and south of Lingdingyang Bay (positive value) (Figure 8A). To better illustrate the spatial movement of the particles, the centers of mass of the concentration field in both experiment 1 results and experiment 2 results were derived to represent the movement of the patchy distribution of particles. Without tidal current, the particles moved northward and concentrated in the sea area north of Neilingding Island.

Although the runoff into the sea decreases greatly in the dry season, its impact on the flow field of Lingdingyang Bay can't be ignored. To further explore the influence of runoff on the red tide drift-diffusion process, we simulated the red tide diffusion without runoff input. It can be found that the center of mass shifted northward when there was no runoff input. More particles spread northward to Humen (negative value)(Figure 8B).

The PRE is located in the subtropical monsoon region, which is obviously affected by the monsoon. This study explores the impact of winds on the drift-diffusion of red tide through experiment 4. Comparing the red tide distribution from no wind, it can be seen

TABLE 3 Skill scores from comparison of model with observations.

Station	Skill score
Shanban Island	0.96
Neilingding Island	0.96
Chiwan	0.96

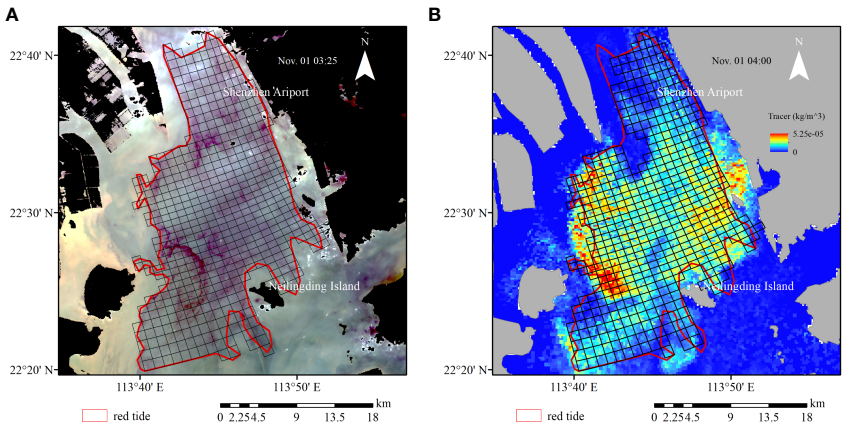

FIGURE 5
(A) True color composite image from the HY-1C satellite on 1 November. **(B)** Particle diffusion results on November 1.

that high concentration particles gathered on both sides of Lingdingyang Bay (positive value) (Figure 8C).

4 Discussion

4.1 Influence of environments on red tide drift-diffusion process

The flow fields of the flood tide and ebb tide in Lingdingyang Bay during red tide are extracted respectively, and the influence of tidal current on the drift-diffusion of red tide is analyzed. On the whole, the tidal current flowed northward from open waters to the estuary during flood tide. The tidal current mainly flowed northward along the deep trough in the Lingdingyang Bay and a part of the tidal current moved northeastward along Lantau Island into the sea area near Hong Kong Island. A part of the northward moving tidal current flowed northwestward along Qi'ao Island, and another part moved northeastward along Neilingding Island (Figure 9A). During ebb tide, the direction of the tidal current was opposite to that during flood tide. When the tidal current flowed through Qi'ao Island and Neilingding Island, part of the tidal current moved southwestward along Qi'ao Island and then flowed southward. Another part of the tidal current moved southeastward along Neilingding Island and then flowed southward (Figure 9B), owing to the effects of the shape and topography of the islands. The simulated tidal current agrees with previous researchers' results (Ding et al., 2015; Fang and Liu, 2020; Wang, 2020). The tidal current resulted in a south-north reciprocating motion of the red tide (Figure 7). The tidal current near Qi'ao Island and Neilingding Island included an east-west component in addition to the south-north component, so the red tide northwest of Neilingding Island would move to the surrounding sea areas with flood and ebb tides. It can be seen from the flow speed distribution that the flow speed south of Neilingding Island was greater than that north of the island. Therefore, this red tide had little impact on the upstream area.

From October to November, Lingdingyang Bay is dominated by northeast wind, followed by easterly wind and northerly wind (Figure 10A). The wind-driven current in Lingdingyang Bay during the red tide period is obtained through model. As shown in Figure 10B, there is northeast wind-driven current in the west coast. When the wind-driven current flows through Qi'ao Island, it turns northwest and then northeast. In the deep trough area in the middle of Lingdingyang, the wind driven current is mainly northward, and then turns to northwest near the coast of Shenzhen. Relevant research shows that wind forcing is an important factor in

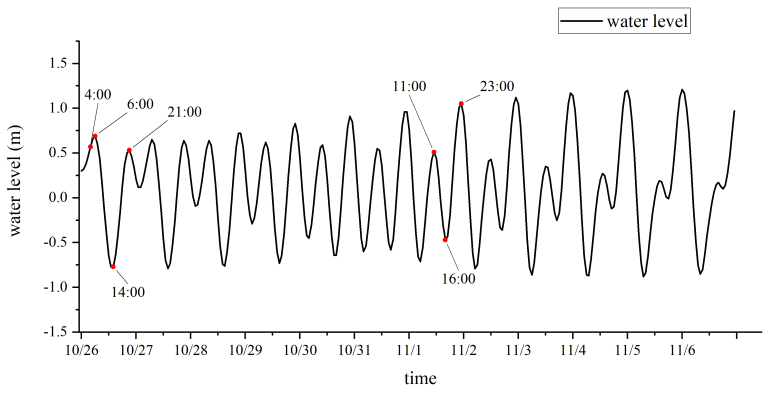

FIGURE 6
Water level variations during red tide.

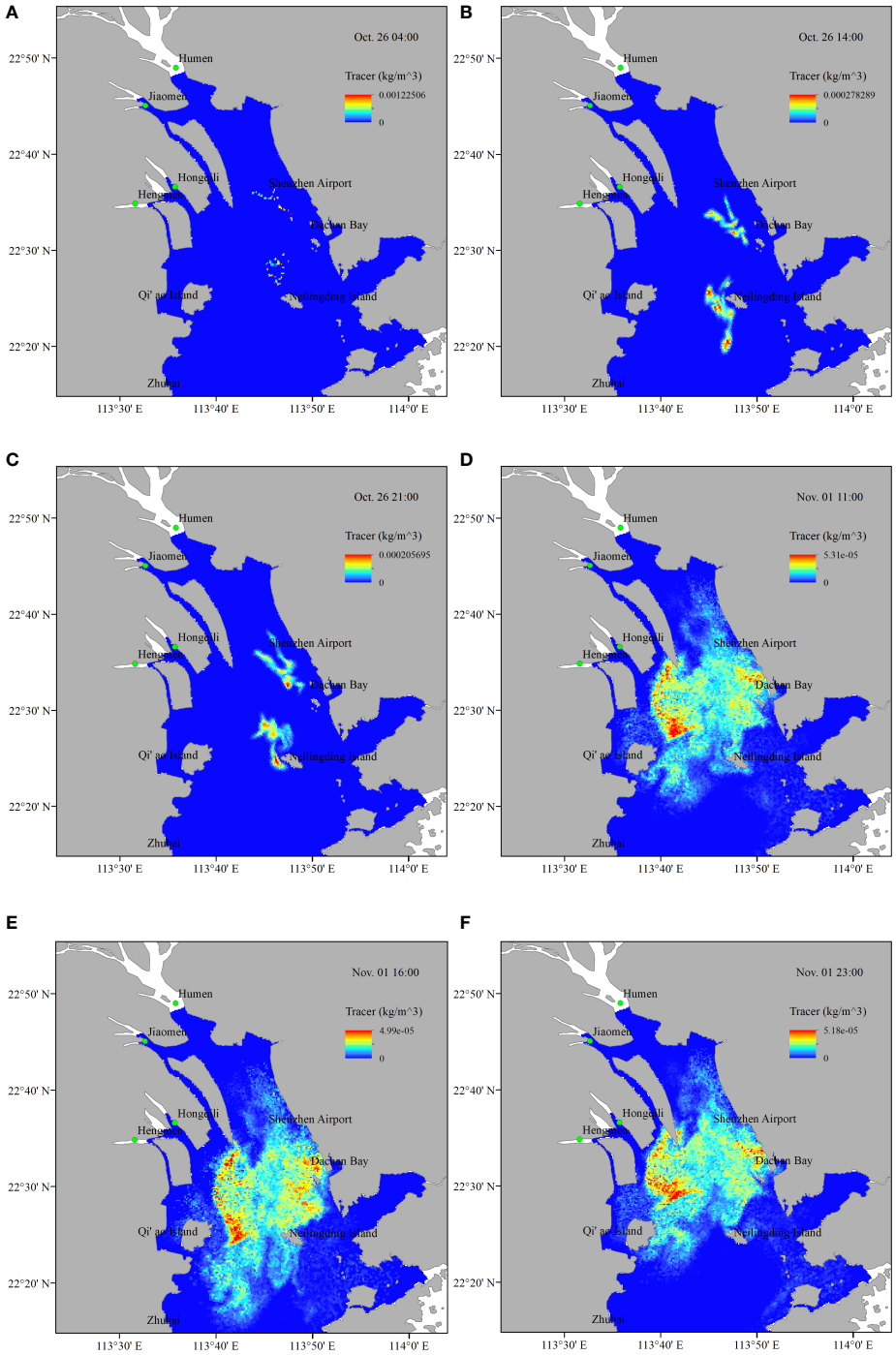

FIGURE 7
Particles cloud distribution results on **(A)** October 26, 04:00; **(B)** October 26, 14:00; **(C)** October 26, 21:00; **(D)** November 1, 11:00; **(E)** November 1, 16:00; and **(F)** November 1, 23:00.

transporting algae cells onshore (Li et al., 2020b). Our research also show that the red tide keeps aggregating along the coast under the influence of the northeast wind. High concentration particles are mainly located along the coast of Shenzhen and the central and western coast of Lingdingyang Bay (Figure 8C).

The runoff-induced residual current at Lingdingyang Bay caused by runoff was calculated by the model. It can be seen that there was relatively weak southward run-off-induced residual current, and the velocity was the strongest at the four outlets and deep trough (Figure 11). The runoff at the PRE flows southward from the estuary to open waters, and it hinders the northward tidal current from the open waters during the flood tide stage. So, the runoff limits the northward drift of red tide.

Moreover, two experiments were conducted to explore the regional differences in red tide drift-diffusion. The simulations show that the red tide in the sea area near Shenzhen Airport mainly moved northward for a short distance (Figure 12A), whereas the red tide near Neilingding Island moved to the surrounding waters and drifted

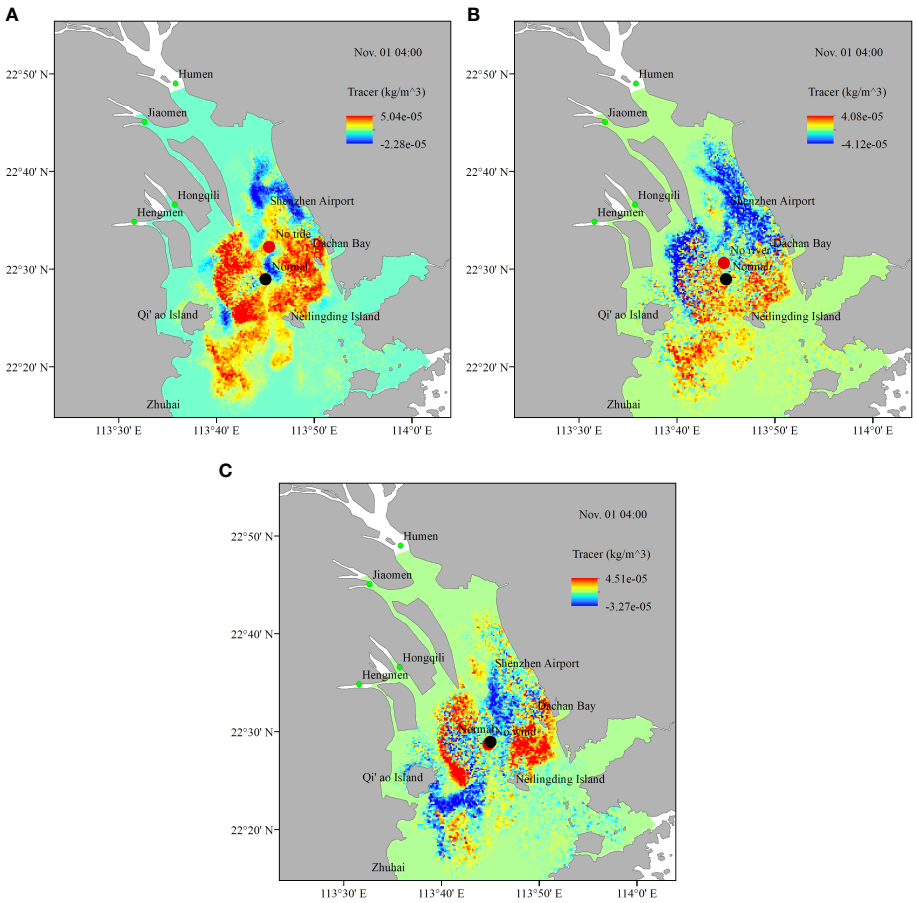

FIGURE 8
The relative differences in the particles cloud distribution between the experiments. **(A)** Experiment 1 (Normal) and 2 (No tide); **(B)** Experiment 1 (Normal) and 3 (No runoff); **(C)** Experiment 1 (Normal) and 4 (No wind).

northeastward, merging with the red tide in the sea area near Shenzhen Airport (Figure 12B). This indicates that the influence range of the red tide outbreak near Neilingding Island is larger than that of the red tide outbreak in the sea area near Shenzhen Airport. In terms of particles concentration, in the process of particles drift-diffusion in the sea area near Neilingding Island, the particles moved westward obviously, while in the process of particles drift-diffusion in the sea area near Shenzhen airport, the particles moved eastward.

Neilingding Island is located in the middle of Lingdingyang Bay, close to the downstream of the estuary. It can be seen from the flow

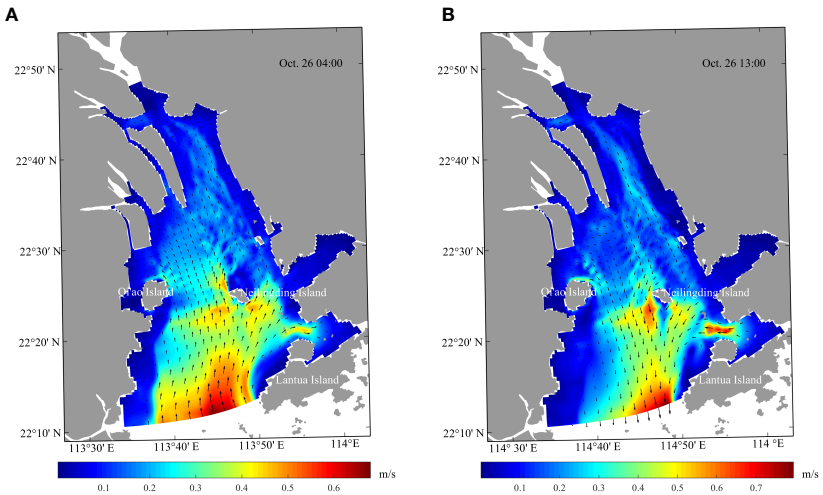

FIGURE 9
Simulated flow fields during **(A)** flood tide; and **(B)** ebb tide.

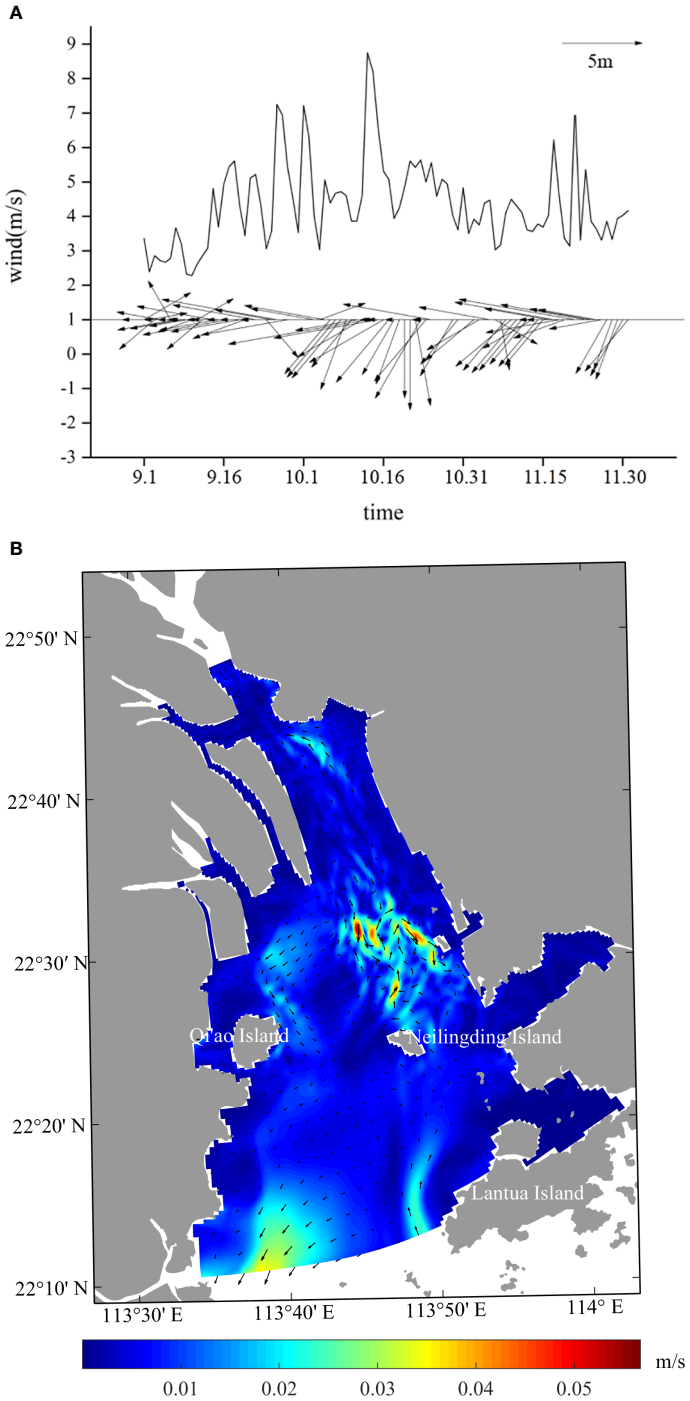

FIGURE 10
(A) Wind condition from Hong Kong International Airport meteorological station over the PRE; **(B)** Wind-induced current.

fields that the sea area here was greatly affected by the tidal current, and the velocity was relatively strong, so the red tide had a large north-south drift-diffusion distance. In the sea area near Shenzhen Airport, the tidal current was relatively small, so the north-south drift-diffusion distance of the red tide was small (Figures 9A, B).

In the process of particles drift-diffusion in the sea area near Neilingding Island, the particles moved significantly to the west, because the sea area was mainly affected by northeast wind-induced current (Figure 10B). Owing to the northwest wind-driven current and runoff, in the process of particles drift-diffusion in the sea area near Shenzhen Airport, the particles moved southward.

4.2 Uncertainties of the model

4.2.1 The differences between the data and the hydrodynamic numerical model results

Due to the irregular shape and highly dynamic water environment of the Pearl River Estuary coastline, it is very

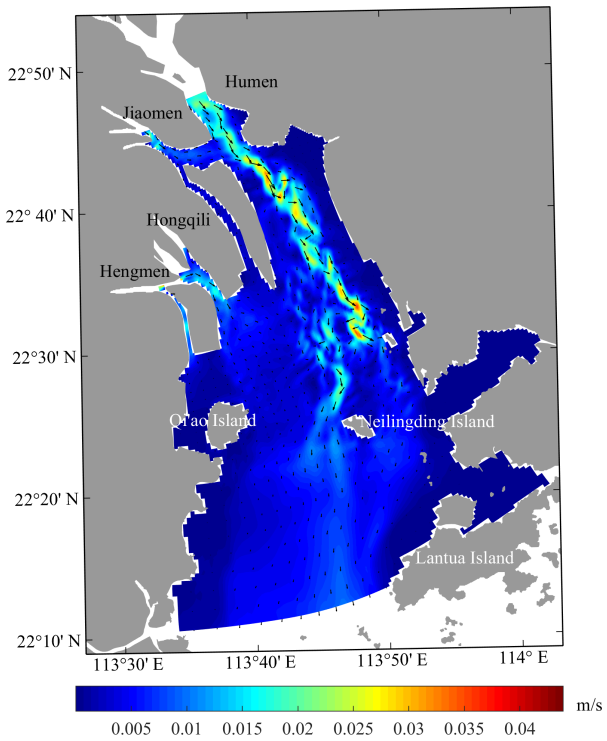

FIGURE 11
Runoff-induced residual current.

complicated to accurately simulate its hydrodynamics (Deltares, 2008). From the verification results, it can be seen that the closer the distance to the inner estuary, the greater the error. (Shanbanzhou Island > Chiwan > Nelingding Island)

There are differences between the location of the model station and the location of the tidal level station. The model reference coordinate system is Cartesian and the tide station is spherical.

The astronomical tidal component is used as the outer sea boundary condition rather than the measured water level, which is conducive to the use of prediction simulation, but the accuracy of simulation in the past period will be reduced (Deltares, 2008).

In addition, the model system errors (Hu, 2010) and the model parameter correction errors, such as roughness, may also lead to differences between simulated water level and observed data.

4.2.2 The differences between the data and the particle tracking model results

Due to the errors in hydrodynamic simulation, the particle simulation has errors. What's more, the red tide process is uncertain. The growth and death of red tide are not considered in the model. In fact, the red tide carries out complex physiological processes in a changing environment. Environmental factors such as

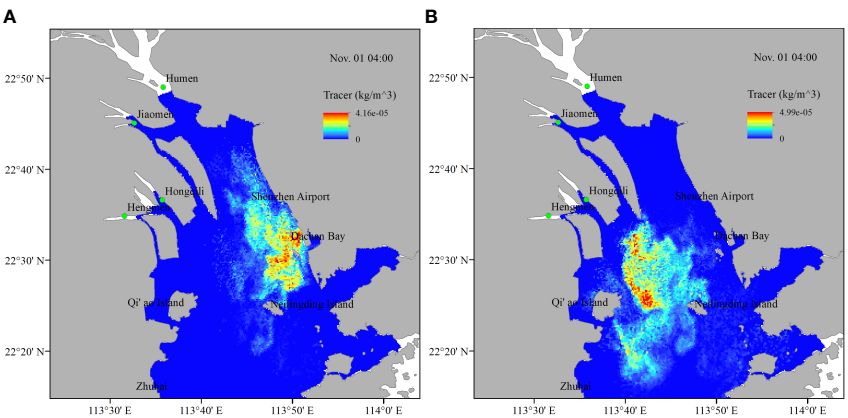

FIGURE 12
(A) Particles cloud distribution in sea area near Shenzhen Airport and **(B)** sea area near Neilingding Island.

light, nutrients, temperature, salinity, etc. will affect the red tide. The ignored physiological process of red tide results in the difference between the model results and the observation. In addition, the remote sensing observation is also uncertain. The red tide distribution data comes from remote sensing images. It is difficult to distinguish red tide in turbid water and cloud-covered areas.

4.3 Application of the model

Many scholars have successfully applied numerical simulation to the study of large-scale algal blooms. Based on the establishment of hydrodynamic model, through understanding the characteristics of different algae, a perfect physical and biological coupling algae model is gradually established to simulate its source, growth, movement, extinction and other processes. Based on the particle tracking models applied to large sea areas or harbors, such as the growth and drift model of the Yellow Sea green tide (Gao et al., 2021), the migration and diffusion model of the Qinhuangdao red tide (Kuang et al., 2016), the diffusion model of alien phytoplankton in the Bohai Bay (Zhang et al., 2021), and the Alexandrium catenella red tide in the Gulf of Maine (Li et al., 2020b), this study also used the particle tracking model to study the small-scale red tide that occurred in the PRE on the basis of ignoring the biological process. The model can well reproduce the development process of the red tide in the PRE, and can make up for the shortage of remote sensing data and measured data. Through the control variable experiments, we can more intuitively understand the effect of environmental factors on red tide. Red tide drifts and diffuses under the combined action of tide, wind and runoff. However, more complex water quality and ecological models are needed to study the accurate red tide process, including considering the effects of light, temperature, salinity and nutrients on the growth and death of algae (Zhou et al., 2021), and the vertical movement of algae (Qi et al., 2017).

5 Conclusions

The coupled Delft3D-FLOW particle tracking model for the Lingdingyang Bay sea area of the PRE can accurately simulate the red tide drift-diffusion process outbreak in the sea area near Shenzhen Airport and northeast of Neilingding Island in the autumn of 2020. Only the hydrodynamic process was considered in the model, without the red tide-related ecological process involved. So, the initial outbreak and extinction stage could not be simulated. However, through the combination of remote sensing data and numerical model, the existing simulation results have relatively accurately described the dynamic distribution of the red tide, which is conducive to further explaining the physical processes and mechanisms related to the drift-diffusion of the red tide.

The drivers influencing the red tide drift-diffusion were analyzed through multiple control variable experiments. The red tide drift-diffusion process was mainly influenced by tidal current and with minimal influence from runoff. What's more, the northeast wind makes the red tide aggregate along the coast.

Comparison with the red tide drift-diffusion process in the sea area near Shenzhen Airport shows that the red tide near Neilingding Island easily diffused toward surrounding waters, because of the strong tidal current, weak runoff in this vast sea area.

Data availability statement

The raw data supporting the conclusions of this article will be made available by the authors, without undue reservation.

Author contributions

YX: data analysis, writing and editing. YX and YS: figure plotting. DL and GX: conceptualization, methodology and reviewing. All authors contributed to the article and approved the submitted version.

Funding

This research is supported by the project supported by Southern Marine Science and Engineering Guangdong Laboratory (Zhuhai) (SML2020SP007), the Guangdong Basic and Applied Basic Research Foundation (2019A1515110840), and the Research Startup Foundation of Guangdong Ocean University (R20009).

Acknowledgments

The authors are thankful to the National Satellite Marine Application Center for making available the HY-1C/HY-1D satellite data and for the data support. The data can be downloaded at https://osdds.nsoas.org.cn.

Conflict of interest

The authors declare that the research was conducted in the absence of any commercial or financial relationships that could be construed as a potential conflict of interest.

Publisher's note

References

Bigdeli, M., Mohammadian, A., Pilechi, A., and Taheri, M. (2022). Lagrangian Modeling of marine microplastics fate and transport: The state of the science. *J. Mar. Sci. Eng.* 10 (4), 481. doi: 10.3390/jmse10040481

Cheng, K., Chan, S., and Lee, J. (2020). Remote sensing of coastal algal blooms using unmanned aerial vehicles (UAVs). *Mar. pollut. Bull.* 152, 110889. doi: 10.1016/j.marpolbul.2020.110889

Chen, L., Yang, M., Xu, Y., and Shen, A. ,. E. (2021). Occurrence of *Prorocentrum donghaiense* dominated bloom based on the field investigation and MODIS image study. *J. Appl. Oceanography* 40 (3), 447–462. doi: 10.3969/J.ISSN.2095-4972.2021.03.010

Chu, A. (2019). *Analysis and modelling of morphodynamics of the Yangtze estuary* (Deltares, The Netherlands: Master's thesis, Delft University of Technology). doi: 10.4233/uuid:068a1257-dfc2-4389-964e-f665aa5cb213

Deltares (2008). *Pearl river delta water quality model final report* (Environmental Protection Department of the Hong Kong Special Administrative Region: Deltares, The Netherlands).

Deltares (2018a). *Delft3D-FLOW simulation of multi-dimensional hydrodynamic flows and transport phenomena, including sediments user manual, version 3.15* (Deltares: The Netherlands).

Deltares (2018b). *Delft3D-PART simulation of mid-field water quality and oil spills, using particle tracking user manual, version 2.15* (Deltares: The Netherlands).

Department of Natural Resources of Guangdong Province (2013-2020). *Guangdong marine disasters bulletin* (Guangzhou, China:Department of Natural Resources of Guangdong Province).

Ding, R., Chen, X., and Qu, N. (2015). Three-dimensional high-resolution numerical study of the tide and circulation in the pearl river estuary and its adjacent waters part 1: Model building and analysis. *Periodical Ocean Univ. China: Natural Sci. Edition* 45 (11), 1–9. doi: 10.16441/j.cnki.hdxb.20150064

Egbert, G. D., and Erofeeva, S. Y. (2002). Efficient inverse modeling of barotropic ocean tides. *Atmos. Ocean. Technol.* 19 (2), 183–204. doi: 10.1175/1520-0426(2002)019<0183:EIMOBO>2.0.CO;2

Fang, S., and Liu, J. (2020). A method of defining main tidal dynamic section and its applications in the lingdingyang estuary. *Eng. J. Wuhan Univ.* 53 (11), 950–957. doi: 10.14188/j.1671-8844.2020-11-002

Gao, L., Fan, De., Song, De., Zong, Y., Bi, N., and Chi, W. (2021). Numerical simulation of the migration path during the growth period of ulva prolifera in the sea near northern jiangsu and the thermohaline environment. *Haiyang Xuebao.* 43 (8), 1–16. doi: 10.12284/hyxb2021056

Hayashi, M., and Yanagi, T. (2008). Analysis of change of red tide species in yodo river estuary by the numerical ecosystem model. *Mar. pollut. Bull.* 57 (1-5), 103–107. doi: 10.1016/j.marpolbul.2008.04.015

Hu, X. (2010). *Numerical study of saltwater intrusion in modaomen of pearl estuary* (Beijing, China: Master's thesis, Tsinghua University)

Kuang, C., Xie, H., Su, P., Gu, J., and Mao, X. (2016). Tracking migration and diffusion of red tides in qinhuangdao coastal water based on FBM method. *China Environ. Sci.* 36 (8), 2505–2515. doi: 10.3969/j.issn.1000-6923.2016.08.033

Lapietra, I., Lisco, S., Mastronuzzi, G., Milli, S., Pierri., C., Sabatier, F., et al. (2022). Morpho-sedimentary dynamics of torre guaceto beach (Southern Adriatic Sea, Italy). *J. Earth Syst. Sci.* 131, 64. doi: 10.1007/s12040-022-01811-6

Li, Y., He, R., Mcgillicuddy, D. J., Anderson, D. M., and Keafer, B. A. (2009). Investigation of the 2006 alexandrium fundyense bloom in the gulf of Maine: *In-situ* observations and numerical modeling. *Cont. Shelf. Res.* 29 (17), 2069–2082. doi: 10.1016/j.csr.2009.07.012

Li, Y., Li, R., and Chang, L. (2020a). Red tide monitoring along the coast of zhejiang province based on GOCI data. *Ecol. Environ. Sci.* 29 (8), 1617–1624. doi: 10.16258/j.cnki.1674-5906.2020.08.013

Li, L., Lu, S., and Cen, J. (2019). Spatio-temporal variations of harmful algal blooms along the coast of guangdong, southern China during 1980-2016. *J. Oceanol. Limnol.* 37 (2), 535–551. doi: 10.1007/s00343-019-8088-y

Li, C., Odermatt, D., Bouffard, D., Wüest, A., and Kohn, T. (2022). Coupling remote sensing and particle tracking to estimate trajectories in large water bodies. *Int. J. Appl. Earth Obs. Geoinf.* 110, 102809. doi: 10.1016/j.jag.2022.102809

Li, J., Xing, Q., Zheng, X., Li, L., and Wang, L. (2022). Noctiluca scintillans red tide extraction method based on UAV images and deep learning. *J. Comput. Applications.* 42 (9), 2969–2974. doi: 10.11772/j.issn.1001-9081.2021071197

Li, Y., Stumpf, R. P., Mcgillicuddy, D. J., and He, R. (2020b). Dynamics of an intense *Alexandrium catenella* red tide in the gulf of Maine: satellite observations and numerical modeling. *Harmful Algae.* 99, 101927. doi: 10.1016/j.hal.2020.101927

Liu, R., Xiao, Y., Ma, Y., Cui, T., and An, J. (2022). Red tide detection based on high spatial resolution broad band optical satellite data. *ISPRS J. Photogramm. Remote Sens.* 184, 131–147. doi: 10.1016/j.isprsjprs.2021.12.009

Liu, J., Zeng, T., Liang, C., Zou, Y., Ye, X., Ding, J., et al. (2020). Application of HY-1C satellite in monitoring of natural disasters. *Satellite Appl.* 6, 26–34. doi: 10.3969/j.issn.1674-9030.2020.06.008

Liu, L., Zhou, J., Zheng, B., Cai, K., and Tang, J. (2013). Temporal and spatial distribution of red tide outbreaks in the Yangtze river estuary and adjacent waters, China. *Mar. pollut. Bull.* 72 (1), 213–221. doi: 10.1016/j.marpolbul.2013.04.002

Li, J., Xing, Q., Zheng, X., Li, L., and Wang, L. (2021). Noctiluca scintillans red tide extraction method based on UAV images and deep learning. *J. Comput. Applications.* 42 (9), 2969–2974. doi: 10.11772/j.issn.1001-9081.2021071197

Lu, Z., and Gan, J. (2015). Controls of seasonal variability of phytoplankton blooms in the pearl river estuary. *Deep-Sea Res. Pt. II.* 117, 86–96. doi: 10.1016/j.dsr2.2013.12.011

Nogueira, E., Bravo, I., Montero, P., Diaz-Tapia, P., Calvo, S., Ben-Gigirey, B., et al. (2022). HABs in coastal upwelling systems: Insights from an exceptional red tide of the toxigenic dinoflagellate. *Alexandrium minutum. Ecol. Indic.* 137, 108790. doi: 10.1016/j.ecolind.2022.108790

Qi, L., Hu, C., Barnes, B. B., and Lee, Z. (2017). VIIRS captures phytoplankton vertical migration in the NE gulf of Mexico. *Harmful Algae.* 66, 40–60. doi: 10.1016/j.hal.2017.04.012

Qin, R., Lin, L., Kuang, C., Su, T., and Mao, X. (2017). A GIS-based software for forecasting pollutant drift on coastal water surfaces using fractional Brownian motion: A case study on red tide drift. *Environ. Modell. Software* 92, 252–260. doi: 10.1016/j.envsoft.2017.03.003

Qu, D., Yu, H., Sun, Y., Zhao, Y., Wei, Q., Yu, H., et al. (2019). Numerical study on the summertime patches of red tide in the adjacent sea of the changjiang (Yangtze) river estuary, China. *Mar. pollut. Bull.* 143, 242–255. doi: 10.1016/j.marpolbul.2019.04.027

Seiler, L., Figueira, R. C. L., Schettini, C. A. F., and Siegle, E. (2020). Three-dimensional hydrodynamic modeling of the santos-são Vicente-bertioga estuarine system, Brazil. *Reg. Stud. Mar. Sci.* 37, 101348. doi: 10.1016/j.marpolbul.2019.04.027

Soto, I. M., Cambazoglu, M. K., Boyette, A. D., Broussard, K., Sheehan, D., Howden, S. D., et al. (2018). Advection of karenia brevis blooms from the Florida panhandle towards Mississippi coastal waters. *Harmful Algae.* 72, 46–64. doi: 10.1016/j.hal.2017.12.008

Tian, Y., Li, T., Hu, S., Xie, X., and Liu, S. (2020). Temporal and spatial characteristics of harmful algal blooms in guangdong coastal area. *Mar. Environ. Science.* 39 (1), 1–8. doi: 10.13634/j.cnki.mes.2020.01.001

Wang, B. (2014). Analysis on the estuarine circulation and its dynamic mechanism in the lingdingyang bay. *Chin. J. Hydrodynamics.* 29 (5), 608–617. doi: 10.3969/j.issn1000-4874.2014.05.013

Wang, G. (2020). *Study on the characteristics of tidal current and material transportation in the pearl river estuary* (Guangzhou, China: Master's thesis, South China University of Technology).

Weisberg, R. H., Liu, Y., Lembke, C., Hu, C., Hubbard, K., and Garrett, M. (2019). The coastal ocean circulation influence on the 2018 West Florida shelf *K.brevis* red tide bloom. *J. Geophys. Res-Oceans.* 124 (4), 2501–2512. doi: 10.1029/2018JC014887

Willmott, C. ,. J. (1981). On the validation of models. *Phys. Geogr.* 2 (2), 184–194. doi: 10.1080/02723646.1981.10642213

Zhang, H., and Li, S. (2010). Effects of physical and biochemical processes on the dissolved oxygen budget for the pearl river estuary during summer. *J. Mar. Syst.* 79 (1-2), 65–88. doi: 10.1016/j.jmarsys.2009.07.002

Zhang, B., Pu, A., Jia, P., Xu, C., Wang, Q., and Tang, W. (2021). Numerical simulation on the diffusion of alien phytoplankton in bohai bay. *Front. Ecol. Evol.* 572. doi: 10.3389/fevo.2021.719844

Zhao, J., and Ghedira, H. (2014). Monitoring red tide with satellite imagery and numerical models: A case study in the Arabian gulf. *Mar. pollut. Bull.* 79 (1-2), 305–313. doi: 10.1016/j.oceaneng.2021.109639

Zhou, F., Ge, J., Liu, D., and Ding, P. (2021). A Lagrangian-based floating macroalgal growth and drift model (FMGDM v1.0): Application in the green tides of the yellow Sea. *Copernicus GmbH.* doi: 10.5194/GMD-2021-20

Zohdi, E., and Abbaspour, M. (2019). Harmful algal blooms (red tide): A review of causes, impacts and approaches to monitoring and prediction. *Int. J. Environ. Sci. Te.* 6 (3), 1789–1806. doi: 10.1007/s13762-018-2108-x

frontiers | Frontiers in Marine Science

TYPE Original Research
PUBLISHED 27 February 2023
DOI 10.3389/fmars.2023.1096435

OPEN ACCESS

EDITED BY
Hui Zhao,
Guangdong Ocean University, China

REVIEWED BY
Jia Wang,
National Oceanic and Atmospheric Administration (NOAA), United States
Xuezhi Bai,
Hohai University, China

*CORRESPONDENCE
Yang Feng
yfeng1982@126.com

†These authors have contributed equally to this work and share first authorship

SPECIALTY SECTION
This article was submitted to Coastal Ocean Processes, a section of the journal Frontiers in Marine Science

RECEIVED 12 November 2022
ACCEPTED 13 February 2023
PUBLISHED 27 February 2023

CITATION
Luo L, Meng Z, Ma W, Huang J, Zheng Y, Feng Y, Li Y, Liu Y, Huang Y and Zhu Y (2023) The second-generation real-time ecological environment prediction system for the Guangdong–Hong Kong–Marco Greater Bay Area: Model setup, validation, improvements, and online visualization. *Front. Mar. Sci.* 10:1096435. doi: 10.3389/fmars.2023.1096435

The second-generation real-time ecological environment prediction system for the Guangdong–Hong Kong–Marco Greater Bay Area: Model setup, validation, improvements, and online visualization

Lin Luo[1†], Zhao Meng[1,2†], Weiwei Ma[3], Jingwen Huang[1,2], Youchang Zheng[1,2], Yang Feng[1*], Yineng Li[1,4,5], Yonglin Liu[1,2], Yuanguang Huang[1] and Yuhang Zhu[1,5]

[1]State Key Laboratory of Tropical Oceanography, South China Sea Institute of Oceanology, Guangzhou, China, [2]College of Marine Science, University of Chinese Academy of Sciences, Beijing, China, [3]Oceanography Department, College of Oceanic and Atmospheric Sciences, Ocean University of China, Qingdao, China, [4]Guangxi Key Laboratory of Marine Disaster in the Beibu Gulf, Beibu Gulf University, Qinzhou, China, [5]Key Laboratory of Science and Technology on Operational Oceanography, Chinese Academy of Sciences, Guangzhou, China

With the rapidly growing population and socioeconomic development of the Guangdong–Hong Kong–Marco Greater Bay Area of China, inputs of diverse contaminants have rapidly increased. This poses threats to the water quality of the Pearl River Estuary (PRE) and adjacent seas. To provide valuable information to assist the governors, stakeholders, and decision-makers in tracking changes in environmental conditions, daily nowcasts and two-day forecasts from the ecological prediction system, namely the Coupled Great Bay Ecological Environmental Prediction System (CGEEPS), has been setup. These forecast systems have been built on the Coupled Ocean–Atmosphere–Wave–Sediment Transport modelling system. This comprises an atmospheric Weather Research Forecasting module and an oceanic Regional Ocean Modelling System module. Daily real-time nowcasts and 2-day forecasts of temperature, salinity, NO2 + NO3, chlorophyll, and pH are continuously available. Visualizations of the forecasts are available on a local website (http://www.gbaycarbontest.xyz:8008/). This paper describes the setup of the environmental forecasting system, evaluates model hindcast simulations from 2014 to 2018, and investigates downscaling and two-way coupling with the regional atmospheric model. The results shown that though CGEEPS lacks accuracy in predicting the absolute value for biological and biogeochemical environmental variables. It is quite informative to predict the spatio-temporal variability of ecological environmental changes associated with extreme weather events. Our study will benefit of developing real-time marine biogeochemical and ecosystem forecast tool for oceanic regions heavily impact by extreme weathers.

KEYWORDS

Pearl River Estuary, Marine biogeochemical and ecosystem, forecast tool, coupled atmosphere-ocean circulation-carbon biogeochemistry model, nowcast and shortrange forecast

1 Introduction

The Pearl River Estuary (PRE) in South China is a large subtropical permanent open estuary fed by the Pearl River, which is the second largest river in China in terms of freshwater discharge (3.3×10^{11} m^3/yr) (Figure 1). Due to the substantial amount of anthropogenic nutrient inputs along with high discharge, the PRE is relatively productive with a high level of biodiversity. It provides crucial habitat and natural resources for multiple marine and freshwater fish species and the Chinese white dolphin, which is designated as a first-class national protected animal (Jefferson and Hung, 2004; Zhou et al., 2019). Oyster aquaculture has also developed rapidly in the PRE since the Ming and Qing dynasties, generating high revenue for the Guangdong government (Liu and Song, 2022). According to Cai and Li (2011), the PRE marine ecosystem is estimated to be valued at $31 billion per year. This represents an important component of the Gross Domestic Product of the Guangdong–Hong Kong–Marco Greater Bay Area.

Over the last few decades, rapid economic growth and progressive urbanization in the Pearl River Delta have led to considerable population growth in large cities in this region, including Hong Kong, Macao, Shenzhen, Zhuhai, and Guangzhou. This population increase poses a threat to the water quality of the PRE due to dumping of new pollutants, such as organophosphorus compounds, pharmaceuticals, and microplastics derived from personal care products (Stedman and Dahl, 2008; Zhou et al., 2016; Wang and Rainbow, 2020). These pollutants can cause severe damage to estuarine ecosystems and reduce biodiversity and fishery resources. This has caused substantial ecological and economic losses. Thus far, the loss value of the PRE is estimated to be approximately $5 billion per year. Therefore, protecting the estuarine environment from further water quality degradation is of considerable interest to stakeholders.

Real-time environmental forecasting systems based on three-dimensional, coupled hydrodynamic-biogeochemistry models are important tools for providing information on spatio-temporal varied environmental conditions (Wang, 2001). These data can be used to assist local governments and private partners to establish specific strategies for water quality improvement. The increase in anthropogenic derived nutrients has fueled larger and more frequent hypoxia in recent years (Li D et al., 2020; Ma et al., 2009; Ye et al., 2017; Qian et al., 2018). Oyster aquaculture has been shown to mitigate eutrophication and hypoxia, whereas the location and size of the farming area require circulation and appropriate biogeochemical conditions (Yu and Gan, 2021).

The coupled hydrodynamic–biogeochemical model usually serves as the internal core of a real-time environmental forecasting system. Web-based visualization systems are another important component that aid in forecasting. Real-time environmental systems with visualization systems can provide an intuitive way for governments and private partners to understand data and facilitate rapid decision-making. These systems have been established in many estuarine areas and oceans adjacent to coastal areas worldwide. For example, the Chesapeake Bay Environmental Forecast System (CBEFS) runs every 6 h over 1–2 km as well as the Chesapeake Bay Regional Ocean Modelling System (ChesROMS) – Estuarine Carbon Biogeochemistry (ECB) Model (Feng et al., 2015). CBEFS can provide real-time nowcast and two-day forecasts of salinity, water temperature, pH, aragonite saturation state, alkalinity, dissolved oxygen, and hypoxic volume in graphics on the local website (www.vims.edu/hypoxia). Another example of a real-time forecasting system is the China high-resolution coastal ocean ecological environment numerical prediction system. This was constructed using the Regional Ocean Modelling System–Carbon Silicate and Nitrogen Ecosystem model (ROMS-CoSiNE) and Semi-implicit Cross-scale Hydroscience-Integrated System Model-CoSiNE

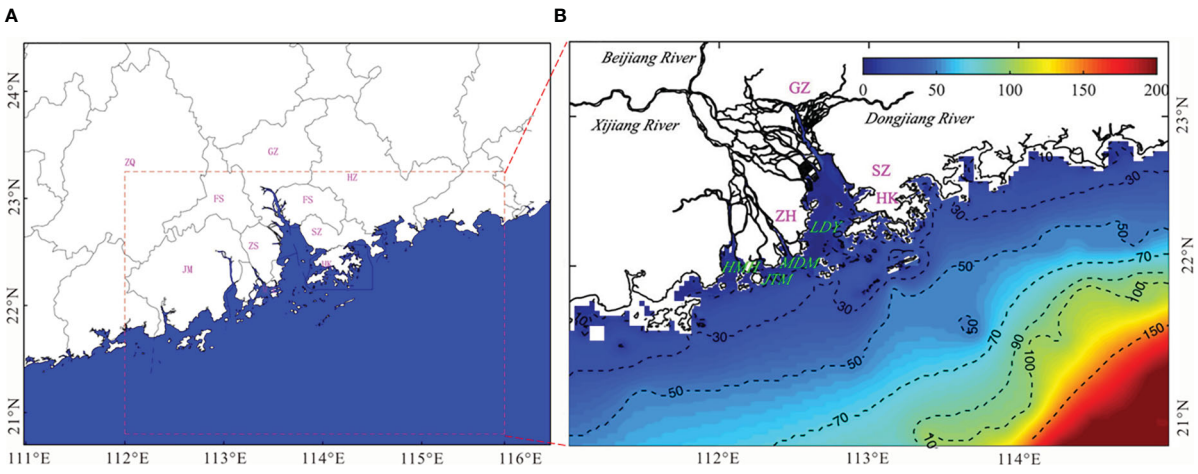

FIGURE 1
(A) Cites of Guangdong–Hong Kong–Marco Greater Bay Area, including Zhao-Qing (ZQ), Guang-Zhou (GZ), Hui-Zhou (HZ), Fo-Shan (FS), Dong-Guan (DG), Jiang-Men (JM), Zhong-Shan (ZS), Shen-Zhen (SZ), Zhu-Hai (ZH), Macau (MC), and Hong Kong (HK). **(B)** The tributaries of Pearl River, the Pearl River Estuary (PRE) and adjacent seas. Abbreviations are sub estuaries, including Ling-Ding-Yang (LDY), Mo-Dao-Men (MDM), Huang-Mao-Hai (HMH), and Ji-Ti-Men (JTM).

(SCHIMS-CoSiNE) for the BoHuang Sea, Yellow Sea, South China Sea, and Xiamen Bay (http://202.108.199.24:8080/BJ_SZYB_Web/default.html). The system can predict water temperature, current, multiple inorganic nutrients, chlorophyll, dissolved oxygen (DO), and pH predictions every 6 h. For the PRE, we constructed the Guangdong–Hong Kong–Marco Greater Bay Area Ecological Security Prediction System V1.0 using the Regional Ocean Modelling System (ROMS), Soil and Water Assessment Tool (SWAT), and Estuarine Carbon Biogeochemistry Model (ECB). The system was run every 24 h and primarily used for forecasting ocean currents, temperature, salinity, NO_2 + NO_3, chlorophyll, and DO (http://zhujiangtest.xyz:8000/).

This study describes an updated version of the real-time Ecological Environmental Forecast System for the Pearl River Estuary, the Coupled Great Bay Ecological Environment Prediction System (CGEEPS). We have introduced a general model configuration and evaluated the model accuracy for multiple hindcast variables and graphic visualization. CGEEPS provides daily nowcasts and two-day forecasts of environmental conditions throughout the PRE for temperature, salinity, NO_2 + NO_3, chlorophyll, DO, and pH. Configuration of the first generation of CGEEPS used a coupled ocean circulation–atmosphere model with a nitrogen-based ocean biogeochemistry component. The river inputs were generated from the land surface model SWAT climatology. We have added a range of updates that build on the first generation model (http://zhujiangtest.xyz:8000/). This includes a carbonate chemistry module that has been previously implemented in an existing nitrogen-based biogeochemistry model. River discharge was updated in near real-time from the China National Water and Rain Information Center (http://xxfb.mwr.cn/) and snatched by the Python request module.

The remainder of this paper is organized as follows. Section 2 presents the configuration of the modelling system core for the Forecast System and the model validation methodology. Section 3 presents the model validation and advantages of coupling it with the atmospheric model in a typhoon passage case. Section 4 summarizes the results and discusses the disadvantages of the current version of the forecasting system and potential future techniques that can be implemented.

2 Materials and methods

2.1 Atmosphere–ocean circulation–carbon biogeochemistry model implementation

The physical model of CGEEPS is built on the Coupled Ocean–Atmosphere–Wave–Sediment Transport (COAWST) modelling system. This comprises an atmospheric Weather Research Forecasting (WRF) module and a ROMS (Warner et al., 2008; Warner et al., 2010). The WRF domain spans from 98 ° to 122 °E and from 16 °to 30°N with an average horizontal resolution of approximately 12 km. This encompasses the entire Pearl River Watershed and northern part of the South China Sea. The ROMS domain ranges from 105° to 121°E and from 16° to 26°N, covering the continental shelf of the North South China Sea (NSCS) and the PRE (Figure 2A). The horizontal grid spacing varies between 2.8 km and 40.7 km with an average resolution of approximately 4 km. The model has 30 vertical layers that follow the terrain with a higher resolution near the surface and bottom boundaries. The vertical *s*-coordinate function is based on that of Shchepetkin and McWilliams (2009). The physical model is configured to use the recursive MPDATA 3-D advection scheme for tracers, four-order horizontal advection of tracers, third-order upwind advection of momentum, and the Mellor and Yamada (1982) turbulence closure scheme for vertical mixing. A viscosity/diffusivity coefficient of $10^{-5}m^2s^{-1}$ was used for biharmonic horizontal mixing in the momentum and tracer equations. Based on the CFL criterion, which is one of the global stability conditions, the internal mode time step of the numerical integration was 900 s, while the external mode time step was 60 s.

The circulation model was coupled with a nitrogen cycle model with consideration of carbonate chemistry and O_2 (Fennel et al., 2006, 2008, 2011). The model has 12 state variables, namely phytoplankton (Phy), chlorophyll (Chl), zooplankton (Zoo), nitrate (NO_3^-), ammonium (NH_4^+), O_2, dissolved inorganic carbon (DIC), total alkalinity (TAlk), and two detritus pools. These include small and large detritus, each split into nitrogen (SDetN and LDetN) and carbon (SDetC and LDetC) (Figure 2B). The mathematical description of the biogeochemical source and sink terms for the state variables is as follows.

$$\frac{\partial \mathrm{Phy}}{\partial t} = \mu_{\max}(T) f(E) L_{\mathrm{N}} \mathrm{Phy} - g_{\max} \frac{\mathrm{Phy}^2}{k_{\mathrm{P}} + \mathrm{Phy}^2} \mathrm{Zoo} - m_{\mathrm{P}} \mathrm{Phy} - \tau(\mathrm{SDetN} + \mathrm{Phy}) \mathrm{Phy} - w_{\mathrm{P}} \frac{\partial \mathrm{Phy}}{\partial z} \quad (1)$$

Where

$$\mu_{max}(T) = \mu_0 1.066^T \quad (2)$$

$$f(E) = \frac{\alpha E}{\sqrt{\mu_{max}^2 + \alpha^2 E^2}} \quad (3)$$

$$L_{NO_3} = \frac{NO_3}{k_{NO_3} + NO_3} \frac{1}{1 + NH_4/k_{NH_4}} \quad (4)$$

$$L_{NH_4} = \frac{NH_4}{k_{NH_4} + NH_4} \quad (5)$$

$$E = E(z) = E_0 \cdot par \cdot exp\left\{-Z(K_w + K_{chl} \int_z^0 Chl(\vartheta) d\vartheta)\right\} \quad (6)$$

$$\frac{\partial \mathrm{Chl}}{\partial t} = \frac{\theta_{max} \mu Phy}{\alpha IChl} \mu_{\max}(T) f(E) L_{\mathrm{N}} \mathrm{Chl} - g_{\max} \frac{\mathrm{Phy}^2}{k_P + \mathrm{Phy}^2} \mathrm{Zoo} - m_{\mathrm{P}} \mathrm{Chl} - \tau(\mathrm{SDetN} + \mathrm{Phy}) \mathrm{Chl} \quad (7)$$

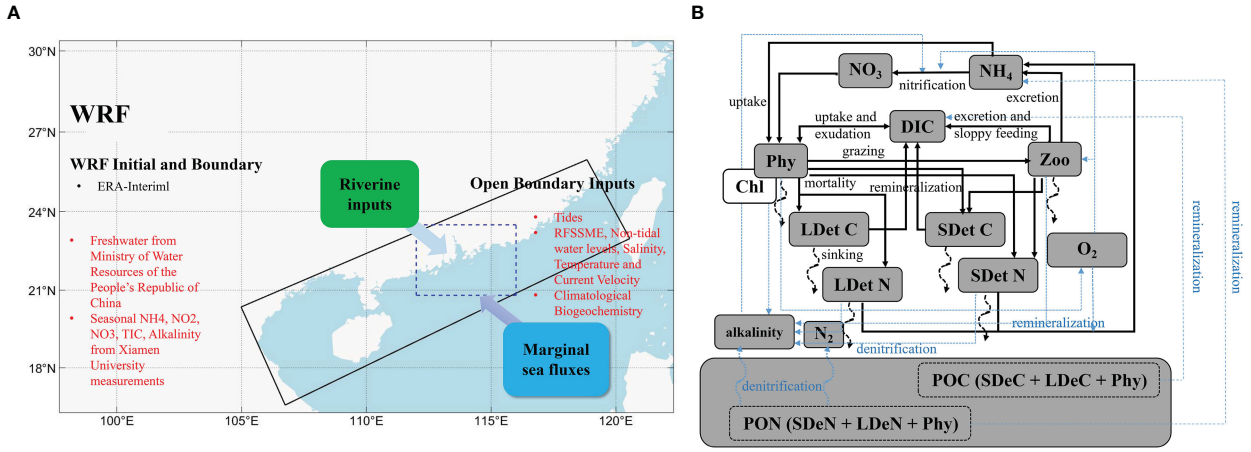

FIGURE 2
General setup of the Coupled Great Bay Ecological Environment Prediction System (CGEEPS) **(A)**; the structure of the biogeochemistry model **(B)**.

$$\frac{\partial \mathrm{Zoo}}{\partial t} = (g_{\max}\frac{\mathrm{Phy}^2}{k_\mathrm{P}+\mathrm{Phy}^2}\beta - l_\mathrm{BM} - l_\mathrm{E}\frac{\mathrm{Phy}^2}{k_\mathrm{P}+\mathrm{Phy}^2}\beta - m_\mathrm{Z}\mathrm{Zoo})\mathrm{Zoo} \quad (8)$$

$$\frac{\partial \mathrm{NO_3^-}}{\partial t} = -\ \mu_{\max}(T)f(E)L_{\mathrm{NO_3^-}}\mathrm{Phy} + \hat{n}\,\mathrm{NH_4^+} \quad (9)$$

$$\frac{\partial \mathrm{NH_4^+}}{\partial t} = -\ \mu_{\max}(T)f(E)L_{\mathrm{NH_4^+}}\mathrm{Phy} - \hat{n}\,\mathrm{NH_4^+} + l_\mathrm{BM}\mathrm{Zoo} + l_\mathrm{E}\frac{\mathrm{Phy}^2}{k_\mathrm{P}+\mathrm{Phy}^2}\beta\mathrm{Zoo} + \hat{r}^\mathrm{N}_\mathrm{SD}\mathrm{SDetN} + \hat{r}^\mathrm{N}_\mathrm{LD}\mathrm{LDetN} \quad (10)$$

$$\frac{\partial \mathrm{SDetN}}{\partial t} = g_{\max}\frac{\mathrm{Phy}^2}{k_\mathrm{P}+\mathrm{Phy}^2}(1-\beta)\mathrm{Zoo} + m_\mathrm{Z}\mathrm{Zoo}^2 + m_\mathrm{P}\mathrm{Phy} - \tau(\mathrm{SDetN}+\mathrm{Phy})\mathrm{SDetN} - \hat{r}^\mathrm{N}_\mathrm{SD}\mathrm{SDetN} - w_\mathrm{SD}\frac{\partial \mathrm{SDetN}}{\partial z} \quad (11)$$

$$\frac{\partial \mathrm{SDetC}}{\partial t} = \theta^\mathrm{Z}_\mathrm{C:N}(g_{\max}\frac{\mathrm{Phy}^2}{k_\mathrm{P}+\mathrm{Phy}^2}(1-\beta)\mathrm{Zoo} + m_\mathrm{Z}\mathrm{Zoo}^2) + \theta^\mathrm{P}_\mathrm{C:N}m_\mathrm{P}\mathrm{Phy} - \tau(\mathrm{SDetC}+\theta^\mathrm{P}_\mathrm{C:N}\mathrm{Phy})\mathrm{SDetC} - \hat{r}^\mathrm{C}_\mathrm{SD}\mathrm{SDetC} - w_\mathrm{SD}\frac{\partial \mathrm{SDetC}}{\partial z} \quad (12)$$

$$\frac{\partial \mathrm{LDetN}}{\partial t} = \tau(\mathrm{SDetN}+\mathrm{Phy})^2 - \hat{r}^\mathrm{N}_\mathrm{LD}\mathrm{LDetN} - w_\mathrm{LD}\frac{\partial \mathrm{LDetN}}{\partial z} \quad (13)$$

$$\frac{\partial \mathrm{LDetC}}{\partial t} = \tau(\mathrm{SDetC}+\theta^\mathrm{P}_\mathrm{C:N}\mathrm{Phy})^2 - \hat{r}^\mathrm{C}_\mathrm{LD}\mathrm{LDetC} - w_\mathrm{LD}\frac{\partial \mathrm{LDetC}}{\partial z} \quad (14)$$

$$\frac{\partial \mathrm{O_2}}{\partial t} = \mu_{\max}(T)f(E)(\frac{L_{N0}\frac{-}{3}}{LN}R_O2:NO\frac{-}{3} + \frac{L_{NH}\frac{+}{4}}{L_N}R_{0_2:NH_4^+})L_N Phy - 2\hat{n}NH\frac{+}{4} - (l_{BM} + l_E\frac{Phy^2}{kp+Phy^2}\beta)R_{0_2:NH_4^+}Zoo - \hat{r}\frac{N}{SD}R_{0_2:NH_4^+}SDetN - \hat{r}\frac{N}{LD}R_{0_2:NH_4^+LDetN} \quad (15)$$

$$\frac{\partial \mathrm{DIC}}{\partial t} = -\ \theta^\mathrm{P}_\mathrm{C:N}\mu_{\max}(T)f(E)L_\mathrm{N}\mathrm{Phy} + \hat{r}^\mathrm{C}_\mathrm{SD}\mathrm{SDetC} + \hat{r}^\mathrm{C}_\mathrm{LD}\mathrm{LDetC} + \hat{r}^\mathrm{C}_\mathrm{RD}\mathrm{RDOC} + \theta^\mathrm{Z}_\mathrm{C:N}(l_\mathrm{BM} + l_\mathrm{E}\frac{\mathrm{Phy}^2}{k_\mathrm{P}+\mathrm{Phy}^2}\beta)\mathrm{Zoo} \quad (16)$$

$$\frac{\partial \mathrm{TAlk}}{\partial t} = \mu_{\max}(T)f(E)\frac{L_{\mathrm{NO_3^-}} - L_{\mathrm{NH_4^+}}}{L_\mathrm{N}}L_\mathrm{N}\mathrm{Phy} - \widehat{2n}\,\mathrm{NH_4^+} + l_\mathrm{BM}\mathrm{Zoo} + l_\mathrm{E}\frac{\mathrm{Phy}^2}{k_\mathrm{P}+\mathrm{Phy}^2}\beta\mathrm{Zoo} + \hat{r}^\mathrm{N}_\mathrm{SD}\mathrm{SDetN} + \hat{r}^\mathrm{N}_\mathrm{LD}\mathrm{LDetN} \quad (17)$$

The parameter definitions, values, and units used in this model for coastal applications are listed in Table S1. The inclusion of inorganic carbon and alkalinity as state variables is critical for the successful simulation of pH using CO2SYS (Lewis and Wallace, 1998), as implemented in MATLAB. Phosphate is not included in this version of the model but will be added in the future to improve the system.

The bathymetry of the model domain was obtained from ETOPO and smoothed to reduce truncation errors, with the minimum water depth set to 5 m. The minimum depth was set to 5 m to ensure global stability, i.e., $h_{min}+\zeta_{max}>0$ (h_{min} is the min undisturbed water depth and ζ_{max} is the max free surface elevation at the coast due to gust

wind-induced storm surges, Wang, 1996). The river discharge data were sourced from the three main branches of the Pearl River (Xijiang, Dongjiang, and Beijing Rivers) and from the Ministry of Water Resources of the People's Republic of China (http://xxfb.mwr.cn). Freshwater inflows for the forecast period of each daily simulation were held constant for the two-day forecast. This was based on the inflow during the nowcast period. The data were summed and assumed to be distributed in the upper part of Lingding Bay, the lower Modaomen sub-estuary, and Huangmaohai Bay. River nutrient concentration was retrieved from water samples collected monthly from the eight river outlets of the Pearl River Delta (Lu et al., 2009) This included NO_3, NH_4, and organic nitrogen. All riverine organic matter was treated as SDetN in the simulations. The phytoplankton, zooplankton, and LDetN values were set to zero. DIC and alkalinity riverine inputs were sourced from the Xiamen University on request. Given that the nutrient and carbon-associated measurements are highly limited, climatological values were used at the open boundary, and the physical module was forced by the daily average temperature, salinity, current velocity, and de-tidal water level from a high-resolution regional South China Sea model (Peng et al., 2015). The biochemical variables used for the boundary conditions of the model were derived from the historical simulation of the CMIP6 model CESM-WACCM. The main inputs and open boundary conditions are presented in Table 1. We spun up the model for over six years before using the available historical cruise data (2014–2018) to validate the model.

2.2 Forecast system configuration

CGEEPS is maintained manually and runs at a specific time of the day to automate the workflow of the prediction system. The forecast system retrieves the necessary information from NOAA ftp to download the seasonal climate forecast from the NCEP coupled forecast system model Version 2 (CFSv2) using the "wget" command. Python was used to interpolate the downloaded data to a fine WRF atmospheric model grid. The Python requests module was used to snatch the river discharge from the China National Water and Rain Information Center. NetCDF operators combined with MATLAB and Python were used to modify the NetCDF input and output files efficiently. The forecast system maintainer replaces dates in a generic ROMS text input file for the simulation to commence on the correct day. The system was run on a workstation with 66 CPUs and simulated for three days, including a one-day nowcast and a two-day forecast. Each successive nowcast resulted from the end of the nowcast for the previous day. MATLAB was used to further postprocess the model NetCDF output to generate portable network graphics (png) files for online visualization.

An ecological security prediction system requires nowcast and forecast boundary conditions. The WRF model was used to produce real-time forecasting meteorological conditions for CGEEPS (Figure 3). The WRF provides evaporation and precipitation, sea surface heat flux, sea surface wind, and air pressure data to the ocean model. The ROMS subsequently feeds the sea surface temperature back to the meteorological model. The exchange frequency was once every 10 min. In this study, the impact on the study area of Hurricane Hato in August 2018 was simulated with and without the WRF.

2.3 Observational data

We used a series of cruise observations from 2014 to 2018 to validate the model (Figure 4; Table 2). The observations are part of an ongoing program from a ship time-sharing project sponsored by the National Natural Science Foundation of China (NSCF) and Xiamen University. Measurements from Conductivity, Temperature, and Depth (CTD) sensors documented the vertical structure and monthly temperature, salinity, and DO. Chlorophyll, NO_3, NH_4, and pH levels were measured in the laboratory.

2.4 Model skill metrics

Quantitative model–data comparisons using multiple skill metrics are critical because they highlight the advantages and

TABLE 1 Major boundary conditions and inputs required to run the atmosphere–ocean circulation– carbon biogeochemistry model.

Input	Variables	Initial Source	Source Resolution
Ocean Boundary	Tides Non-tidal Water Levels Salinity and Temperature Ocean Currents Biogeochemistry	Global Inverse Load Tide Model Real-time regional Forecast System of the South China Sea Marine Environment (RFSSME) CMIP6	1/6° 8 Tidal Harmonics; 0.06°/0.07° 5-day average 1° Monthly
Atmospheric Boundary	Wind Velocity Temperature Relative Humidity Geopotential Height	NCEP version 2 Coupled Forecast System (CFSv2) model https://www.cpc.ncep.noaa.gov/products/CFSv2/CFSv2_body.html	0.5° 6-hour
River Inflow	Discharge Temperature Biogeochemistry	Ministry of Water Resources of the People's Republic of China http://xxfb.mwr.cn Climatology from observation Climatology from observation	Daily Monthly Monthly for nutrients Seasonal for carbonate chemistry

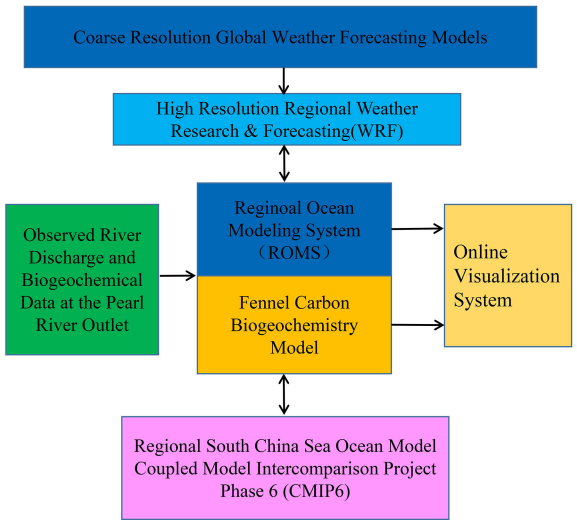

FIGURE 3
Flow chart of the forecast system automated workflow.

potential limitations of a particular model, which must be carefully considered before using the model as a tool for scientific study or decision-making (Jolliff et al., 2009; Stow et al., 2009). In this analysis, multiple skill metrics were examined. This included the correlation coefficient the that measures the tendency of the model and observed values to covary, and was calculated as

$$r = \frac{\sum_{i=1}^{n}(O_i - \bar{O})(M_i - \bar{M})}{\sqrt{\sum_{i=1}^{n}(O_i - \bar{O})^2 \sum_{i=1}^{n}(M_i - \bar{M})^2}} \quad (18)$$

where O_i is the observation at time t_i, M_i is the model estimate at t_i, $\bar{O}$ is the mean of the observations, $\bar{M}$ is the mean of the model estimates, and n is the total number of observations available for comparison with model estimates. The bias, unbiased root–mean–squared difference (unbiased RMSD), and total root–mean–squared difference (RMSD) were calculated as:

$$\text{Bias} = \frac{\sum_{i=1}^{n}(M_i - O_i)}{n} = \bar{M} - \bar{O} \quad (19)$$

$$\text{unbiased RMSD} = \sqrt{\frac{\sum_{i=1}^{n}[(M_i - \bar{M}) - (O_i - \bar{O})]^2}{n}} \quad (20)$$

$$\text{RMSD} = \sqrt{\frac{\sum_{i=1}^{n}(M_i - O_i)^2}{n}} \quad (21)$$

These three skill assessment statistics are particularly useful as bias reports of the size of the model-observation discrepancies. Bias values near zero indicate a close match. However, this can be misleading because negative and positive discrepancies can cancel

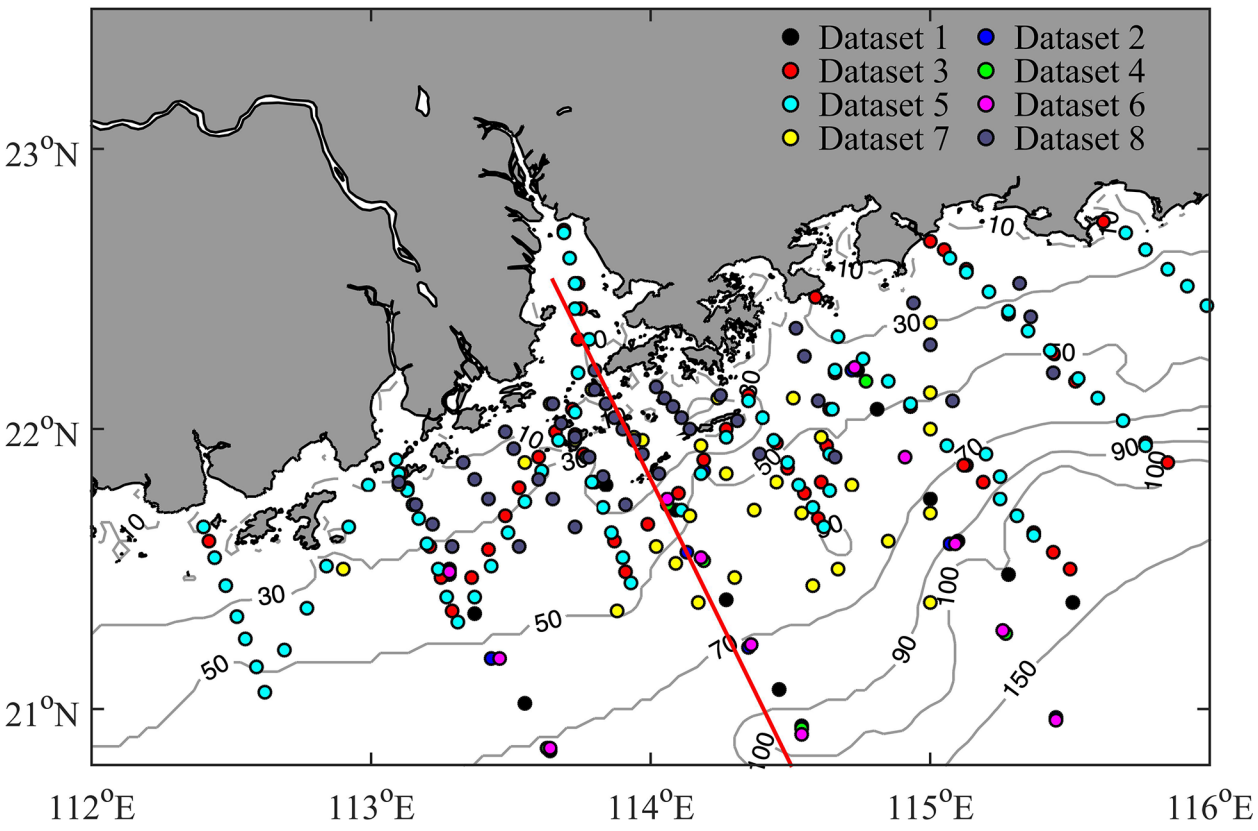

FIGURE 4
Sampling stations on the North South China Sea (NSCS) shelf off the PRE from multiple open cruises. The survey time is listed in Table 1. The red line shows the location of the vertical section in Figures 7, 5, and 11.

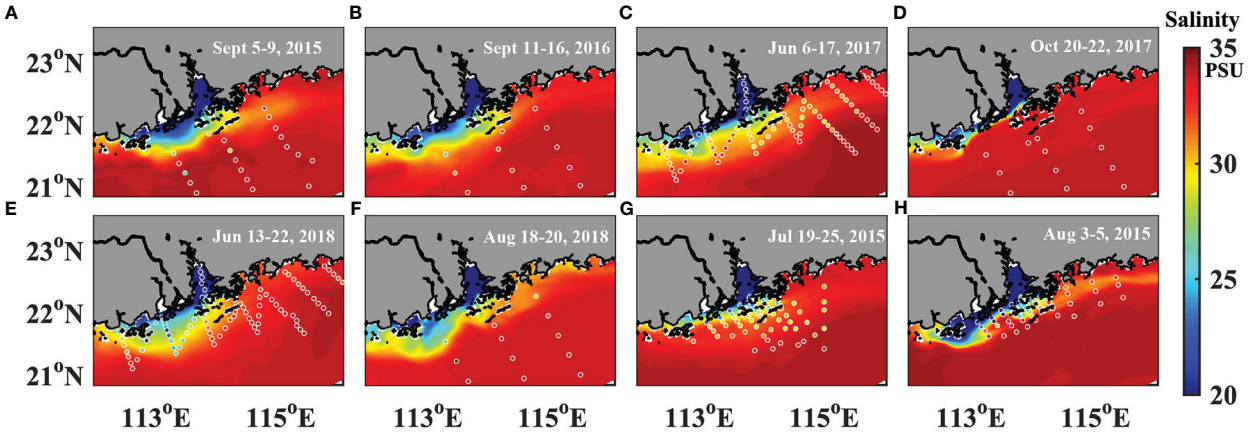

FIGURE 5
Comparison between observed (dots) and simulated (background color) surface salinity (< 2 m) for datasets (1) to (8) (Corresponding to **A–H**). The model results were assessed in the same time period as the observation.

each other. The unbiased RMSD nullifies the effect of the mean and is a pure measure of how model variability differs from observational variability. Total RMSD provides an overall skill metric, given that it includes components for assessing mean (bias) and variability (unbiased RMSD).

2.5 Target and Taylor diagrams for model validation

Multiple model skill metrics are compactly visualized on Taylor (Taylor, 2001) and target diagrams (Hofmann et al., 2008; Friedrichs et al., 2009; Jolliff et al., 2009). For the Taylor diagram, in addition to these skill metrics, the model standard deviation, σ_m has also been calculated.

$$\sigma_m = \sqrt{\frac{\sum_{i=1}^{n}(M_i - \bar{M})^2}{n}} \tag{22}$$

For both types of diagrams, skill statistics are typically normalized by the observational standard deviation (σ_o). This allows plotting of multiple different datasets on the same diagram.

$$\sigma_O = \sqrt{\frac{\sum_{i=1}^{n}(O_i - \bar{O})^2}{n}} \tag{23}$$

The Taylor diagram is plotted using a polar coordinate system and summarizes the skill metrics, including r, σ, and unbiased RMSD. In contrast, the target diagram was plotted using a Cartesian coordinate system and summarized the total RMSD, unbiased RMSD, and bias. On the normalized Taylor diagram, the reference point at (1, 0) represents a perfect skill score. Meanwhile, on the target diagram, the center of the target (0, 0) represents a perfect skill score.

3 Results

3.1 Hindcast simulations for evaluating model accuracy

The hindcast simulation of sea surface salinity was in strong agreement with the observations for all eight cruises (Figure 5). The correlation coefficient was 0.89. The bias and RMSD were 0.83 and 2.77 PSU, respectively. The simulated sea surface salinity showed

TABLE 2 The survey time and variables of datasets 1–8 from the cruises.

Dataset	Time period	Variables	Data Source
(1)	Sept 5-9, 2015	T, S	Shiptime sharing project sponsored by NSCF
(2)	Sept 11-16, 2016	T, S	
(3)	Jun 6-17, 2017	T, S, Chla	
(4)	Oct 20-22, 2017	T, S, Chla	
(5)	Jun 13-22, 2018	T, S, Chla	
(6)	Aug 18-20, 2018	T, S, Chla, DO	
(7)	Jul 19-25, 2015	T, S, pH	Cruise by Xiamen Universtiy
(8)	Aug 3-5, 2015	T, S, pH	

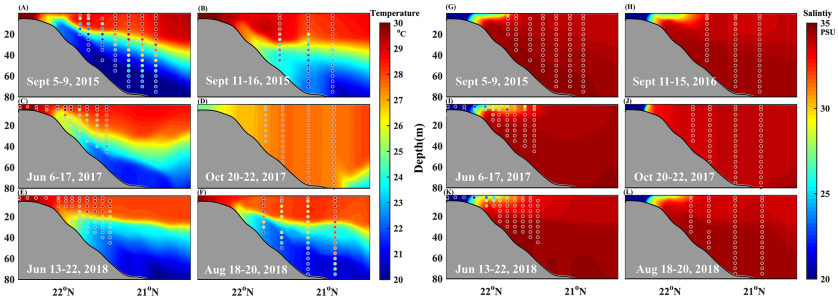

FIGURE 6
Comparison between observed (dots) and simulated (background color) temperature **(A–F)** and salinity **(G–L)** along vertical section for datasets (1) to (6).

that the river plume exhibited multiple shapes during the eight cruises. It spread easterly in July, August, and September 2015 (Figures 5A, B, H) and along the west coast in October 2017 (Figure 5D). The river plume bulged offshore in June and August 2018 (Figures 5E, F), and symmetrical alongshore in September 2016 and June 2017 (Figures 5B, C). The simulated plume morphology is consistent with previous observational facts reported in literature that the Pearl River buoyant plumes formed during summer can be classified into four types, namely offshore bulge spreading, west alongshore spreading, east offshore spreading, and symmetrical alongshore spreading. These were predominantly determined by the combined effect of river discharge and wind (Chen et al., 2017; Luo et al., 2012; Zu and Gan, 2015; Ou et al., 2009). River discharge has regulated the plume size, while wind has played an important role in changing the plume shape. The east and southeast winds drive the buoyant plume westward, resulting in the plume spreading westward alongshore. Given that the river plume resides at the surface, it is susceptible to the surface Ekman effect. The southwest wind upwelled and detached the eastward plume off the coast, which then spread offshore. If the wind is purely in a southerly direction, the plume is confined nearshore and moves both eastward and westward, thus forming a symmetrical structure.

Next, we compared the CGEEPS hindcast temperature and salinity along the vertical transect for six cruises where profiled CTD data were available (Figure 6). The simulated temperature and salinity were in strong agreement with the observations. For temperature, the CGEEPS hindcast replicated the observational fact that there was a strong thermocline in September 2015 and 2016, June 2017 and 2018, and August 2019, but not in October 2017. The correlation coefficient was 0.81. The bias and RMSD was 0.36 and 1.74 °C, respectively. The formation of a strong thermocline was due to upwelling of cold water under southwesterly winds, which generally occurs from June to August.

In addition to the thermocline from upwelling, the low salinity riverine water extended further offshore with the southwesterly wind in both the CGEEPS hindcast simulation and observations. The 28 psu isohaline extended over 22 °N. However, October 2018 was highly favorable for the occurrence of downwelling conditions. The low salinity water was increasingly confined adjacent to the river mouth and the isohalines were vertically distributed. The correlation coefficient was 0.94 and the bias and RMSD were 0.19 and 1.78 psu, respectively.

The high level of skill in terms of temperature and salinity fields suggested that our modelling system was relatively robust in replicating the dynamics of the PRE–ocean system, which is a river-dominated margin (Rabouille et al., 2008).

We subsequently examined how the nitrogen type nutrients, which are a combination of NO_3 + NO_2 + NH_4, were reproduced by CGEEPS. Given that rivers and upwelling are the two main sources of nutrients, we initially observed that the concentrations of N-type nutrients can reach as high as 150 μM inside the estuary and decrease to less than 1 μM as the plume water extends offshore. The nitrate concentration was relatively high (5–10 μM) at 20 m from the bottom owing to upwelling (Figure 7). The correlation coefficient between simulated and observed NO_3 was 0.91; however, the bias seemed to be slightly larger (Bias = 20.79 μM, RMSD = 63.1 μM). We examined the output data and found that NO_3-overestimation predominantly occurred at three stations in the upper reaches of the estuary closer to the river mouth boundary of the model grid. This overestimation was likely because we had set up at the river mouth in the upper part of Lingding Bay rather than at the actual river mouth. If we excluded these three points from the calculation, the bias and RMSD were almost halved (Table 3).

The nutrient distribution was in line with the salinity distribution pattern in the river plume region, which were the two variables with the best performance in the simulation system.

The full model observation skill assessment is presented in Table 3. The comparison was conducted by gathering all the observational points and extracting the model output at the observational stations. This implies that the skill number incorporated both spatial and temporal variability. In addition to the temperature, salinity, and N-type nutrients, we also examined the model performance for surface chlorophyll concentration and bottom DO (Table 3). The comparison results showed that the correlation between the observed and simulated surface chlorophyll content was 0.29. The surface chlorophyll concentration was overestimated by approximately 3 μg–Chl/L, particularly in the plume area. This was likely due to the deficiency of the current ecosystem module in CGEEPS. To date, we have not incorporated the P- and light-limitation effects due to resuspended sediment. We expected that further incorporation of these processes would slow the growth of phytoplankton and decrease the surface chlorophyll concentration.

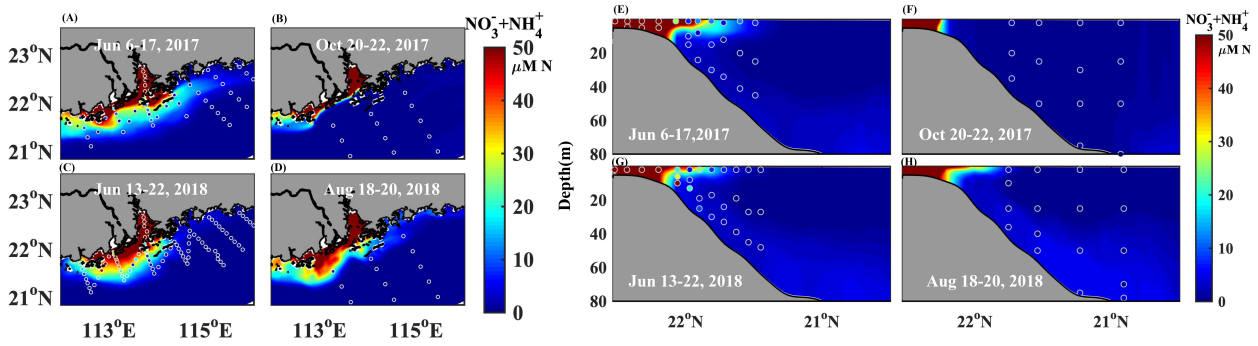

FIGURE 7
Comparison between observed and simulated nitrogen type nutrients (NO_3 + NO_2 + NH_4) for the surface **(A–D)** and along vertical transect **(E–H)** for datasets (3) to (6).

Although the surface chlorophyll concentration had been overestimated, the subsurface high chlorophyll maximum (DCM) structure was reproduced by the model (not shown here). The DCM layer lies immediately above the upwelled high NO_3 concentration, where nutrients and light were determined to be sufficient.

We further estimated the model's overall ability to reproduce bottom DO and surface pH. The model's skill in producing surface chlorophyll concentration and bottom DO was relatively poor. The correlation coefficient was positive at 0.41 for surface pH, but negative at −0.41 for bottom DO. The surface pH was underestimated by approximately −0.11 and the bottom DO was overestimated by approximately 1.2 mg/L. The underestimation of pH was likely associated with the surface temperature being underestimated by the model. This resulted in more dissolved CO_2 being held in the water and more hydrogen ions being released, resulting in lower pH values. The bottom DO was overestimated by the model, which was unexpected because the surface DO chlorophyll overestimated and more oxygen-consuming materials should be available. This overestimation may be because the current version of the biogeochemistry model did not include sediment oxygen consumption (SOC). Currently, the biogeochemistry model assumes that organic matter is immediately consumed upon reaching the bottom, whereas measurements show that organic matter consumption can be taken up over months. Instead of remaining in the same location, it is transported as fluid mud and undergoes numerous cycles of resuspension and deposition. The movement and long-term retention of organic matter in the sediment layer consumes additional oxygen when decomposed by bacteria. The current version of the carbon biogeochemistry model does not include the dissolved form of organic matter, which is another significant pool reserving organic matter and consuming DO. The current model parameter selections are predominantly empirical without optimization, which introduces considerable uncertainty to the simulated biogeochemical variables.

Table 3 provides the overall skill of the model by compiling multiple cruise data. However, it was not known how the model reflects spatial and temporal variability. Next, we performed a cruise-by-cruise comparison, which provided more specific information on the model's skill in replicating the spatial variability of multiple variables. Both Taylor and target diagrams were introduced to graphically and quantitatively visualize multiple model skill metrics (Figure 8). For the predicted environmental variables at the surface and on the bottom, the model performances for salinity and

TABLE 3 Model evaluation statistics for 2015–2018.

Variable	r	Bias	RMSD	ubRMSD
Surface Temperature	0.34	-0.67	1.16	1.22
Surface Salinity	0.89	0.83	2.77	2.64
Surface Chlorophyll	0.29	2.99	5.10	4.12
Bottom DO	-0.41	1.20	1.28	0.44
Surface NO_3 + NO_2	0.91	20.79	63.1	59.6
Surface (Without Lingding Bay NO_3 + NO_2)	0.91	10.2	30.3	28.6
Surface pH	0.41	-0.11	0.26	0.24
Section Salinity	0.94	0.19	1.78	1.77
Section Temperature	0.81	-0.36	1.74	1.70

temperature were uniform for all cruises. For salinity, the bias and RMSD were lower than 2 and 3.6 PSU, respectively, but the correlation coefficients were higher than 0.9. However, for temperature, both the bias and RMSD were low, and the correlation coefficients were also low (Figures 8A, B). In contrast to salinity and temperature, the performance of biogeochemical variables, especially surface chlorophyll, was cruise dependent. The model output showed a small bias and RMSD in October 2017, but a large bias and RMSD in June 2017. Similarly, the correlation coefficient was −0.08 in October 2017 but reached 0.61 in August 2018. Although the overall correlation coefficients for surface pH and chlorophyll concentration were 0.41 and 0.29, respectively, the correlation coefficient for a single cruise can reach as high as 0.7. These results suggest that surface chlorophyll and pH are more challenging to predict than temperature and salinity, because ecological and biogeochemical processes generally have larger uncertainties than physical processes.

Sectional data are only available for salinity and temperature. They showed a small bias and RMSD for all cruises. The correlation coefficients are over 0.7 for most cruises, except in September 2016, when the correlation coefficient for temperature was approximately 0.4.

Currently, data from multiple cruises are not collected at the same locations. Therefore, the ability of the model to reproduce temporal variability has not yet been assessed. Raw cruise data are processed using multiple laboratories. This implied that we could not guarantee that the same criteria and standards would be followed during data collection and preliminary processing. Therefore, the data quality itself may degrade the overall performance. We expect a future observational network and data-sharing platform to be set up in this region, which would benefit the systematic evaluation of the simulation performance in the future.

3.2 Differences in physical and biogeochemical fields by coupling with regional atmospheric model

Most coupled ocean–biogeochemistry model use atmospheric reanalysis products as forcing. One advantage of CGEEPS is the coupling of the regional atmospheric model with the regional ocean model. Compared to reanalysis products, the regional model usually has a high spatio-temporal resolution and the feedback of SST to the atmosphere. The coupled model has unique advantages in terms of simulating hurricane tracks and intensity. Therefore, we examined how the coupling technique has impacted ocean dynamics and biogeochemistry by using Hurricane Hato (2017) as an example.

Hurricane Hato formed over the western North Pacific at 128 ° E, 20.4 °N on August 21, 2017. It moved westward and passed the Luzon Strait at approximately 0000 UTC on August 22 and intensified into a Category 1 typhoon by 0800 UTC on August 22, with maximum sustained near-surface wind speeds increasing to 33 ms^{-1}. At 0000 UTC on August 23, Hato was upgraded to a Category 2 typhoon with a maximum sustained near-surface wind speed of 42 ms^{-1}. Approximately 3 h later, Hato reached its peak intensity with a maximum sustained near-surface wind speed of 48 ms^{-1}. Hato made landfall near Zhuhai City (113.2 °E, 22.1 °N), Guangdong Province, at 0450 UTC on August 23. Soon after its

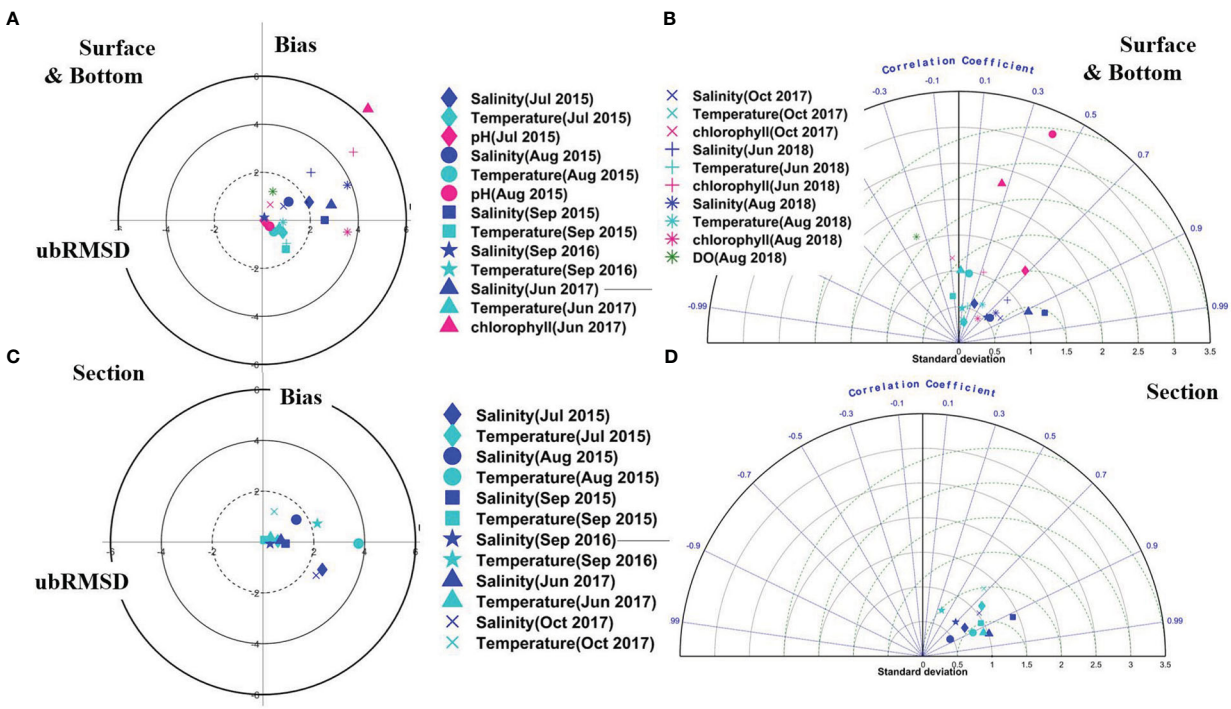

FIGURE 8
Target and Taylor diagrams displaying model skills for multiple hindicast variables between 2015 to 2017 individually on surface and bottom **(A, B)** and Sections **(C, D)**. Each marker shape represents a different cruise.

landfall, Hato weakened rapidly to 30 ms^{-1} over several hours and dissipated by 0800 UTC on August 24.

Two simulations were conducted from August 07 to September 05, 2017, the month when Hurricane Hato (2017) passed through. One was undertaken using two-way coupling with high-resolution regional configured WRF and the other by one-way forcing with coarse-resolution global ERA5. The simulated tracks of typhoons across the NSCS during August 22–24, 2017 are shown in Figure 9. The differences in both physical and biogeochemical fields are shown in Figures 10, 11.

We initially found that the typhoon tracks under the two runs were comparable. This indicates that the track of the typhoon was predominantly controlled by the background of large-scale atmospheric circulation (Figure 9).

For both runs, SST decreased and SSS increased rapidly from August 22 to August 23, 2017 (Figures 10B, C). This was caused by strong vertical mixing induced by the high wind of the hurricane. The SST increased after August 23 and decreased again from August 26. This was caused by upwelling after the eye passed offshore. The magnitude of the temperature drop from August 26 to August 28, 2017, in the two-way coupling WRF run was smaller than that in the one-way ERA5 run. This was likely because SST feedback to the atmosphere during the coupling weakened the strength of the tropical cyclone. The SST recovered from 28 August in both runs. However, the coupled WRF run diverged from the ERA5 one-way run from 31 August by maintaining a high SST at approximately 29°C. At the same time, the tropical cyclone brought heavy precipitation. This resulted in lower SSS in the two-way coupled WRF run than in the ERA5 one-way run.

Due to SST feedback to the atmosphere, we found that the difference between the two runs for surface air temperature (0.57 °C) was larger than SST (0.34 °C) (Figure 10A). The sea surface salinity was maintained at approximately 32 °C until August 27, 2017, and subsequently decreased. This was because river runoff increased after hurricane-induced heavy rainfall, which introduced a substantial amount of freshwater to the region being studied. The simulated results are consistent with the previous studies on ocean SST cooling and enhanced vertical mixing during a passage of a typhoon (Shen et al., 2021).

Surface chlorophyll, bottom DO, and surface pH varied with SSS and SST (Figures 10D–F). The temporal variability of chlorophyll, DO, and pH are strongly related to each other, that is, higher chlorophyll concentrations result in lower DO and higher pH. High surface chlorophyll concentrations indicate high primary production, which indicates that more oxygen-consuming materials are generated and DO decreases. A higher primary production also results in a higher pH because the equilibrium of carbonate ionization moves left after CO_2 is taken up by photosynthesis, thereby decreasing the concentration of hydrogen ions and increasing the pH value.

Owing to the strong vertical mixing induced by the hurricane, the surface chlorophyll concentration decreased, bottom DO increased, and surface pH decreased (Figures 10D–F). During the upwelling period when SST decreased, surface chlorophyll increased, bottom DO decreased, and surface pH also increased, which was caused by high primary production stimulated by sub-surface high nutrients. When the SSS decreased, the surface chlorophyll increased, the bottom DO decreased, and the increase in surface pH became larger.

A comparison between the two-time series and the two runs showed that the surface chlorophyll concentrations yielded larger differences than the SST and SSS differences. During Hato's (2017) passage, although the chlorophyll concentration decreased in both runs, the average surface chlorophyll concentration in the ERA5 run was approximately 2.5 μg–Chl/L higher. The concentration differences were approximately 6.0 μg–Chl/L two weeks later (September 02, 2017). This suggests that the physical and biological processes are highly nonlinear. A minor change in the physical field may be enlarged several times in biogeochemical fields.

For a better view of the differences, we plotted the horizontal distribution of these variables for August 23 and September 02,

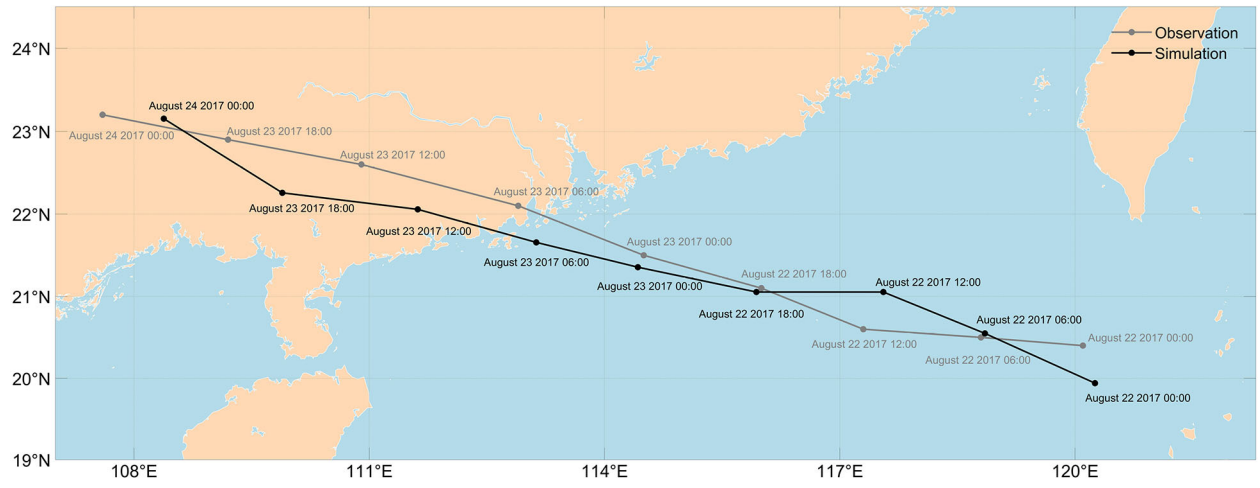

FIGURE 9
The observed and simulated track of Hurricane Hato (2017). The six-hour best-track TC data were obtained from the Shanghai Typhoon Institute.

10.3389/fmars.2023.1096435

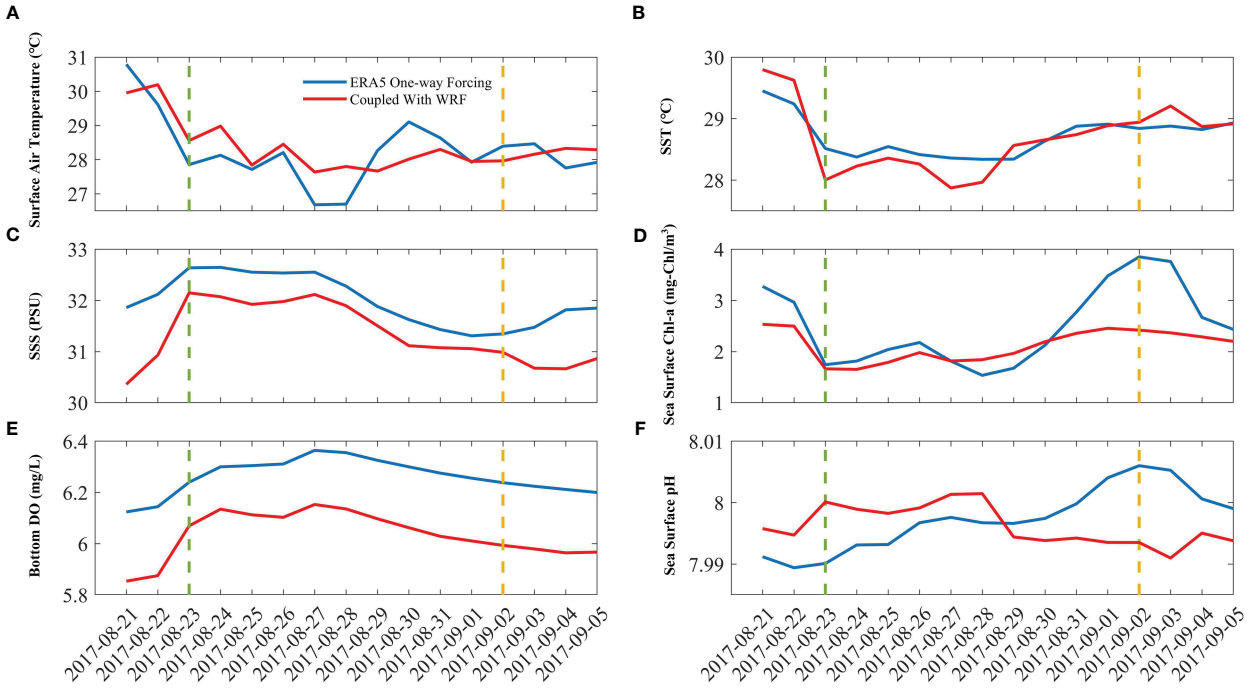

FIGURE 10
Surface air temperature **(A)**, sea surface temperature (SST) **(B)**, sea surface salinity (SSS) **(C)**, sea surface chlorophyll **(D)**, bottom DO **(E)**, and sea surface pH **(F)** when forcing by one-way ERA5 atmosphere (blue lines) and two-way weather research forecasting (WRF; red lines). Vertical dashed lines depict timings for Hato (2017) passing by the PRE. The simulated passage of Hurricane Hato (2017) is shown in Figure 9.

2017. During hurricane Hato's (2017) passage and 11 d after it had passed, was when increased runoff substantially impacted biogeochemical processes.

On August 23, 2017, typhoons Hato induced strong vertical mixing and onshore currents, resulting in low-temperature water mixing up to the surface and confinement to the narrow nearshore band (Figure 11). Low salinity and riverine waters were predominantly confined to Lingding Bay. As a result, there was relatively higher chlorophyll and lower DO within Lingding Bay and adjacent to the nearshore western bank. As river discharge increased and was delivered to the coastal ocean, the plume water extended offshore. As a result, high surface chlorophyll, low DO, and high pH water also extended further offshore. The low salinity, high chlorophyll, and bottom DO water in the one-way ERA5 run occupied a larger area than that in the coupling WRF run. This was likely because the regionally configured WRF had a higher resolution than the one-way ERA5, which induced high sub-grid vertical mixing.

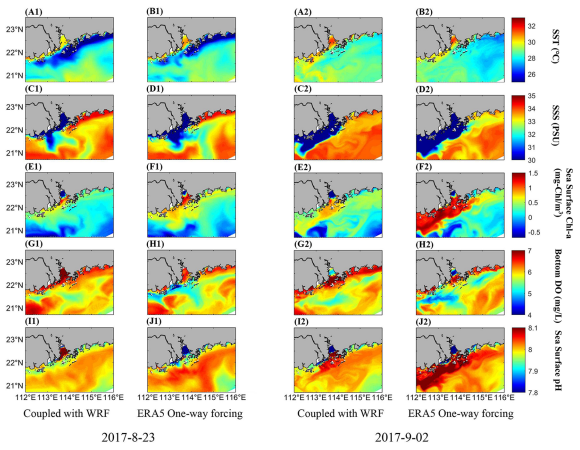

FIGURE 11
Comparison of horizontal distribution of SST, SSS, sea surface chlorophyll, bottom DO, and surface pH between ERA5 one-way atmospheric forcing **(A, C, E, G,** and **I)** and WRF two-way forcing **(B, D, F, H,** and **J)**. Snapshots were selected during (August 23, 2017) and 11 d (September 02, 2017) after the typhoon.

3.3 Forecasts for eutrophication, hypoxia, and ocean acidification

Although our simulation system may not have an exact accuracy in replicating the absolute value of all environmental variables at present, it is relatively informative in predicting variability under extreme weather conditions, such as floods and droughts.

The Pearl River Basin experienced a rainstorm in June 2022, which rapidly increased river discharge to 6×10^4 m^3s^{-1} on June 15 (Figure 12A). CGEEPS successfully captured the surface salinity decrease associated with a sudden increase in runoff (Figure 12B). Compared to June 01, 2022, a low-salinity bulge formed on June 15 beside Lingding Bay (Figure 13B). The sudden increase in runoff also delivered more nutrients from land to the estuarine shelf, leading to phytoplankton blooms and a decrease in bottom

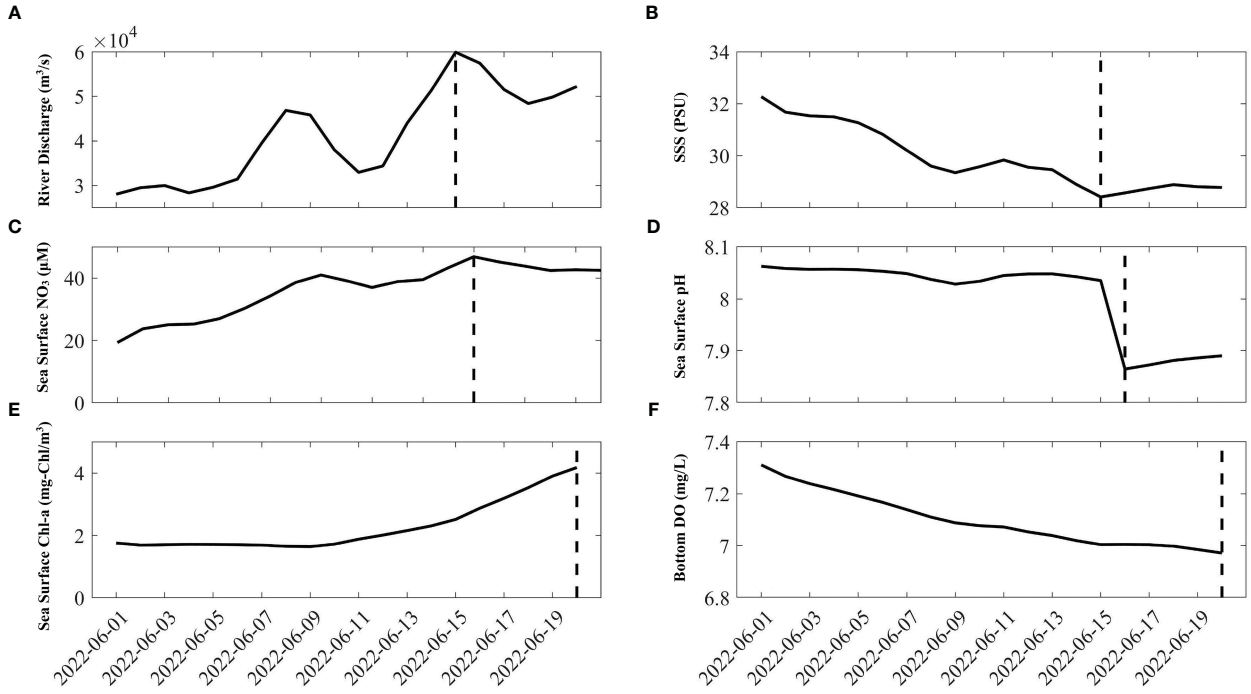

FIGURE 12
The river discharge **(A)** and CGEEPS predicted SSS **(B)**, Sea surface NO_3 **(C)**, pH **(D)**, Chlorophyll **(E)**, and bottom DO **(F)** from June 01, 2022, to June 20, 2022, when the flood happened. Vertical lines denote timing of maximum river runoff, sea surface NO_3, chlorophyll, and minimum sea surface salinity, surface pH and bottom DO.

dissolved oxygen (Figures 12E, F). At the surface, the low-salinity bulge was accompanied by a high NO_3 concentration (Figure 13D). However, the surface chlorophyll water was not synchronized with surface salinity and NO_3, which was relatively low within Lingding Bay and nearshore, but relatively high offshore (Figure 13H).The surface chlorophyll concentration depends on the relative importance of flushing and phytoplankton growth. High runoff reduces the residence time of phytoplankton, flushing them nearshore. Although the nutrient concentration was relatively high, there was insufficient time for phytoplankton to take up nutrients. Therefore, surface chlorophyll concentration was maintained at a low level. In contrast, phytoplankton had sufficient time to uptake NO_3 and bloom in the offshore region. We observed that high surface chlorophyll water was accompanied by higher pH levels. The pH was regulated by primary production. River runoff also brought a mass of DIC, resulting in a significant decrease in pH adjacent to the river mouth (Figure 13H). We also observed a sudden decrease in pH on June 16 from the time series after the peak discharge (Figure 12D).

These results suggest that the PRE and adjacent seas became more eutrophic, hypoxic, and acidic due to flooding. CGEEPS can capture such temporal and spatially varying environmental conditions, which can facilitate stakeholders making daily decisions regarding their usage of the bay's resources.

To make it easier for the governments and private users to access and understand relevant information, the information provided by the CGEEPS system should be presented in an easily accessible format. In addition to the near-real-time simulation system, CGEEPS also includes a real-time online data visualization system in which the visualized graph is published in a webpage format. Graphics generated from CGEEPS can nowcast environmental variables daily and forecast them over two days (Figures 14, 15). The focus has been on the horizontal distribution of variables in the first generation of the forecast system (http://zhujiangtest.xyz:8000/). To better inform governance and stakeholders, we have recently extended it to produce a vertical profiles and maps to display the subsurface structure, which is informative for visualizing eutrophic, hypoxic, and acidic water.

4 Discussion

Daily nowcasts and two-day forecasts from the ecological prediction system, the CGEEPS, were set up in the PRE and adjacent seas. The forecast systems were built on the COAWST modelling system. This comprises an atmospheric WRF module, an oceanic ROMS module, and a carbon-based biogeochemistry module (FENNEL). The forecast system can now provide real-time nowcast and two-day forecasts for temperature, salinity, NH_4 + NO_2 + NO_3, chlorophyll, DO, and pH. Hindcast comparison with available historical data from summer 2015–2018 has shown that the prediction system can replicate the temperature, salinity, and N-type nutrients for surface and vertical transects. However, the model performance for chlorophyll, DO, and pH was relatively poor. We also compared how the predicted biogeochemical fields differed from those predicted using coarse-resolution atmospheric

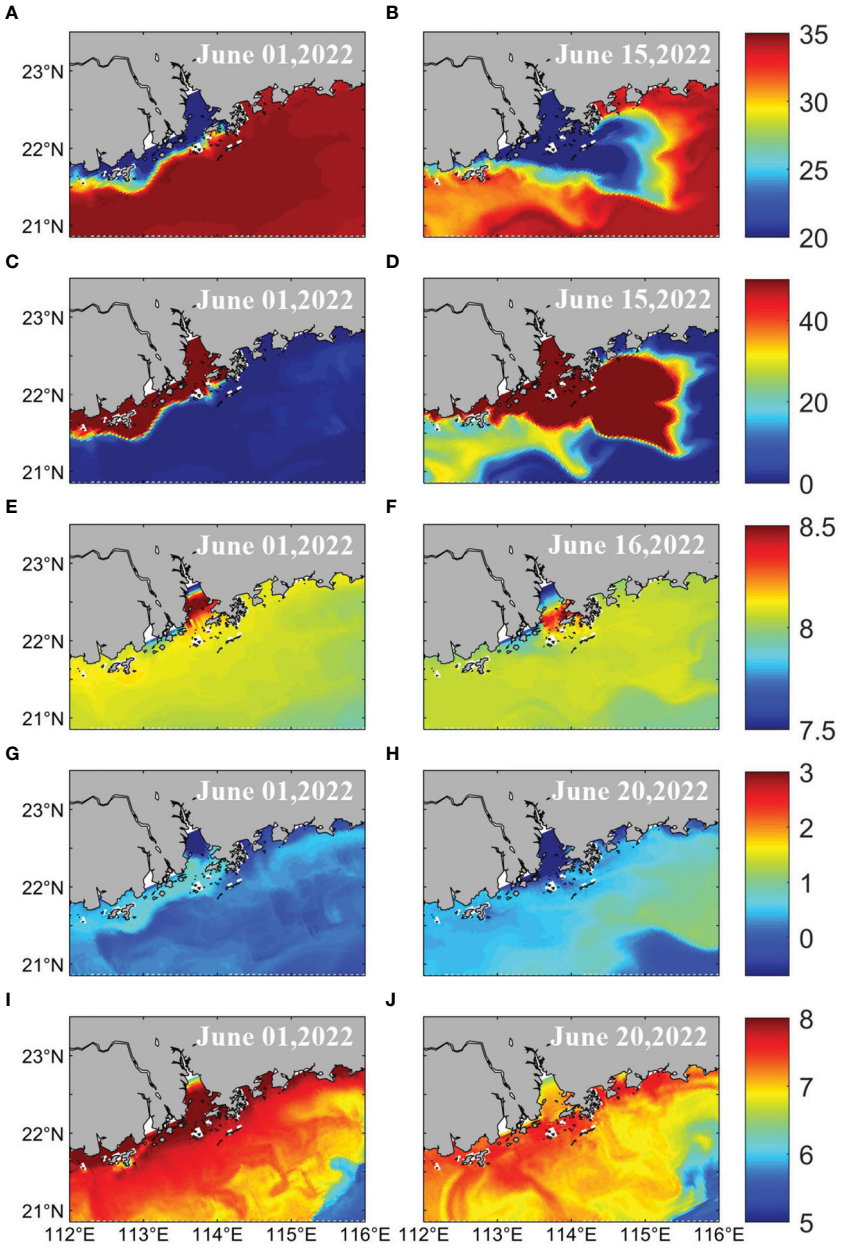

FIGURE 13
Comparison of SSS **(A, B)**, Sea Surface NO_3 **(C, D)**, pH **(E, F)**, Chlorophyll **(G, H)**, and bottom DO **(I, J)** before (June 01, 2022) and after flood occurrence (June 15, 2022). The snapshot dates are June 15, 2022 for surface salinity and NO_3; June 16, 2022 for surface pH; and June 20, 2022 for surface Chlorophyll and bottom DO.

reanalysis products. Using Hurricane Hato (2017) as an example, we found that stronger sub-grid vertical mixing was introduced after coupling with WRF. As a result, the surface salinity was lower than that when using coarse-resolution one-way ERA5 forcing. Due to the non-linear interaction between the physical and biogeochemical fields, the differences in surface chlorophyll became much greater than the salinity. Results suggest that the ecological environment prediction system was highly sensitive to physical forcing. The improved physical model would be beneficial to the system accuracy. We also determined how the physical and biological variables were predicted during the June 2022 rainstorm event. Results have shown that CGEEPS successfully captured data showing that the PRE and adjacent seas became fresher, more eutrophic, hypoxic, and acidic due to the Pearl River floods associated with the rainstorm. Results suggest that CGEEPS is capable of capturing the spatio-temporal variability of ecological environmental changes associated with extreme weather events.

At present, our ecological prediction system lacks accuracy in predicting some biological and biogeochemical environmental variables. We expect future improvements to increase system predictability, including: 1) more precise description of the water column and sediment processes, and 2) optimizing the parameter scheme of biogeochemical models. In addition to the modelling system itself, we found that building an observational network and

FIGURE 14
Real-time graphics displaying the surface **(A)** and vertical transect **(B)** of salinity (Screen shot from July 07, 2022).

data-sharing platform for this region was important. Compared to the Texas–Louisiana shelf, which is heavily impacted by the Mississippi River and Chesapeake Bay in the US, current observational data used to validate the system are relatively sparse and not spatially uniform. This increases the difficulty in evaluating the performance of the prediction system after new processes are introduced. An observational network has served as the basis for better parameterization of the ecosystem model. Another disadvantage of CGEEPS is that the system is currently operated and maintained manually, and we expect to use the Cron software utility to completely automate the CGEEPS workflow in the next phase of development.

Despite these disadvantages, CGEEPS is the first ecological environmental prediction system for the China Great Bay Area. The Hong Kong University of Science and Technology model data platform (http://ocean.ust.hk:8080/SiteMapApi/new/index.jsp) provides data visualization for daily averaged ocean circulation, ecosystem, and hypoxia, but no forecasts for these fields. Another example is the real-time Regional Forecast System of the SCS Marine Environment (https://epanf.scsio.ac.cn/), which is used to predict ocean circulation, waves, and several other important ocean–atmospheric dynamic variables rather than ecological environmental conditions (Zhu et al., 2020). Real-time environmental forecasting systems based on coupled ocean–atmosphere have also been set up worldwide. The Coupled Northwest Atlantic Prediction System (CNAPS), which is run by the North Carolina State University, predicts marine weather, ocean waves, and ocean circulation daily over an extensive area of the coastal northwest Atlantic Ocean. Another example is the South Eastern Levantine Israeli Prediction System (SLEIPS), which was setup through the Princeton Ocean Model (POM) and Variational Initial and Forcing Platform (VIFOP) for the coastal zone of the south eastern corner of the Levantine Basin (https://isramar.ocean.org.il/isramar2009/selips/), which provides temperature, salinity, and sea current prediction every 24 h. Compared with these prediction systems, CGEEPS is capable of predicting ecological environmental variables based on the coupled ocean–atmosphere–biogeochemistry technique. However, many

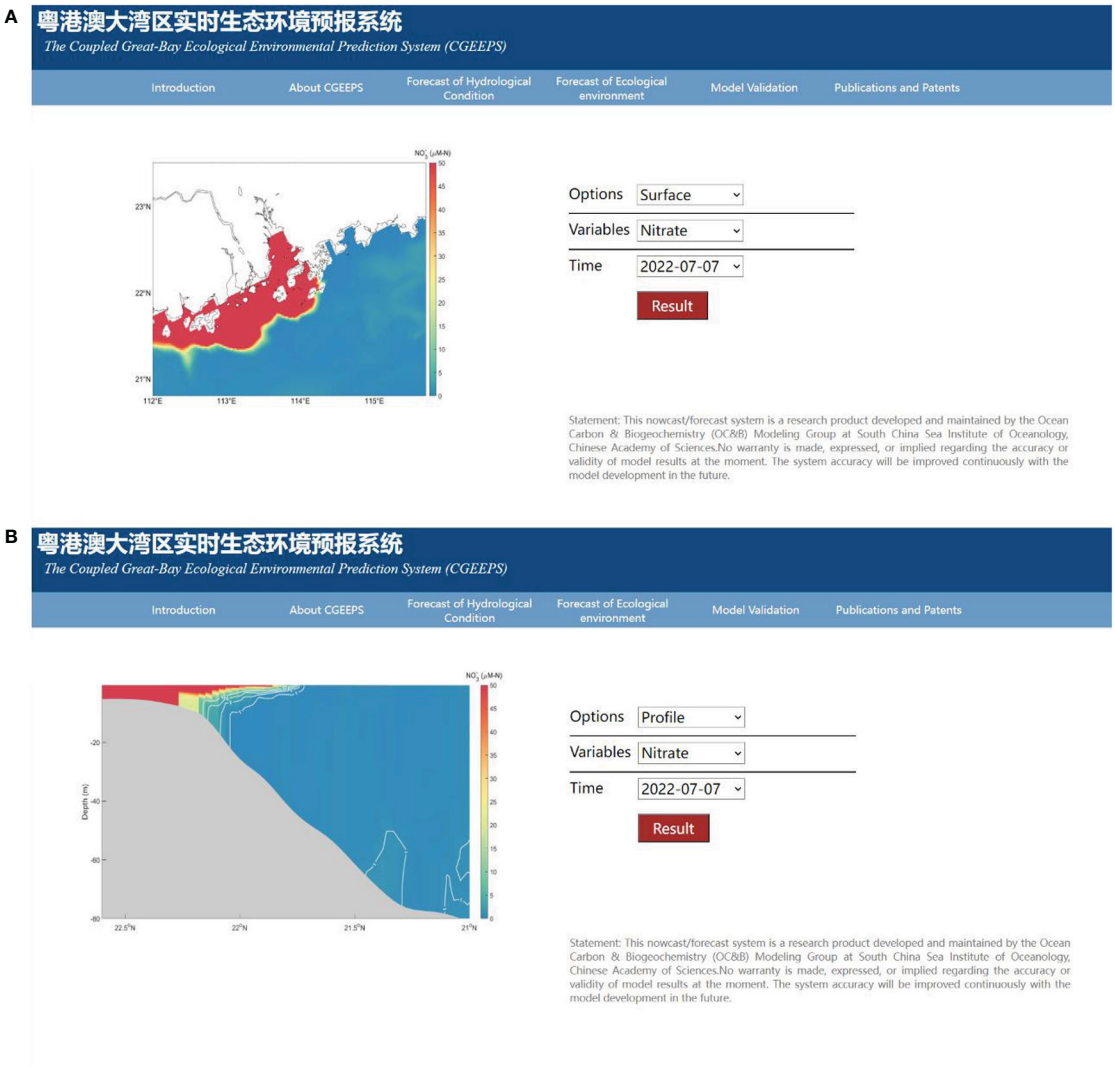

FIGURE 15
Real-time graphics displaying the surface **(A)** and vertical transect **(B)** of nitrate (Screen shot from July 07, 2022).

challenges on prediction accuracy were present because biogeochemical models are highly unconstrained and observation streams are much sparser than physical streams (Fennel et al., 2019).

Therefore, we implemented a coupled ocean–atmosphere technique for ecosystem and biogeochemistry prediction. However, for river-dominated ocean margins, such as the Pearl River estuarine–coastal system, the land delivers substantial amounts of nutrients, organic matter, and suspended sediments. These materials regulate the biogeochemical cycle of estuarine–coastal ocean systems; therefore, coupling with process-based land ecosystem models is required in the future. Such a land–estuary–ocean biogeochemistry model has been developed for the Chesapeake Bay system (Feng et al., 2015). However, only land delivered materials in one-year was cycling used, and river discharge was still the USGS measurements (Bever et al., 2021). Model coupling techniques, such as CPL7, are required to develop an operational system (Sun et al., 2020).

Coastal marine ecosystems are subject to multiple stressors, such as climate change and human land activities. Implementation of an ecological environmental prediction system is important for protective and adaptive measures in ocean ecosystems. The prediction tool that we have constructed is based on realistic representations of ocean circulation coupled with biogeochemical and ecological models, which can forecast short-term (days to weeks) to seasonal (months) time intervals. In addition to this type of model, statistics based artificial intelligence models have emerged and have been applied to coastal ocean biogeochemistry studies in recent years (Chen et al., 2019; Li X et al., 2020; Ou et al., 2022; Yu et al., 2022). Compared with the coupled hydrodynamic–biogeochemistry model, artificial intelligent models are more efficient and require less computational resources. However, the application of such models to ocean biogeochemistry is still in its early stages. Therefore, the predictability and results explainable for such a model require further investigation.

5 Concluding remarks

Warming, acidification, deoxygenation, and eutrophication of estuarine–coastal oceans have manifested in recent decades due to climate change and human land activities. Ecological environmental prediction systems are important tools that help decision-makers and the public implement protective and adaptive measures for ocean ecosystems. Based on the coupled ocean–atmosphere–biogeochemistry model, we constructed a real-time ecological environmental forecast system for the Pearl River Estuary (PRE), namely the Coupled Great Bay Ecological Environment Prediction System (CGEEPS). Compared to previous ecological prediction systems built for this region, CGEEPS can not only provide real-time nowcasts and two-day forecasts for chlorophyll but also DO and pH. Although limited in its absolute accuracy, the system is still informative for eutrophication, deoxygenation, and acidification, especially under extreme weather events. We expect the expansion of biogeochemical and ecological observational systems built for this region to help develop and apply such prediction tools in the future. Ultimately, the predicted data products can benefit the economic, environmental, and public safety needs of stakeholders and governments.

Data availability statement

The datasets presented in this study can be found in online repositories. The names of the repository/repositories and accession number(s) can be found below:; http://www.gbaycarbontest.xyz:8008/.

Author contributions

LL, ZM: These authors contributed equally to this work and share first authorship. They are responsible for the writing of this paper. WM, JH, YLi, YLiu, YH, YZhu: These authors contributed equally to this work. They are responsible for the setup, calibration, operation and maintenance of the Coupled Great Bay Ecological Environmental Prediction System. YF: She share senior authorship. She is in charge of the whole project. All authors contributed to the article and approved the submitted version.

Funding

This research was supported by the State Key Laboratory of Tropical Oceanography Independent Research Fund (grant no. LTOZZ2103), the State Key Laboratory of Tropical Oceanography, South China Sea Institute of Oceanology, Chinese Academy of Sciences (grant no. LTO2215), the Major Projects of the National Natural Science Foundation of China (Grant Nos. 41890851, U21A6001), and the Strategic Priority Research Program of the Chinese Academy of Sciences (Grant No. XDA19060503).

Acknowledgments

The authors thank use of the HPCC at the South China Sea Institute of Oceanology, Chinese Academy of Sciences.

Conflict of interest

The authors declare that the research was conducted in the absence of any commercial or financial relationships that could be construed as a potential conflict of interest.

Publisher's note

Supplementary material

The Supplementary Material for this article can be found online at: https://www.frontiersin.org/articles/10.3389/fmars.2023.1096435/full#supplementary-material

SUPPLEMENTARY TABLE 1
Definitions of biogeochemical parameters used in state variable equations.

References

[NOAA]National Oceanic and Atmospheric Administration (2020a) *Chesapeake Bay operational forecast system (CBOFS)* (Accessed May 1, 2020). Internet.

[NOAA]National Oceanic and Atmospheric Administration (2020b) *Sea Nettles probability of encounters* (Accessed May 1, 2020). internet.

Bever, A. J., Friedrichs, M. A. M., and St-Laurent, P. (2021). Real-time environmental forecasts of the Chesapeake bay: Model setup, improvements, and online visualization. *Environ. Model. Software* 140, 105036. doi: 10.1016/j.envsoft.2021.105036

Cai, M., and Li, K. (2011). Economic losses from marine pollution adjacent to pearl river estuary, China. *Proc. Eng.* 18, 43–52. doi: 10.1016/j.proeng.2011.11.008

Chen, Z., Gong, W., Cai, H., Chen, Y., and Zhang, H. (2017). Dispersal of the pearl river plume over continental shelf in summer. *Estuarine Coast. Shelf Sci.* 194, 252–262. doi: 10.1016/j.ecss.2017.06.025

Chen, S., Hu, C., Barnes, B. B., Wanninkhof, R., Cai, W.-J., Barbero, L., et al. (2019). A machine learning approach to estimate surface ocean PCO2 from satellite measurements. *Remote Sens. Environ.* 228, 203–226. doi: 10.1016/j.rse.2019.04.019

Feng, Y., Friedrichs, M. A., Wilkin, J., Tian, H., Yang, Q., Hofmann, E. E., et al. (2015). Chesapeake Bay nitrogen fluxes derived from a land-estuarine ocean biogeochemical modeling system: Model description, evaluation, and nitrogen budgets. *J. Geophysical Research: Biogeosciences* 120 (8), 1666–1695. doi: 10.1002/2015JG002931

Fennel, K., Wilkin, J., Levin, J., Moisan, J., O'Reilly, J., and Haidvogel., D. (2006). Nitrogen cycling in the middle Atlantic bight: Results from a three-dimensional model and implications for the north Atlantic nitrogen budget. *Global. Biogeochem. Cycles* 20, GB3007. doi: 10.1029/2005GB002456

Fennel, K., Wilkin, J., Previdi, M., and Najjar, R. (2008). Denitrification effects on air-sea CO2 flux in the coastal ocean: Simulations for the northwest north Atlantic. *Geophys. Res. Lett.* 35, L24608. doi: 10.1029/2008GL036147

Fennel, K., Hetland, R., Feng, Y., and DiMarco., S. (2011). A coupled physical-biological model of the northern gulf of Mexico shelf: model description, validation and analysis of phytoplankton variability. *Biogeosciences* 8 (7), 1881–1899. doi: 10.5194/bg-8-1881-2011

Fennel, K., Gehlen, M., Brasseur, P., Brown, C. W., Ciavatta, S., Cossarini, G., et al. (2019). Advancing marine biogeochemical and ecosystem reanalyses and forecasts as tools for monitoring and managing ecosystem health. *Front. Mar. Sci.* 6. doi: 10.3389/fmars.2019.00089

Friedrichs, M. A. M., Carr, M. E., Barber, R. T., Scardi, M., Antoine, D., Armstrong, R. A., et al. (2009). Assessing the uncertainties of model estimates of primary productivity in the tropical pacific ocean. *J. Mar. Syst.* 76 (1-2), 113–133. doi: 10.1016/j.jmarsys.2008.05.010

HKUST Hong Kong University of Science and Technology (2020) *Ocean circulation, ecosystem and hypoxia around Hong Kong waters (OCEAN-HK)* (Accessed August 6, 2020). Internet.

Hofmann, E., Druon, J.-N., Fennel, K., Friedrichs, M., Haidvogel, D., Lee, C., et al. (2008). Eastern US Continental shelf carbon budget: Integrating models, data assimilation, and analysis. *Oceanography* 21 (1), 86–104. doi: 10.1111/j.1468-2958.1996.tb00396.x

Jefferson, T. A., and Hung, S. K. (2004). A review of the status of the indo-pacific humpback dolphin (Sousa chinensis) in Chinese waters. *Aquat. Mammals* 30 (1), 149–158. doi: 10.1578/AM.30.1.2004.149

Jolliff, J. K., Kindle, J. C., Shulman, I., Penta, B., Friedrichs, M. A. M., Helber, R., et al. (2009). Summary diagrams for coupled hydrodynamic-ecosystem model skill assessment. *J. Mar. Syst.* 76 (1-2), 64–82. doi: 10.1016/j.jmarsys.2008.05.014

Lewis, E. R., and Wallace, D. W. R. (1998). *Program developed for CO2 system calculations* (Oak Ridge, Tennessee: Oak Ridge National Laboratory Press). doi: 10.15485/1464255

Li, X., Bellerby, R. G. J., Ge, J., Wallhead, P., Liu, J., and Yang, A. (2020). Retrieving monthly and interannual total-scale pH (pH T) on the East China Sea shelf using an artificial neural network: ANN-pH T-v1. *Geoscientific Model. Dev.* 13 (10), 5103–5117. doi: 10.5194/GMD-13-5103-2020

Li, D., Gan, J., Hui, R., Liu, Z., Yu, L., Lu, Z., et al. (2020). Vortex and biogeochemical dynamics for the hypoxia formation within the coastal transition zone off the pearl river estuary. *J. Geophysical Research: Oceans* 125 (8), e2020JC016178. doi: 10.1029/2020JC016178

Liu, J.-x., and Song, C. (2022). A historical investigation of oyster breeding industryin pearl river estuary during Ming and Qing dynasties. *Chin. Fisheries Economics* 40 (01), 115–122.

LiveOcean: Pacific Northwest ocean and estuary forecasts (2020) *Internet* (Accessed May 1, 2020).

Lu, F.-H., Ni, H.-G., Liu, F., and Zeng, E. Y. (2009). Occurrence of nutrients in riverine runoff of the pearl river delta, south China. *J. Hydrology* 376 (1-2), 107–115. doi: 10.1016/j.jhydrol.2009.07.018

Luo, L., Zhou, W., and Wang, D. (2012). Responses of the river plume to the external forcing in pearl river estuary. *Aquat. Ecosystem Health Manage.* 15 (1), 62–69. doi: 10.1080/14634988.2012.655549

Ma, Y., Wei, W., Xia, H., Yu, B., Wang, D., Ma, Y., et al. (2009). History change and influence factor of nutrient in lingdinyang Sea area of zhujiang river estuary. *Actaoceanologica Sin.* 31 (2), 69–77. Chinese edition/Haiyang Xuebao.

Mellor, G. L., and Yamada, T. (1982). Development of a turbulence closure model for geophysical fluid problems. *Rev. Geophys* 20, 851–875. doi: 10.1029/RG020i004p00851

Ou, Y., Li, B., and Xue, Z. G. (2022). Hydrodynamic and biochemical impacts on the development of hypoxia in the Louisiana–texas shelf – part 2: Statistical modeling and hypoxia prediction. *Biogeosciences* 19 (15), 3575–3593. doi: 10.5194/bg-19-3575-2022

Ou, S., Zhang, H., and Wang, D.-x. (2009). Dynamics of the buoyant plume off the pearl river estuary in summer. *Environ. Fluid Mechanics* 9 (5), 471–492. doi: 10.1007/s10652-009-9146-3

Peng, S., Li, Y., Gu, X., Chen, S., Wang, D., Wang, H., et al. (2015). A real-time regional forecasting system established for the south China Sea and its performance in the track forecasts of tropical cyclones during 2011–13. *Weather Forecasting* 30 (2), 471–485. doi: 10.1175/WAF-D-14-00070.1

Qian, W., Gan, J., Liu, J., He, B., Lu, Z., Guo, X., et al. (2018). Current status of emerging hypoxia in a eutrophic estuary: The lower reach of the pearl river estuary, China. *Estuarine Coast. Shelf Sci.* 205, 58–67. doi: 10.1016/j.ecss.2018.03.004

Rabouille, C., Conley, D. J., Dai, M. H., Cai, W.-J., Chen, C. T. A., Lansard, B., et al. (2008). Comparison of hypoxia among four river-dominated ocean margins: The changjiang (Yangtze), Mississippi, pearl, and rhône rivers. *Continental Shelf Res.* 28 (12), 1527–1537. doi: 10.1016/j.csr.2008.01.020

Shchepetkin, A. F., and McWilliams, J. C. (2009). Computational kernel algorithms for fine-scale, multiprocess, longtime oceanic simulations. *Handb. Numerical Analysis.* 14 (08), 121–183. doi: 10.1016/S1570-8659(08)01202-0

Shen, D., Li, X., Wang, J., Bao, S., and Pietrafesa, L. J. (2021). Dynamical oceanresponses to typhoon malakas, (2016) in the vicinity of Taiwan. *J. Geophysical Research: Oceans* 126 (2), e2020JC016663. doi: 10.1029/2020JC016663

Stedman, S., and Dahl, T. E. (2008). Coastal wetlands of the eastern united states: 1998 to 2004, status and trends. *Natl. Wetlands Newslett.* 30 (4), 18–20.

Stow, C. A., Jolliff, J., McGillicuddy, D.J. Jr, Doney, S. C., Allen, J. I., Friedrichs, M. A., et al. (2009). Skill assessment for coupled biological/physical models of marine systems. *J. Mar. Syst.* 76 (1-2), 4–15. doi: 10.1016/j.jmarsys.2008.03.011

Sun, L., Liang, X. Z., and Xia, M. (2020). Developing the coupled CWRF-FVCOM modeling system to understand and predict atmosphere-watershed interactions over the great lakes region. *J. Adv. Modeling Earth Syst.* 12 (12), e2020MS002319. doi: 10.1029/2020MS002319

Taylor, K. E. (2001). Summarizing multiple aspects of model performance in a single diagram. *J. Geophysical Research: Atmospheres* 106 (D7), 7183–7192. doi: 10.1029/2000JD900719

Wang, J. (1996). Global linear stability of the two-dimensional shallow-water equations: An application of the distributive theorem of roots for polynomials on the unit circle. *Monthly Weather Rev.* 124 (6), 1301–1310. doi: 10.1175/1520-0493(1996)124<1301:GLSOTT>2.0.CO;2

Wang, J. A. (2001). Nowcast/forecast system for coastal ocean circulation using simple nudging data assimilation. *J. Atmospheric Oceanic Technol.* 18 (6), 1037–1047. doi: 10.1175/1520-0426(2001)018<1037:ANFSFC>2.0.CO;2

Wang, W.-X., and Rainbow, P. S. (2020). Pollution in the pearl river estuary. *Estuaries World.* 23 (686), 23, 13–35. doi: 10.1007/978-3-662-61834-9_3

Warner, J. C., Armstrong, B., He, R., and Zambon, J. B. (2010). Development of a coupled ocean–atmosphere–wave–sediment transport (COAWST) modeling system. *Ocean Model.* 35 (3), 230–244. doi: 10.1016/j.ocemod.2010.07.010

Warner, J. C., Sherwood, C. R., Signell, R. P., Harris, C. K., and Arango, H. G. (2008). Development of a three-dimensional, regional, coupled wave, current, and sediment-transport model. *Comput. Geosciences* 34 (10), 1284–1306. doi: 10.1016/j.cageo.2008.02.012

Ye, F., Guo, W., Shi, Z., Jia, G., and Wei, G. (2017). Seasonal dynamics of particulate organic matter and its response to flooding in the pearl river estuary, China, revealed by stable isotope (δ13C and δ15N) analyses. *J. Geophysical Research: Oceans* 122 (8), 6835–6856. doi: 10.1002/2017JC012931

Yu, L., and Gan, J. (2021). Mitigation of eutrophication and hypoxia through oyster aquaculture: an ecosystem model evaluation off the pearl river estuary. *Environ. Sci. Technol.* 55 (8), 5506–5514. doi: 10.1021/acs.est.0c06616

Yu, L., and Gan, J. (2022). Reversing impact of phytoplankton phosphorus limitation on coastal hypoxia due to interacting changes in surface production and shoreward bottom oxygen influx. *Water. Res.* 212, 118094. doi: 10.1016/j.watres.2022.118094

Zhou, L., Wang, G., Kuang, T., Guo, D., and Li, G. (2019). Fish assemblage in the pearl river estuary: Spatial-seasonal variation, environmental influence and trends over the past three decades. *J. Appl. Ichthyology* 35 (4), 884–895. doi: 10.1111/jai.13912

Zhou, L., Zeng, L., Fu, D., Xu, P., Zeng, S., Tang, Q., et al. (2016). Fish density increases from the upper to lower parts of the pearl river delta, China, and is influenced by tide, chlorophyll-a, water transparency, and water depth. *Aquat. Ecol.* 50 (1), 59–74. doi: 10.1007/s10452-015-9549-9

Zhu, Y., Li, Y., and Peng, S. (2020). The track and accompanying Sea wave forecasts of the supertyphoon mangkhut, (2018) by a real-time regional forecast system. *J. Atmospheric Oceanic Technol.* 37 (11), 2075–2084. doi: 10.1175/JTECH-D-19-0196.1

Zu, T., and Gan, J. (2015). A numerical study of coupled estuary–shelf circulation around the pearl river estuary during summer: Responses to variable winds, tides and river discharge. *Deep Sea Res. Part II: Topical Stud. Oceanography* 117, 53–64. doi: 10.1016/j.dsr2.2013.12.010

frontiers | Frontiers in Marine Science

TYPE Original Research
PUBLISHED 31 March 2023
DOI 10.3389/fmars.2023.1095663

OPEN ACCESS

EDITED BY
Vetrimurugan Elumalai,
University of Zululand, South Africa

REVIEWED BY
Dingfeng Yu,
Qilu University of Technology, China
Qianguo Xing,
Institute of Coastal Zone Research (CAS), China

*CORRESPONDENCE
Dazhao Liu
lddz@163.com
Guangjun Xu
gjxu_gdou@yeah.net

SPECIALTY SECTION
This article was submitted to Coastal Ocean Processes, a section of the journal Frontiers in Marine Science

RECEIVED 11 November 2022
ACCEPTED 22 March 2023
PUBLISHED 31 March 2023

CITATION
Sun Y, Xu Y, Liu D and Xu G (2023) Analysis of environmental factors impact on water transparency off southeastern Vietnam. *Front. Mar. Sci.* 10:1095663. doi: 10.3389/fmars.2023.1095663

Analysis of environmental factors impact on water transparency off southeastern Vietnam

Yan Sun[1,2], Yuanxing Xu[2,3], Dazhao Liu[2,3]* and Guangjun Xu[3,4]*

[1]College of Chemistry and Environment, Guangdong Ocean University, Zhanjiang, China, [2]Guangdong Provincial Engineering and Technology Research Center of Marine Remote Sensing and Information Technology, Zhanjiang, China, [3]College of Electronic and Information Engineering, Guangdong Ocean University, Zhanjiang, China, [4]Southern Marine Science and Engineering Guangdong Laboratory (Zhuhai), Zhuhai, China

Seawater transparency, one of the important parameters to evaluate the marine ecological environment and functions, can be measured using the Secchi disk depth (SDD). In this study, we use multi-source remote sensing data and other fused data from 2011 to 2020 to study the spatial distribution and variation of SDD off southeastern Vietnam. The monthly average of SDD in the study area has obvious seasonal variation characteristics and shows a double peak characteristic. An important observation is a significant decrease in transparency from July to September each year, which is far lower than other nearby seas. To study this low SDD phenomenon, the generalized additive model (GAM) is used to determine the main environmental factors. The response relationship between SDD and environmental factors on different time scales is explained through empirical mode decomposition (EMD) analysis experiments. The results show that the comprehensive explanation rate of the GAM model is 72.1%, and the main environmental factors affecting SDD all have non-linear response relationships with SDD. The contributions are ranked as sea surface salinity (SSS)> offshore current velocity (Cu)> wind direction (WD)> offshore Ekman transport (ETu)> sea surface temperature (SST)> mean direction of wind waves (MDWW). SDD is positively correlated with SSS and SST, and negatively correlated with Cu and ETu. SSS, Cu, ETu, and SST have a significant effect on SDD at interannual scales. Long-term changes in SDD are driven by SSS, Cu, WD, and SST. Generally, SSS has the most comprehensive impact on SDD. WD indirectly has a non-negligible impact on SDD by changing ocean dynamics processes.

KEYWORDS

Secchi disk depth, environmental factors, off southeastern Vietnam, generalized additive model, empirical mode decomposition

1 Introduction

The Secchi disk depth (SDD), an old method to determine seawater transparency efficiently and easily, is still widely used today (Wernand, 2010). SDD is an important approach to characterizing the optical properties of seawater (Tang and Chen, 2016; Zhou et al., 2018). It is also an important indicator of the marine ecological environment and aquatic health, which can change the heat flux transport, photosynthesis of phytoplankton, and circulation of underwater nutrients (Kirk, 1994; Rodrigues et al., 2017; Harvey et al., 2019; Zhou et al., 2021). The study of SDD contributes to understanding seawater quality, primary productivity, and aquatic ecosystems of phytoplankton.

From previous studies, we know that SDD is affected by chlorophyll, salinity, suspended particulate matter (SPM), chromophoric dissolved organic matter (CDOM), wind, and nutrients (Gordon et al., 1983; Cloern, 1987; Erlandsson and Stigebrandt, 2006; Philippart et al., 2013; Aas et al., 2014; Hayami et al., 2015; Li et al., 2017; Bohn et al., 2018; Wang et al., 2019; Zou et al., 2020). These environmental parameters affecting SDD are related to deterministic events, such as abundant sediment transports in the estuary with low salinity plume, changes in nutrient concentrations due to upwelling, and seasonally varying sea surface temperature (SST) (Wang et al., 2015; Duy Vinh et al., 2016);. In addition, random events (e.g., algal blooms) can also have an important impact on SDD (Klemas, 2012; Yang et al., 2022). In past research on SDD, in addition to remote sensing monitoring technology, there is often analysis of the temporal and spatial changes of SDD and environmental driving forces (Philippart et al., 2013; Hayami et al., 2015; Nishijima et al., 2016; Nishijima et al., 2018; Luis et al., 2019; Idris et al., 2022). However, in special sea areas with complex environments, few quantitative studies on the effects of multiple environmental indicators on SDD have been conducted (Alsahli and Nazeer, 2021). Moreover, the correlation analysis between periodic events and SDD has not been adequately studied.

The study area of this paper is located in the southeast sea of Vietnam. Its hydrodynamic environment is complex, and the topography changes greatly (Tang et al., 2004). The sea area is a system of multiple complex interactions. In addition, SDD does not completely depend on a single environmental factor but results from multiple factors in the water. The composition of distinct water bodies is different, and the distribution and driving force of SDD is also different. This study aims to address the following research question: How does the SDD change in the southeastern Vietnamese waters? What fundamental environmental factors modulate SDD in this sea area? On what time scale do these environmental factors significantly affect SDD?

In this study, we use 2011-2020 multi-source remote sensing fusion data including various marine dynamic data, meteorological data, SST, sea surface salinity (SSS). Then, we use the generalized additive models (GAM) and the empirical mode decomposition (EMD) modal decomposition method to analyze the variation characteristics of SDD, screen out the main environmental factors affecting SDD in the study area, and quantitatively calculate the contribution of driving factors. Finally, the time scale and cycle that affect SDD are clarified, and the reasons for the significant difference in SDD between the study area and other sea areas.

2 Data and methods

2.1 Study area

Figure 1 shows the South China Sea (SCS) bathymetry. The study area (10°~14°E, 105°~114°N), which is the sea area off the southeastern coast of Vietnam, is plotted in the red rectangle. The water depths in the study area span from a few meters near shore to more than 6000 m offshore. Overall, water depth becomes shallower moving closer to land. In addition, the hydrodynamic environment of the study area is complex. With the Mekong Delta on the left nearshore, the average annual flow of the Mekong is 15,000 m^3, and there is the western boundary current along the Vietnamese coastline. In summer, at about 11.2°N, the western boundary current may split into an eastward flow known as the summertime eastward jet (Cai et al., 2007; Sun and Lan, 2021). Moreover, upwelling also occurs in the study area during summer. Overall, the region has complex biological, chemical, and physical characteristics (Tang et al., 2004; Chang et al., 2008).

2.2 SDD and environmental factors data

A total of 10 years (2010-2020) satellite-derived monthly SDD data are obtained from the Satco2 (http://www.geodata.cn). The spatial resolution of the data is 1.8 km. Previous studies have used this dataset to conduct research on marine elements in the SCS. The relationship model between SDD and water inherent optics is

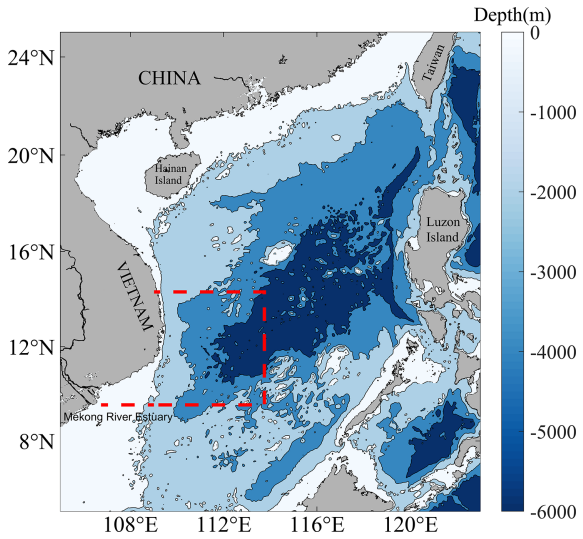

FIGURE 1
Bathymetry (m) of the SCS region. The red dashed box is the study area. The bathymetry data is obtained from ETOPO1.

expressed as follows (He et al., 2014; He et al., 2017):

$$Z_d = 0.25(a + b_b)\ln[\frac{\rho_\rho \alpha\beta(a+b_b)}{(C_a f b_b)}] \quad (1)$$

where ρ_ρ is the surface reflectance of the transparency disk, α is the refraction factor, β is the water surface reflection factor, C_a is the ratio threshold, f is a variable ranging from 0.32 to 0.37, a is the absorption coefficient, and b_b is the backscattering coefficient. For case I water, a and b are estimated as follows:

$$a(\lambda) = [a_w(\lambda) + 0.06A(\lambda)Chl^{0.65}][1 + 0.2e^{-0.014(\lambda-440)}] \quad (2)$$

$$b_b(\lambda) = b_{bw}(\lambda) + [0.3Chl^{0.62} - b_w(550)]\{0.002 + 0.02[0.2 - 0.25\log(Chl)\frac{550}{\lambda}]\} \quad (3)$$

where λ is the observation wavelength, a_w, b_w, and b_{bw} are the absorption, scattering and backscattering coefficients of pure water, respectively, and e is the *Chl* concentration. In addition, for case II water, the absorption (a_p) and scattering coefficient (b_{bp}) of suspended sediment should be increased on the basis of case I water:

$$a_p(\lambda) = s[0.025 + 0.038e^{-0.0055(\lambda-440)}] \quad (4)$$

$$b_{bp}(\lambda) = 0.019s[0.28 - 0.000167(\lambda - 400)] \quad (5)$$

where s is the concentration of suspended sediment.

SST, SSS and sea surface velocity data with a spatial resolution of 9 km (0.083°) are derived from global ocean reanalysis data simulated by The Copernicus Marine Environment Monitoring Service (CMEMS). The data extends from surface to 5500 m and is divided into 50 layers in the vertical direction. It adopts GEBCO data for layering nearshore and adopts ETOPO1 with a resolution of 1 arc minute to realize layering in the deep ocean, thus providing high-quality ocean environmental data (Wang et al., 2021).

The monthly average ocean wave and sea surface wind field data are derived from the ERA5 dataset of the European Center for Medium-Range Weather Forecasts (ECMWF). This dataset is the fifth-generation reanalysis dataset of global climate and weather over the past 40-70 years, including real-time updates from 1979 to the present. The dataset provides a large number of atmospheric, ocean wave and land surface parameters. The temporal resolution is hourly and monthly, and the spatial resolution of the reanalysis data is 0.25° (resolution of ocean wave data is 0.5°). The applicability of this product in the SCS has been verified and is in good agreement with buoy data (Shi et al., 2021).

The coastal upwelling region in the SCS is driven by classic wind-stressed Ekman dynamics (Zeng et al., 2022). In the upwelling region of southeastern Vietnam, Ekman transport along the shore (ETv) and offshore (ETu) and Ekman pumping (EPV) can transport nutrients from the coast or ocean bottom to the upper layer. This can promote the growth of phytoplankton and indirectly affect SDD. Ekman transport is calculated from wind components at 10 m above the sea surface (Equation 6, 7) (Cropper et al., 2014).

$$Q_x = \frac{\rho_a C_d}{\rho f}(W_x^2 + W_y^2)^{\frac{1}{2}} W_x \quad (6)$$

$$Q_y = -\frac{\rho_a C_d}{\rho f}(W_x^2 + W_y^2)^{\frac{1}{2}} W_y \quad (7)$$

where W is the wind speed near surface, ρ is the sea water density (1025 kg/m^3), and C_d is the dimensionless viscosity (1.4×10^{-3}). f is the Coriolis parameter, defined as twice the component of the angular velocity of earth (Ω) at latitude θ $f = 2\Omega sin\theta$. x and y correspond to the zonal and meridional components of wind, respectively.

EPV is calculated as follows:

$$EPV = \frac{curl(\tau)}{\rho f} \quad (8)$$

where τ is surface wind stress.

The mixed layer depth (MLD) and barrier layer depth (BLD) distribution in the ocean is closely related to the internal motion of the ocean, marine organisms and marine meteorological elements. BLD is the water layer between the isothermal layer depth (ILD) and MLD, expressed as BLD=ILD-MLD. In this study, the gradient method is used to determine ILD and MLD. Different determination methods are used in offshore waters with a water depth of less than 200 m and in the open seas with larger water depths (Godfrey and Lindstrom, 1989; Chu et al., 2002):

offshore(≤200 m)

$$\frac{\partial T}{\partial z} = 0.2\,°C\cdot m^{-1} \quad \frac{\partial \sigma_t}{\partial z} = 0.1 \quad kg\cdot m^{-4} \quad (9)$$

open sea(≥200 m)

$$\frac{\partial T}{\partial z} = 0.05\,°C\cdot m^{-1} \quad \frac{\partial \sigma_t}{\partial z} = 0.015 \quad kg\cdot m^{-4} \quad (10)$$

where σt is the density of seawater obtained from temperature and salinity by TEOS10 (http://www.teos-10.org/), and T is sea water temperature.

2.3 Method

2.3.1 Empirical mode decomposition

Compared with the traditional wavelet analysis, the EMD proposed and improved by Huang can obtain more refined time-frequency local features. It smoothly processes complex signals and extracts the fluctuation or trend components of different scales from the original sequence. The output is several intrinsic mode functions (IMFs) of different scales and a trend item. The trend change characteristics have no relationship with past or future data. This method is widely used in atmospheric and oceanic research (Chen et al., 2013; Chen et al., 2014).

IMFs must satisfy two conditions (Huang et al., 1998). (a) The number of extreme points and zero crossing points throughout the data should be less than or equal to 1. (b) Any point where the mean of the envelope is defined by the local maximum or local minimum is 0. An IMF that meets these conditions has amplitude and frequency that vary as a function of time. EMD is ultimately decomposed into IMFs, and a residual term r(n) is obtained:

$$X(t) = \sum_{i=1}^{n} IMF_i + r(n) \quad (11)$$

where $X(t)$ is decomposed by EMD to obtain several IMFs. Based on the Hilbert transformation of each IMF, the instantaneous frequency and instantaneous amplitude of each component are obtained. For any signal $X(t)$, it can be expressed as:

$$H(X(t)) = y(t) = \frac{1}{\pi} pv \int \frac{X(u)}{t-u} du \tag{12}$$

In the above equation, pv is the Cauchy's principal value, and the analytic signal corresponding to $X(t)$ is:

$$Z(t) = X(t) + iy(t) = a(t)e^{i\theta(t)} \tag{13}$$

where a(t) and $\theta(t)$ are the instantaneous amplitude and instantaneous phase of the signal, respectively, expressed as

$$a(t) = \sqrt{X(t)^2 + y(t)^2} \tag{14}$$

$$\theta(t) = arctan(\frac{y(t)}{X(t)}) \tag{15}$$

Further derivation of $\theta(t)$ function obtained from the original analysis signal yields the instantaneous frequency of the signal as follows:

$$\omega(t) = \frac{d\theta(t)}{dt} \tag{16}$$

If the amplitude is plotted on the plane of time and frequency, the Hilbert spectrum of the original signal X(t) can be obtained.

This study mainly uses EMD to carry out multi-scale analysis and correlation analysis on the time series of SDD and related influencing factors in the study area. The Hilbert spectrum analysis is then applied to the obtained IMF modal components to finally obtain the Hilbert spectrum with clear physical meaning. This method can better describe the non-linear process and can effectively obtain the variation trend characteristics of SDD in different and multiple periods, in order to further determine the contribution of various environmental factors.

2.3.2 Generalized additive models

GAM is an important achievement in statistical research in recent years (Guisan et al., 2002). Its advantage is that it can explain the highly non-linear or monotonic relationship between response variables and environmental factors. The model is data-driven rather than assuming specific parameters between data in advance. It has high flexibility and can better explain the relationship between the response variable and the explanatory variable, and the importance of each explanatory variable. GAM can be expressed as:

$$g(Y) = \alpha + \sum_{i}^{n} f_i(x_i) + \epsilon \tag{17}$$

where $g(Y)$ is the connection function of the response variable SDD (the data of the response variable can be of any exponential distribution form), α is the intercept, ϵ is the residual, n is the number of parameters, X_i is the ith explanatory variable, and $f_i(x_i)$ is the smoothing function used to describe the relationship between $g(Y)$ and the ith explanatory variable.

This study used the effective degree of freedom (EDF), P-value, deviance explained (D-E) and F-statistic to characterize the quality of the model's statistical results. In addition, the larger the F-statistic, the higher the importance of the corresponding variable. When EDF=1, it represents a linear relationship between the variables and when EDF > 1, it indicates that the function is a non-linear curve equation. The larger the EDF, the more significant the non-linear relationship (Requia et al., 2019). P-value represents the significance level of the statistical results, D-E represent the model's interpretation rate for the change of the response variable, and values closer to 1 mean that the model works better.

Based on the inversion principle of SDD, generally, the factors that most directly affect SDD include SPM, chlorophyll and CDOM. In contrast, other environmental factors indirectly affect SDD by affecting the spatial and temporal distribution of the above three environmental factors. In this study, one environmental factor is selected as the explanatory variable of GAM each time, and the relationship and contribution of each factor to SDD changes are analyzed. The environmental variables include SSS, SST, ET (Ekman transport), EPV, CV (current velocity), ILD, BLD, wind and nine wave parameters:mean direction of total swell, significant height of total swell, mean period of total swell, MDWW (mean direction of wind waves), mean period of wind waves, mean wave direction, mean wave period, SWH (significant height of combined wind waves and swell), and significant height of wind waves. The construction and data analysis of the GAM model are completed using the R mgcv package.

3 Results

3.1 Spatial distribution and variation characteristics of SDD

The monthly mean SDD in the study area from 2011 to 2020, shows the variation range of the monthly mean SDD in the study area is 26.6~34.9 m during the 10 years (Figure 2). SDD has obvious seasonal variation characteristics, reaching a maximum in May, decreasing rapidly, and reaching a minimum in August each year. Concretely, the average SDD in June (summer) is 32.4 m, when the water clarity of the study area is higher, but it was still very low in September, which was already autumn (mean SDD value is 28.6 m). Apparently, the most turbid time of the year is July to September.

We average the SDD in the SCS and surrounding seas by season according to the monthly variation characteristics of SDD (Figure 3), in order to better understand the spatial and temporal distribution of SDD from 2011 to 2020. Note that the definition of the four seasons is delayed by one month compared to the commonly used time, e.g., summer is July-September. This approach has been applied in previous studies related to primary productivity in SCS (Zhao and Wang, 2018), so we consider it acceptable in studies of SDD directly related to primary productivity. Overall, SDD have a gradient change in spatial distribution, and the SDD pattern is basically the same along the coast. More SDD low-value areas are distributed in the near shore and estuarine areas. According to the seasonal average distribution,

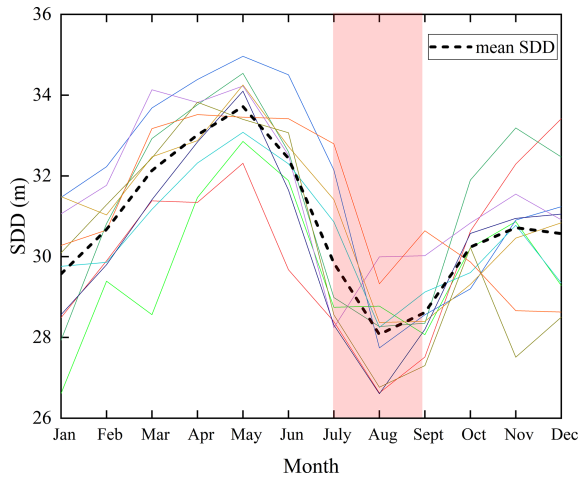

FIGURE 2
Annual cycle of SDD calculated from 2011 to 2020 in the study area. Different color lines represent the SDD of different years. Black dashed line represents the mean value of SDD. The red area represents the low value of SDD from July to September.

the average value of SDD from July to September is significantly lower than in other sea areas (Figure 3C). The main axis of the low-value area is parallel to the southern coastline of the Indo-China Peninsula, showing tongue-shaped, which seems to be an extension of the low-value area of the Mekong Estuary. This phenomenon does not appear in other seasons (Figures 3A, B, D).

3.2 Multi-scale analysis of SDD

Taking the monthly time series of SDD in the study area from 2011 to 2020 with a total of 120 sample points, the SDD is decomposed by the EMD method (Figure 4). The plot shows the EMD decomposition result of SDD monthly average value, where ORG is the original time series of SDD, IMF1-5 are the five signal components, which reflect the SDD fluctuation characteristics of different time scales from high frequency to low frequency, and trend denotes the trend term. In addition, the period of each component is calculated by the distance between adjacent maximum (minimum) values, and the average value and variance of each component. The average periods of IMF1-5 components are 6 months, 11 months, 16 months, 24 months, and 60 months, respectively.

Specifically, the first signal component (IMF1) of SDD indicated an aperiodic oscillation, it contains a high-frequency oscillation process. During 0-20 months and 50-70 months, the amplitude of SDD changes is about 1.5 m, and the amplitude can reach 4.7 m in other time intervals. IMF2 is the interannual component expressing the interannual variation process, and its maximum amplitude is 4.4 m. IMF3 is a component with a period of 16 months. Its amplitude is larger between 50 and 70 months, which may be caused by low-frequency anomalous events in the corresponding period. IMF4 represents SDD changes on a time scale of about two years, with smaller changes in amplitude. The variation characteristics of IMF5 are relatively gentle, with a low-frequency variation signal on the five-year time scale. The last signal component (Trend) is a non-monotonic signal. SDD first increases and then decreases during the ten years. It reaches a maximum of 34.96 m around the 60th month and decreases in the next five years. The SDD remains at 30.5~31 m during the ten years.

In order to analyze the variation characteristics of SDD, the Hilbert transform is performed on the IMF1-5 components of SDD signal. The time spectrum of the signal is plotted in Figure 5. Signals with average frequencies around 0.08/month and 0.15/month fluctuate widely, while low-frequency signals (less than 0.05/month) exhibit a near-stationary band. In terms of energy distribution, high energy is mostly distributed in higher frequency signals, which indicates that the SDD in the study area has the largest fluctuations on the time scale of about half a year to one year. This further confirms the signal analysis in Figure 4.

3.3 GAM analysis of SDD and environmental factors

According to the principle of SDD inversion calculation and the actual situation of the study area, the significant reduction in SDD phenomenon is often caused by the joint action of various influencing factors (Gordon et al., 1975);. Therefore, we include multiple oceanographic and meteorological elements in the analysis, use the variance inflation factor standard to eliminate the multi-collinearity environmental factors (Wood, 2004). Finally, SSS, SST, MDWW, SWH, ETu, ETv, BLD, EPV, Cu (offshore current), Cv (alongshore current), MLD, WD, and ILD environmental factors are screened as explanatory variables.

The GAM results shows that the combined explanation rate of the model is 72.1%, and all selected driving factors significantly affect the changes in SDD at P-value< 0.01, which were all statistically significant. The environmental factors that explain the SDD variation with a high rate (15.3%-38.2%) with effects ranked as SSS > Cu > WD > ETu > SST > MDWW, and they fit well with the model equations constructed by SDD (Table 1). Although the rest of the factors pass the P-value significance test, their explanatory power for SDD changes is relatively low (less than 15%) and the model fit is also poor. In addition, the EDF of each explanatory variable is greater than 1, indicating that the constructed function is a non-linear equation and there is a significant non-linear relationship between the explanatory variables and SDD.

The smooth regression function of related environmental factors is calculated using the GAM model established between multiple driving factors and SDD response variables. The effect diagram of the impact of environmental factors on SDD changes with an explanation rate greater than 15% is obtained (Figure 6). The gray shading in the figure represents the upper and lower bounds of the confidence interval, and the solid line represents the smooth fitting curve.

According to the results, each environmental factor shows a non-linear relationship with the change in SDD. Specifically, SDD is positively correlated with SSS and SST. When SSS is 30.5-31.5 PSU and SST is 28-30.5 °C, the confidence interval is small and the

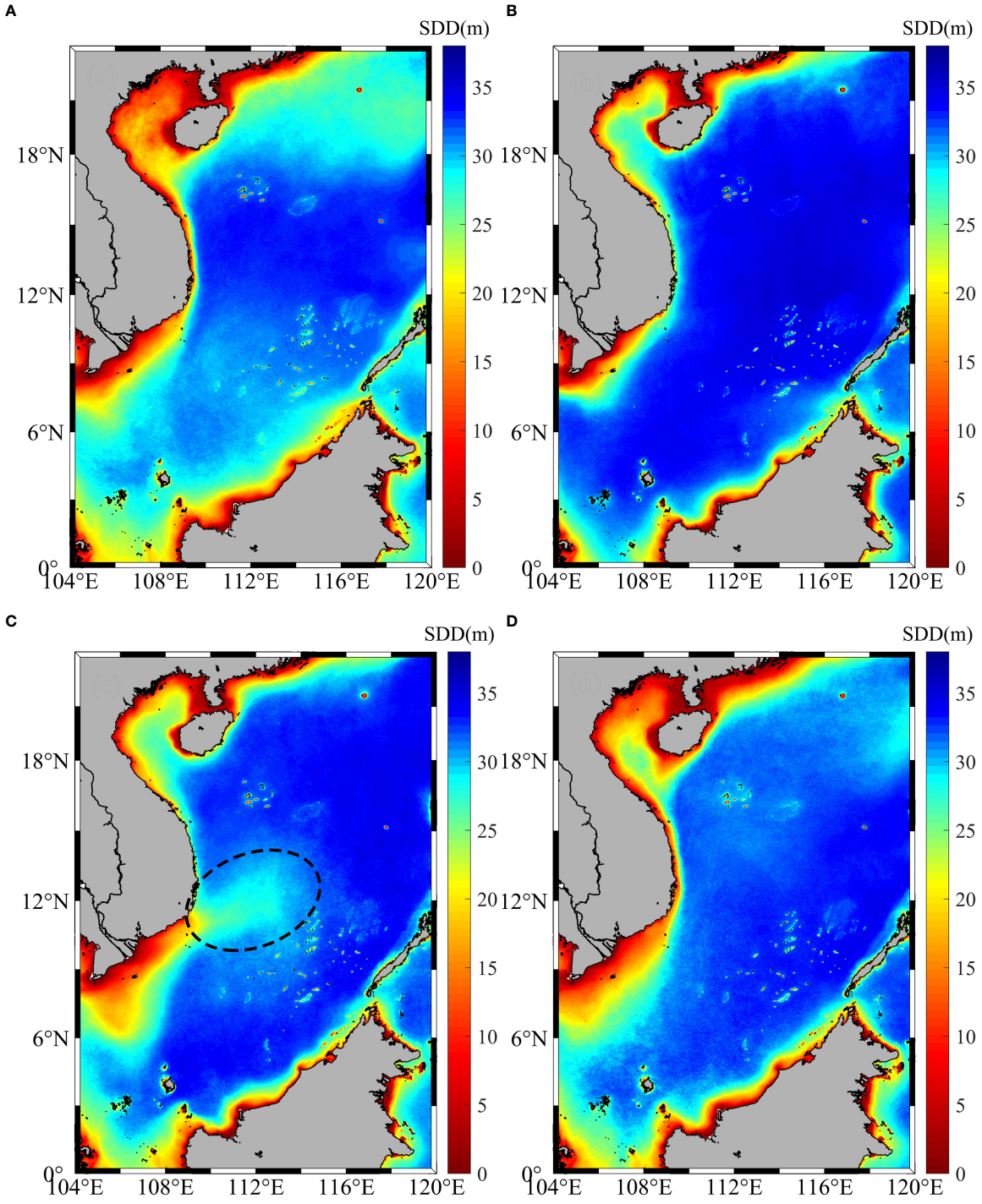

FIGURE 3
Distributions of mean SDD (background color, m) for **(A)** January-March **(B)** April-June **(C)** July-September **(D)** October-December from 2011-2020. The dotted line is the low value area of SDD.

reliability is high. In addition, SSS and SST have the most significant impact on SDD (Figures 6A, E). Cu and ETu have similar effects on SDD, with a general decrease in SDD as Cu and ETu increase (Figures 6B, D). It should be noted that when Cu is greater than 0.5 m/s, SDD reaches the minimum, and then there is no obvious trend, indicating that the response of SDD to Cu in the study area is phased and does not decrease with the increase in Cu. The relationship between WD and SDD is diverse. SDD is relatively high when WD is 0-90° and the confidence interval is small (Figure 6C). SDD increases with the increase in WD in this interval. When WD is between 90° and 230°, SDD first rises and then falls, reaching two peaks at 130° and 230°, respectively. SDD increases with the increase of WD. The relationship between MDWW and SDD is complex (Figure 6F). MDWW and SDD are positively correlated when the wave direction is between 0 and 180°. When MDWW is between 180° and 290°, SDD decreases and then

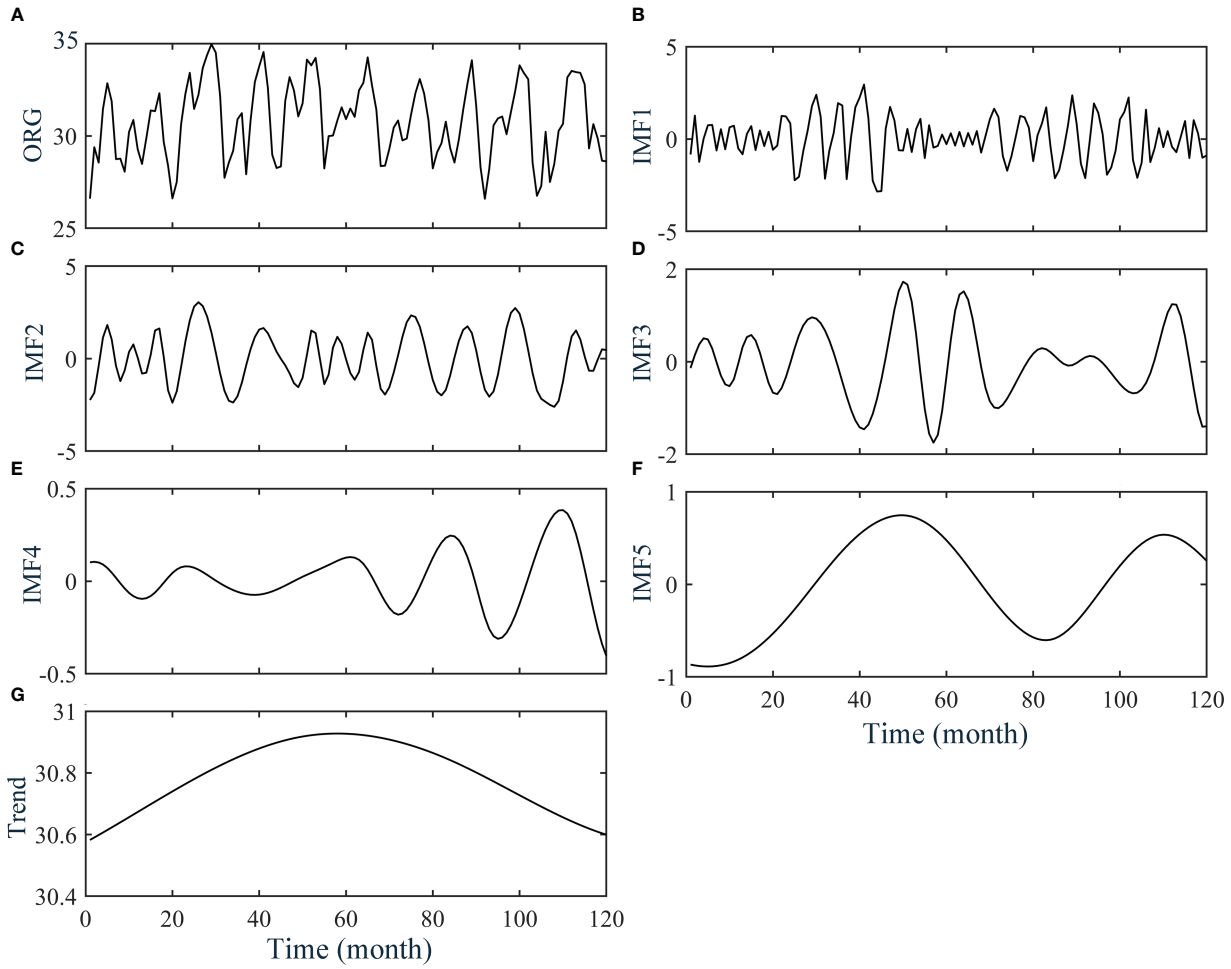

FIGURE 4
Decomposition results of SDD time series using the EMD. **(A)** is original component, **(B–F)** are IMFs, and **(G)** is the trend component.

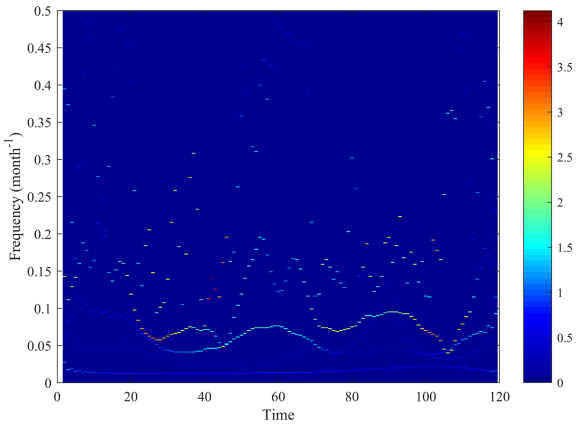

FIGURE 5
Hilbert-Huang spectrum analysis of SDD. The color represents the energy value, where the higher the value, the higher the energy event.

increases. The SDD in the interval is significantly affected by MDWW. When MDWW is greater than 290°, SDD decreases again.

4 Discussion

4.1 Multi-scale correlation analysis of SDD and main environmental factors

In this paper, EMD is used to objectively deal with nonlinear and nonsmooth processes. We perform EMD transformations on the main factors obtained from the GAM and analyze their response to changes in SDD at different time scales. Based on the EMD signal decomposition, we use the Pearson correlation coefficient to analyze the correlation between SDD and various influencing factors on multiple time scales to obtain the contribution of the correlation factors that affect SDD changes on different time scales (Figure 7).

Specifically, with the exception of SDD IMF1, SSS has a regulating effect on all SDD signal components with a period greater than or equal to 11 months, and the correlation

TABLE 1 GAM fitting results of SDD and environmental factors.

Variable	EDF	F-statistic	p-value	Contribution (%)
SSS	8.225	607.6	$<2\times10^{-16}$**	38.2
Cu	8.529	335.6	$<2\times10^{-16}$**	25.7
WD	8.907	269.1	$<2\times10^{-16}$**	21.8
ETu	8.43	208.9	$<2\times10^{-16}$**	17.7
SST	8.894	196.9	$<2\times10^{-16}$**	17
MDWW	8.797	173.8	$<2\times10^{-16}$**	15.3
MLD	7.429	174.2	$<2\times10^{-16}$**	14.2
EPV	8.688	120.3	$<2\times10^{-16}$**	11.1
Cv	7.771	77.89	$<2\times10^{-16}$**	7.24
ETv	8.661	38.63	$<2\times10^{-16}$**	3.9
ILD	7.864	8.57	$<2\times10^{-16}$**	2.3
SWH	7.969	21.63	$<2\times10^{-16}$**	2.2
BLD	6.532	14.84	$<2\times10^{-16}$**	1.35

** indicates significant correlation (P<0.01).

coefficients of the two can reach 0.565, 0.429, 0.444, 0.315, and 0.883, respectively, which indicates that SDD is significantly driven by SSS on interannual or longer time scales, and they are positively correlated. Cu has a significant negative correlation with SDD period of less than 11 months and signal components greater than 60 months, which means that SDD is affected on short time scales within 1 year and long time scales greater than 5 years. WD is similar to MDWW, both of which have a moderate effect on SDD changes greater than 16 months. The effects of ETu and SST exist mainly on longer time scales (Based on available theoretical and GAM results, ETu is negatively correlated with SDD, so the positive correlation results between SDD Trend and ETu Trend are not considered. The anomalous positive correlation of the long-term trend correlation may be related to the amount of data). In addition,

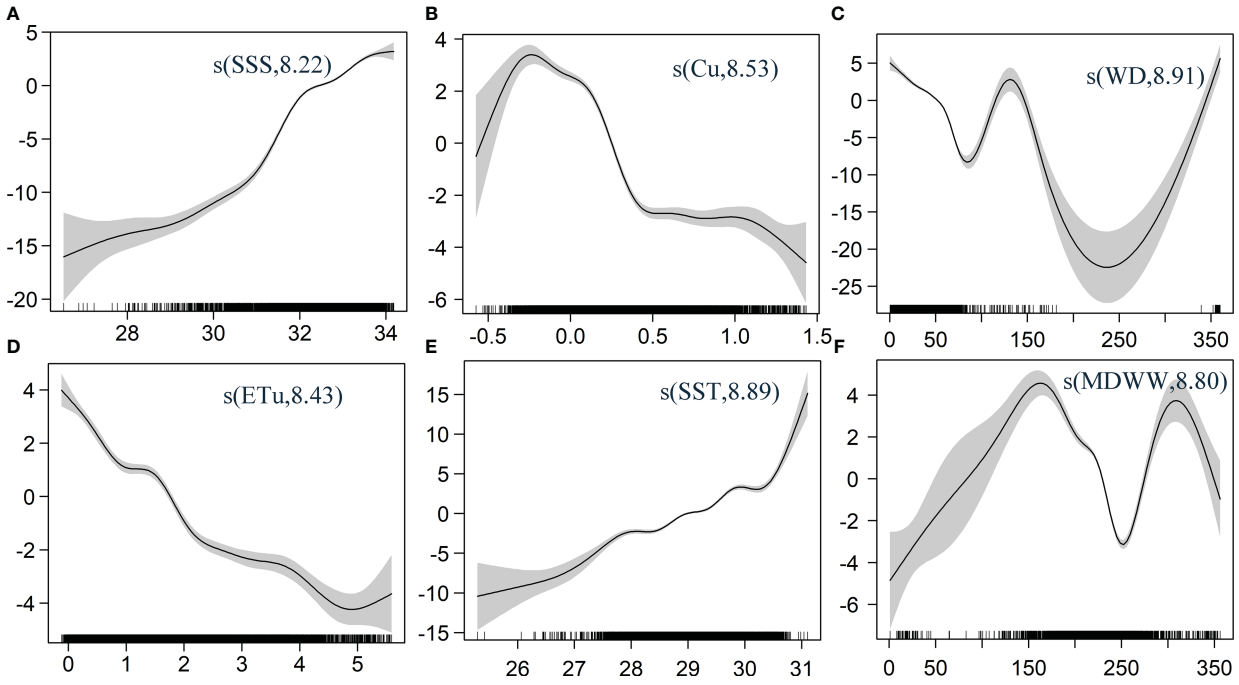

FIGURE 6
Response curves of SDD to changes in **(A)** SSS, **(B)** Cu, **(C)** WD, **(D)** ETu, **(E)**SST and **(F)** MDWW. The Y-axis in each subplot represents the smoothing function term for each factor, and the numbers in brackets represent degrees of freedom.

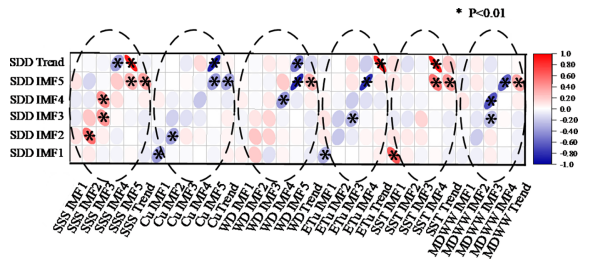

FIGURE 7
Correlation analysis of SDD and environmental factors at various time scales. The shape and color of the ellipse in the figure represent the degree of the correlation, the direction of the ellipse represents positive or negative correlation, and * means that the data has been tested for significance at 0.01.

they are both significantly correlated with SDD IMF1, which indicates that ETu and SST also have a non-negligible effect on the semiannual-scale SDD oscillation.

In general, SSS, Cu, ETu, and SST significantly impact SDD on a six-month to one-year scale. On a time scale of about two years (SDD IMF3, SDD IMF4), SDD is significantly driven by SSS, WD, ETu, and MDWW. All factors play a significant role in the approximately five-year scale signal of SDD. Therefore, we can conclude that SSS influences the signal components of SDD at five different time scales, indicating that SSS is an important environmental factor affecting SDD at most of the time. The modulating effect of SSS on SDD is the most comprehensive, followed by the effect of Cu, which has an important impact on the four signal components of SDD.

4.2 Analysis of the response mechanism of SDD to environmental factors

According to the distribution of SSS and SST, it can be concluded that the study sea area is characterized by low temperature and low salinity. The Mekong River brings a large number of low-salinity plumes during the rainy season, which makes the estuary and its adjacent waters low in salt content (SSS minimum is below 22 PSU) (Figure 8A) (Hordoir et al., 2006). Based on our results, there is a significant positive correlation between SSS and SDD. SDD decreases with the decrease in SSS, and appropriate salinity promotes the mass growth and

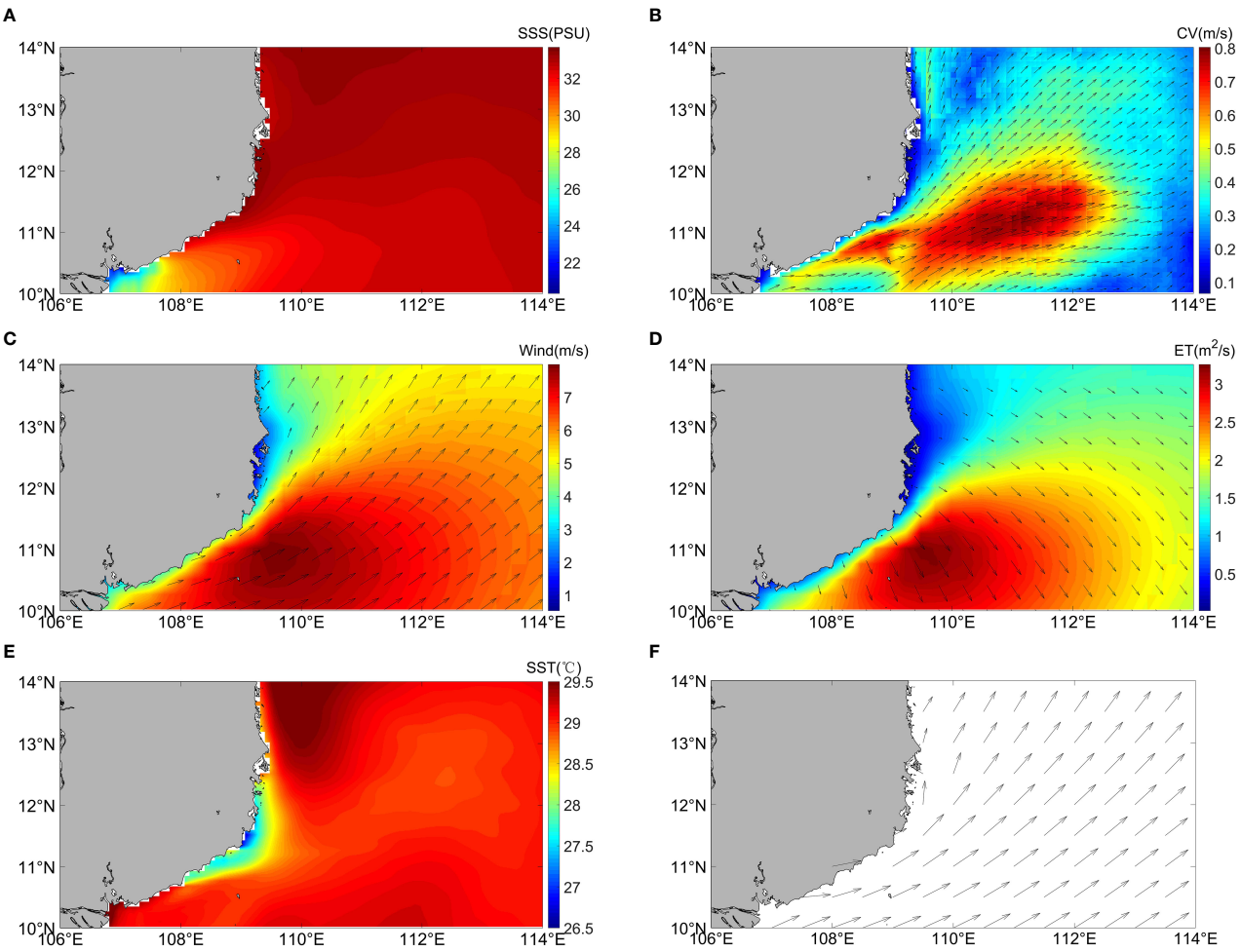

FIGURE 8
Spatial distribution of **(A)** SSS; **(B)** Cu; **(C)** WD; **(D)** ET; **(E)** SST; **(F)** MDWW. (July to September).

reproduction of phytoplankton, thereby reducing the transparency of seawater (Jeppesen et al., 2007). At the same time, part of the study area is in the upwelling region, and the distribution of SST shows the cold spot phenomenon near shore (Wang et al., 2013; Dang et al., 2022). This is due to the deep cold water brought by the upwelling, causing the SST in the upwelling area to be less than 26.5 °C at minimum (Figure 8E). Based on the Pearson analysis between the GAM analysis and EMD, SST and SDD are positively correlated. The decrease in SST reduces the thickness of the thermocline and the vertical stability of seawater. Nutrients are more easily mixed, so SDD decreases as SST decreases. It is worth noting that due to the strong seasonal changes in SST, the changes to the marine biological environment are relatively slow, so the impact of SST on SDD is mainly reflected on a longer time scale in addition to the semi-annual scale. In short, the upwelling sea area carries a large amount of nutrients and SPM (Li et al., 2015). It can be concluded that the plume and upwelling of the Mekong River affect the distribution of SSS and SST, which indirectly causes the SDD in the study area to decrease significantly.

In marine systems, regional SDD is sensitive to hydrodynamic and meteorological conditions (Zhou et al., 2022). WD from July to September is mostly southwesterly (Figure 8C), and the distribution of the wind stress curl field is favorable to the formation of summertime eastward jet (Sun and Lan, 2021), which has a significant impact on the regional climate and ecological environment. The summertime eastward jet generally intensifies in July, reaches its maximum in August, and then gradually weakens in September, which is consistent with the appearance of the low value region of SDD. As shown in the distribution of the sea surface current field (Figure 8B), the prevailing southwest wind promotes Cu in the offshore direction, which increases the intensity of Cu in the study area and promotes the transfer of low salinity cold water from the Mekong River to the east, thus indirectly causing significantly low SDD (Van Der Woerd and Pasterkamp, 2008). Cu can lead to the summertime Chl-a jet phenomenon (Chl-a concentrations above 0.13 mg m^{-3}) (Zeng et al., 2022), which can have a direct impact on SDD. In addition, Cu driven by wind also has periodic changes due to seasonal changes in WD. Therefore, Cu impacts the variation of SDD on a semi-annual to annual scale. Another environmental factor driven by wind, MDWW, also plays a role in SDD. MDWW is mostly southwestern from July to September (Figure 8F). The GAM model results show that SDD is significantly lower when the direction of weaves is 180-270° due to MDWW transporting more nutrients with SPM and contributed to the reduction of SDD. Finally, Ekman transport, as one of the environmental variables affecting SDD, is also driven by wind (Dippner et al., 2007; Wang et al., 2013). The offshore direction of ET in the study area is southeast and perpendicular to the shoreline (Figure 8D), favoring the creation of more phytoplankton growth and causing a decrease in SDD.

It is noteworthy that each environmental factor we analyzed acts indirectly on SDD by affecting chlorophyll or SPM. The sources of chlorophyll, representing primary productivity, are nearshore transport and locally generated (Liu and Tang, 2022), which affect SDD through physical and biological processes. Both summertime eastward jet and upwelling significantly affect local chlorophyll, which explains the relationship between SDD response to EPV intensity and summertime eastward jet in the GAM analysis, i.e., these processes are significantly associated with changes in SDD, but their contribution to SDD changes is limited due to seasonal fluctuations in EPV and hydrodynamics. The effect of MLD on SDD is similar to the EPV effect. MLD is influenced by monsoons and eddies, especially in summer when the MLD increases and phytoplankton can obtain abundant nutrients in surface waters, which has a great impact on local SDD. However, due to its seasonal variation, the effect of MLD on SDD is limited during the whole year.

5 Conclusions

In this study, we use multi-source satellite remote sensing data and reanalysis data to study the spatial distribution and variation characteristics of SDD in the study area (10°~14°E, 105°~114°N) from 2011 to 2020. The monthly mean time series shows that the SDD values in the study area are bimodal and varied significantly seasonally, with the highest and lowest values occurring in May and August each year, respectively. The spatial and temporal distributions show a distinct zone of low SDD values (average 28.8 m) from July to September each year compared to nearby waters, with its main axis parallel to the southern shoreline of the Mekong estuary in a tongue shape.

To explore the SDD low value phenomenon, a non-parametric model, GAM, is used to identify the dominant environmental factors affecting SDD variation and analyze the relationship between the dominant environmental factors and SDD variation. The combined explanation rate of the model is 72.1%, and the environmental factors' influence contribution is ranked SSS > Cu > WD > ETu > SST > MDWW, with different degrees of nonlinear response relationships. Among them, SDD is positively correlated with SSS and SST, and negatively correlated with Cu and ETu. Moreover, in order to explore at what time scales environmental factors influence SDD, this paper performs an EMD decomposition of the main environmental factors. The analysis results show that the variation of SSS, Cu, ETu, and SST on the interannual scale have important effects on SDD, while on longer time scales, SSS, Cu, WD, and SST had effects on SDD. In general, SSS has the largest comprehensive impact on SDD. WD is also an important segment that can indirectly affect SDD by altering ocean dynamic processes.

Data availability statement

The raw data supporting the conclusions of this article will be made available by the authors, without undue reservation.

Author contributions

YS: data analysis, writing and editing. YS and YX: figure plotting. DL and GX: conceptualization, methodology and

reviewing. All authors contributed to the article and approved the submitted version.

Funding

This research is supported by the project supported by Southern Marine Science and Engineering Guangdong Laboraory (Zhuhai) (SML2020SP007), the Guangdong Basic and Applied Basic Research Foundation (2019A1515110840), and the Research Startup Foundation of Guangdong Ocean University (R20009).

Acknowledgments

Thanks to the SDD data support from "National Earth System Science Data Sharing Infrastructure, National Science & Technology Infrastructure of China. (http://www.geodata.cn)"; Thanks to the SDD data support from "National Earth System Science Data Sharing Infrastructure, National Science & Technology Infrastructure of China. (http://www.geodata.cn)" the Copernicus for providing the monthly SST, SSS, and ocean current data; the ECMWF for providing the wave and wind data. Thanks to Dr. Kenny T.C. Lim Kam Sian for the contributions to this manuscript.

Conflict of interest

The authors declare that the research was conducted in the absence of any commercial or financial relationships that could be construed as a potential conflict of interest.

Publisher's note

All claims expressed in this article are solely those of the authors and do not necessarily represent those of their affiliated organizations, or those of the publisher, the editors and the reviewers. Any product that may be evaluated in this article, or claim that may be made by its manufacturer, is not guaranteed or endorsed by the publisher.

References

Aas, E., Høkedal, J., and Sørensen, K. (2014). Secchi depth in the oslofjord–skagerrak area: theory, experiments and relationships to other quantities. *Ocean Sci.* 10 (2), 177–199. doi: 10.3390/rs11192226

Alsahli, M. M., and Nazeer, M. (2021). Spatiotemporal variability of secchi depths of the north Arabian gulf over the last two decades. *Estuar. Coast. Shelf Sci.* 260, 107487. doi: 10.1016/j.ecss.2021.107487

Bohn, V. Y., Carmona, F., Rivas, R., Lagomarsino, L., Diovisalvi, N., and Zagarese, H. E. (2018). Development of an empirical model for chlorophyll-a and secchi disk depth estimation for a pampean shallow lake (Argentina). *Egypt. J. Remote Sens. Space Sci.* 21 (2), 183–191. doi: 10.1016/j.ejrs.2017.04.005

Cai, S., Long, X., and Wang, S. (2007). A model study of the summer southeast Vietnam offshore current in the southern south China Sea. *Cont. Shelf Res.* 27 (18), 2357–2372. doi: 10.1016/j.csr.2007.06.002

Chang, C. W. J., Hsu, H. H., Wu, C. R., and Sheu, W. J. (2008). Interannual mode of sea level in the south China Sea and the roles of El Niño and El Niño modoki. *Geophys. Res. Lett.* 35 (3), L03601. doi: 10.1029/2007GL032562

Chen, X., Feng, Y., and Huang, N. E. (2014). Global sea level trend during 1993–2012. *Glob. Planet Change* 112, 26–32. doi: 10.1016/j.gloplacha.2013.11.001

Chen, X., Zhang, Y., Zhang, M., Feng, Y., Wu, Z., Qiao, F., et al. (2013). Intercomparison between observed and simulated variability in global ocean heat content using empirical mode decomposition, part I: modulated annual cycle. *Clim. Dyn.* 41 (11), 2797–2815. doi: 10.1007/s00382-012-1554-2

Chu, P. C., Liu, Q., Jia, Y., and Fan, C. (2002). Evidence of a barrier layer in the sulu and celebes seas. *J. Phys. Oceanogr.* 32 (11), 3299–3309. doi: 10.1175/1520-0485(2002)032<3299:EOABLI>2.0.CO;2

Cloern, J. E. (1987). Turbidity as a control on phytoplankton biomass and productivity in estuaries. *Cont. Shelf Res.* 7, 1367–1381. doi: 10.1016/0278-4343(87)90042-2

Cropper, T. E., Hanna, E., and Bigg, G. R. (2014). Spatial and temporal seasonal trends in coastal upwelling off Northwest Africa 1981–2012. *Deep. Res. Part I Oceanogr. Res. Pap.* 86, 94–111. doi: 10.1016/j.dsr.2014.01.007

Dang, X., Bai, Y., Gong, F., Chen, X., Zhu, Q., Huang, H., et al. (2022). Different responses of phytoplankton to the ENSO in two upwelling systems of the south China Sea. *Estuar. Coasts.* 45 (2), 485–500. doi: 10.1007/s12237-021-00987-2

Dippner, J. W., Nguyen, K. V., Hein, H., Ohde, T., and Loick, N. (2007). Monsoon-induced upwelling off the Vietnamese coast. *Ocean Dynam.* 57 (1), 46–62. doi: 10.1007/s10236-006-0091-0

Duy Vinh, V., Ouillon, S., Van Thao, N., and Ngoc Tien, N. (2016). Numerical simulations of suspended sediment dynamics due to seasonal forcing in the Mekong coastal area. *Water* 8 (6), 255. doi: 10.3390/w8060255

Erlandsson, C. P., and Stigebrandt, A. (2006). Increased utility of the secchi disk to assess eutrophication in coastal waters with freshwater run-off. *J. Mar. Syst.* 60, 19–29. doi: 10.1016/j.jmarsys.2005.12.001

Godfrey, J. S., and Lindstrom, E. J. (1989). The heat budget of the equatorial western pacific surface mixed layer. *J. Geophys. Res. Oceans* 94 (C6), 8007–8017. doi: 10.1029/JC094iC06p08007

Gordon, H. R., Brown, O. B., and Jacobs, M. M. (1975). Computed relationships between the inherent and apparent optical properties of a flat homogeneous ocean. *Appl. Opt.* 14 (2), 417–427. doi: 10.1364/AO.14.000417

Gordon, H., Clark, D., Brown, J., Brown, O., Evans, R., and Broenkow, W. (1983). Phytoplankton pigment concentrations in the middle Atlantic bight: comparison between ship determinations and coastal zone color scanner estimates. *Appl. Opt.* 22, 20–36. doi: 10.1364/AO.22.000020

Guisan, A., Edwards, T. C.Jr., and Hastie, T. (2002). Generalized linear and generalized additive models in studies of species distributions: Setting the scene. *Ecol. Modell.* 157 (2-3), 89–100. doi: 10.1016/S0304-3800(02)00204-1

Harvey, E. T., Walve, J., Andersson, A., Karlson, B., and Kratzer, S. (2019). The effect of optical properties on secchi depth and implications for eutrophication management. *Front. Mar. Sci.* 5. doi: 10.3389/fmars.2018.00496

Hayami, Y., Maeda, K., and Hamada, T. (2015). Long term variation in transparency in the inner area of ariake Sea. *Estuar. Coast. Shelf Sci.* 163, 290–296. doi: 10.1016/j.ecss.2014.11.029

He, X., Bai, Y., Chen, C. T. A., Hsin, Y. C., Wu, C. R., Zhai, W., et al. (2014). Satellite views of the episodic terrestrial material transport to the southern Okinawa trough driven by typhoon. *J. Geophys. Res. Oceans* 119 (7), 4490–4504. doi: 10.1002/2014JC009872

He, X., Pan, D., Bai, Y., Wang, T., Chen, C. T. A., Zhu, Q., et al. (2017). Recent changes of global ocean transparency observed by SeaWiFS. *Cont. Shelf Res.* 143, 159–166. doi: 10.1016/j.csr.2016.09.011

Hordoir, R., Nguyen, K. D., and Polcher, J. (2006). Simulating tropical river plumes, a set of parametrizations based on macroscale data: A test case in the Mekong delta region. *J. Geophys. Res. Oceans* 111, C09036. doi: 10.1029/2005JC003392

Huang, N. E., Shen, Z., Long, S. R., Wu, M. C., Shih, E. H., Zheng, Q., et al. (1998). The empirical mode decomposition and the Hilbert spectrum for non stationary time series analysis. *Proc. R. Soc Lond.* 454, 903–995. doi: 10.1098/rspa.1998.0193

Idris, M. S., Siang, H. L., Amin, R. M., and Sidik, M. J. (2022). Two-decade dynamics of MODIS-derived secchi depth in peninsula Malaysia waters. *J. Mar. Syst.* 236, 103799. doi: 10.1016/j.jmarsys.2022.103799

Jeppesen, E., Søndergaard, M., Pedersen, A. R., Jürgens, K., Strzelczak, A., Lauridsen, T. L., et al. (2007). Salinity induced regime shift in shallow brackish lagoons. *Ecosystems* 10 (1), 48–58. doi: 10.1007/s10021-006-9007-6

Kirk, J. T. O. (1994). *Light and photosynthesis in aquatic ecosystems. 2nd ed* (Cambridge, UK: Cambridge University Press).

Klemas, V. (2012). Remote sensing of algal blooms: An overview with case studies. *J. Coast. Res.* 28 (1A), 34–43. doi: 10.2112/JCOASTRES-D-11-00051.1

Li, Y., Xu, X., Yin, X., Fang, J., Hu, W., and Chen, J. (2015). Remote-sensing observations of typhoon soulik, (2013) forced upwelling and sediment transport enhancement in the northern Taiwan strait. *Int. J. Remote Sens.* 36 (8), 2201–2218. doi: 10.1080/01431161.2015.1035407

Li, J., Yu, Q., Tian, Y. Q., and Becker, B. L. (2017). Remote sensing estimation of colored dissolved organic matter (CDOM) in optically shallow waters. *ISPRS J. Photog. Remote Sens.* 128, 98–110. doi: 10.1016/j.isprsjprs.2017.03.015

Liu, F., and Tang, S. (2022). A double-peak intraseasonal pattern in the chlorophyll concentration associated with summer upwelling andmesoscale eddies in the western south China Sea. *J. Geophys. Res. Oceans* 127 (1), e2021JC017402. doi: 10.1029/2021JC017402

Luis, K. M., Rheuban, J. E., Kavanaugh, M. T., Glover, D. M., Wei, J., Lee, Z., et al. (2019). Capturing coastal water clarity variability with landsat 8. *Mar. Pollut. Bull.* 145, 96–104. doi: 10.1016/j.marpolbul.2019.04.078

Nishijima, W., Umehara, A., Sekito, S., Okuda, T., and Nakai, S. (2016). Spatial and temporal distributions of secchi depths and chlorophyll a concentrations in the suo Nada of the seto inland Sea, Japan, exposed to anthropogenic nutrient loading. *Sci. Total Environ.* 571, 543–550. doi: 10.1016/j.scitotenv.2016.07.020

Nishijima, W., Umehara, A., Sekito, S., Wang, F., Okuda, T., and Nakai, S. (2018). Determination and distribution of region-specific background secchi depth based on long-term monitoring data in the seto inland sea. Japan. *Ecol. Indic.* 84, 583–589. doi: 10.1016/j.ecolind.2017.09.014

Philippart, C., Salama, M. S., Kromkamp, J. C., van der Woerd, H. J., Zuur, A. F., and Cadee, G. C. (2013). Four decades of variability in turbidity in the western wadden Sea as derived from corrected secchi disk readings. *J. Sea Res.* 82, 67–79. doi: 10.1016/j.seares.2012.07.005

Requia, W. J., Jhun, I., Coull, B. A., and Koutrakis, P. (2019). Climate impact on ambient PM2. 5 elemental concentration in the united states: A trend analysis over the last 30 years. *Environ. Int.* 131, 104888. doi: 10.1016/j.envint.2019.05.082

Rodrigues, T., Alcântara, E., Watanabe, F., and Imai, N. (2017). Retrieval of secchi disk depth from a reservoir using a semi-analytical scheme. *Remote Sens. Environ.* 198, 213–228. doi: 10.1016/j.rse.2017.06.018

Shi, H., Cao, X., Li, Q., Li, D., Sun, J., You, Z., et al. (2021). Evaluating the accuracy of ERA5 wave reanalysis in the water around China. *J. Ocean Univ. China* 20 (1), 1–9. doi: 10.3390/atmos13060935

Sun, Y., and Lan, J. (2021). Summertime eastward jet and its relationship with western boundary current in the south China Sea on the interannual scale. *Clim. Dyn.* 56 (3), 935–947. doi: 10.1007/s00382-020-05511-z

Tang, S., and Chen, C. (2016). Novel maximum carbon fixation rate algorithms for remote sensing of oceanic primary productivity. *IEEE J. Selected. Topics. Appl. Earth Observ. Remote Sensing.* 9 (11), 5202–5208. doi: 10.1109/JSTARS.2016.2574898

Tang, D. L., Kawamura, H., Doan-Nhu, H., and Takahashi, W. (2004). Remote sensing oceanography of a harmful algal bloom off the coast of southeastern Vietnam. *J. Geophys. Res. Oceans* 109, 2045. doi: 10.1029/2003JC002045

Van Der Woerd, H. J., and Pasterkamp, R. (2008). HYDROPT: A fast and flexible method to retrieve chlorophyll-a from multispectral satellite observations of optically complex coastal waters. *Remote Sens. Environ.* 112 (4), 1795–1807. doi: 10.1080/01431161.2015.1035407

Wang, H., Fu, D., Liu, D., Xiao, X., He, X., and Liu, B. (2021). Analysis and prediction of significant wave height in the beibu gulf, south China Sea. *J. Geophys. Res. Oceans* 126 (3), e2020JC017144. doi: 10.1029/2020JC017144

Wang, D., Gouhier, T. C., Menge, B. A., and Ganguly, A. R. (2015). Intensification and spatial homogenization of coastal upwelling under climate change. *Nature* 518, 390–394. doi: 10.1038/nature14235

Wang, F., Umehara, A., Nakai, S., and Nishijima, W. (2019). Distribution of region-specific background secchi depth in Tokyo bay and ise bay, Japan. *Ecol. Indic.* 98, 397–408. doi: 10.3390/rs11161948

Wang, D., Wang, H., Li, M., Liu, G., and Wu, X. (2013). Role of ekman transport versus ekman pumping in driving summer upwelling in the south China Sea. *J. Ocean Univ. China* 12 (3), 355–365. doi: 10.1007/s11802-013-1904-7

Wernand, M. R. (2010). On the history of the secchi disc. *J. Eur. Opt. Soc.* 5, 10013s. doi: 10.2971/jeos.2010.10013s

Wood, S. N. (2004). Stable and efficient multiple smoothing parameter estimation for generalized additive models. *J. Am. Stat. Assoc.* 99 (467), 673–686. doi: 10.1198/016214504000000980

Yang, L., Yu, D., Yao, H., Gao, H., Zhou, Y., Gai, Y., et al. (2022). Capturing secchi disk depth by using sentinel-2 MSI imagery in jiaozhou bay, China from 2017 to 2021. *Mar. Pollut. Bull.* 185, 114304. doi: 10.1016/j.marpolbul.2022.114304

Zeng, J., Liu, C., Li, X., Zhao, H., and Lu, X. (2022). Comparative study of the variability and trends of phytoplankton biomass between spring and winter upwelling systems in the south China Sea. *J. Mar. Syst.* 231, 103738. doi: 10.1016/j.jmarsys.2022.103738

Zhao, H., and Wang, Y. (2018). Phytoplankton increases induced by tropical cyclones in the south China Sea during 1998–2015. *J. Geophys. Res. Oceans* 123 (4), 2903–2920. doi: 10.1002/2017JC013549

Zhou, Y., Yu, D., Cheng, W., Gai, Y., Yao, H., Yang, L., et al. (2022). Monitoring multi-temporal and spatial variations of water transparency in the jiaozhou bay using GOCI data. *Mar. Pollut. Bull.* 180, 113815. doi: 10.1016/j.marpolbul.2022.113815

Zhou, Y., Yu, D., Yang, Q., Pan, S., Gai, Y., Cheng, W., et al. (2021). Variations of water transparency and impact factors in the bohai and yellow seas from satellite observations. *Remote Sens.* 13 (3), 514. doi: 10.3390/rs13030514

Zhou, Q., Zhang, Y., Li, K., Huang, L., Yang, F., Zhou, Y., et al. (2018). Seasonal and spatial distributions of euphotic zone and long-term variations in water transparency in a clear oligotrophic lake fuxian, China. *J. Environ. Sci.* 72, 185–197. doi: 10.1016/j.jes.2018.01.005

Zou, W., Zhu, G., Cai, Y., Vilmi, A., Xu, H., Zhu, M., et al. (2020). Relationships between nutrient, chlorophyll a and secchi depth in lakes of the Chinese eastern plains ecoregion: Implications for eutrophication management. *J. Environ. Manage.* 260, 109923. doi: 10.1016/j.jenvman.2019.109923

Frontiers in Marine Science

Explores ocean-based solutions for emerging global challenges

The third most-cited marine and freshwater biology journal, advancing our understanding of marine systems and addressing global challenges including overfishing, pollution, and climate change.

Discover the latest Research Topics

See more →

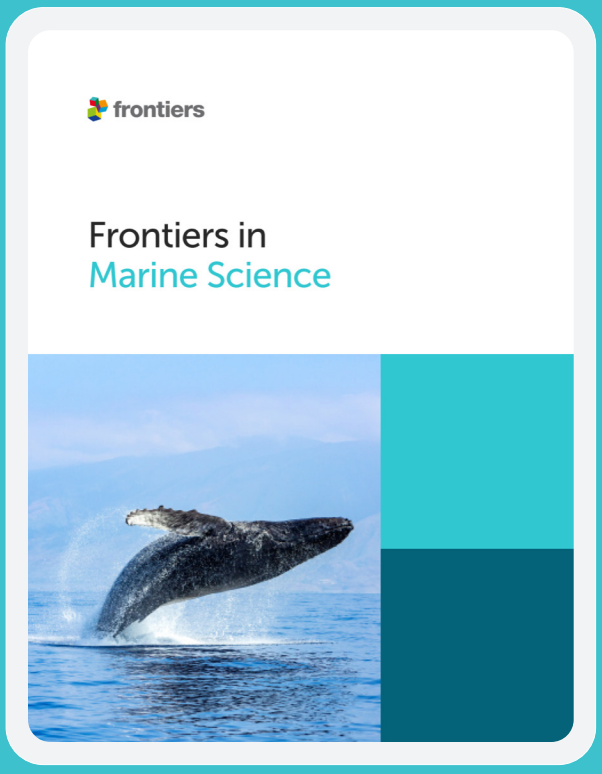

Frontiers

Avenue du Tribunal-Fédéral 34
1005 Lausanne, Switzerland
frontiersin.org

Contact us

+41 (0)21 510 17 00
frontiersin.org/about/contact